



Universidade de Aveiro Departamento de Química
Ano 2013

**Sérgio Manuel Felipe
Vilela**

**Redes Metalo-Orgânicas Baseadas em Ligandos
Fosfonato**

**Metal-Organic Frameworks Based on Phosphonate
Linkers**



**Sérgio Manuel Felipe
Vilela**

**Redes Metalo-Orgânicas Baseadas em Ligandos
Fosfonato**

**Metal-Organic Frameworks Based on Phosphonate
Linkers**

Tese apresentada à Universidade de Aveiro para cumprimento dos requisitos necessários à obtenção do grau de Doutor em Química, realizada sob a orientação científica do Doutor Filipe Alexandre Almeida Paz, Investigador Auxiliar do Laboratório Associado CICECO do Departamento de Química da Universidade de Aveiro, e co-orientação do Doutor João Paulo Costa Tomé, Investigador Principal da Unidade de Investigação QOPNA do Departamento de Química da Universidade de Aveiro.

Apoio financeiro da FCT: SFRH/BD/66371/2009 e
PTDC/QUI-QUI/098098/2008 (FCOMP-01-0124-FEDER-010785)

FCT Fundação para a Ciência e a Tecnologia
MINISTÉRIO DA CIÊNCIA, TECNOLOGIA E ENSINO SUPERIOR



Dedico esta tese à minha Mãe, ao meu Irmão e à memória do meu Pai que sempre me acompanharam, agradeceram e incentivaram.

o júri

presidente

Prof. Doutor Fernando Manuel dos Santos Ramos
professor catedrático da Universidade de Aveiro

Prof. Doutor João Carlos Matias Celestino Gomes da Rocha
professor catedrático da Universidade de Aveiro

Prof. Doutor Jorge Andrés Rodríguez Navarro
professor catedrático da Faculdade de Ciências da Universidade de Granada

Doutor Luís Manuel Cunha e Silva
investigador auxiliar da Faculdade de Ciências da Universidade do Porto

Prof. Doutora Susana Graça da Costa
professor auxiliar da Escola de Ciências da Universidade do Minho

Doutor Filipe Alexandre Almeida Paz
investigador auxiliar do Laboratório Associado CICECO da Universidade de Aveiro

Doutor Duarte Ananias Marques
investigador auxiliar do Laboratório Associado CICECO da Universidade de Aveiro

agradecimentos

Não poderia iniciar esta secção sem agradecer, em primeiro lugar, à Fundação para a Ciência e a Tecnologia pela bolsa de doutoramento que me facultou (com a referência SFRH/BD/66371/2009) conducente à realização do meu plano de trabalhos proposto à 4 anos atrás.

Ao CICECO, Laboratório Associado da Universidade de Aveiro, que me disponibilizou todas as condições logísticas e materiais necessárias para desenvolver o meu projeto de investigação.

Um agradecimento especial ao Doutor Filipe Paz e ao Doutor João Tomé, meus orientadores, que sempre me mostraram como levar este projeto a bom porto. A Eles, um muito obrigado pela orientação, colaboração, amizade, pelos conselhos e “puxões de orelhas” que fizeram com que me torna-se uma pessoa mais autónoma e capaz na concretização deste desafio.

Agradeço ao Professor João Rocha pela disponibilidade que sempre demonstrou na apreciação dos resultados que foram sendo obtidos e, também, pelos ensinamentos transmitidos durante alguns momentos de avaliação ao qual fui submetido no Programa Doutoral em Química.

Ao Professor Artur Silva um muito obrigado pela disponibilidade e prestabilidade com que me foi ajudando a desvendar alguns enigmas escondidos por detrás dos espectros de RMN. Pela transmissão de conhecimento através de algumas unidades curriculares lecionadas por ele e, sem esquecer de o congratular pelo trabalho singular de coordenação que tem vindo a desempenhar em prol dos alunos do Programa Doutoral em Química da Universidade de Aveiro.

Um novo obrigado ao Doutor Filipe Paz pela resolução das estruturas cristalinas de alguns ligandos orgânicos e MOFs produzidos durante o desenvolvimento dos meus trabalhos de investigação. Nesta vertente, aproveito para deixar umas palavras de apreço ao José Fernandes que colaborou comigo na realização de alguns trabalhos cristalográficos.

Agradeço também ao Doutor Duarte Ananias pela sua colaboração conducente ao estudo das propriedades fotoluminescentes de alguns materiais que preparei e se encontram descritos nesta dissertação.

Obrigado à Doutora Anabela Valente e à sua equipa, principalmente à Sofia Bruno e Ana Gomes, pela colaboração na investigação da atividade catalítica de alguns compostos expostos neste projeto.

agradecimentos

Deixo também aqui uma palavra de apreço ao Professor Jorge Navarro pela oportunidade que me deu em conhecer e trabalhar com o seu grupo de investigação (em particular, com a Carmen, Kiko, Sara e Elena) tendo como finalidade a avaliação da capacidade de alguns compostos porosos em processos de separação de gases. A todos “Muchas Gracias”!

À Patrícia Silva, Ricardo Mendes e Daniela Firmino, colegas do grupo de investigação em MOFs da Universidade de Aveiro, o meu obrigado pela ajuda e disponibilidade que prestaram durante a realização de algumas tarefas.

Um grande obrigado ao pessoal técnico do Departamento de Química da Universidade de Aveiro pelo profissionalismo e competência com que desempenham as suas funções em prol do desenvolvimento científico neste departamento e, neste caso, no meu.

Deixo um agradecimento à Rosário Soares pela preciosa ajuda e, muitas vezes, orientação na análise dos meus materiais através de difração de raios-X de pós. Um obrigado também à Margarete pela sua disponibilidade e amizade.

À malta da orgânica, principalmente aos alunos do Doutor João Tomé, deixo aqui um grande abraço e um muito obrigado por tudo. Por tudo mesmo! Não vou individualizar situações, pois não há necessidade.

Às meninas que dividem o gabinete comigo e às outras que vão por lá aparecendo, a contar, claro, com o João Rodrigues um forte abraço e obrigado pela companhia, amizade e os docinhos.

Um obrigado também a todos os colegas e amigos do CICECO com quem tenho o prazer de partilhar as horas de almoço e algumas saídas por aí.

Aos futeboleiros das sextas à tarde, com quem troco umas bolas, um abraço e os “Branços” sempre à vitória!

À D. Susana e ao Sr. Manuel agradeço a amizade, atenção, compreensão, prestabilidade e carinho.

A minha última palavra de gratidão e apreço vai para todos os meus amigos que de alguma forma me apoiaram durante esta “corrida” e, para aqueles que estiveram ainda mais próximos em alturas complicadas: Ricardo, Leandro, Flávio e Nuno, aquele abraço!

palavras-chave

Redes Metalo-Orgânicas, Fosfonatos, Terras Raras, Catálise, Fotoluminescência, Separação de Gases

resumo

Ao longo das últimas décadas, as Redes Metalo-Orgânicas (MOFs), conhecidas também por Polímeros de Coordenação, têm atraído atenções dos investigadores de todas as partes do mundo devido às suas arquiteturas fascinantes e propriedades únicas. Estes materiais multidimensionais têm encontrado potenciais aplicações em áreas distintas: armazenamento e separação de gases, troca iónica, catálise, magnetismo, em sensores óticos, entre outras.

O grupo de investigação em MOFs da Universidade de Aveiro tem preparado novos materiais a partir da combinação de ligandos orgânicos com grupos fosfonato e, principalmente, lantanídeos. Esta dissertação descreve as descobertas mais recentes nesta área envolvendo a síntese de MOFs multidimensionais baseados em quatro moléculas com grupos fosfonato. Os ligandos orgânicos usados neste projeto foram desenhados e preparados após seleção e otimização das condições reacionais e métodos de síntese. Reações entre estes ligandos orgânicos e terras-raras levaram à formação de várias famílias de MOFs 1D, 2D e 3D. A preparação destes materiais envolveu o uso de métodos de síntese distintos: síntese hidro(solvo)térmica, assistida por micro-ondas ou ultrassons, “*one-pot*” e ionotérmica. A seleção criteriosa dos ligandos orgânicos mostrou ter um papel fundamental nas arquiteturas finais dos materiais: enquanto as moléculas com grupos fosfonato mais flexíveis originaram estruturas 1D, 2D e 3D densas, um dos ligandos com a sua estrutura mais rígida levou à formação de uma MOF 3D porosa. A estrutura cristalina de todos os materiais foi resolvida através de difração de raios-X de pó ou monocristal. Todos os materiais foram ainda caracterizados usando várias técnicas em estado sólido (FT-IV, microscopia eletrónica (SEM e EDS), RMN em estado sólido, análise elementar e termogravimétrica). Algumas MOFs exibiram uma estabilidade térmica e robustez notáveis até aproximadamente 400 °C.

As propriedades de algumas MOFs foram investigadas. Estudos de fotoluminescência revelaram que os ligandos orgânicos selecionados são sensibilizadores apropriados para os catiões Tb^{3+} levando à formação de materiais emissores de luz verde intensa. A supressão de grupos “quencher” O–H, através de processos de deuteração ou desidratação melhorou substancialmente a fotoluminescência dos materiais contendo catiões Eu^{3+} . Algumas MOFs mostraram elevada atividade catalítica, em meio heterogéneo, e uma excelente regioseletividade na reação “ring-opening” do óxido de estireno (PhEtO) com metanol (100% de conversão de PhEtO a 55 °C durante 30 minutos). A MOF porosa foi usada em processos de separação de gases. Este composto exibiu uma boa capacidade para separar propano de propileno. Este material contendo catiões K^+ no interior da sua rede exibiu uma afinidade elevada para CO_2 mostrando também capacidade para separar acetileno deste gás inimigo do ambiente.

keywords

Metal-Organic Frameworks, Phosphonates, Rare Earths, Catalysis, Photoluminescence, Gas Separation

abstract

During the last few decades, Metal-Organic Frameworks (MOFs), also known as Coordination Polymers, have attracted worldwide research attentions due to their incremented fascinating architectures and unique properties. These multi-dimensional materials have been potential applications in distinct areas: gas storage and separation, ion exchange, catalysis, magnetism, in optical sensors, among several others.

The MOF research group at the University of Aveiro has prepared MOFs from the combination of phosphonate organic primary building units (PBUs) with, mainly, lanthanides. This thesis documents the last findings in this area involving the synthesis of multidimensional MOFs based on four di- or tripodal phosphonates ligands. The organic PBUs were designed and prepared by selecting and optimizing the best reaction conditions and synthetic routes. The self-assembly between phosphonate PBUs and rare-earths cations led to the formation of several 1D, 2D and 3D families of isotypical MOFs. The preparation of these materials was achieved by using distinct synthetic approaches: hydro(solvo)thermal, microwave- and ultrasound-assisted, one-pot and ionothermal synthesis. The selection of the organic PBUs showed to have an important role in the final architectures: while flexible phosphonate ligands afforded 1D, 2D and dense 3D structures, a large and rigid organic PBU isolated a porous 3D MOF. The crystal structure of these materials was successfully unveiled by powder or single-crystal X-ray diffraction. All multidimensional MOFs were characterized by standard solid-state techniques (FT-IR, electron microscopy (SEM and EDS), solid-state NMR, elemental and thermogravimetric analysis). Some MOF materials exhibited remarkable thermal stability and robustness up to *ca.* 400 °C.

The intrinsic properties of some MOFs were investigated. Photoluminescence studies revealed that the selected organic PBUs are suitable sensitizers of Tb³⁺ leading to the isolation of intense green-emitting materials. The suppression of the O–H quenchers by deuteration or dehydration processes improves substantially the photoluminescence of the optically-active Eu³⁺-based materials. Some MOF materials exhibited high heterogeneous catalytic activity and excellent regioselectivity in the ring-opening reaction of styrene oxide (PhEtO) with methanol (100% conversion of PhEtO at 55 °C for 30 min). The porous MOF material was employed in gas separation processes. This compound showed the ability to separate propane over propylene. The ion-exchanged form of this material (containing K⁺ cations into its network) exhibited higher affinity for CO₂ being capable to separate acetylene over this environment non-friendly gas.

Table of Contents

Abbreviations	vii
----------------------------	------------

Publications Presented in this Thesis	ix
--	-----------

Chapter 1

Metal-Organic Frameworks: Concepts, Properties and Potential

Applications	1
1.1. Supramolecular Chemistry	3
1.2. Metal-Organic Frameworks	4
1.2.1. The Genesis and Terminology of the Name	4
1.2.2. Interests in MOFs	6
1.2.3. Building Components for the Preparation of MOFs	7
1.2.3.1. Metal Centers	8
1.2.3.2. Organic Linker Components	12
1.2.4. Synthetic Methods for the Preparation of MOFs	15
1.3. Properties and Potential Applications of MOFs	19
1.3.1. Porosity	19
1.3.1.1. Methane and Hydrogen Storage	23
1.3.1.2. CO ₂ Capture	27
1.3.2. Heterogeneous Catalysis	29
1.3.3. Luminescence	33
1.4. Phosphonate-Based MOFs	37
1.4.1. Properties and Potential Applications	38
1.4.2. Examples of Functional MOFs Prepared from Phosphonate-Based Organic Ligands	39
1.5. Outline and Main Objectives of this PhD Thesis	48
1.6. References	51

Chapter 2

Synthesis of Bi- and Tripodal Phosphonate Organic Ligands	63
2.1. Introduction	65
2.1.1. Structure, Properties and Applications of Phosphonic Acids and Ester Derivatives	65
2.1.2. Synthetic Methods to Prepare Phosphonic Acid Linkers and their Phosphonate Intermediates	67

2.2. Strategy	70
2.3. 1,4-Phenylenebis(methylene)diphosphonic acid (H₄pmd)	71
2.3.1. Synthesis.....	71
2.3.2. Structural Elucidation.....	72
2.4. (Benzene-1,3,5-triyltris(methylene))triphosphonic acid (H₆bmt)	72
2.4.1. Synthesis.....	72
2.4.2. Structural Elucidation.....	73
2.5. ((2,4,6-Trifluorobenzene-1,3,5-triyl)tris(methylene))triphosphonic acid (H₆tftp)	75
2.5.1. Synthesis.....	75
2.5.2. Structural Elucidation.....	77
2.6. Large tripodal phosphonate ligand H₆L	80
2.6.1. Synthesis.....	80
2.6.2. Structural Elucidation.....	82
2.7. Results and Discussion	84
2.8. References	88

Chapter 3

1D and 3D MOFs from the Self-Assembly of Lanthanides with

1,4-Phenylenebis(methylene)diphosphonic acid

91

3.1. Initial Considerations	93
3.2. From Micro- to Nano-Sized Lanthanide-Biphosphonate Coordination Polymers	94
3.2.1. Synthesis.....	94
3.2.1.1. Synthetic Strategy.....	94
3.2.1.2. Convencional Hydrothermal Synthesis	94
3.2.1.3. Microwave-Assisted Hydrothermal Synthesis.....	96
3.2.1.4. [Ln(Hpmd)(H ₂ O)] Materials as Isolated Nanoparticles	98
3.2.2. Crystal Structure Description	101
3.2.3. Thermogravimetry and Variable Temperature Powder X-ray Diffraction Studies.....	103
3.2.4. Vibrational Spectroscopy Studies	104
3.2.5. Photoluminescence	106
3.2.6. Heterogeneous Catalysis	112
3.3. Lanthanum-Biphosphonate Coordination Polymers Isolated by Microwave-Assisted and One-Pot Synthesis	115
3.3.1. Synthesis.....	115
3.3.1.1. Synthetic Strategy.....	115
3.3.1.2. Microwave-Assisted Synthesis	115
3.3.1.3. One-Pot Synthesis.....	117
3.3.2. Crystal Morphology.....	118

3.3.3. Crystal Structure Description	121
3.3.4. Thermogravimetric Studies of Phase-Pure Materials 4 and 5	128
3.3.5. FT-IR Spectroscopy	129
3.3.6. Solid-State Nuclear Magnetic Resonance (NMR)	131
3.4. Results and Discussion	133
3.5. References	136

Chapter 4

From 1D to 3D Functional MOFs based on (Benzene-1,3,5-triyltris-methylene))triphosphonic acid	139
4.1. Initial Considerations	141
4.2. Microwave-Assisted Synthesis of 1D Lanthanide-Organic Frameworks	142
4.2.1. Microwave-Assisted Hydrothermal Synthesis	142
4.2.2. Crystal Structure of [La(H ₄ bmt)(H ₅ bmt)(H ₂ O) ₂]·3H ₂ O	144
4.2.3. Thermogravimetry and Thermogravimetry	147
4.2.4. FT-IR Spectroscopic Studies	149
4.2.5. Solid-State NMR: [La(H ₄ bmt)(H ₅ bmt)(H ₂ O) ₂]·3H ₂ O	151
4.2.6. Photoluminescence	152
4.2.7. Heterogeneous catalysis	155
4.3. Hydrothermal Synthesis of Layered 2D Lanthanide-Organic Frameworks	158
4.3.1. Hydrothermal Synthesis	158
4.3.2. Crystal Structure Description of [Eu ₂ (H ₃ pmt) ₂]·H ₂ O	160
4.3.3. Thermogravimetry and Thermogravimetry	161
4.3.4. FT-IR Spectroscopic Studies	162
4.4. Conventional Hydrothermal Synthesis of 3D Lanthanide-Organic Frameworks	164
4.4.1. Hydrothermal Synthesis	164
4.4.2. Crystal Structure of [La ₂ (H ₃ bmt) ₂ (H ₂ O) ₂]·H ₂ O	166
4.4.3. Thermogravimetry and Thermogravimetry	169
4.4.4. Solid-State NMR and FT-IR Spectroscopy Studies	170
4.4.5. Photoluminescence	172
4.4.6. Heterogeneous catalysis	178
4.5. Results and Discussion	180
4.6. References	183

Chapter 5

Layered Lanthanide-Organic Frameworks Based on ((2,4,6-Trifluorobenzene-1,3,5-triyl)tris-(methylene))triphosphonic acid	185
5.1. Initial Considerations	187
5.2. Strategy	188
5.3. Synthesis	188
5.3.1. Hydrothermal Synthesis of isotypical [Ln(H ₃ tftp)(H ₂ O)] materials	188
5.3.2. Isolation of large single-crystals of isotypical [Ln(H ₃ tftp)(H ₂ O)] materials	191
5.4. Crystal Structure Description of [La(H ₃ tftp)(H ₂ O)]	191
5.5. Thermogravimetry and Variable Temperature Powder X-ray Diffraction Studies	195
5.6. Solid-State NMR and FT-IR Spectroscopic Studies	196
5.7. Photoluminescence	199
5.8. Results and Discussion	202
5.8. References	204

Chapter 6

Porous Yttrium-Triphosphonate MOF: Synthesis and Properties	207
6.1. Initial Considerations	209
6.2. Synthesis	214
6.2.1. Synthetic Strategy	214
6.3. Crystal Structure Description of the Porous Material [Y(H ₃ L)]·xH ₂ O·yMeOH	218
6.4. Thermogravimetry and Variable Temperature Powder X-ray Diffraction Studies	220
6.5. FT-IR Spectroscopy	221
6.6. Adsorption Properties	221
6.6.1. Static Adsorption Experiments	222
6.6.2. Pulse Gas Chromatography Experiments	223
6.6.3. Gas Separation Breakthrough Studies	225
6.6.4. Preparation and Adsorption Properties of the Ion-exchanged [Y(H ₃ L)]·xSolvent_K	227
6.7. Stability Studies under Constant CO ₂ Flow	230
6.8. Photoluminescence Studies	234
6.9. Results and Discussion	237
6.10. References	241

Chapter 7

General Conclusions	243
References.....	248

Chapter 8

Experimental Section	249
8.1. General Characterization Methods	251
8.2. Reagents and Solvents	252
8.3. Single-Crystal X-ray Diffraction Studies	252
8.4. Structural Determination: Laboratory Powder X-ray Diffraction	253
8.5. Variable-Temperature Powder X-ray Diffraction	253
8.6. Photoluminescence Spectroscopy	254
8.7. Heterogeneous Catalysis	254
8.8. Adsorption Studies	255
8.8.1. Gas Adsorption Measurements	255
8.8.2. Variable-Temperature Pulse Gas Chromatography.....	255
8.8.3. Breakthrough Experiments for Gas Separation	255
8.9. Synthesis of Bi- and Tripodal Phosphonate Organic Ligands	256
8.9.1. 1,4-Phenylenebis(methylene)diphosphonic acid (H₄pmd)	256
8.9.2. (Benzene-1,3,5-triyltris(methylene))triphosphonic acid (H₆bmt)	256
8.9.3. ((2,4,6-Trifluorobenzene-1,3,5-triyl)tris(methylene))triphosphonic acid (H₆tftp)	257
8.9.4. Large tripodal phosphonate ligand H₆L	259
8.10. 1D and 3D MOFs from the Self-Assembly of Lanthanides with 1,4- Phenylenebis(methylene)diphosphonic acid	260
8.10.1. From Micro- to Nano-Sized Lanthanide-Biphosphonate Coordination Polymers.....	260
8.10.1.1 Conventional Hydrothermal Synthesis	260
8.10.1.2 Microwave-Assisted Hydrothermal Synthesis	261
8.10.1.3 [Ln(Hpmb)(H ₂ O)] Materials as Isolated Nanoparticles.....	262
8.10.1.4 Theoretical Calculations	262
8.10.2. Lanthanum-Biphosphonate Coordination Polymers Isolated by Microwave-Assisted and One-Pot Synthesis	263
8.10.2.1 Microwave-Assisted Synthesis.....	263
8.10.2.2 One-Pot Synthesis.....	263
8.10.2.3 Characterization Data for the isolated Phase-pure MOFs 4 and 5 and for compounds 6 , 7 and 8	263
8.11. From 1D to 3D Functional MOFs based on (Benzene-1,3,5- triyltris(methylene))triphosphonic Acid	265
8.11.1. Microwave-Assisted Synthesis of 1D Lanthanide-Organic Frameworks	265

8.11.2. Hydrothermal Synthesis of Layered 2D Lanthanide-Organic Frameworks	266
8.11.3. Conventional Hydrothermal Synthesis of 3D Lanthanide-Organic Frameworks	267
8.12. Layered Lanthanide-Organic Frameworks Based on ((2,4,6-Trifluorobenzene-1,3,5-triyl)tris(methylene))triphosphonic acid.....	269
8.12.1. Hydrothermal Synthesis of isotypical [Ln(H ₃ tftp)(H ₂ O)] materials.....	269
8.13. Porous Yttrium-Triphosphonate MOF: Synthesis and Properties.....	270
8.13.1. Conventional Solvothermal Synthesis	270
8.13.2. Preparation of compound [Y(H ₃ L)]·xH ₂ O·yMeOH as large single-crystals.....	271
References.....	272
Appendices	275

Abbreviations

^1H NMR	proton nuclear magnetic resonance
^{13}C NMR	carbon 13 nuclear magnetic resonance
^{19}F NMR	fluorine 19 nuclear magnetic resonance
^{31}P NMR	phosphorous 31 nuclear magnetic resonance
bdc	benzene-1,4-dicarboxylic acid
CMOF	Chiral Metal-Organic Framework
CN	coordination number
CP	coordination polymer
CPMAS	cross-polarization magic-angle spinning
d	doublet
DEF	<i>N,N'</i> -diethylformamide
DMF	<i>N,N'</i> -dimethylformamide
DMSO	dimethyl sulfoxide
DMSO- <i>d</i> ₆	deuterated dimethyl sulfoxide
DOE	Department of Energy
dq	double quartet
dt	double triplet
EDG	electron-donating group
EDS	energy dispersive spectroscopy
EDW	electron-withdrawing group
ELM	elastic layer-structured metal-organic framework
ESI	electrospray ionization
FT-IR	Fourier transform infrared
HPDEC	high power decoupling
HR-MS	high resolution mass spectrometry
IL	ionic liquid
IUPAC	International Union of Pure and Applied Chemistry
<i>J</i>	coupling constant
Ln	Lanthanide
LnOF	Lanthanide-Organic Framework
MAS	magic-angle spinning
MIL	Materials Institute Lavoisier
MOF	Metal-Organic Framework

MOP	Metal-Organic Polyhedra
MS	mass spectrometry
MWAS	microwave-assisted synthesis
m/z	mass/charge ratio
$(M + H)^-$	deprotonated molecular ion
$(M - H)^+$	protonated molecular ion
$(M + Na)^+$	sodiated molecular ion
NMR	nuclear magnetic resonance
PBU	primary building unit
PCN	Porous Coordination Network
ppm	part per million
PXRD	powder X-ray diffraction
s	singlet
SEM	scanning electron microscopy
STP	standard temperature and pressure
t	triplet
texbp	tetraethyl- <i>p</i> -xylylenebisphosphonate
TEOS	tetraethyl orthosilicate
TGA	thermogravimetric analysis
THF	tetrahydrofuran
TLC	thin layered chromatography
TOF MS ES	time-of-flight mass spectrometry electrospray
UMCM	University of Michigan Crystalline Material
USAS	ultrasound-assisted synthesis
VOC	volatile organic compound
VTPXRD	variable-temperature powder X-ray diffraction
δ	chemical shift (in ppm)
ZIFs	zeolitic imidazolate frameworks

Publications Presented in this Thesis

- 1. Multifunctional Micro- and Nanosized Metal-Organic Frameworks Assembled from Bisphosphonates and Lanthanides*
Sérgio M. F. Vilela, Duarte Ananias, José A. Fernandes, Patrícia Silva, Ana C. Gomes, Nuno J. O. Silva, Marcelo O. Rodrigues, João P. C. Tomé, Anabela A. Valente, Paulo Ribeiro-Claro, Luís D. Carlos, João Rocha, Filipe A. Almeida Paz
J. Mater. Chem. C, **2013**, DOI: 10.1039/C3TC32114B
- 2. Photoluminescent Layered Lanthanide-Organic Framework Based on a Novel Trifluorotriphosphonate Organic Linker*
Sérgio M. F. Vilela, José A. Fernandes, Duarte Ananias, Luís D. Carlos, João Rocha, João P. C. Tomé, Filipe A. Almeida Paz
CrystEngComm, **2013**, DOI: 10.1039/c1033ce41482e
- 3. Lanthanide-polyphosphonate coordination polymers combining catalytic and photoluminescence properties*
Sérgio M. F. Vilela, Ana D. G. Firmino, Ricardo F. Mendes, José A. Fernandes, Duarte Ananias, Anabela A. Valente, Holger Ott, Luís D. Carlos, João Rocha, João P. C. Tomé, Filipe A. Almeida Paz
Chem. Commun., **2013**, 49, 6400-6402
- 4. Structural Diversity of Lanthanum-Organic Frameworks Based on 1,4-Phenylenebis-(methylene)diphosphonic Acid*
Sérgio M. F. Vilela, Ricardo F. Mendes, Patrícia Silva, José A. Fernandes, João P. C. Tomé, Filipe A. Almeida Paz
Cryst. Growth Des., **2013**, 13, 543-560
- 5. Multi-functional metal-organic frameworks assembled from a tripodal organic ligand*
Sérgio M. F. Vilela, Duarte Ananias, Ana C. Gomes, Anabela A. Valente, Luís D. Carlos, José A. S. Cavaleiro, João Rocha, João P. C. Tomé, Filipe A. Almeida Paz
J. Mat. Chem., **2012**, 22, 18354-1837
- 6. Ligand design for functional metal-organic frameworks*
Filipe A. Almeida Paz, Jacek Klinowski, Sérgio M. F. Vilela, João P. C. Tomé, José A. S. Cavaleiro, João Rocha
Chem. Soc. Rev., **2012**, 41, 1088-1110
- 7. 1,3,5-Tris(bromomethyl)benzene*
José A. Fernandes, Sérgio M. F. Vilela, Paulo J. Ribeiro-Claro, Filipe A. Almeida Paz
Acta Crystallogr., Sect. C: Cryst. Struct. Commun., **2011**, C67, o198-o200

Chapter 1

Metal-Organic Frameworks: Concepts, Properties and Potential Applications

1.1. Supramolecular Chemistry

For several decades, since 1828, date in which Friedrich Wöhler synthesized urea, molecular chemistry have developed a huge number of powerful and highly sophisticated methods to construct and prepare complex molecular structures through the creation or break of covalent bonds between atoms while carefully controlling the reaction conditions. During several years, organic chemistry grew very quickly, becoming one of the most important areas of chemistry. After several efforts, Robert B. Woodward and Albert Eschenmozer, supported by a great number of collaborators, synthesized the so known Vitamin B₁₂.¹ Nevertheless, molecular chemistry has just concerned in covalent bonds forgetting other interactions.

Worldwide Chemists have been interested in other non-covalent interactions and, consequently, a new direction in chemistry, called supramolecular chemistry, has gained a tremendous power in the last decades. This fact has been supported and documented in several published monographs.¹⁻⁵ The term supramolecular chemistry was introduced, for the first time, in 1978 by Jean-Marie Lehn, who won, with the two reputable researchers Donald J. Cram and Charles J. Pedersen, the Nobel Prize in chemistry in 1987 due to the high progress that they have developed in this field.³ Thus, supramolecular chemistry is defined as “chemistry beyond the molecule”. In other words, this field concerns with the study of molecular ensembles and intermolecular bonds.⁶⁻⁷ Figure 1.1 illustrates a supramolecular complex achieved through intermolecular interactions.

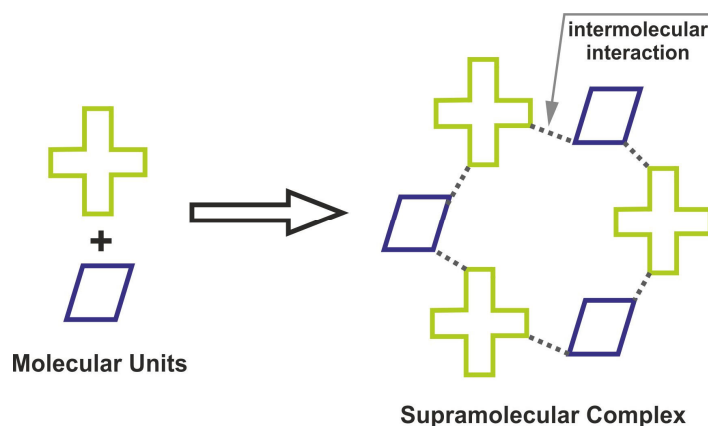


Figure 1.1 – Formation of a supramolecular complex from the self-assembly, through intermolecular interactions, of molecular units.

Supramolecular chemistry is a relatively recent area, which has grown rapidly. Nowadays, this area has becoming very strong due to the collaboration between researchers belonging to distinct interdisciplinary disciplines (chemistry, physics, biology and technology). As mentioned above, supramolecular chemistry is focused on the construction of functional and highly complex chemical systems resulting of non-covalent connections between molecular components.^{3,5,8-9} It is emphasized:

- hydrogen bonding
- π - π stacking
- van der Waals forces
- ion-ion interactions
- electrostatic interactions
- ion-dipole interactions
- dipole-dipole interactions
- cation- π interactions

Compared to the high energetic covalent bonds (200-400 kJ mol⁻¹), the non-covalent interactions have smaller energies: i) 4-40 kJ mol⁻¹ for ion-ion electrostatic interactions; ii) 1-80 kJ mol⁻¹ for hydrogen bonding; and iii) less than 4 kJ mol⁻¹ for van der Waals forces, dipole-dipole and ion-dipole interactions.² Although weak, some of the numerous interactions contained in supermolecules, the subject of study in supramolecular chemistry, have a great influence in the final properties of them.

Within the supramolecular chemistry area, one of the most important sub-areas is, undoubtedly, the supramolecular coordination chemistry. This comprises the generation of supramolecular coordination systems possessing metal ions centers embedded in their structure. The existence of both organic and inorganic components confers, in several cases, more than one property to the complex allowing its application in distinct fields.¹⁰⁻¹¹ In the literature it is possible to find a considerable number of supramolecular coordination complexes. One of these families is composed of highly crystalline and, sometimes, porous architectures normally known as Coordination Polymers, Metal-Organic Frameworks (MOFs), Porous Coordination Polymers (PCPs) or Coordination Frameworks.

1.2. Metal-Organic Frameworks

Metal-Organic Frameworks (MOFs), also known as coordination polymers, are one of the most recent classes of functional materials and a hot topic which has been attracted worldwide research attention. Tremendous efforts have been devoted towards the chemistry of new and fascinating architectures, some of which exhibiting interesting and unique properties. Noteworthy, these materials are on the interface between molecular coordination chemistry and materials science. The large number of reviews published in the most prestigious scientific journals, scientific papers, monographs and books, have reflected the high interest from the scientific community around these materials.¹²⁻⁴⁶

1.2.1. The Genesis and Terminology of the Name

Since the appearance of crystalline, multidimensional and functional coordination materials, their nomenclature is a hot topic. However, in some scientific meetings,

worldwide researchers, working in this field, still did not achieve a consensus. This family of materials has been identified as Coordination Polymers (CPs), Metal-Organic Frameworks (MOFs), Coordination Networks, Porous Coordination Polymers (PCPs), Hybrid Organic-inorganic Materials, Organic Zeolite Analogues, among others.^{19,47-48}

The term CP is usually used to describe a class of materials formed by an extended network of metal centers or clusters connected, through coordination bonds, to organic bridging ligands. This term is too vague because it does not refer to the final structure or morphology of the solid material. For example, CPs does not clarify if the compound is crystalline or amorphous, or if it is porous or dense. Thus, very often the term MOF has been used to define crystalline and highly porous compounds which involve strong metal-to-ligand interactions resulting usually in three-dimensional fascinating structures with high thermal and mechanical stability.¹⁸⁻¹⁹

Because the terms CPs and MOFs provide some ambiguity, several efforts have been done in order to have a decision about the nomenclature of this type of materials. In 2009, Biradha, Ramanan and Vittall published a pedagogic work relating about this theme. Although some explanations about both CPs and MOFs, the uncertainty about which term should be used for 1D, 2D or 3D crystalline coordination materials remained.⁴⁸ Three years later, in 2012, the nomenclature of CPs *versus* MOFs (after an initial project of the IUPAC (*International Union of Pure and Applied Chemistry*) Inorganic Chemistry division called “*Coordination polymers and metal-organic frameworks: terminology and nomenclature guidelines*”) was also discussed in a scientific meeting counting with the participation of several experts of this research area.⁴⁷ From this discussion, it was reported two hierarchies of solid state coordination chemistry. In Figure 1.2 is depicted one of these hierarchies where CPs and MOFs are contained. Despite this attempt, it is still not clear what is the appropriated term to use for the nomenclature of crystalline coordination materials.

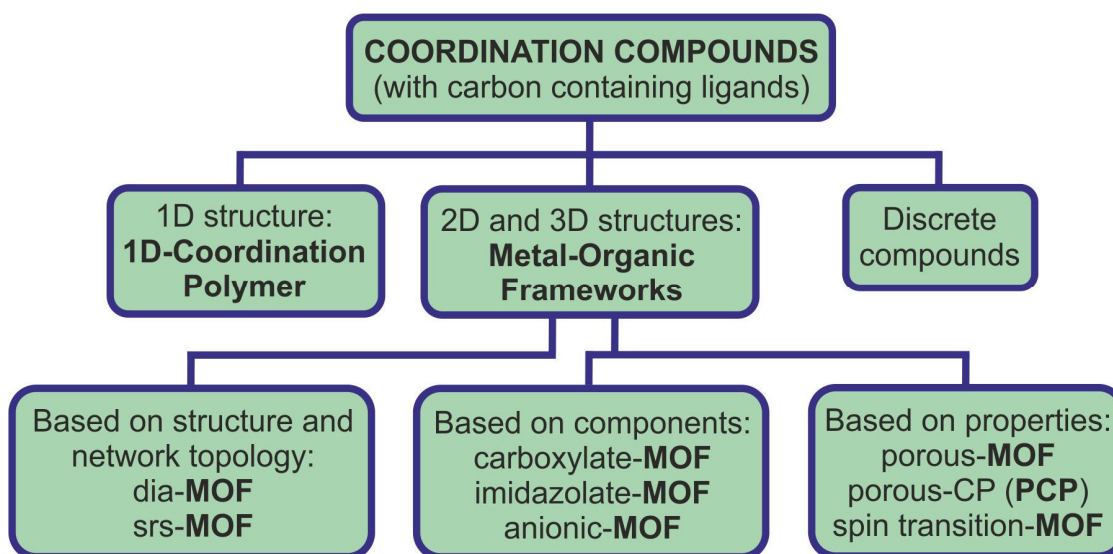


Figure 1.2 – Illustration of a proposal hierarchy by the group of researchers in charge for IUPAC to define the terms Coordination Polymers and Metal-Organic Frameworks. Reproduced from reference 47.

In this thesis it will be considered as MOFs all the crystalline compounds, which result from the self-assembly of organic linkers (in our case, phosphonate-based organic molecules) with metal centers (lanthanides), independently of their dimensionality or porosity.

1.2.2. Interests in MOFs

In the last years, the interest in both CPs and MOFs has grown exponentially. Searches in the ISI Web of Knowledge database can easily unveil a huge number of scientific papers reporting the synthesis, characterization and the properties of CP- or MOF-type materials. The first report describing the design and synthesis of a new class of scaffolding-like materials, using zinc and tetracyanotetraphenylmethane as the primary building units (PBUs) was published by Hoskins & Robson in 1990. This work constitutes a preliminary attempt to construct, through strong and highly directional coordinative bonds (several hundreds of KJ mol^{-1}), multi-dimensional diamondoid-type metal-organic frameworks. This pioneering work has been motivated worldwide researchers to focus their attention in the design and synthesis of new materials, resulting from the self-assembly of organic molecules and metallic centers. These compounds compose the first generation of MOFs.⁴⁹ Evolving in time, scientists belonging to this field started to use secondary building units (second generation)⁵⁰ passing then for the production of large metal-organic polyhedral cages (third generation networks known as MOPs).⁵¹

Consequence of the progressive evolution on the production of this class of compounds has been reflected on the exponential growth of publications in international journals since 1990 (Figure 1.3).⁵²

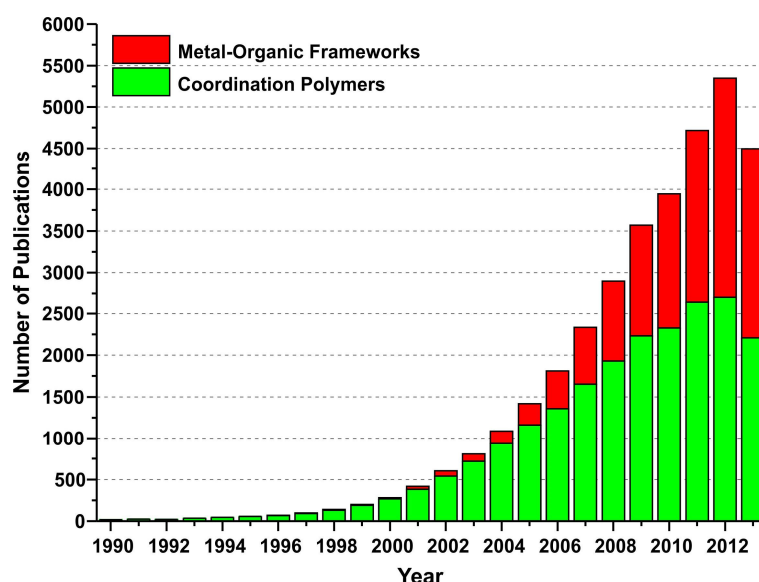


Figure 1.3 – Published scientific papers containing the terms “Coordination Polymer(s)” and/or “Metal-Organic Framework(s)” in their titles, abstracts or keywords until 14 November 2013. Reproduced from ISI Web of Science (reference 52).

When compared with other microporous inorganic materials, as for instance zeolites, the architecture and functionalization of the pores of MOFs are easier to be controlled due to the flexible design of the organic component which is amenable to chemical modifications through organic synthesis.⁵³⁻⁵⁴ This is not the only advantage of MOFs when compared with other systems. MOFs have another features and properties overlapping to other structures, of those we may highlight: i) the considerable resistance to structural collapse due to the very strong coordination bonds; ii) MOF-type materials are more porous and possess world records in terms of surface area; and iii) complexes with geometrically well-defined structures. The latter characteristic is extremely important to promote the isolation of materials with high crystallinity, and is an essential criterion for the establishment of structure-property relationships.^{19,55} All these characteristics in MOFs can lead to entering properties such as porosity (to store and capture guests), high internal surface area (with the possibility to have functional groups available to originate catalytic processes), conductivity, magnetism, among many others.

1.2.3. Building Components for the Preparation of MOFs

The design and synthesis of MOFs involve a very interesting intellectual challenge because the final architecture strongly depends of the combination of two distinct components: metal centers and organic ligands. These are known as primary building units (PBUs). The number and orientation of the bonding sites (coordination numbers and coordination geometries) of the PBUs are responsible for some features of the material such as shape, pore size and topology. The dimensionality (1D, 2D or 3D), other feature of the final structure of MOF materials, also depends of the employed PBUs. Figure 1.4 depicts the process to produce the resulting multidimensional MOFs.

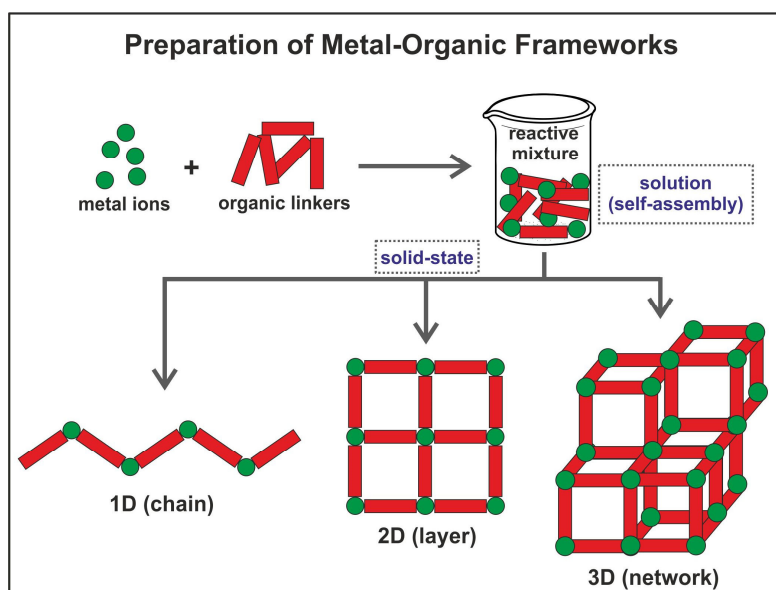


Figure 1.4 – Schematic representation of MOFs with different dimensionalities (1D, 2D and 3D).

1.2.3.1. Metal Centers

During the last two decades, worldwide research groups interested in the preparation of MOFs have selected the metallic centers concerning their both final structure and properties. Therefore having into account the structure-properties relationship of the resulting MOF materials, a vast number of metallic elements from the periodic table have been employed in their preparation, such as: alkaline earths metals (*i.e.*, Ca^{2+} , Mg^{2+} and Sr^{2+}), transition metals (*i.e.*, Mn^{2+} , Fe^{2+} , Co^{2+} , Cu^{2+} and Zn^{2+}) and rare-earth metals, including lanthanides (*i.e.*, La^{3+} , Ce^{3+} , Eu^{3+} , Gd^{3+} and Tb^{3+}).¹³ Due to their different geometries, metallic centers display an important role in terms of the dimensionality and topology of the final structures of MOFs. In the case of transition metals, according to their oxidation state, they may possess coordination number (CN) varying from 2 to 7, giving rise to different coordination geometries (Figure 1.5).⁵⁶⁻⁵⁷

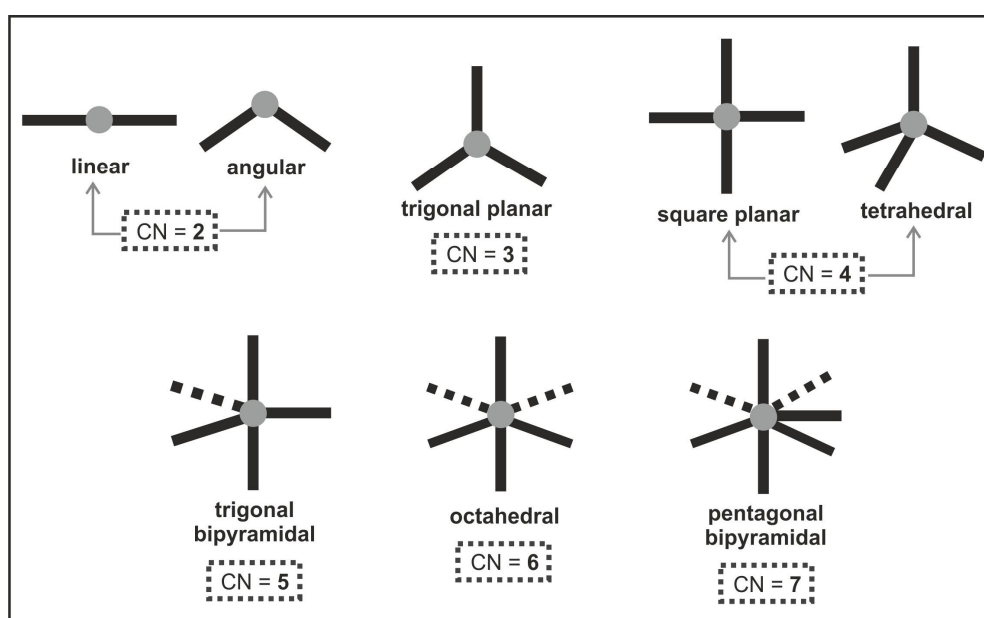


Figure 1.5 – Some coordination geometries of transition metals (CN = coordination number).

Rare-earth elements have been widely employed in the synthesis of multidimensional MOFs.^{24,34,58} Because during my PhD project I only used this type of metal elements, mainly lanthanides, in this topic it will be provided a more detailed information about their characteristics and properties.

According to IUPAC, rare-earths are considered the elements with the atomic number 21 (Sc), 39 (Y) and 57 (La) to 71 (Lu). Additionally, the elements from 58 (Ce) to 71 (Lu) are also called as lanthanides. The occurrence of the La to Lu lanthanide elements is not common. Therefore, these are more abundant in Australia, Brazil, China and Malaysia, being these the major exporting countries.⁵⁹⁻⁶¹ In terms of solubility, lanthanide minerals are very soluble in water, however, their abundance is very low in all natural

waters. These elements do not present, generally, toxicity for Life, with exception of promethium (radioactive element) which does not occur naturally.⁵⁹

Table 1.1 – Properties of the Lanthanide series. Electronic configuration of Xe: $1s^2 2s^2 2p^6 3s^2 3p^6 4s^2 3d^{10} 4p^6 5s^2 4d^{10} 5p^6$.

Element	Name	Atomic Number	Ionic Radii for Ln ³⁺ (ppm)	Electronic Configuration	Oxidation States
La	Lanthanum	57	103.2	[Xe]5d ¹ 6s ²	La ³⁺
Ce	Cerium	58	101.0	[Xe]4f ¹ 5d ¹ 6s ²	Ce ³⁺ , Ce ⁴⁺
Pr	Praseodymium	59	99.0	[Xe] 4f ³ 6s ²	Pr ³⁺ , Pr ⁴⁺
Nd	Neodymium	60	98.3	[Xe] 4f ⁴ 6s ²	Nd ²⁺ , Nd ³⁺ , Nd ⁴⁺
Pm	Promethium	61	97.0	[Xe] 4f ⁵ 6s ²	Pm ³⁺
Sm	Samarium	62	95.8	[Xe] 4f ⁶ 6s ²	Sm ²⁺ , Sm ³⁺
Eu	Europium	63	94.7	[Xe] 4f ⁷ 6s ²	Eu ²⁺ , Eu ³⁺
Gd	Gadolinium	64	93.8	[Xe] 4f ⁷ 5d ¹ 6s ²	Gd ³⁺
Tb	Terbium	65	92.3	[Xe] 4f ⁹ 6s ²	Tb ³⁺ , Tb ⁴⁺
Dy	Dysprosium	66	91.2	[Xe] 4f ¹⁰ 6s ²	Dy ²⁺ , Dy ³⁺ , Dy ⁴⁺
Ho	Holmium	67	90.1	[Xe] 4f ¹¹ 6s ²	Ho ³⁺
Er	Erbium	68	89.0	[Xe] 4f ¹² 6s ²	Er ³⁺
Tm	Thulium	69	88.0	[Xe] 4f ¹³ 6s ²	Tm ²⁺ , Tm ³⁺
Yb	Ytterbium	70	86.8	[Xe] 4f ¹⁴ 6s ²	Yb ²⁺ , Yb ³⁺
Lu	Lutetium	71	86.1	[Xe] 4f ¹⁴ 5d ¹ 6s ²	Lu ³⁺

Lanthanides have some characteristics in their chemistry differencing them from the *d*-block elements and, consequently, render them more reactive than transition metals:

- i) the 4f orbitals of the Ln^{3+} do not have a direct effect on the bonding, due to the shielding by the $5s^2$ and $5p^6$ orbitals. This feature make their magnetic and spectroscopy properties largely uninfluenced by the ligand;
- ii) very sharp electronic peaks in their electronic spectra when compared with those of transition metals;
- iii) lanthanide elements prefer anion ligands with high electronegative donor atoms (*i.e.*, oxygen or fluorine atoms);
- iv) they originate hydrated compounds, leading to an uncertainty to assign coordination numbers;
- v) at neutral pH, it occurs a precipitation of insoluble hydroxide lanthanides. This process does not may happen in this case of the presence of complexing species;
- vi) the chemistry of lanthanides is, mostly, based on the 3+ oxidation state in, certainly, aqueous reaction solutions;
- vii) in opposition to what happens with transition metals, $\text{Ln}=\text{O}$ or $\text{Ln}\equiv\text{N}$ multiple bonds do not form.

In Table 1.1 are described some properties of the lanthanide elements (Ln^{3+} ionic radii, electronic configurations and oxidation states).⁶⁰

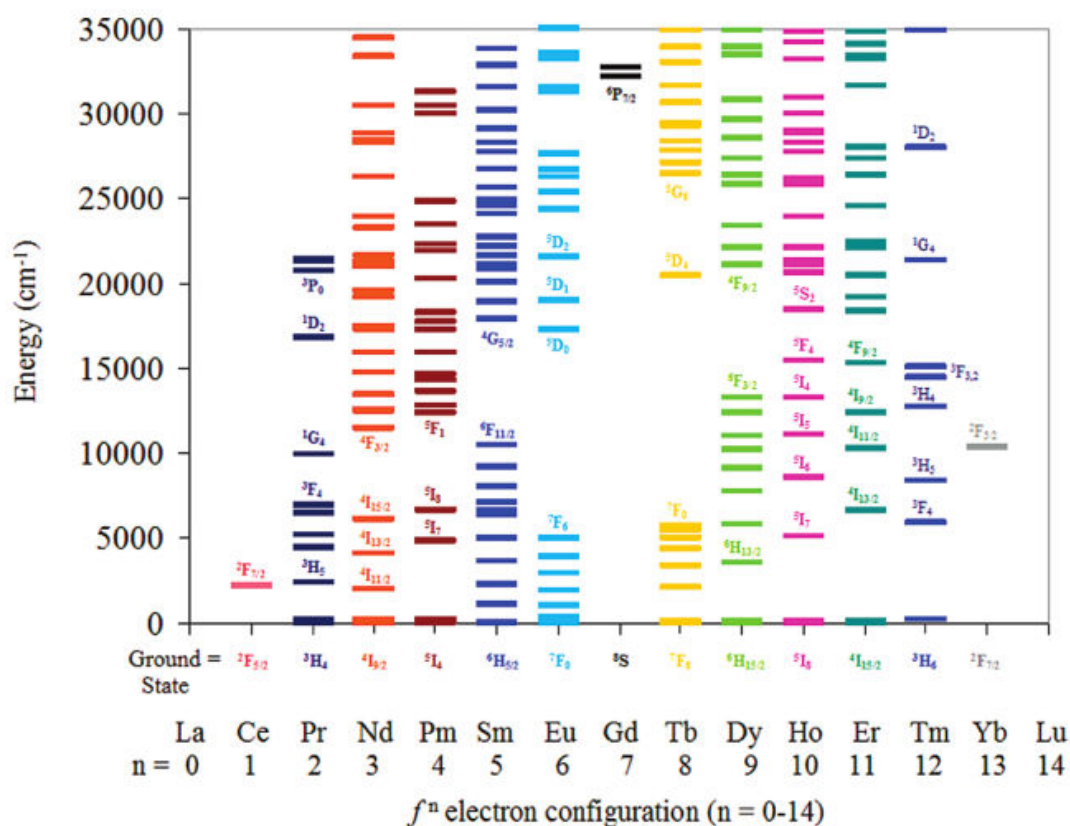


Figure 1.6 - Diagram of the electronic energy levels for lanthanide cations (Ln^{3+}); n corresponds to the number of electrons in the 4f orbitals. Reproduced from reference 34.

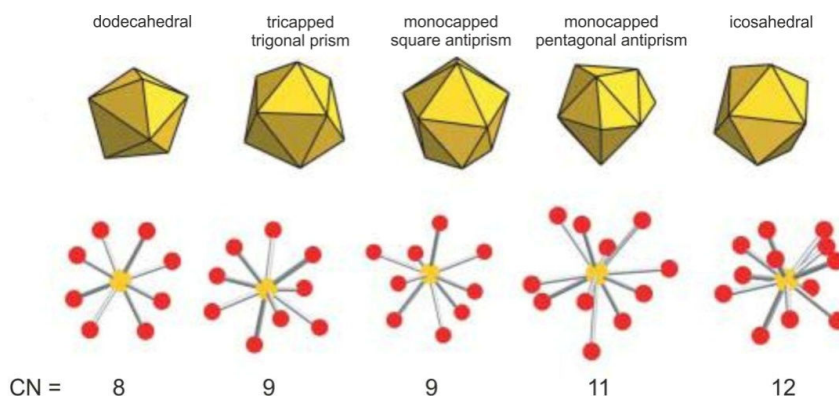


Figure 1.8 – Coordination geometries of lanthanide elements (CN = coordination number). Reproduced from reference 58.

1.2.3.2. Organic Linker Components

Many types of organic linkers have been employed in the construction of MOFs. These molecules are responsible for the bridges between metal centers. To originate a structure infinitely expanded the organic molecules have to be multidentate with, at least, two donor atoms such as O, S or N. The molecules differ from each other according their complexity and functional groups. They can be of aromatic or aliphatic nature and, sometimes, they contain heteroelements in their structure. In terms of functional groups the organic ligands must have at least two, which can be carboxylic acids, esters, amines, phosphonates, sulphonates, nitrile, pyridyl, imidazole, pyrazole, triazole and tetrazoles groups (Figure 1.9) or even a combination of them. The shape (rigid or not) and length (i.e., distance between coordinating groups) further determine some properties of the final structures.^{18,28,68-69}

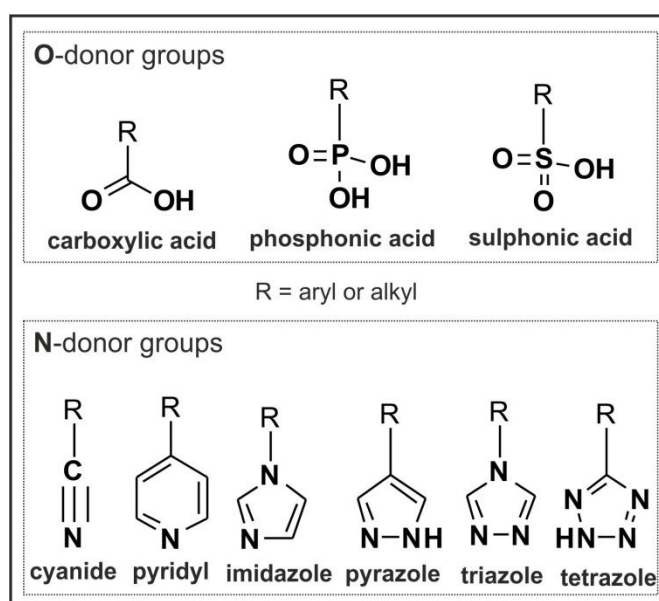


Figure 1.9 – Functional groups commonly found in the organic linkers used for the preparation of MOFs.

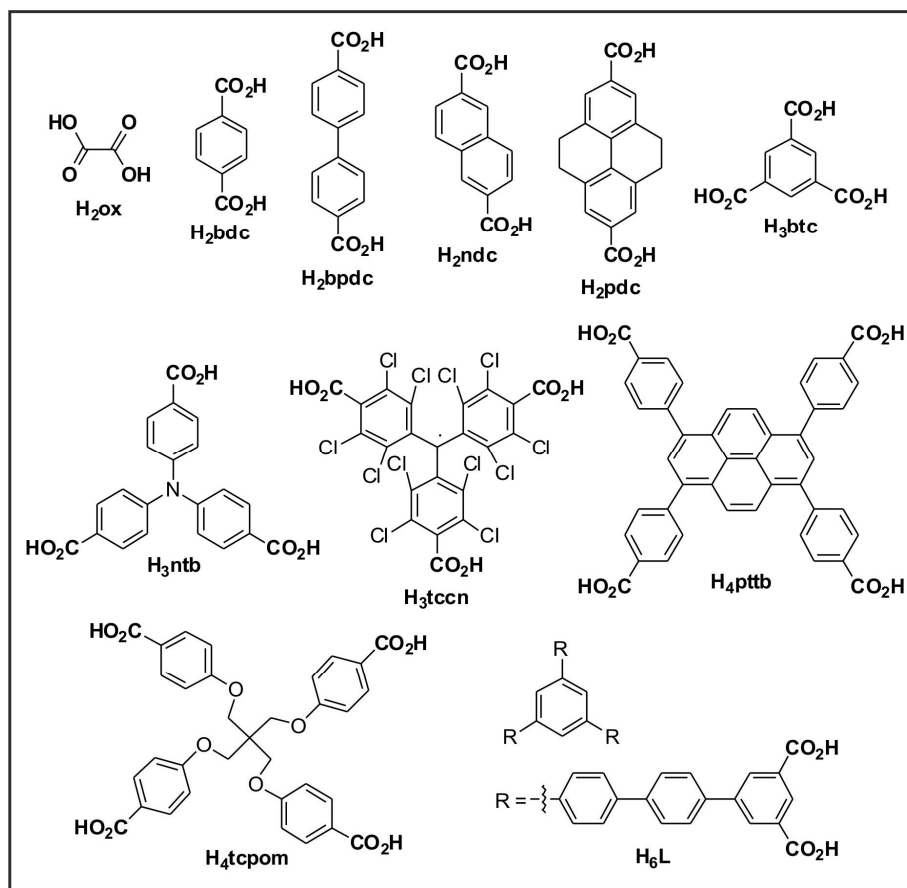


Figure 1.10 – Organic ligands based on carboxylic acid groups for the preparation of MOFs: **H₂ox** – oxalic acid;
H₂bdc – benzene-1,4-dicarboxylic acid (terephthalic acid);
H₂bpdc – bisphenyl-4,4'-dicarboxylic acid;
H₂ndc – naphthalene-2,6-dicarboxylic acid;
H₂pdc – 4,5,9,10-tetrahydropyrene-2,7-dicarboxylic acid;
H₃btc – benzene-1,3,5-tricarboxylic acid (trimesic acid);
H₃ntb – 4,4',4''-nitriлотrisbenzoic acid;
H₃tcen – tris(2,3,5,6-tetrachloro-4-carboxy)methyl radical;
H₄pttb – 4,4',4'',4'''-(pyrene-1,3,6,8-tetrayl)tetrabenzoic acid;
H₄tcpom – tetrakis[4-(carboxyphenyl)oxymethyl]methane.

A careful selection of the organic ligands to construct a MOF is essential, because these may display a very important role in the functionality and porosity of the resulting materials and, additionally, may provide the possibility of post-synthetic modification of the MOF material.⁷⁰ The majority of the research groups working in this area opt for commercially available organic molecules. Their availability may be an advantage for a fast and cheaper preparation of MOFs. Therefore, it has been more frequent to find published scientific works reporting the synthesis of MOFs composed of commercially available organic ligands than those produced from designed and prepared ones by researchers in the own laboratories using conventional (step-by-step from the ligand precursors to the desired linker) and non-conventional *in situ* synthesis. In the later, the organic precursors are converted *in situ* into the final molecule which coordinates to the

metal centers. Several processes explain this *in situ* preparation: hydroxylation, decarboxylation, alkylation, and hydrolysis.^{69,71-72} Although more time consuming and, sometimes, more expensive, the synthesis of new organic ligands may confer to the resulting MOF the desired properties. In order to explain the relationship between the properties of the resulting materials and the nature and structure of the designed and synthesized organic ligands, the MOF research group University of Aveiro published a critical review discussing this topic.⁷³ Having this into account, during my PhD project I prepared four organic phosphonate-based organic PBUs (chapter 2) to be used in the preparation of functional and multidimensional MOFs (chapters 3, 4, 5 and 6).

As mentioned above, a huge number of organic linkers have been used for the self-assembly of MOFs. In the Figures 1.10, 1.11, 1.12 and 1.13 are represented some of them (commercially available or prepared by some research groups) illustrating the functionality and size diversity of the organic PBUs.^{27,57,74-100} Examples of phosphonate-based ligands are represented in the following section.

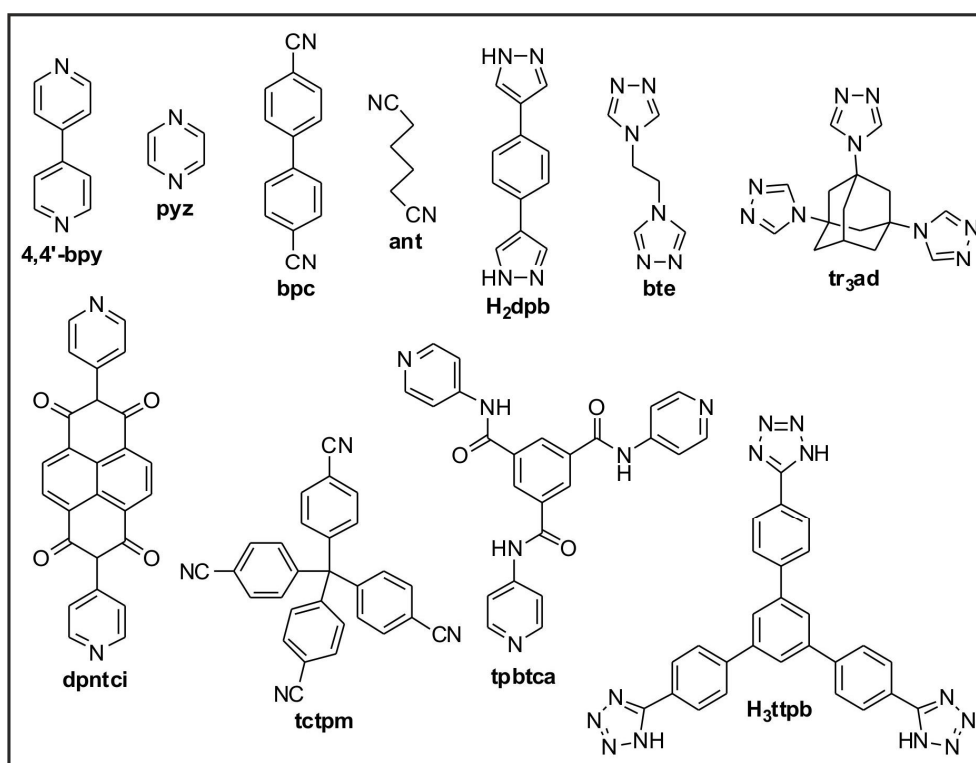


Figure 1.11 – N-Donor organic ligands for the preparation of MOFs:

4,4'-bpy - 4,4'-bipyridine;

pyz - pyrazine;

bpc - 4,4'-dicyanodiphenyl;

ant - 1,4-dicyanobutane;

H₂dpb – 1,4-di(1*H*-pyrazol-4-yl)benzene;

bte – 1,2-bis(1,2,4-triazol-4-yl)ethane;

tr₃ad - 1,3,5-tris(1,2,4-triazol-4-yl)adamantane;

dpntci – *N,N'*-di(4-pyridyl)-1,4,5,8-naphthalenetetracarboxydiimide;

tctpm – 4,4',4'',4'''-methanetetrayltetrabenzonitrile;

tpbtca – *N¹,N³,N⁵*-tri(pyridin-4-yl)benzene-1,3,5-tricarboxamide;

H₃ttpb – 1,3,5-tris[4-(2*H*-tetrazol-5-yl)phenyl]benzene.

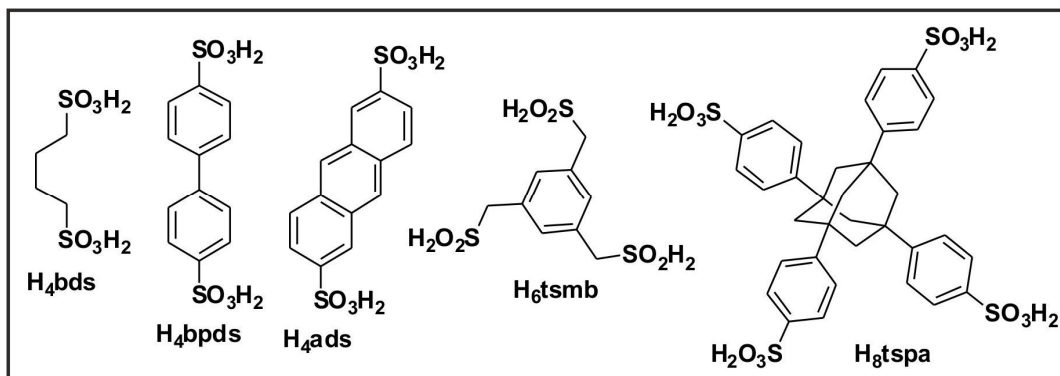


Figure 1.12 – Organic ligands based on sulfonic acid groups for the preparation of MOFs: **H₄bds** – butane-1,4-disulfonic acid; **H₄bpds** - biphenyl-4,4'-disulphonic acid; **H₄ads** – anthracene-2,6-disulfonic acid; **H₆tsmb** – 1,3,5-tris(sulfonomethyl)benzene; **H₈tspa** – 1,3,5,7-tetra(4-sulfonophenyl)adamantine.

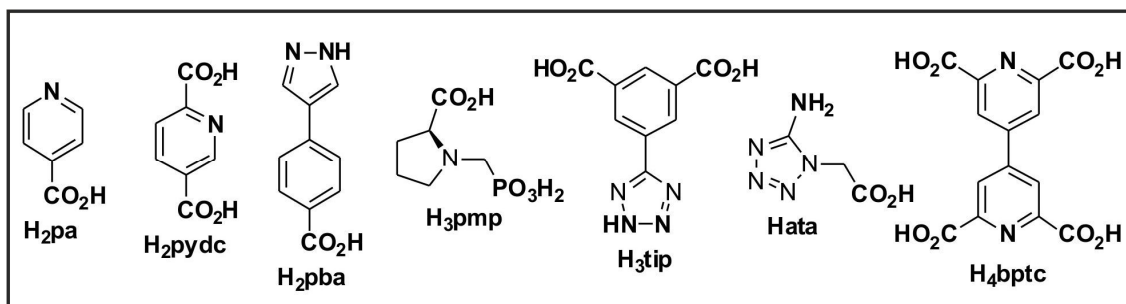


Figure 1.13 – Mixed O- and/or N-donor organic ligands for the preparation of MOFs: **H₂pa** – isonicotinic acid; **H₂pydc** – 2,5-pyridinedicarboxylic acid; **H₂pba** – 4-(1*H*-pyrazol-4-yl)benzoic acid; **H₃pmp** – (*S*)-*N*-(phosphonomethyl)proline; **H₃tip** – 5-(1*H*-tetrazol-5-yl)isophthalic acid; **Hata** – (5-amino-1*H*-tetrazol-1-yl)acetic acid; **H₄bptc** – 4,4'-bipyridine-2,2',6,6'-tetracarboxylic acid.

1.2.4. Synthetic Methods for the Preparation of MOFs

PBUs are, undoubtedly, very important components concerning the crystalline structure of the resulting MOF materials. Nevertheless, other parameters (*i.e.*, reaction conditions and synthetic methodologies) are also essential for the construction of these compounds. The specific reaction conditions that can be changed are (Figure 1.14):

- i) metal source (*i.e.*, nitrate, chloride, oxide or acetate);
- ii) molar ratio/concentration of the PBUs in solution;
- iii) solvent (*e.g.*, water, DMF, DMSO, methanol, ethanol or a mixture of them);

- iv) reaction time (depending of the synthetic approach employed, the reaction time may vary from few minutes to several weeks);
- v) pressure (ambient pressure, if the reaction occurs in an open reactor; autogenous pressure if a closed vessel is selected, or controlled pressure when the reaction occurs in a microwave-assisted equipment);
- vi) temperature (from ambient to 250 °C);
- vii) pH (adjust with acids or bases, as for instance, HCl or NaOH).

Although all the reaction conditions display an important role in the preparation of MOFs, it was found that there is a relationship between the last two (temperature and pH) and the final structure of these materials.^{18,101-103}

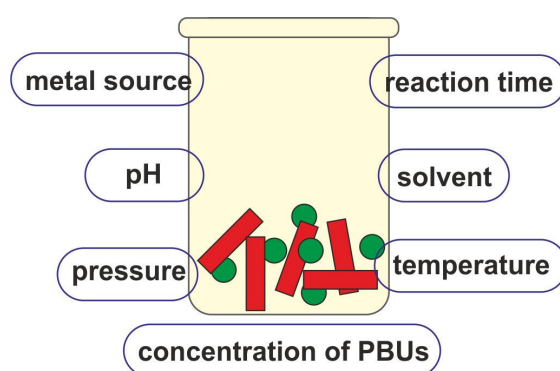


Figure 1.14 – Reaction variables that may be optimized for the preparation of MOFs.

Depending of the final purpose, multidimensional MOFs may be prepared employing different and distinct synthetic methodologies. Some of them (*i.e.*, microwave-, ultrasound-assisted and one-pot synthesis) are faster, being more attractive for industry. However, the possibility to obtain the desired materials as large single-crystals is very often a difficult task to achieve. In opposition, slow diffusion and hydro(solvo)thermal approaches lead to large single-crystal particles, but they are, normally, time-consuming methodologies. In the following paragraphs some details of various synthetic methodologies will be described.

Slow diffusion can be employed when MOFs are pretended as large single-crystals (fundamental for X-ray diffraction studies). This methodology consists on the slowly “bring into contact” of different solutions containing reactive species (organic ligands and metal centers). Therefore, this method consists in the preparation of saturated solutions (having different density) containing the metal salts and organic ligands dissolved in a suitable solvent or a mixture of solvents. After the first solution being transferred for a suitable reaction vessel, a less dense solvent is added. Finally the second solution is transferred to the vessel and a system composed of three layers is formed. This reaction system mixture is kept in an open, or partially open, system at ambient or low temperature

while the layers start to mixture, leading to the contact of the organic and inorganic components and, consequently, to the formation of the MOF material. Although very simple, this synthetic approach is typically very slow, taking several days, weeks or even months.¹⁰⁴⁻¹⁰⁷



Figure 1.15 – Representation of the instrumentation used in hydro(solvo)thermal synthesis: oven and autoclave (inset).

Hydro(solvo)thermal synthesis was originally developed for the synthesis of zeolites. This method is, undoubtedly, the most widely used in the self-assembly of multidimensional MOFs. The prepared reaction mixtures are transferred to a closed system (autoclave) and then placed inside an oven. The operation temperature range is between 80 and 250 °C. Sometimes it is necessary to perform heating and cooling temperature ramps to isolate large single-crystals. The system is under autogenous pressure. Besides water, another solvents are used such as tetrahydrofuran (THF), toluene, *N,N*-dimethylformamide (DMF), among several others. DMF has become a popular solvent

due to its high boiling point and capacity to dissolve metal salts and organic ligands, mainly carboxylic acids.¹⁰⁸⁻¹¹⁰

Ionothermal synthesis was developed by Morris in 2004.¹¹¹ This recent methodology employs ionic liquids (ILs) and eutectic mixtures which provides different reaction conditions when compared to the conventional solvo(hydro)thermal synthesis. ILs act at the same time as the reaction solvent, template, or charge-compensating group. Because there are a large number of possible binary ionic liquids and eutectic mixtures, this method have been used in the construction of several porous materials by selecting solvents with different properties.¹¹²⁻¹¹⁴

Microwave-assisted synthesis (MWAS) is not very common, when compared, for instance, with the hydro(solvo)thermal method. Very interesting results have been, however, published by using this approach. Researchers have preferred this synthetic method because it is a simpler and energy-efficient heating process, it allows the reduction of the crystallization times, improve yields, the possibility to control the morphology of the structure, phase selectivity, narrow particle distribution and also allows an easy variation of the reaction parameters. This method has the main disadvantage of not typically allowing the



Figure 1.16 – Representation of the apparatus used in microwave-assisted synthesis. Inset is a common reactor for this equipment.

isolation of large single crystals for X-ray diffraction.^{109,115-117}

Electrochemical Synthesis is not very usual for the preparation of MOFs. This approach consists in an electron transference between the electrode and the electrolyte (ionic conductor) or species in solution. Müller and collaborators prepared the well-known HKUST-1 using an electrochemical cell containing copper plates as the anode, a solution of benzene-1,3,5-tricarboxylic acid in methanol and a copper cathode. It was applied a voltage of 12-19 V and 1.3 A of intensity. After 150 minutes the desired HKUST-1 MOF was isolated.¹¹⁸ Some years latter Van Assche *et al.* reported the preparation of the same material as thin HKUST-1 layers.¹¹⁹ This method has been used on industrial scale to produce MOF materials.

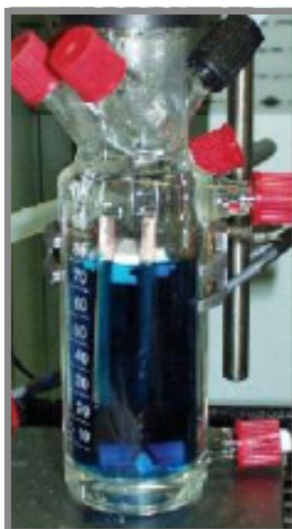


Figure 1.17 – Picture of the system used by Müller *et al.* to produce the HKUST-1 MOF by electrochemistry synthesis.

Ultrasound-assisted synthesis (USAS), as well as MWAS, allows an easy adaptability of the reaction conditions tested in the conventional heating approaches. USAS have been widely used due to its capacity to isolate MOFs as phase-pure, with homogeneous particle size and morphology and in rapid synthesis kinetics. Therefore, ultrasonication promotes homogeneous nucleation in very short crystallization periods of time owing the creation, growth and collapse of an acoustic cavitation that leads to very high temperatures (5000-25000 K) and pressures and the possibility for fast heating and cooling processes.¹²⁰⁻¹²³ USAS have been seen as a very good synthetic approach for the preparation of nano-sized MOFs.^{121,124-125}



Figure 1.18 – Schematic representation of a ultrasound equipment.

One-pot synthesis is, probably, the easiest synthetic methodology used for the production of MOFs. One-pot approach is based on the stirring of the reactants (organic ligands and metal centers) at ambient pressure and temperature (being this latter parameter easily altered for higher values using, as for instance, a regular heating plate). This *bench* methodology has gained relevant research interests due to its simplicity and low energy consumption. Additionally, the possibility to prepare MOFs at ambient temperature, during short periods of time with particle size ranging from few nanometers to several hundred of micrometers, boosted in recent years the use of this approach as a strong synthetic alternative.¹²⁶⁻¹³²



Figure 1.19 – Schematic representation of the one-pot synthesis of a MOF produced in our laboratory.

1.3. Properties and Potential Applications of MOFs

Multidimensional MOFs have found potential applications in several and distinct areas due to their unique properties. In the next sub-sections it will be described in more detail some of the properties of MOFs which were investigated during my PhD project: i) porosity; ii) heterogeneous catalytic activity; and iii) luminescence.

1.3.1. Porosity

In opposition that described for other solid-state materials (*e.g.*, active carbons), MOFs are widely known by the close control over their crystalline structures. The quest for novel and functional multidimensional MOFs is an enormous challenge having attracted the interest of several worldwide research groups. Porosity is, undoubtedly, the most desired property for MOF materials with researchers working in this field have been looking for materials: i) capable to store species (*e.g.*, CH₄, H₂); ii) for gas separation processes (as for instance, retention of CO₂ from a mixture of gases); iii) with large pores to allow the interaction between catalytic active sites and some molecules to be transformed; and iv) to accommodate biologically active molecules to be used, as for instance, in drug delivering processes. For that, MOFs should have large and accessible channels without self-penetration, be charged (typically anionic) to allow the ion exchange and be chemically stable when in contact with solvents, mainly water, for their application as functional materials.¹³³ According to IUPAC notation porous materials are classified into several types based on their width of the pore: i) microporous (20 Å or less); ii) mesoporous (in the range of 20-500 Å); and iii) macroporous (pores with sizes larger than

500 Å).¹³⁴ Besides porosity, other important requirement for MOFs is their zeolite-type behavior for reversible exchange of guest chemical species (Figure 1.20).³² Nevertheless, porosity is the basis to occur the zeolitic behavior in MOFs, as for instance, in ion exchange, adsorption and desorption, enantiomer separation or selective catalytic processes.

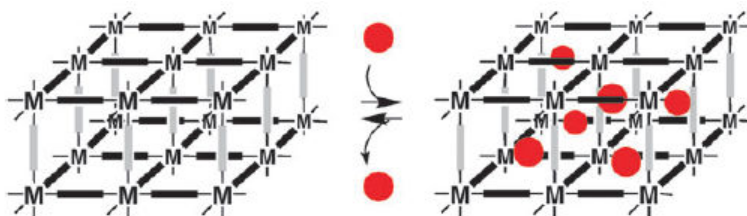


Figure 1.20 – Schematic representation of the zeolite-type behavior which occurs in reversible guest molecules exchange process through the porous network of MOFs. Reproduced from reference 32.

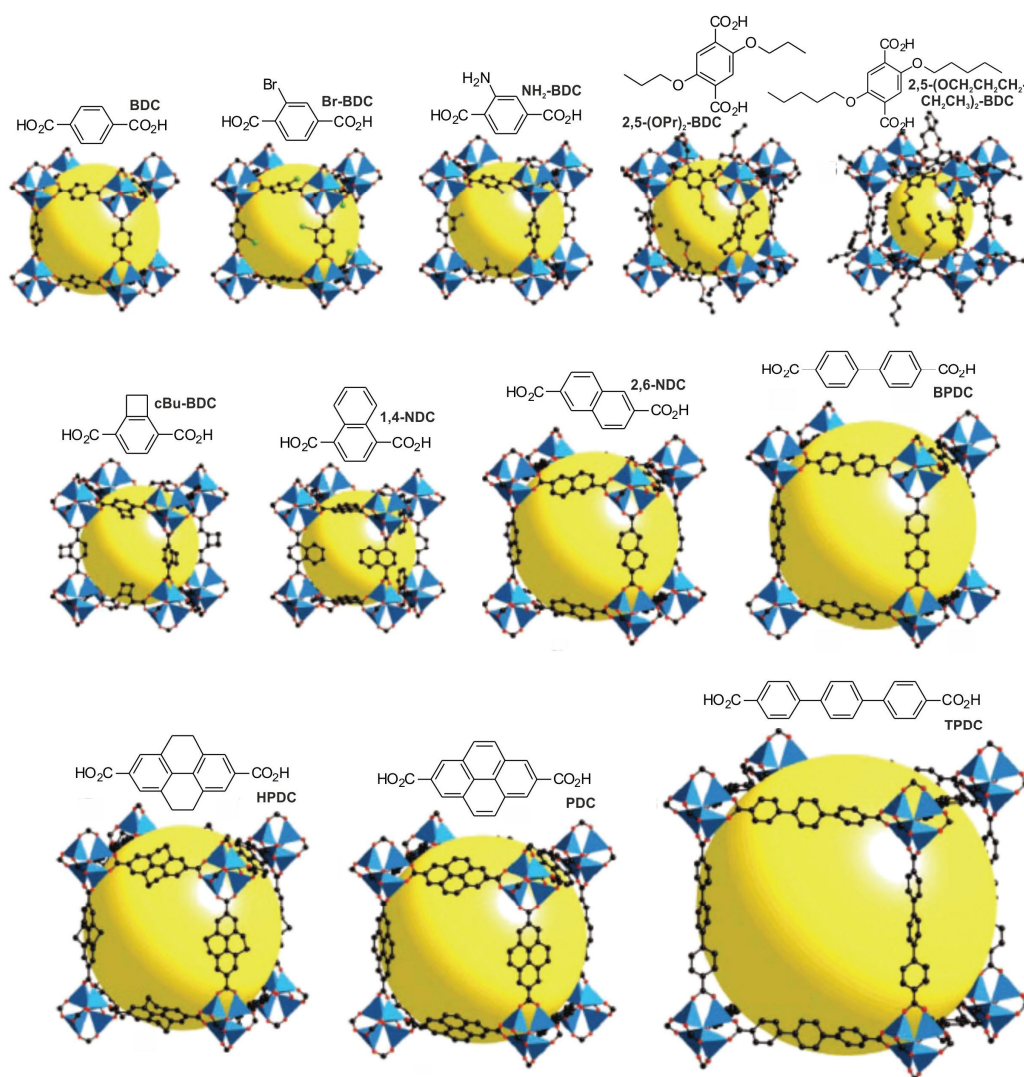


Figure 1.21 – Representation of the crystalline and cubic topology of the IRMOF family and the respective organic ligands. Reproduced from reference 34.

The ability to separate metallic cations using large enough organic ligands to create porosity, while maintaining structural robustness, is a great challenge. Keeping this in mind, scientists have carefully selected, from commercially sources or designed and prepared by themselves, a large number of organic PBUs. Omar Yaghi, very often called as godfather of MOFs, and coworkers published a very interesting work reporting the rational design and reticular synthesis of a family of open-framework MOFs, known as IRMOFs (isoreticular metal-organic frameworks), based on the extension of MOF-5 (Figure 1.21).⁵⁴ For that, it was used Zn^{2+} cations and several organic ligands (the commercially available terephthalic acid (BDC) and other organic linkers which could expand the pores while maintaining the cubic topology of the parent materials).^{34,75}

Some group leaders, as for instance Susumu Kitagawa, Gerard Férey, Joseph Hupp, Jeffrey Long, Martin Schröder, among others, have dedicated enormous effort into the preparation of functional porous MOFs. Having into account the porosity of MOFs, various intriguing porous structures have been reported. Table 1.2 lists known porous MOFs produced since 1999 until 2013. The crystalline structure of such materials are depicted in Figure 1.22.^{45,54,135-168}

Table 1.2 – Known porous MOFs prepared between 1999 and 2013. Information about their porosity (pore diameter (in Å)), organic and inorganic components as well as the reaction conditions used for their preparation are also summarized.

MOF-Like material	Year Published	Pore/Cage Diameter (Å)	Components and reaction conditions
MOF-5	1999	11.2	$Zn(NO_3)_2 \cdot 4H_2O$, benzene-1,4-dicarboxylic acid, DEF, 85 °C, 2 days.
HKUST-1	1999	9.0	$Cu(NO_3)_2 \cdot 2.5H_2O$, benzene-1,3,5-tricarboxylic acid, H_2O , 110 °C, 18 h.
CuSiF ₆ (4,4'-bpy)	2000	8.0	$Cu(BF_4)_2 \cdot 6H_2O$, 4,4'-bipyridine, H_2O /ethylene glycol, ambient temperature, 1 week.
MOF-14	2001	16.0	$Zn(NO_3)_2 \cdot 4H_2O$, pyrene-2,7-dicarboxylic acid, DEF, 85 °C, 2 days.
MOP-1	2001	15.0	$Cu(NO_3)_2 \cdot 2.5H_2O$, benzene-1,3-dicarboxylic acid, DMF/EtOH, 80 °C, 24 h.
ELM-11	2001	layered	$Cu(BF_4)_2 \cdot xH_2O$, 4,4'-bipyridine, CH_3CN /diethyl ether, ambient temperature, several days.
MIL-47	2002	11.0	VCl_3 , terephthalic acid, H_2O , 200 °C, 4 days.
MIL-53	2002	13.0	$Cr(NO_3)_3 \cdot 9H_2O$, terephthalic acid, H_2O , 220 °C, 3 days.

MIL-88	2004	13.9	Fe(III)(CH ₃ COO) ₂ , fumaric acid, H ₂ O/MeOH, 100 °C, 3 days.
MOF-177	2004	14.4	Zn(NO ₃) ₂ ·4H ₂ O, 4,4',4''-benzene-1,3,5-triyltribenzoic acid, DEF, 85 °C, 2 days.
Cr-MIL-100	2004	29.0	metallic chromium, benzene-1,3,5-tricarboxylic acid, H ₂ O, 220 °C, 4 days.
Cr-MIL-101	2005	34.0	Cr(NO ₃) ₃ ·9H ₂ O, terephthalic acid, H ₂ O, 220 °C, 8 h.
Ni-CPO-27	2006	11.0	Ni(II)(CH ₃ COO) ₂ , 2,5-dihydroxyterephthalic acid, THF/H ₂ O, 110 °C, 3 days.
UiO-66	2008	9.0	ZrCl ₄ , terephthalic acid, DMF, 120 °C, 24 h.
ZIF-8	2008	11.6	Zn(NO ₃) ₂ ·4H ₂ O, 2-methylimidazole, DMF, 140 °C, 24 h.
PCN-14	2008	18.5	Cu(NO ₃) ₂ ·2.5H ₂ O, 5,5'-(9,10-anthracenediyl)di-isophthalic acid, THF, ambient temperature, overnight.
DO-MOF	2009	8.8	Zn(NO ₃) ₂ ·6H ₂ O, L1/L2, DMF, 80 °C, 2 days.
Be₁₂(OH)₁₂(BTB)₄	2009	27.0	Be(NO ₃) ₂ , benzene-1,3,5-tricarboxylic acid, DMSO/DMF/H ₂ O, 130 °C, 10 days.
UMCM-2	2009	32.0	Zn(NO ₃) ₂ ·6H ₂ O, 4,4',4''-benzene-1,3,5-triyl-tris(benzoic acid)/thieno[3,2-b]thiophene-2,5-dicarboxylic acid, DMF, 85 °C, 3 days.
NOTT-116	2010	24.0	Cu(NO ₃) ₂ ·3H ₂ O, H ₆ L, DMF/H ₂ O, 85 °C, 18 h.
MOF-200	2010	28.0	Zn(NO ₃) ₂ ·4H ₂ O, 4,4',4''-(benzene-1,3,5-triyl-tris(benzene-4,1-diyl)-tribenzoic acid.
UTSA-20	2011	8.5	Cu(NO ₃) ₂ ·2H ₂ O, 3,3',3'',5,5',5''-benzene-1,3,5-triylhexabenzocic acid, DMF, 65 °C, 48 h.
IRMOF-74-XI	2012	98.0	MgCl ₂ , DOT-XI, DMF, 130 °C, 24 h.
NU-125	2013	24.0	Cu(NO ₃) ₂ ·2.5H ₂ O, LH ₆ , DMF, 80 °C, 24 h.

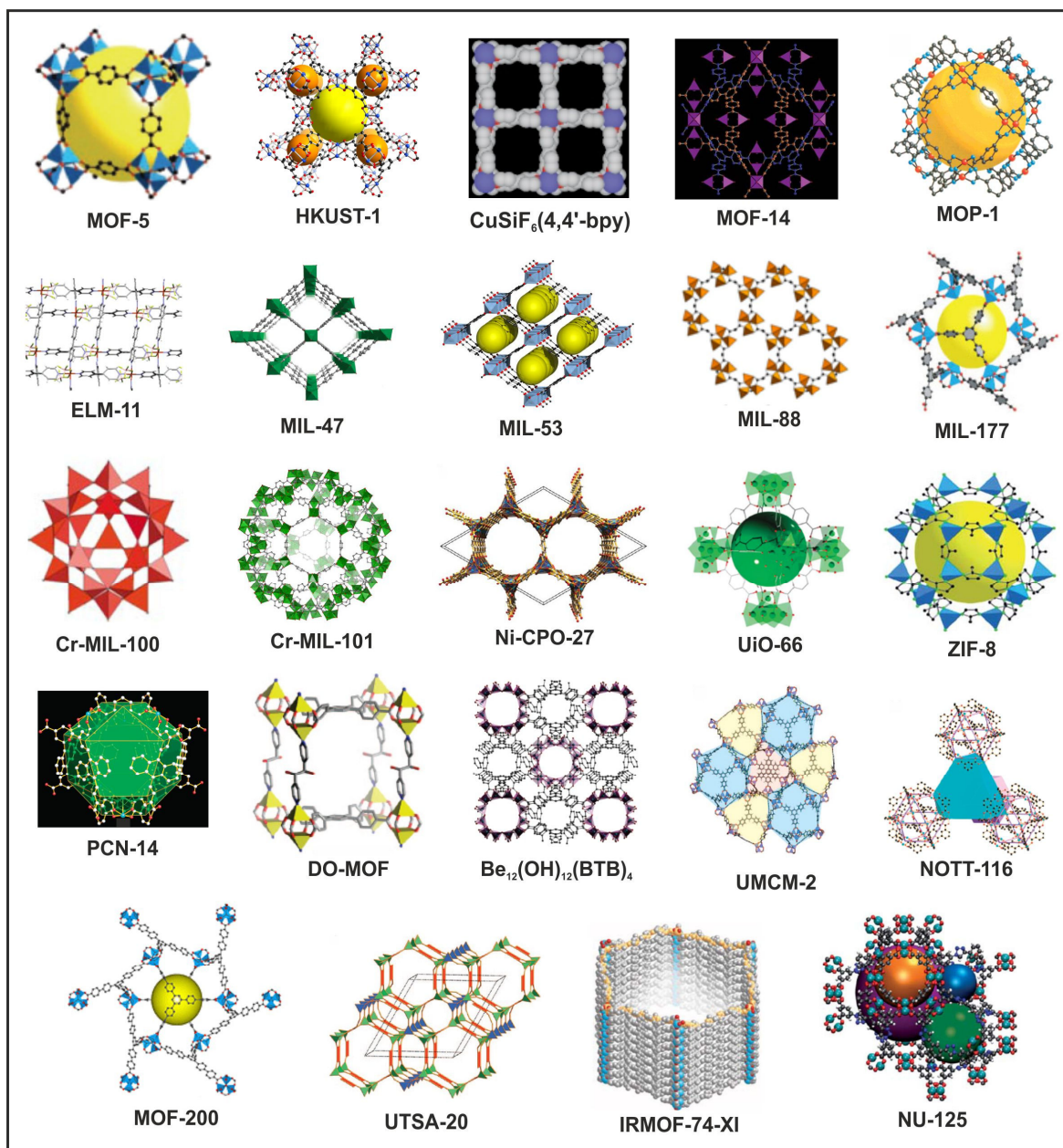


Figure 1.22 – Porous MOFs used toward the quest for materials capable of accommodate/retain chemical species in their pores.

1.3.1.1. Methane and Hydrogen storage

The prime challenge of the 21st century faced by chemists is, undoubtedly, energy storage: i) hydrogen appears as an environmentally friendly energy carrier and clean fuel; and ii) methane, a component of natural gas, seems to be an attractive fuel, since it is very abundant and its burning process is clean. Therefore, both gases are excellent and realistic alternatives to the common fossil fuels. Additionally, the necessity to store and to use them as fuels in a cheap, safe and convenient way is a great requirement and a great challenge.

For that, several research groups have produced various porous MOF materials to facilitate the storage of H₂ and CH₄, as for instance, in automobiles while fulfilling the requirements mentioned above. The U.S. Department of Energy (DOE) published recently the following storage target values: for H₂, at near-ambient temperature (-40 to 85 °C) and amenable pressures (< 100 bar), the target is 9.0 wt% and 81 g L⁻¹ by 2015; for CH₄ is 180 (STP) cm³ cm⁻³ (25 °C, 35 bar) (*Note*: STP means standard temperature and pressure).¹⁶⁹

Zeolites (exhibiting CH₄ uptake below 100 (STP) cm³ cm⁻³) and porous carbon materials (showing a CH₄ uptake in the range of 50-160 (STP) cm³ cm⁻³) possess good capacities in CH₄ adsorption.¹⁷⁰⁻¹⁷¹ Although some porous carbon materials have values of methane uptake close of the DOE target, this type of compounds have, as strong limitation, the increase of their high surface area (\approx 2000 - 3500 m² g⁻¹).¹⁶⁹

One inconvenient to store the natural gas CH₄ is based on its low energy density. This fact leads to a necessity to store it either at very high pressures as well as a liquid to use it in vehicles.¹⁷² Nevertheless, various researchers have reported that some MOFs have exhibited a great capacity to adsorb CH₄. In 2000, Kitagawa *et al.* reported the preparation of [CuSiF₆(4,4'-bpy)] MOF shown as a new potential inorganic-organic hybrid material to adsorb methane.¹³⁸ Since then, dozens of MOF materials have been reported having high capacity to adsorb CH₄, of which it is emphasized: HKUST-1,¹⁷³ MIL-101,¹⁷³ USTA-20,¹⁶⁷ NU-125,¹⁶⁸ NOT-122¹⁷⁴ and PCN-14.¹⁵⁷

Recently Yildirim *et al.* published a very interesting work reporting the capacity of six well-known MOFs (NU-11, NU-125, UTSA-20, PCN-14, Ni-MOF-74 (Ni-CPO-27) and HKUST-1) for CH₄ uptake (Figure 1.23).¹⁷⁵ Investigations performed reveal that these porous materials present very good capacity towards CH₄ adsorption. Although Ni-MOF-74 can adsorb very high CH₄ quantity, the commercially available in gram scale HKUST-1, exceeds any value reported to date. At ambient temperature the volumetric CH₄ uptake is about 230 cm³ cm⁻³ at 35 bar and 270 cm³ cm⁻³ at 65 bar. These values reach the new volumetric target recently set by the DOE, if the packing efficiency loss is ignored. Despite these excellent results, there are other issues to have into account, as for instance, the cost and the chemical stability of these materials.

Because H₂ is a viable energy source to replace common fossil combustibles (one of the most responsible for the greenhouse effect), several research groups have dedicated enormous efforts in order to produce porous materials with capacity to store this gas in a safe and cheap manner and, consequently, use it as energy for vehicles. As for CH₄, the H₂ storage requires specific conditions i) very high pressure gas; ii) liquid hydrogen; iii) intercalating of H₂ in metals; iv) porous materials to adsorb H₂.¹³⁴ MOF materials emerged as a very strong alternative to display the role as containers for H₂ due to their high surface areas.

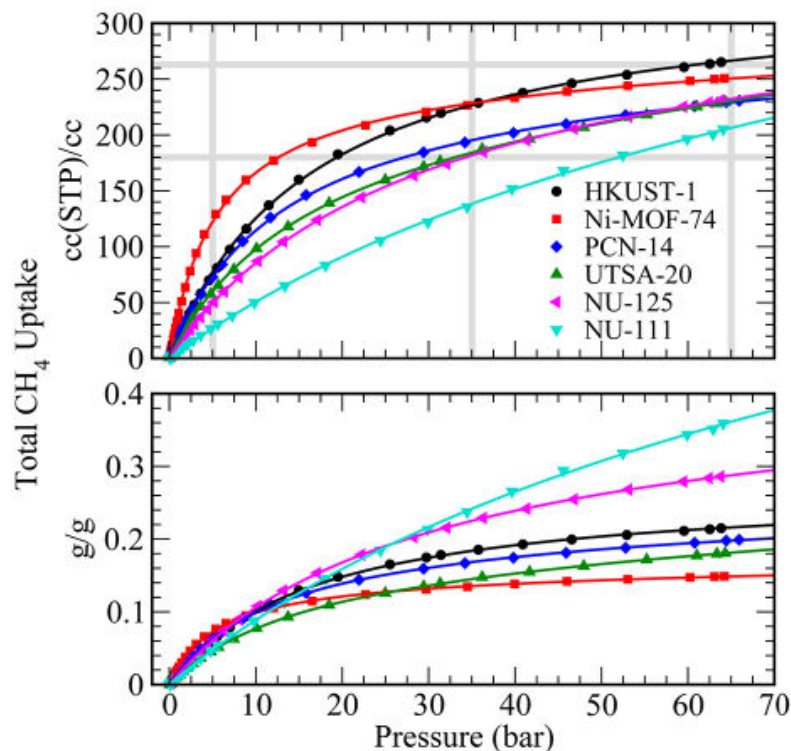


Figure 1.23 – Graphics of the total volumetric (top) and gravimetric (bottom) uptakes for six MOF materials. The old and new DOE targets for volumetric CH₄ uptake are represented as gray lines. The target gravimetric value is 0.5 g of CH₄ per gram of sorbent. Reproduced from reference 175.

The H₂ storage capacity of several known MOFs has been studied. Both small pore sizes (in order to allow the interaction of H₂ with the wall of the MOF materials) and the incorporation of coordinatively unsaturated metal centers (to bind H₂) are two important requirements to retain H₂ molecules. Nevertheless, other strategies have been adopted to improve the ability of porous MOFs to uptake H₂: i) postsynthetic processes;¹⁵⁹ ii) variation in the pore features;^{159,176-178} and iii) use of mixed crystals of known MOF materials prepared in different solvents.¹³⁵

To try understand about the mechanism of H₂ adsorption in the pores of MOFs, Belof *et al.*¹⁷⁹ evaluated how H₂ binds in two indium frameworks: [In₃O(C₈O₄H₄)₃(H₂O)_{1.5}(C₃N₂H₃)(C₃N₂H₄)_{0.5}]·DMF·0.5(CH₃CN) and [In₃O(C₁₆N₂O₈H₆-1.5(H₂O)₃](H₂O)₃(NO₃), initially prepared by Liu and collaborators (Figure 1.24).¹⁸⁰ It was shown that: i) the MOF material, alongside its high surface area, has a huge number of interdigitated pores; ii) open frameworks with low density MOFs allow H₂ adsorption due to H₂-H₂ interactions which occur in the middle of the channels; and iii) the inner surface should have local polar groups in order to promote MOF-H₂ interactions. This last characteristic is directly attributed to the properties of the organic PBUs. To support that, it was proved that the structure of Liu *et al.*¹⁸⁰ containing an organic spacer with a N=N connection provides significant MOF-H₂ interactions.

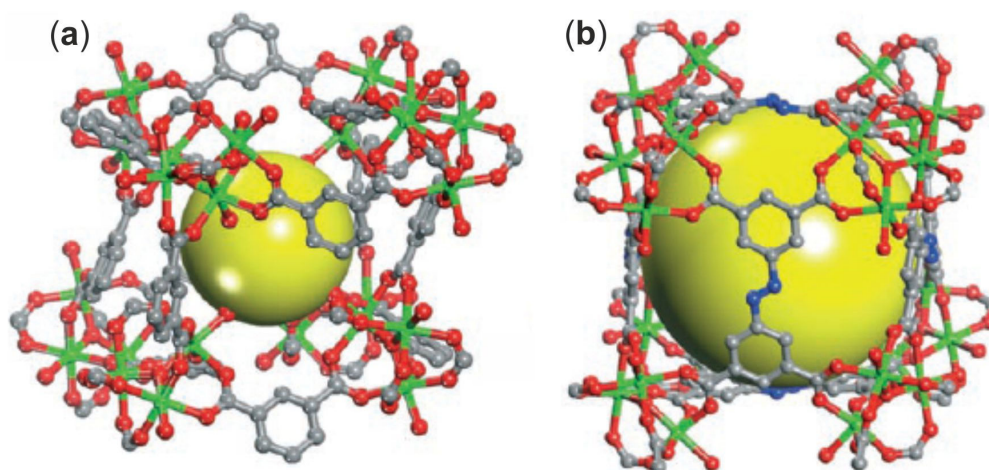


Figure 1.24 – Ball-and-stick representation of the cuboidal cage of $[\text{In}_3\text{O}(\text{C}_8\text{O}_4\text{H}_4)_3(\text{H}_2\text{O})_{1.5}(\text{C}_3\text{N}_2\text{H}_3)(\text{C}_3\text{N}_2\text{H}_4)_{0.5}]\cdot\text{DMF}\cdot 0.5(\text{CH}_3\text{CN})$ (a) and $[\text{In}_3\text{O}(\text{C}_{16}\text{N}_2\text{O}_8\text{H}_6)_{1.5}(\text{H}_2\text{O})_3](\text{H}_2\text{O})_3(\text{NO}_3)$ (b). (C atoms = gray, O atoms = red, H atoms = white, N atoms = blue and In atoms = green). Reproduced from reference 180.

Dietzel and collaborators prepared and investigated the ability of the dehydrated form of the 3D Ni-CPO-27 material towards H_2 adsorption.¹⁴⁹ The porosity of this material was conserved after evacuation (at high temperatures) of the water molecules leading to an increase of its surface area. This process improves the accessibility of H_2 to the unsaturated metal sites. The H_2 uptake capacity of Ni-CPO-27 is of 1.8 wt% at 77 K.

Yaghi's group isolated twelve zeolitic imidazolate frameworks (ZIFs), termed ZIF-1 to -12), based on imidazolate-type organic ligands coordinated to Zn^{2+} or Co^{2+} metal cations.¹⁶⁶ The crystalline structure of these materials consists in the net of seven distinct aluminosilicates zeolites (the tetrahedral Si(Al) and the bridging O element where replaced by Zn^{2+} or Co^{2+} and the imidazolate molecules). H_2 uptake experiments were performed for both ZIF-8 and -11 showing reversible hydrogen behaviour. The H_2 uptake for both materials was similar [$145 \text{ cm}^3\text{g}^{-1}$ STP for ZIF-8 and $154 \text{ cm}^3\text{g}^{-1}$ STP for ZIF-11 (slightly higher due to its higher surface area)]. In high-pressure (up to 80 bar) at 77 K ZIF-8 exhibited $350 \text{ cm}^3\text{g}^{-1}$ STP at 55 bar.

NOTT- n (where $n = 1, 2, 3, \dots$) porous materials, known due to their polyhedral cages with different sizes, have been prepared by the group led by Schröder and their H_2 uptake capacities have been measured. NOTT-112, -116 and -122 produced from the self-assembly of Cu^{2+} cations with different hexacarboxylate organic linkers showed interesting H_2 uptake abilities.^{156,174} Therefore, NOTT-112, -116 and -122 have H_2 uptakes of 2.3 wt%, 1.9 wt% and 2.6 wt%, respectively, at 77 K and 1 bar. Only few materials are able to adsorb amounts of H_2 higher than that observed for NOTT-122 under the above mentioned conditions.¹⁷⁴

In 2009, Mulfort *et al.* published a strategy to improve the H_2 uptake in MOF materials.¹⁵⁹ Their work consists in a post-synthesis procedure in order to convert pendent alcohols moieties to metal alkoxides (Figure 1.25). The as-prepared porous DO-MOF material (having in its structure Zn^{2+} metallic centers and two different organic ligands: a

tetracarboxylate and a bipyridine molecules) was added to a mixture composed of THF, to replace the guest solvent molecules of DMF, and an excess of $\text{Li}^+[\text{O}(\text{CH}_3)_3]^-$ in $\text{CH}_3\text{CN}/\text{THF}$. After that, the H_2 uptake capacity of the as-prepared DO-MOF, as well as the DO-MOF-Li, were investigated and the results suggested that at 77 K (1 atm) the DO-MOF-Li material has a higher H_2 uptake (1.32 wt%) than the original DO-MOF (1.23 wt%).

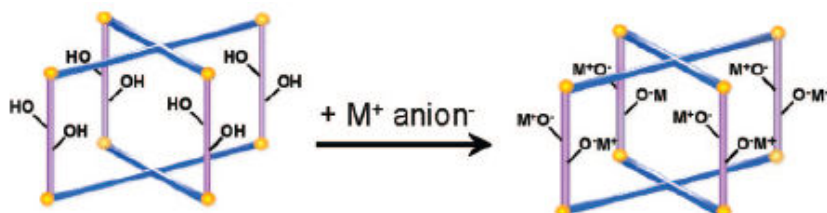


Figure 1.25 – Schematic representation of the formation of metal alkoxides within the porous DO-MOF. Reproduced from reference 159.

1.3.1.2. CO_2 Capture

CO_2 is the major responsible of the greenhouse effect in atmosphere. It is reported that during the last half century the concentration of CO_2 in the atmosphere increased from about 310 to over 380 ppm, being expected to achieve 550 ppm by 2050, even if CO_2 emissions may be stabilized in the next four decades.¹⁸¹⁻¹⁸³ One of the consequences of the CO_2 accumulation in the atmosphere is the global warming. This environmental problem results, mainly, of the high CO_2 emission from the industries and from the combustion of fossil combustibles used in vehicles. Having into account this problem, it is important to develop strategies in order to decrease CO_2 emissions. One was mentioned in the previous topic (*i.e.*, the replacement of common fossil combustibles by environmentally friendly H_2 and CH_4). Another alternative consists in the preparation of porous structures with high affinity to CO_2 and to avoid its release for the atmosphere. The United States DOE established a program envisaging the retention of 90% of CO_2 emissions *via* the post-combustion process allowing an increase in the cost of electricity no more than 35% by 2020.¹⁸³

Porous MOF-based materials have been proposed to help in the resolution of this sever environmental issue. In the last two decades, MOFs have emerged as a new type of functional CO_2 adsorbent materials and a rapid progress and extensive development in the preparation of these materials with high capacity to sequester CO_2 have been observed.^{31,40,44,181} MOF-based material should have some characteristics and requirements towards CO_2 adsorption: i) to be porous with good accessibility to its channels; ii) thermally stable; iii) existence of functional groups (*e.g.*, NH_2 moieties) into the pores to interact with CO_2 ; iv) insertion of metal ions; and v) the presence of open metal sites.¹⁸³ Alongside these mentioned features, the low production cost of MOFs is another important requirement envisaging their industrial availability. The reduction of CO_2 emissions

comprises three main separation procedures, such as separation from fuel gas, power plant combustion flows and natural gas sources.¹⁸⁴

A huge amount of reports have described the ability of MOFs to retain considerable amounts of CO₂ into their channels. Among these are included some well-known structures, such as NOTT-122 (9.0 mmol g⁻¹),¹⁷⁴ HKUST-1 (10.7 mmol g⁻¹),¹⁸⁵ MOF-5 (21.7 mmol g⁻¹),¹⁸⁵ MOF-117 (33.5 mmol g⁻¹),¹⁸⁵ MIL-100(Cr) (18.0 mmol g⁻¹),¹⁸⁶ MIL-101(Cr) (40.0 mmol g⁻¹),¹⁸⁶ NU-100 (46.4 mmol g⁻¹),¹⁸⁷ UMCM-1 (23.5 mmol g⁻¹),¹⁸⁸ MOF-200 (54.5 mmol g⁻¹)¹⁶³ and MOF-210 (54.5 mmol g⁻¹).¹⁶³

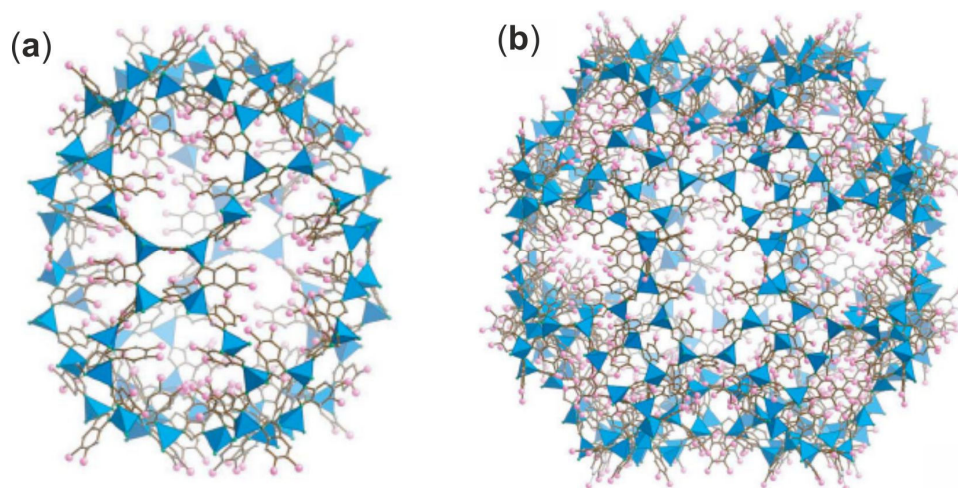


Figure 1.26 – Porous (a) ZIF-95 and (b) ZIF-100. Reproduced from reference 189.

Despite the high affinity of some porous MOF materials toward CO₂, the capacity of these to separate this gas from a mixture of gases is not, very often, represented or investigated. Nevertheless, a considerable number of scientific reports have emerged reporting the selective adsorption of CO₂ over other gases (*i.e.*, N₂, CH₄, O₂ or CO). Thus, this comprises binary (*e.g.*, CO₂/CO, CO₂/N₂ or CO₂/CH₄) and ternary (CO₂/N₂/CH₄, CO₂/N₂/H₂O or CO₂/N₂/O₂) gas mixtures.¹⁸⁹⁻¹⁹⁴ In 2008 Wang *et al.* reported two porous zeolite-type imidazolate frameworks, coined as ZIF-95 and ZIF-100, possessing very complex cages with 264 vertices, and constructed from about 7524 atoms (Figure 1.26).¹⁸⁹ After breakthrough experiments it was reported that ZIF-95 and ZIF-100 have a great ability to selectively adsorb CO₂ from mixtures of CO₂/CH₄, CO₂/CO and CO₂/N₂ (50:50 v/v). The average selectivities of CO₂ over CH₄, CO and N₂ were of 4.3 : 1, 11.4 : 1 and 18.0 : 1, respectively, for ZIF-95 and of 5.9 : 1, 17.3 : 1 and 25 : 1, respectively, for ZIF-100. The research group led by Yaghi employed the known porous Mg-MOF-74 material in CO₂ separation processes.^{44,190} Therefore, after breakthrough experiments where it was used a mixture of CH₄/CO₂ (4:1) it was observed that CO₂ is substantially more adsorbed than CH₄ with a dynamic capacity of 8.9 wt% CO₂ uptake (Figure 1.27). It was also reported that CO₂ can be easily released from the Mg-MOF-74 structure using a significant lower temperature at 80 °C.

Although some MOF materials have very interesting capacity for the sequestration of CO₂, enormous efforts have been done to enhance it and, consequently, to improve the selective adsorption of CO₂ over other gases. A number of strategies have been developed: i) insertion of pendant moieties, as for instance, –NH₂ or –OH groups in the organic PBUs;¹⁹⁵⁻¹⁹⁶ ii) preparation of MOFs with organic ligands derived of nitrogen-containing heterocycles;^{174,197} iii) interpenetration and catenation;¹⁹⁸⁻¹⁹⁹ and iv) exposed metal cation sites.²⁰⁰

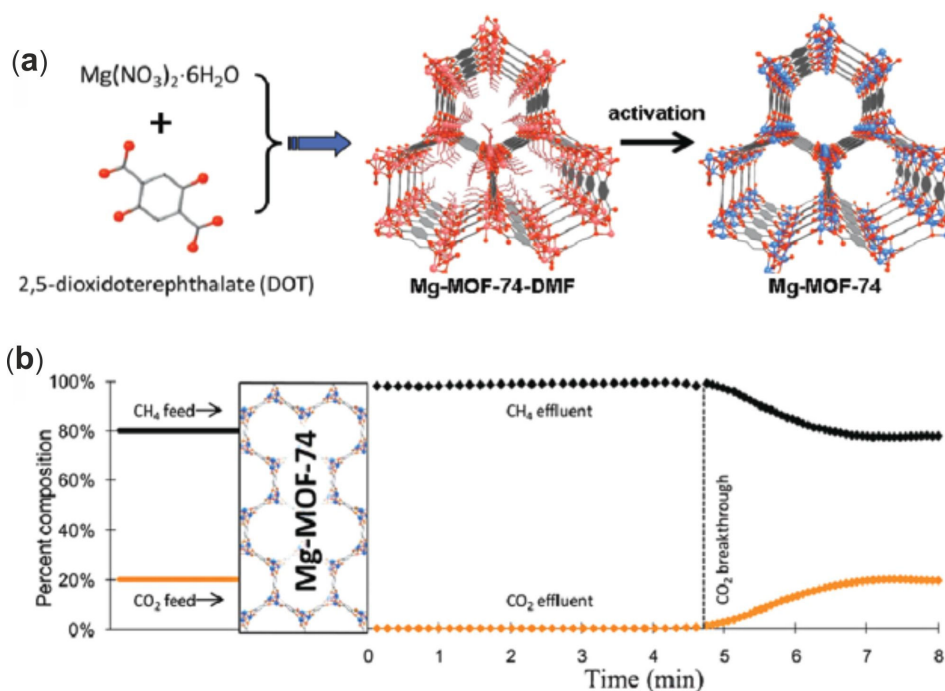


Figure 1.27 – (a) Schematic representation of the preparation and structure of the as-prepared Mg-MOF-74-DMF and the activated Mg-MOF-74 materials (C atoms = gray, O atoms = red, terminal ligands and 6-coordinated Mg atoms = pink and 5-coordinated Mg atoms = blue). (b) Breakthrough curves resulting of the separation process using a mixture of CH₄/CO₂ (4:1). Reproduced from reference 190.

1.3.2. Heterogeneous catalysis

Catalysis is a research area with great and continuous importance aiming at the conversion of several chemical species, some of them dangerous to humans and the environment, into inoffensive products and in another cases desired molecules for applications. Alongside with the quest for porosity, application of multi-dimensional MOFs in heterogeneous catalysis has been intensely investigated. Zeolites are the most common materials used in industrial heterogeneous catalysis. The preparation of catalytic-active MOFs does not aim to replace zeolite materials, but, on the contrary, to fill some gaps never achieved for this type of materials, as for instance, in enantioselective heterogeneous catalysis.

The recyclability of a heterogeneous catalyst is one of the main objectives of researchers working in catalytic processes. Additionally, this can be called as an eco-friendly procedure (recycle the catalyst without loss of activity). Because several MOFs have been shown to be good stable solid materials in many organic solvents, their recovering after catalytic essays can be easily performed. For a MOF to have excellent catalytic behavior it is absolutely imperative the presence of active catalytically sites from the metal or organic molecules (Figure 1.28).^{22,25} Therefore, the capacity to insert functional groups into porous of MOFs and the presence of well-defined channels (allowing size and shape selectivity) make these materials excellent candidates for heterogeneous catalysis.²⁰¹ A good MOF catalyst should have: i) functionalized organic ligands to display the role, as for instance, Brönsted acids; ii) coordinatively unsaturated metal sites; and iii) the potentiality to incorporate metal complexes into the organic ligand and pores/channels.³²

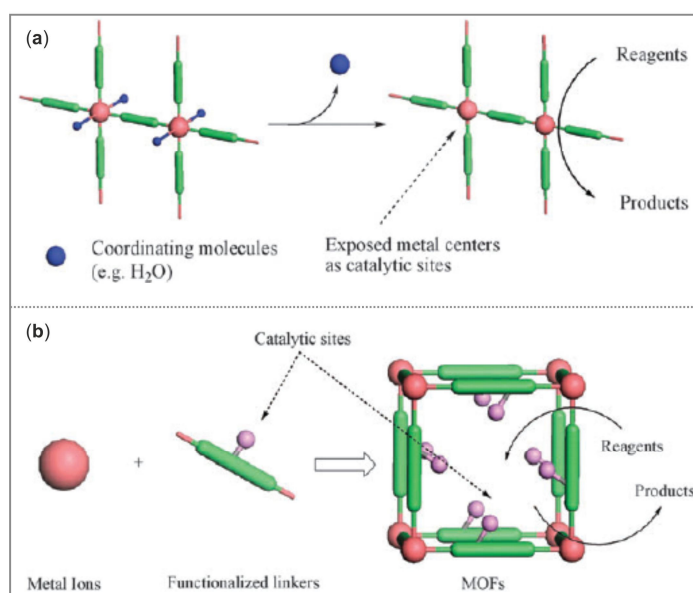


Figure 1.28 – Schematic representation of coordinatively unsaturated metal (a) and functionalized bridging organic ligands (b) as catalytic active sites. Reproduced from reference 22.

How is it possible to prepare organic PBUs which may introduce catalytic behavior in MOFs? Some strategies have been reported to achieve this goal, of which the most important are: i) immobilization of coordinative unsaturated open metal sites and ii) the inclusion of functional organic groups able to improve recognition. The advantage of the latter strategy is that, for example, a base-type catalyst can be created because there are several organic functional groups which can serve as active base sites.⁸⁹

Hasegawa *et al.* synthesized an organic ligand, termed as (1,3,5-benzene tricarboxylic acid tris[*N*-(4-pyridyl)amide]) (4-btapa), with three amide groups as guest interaction sites and three pyridyl groups to coordinate to metallic centers. The self-assembly of 4-btapa with Cd^{2+} cations gave rise to a 3D porous network, formulated as

$\{[\text{Cd}(4\text{-btapa})_2(\text{NO}_3)_2] \cdot 6\text{H}_2\text{O} \cdot 2\text{DMF}\}_n$. This heterogeneous catalyst was used in the Knoevenagel condensation between benzaldehyde with active methylene compounds (malononitrile, ethyl cyanoacetate and cyano-acetic acid *tert*-butyl ester). Obtained data demonstrated the selective heterogeneous base catalytic properties of the MOF-based compound, which depends on the size of the reactants: the malononitrile was a very good substrate, producing 98% conversion of the adduct, while the other substrates reacted negligibly (Figure 1.29).

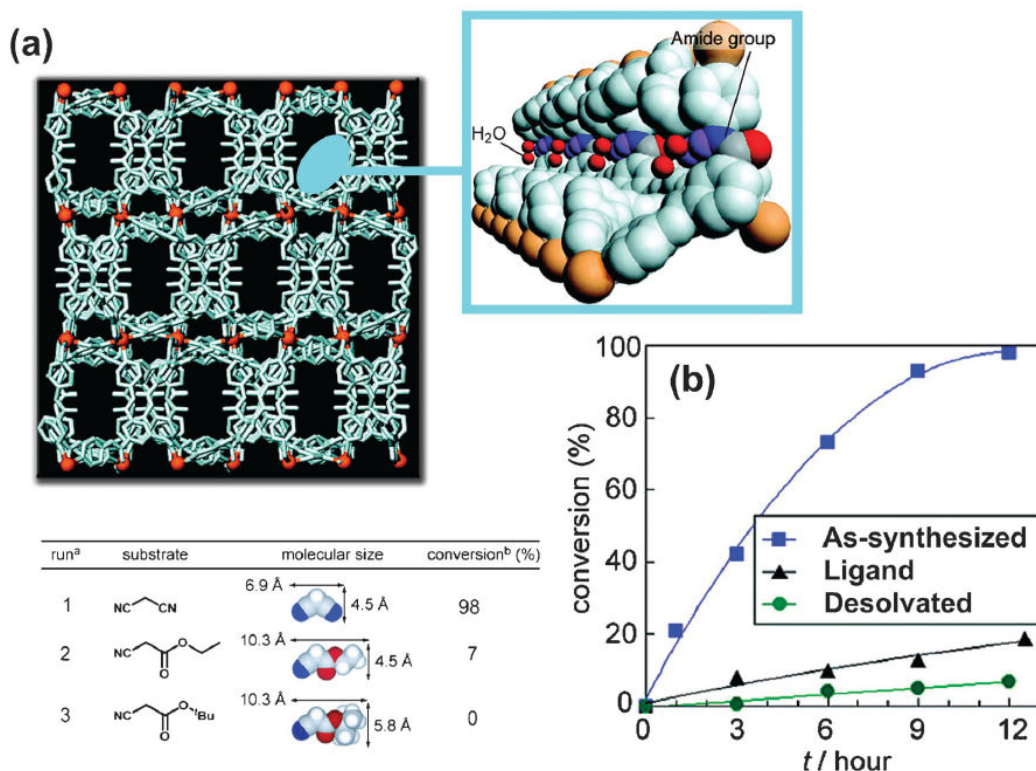
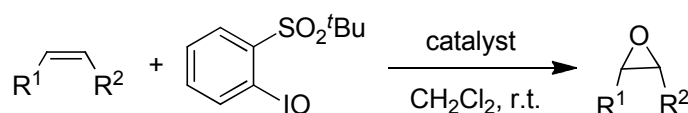


Figure 1.29 – (a) Crystal packing of $\{[\text{Cd}(4\text{-btapa})_2(\text{NO}_3)_2] \cdot 6\text{H}_2\text{O} \cdot 2\text{DMF}\}_n$ showing their zigzag channels. (top right) View of the ordered amide groups on the channels surface interacting with water molecules *via* hydrogen bonds. Cd atoms = light brown, O atoms = red, N atoms = blue, C atoms = gray and H atoms = purple. (b) Conversion for the Knoevenagel condensation reaction of benzaldehyde with malononitrile catalyzed by the as-synthesized (blue squares) and desolvated (green circles) materials and organic ligand (black triangles). (bottom left) Table summarizing the results of the Knoevenagel condensation reaction for the various substrates. Reproduced from reference 89.

In 2010 Lin's group reported the preparation of a family of five isorecticular chiral MOFs, termed as CMOFs 1-5, to be employed in the asymmetric epoxidation of a variety of unfunctionalized alkenes.²⁰² The CMOF materials were prepared from the reaction of elongated dicarboxylate chiral Mn-Salen catalytic subunits with $\text{Zn}(\text{NO}_3)_2 \cdot 6\text{H}_2\text{O}$ under solvothermal conditions. Catalytic studies involved the use of 1*H*-indene (as substrate), and 2-(*tert*-butylsulfonyl)iodosylbenzene (as oxidant) in the presence of the catalysts CMOFs 1-5 (Scheme 1.1).

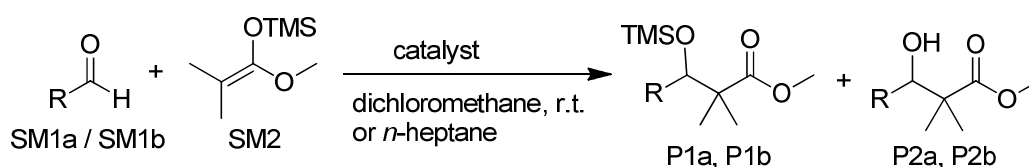


Scheme 1.1 – Schematic representation of the enantioselective epoxidation of alkenes using CMOFs 1-5 as catalysts. R¹ and R² represent different alkane molecules (see reference 202 for further details).

The results suggest that the CMOFs 1-5 exhibit to be highly effective catalysts for asymmetric epoxidation of alkenes. The Mn³⁺ ions, belonging to the dicarboxylate chiral Mn-Salen subunits, display a fundamental role in the catalytic process. The catalyst CMOF-4 revealed high capacity to afford one of the desired epoxidation products in 90% conversion and 92% ee (enantiomeric excess). Additionally, this family of materials showed good reusability.

Two years ago Gedrich *et al.* reported the synthesis of two chiral MOFs with wide-open pores (> 30 Å).²⁰³ These materials were prepared from reactive mixtures composed of large chiral tripodal carboxylate-based ligands (termed as H₃ChirBTB-1 and -2, with 4,4',4''-benzene-1,3,5-triyltribenzoate (BTB) backbones decorated with three chiral oxazolidinone substituents) and Zn(NO₃)₂·4H₂O in DEF. The resulting porous MOF materials, formulated as [Zn₃(ChirBTB-1)₂] and [Zn₃(ChirBTB-2)₂], were used as catalysts in Mukaiyama aldol reactions with 1-methoxy-1-(trimethylsilyloxy)-2-methyl-1-propene and benzaldehyde or 1-naphthaldehyde (Scheme 1.2).

Both porous MOFs showed to be highly active Lewis acid catalysts exhibiting considerable enantioselectivity in the Mukaiyama aldol reactions. Table 1.3 lists the results obtaining during the catalytic tests.



SM1a, P1a, P2a: R = Ph
SM1b, P1b, P2b: R = 1-naphthyl

Scheme 1.2 – Schematic representation of the Mukaiyama aldol reactions with 1-methoxy-1-(trimethylsilyloxy)-2-methyl-1-propene (SM2) and benzaldehyde (SM1a) or 1-naphthaldehyde (SM1b).

To enhance the catalytic performance of MOFs, researchers have employed two strategies: i) postsynthetic modifications into the porous surface of MOFs; and ii) encapsulation of nanoparticles using the porous MOF structure as host matrices to support the catalysis.^{31,204} Therefore, and besides the catalytic reactions exposed above, MOFs have been involved in several other catalytic transformations, of which we emphasize:

- Aerobic oxidation of alcohols;²⁰⁵
- C-C coupling reactions;²⁰⁶

- CO to CO₂ oxidation;²⁰⁷
- Cyanosilylation of aldehydes;²⁰⁸
- Hydrogenation of aromatic ketones;²⁰⁹
- Ring-opening reaction of epoxides.²¹⁰

Table 1.3 – Results of the Mukaiyama aldol reactions using dichloromethane or *n*-heptane as solvent. Reproduced from reference 203.

Entry	Aldehyde	MOF	Reaction time	Yield (%)	<i>ee</i> value (%)
dichloromethane					
1	SM1a	[Zn ₃ (ChirBTB-1) ₂]	48 h	83 ^[a]	0
2	SM1b	“	17 d	31 ^[a]	40 ^[b,c]
3	SM1b	“	17 d	22 ^[a]	10 ^[b,d]
4	SM1a	[Zn ₃ (ChirBTB-2) ₂]	13 d	66 ^[a]	8 ^[e]
5	SM1a	“	13 d	54 ^[a]	8 ^[e,d]
6	SM1b	“	14 d	0 ^[a]	-
<i>n</i>-heptane					
7	SM1a	[Zn ₃ (ChirBTB-1) ₂]	48 h	77 (98) ^[f]	9 ^[e]
8	SM1b	“	48 h	77 ^[f]	16 ^[b]
			7 d	84 ^[f]	
9	SM1a	[Zn ₃ (ChirBTB-1) ₂]	48 h	43 (82) ^[f]	6 ^[e]
			12 d	74 (94) ^[f]	

Isolated yields of P1a after determined by [a] column chromatography and [b] by chiral HPLC. [c] However, a different batch of material gave a 10 % *ee* in the first cycle. [d] Second cycle. [e] Determined by chiral GC. [f] Yields of P1a determined during kinetic measurements; yields of P1a + P2a are represented in parentheses.

1.3.3. Luminescence

The luminescence properties of MOFs have attracted the interest of many groups.^{24,33-34,103,211} Luminescence is normally used to describe the process where light is produced by the adsorption of energy,³⁴ and contains two basic forms: i) fluorescence which is spin-allowed, possessing typical lifetimes in the range from nano- to microseconds; and ii) phosphorescence being spin-forbidden and having lifetimes which can reach several seconds.²⁴ The luminescent properties comprise the following features:³⁴

- luminescence spectra containing the fluorescence intensity as a function of a wavelength;

- quantum yield which is traduced as the efficiency of the fluorescence process. This parameter is defined as the ratio of the number of emitted photons come from the fluorescence process in relation of the photons absorbed;
- lifetime that is related with the average time in which the molecule stays in its excited state before emitting photon. This parameter is determined as being inversely proportional to the sum rate constants of radiative and non-radiative processes.

The possibility to simultaneously fine-tune the organic and inorganic components allows the modification of the optical properties of the final materials. Light emission may appear either from individual organic ligands or metallic centers, or from materials resulting from their interconnection. Thus, the luminescent properties of a given MOF may arise from: i) organic ligand-based luminescence, including both the phenomena ligand-to-metal charge transfer (LMCT) and metal-to-ligand charge transfer (MLCT); ii) adsorbate-based emission and sensitization, the so called *antenna effect*; iii) surface functionalization; and iv) scintillation.²⁴ In Figure 1.30 are depicted the luminescent phenomena observed in a MOF-based material. MOFs, possessing permanent porosity, may unveil some luminescent features which are not possible to observe in other materials:

- The capacity of MOF materials to accumulate molecules (as for instance, solvent molecules) into their channels, allowing a close proximity between these and the luminescent centers, may affect the overall emission properties;
- The existence of rigidity in a MOF material constrains the organic ligands in some way that may lead to an increase of the fluorescence lifetimes and quantum efficiency. This feature is not observed for free complexes in solution;
- Because MOFs exist solely, their surfaces can be functionalized in solid state. This leads to new properties with potential for different optical applications.

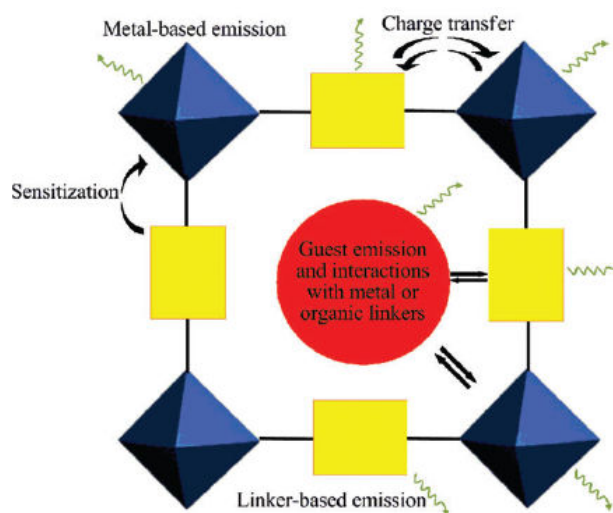


Figure 1.30 – Representation of the various luminescent phenomena observed in a MOF. The organic linkers are represented as yellow rectangles, the metallic centers as blue octahedra and the guest molecules as red circle. Reproduced from reference 24.

Regarding the organic ligands, these have luminescent groups, being normally conjugated organic compounds (*i.e.*, naphthalene, pyridine, pyrene, anthracene, stilbene), which absorb in the UV and visible region and the emission may occur directly from the molecule or involving a charge transfer process with coordinated metal ions. The metallic centers, as for instance, transition metals with unpaired electrons may be efficient quenchers. However, MOFs constructed from N- or O-donor ligands and d^{10} -elements, as for instance Zn^{II} or Cd^{II} , can exhibit luminescence. Metal-centered luminescence is seen in MOFs containing lanthanide ions, Ln(III), as nodes. The proximity between a fluorophore organic ligand and a Ln(III) ion can lead to the *antenna effect* (Figure 1.31) increasing the luminescence intensity.³²⁻³³

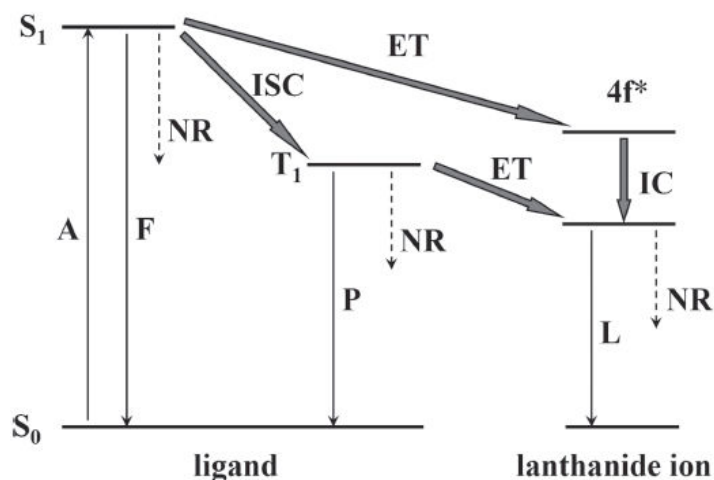


Figure 1.31 – Schematic representation of the photophysical processes involved in the *antenna effect*. Legend: A = absorption, F = fluorescence, P = phosphorescence, L = lanthanide-centered luminescence, ISC = intersystem crossing, ET = energy transfer, IC = internal conversion, S = singlet, T = triplet. Plain and dotted arrows are attributed to radiative and non-radiative (NR) transitions. Reproduced from reference 34.

Luminescent MOFs have been constructed from the self-assembly of distinct organic linkers and metallic centers (lanthanides and transition metals). Some have potential applications as small-molecules and ions sensors, pH sensors, luminescent labels for fluoro-immunoassays, high-technology optics, among others.^{24,34,90,211-219}

In 2011 the research group led by Kitagawa reported a remarkable example of a luminescent MOF. This material consists in a porous framework, $[Zn_2(bdc)_2(dpNDI)]_n$,⁹⁰ prepared from a mixture composed of benzene-1,4-dicarboxylic acid (H_2bdc) and N,N' -di(4-pyridyl)-1,4,5,8-naphthalenediimide ($dpNDI$) organic linkers and $Zn(NO_3)_2 \cdot 6H_2O$ in DMF, under solvothermal conditions. Even though the new $dpNDI$ linker predictably has a low fluorescence quantum yield, the authors deduced that this molecule could strongly interact with aromatic volatile organic compounds (VOC). The obtained materials exhibited a strong color change in the visible region of the spectrum which was a consequence of the adsorbed aromatic VOC. The incorporation of benzene, toluene, xylene, anisole and iodobenzene into the porous framework of desolvated

$[\text{Zn}_2(\text{bdc})_2(\text{dpNDI})]_n$, led to new products (*i.e.*, $[\text{Zn}_2(\text{bdc})_2(\text{dpNDI})]_n > \text{VOC}$) displaying intense blue, cyan, green, yellow, and red photoluminescence, respectively (Figure 1.32). It was that this chemoresponse was of a non-linear nature owing the coupling of structural transformation with the amount of adsorbed guest molecules.

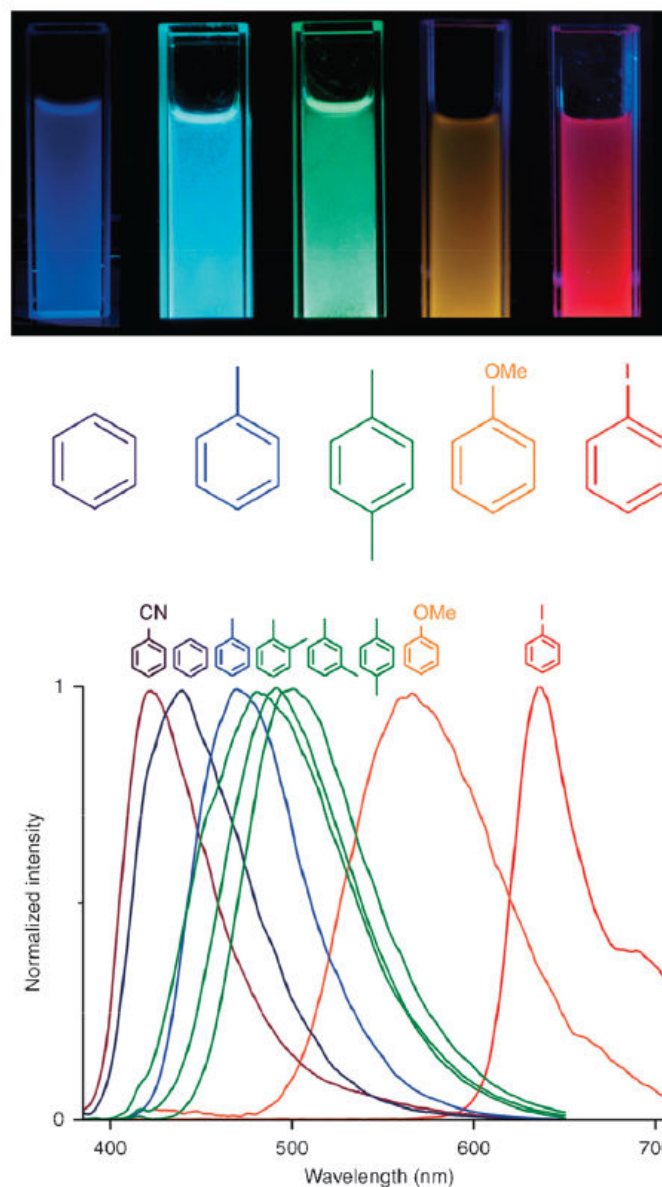


Figure 1.32 – (*top*) luminescence of the powdered $[\text{Zn}_2(\text{bdc})_2(\text{dpNDI})]_n$ material suspended in the aromatic VOC liquids, with their structures below, after excitation at 365 nm using a commercial ultraviolet lamp. (*bottom*) Collected normalized spectra of the $[\text{Zn}_2(\text{bdc})_2(\text{dpNDI})]_n > \text{VOC}$ compounds excited at 370 nm. Reproduced from the reference 33.

Taking advantage of the luminescence emitted by lanthanide ions, Li *et al.*²¹⁴ reported the preparation of a new luminescent lanthanide-based MOF exhibiting efficient turn-on generated by solvent vapor with excellent selectivity for DMF. The basis for this work addressed the fact that serious health concerns are associated with DMF exposure

due to both skin contact and inhalation in several industries responsible for the production of synthetic fibers, coatings, films and leather tanning. Studies show that the contact with DMF may be related with hepatotoxicity and carcinogenesis issues. Thus, a reactive mixture containing $\text{Eu}(\text{NO}_3)_3$ and the 2',5'-bis(methoxymethyl)-[1,1':4',1''-terphenyl]-4,4''-dicarboxylic acid (H_2L) in DMF/ H_2O (4:1 v/v) at 80 °C for 3 days was prepared. The new luminescent MOF was formulated as $[\text{Eu}_2(\text{L})_3(\text{H}_2\text{O})_4]\cdot 3\text{DMF}$ (Figure 1.33a). In order to replace the DMF guest molecules by H_2O , $[\text{Eu}_2(\text{L})_3(\text{H}_2\text{O})_4]\cdot 3\text{DMF}$ was immersed in distilled water for three days giving rise to a water-exchanged MOF. The sensing ability of the new water-exchanged material was investigated for several solvents (*e.g.*, acetone, benzene, dichloromethane, DMF, ethanol, hexane, THF, among others). After incubation of the material for 24 h under a range of solvent vapors, the luminescent response of the water-exchanged MOF was measured. Results suggested that the MOF material displays a superior turn-on after DMF vapor exposure, being the luminescence enhanced more than eight times Figure (1.33b).

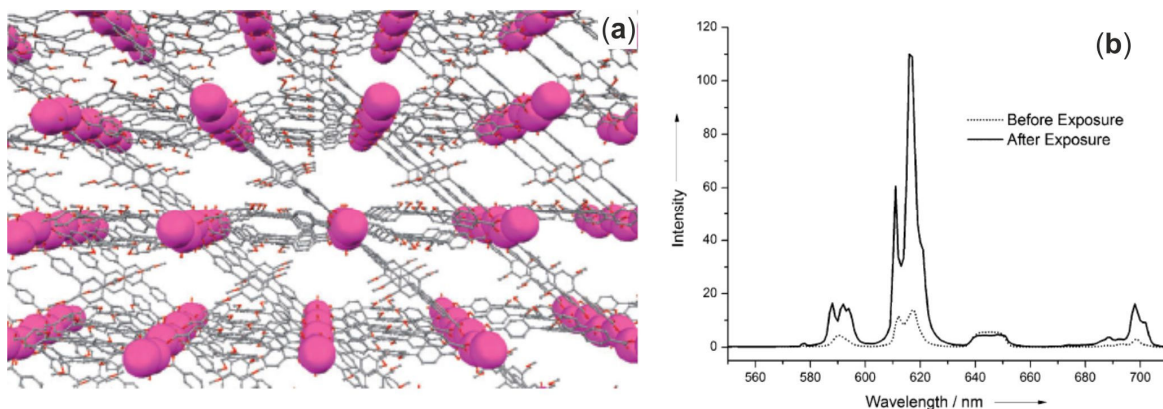


Figure 1.33 – (a) View of the 1D open channels of $[\text{Eu}_2(\text{L})_3(\text{H}_2\text{O})_4]\cdot 3\text{DMF}$ material. C atoms = gray, O atoms = red and Eu atoms = pink spheres. (b) Emission spectra of the water-exchange MOF before and after DMF vapor exposure.

1.4. Phosphonate-Based MOFs

The choice of organic linkers for the preparation of multidimensional MOFs is an important step and, undoubtedly, an enormous challenge. Organic PBUs may be obtained from the various commercially available sources or designed and prepared by each research group. In this section it will be presented examples of phosphonate-based organic linkers of both types. Particularly attention will be given to those designed and synthesized by the research groups for the preparation of functional and multidimensional MOFs.

In Figure 1.34 are represented some examples of commercially available organic ligands (multipodal aromatic, aliphatic, rigid or flexible phosphonate-based molecules) that have been used in the preparation of multidimensional MOFs.

In the literature, it is possible to see that phosphonate-based MOFs contain, essentially, transition metals and lanthanides in their structures.^{231,234-236} The self-assembly of MOFs combining phosphonates with lanthanides seems to be a good choice, because the large number of O-donor atoms present in the organic linker fills the requirement of lanthanides which can exhibit high coordination number. This fact may lead to the formation of unusual and different architectures to those of the transition metals. In addition, the photoluminescent properties of lanthanides make them highly attractive for the synthesis of functional MOFs.^{232,237}

The preparation of phosphonate-based MOFs requires the adjustment of many synthetic variables: phosphonate and metal source, solvent, metal:P molar ratio, concentration, pH, and, very important, reaction time and temperature. Therefore, the variation of these reaction parameters displays a very relevant role in the final structure of MOFs.²²⁹

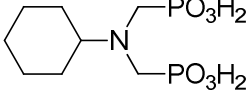

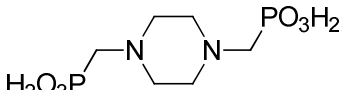
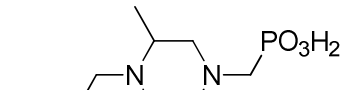
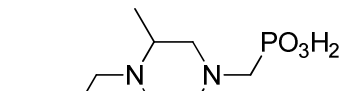
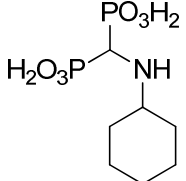
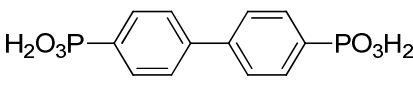
Due to the properties of the multifunctional phosphonate-based MOFs, these materials have potentiality to be applied in distinct fields, such as gas storage and separation, ion exchange, heterogeneous catalysis and as optical sensors.

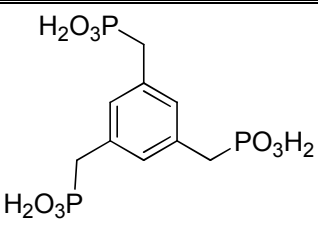
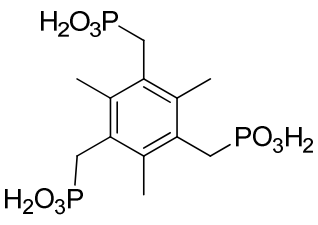
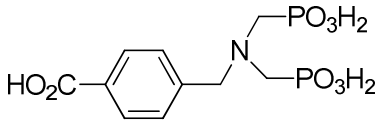
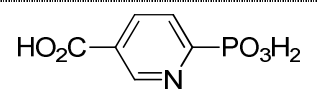
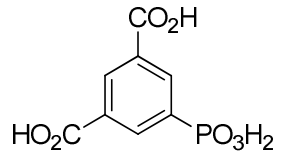
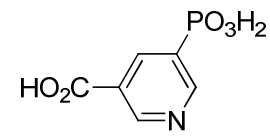
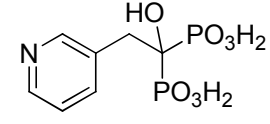
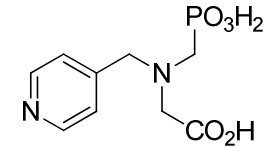
1.4.2. Examples of Functional MOFs Prepared from Phosphonate-Based Organic Ligands

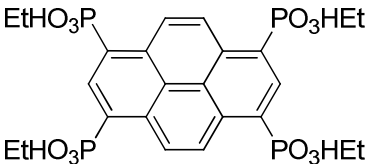
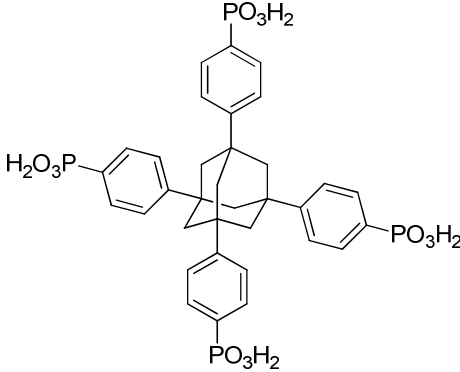
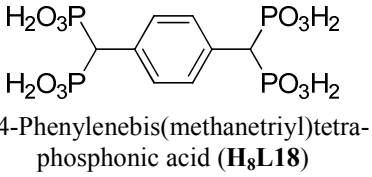
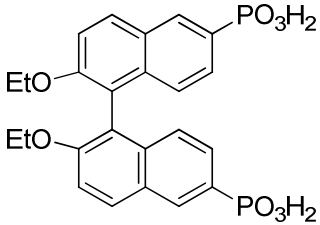
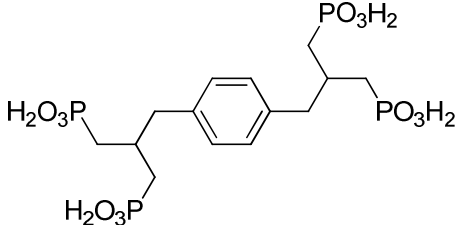
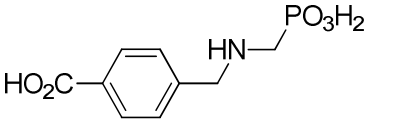
In section 1.3 it was described some properties and potential applications of multidimensional MOFs prepared from carboxylates and N-donor organic ligands. Nevertheless, any example of phosphonate-based MOFs was not mentioned. The research group in which I was working has dedicated enormous efforts in the preparation of functional MOFs containing phosphonate organic ligands and lanthanide ions. In the last years I have been interested in the preparation of MOFs using lanthanides as metallic centers and phosphonate organic linkers. These molecules were thought in order to envisage the final structure (1D, 2D, 3D, dense or porous) and properties (*i.e.*, catalytic behavior, photoluminescence and adsorption) of the resulting MOF materials.

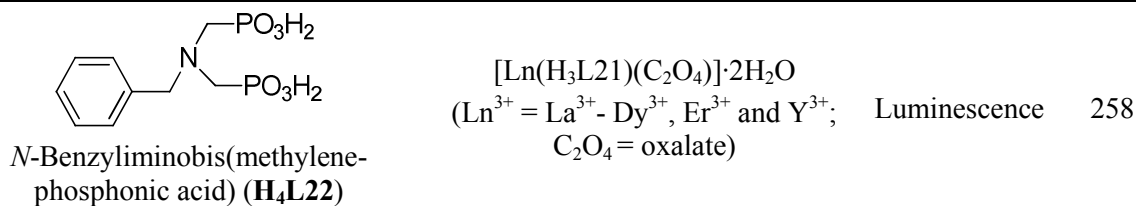
In this subsection, several examples of designed and prepared, by worldwide research groups, phosphonate-based molecules will be listed as well as the corresponding MOFs. Additionally, the synthesis of few examples of organic linkers, phosphonate-based-MOFs and their properties will be described in more detail. Table 1.3 lists several examples of phosphonate-based organic linkers as well as the MOFs prepared using these molecules and their properties.

Table 1.4 – Examples of phosphonate-based ligands designed and prepared by several research groups. MOF materials prepared using these linkers, respective properties and references.

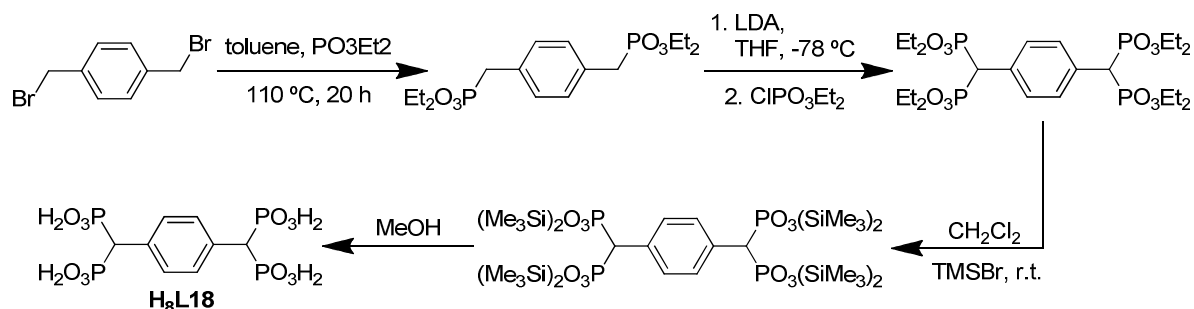
Organic ligands	MOFs	Properties	[Ref]
 ((cyclohexylazanediy)bis(methylene)di-phosphonic acid (H₄L1)	$[\text{Cd}_{0.25}(\text{L1})(\text{H}_2\text{O})_2\text{F}] \cdot \text{H}_2\text{O}$ $[\text{Cd}_{3.5}(\text{HL1})(\text{OP1})_2]$ $[\text{Sn}_3\text{O}(\text{L1})]$	Luminescence	238
 aminomethylphosphonic acid (H₄L2)	$[\text{Zn}(\text{L2})\text{Cl}]$ $[\text{Cd}(\text{L2})(\text{NO}_3)]$ $\{[\text{Hg}_2(\text{L2})_2](\text{H}_2\text{O})_2(\text{NO}_3)\}$ $\{[\text{Pb}(\text{L2})](\text{NO}_3)\}$ $\{[\text{Ag}_6(\text{L2})_4](\text{CF}_3\text{SO}_3)_2(\text{H}_2\text{O})_2\}$ $\{[\text{Ag}_3(\text{L2})_2](\text{NO}_3)(\text{H}_2\text{O})\}$ $[\text{Ag}(\text{L2})\text{Cu}_2(\text{NO}_3)]$	-	239
 <i>N,N'</i> -piperazinebis(methylenephosphonic acid) (H₄L3)	$[\text{Ln}(\text{L3})] \cdot 4\text{H}_2\text{O}$ $(\text{Ln}^{3+} = \text{La}^{3+}, \text{Ce}^{3+} \text{ and } \text{Nd}^{3+})$ $[\text{Ln}_2(\text{L3})(\text{H}_2\text{O})] \cdot x\text{H}_2\text{O}$ $(\text{Ln}^{3+} = \text{La}^{3+} \text{ and } \text{Ce}^{3+})$ $[\text{Ni}_2(\text{L3})(\text{H}_2\text{O})_2] \cdot 5.4\text{H}_2\text{O}$ $[\text{Ni}_2(\text{L3})] \cdot x\text{H}_2\text{O} (x = 8, 2 \text{ or } 0)$	Gas adsorption	233 240 241
 2-methyl- <i>N,N'</i> -piperazinebis(methylenephosphonic acid) (H₄L4)	$[\text{Ln}(\text{HL4})] \cdot x\text{H}_2\text{O}$ $(\text{Ln} = \text{Ce}^{3+} \text{ and } \text{Nd}^{3+})$	-	240 241
 2,5-dimethyl- <i>N,N'</i> -piperazinebis(methylene-phosphonic acid) (H₄L5)	$[\text{Ln}(\text{L5})] \cdot 4\text{H}_2\text{O}$ $(\text{Ln}^{3+} = \text{La}^{3+}, \text{Ce}^{3+} \text{ and } \text{Nd}^{3+})$ $[\text{Ln}(\text{HL5})] \cdot x\text{H}_2\text{O}$ $(\text{Ln}^{3+} = \text{Ce}^{3+} \text{ and } \text{Nd}^{3+})$ $[\text{Co}_4(\text{L5})_{1.5}(\text{CH}_3\text{CO}_2)_{1.5}(\text{OH}, \text{H}_2\text{O})]$	-	240
 <i>N</i> -cyclohexylaminomethanediphosphonic acid (H₅L6)	$[\text{Co}_3(\text{L6})_2(\text{H}_2\text{O})_2]$ $[\text{Mn}_3(\text{L6})_2(\text{H}_2\text{O})_2]$	Magnetism	242
 (1,1'-biphenyl)-4,4'-diyldiphosphonic acid (H₄L7)	$[\text{M}(\text{L7})]$ $(\text{M} = \text{Li}^+, \text{Na}^+, \text{K}^+, \text{Rb}^+ \text{ and } \text{Cs}^+)$	-	243

 <p>benzene-1,3,5-tris(methylenephosphonic acid) (H₆L8)</p>	[Cu ₃ (L8)(H ₂ O) _{3,6}]·H ₂ O	Magnetism	244
 <p>2,4,6-trimethylbenzene-1,3,5-tris(methylenephosphonic acid) (H₆L9)</p>	[Cu ₅ (H ₂ L9)(btb) ₂ (OH) ₂]·3H ₂ O [btb = 1,4-bis(1,2,4-triazol-1-yl)butane] [Cu ₄ (L9) ₂ (H ₂ O) ₄] [Co ₆ (L9) ₂ (H ₂ O) ₄]	Photocatalysis Magnetism	244 245 246
 <p>4-((bis(phosphonomethyl)amino)methyl)benzoic acid (H₅L10)</p>	[La(H ₄ L10)(H ₃ L10)(H ₂ O)]·2H ₂ O [Er(H ₃ L10)(H ₄ L10)]	Luminescence	247
 <p>6-phosphonic-nicotinic acid (H₃L11)</p>	[Co ₃ (L11)(OL)(H ₂ O) ₂] (OL = 1,4-bis(imidazole-1-ylmethyl)benzene)	Magnetism	248
 <p>5-phosphonobenzene-1,3-dicarboxylic acid (H₄L12)</p>	[Zn ₃ (L12) ₂]·2H ₃ O [Zn ₃ (L12) ₂]·Hpd·H ₃ O·4H ₂ O (pd = pyrrolidine) [Co _{1.5} Zn _{1.5} (OP12) ₂]·2H ₃ O	Catalysis	249
 <p>2-phosphonic-isonicotinic acid (H₃L13)</p>	[Zn(HL13)(H ₂ O)] [Cd(HL13)]	-	250
 <p>1-hydroxyl-2-(3-pyridyl)ethylidene-1,1-diphosphonic acid (H₄L14)</p>	[Zn ₂ (L14)(H ₂ O)] [Cu ₄ (L14)(H ₂ O) ₄]·(H ₂ O) _{1.25}	Magnetism Luminescence	251
 <p>2-((phosphonomethyl)(pyridin-4-ylmethyl)amino)acetic acid (H₃L15)</p>	(H ₃ O) ₄ [Cd ₇ (L15) ₆]·16H ₂ O (H ₃ O) ₄ [Mn ₇ (L15) ₆]·17H ₂ O [Co(HL15)(H ₂ O)]·2H ₂ O [Ni(HL15)(H ₂ O)]·2H ₂ O	Magnetism Luminescence	252

	[Ba(L16)]	Gas adsorption	253
Tetraethyl-1,3,6,8-pyrenetetraphosphonate (H₄L16)			
	[Cu ₃ (H ₃ L17)(OH)(H ₂ O) ₃]- ·H ₂ O·MeOH	Gas adsorption	254
1,3,5,7-Tetrakis(4-phosphonophenyl)-adamantane (H₈L17)			
	<p>[Ln(H₅L18)]·4H₂O (Ln³⁺ = La³⁺, Nd³⁺, Gd³⁺, Dy³⁺)</p> <p>[Ln₂(H₂L18)]·8H₂O (Ln³⁺ = La³⁺, Nd³⁺, Gd³⁺, Dy³⁺)</p> <p>[NaLn(H₄OL18)]·4H₂O (Ln³⁺ = La³⁺, Nd³⁺, Gd³⁺, Dy³⁺)</p>	Ion exchange	237 255
1,4-Phenylenebis(methanetriyl)tetrakisphosphonic acid (H₈L18)			
	[Ln(H ₂ L19)(H ₃ L19)(H ₂ O)]·xH ₂ O (Ln ³⁺ = La ³⁺ , Ce ³⁺ , Pr ³⁺ , Nd ³⁺ , Sm ³⁺ , Gd ³⁺ , Tb ³⁺ and x = 9-14)	Catalysis	208
2,2'-Diethoxy-1,1'-binaphthalene-6,6'-diphosphonic acid (H₄L19)			
	[Cu ₃ (H ₂ L20)(bipy) ₂]·24H ₂ O (bipy = 4,4'-bipyridine)	Gas adsorption	256
((1,4-phenylenebis(methylene))bis-(propane-1,2,3-triyl))tetrakisphosphonic acid (H₈L20)			
	[Zn(HL21)] [CdCl(H ₂ L21)]	Luminescence	257
4-(((phosphonomethyl)amino)methyl)-benzoic acid (H₄L21)			



Plabst and Bein developed an interesting organic PBU, 1,4-phenylenebis(methane)-tetraposphonic acid (**H₈L18**) (Scheme 1.3), used to design new multi-dimensional MOFs with lanthanide centers.²³⁷ **H₈L18** contains two bisphosphonate groups which are capable to coordinate to metallic centers through different coordination fashions. The procedure to prepare the materials was based in a mixture of **H₈L18** and $\text{Ln}(\text{NO}_3)_3 \cdot 6\text{H}_2\text{O}$ salts under hydrothermal conditions. The metal:ligand molar ratios in the synthesis solution were selected as 1:1, 2:1, 4:1 and 6:1. The pH was adjusted with NaOH in a range from pH=1 to pH=7-8. The reaction mixtures were kept for 7 days at 75, 100, 150, or 180 °C giving rise to three structures types with general formula $[\text{Ln}(\text{H}_5\text{L18})] \cdot 4\text{H}_2\text{O}$, $[\text{Ln}_2(\text{H}_2\text{L18})] \cdot 8\text{H}_2\text{O}$ and $[\text{NaLn}(\text{H}_4\text{L18})] \cdot 4\text{H}_2\text{O}$ (where $\text{Ln}^{3+} = \text{La}^{3+}, \text{Nd}^{3+}, \text{Gd}^{3+}$ and Dy^{3+}).



Scheme 1.3 - Synthesis of 1,4-phenylenebis(methane)tetraposphonic acid (**H₈L18**).
 Reproduced from reference 255.

$[\text{NaLn}(\text{H}_4\text{L18})] \cdot 4\text{H}_2\text{O}$ (Figure 1.35) contains Na^+ and water molecules as guests in the channels. This MOF was used as the subject of study to evaluate the exchange of Na^+ with other monovalent cations (Li^+ , K^+ , Rb^+ and Cs^+), divalent cations (Mg^{2+} , Ca^{2+} , Sr^{2+} , Ba^{2+} , Ni^{2+} , Cu^{2+} , Zn^{2+} and Mn^{2+}) and the trivalent Fe^{3+} .²⁵⁵ Results suggested that Na^+ can be exchanged with monovalent cations, while the divalent and trivalent ones were rejected. This type of behavior is rare in open-framework ion-exchanging materials because it is normally related to size instead of charge. Therefore, $[\text{NaLn}(\text{H}_4\text{L18})] \cdot 4\text{H}_2\text{O}$ appears to be an excellent candidate for the design of selective ion-exchange materials.

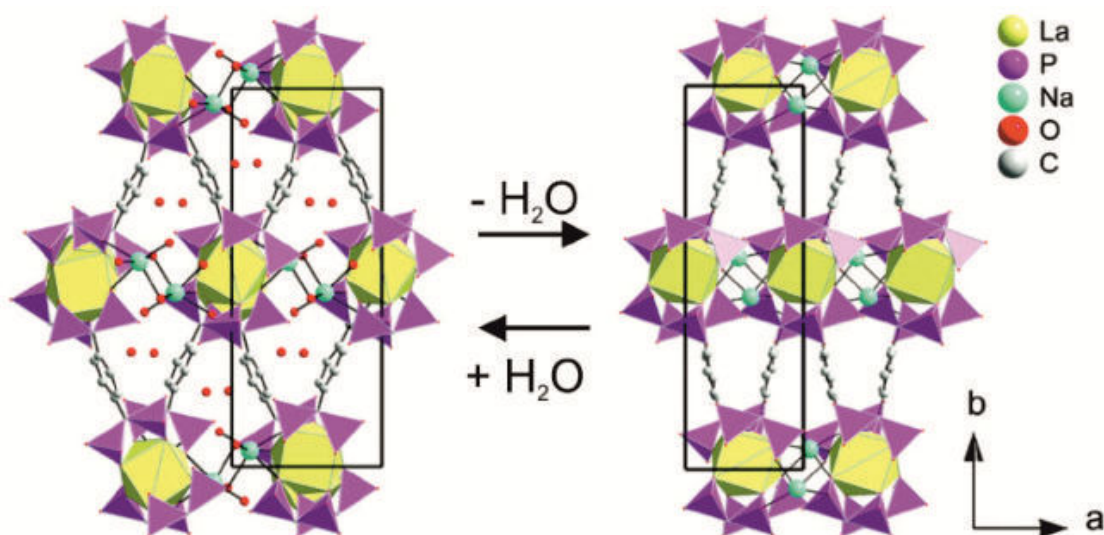
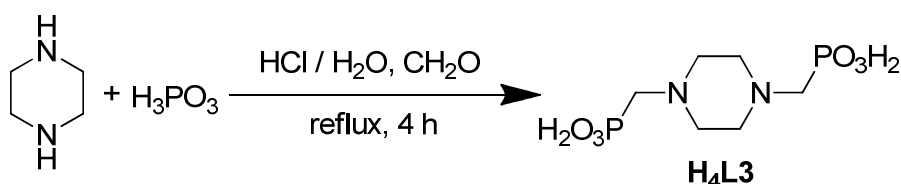


Figure 1.35 – Schematic representation of the contraction and expansion of the 3D porous $[\text{NaLn}(\text{H}_4\text{L18})]\cdot 4\text{H}_2\text{O}$ material. Reproduced from reference 255.

N,N'-Piperazinebis(methylenephosphonic acid) (**H₄L3**) organic ligand (Scheme 1.4) is particularly interesting due to its flexibility. This molecule is able to generate structures in which the coordination of the ligand to the metal is made via two or three oxygen atoms of the phosphonate groups and also via the nitrogen atoms of the piperazine ring.^{233,241,259-260}



Scheme 1.4 - Synthesis of *N,N'*-piperazinebis(methylenephosphonic acid) (**H₄L3**). Reproduced from reference 233.

Miller *et al.* isolate a highly symmetrical and porous framework, $[\text{Ni}_2(\text{L3})]\cdot x\text{H}_2\text{O}$ (with $x = 8, 2$ or 0), also coined as Ni-STA12 (Figure 1.36) from the self-assembly of **H₄L3** with Ni^{2+} cations.²³³

Studies of H_2 , CO , CO_2 and CH_4 adsorption were performed and monitored through infrared spectroscopy to identify the sites responsible for the capture of these molecules. It was found that the evacuated Ni-STA12 material has an uptake of CO_2 ten times more than of CH_4 . This occurs due to the strong interactions of CO_2 with all coordinative unsaturated Ni^{2+} sites. A similar conclusion was found for the H_2 and CO , in other words, this species can interact with Ni^{2+} cations (weak Lewis acid sites). There is no information about the interactions between H_2 and $\text{P}=\text{O}$ moiety.

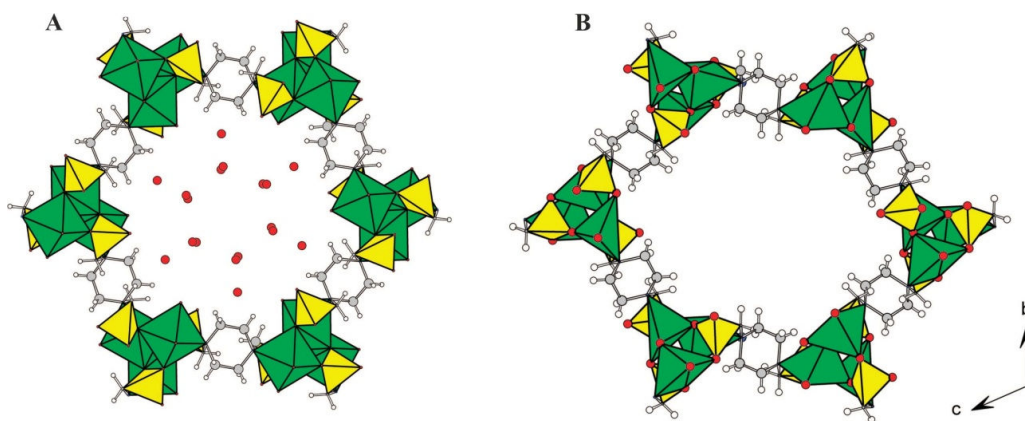
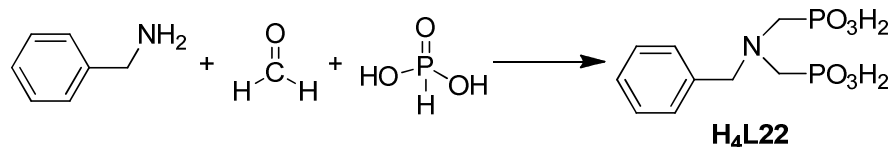


Figure 1.36 – Framework structure of Ni-STA12: (A) fully hydrated and (B) dehydrated. (Nickel octahedra in green, phosphonate octahedra in yellow, carbon atoms in grey and hydrogen atoms in white; oxygen atoms of physisorbed water molecules are in red). Reproduced from reference 233.

In 2011, Zhu *et al.* designed and synthesized a new flexible phosphonate-based organic ligand: *N*-benzyliminobis(methylene-phosphonic acid) (**H₄L22**) (Scheme 1.5). After preparing a reaction mixture containing **H₄L22**, oxalic acid (as co-ligand) and the respective LnCl₃·6H₂O salts (where Ln³⁺ = La³⁺-Dy³⁺, Er³⁺ and Y³⁺) in distilled water, it was isolated a family of isotypical lanthanide-based 2D, formulated as [Ln(H₃L22)(C₂O₄)]·2H₂O (Ln³⁺ = La³⁺-Dy³⁺, Er³⁺ and Y³⁺) layered structures (Figure 1.37).²⁵⁸



Scheme 1.5 - Synthesis of *N*-benzylaminobis(methylenephosphonic acid) (**H₄L22**).

Oxalate was chosen due to two main reasons: i) the presence of high and versatile coordination modes to coordinate with lanthanides (having high coordination number) and, mainly, ii) π -conjugated character which make it an effective bridge for charger transfer between lanthanide metallic centers, rendering it very helpful as a lanthanide luminescent sensitizer. Photoluminescence of Sm³⁺-, Eu³⁺-, Tb³⁺- and Dy³⁺-based materials were measured. A comparative study between hydrated and dehydrated Eu-based compounds was performed. As expected, the hydrated sample emits less than the dehydrated one. This is due to the quenching effect from O-H groups of the water molecules. Studies also revealed a lower emission intensity for the Sm³⁺-based material when compared with compounds having Eu³⁺, Tb³⁺ and Dy³⁺ cations in their structure. This mean that there is lower efficiency of energy-transfer from organic molecules to metallic centers in [Sm(H₃L22)(C₂O₄)]·2H₂O.

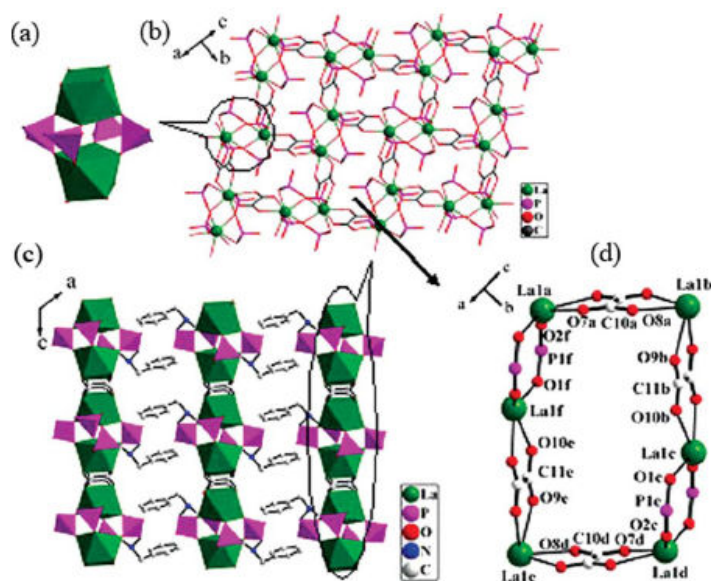
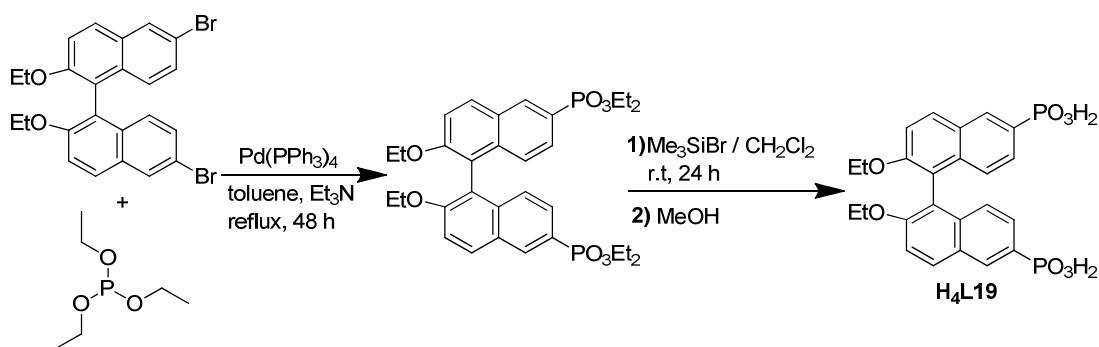


Figure 1.37 – Crystal structure of $[\text{La}(\text{H}_3\text{L}22)(\text{C}_2\text{O}_4)] \cdot 2\text{H}_2\text{O}$: (a) polyhedral drawing of the $\{(\text{LaO}_8)(\text{CPO}_3)_4\}$ unit; (b) 2D layer in $[\text{La}(\text{H}_3\text{L}22)(\text{C}_2\text{O}_4)] \cdot 2\text{H}_2\text{O}$; (c) layered structure of $[\text{La}(\text{H}_3\text{L}22)(\text{C}_2\text{O}_4)] \cdot 2\text{H}_2\text{O}$ viewed along of the b -axis; (d) representation of the 24-atom window present in $[\text{La}(\text{H}_3\text{L}22)(\text{C}_2\text{O}_4)] \cdot 2\text{H}_2\text{O}$. Reproduced from reference 258.

Several reports describing the catalytic behavior of phosphonate-based MOFs, mainly with transition metals, have been published. After a slow evaporation of a mixture composed of the chiral 2,2'-diethoxy-1,1'-binaphthalene-6,6'-diphosphonic acid (**H₄L19**) (Scheme 1.6) and nitrate or perchlorate Ln^{3+} salts in MeOH/HCl, Evans *et al.* isolated homochiral porous lanthanide-based lamellar materials, structurally robust to solvent evacuation (at ambient temperature): $[\text{Ln}(\text{H}_2\text{L}19)(\text{H}_3\text{L}19)(\text{H}_2\text{O})_4] \cdot x\text{H}_2\text{O}$ (with $\text{Ln}^{3+} = \text{La}^{3+}$, Ce^{3+} , Pr^{3+} , Nd^{3+} , Sm^{3+} , Gd^{3+} , Tb^{3+} and $x = 9-14$).²⁰⁸



Scheme 1.6 - Synthesis of 2,2'-diethoxy-1,1'-binaphthalene-6,6'-diphosphonic acid (**H₄L19**). Reproduced from reference 208.

The compound containing Gd^{3+} , $[\text{Gd}(\text{H}_2\text{L}19)(\text{H}_3\text{L}19)(\text{H}_2\text{O})_4] \cdot x\text{H}_2\text{O}$, was studied by single-crystal X-ray diffraction revealing a layered structure (Figure 1.38). The good

structure stability and reversibility of the dehydration process of these materials allowed the authors to explore their applications in heterogeneous catalysis. Because the presence of both Lewis and Brønsted acid sites in the materials, these could be adequate to catalyze various organic transformations such as the cyanosilylation of aldehydes and ring opening of *meso*-carboxylic anhydrides (1-naphthaldehyde and propionaldehyde were converted to their cyanohydrin products with >50% yield) and cyanosilylation of aldehydes (conversion of benzaldehyde into mandelonitrile with yield of about 70%).

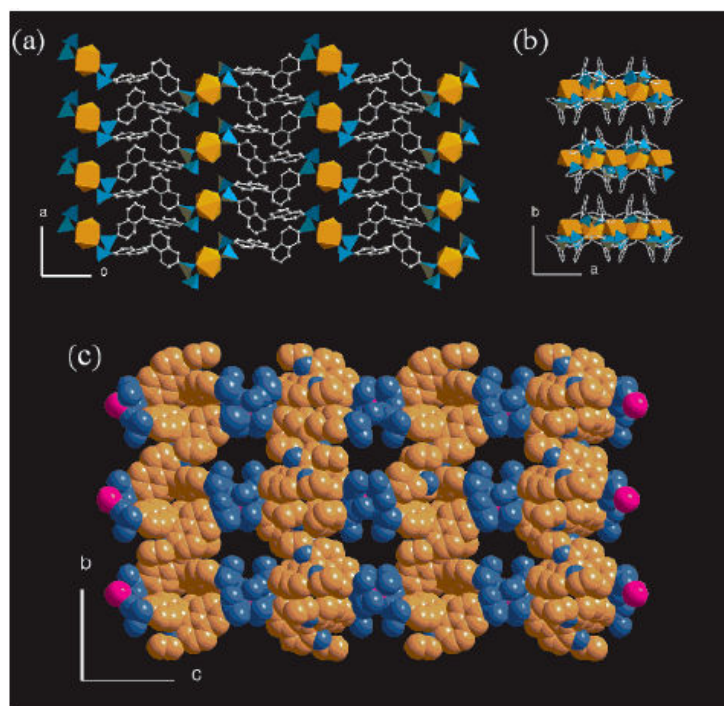


Figure 1.38 – (a) View of the layered structure of $[\text{Gd}(\text{H}_2\text{L19})(\text{H}_3\text{L19})(\text{H}_2\text{O})_4] \cdot x\text{H}_2\text{O}$ down the b axis. (b) Stacking of adjacent layers along the c axis. The coordination environments of Gd^{3+} and P atoms are represented as orange and blue polyhedra, respectively. (c) Space-filling model of $[\text{Gd}(\text{H}_2\text{L19})(\text{H}_3\text{L19})(\text{H}_2\text{O})_4] \cdot x\text{H}_2\text{O}$ viewed down the a axis. Reproduced from reference 208.

1.5. Outline and Main Objectives of this PhD Thesis

The scope of this PhD project is based on the preparation of functional and multidimensional MOFs from the self-assembly of rare-earths as metallic centers with phosphonate-based organic ligands, selected and prepared by myself. Therefore, for the first task of this work it is proposed the synthesis of four different organic ligands (Figure 1.39):

- i) 1,4-phenylenebis(methylene)diphosphonic acid (**H₄pmd**): to expand the family of Lanthanide-Organic Frameworks (composed by the compounds [Ce(Hpmd)(H₂O)] and [Pr(Hpmd)(H₂O)]²⁶¹ initialized by the research group where I was working. The incorporation of other lanthanide cations as, for instance the optically-active Eu³⁺ and Tb³⁺, can lead to the formation of functional MOFs with luminescent properties;
- ii) (benzene-1,3,5-triyltris-(methylene))triphosphonic acid (**H₆bmt**): to self-assembly with the series of lanthanides, by using distinct synthetic approaches, to isolate novel multidimensional MOFs with catalytic behavior and photoluminescent properties;
- iii) ((2,4,6-trifluorobenzene-1,3,5-triyl)tris(methylene))triphosphonic acid (**H₆tftp**): analogue of the **H₆bmt** organic linker. To prepare MOF materials with the same crystalline phase of those isolate by employing **H₆bmt**. To assess the influence of the replacement of C-H by C-F moieties in the photoluminescent properties of the resulting materials;
- iv) a large tripodal organic linker, termed as **H₆L**: to coordinate with rare-earth cations in order to isolate highly porous MOFs with adsorption and catalytic properties.

Based on the literature and in previous works, it is aimed to prepare all the organic molecules using specific synthetic routes, as for instance, Michaelis-Arbusov and catalytic cross-coupling reactions to prepare the intermediate phosphoethyl esters and acid hydrolysis to isolate the desired phosphonic acid organic ligand. The synthesis of all compounds will be carried out using conventional heating organic methods and, always possible, microwave-assisted synthesis. The evolution of all reactions will be performed by thin layer chromatography (TLC) and the purification of the intermediates and final compounds will be carried out by flash column chromatography and, if needed, employing crystallization processes using adequate organic solvents.

All organic compounds will be fully characterized by standard liquid-state techniques (NMR spectroscopy and mass spectrometry) and single-crystal X-ray diffraction.

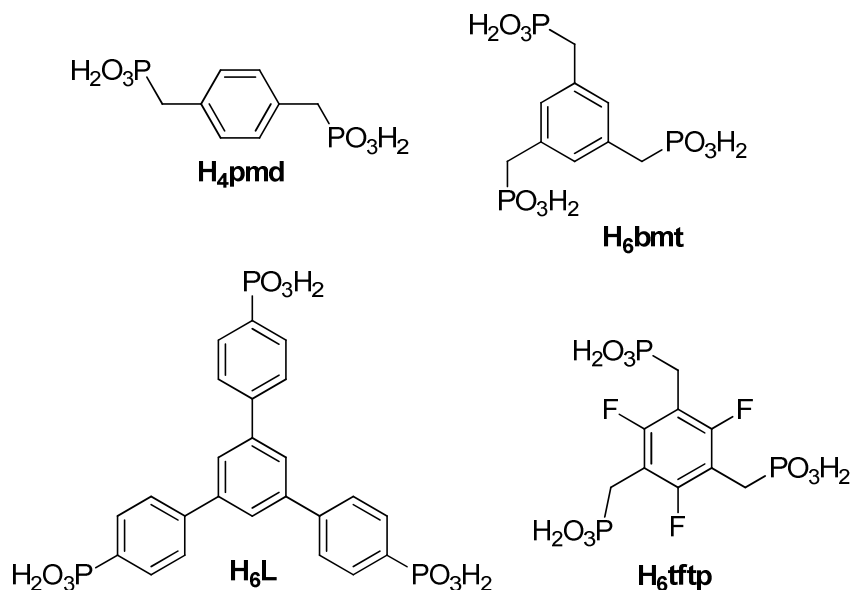


Figure 1.39 – Representation of the molecular structures of the phosphonic organic ligands prepared during the PhD project.

The synthesis of the MOF materials will be based on the use of distinct synthetic methodologies: i) hydro(solvo)thermal synthesis; ii) microwave- and ultrasound-assisted synthesis; and iii) a *bench* method called “one-pot” synthesis. To prepare functional MOFs as phase-pure and with large crystal sizes to be studied by single-crystal X-ray diffraction, it will be necessary to optimize the various reaction parameters (*i.e.*, reaction temperature and time, pH of the reaction solutions, solvents or mixtures of solvents, irradiation power and pressure, for the case of the microwave-assisted synthesis, among others). Materials will be characterized by using several standard solid-state techniques (powder or single-crystal X-ray diffraction, vibrational spectroscopy (FT-IR and FT-Raman), electron microscopy (SEM and EDS), solid-state NMR, thermogravimetric and elemental analyses) to investigate the crystalline structure.

Investigations on the intrinsic properties of the resulting MOF materials (*i.e.*, photoluminescence, catalytic behavior and gas adsorption) only may possible with the close collaboration with some researchers and group leaders expert in these scientific fields. Thus, the photoluminescent properties of the optically-active MOFs will be performed by Dr. Duarte Ananias and the catalytic behavior of the materials will be investigated in the Dr. Anabela Valente’s research group, both Auxiliary Researchers of the Associated Laboratory CICECO (Department of Chemistry of the University of Aveiro). Regarding to the gas adsorption properties of the porous Y³⁺-based MOF, these will be investigated in collaboration with the research group led by Prof. Dr. Jorge Navarro at the Faculty of Sciences of the University of Granada (Spain).

Therefore, because it is supposed to isolate functional MOFs, we propose the study of their:

- i) photoluminescent properties (*i.e.*, for the materials containing optically-active lanthanide metallic centers);

- ii) heterogeneous catalytic behavior, because the MOF materials are, normally, stable powdered compounds in several organic solvents. It is proposed to evaluate the catalytic activity of the resulting MOFs in the ring-opening reaction of styrene oxide with methanol;
- iii) adsorption properties, mainly, for the MOFs construct from the large tripodal H₆L organic ligand: to investigate their abilities, as for instance, for selective gas separation processes using binary (*e.g.*, C₃H₆/ C₃H₈ and CO₂/C₂H₂) and ternary (*e.g.*, CO₂/C₂H₂/CH₄ and CO₂/C₂H₂/N₂) gas mixtures.

1.6. References

- (1) Lehn, J. M. *Supramolecular Chemistry - Concepts and Perspectives*; VCH, 1995.
- (2) Dodziuk, H. *Introduction to Supramolecular Chemistry*; Kluwer Academic Publishers, 2002.
- (3) Steed, J. W.; L., A. J. *Supramolecular Chemistry*; John Wiley & Sons, Ltd, 2000.
- (4) Schneider, H. J.; Yatsimirsky, A. K. *Principle and Methods in Supramolecular Chemistry*; John Wiley & Sons, Ltd, 2000.
- (5) Steed, J. W.; Turner, D. R.; Wallace, K. J. *Core Concepts in Supramolecular Chemistry and Nanochemistry*; John Wiley & Sons, Ltd, 2007.
- (6) Lehn, J. M.; *J. Inclusion Phenom.*, **1988**, 6, 351-396.
- (7) Lehn, J. M.; *Angew. Chem. Int. Ed.*, **1988**, 27, 89-112.
- (8) Bertani, R.; Sgarbossa, P.; Venzo, A.; Lelj, F.; Amati, M.; Resnati, G.; Pilati, T.; Metrangolo, P.; Terraneo, G.; *Coord. Chem. Rev.*, **2010**, 254, 677-695.
- (9) Lehn, J. M.; *Chem. Soc. Rev.*, **2007**, 36, 151-160.
- (10) Weck, M.; *Polym. Int.*, **2007**, 56, 453-460.
- (11) Zhou, C. H.; Gan, L. L.; Zhang, Y. Y.; Zhang, F. F.; Wang, G. Z.; Jin, L.; Geng, R. X.; *Sci. China Ser. B-Chem.*, **2009**, 52, 415-458.
- (12) MacGillivray, L. R. *Metal-Organic Frameworks: Design and Applications*; John Wiley & Sons, Inc., 2010.
- (13) Valtchev, V.; Mintova, S.; Tsapatsis, M. *Ordered Porous Solids - Recent Advances and Prospects*; Elsevier, 2009.
- (14) Ma, L.; Lin, W. *Functional Metal-Organic Frameworks: Gas Storage, Separation and Catalysis: Topics in Current Chemistry*; Springer, 2010.
- (15) Farrusseng, D. *Metal-Organic Frameworks: Applications from Catalysis to Gas Storage*; John Wiley & Sons, Inc., 2011.
- (16) Serre, C.; Dietzel, P.; Kitagawa, S. *Microporous and Mesoporous Materials*; Elsevier, 2012.
- (17) Xu, Q. *Nanoporous Materials: Synthesis and Applications*; Taylor & Francis Group, 2013.
- (18) Férey, G.; *Chem. Soc. Rev.*, **2008**, 37, 191-214.
- (19) Rowsell, J. L. C.; Yaghi, O. M.; *Microporous Mesoporous Mater.*, **2004**, 73, 3-14.
- (20) Kitagawa, S.; Kitaura, R.; Noro, S.; *Angew. Chem., Int. Ed.*, **2004**, 43, 2334-2375.
- (21) James, S. L.; *Chem. Soc. Rev.*, **2003**, 32, 276-288.
- (22) Ma, L. Q.; Abney, C.; Lin, W. B.; *Chem. Soc. Rev.*, **2009**, 38, 1248-1256.
- (23) Czaja, A. U.; Trukhan, N.; Muller, U.; *Chem. Soc. Rev.*, **2009**, 38, 1284-1293.
- (24) Allendorf, M. D.; Bauer, C. A.; Bhakta, R. K.; Houk, R. J. T.; *Chem. Soc. Rev.*, **2009**, 38, 1330-1352.
- (25) Corma, A.; Garcia, H.; Xamena, F. X. L.; *Chem. Rev.*, **2010**, 110, 4606-4655.

- (26) Shimizu, G. K. H.; Vaidhyanathan, R.; Taylor, J. M.; *Chem. Soc. Rev.*, **2009**, *38*, 1430-1449.
- (27) Yaghi, O. M.; O'Keeffe, M.; Ockwig, N. W.; Chae, H. K.; Eddaoudi, M.; Kim, J.; *Nature*, **2003**, *423*, 705-714.
- (28) Cook, T. R.; Zheng, Y. R.; Stang, P. J.; *Chem. Rev.*, **2013**, *113*, 734-777.
- (29) Wang, Z. Q.; Cohen, S. M.; *Chem. Soc. Rev.*, **2009**, *38*, 1315-1329.
- (30) Zacher, D.; Shekhah, O.; Woll, C.; Fischer, R. A.; *Chem. Soc. Rev.*, **2009**, *38*, 1418-1429.
- (31) Xuan, W. M.; Zhu, C. F.; Liu, Y.; Cui, Y.; *Chem. Soc. Rev.*, **2012**, *41*, 1677-1695.
- (32) Janiak, C.; Vieth, J. K.; *New J. Chem.*, **2010**, *34*, 2366-2388.
- (33) Kreno, L. E.; Leong, K.; Farha, O. K.; Allendorf, M.; Van Duyne, R. P.; Hupp, J. T.; *Chem. Rev.*, **2012**, *112*, 1105-1125.
- (34) Cui, Y. J.; Yue, Y. F.; Qian, G. D.; Chen, B. L.; *Chem. Rev.*, **2012**, *112*, 1126-1162.
- (35) Gagnon, K. J.; Perry, H. P.; Clearfield, A.; *Chem. Rev.*, **2012**, *112*, 1034-1054.
- (36) Cohen, S. M.; *Chem. Rev.*, **2012**, *112*, 970-1000.
- (37) Horcajada, P.; Gref, R.; Baati, T.; Allan, P. K.; Maurin, G.; Couvreur, P.; Ferey, G.; Morris, R. E.; Serre, C.; *Chem. Rev.*, **2012**, *112*, 1232-1268.
- (38) Yoon, M.; Srirambalaji, R.; Kim, K.; *Chem. Rev.*, **2012**, *112*, 1196-1231.
- (39) Wang, C.; Zhang, T.; Lin, W. B.; *Chem. Rev.*, **2012**, *112*, 1084-1104.
- (40) Sumida, K.; Rogow, D. L.; Mason, J. A.; McDonald, T. M.; Bloch, E. D.; Herm, Z. R.; Bae, T. H.; Long, J. R.; *Chem. Rev.*, **2012**, *112*, 724-781.
- (41) O'Keeffe, M.; Yaghi, O. M.; *Chem. Rev.*, **2012**, *112*, 675-702.
- (42) Stock, N.; Biswas, S.; *Chem. Rev.*, **2012**, *112*, 933-969.
- (43) Suh, M. P.; Park, H. J.; Prasad, T. K.; Lim, D. W.; *Chem. Rev.*, **2012**, *112*, 782-835.
- (44) Li, J. R.; Sculley, J.; Zhou, H. C.; *Chem. Rev.*, **2012**, *112*, 869-932.
- (45) Furukawa, H.; Cordova, K. E.; O'Keeffe, M.; Yaghi, O. M.; *Science*, **2013**, *341*, 974-986.
- (46) Carne-Sanchez, A.; Imaz, I.; Cano-Sarabia, M.; MasPOCH, D.; *Nat. Chem.*, **2013**, *5*, 203-211.
- (47) Batten, S. R.; Champness, N. R.; Chen, X. M.; Garcia-Martinez, J.; Kitagawa, S.; Ohrstrom, L.; O'Keeffe, M.; Suh, M. P.; Reedijk, J.; *CrystEngComm*, **2012**, *14*, 3001-3004.
- (48) Biradha, K.; Ramana, A.; Vittal, J. J.; *Cryst. Growth Des.*, **2009**, *9*, 2969-2970.
- (49) Yaghi, O. M.; Li, H. L.; Davis, C.; Richardson, D.; Groy, T. L.; *Acc. Chem. Res.*, **1998**, *31*, 474-484.
- (50) Eddaoudi, M.; Moler, D. B.; Li, H. L.; Chen, B. L.; Reineke, T. M.; O'Keeffe, M.; Yaghi, O. M.; *Acc. Chem. Res.*, **2001**, *34*, 319-330.
- (51) Tranchemontagne, D. J. L.; Ni, Z.; O'Keeffe, M.; Yaghi, O. M.; *Angew. Chem., Int. Ed.*, **2008**, *47*, 5136-5147.

- (52) ISI Web of Knowledge; 2013. <http://isiwebofknowledge.com/>.
- (53) Carson, C. G.; Hardcastle, K.; Schwartz, J.; Liu, X. T.; Hoffmann, C.; Gerhardt, R. A.; Tannenbaum, R.; *Eur. J. Inorg. Chem.*, **2009**, 2338-2343.
- (54) Li, H.; Eddaoudi, M.; O'Keeffe, M.; Yaghi, O. M.; *Nature*, **1999**, *402*, 276-279.
- (55) Férey, G.; Mellot-Draznieks, C.; Serre, C.; Millange, F.; *Acc. Chem. Res.*, **2005**, *38*, 217-225.
- (56) Noro, S.; Kitagawa, S.; Akutagawa, T.; Nakamura, T.; *Prog. Polym. Sci.*, **2009**, *34*, 240-279.
- (57) Robin, A. Y.; Fromm, K. M.; *Coord. Chem. Rev.*, **2006**, *250*, 2127-2157.
- (58) Cahill, C. L.; de Lill, D. T.; Frisch, M.; *CrystEngComm*, **2007**, *9*, 15-26.
- (59) Cox, P. A. *The Elements on Earth: Inorganic Chemistry in the Environment*; Oxford University Press Inc., 1995.
- (60) Cotton, S. *Lanthanide and Actinide Chemistry*; John Wiley & Sons, Ltd, 2006.
- (61) Karlin, K. D. *Progress in Inorganic Chemistry*; John Wiley & Sons, Ltd, 2012; Vol. 57.
- (62) Moore, E. G.; Samuel, A. P. S.; Raymond, K. N.; *Acc. Chem. Res.*, **2009**, *42*, 542-552.
- (63) Armelao, L.; Quici, S.; Barigelletti, F.; Accorsi, G.; Bottaro, G.; Cavazzini, M.; Tondello, E.; *Coord. Chem. Rev.*, **2010**, *254*, 487-505.
- (64) Pevec, A.; Mrak, M.; Demsar, A.; Petricek, S.; Roesky, H. W.; *Polyhedron*, **2003**, *22*, 575-579.
- (65) Cotton, S. A.; *Coord. Chem. Rev.*, **1997**, *160*, 93-127.
- (66) Edelmann, F. T.; Gunko, Y. K.; *Coord. Chem. Rev.*, **1997**, *165*, 163-237.
- (67) Aspinall, H. C.; Tillotson, M. R.; *Polyhedron*, **1994**, *13*, 3229-3234.
- (68) Fromm, K. M.; *Coord. Chem. Rev.*, **2008**, *252*, 856-885.
- (69) Yang, Q. F.; Cui, X. B.; Yu, J. H.; Lu, J.; Yu, X. Y.; Zhang, X.; Xu, J. Q.; Hou, Q.; Wang, T. G.; *CrystEngComm*, **2008**, *10*, 1531-1538.
- (70) Tanabe, K. K.; Cohen, S. M.; *Chem. Soc. Rev.*, **2011**, *40*, 498-519.
- (71) Chen, X. M.; Tong, M. L.; *Acc. Chem. Res.*, **2007**, *40*, 162-170.
- (72) Evans, O. R.; Lin, W. B.; *Acc. Chem. Res.*, **2002**, *35*, 511-522.
- (73) Paz, F. A. A.; Klinowski, J.; Vilela, S. M. F.; Tomé, J. P. C.; Cavaleiro, J. A. S.; Rocha, J.; *Chem. Soc. Rev.*, **2012**, *41*, 1088-1110.
- (74) Eddaoudi, M.; Kim, J.; O'Keeffe, M.; Yaghi, O. M.; *J. Am. Chem. Soc.*, **2002**, *124*, 376-377.
- (75) Eddaoudi, M.; Kim, J.; Rosi, N.; Vodak, D.; Wachter, J.; O'Keeffe, M.; Yaghi, O. M.; *Science*, **2002**, *295*, 469-472.
- (76) Yan, Y.; Yang, S. H.; Blake, A. J.; Lewis, W.; Poirier, E.; Barnett, S. A.; Champness, N. R.; Schroder, M.; *Chem. Commun.*, **2011**, *47*, 9995-9997.
- (77) Lee, E. Y.; Jang, S. Y.; Suh, M. P.; *J. Am. Chem. Soc.*, **2005**, *127*, 6374-6381.

- (78) Thallapally, P. K.; Fernandez, C. A.; Motkuri, R. K.; Nune, S. K.; Liu, J.; Peden, C. H. F.; *Dalton Trans.*, **2010**, 39, 1692-1694.
- (79) Tian, J. A.; Motkuri, R. K.; Thallapally, P. K.; McGrail, B. P.; *Cryst. Growth Des.*, **2010**, 10, 5327-5333.
- (80) Tian, J. A.; Motkuri, R. K.; Thallapally, P. K.; *Cryst. Growth Des.*, **2010**, 10, 3843-3846.
- (81) Maspocho, D.; Ruiz-Molina, D.; Wurst, K.; Domingo, N.; Cavallini, M.; Biscarini, F.; Tejada, J.; Rovira, C.; Veciana, J.; *Nat. Mater.*, **2003**, 2, 190-195.
- (82) Maspocho, D.; Ruiz-Molina, D.; Wurst, K.; Rovira, C.; Veciana, J.; *Chem. Commun.*, **2004**, 1164-1165.
- (83) Maspocho, D.; Domingo, N.; Molina, D. R.; Wurst, K.; Hernandez, J. M.; Vaughan, G.; Rovira, C.; Lloret, F.; Tejada, J.; Veciana, J.; *Chem. Commun.*, **2005**, 5035-5037.
- (84) Aharen, T.; Habib, F.; Korobkov, I.; Burchell, T. J.; Guillet-Nicolas, R.; Kleitz, F.; Murugesu, M.; *Dalton Trans.*, **2013**, 42, 7795-7802.
- (85) Senchyk, G. A.; Bukhan'ko, V. O.; Lysenko, A. B.; Krautscheid, H.; Rusanov, E. B.; Chernega, A. N.; Karbowski, M.; Domasevitch, K. V.; *Inorg. Chem.*, **2012**, 51, 8025-8033.
- (86) Senchyk, G. A.; Lysenko, A. B.; Boldog, I.; Rusanov, E. B.; Chernega, A. N.; Krautscheid, H.; Domasevitch, K. V.; *Dalton Trans.*, **2012**, 41, 8675-8689.
- (87) Choi, H. J.; Dincă, M.; Long, J. R.; *J. Am. Chem. Soc.*, **2008**, 130, 7848-7850.
- (88) Dinca, M.; Dailly, A.; Tsay, C.; Long, J. R.; *Inorg. Chem.*, **2008**, 47, 11-13.
- (89) Hasegawa, S.; Horike, S.; Matsuda, R.; Furukawa, S.; Mochizuki, K.; Kinoshita, Y.; Kitagawa, S.; *J. Am. Chem. Soc.*, **2007**, 129, 2607-2614.
- (90) Takashima, Y.; Martinez Martinez, V.; Furukawa, S.; Kondo, M.; Shimomura, S.; Uehara, H.; Nakahama, M.; Sugimoto, K.; Kitagawa, S.; *Nature Commun.*, **2011**, 2.
- (91) Hoffart, D. J.; Dalrymple, S. A.; Shimizu, G. K. H.; *Inorg. Chem.*, **2005**, 44, 8868-8875.
- (92) Chandler, B. D.; Cramb, D. T.; Shimizu, G. K. H.; *J. Am. Chem. Soc.*, **2006**, 128, 10403-10412.
- (93) Custelcean, R.; Moyer, B. A.; *Eur. J. Inorg. Chem.*, **2007**, 1321-1340.
- (94) Galli, S.; Masciocchi, N.; Colombo, V.; Maspero, A.; Palmisano, G.; Lopez-Garzon, F. J.; Domingo-Garcia, M.; Fernandez-Morales, I.; Barea, E.; Navarro, J. A. R.; *Chem. Mater.*, **2010**, 22, 1664-1672.
- (95) Padial, N. M.; Procopio, E. Q.; Montoro, C.; Lopez, E.; Oltra, J. E.; Colombo, V.; Maspero, A.; Masciocchi, N.; Galli, S.; Senkovska, I.; Kaskel, S.; Barea, E.; Navarro, J. A. R.; *Angew. Chem., Int. Ed.*, **2013**, 52, 8290-8294.
- (96) Lin, X.; Blake, A. J.; Wilson, C.; Sun, X. Z.; Champness, N. R.; George, M. W.; Hubberstey, P.; Mokaya, R.; Schroder, M.; *J. Am. Chem. Soc.*, **2006**, 128, 10745-10753.
- (97) Nouar, F.; Eubank, J. F.; Bousquet, T.; Wojtas, L.; Zaworotko, M. J.; Eddaoudi, M.; *J. Am. Chem. Soc.*, **2008**, 130, 1833-1835.

- (98) Yue, Q.; Yang, J.; Li, G. H.; Li, G. D.; Chen, J. S.; *Inorg. Chem.*, **2006**, *45*, 4431-4439.
- (99) Li, Q. Y.; Yang, G. W.; Tang, X. Y.; Ma, Y. S.; Yao, W.; Zhou, F.; Chen, J.; Zhou, H.; *Cryst. Growth Des.*, **2010**, *10*, 165-170.
- (100) Cheng, J. W.; Zheng, S. T.; Yang, G. Y.; *Inorg. Chem.*, **2008**, *47*, 4930-4935.
- (101) Forster, P. M.; Burbank, A. R.; Livage, C.; Ferey, G.; Cheetham, A. K.; *Chem. Commun.*, **2004**, 368-369.
- (102) Zhang, W. H.; Wang, Y. Y.; Lermontova, E. K.; Yang, G. P.; Liu, B.; Jin, J. C.; Dong, Z.; Shi, Q. Z.; *Cryst. Growth Des.*, **2010**, *10*, 76-84.
- (103) Kuppler, R. J.; Timmons, D. J.; Fang, Q. R.; Li, J. R.; Makal, T. A.; Young, M. D.; Yuan, D. Q.; Zhao, D.; Zhuang, W. J.; Zhou, H. C.; *Coord. Chem. Rev.*, **2009**, *253*, 3042-3066.
- (104) Chen, X. Y.; Zhao, B.; Shi, W.; Xia, J.; Cheng, P.; Liao, D. Z.; Yan, S. P.; Jiang, Z. H.; *Chem. Mater.*, **2005**, *17*, 2866-2874.
- (105) Tao, J.; Yin, X.; Huang, R. B.; Zheng, L. S.; Ng, S. W.; *Inorg. Chem. Commun.*, **2002**, *5*, 975-977.
- (106) Wang, D. X.; He, H. Y.; Chen, X. H.; Feng, S. Y.; Niu, Y. Z.; Sun, D. F.; *CrystEngComm*, **2010**, *12*, 1041-1043.
- (107) Wu, J. Y.; Chao, T. C.; Zhong, M. S.; *Cryst. Growth Des.*, **2013**, *13*, 2953-2964.
- (108) Qiu, S. L.; Zhu, G. S.; *Coord. Chem. Rev.*, **2009**, *253*, 2891-2911.
- (109) Wu, X. F.; Bao, Z. B.; Yuan, B.; Wang, J.; Sun, Y. Q.; Luo, H. M.; Deng, S. G.; *Microporous Mesoporous Mater.*, **2013**, *180*, 114-122.
- (110) Shen, L. J.; Wu, W. M.; Liang, R. W.; Lin, R.; Wu, L.; *Nanoscale*, **2013**, *5*, 9374-9382.
- (111) Cooper, E. R.; Andrews, C. D.; Wheatley, P. S.; Webb, P. B.; Wormald, P.; Morris, R. E.; *Nature*, **2004**, *430*, 1012-1016.
- (112) Liu, L.; Wragg, D. S.; Zhang, H. Y.; Kong, Y.; Byrne, P. J.; Prior, T. J.; Warren, J. E.; Lin, Z. J.; Dong, J. X.; Morris, R. E.; *Dalton Trans.*, **2009**, 6715-6718.
- (113) Xu, L.; Yan, S. H.; Choi, E. Y.; Lee, J. Y.; Kwon, Y. U.; *Chem. Commun.*, **2009**, 3431-3433.
- (114) Parnham, E. R.; Morris, R. E.; *Acc. Chem. Res.*, **2007**, *40*, 1005-1013.
- (115) Li, J. T.; Ma, Y. S.; Li, S. G.; Cao, D. K.; Li, Y. Z.; Song, Y.; Zheng, L. M.; *Dalton Trans.*, **2009**, 5029-5034.
- (116) Ni, Z.; Masel, R. I.; *J. Am. Chem. Soc.*, **2006**, *128*, 12394-12395.
- (117) Sabouni, R.; Kazemian, H.; Rohani, S.; *Chem. Eng. Technol.*, **2012**, *35*, 1085-1092.
- (118) Müller, U.; Schubert, M.; Teich, F.; Puetter, H.; Schierle-Arndt, K.; Pastre, J.; *J. Mater. Chem.*, **2006**, *16*, 626-636.
- (119) Van Assche, T. R. C.; Desmet, G.; Ameloot, R.; De Vos, D. E.; Terryn, H.; Denayer, J. F. M.; *Microporous Mesoporous Mater.*, **2012**, *158*, 209-213.
- (120) Jung, D. W.; Yang, D. A.; Kim, J.; Ahn, W. S.; *Dalton Trans.*, **2010**, *39*, 2883-2887.

- (121) Son, W. J.; Kim, J.; Ahn, W. S.; *Chem. Commun.*, **2008**, 6336-6338.
- (122) Li, Z. Q.; Qiu, L. G.; Xu, T.; Wu, Y.; Wang, W.; Wu, Z. Y.; Jiang, X.; *Mater. Lett.*, **2009**, *63*, 78-80.
- (123) Haque, E.; Khan, N. A.; Park, J. H.; Jung, S. H.; *Chem.-Eur. J.*, **2010**, *16*, 1046-1052.
- (124) Sadeghzadeh, H.; Morsali, A.; *J. Inorg. Organomet. Polym. Mater.*, **2010**, *20*, 733-738.
- (125) Shaabani, B.; Mirtamizdoust, B.; Viterbo, D.; Croce, G.; Hammud, H.; Hojati-Lalemi, P.; Khandar, A.; *Z. Anorg. Allg. Chem.*, **2011**, *637*, 713-719.
- (126) Sudik, A. C.; Côté, A. P.; Wong-Foy, A. G.; O'Keeffe, M.; Yaghi, O. M.; *Angew. Chem., Int. Ed.*, **2006**, *45*, 2528-2533.
- (127) Imaz, I.; Hernando, J.; Ruiz-Molina, D.; MasPOCH, D.; *Angew. Chem., Int. Ed.*, **2009**, *48*, 2325-2329.
- (128) Ma, M.; Zacher, D.; Zhang, X. N.; Fischer, R. A.; Metzler-Nolte, N.; *Cryst. Growth Des.*, **2011**, *11*, 185-189.
- (129) Wang, L. Y.; Lu, S.; Zhou, Y. X.; Guo, X. D.; Lu, Y. L.; He, J.; Evans, D. G.; *Chem. Commun.*, **2011**, *47*, 11002-11004.
- (130) Zhang, L.; Hu, Y. H.; *Phys. Lett. A*, **2011**, *375*, 1514-1517.
- (131) Cho, W.; Lee, H. J.; Oh, M.; *J. Am. Chem. Soc.*, **2008**, *130*, 16943-16946.
- (132) Imaz, I.; MasPOCH, D.; Rodriguez-Blanco, C.; Perez-Falcon, J. M.; Campo, J.; Ruiz-Molina, D.; *Angew. Chem., Int. Ed.*, **2008**, *47*, 1857-1860.
- (133) Sava, D. F.; Kravtsov, V. C.; Nouar, F.; Wojtas, L.; Eubank, J. F.; Eddaoudi, M.; *J. Am. Chem. Soc.*, **2008**, *130*, 3768-3770.
- (134) Rouquerol, J.; Avnir D.; Fairbridge C. W.; Everett D. H.; Haynes J. H.; Pernicone N.; Ramsay J. D. F.; Sing K. S. W.; Unger K. K.; *Pure & Appl. Chem.*, **1994**, *66*, 1739-1758.
- (135) Saha, D.; Deng, S. G.; *Int. J. Hydrogen Energy*, **2009**, *34*, 2670-2678.
- (136) Chui, S. S. Y.; Lo, S. M. F.; Charmant, J. P. H.; Orpen, A. G.; Williams, I. D.; *Science*, **1999**, *283*, 1148-1150.
- (137) Ye, S.; Jiang, X.; Ruan, L. W.; Liu, B.; Wang, Y. M.; Zhu, J. F.; Qiu, L. G.; *Microporous Mesoporous Mater.*, **2013**, *179*, 191-197.
- (138) Noro, S.; Kitagawa, S.; Kondo, M.; Seki, K.; *Angew. Chem., Int. Ed.*, **2000**, *39*, 2082-2084.
- (139) Chen, B. L.; Eddaoudi, M.; Hyde, S. T.; O'Keeffe, M.; Yaghi, O. M.; *Science*, **2001**, *291*, 1021-1023.
- (140) Millange, F.; El Osta, R.; Medina, M. E.; Walton, R. I.; *CrystEngComm*, **2011**, *13*, 103-108.
- (141) Klimakow, M.; Klobes, P.; Thunemann, A. F.; Rademann, K.; Emmerling, F.; *Chem. Mater.*, **2010**, *22*, 5216-5221.
- (142) Onishi, S.; Ohmori, T.; Ohkubo, T.; Noguchi, H.; Di, L.; Hanzawa, Y.; Kanoh, H.; Kaneko, K.; *Appl. Surf. Sci.*, **2002**, *196*, 81-88.

- (143) Kondo, A.; Noguchi, H.; Ohnishi, S.; Kajiro, H.; Tohdoh, A.; Hattori, Y.; Xu, W. C.; Tanaka, H.; Kanoh, H.; Kaneko, K.; *Nano Lett.*, **2006**, *6*, 2581-2584.
- (144) Barthelet, K.; Marrot, J.; Riou, D.; Férey, G.; *Angew. Chem., Int. Ed.*, **2002**, *41*, 281-284.
- (145) Dechambenoit, P.; Long, J. R.; *Chem. Soc. Rev.*, **2011**, *40*, 3249-3265.
- (146) Serre, C.; Millange, F.; Thouvenot, C.; Nogues, M.; Marsolier, G.; Louer, D.; Férey, G.; *J. Am. Chem. Soc.*, **2002**, *124*, 13519-13526.
- (147) Serre, C.; Millange, F.; Surble, S.; Férey, G.; *Angew. Chem., Int. Ed.*, **2004**, *43*, 6286-6289.
- (148) Chae, H. K.; Siberio-Perez, D. Y.; Kim, J.; Go, Y.; Eddaoudi, M.; Matzger, A. J.; O'Keeffe, M.; Yaghi, O. M.; *Nature*, **2004**, *427*, 523-527.
- (149) Dietzel, P. D. C.; Panella, B.; Hirscher, M.; Blom, R.; Fjellvag, H.; *Chem. Commun.*, **2006**, 959-961.
- (150) Cavka, J. H.; Jakobsen, S.; Olsbye, U.; Guillou, N.; Lamberti, C.; Bordiga, S.; Lillerud, K. P.; *J. Am. Chem. Soc.*, **2008**, *130*, 13850-13851.
- (151) Lau, C. H.; Babarao, R.; Hill, M. R.; *Chem. Commun.*, **2013**, *49*, 3634-3636.
- (152) Férey, G.; Serre, C.; Mellot-Draznieks, C.; Millange, F.; Surble, S.; Dutour, J.; Margiolaki, I.; *Angew. Chem., Int. Ed.*, **2004**, *43*, 6296-6301.
- (153) Férey, G.; Mellot-Draznieks, C.; Serre, C.; Millange, F.; Dutour, J.; Surble, S.; Margiolaki, I.; *Science*, **2005**, *309*, 2040-2042.
- (154) Lebedev, O. I.; Millange, F.; Serre, C.; Van Tendeloo, G.; Férey, G.; *Chem. Mater.*, **2005**, *17*, 6525-6527.
- (155) Banerjee, R.; Phan, A.; Wang, B.; Knobler, C.; Furukawa, H.; O'Keeffe, M.; Yaghi, O. M.; *Science*, **2008**, *319*, 939-943.
- (156) Yan, Y.; Telepeni, I.; Yang, S. H.; Lin, X.; Kockelmann, W.; Dailly, A.; Blake, A. J.; Lewis, W.; Walker, G. S.; Allan, D. R.; Barnett, S. A.; Champness, N. R.; Schröder, M.; *J. Am. Chem. Soc.*, **2010**, *132*, 4092-4094.
- (157) Ma, S. Q.; Sun, D. F.; Simmons, J. M.; Collier, C. D.; Yuan, D. Q.; Zhou, H. C.; *J. Am. Chem. Soc.*, **2008**, *130*, 1012-1016.
- (158) Eddaoudi, M.; Kim, J.; Wachter, J. B.; Chae, H. K.; O'Keeffe, M.; Yaghi, O. M.; *J. Am. Chem. Soc.*, **2001**, *123*, 4368-4369.
- (159) Mulfort, K. L.; Farha, O. K.; Stern, C. L.; Sarjeant, A. A.; Hupp, J. T.; *J. Am. Chem. Soc.*, **2009**, *131*, 3866-3868.
- (160) Bury, W.; Fairen-Jimenez, D.; Lalonde, M. B.; Snurr, R. Q.; Farha, O. K.; Hupp, J. T.; *Chem. Mater.*, **2013**, *25*, 739-744.
- (161) Koh, K.; Wong-Foy, A. G.; Matzger, A. J.; *J. Am. Chem. Soc.*, **2009**, *131*, 4184-4185.
- (162) Sumida, K.; Hill, M. R.; Horike, S.; Dailly, A.; Long, J. R.; *J. Am. Chem. Soc.*, **2009**, *131*, 15120-15121.
- (163) Furukawa, H.; Ko, N.; Go, Y. B.; Aratani, N.; Choi, S. B.; Choi, E.; Yazaydin, A. O.; Snurr, R. Q.; O'Keeffe, M.; Kim, J.; Yaghi, O. M.; *Science*, **2010**, *329*, 424-428.

- (164) Deng, H. X.; Grunder, S.; Cordova, K. E.; Valente, C.; Furukawa, H.; Hmadeh, M.; Gandara, F.; Whalley, A. C.; Liu, Z.; Asahina, S.; Kazumori, H.; O'Keeffe, M.; Terasaki, O.; Stoddart, J. F.; Yaghi, O. M.; *Science*, **2012**, *336*, 1018-1023.
- (165) Li, D.; Kaneko, K.; *Chem. Phys. Lett.*, **2001**, *335*, 50-56.
- (166) Park, K. S.; Ni, Z.; Cote, A. P.; Choi, J. Y.; Huang, R. D.; Uribe-Romo, F. J.; Chae, H. K.; O'Keeffe, M.; Yaghi, O. M.; *Proc. Natl. Acad. Sci.*, **2006**, *103*, 10186-10191.
- (167) Guo, Z. Y.; Wu, H.; Srinivas, G.; Zhou, Y. M.; Xiang, S. C.; Chen, Z. X.; Yang, Y. T.; Zhou, W.; O'Keeffe, M.; Chen, B. L.; *Angew. Chem., Int. Ed.*, **2011**, *50*, 3178-3181.
- (168) Wilmer, C. E.; Farha, O. K.; Yildirim, T.; Eryazici, I.; Krungleviciute, V.; Sarjeant, A. A.; Snurr, R. Q.; Hupp, J. T.; *Energy Environ. Sci.*, **2013**, *6*, 1158-1163.
- (169) Multi-Year Research, Development and Demonstration Plan: Planned Program Activities for 2003–2010: Technical Plan, United States Department of Energy; <http://www.eere.energy.dov/hydrogenandfuelcells/mypp/>.
- (170) Menon, V. C.; Komarneni, S.; *J. Porous Mater.*, **1998**, *5*, 43-58.
- (171) Lozano-Castello, D.; Alcaniz-Monge, J.; de la Casa-Lillo, M. A.; Cazorla-Amoros, D.; Linares-Solano, A.; *Fuel*, **2002**, *81*, 1777-1803.
- (172) Konstas, K.; Osl, T.; Yang, Y. X.; Batten, M.; Burke, N.; Hill, A. J.; Hill, M. R.; *J. Mater. Chem.*, **2012**, *22*, 16698-16708.
- (173) Senkovska, I.; Kaskel, S.; *Microporous Mesoporous Mater.*, **2008**, *112*, 108-115.
- (174) Yan, Y.; Suyetin, M.; Bichoutskaia, E.; Blake, A. J.; Allan, D. R.; Barnett, S. A.; Schröder, M.; *Chem. Sci.*, **2013**, *4*, 1731-1736.
- (175) Peng, Y.; Krungleviciute, V.; Eryazici, I.; Hupp, J. T.; Farha, O. K.; Yildirim, T.; *J. Am. Chem. Soc.*, **2013**, *135*, 11887-11894.
- (176) Yang, S. J.; Cho, J. H.; Lee, K.; Kim, T.; Park, C. R.; *Chem. Mater.*, **2010**, *22*, 6138-6145.
- (177) Lin, X.; Telepeni, I.; Blake, A. J.; Dailly, A.; Brown, C. M.; Simmons, J. M.; Zoppi, M.; Walker, G. S.; Thomas, K. M.; Mays, T. J.; Hubberstey, P.; Champness, N. R.; Schroder, M.; *J. Am. Chem. Soc.*, **2009**, *131*, 2159-2171.
- (178) Yang, S. H.; Lin, X.; Blake, A. J.; Walker, G. S.; Hubberstey, P.; Champness, N. R.; Schroder, M.; *Nat. Chem.*, **2009**, *1*, 487-493.
- (179) Belof, J. L.; Stern, A. C.; Eddaoudi, M.; Space, B.; *J. Am. Chem. Soc.*, **2007**, *129*, 15202-15210.
- (180) Liu, Y. L.; Eubank, J. F.; Cairns, A. J.; Eckert, J.; Kravtsov, V. C.; Luebke, R.; Eddaoudi, M.; *Angew. Chem., Int. Ed.*, **2007**, *46*, 3278-3283.
- (181) Liu, J.; Thallapally, P. K.; McGrail, B. P.; Brown, D. R.; *Chem. Soc. Rev.*, **2012**, *41*, 2308-2322.
- (182) Wang, Q. A.; Luo, J. Z.; Zhong, Z. Y.; Borgna, A.; *Energy Environ. Sci.*, **2011**, *4*, 42-55.
- (183) Zhang, Z. J.; Zhao, Y. G.; Gong, Q. H.; Li, Z.; Li, J.; *Chem. Commun.*, **2013**, *49*, 653-661.

- (184) D'Alessandro, D. M.; Smit, B.; Long, J. R.; *Angew. Chem., Int. Ed.*, **2010**, *49*, 6058-6082.
- (185) Millward, A. R.; Yaghi, O. M.; *J. Am. Chem. Soc.*, **2005**, *127*, 17998-17999.
- (186) Llewellyn, P. L.; Bourrelly, S.; Serre, C.; Vimont, A.; Daturi, M.; Hamon, L.; De Weireld, G.; Chang, J. S.; Hong, D. Y.; Hwang, Y. K.; Jhung, S. H.; Ferey, G.; *Langmuir*, **2008**, *24*, 7245-7250.
- (187) Farha, O. K.; Yazaydin, A. O.; Eryazici, I.; Malliakas, C. D.; Hauser, B. G.; Kanatzidis, M. G.; Nguyen, S. T.; Snurr, R. Q.; Hupp, J. T.; *Nat. Chem.*, **2010**, *2*, 944-948.
- (188) Mu, B.; Schoenecker, P. M.; Walton, K. S.; *J. Phys. Chem. C*, **2010**, *114*, 6464-6471.
- (189) Wang, B.; Cote, A. P.; Furukawa, H.; O'Keeffe, M.; Yaghi, O. M.; *Nature*, **2008**, *453*, 207-U206.
- (190) Britt, D.; Furukawa, H.; Wang, B.; Glover, T. G.; Yaghi, O. M.; *Proc. Natl. Acad. Sci.*, **2009**, *106*, 20637-20640.
- (191) Li, J. R.; Tao, Y.; Yu, Q.; Bu, X. H.; Sakamoto, H.; Kitagawa, S.; *Chem.-Eur. J.*, **2008**, *14*, 2771-2776.
- (192) Kizzie, A. C.; Wong-Foy, A. G.; Matzger, A. J.; *Langmuir*, **2011**, *27*, 6368-6373.
- (193) Bastin, L.; Barcia, P. S.; Hurtado, E. J.; Silva, J. A. C.; Rodrigues, A. E.; Chen, B. L.; *J. Phys. Chem. C*, **2008**, *112*, 1575-1581.
- (194) Nakagawa, K.; Tanaka, D.; Horike, S.; Shimomura, S.; Higuchi, M.; Kitagawa, S.; *Chem. Commun.*, **2010**, *46*, 4258-4260.
- (195) Colombo, V.; Montoro, C.; Maspero, A.; Palmisano, G.; Masciocchi, N.; Galli, S.; Barea, E.; Navarro, J. A. R.; *J. Am. Chem. Soc.*, **2012**, *134*, 12830-12843.
- (196) Mu, W.; Liu, D. H.; Yang, Q. Y.; Zhong, C. L.; *Microporous Mesoporous Mater.*, **2010**, *130*, 76-82.
- (197) Chen, S. S.; Chen, M.; Takamizawa, S.; Wang, P.; Lv, G. C.; Sun, W. Y.; *Chem. Commun.*, **2011**, *47*, 4902-4904.
- (198) Kim, J.; Yang, S. T.; Choi, S. B.; Sim, J.; Ahn, W. S.; *J. Mater. Chem.*, **2011**, *21*, 3070-3076.
- (199) Cheon, Y. E.; Park, J.; Suh, M. P.; *Chem. Commun.*, **2009**, 5436-5438.
- (200) Bordiga, S.; Regli, L.; Bonino, F.; Groppo, E.; Lamberti, C.; Xiao, B.; Wheatley, P. S.; Morris, R. E.; Zecchina, A.; *Phys. Chem. Chem. Phys.*, **2007**, *9*, 2676-2685.
- (201) Fang, Q. R.; Yuan, D. Q.; Sculley, J.; Li, J. R.; Han, Z. B.; Zhou, H. C.; *Inorg. Chem.*, **2010**, *49*, 11637-11642.
- (202) Song, F. J.; Wang, C.; Falkowski, J. M.; Ma, L. Q.; Lin, W. B.; *J. Am. Chem. Soc.*, **2010**, *132*, 15390-15398.
- (203) Gedrich, K.; Heitbaum, M.; Notzon, A.; Senkowska, I.; Frohlich, R.; Getzschmann, J.; Mueller, U.; Glorius, F.; Kaskel, S.; *Chem.-Eur. J.*, **2011**, *17*, 2099-2106.
- (204) Moon, H. R.; Lim, D. W.; Suh, M. P.; *Chem. Soc. Rev.*, **2013**, *42*, 1807-1824.

- (205) Ishida, T.; Nagaoka, M.; Akita, T.; Haruta, M.; *Chem.-Eur. J.*, **2008**, *14*, 8456-8460.
- (206) Yuan, B. Z.; Pan, Y. Y.; Li, Y. W.; Yin, B. L.; Jiang, H. F.; *Angew. Chem., Int. Ed.*, **2010**, *49*, 4054-4058.
- (207) Aijaz, A.; Karkamkar, A.; Choi, Y. J.; Tsumori, N.; Ronnebro, E.; Autrey, T.; Shioyama, H.; Xu, Q.; *J. Am. Chem. Soc.*, **2012**, *134*, 13926-13929.
- (208) Evans, O. R.; Ngo, H. L.; Lin, W. B.; *J. Am. Chem. Soc.*, **2001**, *123*, 10395-10396.
- (209) Hu, A. G.; Ngo, H. L.; Lin, W. B.; *J. Am. Chem. Soc.*, **2003**, *125*, 11490-11491.
- (210) Tanaka, K.; Oda, S.; Shiro, M.; *Chem. Commun.*, **2008**, 820-822.
- (211) Bunzli, J. C. G.; Piguet, C.; *Chem. Soc. Rev.*, **2005**, *34*, 1048-1077.
- (212) Rocha, J.; Carlos, L. D.; Paz, F. A. A.; Ananias, D.; *Chem. Soc. Rev.*, **2011**, *40*, 926-940.
- (213) Takashima, Y.; Martinez, V. M.; Furukawa, S.; Kondo, M.; Shimomura, S.; Uehara, H.; Nakahama, M.; Sugimoto, K.; Kitagawa, S.; *Nat. Commun.*, **2011**, *2*.
- (214) Li, Y.; Zhang, S. S.; Song, D. T.; *Angew. Chem., Int. Ed.*, **2013**, *52*, 710-713.
- (215) Harbuzaru, B. V.; Corma, A.; Rey, F.; Jorda, J. L.; Ananias, D.; Carlos, L. D.; Rocha, J.; *Angew. Chem., Int. Ed.*, **2009**, *48*, 6476-6479.
- (216) Chen, B. L.; Wang, L. B.; Zapata, F.; Qian, G. D.; Lobkovsky, E. B.; *J. Am. Chem. Soc.*, **2008**, *130*, 6718-6719.
- (217) An, J. Y.; Shade, C. M.; Chengelis-Czegan, D. A.; Petoud, S.; Rosi, N. L.; *J. Am. Chem. Soc.*, **2011**, *133*, 1220-1223.
- (218) Fang, Q. R.; Zhu, G. S.; Jin, Z.; Ji, Y. Y.; Ye, J. W.; Xue, M.; Yang, H.; Wang, Y.; Qiu, S. L.; *Angew. Chem., Int. Ed.*, **2007**, *46*, 6638-6642.
- (219) Liu, K.; You, H. P.; Zheng, Y. H.; Jia, G.; Song, Y. H.; Huang, Y. J.; Yang, M.; Jia, J. J.; Guo, N.; Zhang, H. J.; *J. Mater. Chem.*, **2010**, *20*, 3272-3279.
- (220) Konar, S.; Zon, J.; Prosvirin, A. V.; Dunbar, K. R.; Clearfield, A.; *Inorg. Chem.*, **2007**, *46*, 5229-5236.
- (221) Clearfield, A.; Smith, G. D.; *Inorg. Chem.*, **1969**, *8*, 431-436.
- (222) Zon, J.; Kong, D. Y.; Gagnon, K.; Perry, H.; Holliness, L.; Clearfield, A.; *Dalton Trans.*, **2010**, *39*, 11008-11018.
- (223) Clearfield, A.; *Dalton Trans.*, **2008**, 6089-6102.
- (224) Kong, D.; Zon, J.; McBee, J.; Clearfield, A.; *Inorg. Chem.*, **2006**, *45*, 977-986.
- (225) Mao, J. G.; Wang, Z. K.; Clearfield, A.; *Inorg. Chem.*, **2002**, *41*, 2334-2340.
- (226) Clearfield, A.; *Curr. Opin. Solid State Mat. Sci.*, **2002**, *6*, 495-506.
- (227) Clearfield, A.; *Curr. Opin. Solid State Mat. Sci.*, **1996**, *1*, 268-278.
- (228) Chen, Z. X.; Ling, Y.; Yang, H. Y.; Guo, Y. F.; Weng, L. H.; Zhou, Y. M.; *CrystEngComm*, **2011**, *13*, 3378-3382.
- (229) Natarajan, S.; Mahata, P.; *Curr. Opin. Solid State Mat. Sci.*, **2009**, *13*, 46-53.

- (230) Liu, H. Y.; Zhang, Z. J.; Shi, W.; Zhao, B.; Cheng, P.; Liao, D. Z.; Yan, S. P.; *Dalton Trans.*, **2009**, 4416-4419.
- (231) Fu, R. B.; Hu, S. M.; Wu, X. T.; *Dalton Trans.*, **2009**, 9843-9848.
- (232) Tang, S. F.; Song, J. L.; Li, X. L.; Mao, J. G.; *Cryst. Growth Des.*, **2007**, *7*, 360-366.
- (233) Miller, S. R.; Pearce, G. M.; Wright, P. A.; Bonino, F.; Chavan, S.; Bordiga, S.; Margiolaki, I.; Guillou, N.; Feerey, G.; Bourrelly, S.; Llewellyn, P. L.; *J. Am. Chem. Soc.*, **2008**, *130*, 15967-15981.
- (234) Iremonger, S. S.; Liang, J. M.; Vaidhyanathan, R.; Shimizu, G. K. H.; *Chem. Commun.*, **2011**, *47*, 4430-4432.
- (235) Taylor, J. M.; Mah, R. K.; Moudrakovski, I. L.; Ratcliffe, C. I.; Vaidhyanathan, R.; Shimizu, G. K. H.; *J. Am. Chem. Soc.*, **2010**, *132*, 14055-14057.
- (236) Gan, X. M.; Binyamin, I.; Pailloux, S.; Duesler, E. N.; Paine, R. T.; *Dalton Trans.*, **2006**, 3912-3917.
- (237) Plabst, M.; Bein, T.; *Inorg. Chem.*, **2009**, *48*, 4331-4341.
- (238) Jiao, C. Q.; Sun, Z. G.; Zhu, Y. Y.; Chen, K.; Zhu, J.; Li, C.; Wang, C. L.; Sun, S. H.; Tian, H.; Chu, W.; Zheng, M. J.; Shao, W. Y.; Lu, Y. F.; *Inorg. Chim. Acta*, **2012**, *387*, 186-194.
- (239) Samanamu, C. R.; Zamora, E. N.; Montchamp, J. L.; Richards, A. F.; *J. Solid State Chem.*, **2008**, *181*, 1462-1471.
- (240) Mowat, J. P. S.; Groves, J. A.; Wharmby, M. T.; Miller, S. R.; Li, Y.; Lightfoot, P.; Wright, P. A.; *J. Solid State Chem.*, **2009**, *182*, 2769-2778.
- (241) Groves, J. A.; Miller, S. R.; Warrender, S. J.; Mellot-Draznieks, C.; Lightfoot, P.; Wright, P. A.; *Chem. Commun.*, **2006**, 3305-3307.
- (242) Su, Y. H.; Cao, D. K.; Duan, Y.; Li, Y. Z.; Zheng, L. M.; *J. Solid State Chem.*, **2010**, *183*, 1588-1594.
- (243) Kinnibrugh, T. L.; Garcia, N.; Clearfield, A.; *J. Solid State Chem.*, **2012**, *187*, 149-158.
- (244) Yang, C. I.; Song, Y. T.; Yeh, Y. J.; Liu, Y. H.; Tseng, T. W.; Lu, K. L.; *CrystEngComm*, **2011**, *13*, 2678-2686.
- (245) Zhou, S.; Kong, Z. G.; Wang, Q. W.; Li, C. B.; *Inorg. Chem. Commun.*, **2012**, *25*, 1-4.
- (246) Tang, S. F.; Pan, X. B.; Lv, X. X.; Yan, S. H.; Xu, X. R.; Li, L. J.; Zhao, X. B.; *CrystEngComm*, **2013**, *15*, 1860-1873.
- (247) Tang, S. F.; Song, J. L.; Mao, J. G.; *Eur. J. Inorg. Chem.*, **2006**, 2011-2019.
- (248) Wang, P. F.; Duan, Y.; Clemente-Juan, J. M.; Song, Y.; Qian, K.; Gao, S.; Zheng, L. M.; *Chem.-Eur. J.*, **2011**, *17*, 3579-3583.
- (249) Deng, M. L.; Ling, Y.; Xia, B.; Chen, Z. X.; Zhou, Y. M.; Liu, X. F.; Yue, B.; He, H. Y.; *Chem.-Eur. J.*, **2011**, *17*, 10323-10328.
- (250) Yang, Y. F.; Ma, Y. S.; Bao, S. S.; Zheng, L. M.; *Dalton Trans.*, **2007**, 4222-4226.
- (251) Fu, R. B.; Hu, S. M.; Wu, X. T.; *CrystEngComm*, **2011**, *13*, 2331-2335.

- (252) Fu, R. B.; Hu, S. M.; Wu, X. T.; *CrystEngComm*, **2013**, *15*, 802-807.
- (253) Taylor, J. M.; Vaidhyanathan, R.; Iremonger, S. S.; Shimizu, G. K. H.; *J. Am. Chem. Soc.*, **2012**, *134*, 14338-14340.
- (254) Taylor, J. M.; Mahmoudkhani, A. H.; Shimizu, G. K. H.; *Angew. Chem., Int. Ed.*, **2007**, *46*, 795-798.
- (255) Plabst, M.; McCusker, L. B.; Bein, T.; *J. Am. Chem. Soc.*, **2009**, *131*, 18112-18118.
- (256) Taddei, M.; Costantino, F.; Ienco, A.; Comotti, A.; Dau, P. V.; Cohen, S. M.; *Chem. Commun.*, **2013**, *49*, 1315-1317.
- (257) Chu, W.; Zhu, Y. Y.; Sun, Z. G.; Jiao, C. Q.; Li, J.; Sun, S. H.; Tian, H.; Zheng, M. J.; *Rsc Adv.*, **2013**, *3*, 623-631.
- (258) Zhu, Y. Y.; Sun, Z. G.; Tong, F.; Liu, Z. M.; Huang, C. Y.; Wang, W. N.; Jiao, C. Q.; Wang, C. L.; Li, C.; Chen, K.; *Dalton Trans.*, **2011**, *40*, 5584-5590.
- (259) Serre, C.; Groves, J. A.; Lightfoot, P.; Slawin, A. M. Z.; Wright, P. A.; Stock, N.; Bein, T.; Haouas, M.; Taulelle, F.; Ferey, G.; *Chem. Mater.*, **2006**, *18*, 1451-1457.
- (260) Groves, J. A.; Wright, P. A.; Lightfoot, P.; *Inorg. Chem.*, **2005**, *44*, 1736-1739.
- (261) Shi, F. N.; Trindade, T.; Rocha, J.; Paz, F. A. A.; *Cryst. Growth Des.*, **2008**, *8*, 3917-3920.

Chapter 2

Synthesis of Bi- and Tripodal Phosphonate Organic Ligands

2.1. Introduction

Organophosphorus compounds are a family of organic molecules possessing carbon-phosphorus (C–P) bonds. The first organophosphorus molecules emerged for the first time in the middle ages. This family of compounds was in 1820 systematically studied by Lassaigne while performing the phosphoric acid esterification. Several years later, Thnard's group isolates a series of phosphine derivatives and after this work the progress in the phosphorous-based organic molecules was very fast. Therefore, in the middle of the XIX century, this field of research was dominated by A. Michaelis, being then continued by A. E. Arbusov and his son B. A. Arbusov. The latter, in collaboration with some British and German researchers, continued the evolution of this area. Some properties of this type of organophosphorus compounds, as for instance, toxicity and the possibility to be used as insecticides were discovered in 1930 by Shrader and co-workers, being, then, industrially produced. Later, in 1949, the chemistry of the organophosphorus compounds was studied by G. M. Kosolapoff. Coffey reviewed recently this type of chemistry.¹⁻³

2.1.1. Structure, Properties and Applications of Phosphonic Acids and Ester Derivatives

Phosphonic acid compounds have been described as phosphoric acid derivatives. The difference resides in the replacement of a hydroxyl group by an organic substituent (R = aryl or alkyl), with RPO_3H_2 as general formula: the phosphorous atom, in this case, is pentavalent connected to three atoms (two oxygens and one R) by simple bonds and to one oxygen by one double bond. Additionally, the phosphorous of phosphonic acids has sp^3 hybridization conferring it a close tetrahedral geometry.⁴⁻⁵ In Figure 2.1 it is represented the molecular formula of the phosphonic acid (as well as its geometry), phosphonate (deprotonated form of the phosphonic acid) and the ester of the phosphonic acid. Regarding to the acidic properties of the phosphonic acids, acidity of the first proton can vary in a $\text{p}K_{\text{a}1}$ range between 0.5 and approximately 3, while for the second proton the $\text{p}K_{\text{a}2}$ value is comprised in the 5-9 range. This variation in the $\text{p}K_{\text{a}1}$ and $\text{p}K_{\text{a}2}$ values may be based on the presence of some electron-donating (EDG) or/and electron-withdrawing (EWG) groups.⁴

Due to their properties, phosphonic acids have found applications in distinct areas such as: organic synthesis reactants, antioxidants of industrial oils, production of non-flammable plastics, surface applications to prevent corrosion processes, as agrochemicals (*i.e.*, insecticides, herbicides and fungicides) and for medical purposes (antitumor, anti-hepatitis B and -HIV virus and in clinical dentistry).⁴⁻⁸ In Figure 2.2 are depicted some of the commercially available phosphonate-based and phosphonic acid compounds which have been employed in different fields: i) phosphonoformic acid (Foscavir[®]) an antiviral agent; ii) the herbicide *N*-(phosphonomethyl)glycine (Roundup[®]); iii) 3-amino-1-

hydroxypropanediyl-1,1-bis-phosphonic acid (Aredia[®]) a medical drug for hypercalcemia treatment; and iv) (*R*)-1-6-aminopurin-9-yl)propan-2-yloxymethylphosphonic acid (Viread[®]).

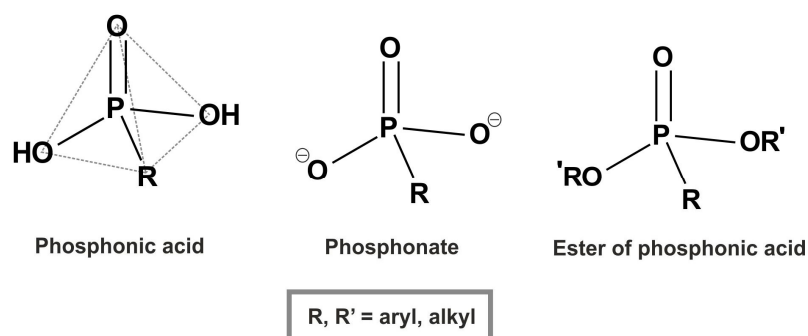


Figure 2.1 – General structure of the phosphonic acid group, illustrating its tetrahedral geometry, phosphonate and ester of phosphonic acid.

Phosphonic acid-based organic molecules have been employed in the synthesis of metal phosphonate-based compounds. Alberti and collaborators reported in 1978 for the first time this type of compounds consisting in zirconium phosphonate layered structures formulated as $[\text{Zr}(\text{HOCH}_2\text{PO}_3)_2] \cdot \text{H}_2\text{O}$, $[\text{Zr}(\text{C}_2\text{H}_6\text{PO}_3)]$ and $[\text{Zr}(\text{C}_6\text{H}_6\text{PO}_3)]$.⁹ Since then, the interest in the preparation of metal phosphonate chemistry have been substantially increased.¹⁰ The physical and chemical properties of organophosphorus compounds, especially phosphonate-based or phosphonic acid organic molecules, led us to employ enormous efforts in their preparation for the construction of multidimensional Metal-Organic Frameworks (MOFs).

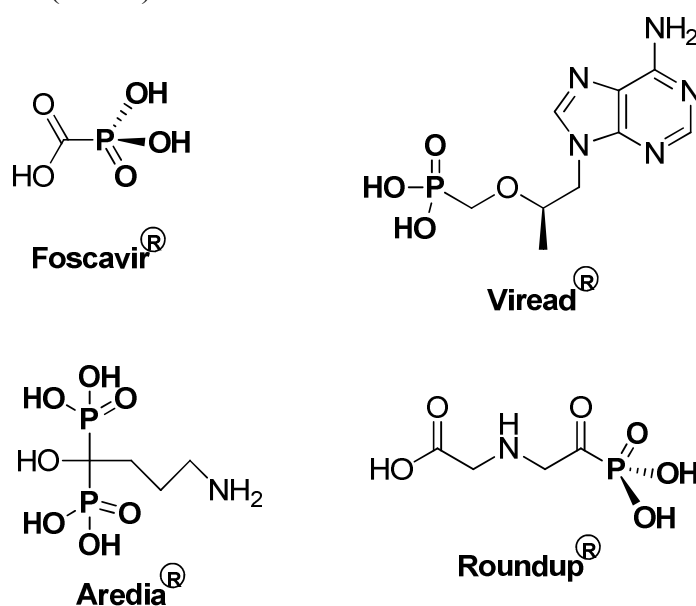


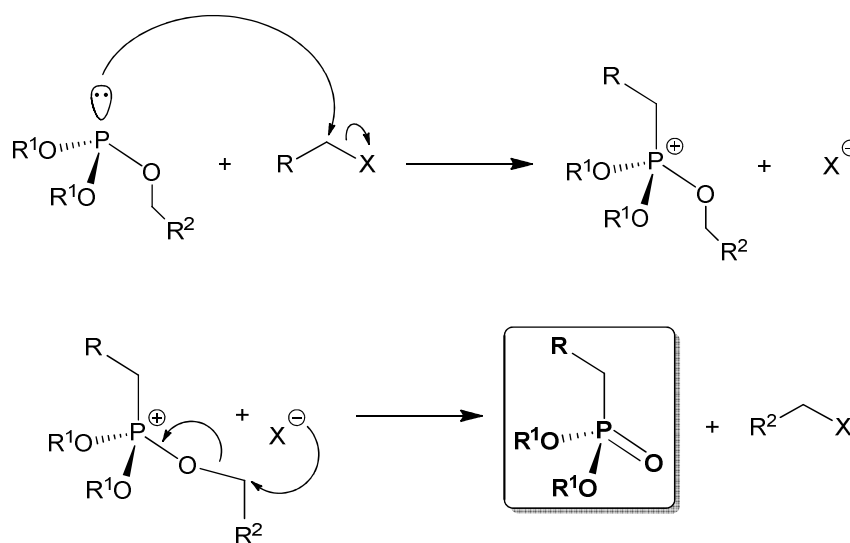
Figure 2.2 – Molecular structures of the commercially available Foscavir[®], Roundup[®], Aredia[®] and Viread[®] used in different fields.

2.1.2. Synthetic Methods to Prepare Phosphonic Acid Linkers and their Phosphonate Intermediates

In an historical perspective, and as mentioned above, we must go back to the XIX century, more precisely in 1897, date on which Michaelis and Becker reported the generation of a carbon-phosphorous (C–P) bond, involving the phosphorylation, by using salts of dialkylphosphites, of a saturated carbon under heating.¹¹⁻¹³ Since then, this type of nucleophilic phosphorylation has been used and improved in order to prepare new phosphonate-based organic ligands in high yields. Therefore, in the literature it is commonly found several synthetic methodologies in order to isolate phosphonated compounds, such as: i) Michaelis-Arbusov reaction; ii) Michaelis-Becker reaction; iii) Mannich-type condensation; and iv) catalytic cross-coupling reaction (nickel or palladium). In the next sub-sections, it is only highlighted and described the Michaelis-Arbusov reaction and the catalytic cross-coupling method, using palladium as catalyst. It is also describe the transformation of the dialkyl phosphonate intermediates into organic phosphonic acids.

Michaelis-Arbusov Reaction

This type of reaction has been reported in several articles and reviews since 1949, being used very often in the synthesis of new phosphonate-based organic compounds.¹⁴⁻¹⁹ The Michaelis-Arbusov reaction is one of the most versatile synthetic routes to produce C–P bonds, involving the reaction of an primary alkyl halide, possessing commonly Cl, Br or I elements, with trialkyl phosphite, with the formula P(OR)₃ [where R = –CH₃, –CH₂CH₃, –CH(CH₃)₂, and others]. This reaction is normally performed at 110-200 °C, depending of the R group and used solvents as, for instance, toluene or xylene,^{17-18,20} being more common its use without organic solvents. Normally, the trialkyl phosphite has been used as reagent and solvent.

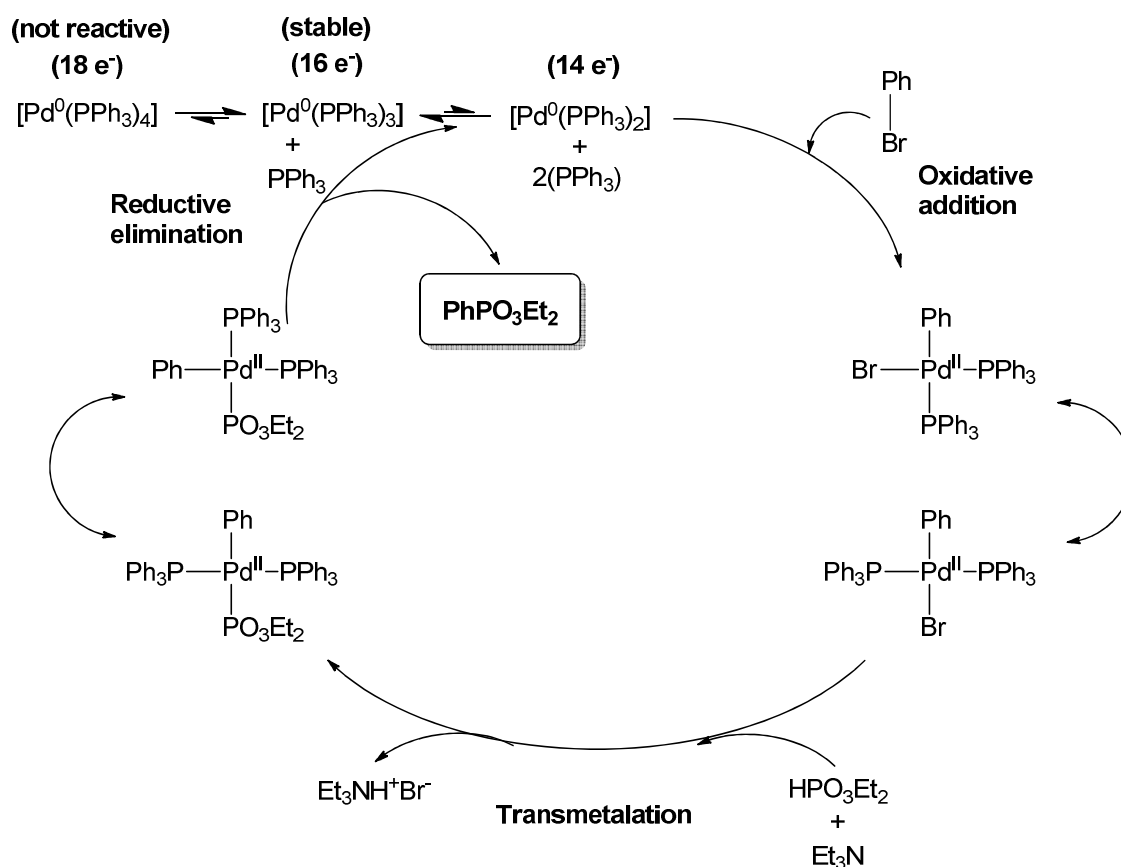


Scheme 2.1 – Schematic representation of the mechanism of the Michaelis-Arbusov reaction.

Mechanistically, the Michaelis-Arbusov reaction comprises two reaction steps (Scheme 2.1). First, a nucleophilic attack (S_N2) of the trialkyl phosphite, promoted by the free electron pair present in the phosphorus atom, to the α -carbon of the alkyl halide. This phenomenon leads to the formation of an ionic phosphonium salt intermediate and a halide anion. Then, because the phosphonium intermediate is unstable under heat, the halide anion, being the leaving group in the first reaction step and acting as a nucleophile in the second one, attacks one carbon that is directly connected to oxygen of one of the alkoxy groups (in a S_N2 reaction) affording the phosphonate ester. In summary, during this transformation the trivalent phosphorus is converted in a pentavalent one.^{4,12,21}

Catalytic Cross-coupling Reaction

The general main objective of a transition metal-catalyzed organic synthesis comprises the formation of a carbon-carbon (C–C) bond. The Pd-catalyzed coupling reaction is one of the most employed and efficient methodologies regarding the construction of C–C bonds. In addition to Pd-catalysts (e.g., $Pd(OAc)_2$ and $[Pd(PPh_3)_4]$), transition metal-catalysts (as for instance, $NiBr_2$ and $NiCl_2$) have also been extensively used for the formation of carbon-phosphorus (C–P) and carbon-boron (C–B) bonds in order to produce respective aryl or alkenyl phosphonate or boronic acid organic molecules.²²⁻²⁵



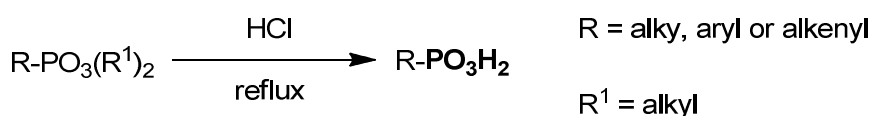
Scheme 2.2 – Schematic representation of the mechanism of palladium-catalyzed cross-coupling.

Contrary to what happens in the Michaelis-Arbusov approach, involving the use of primary alkyl halide, the reaction between alkenyl or aryl halides with trialkyl phosphite does not occur because the halide is an electrophilic poor molecule. The use of a transition metal-catalyst is required.

Catalytic cross-coupling reaction is complicated involving three main steps: i) oxidative addition; ii) transmetalation; and iii) reductive elimination (Scheme 2.2). In addition, electronic and steric features of the organic halides, the palladium source as well as the anionic additives and ligands display a very important role in the success of the formation of the C–P bond. Therefore, mechanistically the catalytic cross-coupling reaction starts with the formation of an active Pd⁰ complex. Then, it arises a palladium complex due to the oxidative addition of an aryl or alkenyl substrate. Pd becomes Pd^{II}. In the next step, the trialkyl phosphite coordinates to the metal center giving rise to a new palladium complex (ligand–phosphite–Pd^{II}–aryl (or alkenyl) complex) and to the consequent formation of a Pd–P bond. Finally, in the last step a reductive elimination occurred, being the Pd⁰ regenerated and the C–P bond formed in order to isolate the desired organic phosphonic ligand.^{4,12}

From Phosphonate Intermediates to the Final Acid Phosphonic Organic Compounds

The transformation of the dialkyl phosphonates into the respective phosphonic acid compounds is a relatively simple step. This methodology comprises a conventional acid hydrolysis from the preparation of a reaction mixture containing the dialkyl phosphonate intermediate with an aqueous solution of HCl (6 M) or even concentrated HCl (Scheme 2.3). The solution is refluxed during few to several hours depending of the number of existing phosphonate groups and/or the complexity of the organic molecule.^{21,24,26 27}



Scheme 2.3 – Acid hydrolysis of the dialkyl phosphonates to isolate the desired phosphonic acid organic linkers.

This chapter only focus the synthesis of four phosphonic organic ligands: i) the dipodal 1,4-phenylenebis(methylene)diphosphonic acid (**H₄pmd**); ii) the tripodal (benzene-1,3,5-triyltris(methylene))tri-phosphonic acid (**H₆bmt**); iii) the fluorinated tripodal ((2,4,6-trifluorobenzene-1,3,5-triyl)tris(methylene))-triposphonic acid (**H₆tftp**); and iv) the large tripodal **H₆L** (depicted in Figure 1.39 of the Chapter 1). All synthetic routes, purification processes and characterization (NMR spectroscopy, mass spectrometry and single-crystal X-ray diffraction) are described in detail.

2.2. Strategy

Our research group initialized the quest for MOF materials composed of highly flexible and aliphatic carboxylate organic molecules obtained commercially. Nevertheless, and progressing in time, the carboxylate groups have been replaced by phosphonate ones (Figure 2.3).²⁸⁻³⁷

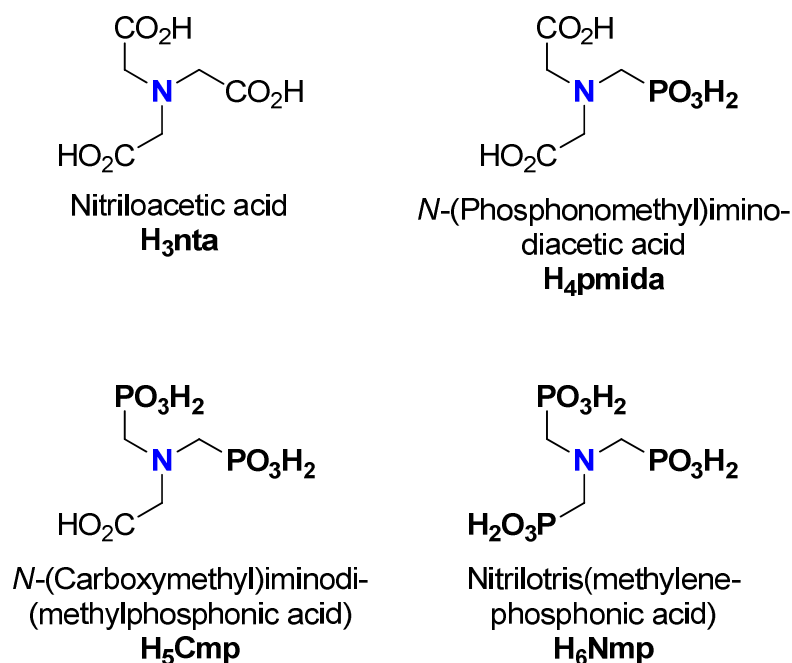


Figure 2.3 – Highly flexible and aliphatic carboxylate and/or phosphonate organic ligands used for our research group to prepare MOFs.

From these previous investigations it was possible to draw some conclusions:

- (i) the presence of central nitrogen atom core together with methylene groups, despite being a suitable moiety to employ in divergent tripodal organic PBUs, promotes a high degree of flexibility of the organic molecule and consequently supramolecular isomerism. This fact, may be related with the preparation of microcrystalline MOF powders;
- (ii) two-dimensional MOF materials are usually isolated because the organic PBUs act as chelating agents of the metal cations and branching is only facilitated in two directions of the space;
- (iii) because many of these previously reported structures contain *f*-block elements, we observed that the absence of suitable sensitizers in the organic PBUs (e.g., aromatic rings) led to poor photoluminescent properties. To boost emission of the isolated Lanthanide–Organic Frameworks (LnOFs) specific groups have to be included, such as aromatic rings, so as to promote an effective *antenna effect*;

(iv) in addition, the central nitrogen atom appears protonated in the synthesized MOF structures (as also occurs in the zwitterionic forms of the starting organic PBUs), which constitutes an additional quencher (non-radiative) of the photoluminescent properties.

Comparing carboxylic with phosphonic acids ligands, the latter are more acidic, the number of electrons is twice higher and they are non-planar possessing tetrahedral geometry. This set of characteristics allows the formation of stronger hydrogen bonds, being a very good request for the design of crystalline structures and for the self-assembly of supramolecular arrays.¹⁰

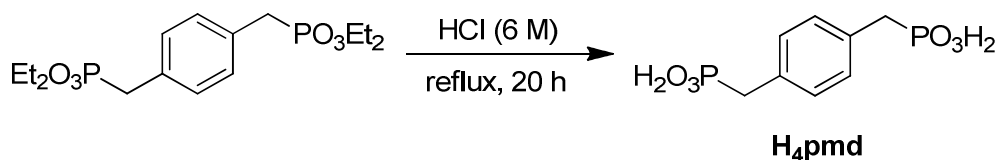
Keeping into account all these information, we have done enormous efforts towards the preparation of di- and tripodal aromatic phosphonate-based molecules. With that we prospect the construction of multidimensional MOF materials aiming the improvement of their final properties (e.g., photoluminescence).

2.3. 1,4-Phenylenebis(methylene)diphosphonic acid (**H₄pmd**)

2.3.1. Synthesis

1,4-Phenylenebis(methylene)diphosphonic acid (**H₄pmd**) linker was for the first time used by our group for the preparation of LnOFs. In 2008 it was reported the synthesis of two layered LnOFs, formulated as [Ln(Hpmd)(H₂O)] (Ln³⁺ = Ce³⁺ and Pr³⁺) based on **H₄pmd**.³⁸ In that work, H₄pmd was generated *in situ*, involving the use of ionic liquids from his tetraethyl ester derivative 1,4-phenylenebis(methylene)bisphosphonate (commercially available). Although being novel, the method proved to be difficult and the extension for other lanthanides it was not possible to perform.

The **H₄pmd** organic linker was herein isolated using a different synthetic route. An aqueous suspension composed of HCl (6M) with the commercially available tetraethyl 1,4-phenylenebis(methylene)-bisphosphonate was prepared and refluxed for 20 h (Scheme 2.4). The solvent was completely distilled and the desired linker, 1,4-phenylenebis(methylene)diphosphonic acid (**H₄pmd**), was obtained as crystalline white powder with 96% yield (see the Experimental Section for further details).



Scheme 2.4 - Synthetic route to 1,4-phenylenebis(methylene)diphosphonic acid (**H₄pmd**).

2.3.2. Structural Elucidation

To confirm the structure of the 1,4-phenylenebis(methylene)diphosphonic acid (H_4pmd) organic molecule it was collected the respective 1H , ^{13}C and ^{31}P NMR spectra using $DMSO-d_6$ as solvent. Analyzing the 1H spectrum, it is observed one doublet ($J(^1H-^{31}P) = 19.9$ Hz) at δ 2.91 ppm corresponding to the resonance of the protons of the methylene ($-CH_2$) group with the phosphorous belonging to the $-PO_3H_2$ groups. In the aromatic zone appears one singlet at 7.15 ppm corresponding to the aromatic protons. In the ^{13}C NMR spectrum at δ 35.0 ppm it is observed a doublet ($J(^{13}C-^{31}P) = 132.6$ Hz) which is related with the resonance of the carbons belonging to the $-CH_2$ groups with phosphorous. At δ 129.4 and 131.8 ppm are presented the aromatic $-CH$ and the aromatic $-C-CH_2$, respectively. The ^{31}P NMR spectrum only has one triplet ($J(^{31}P-^1H) = 22.2$ Hz) centered at δ 21.7 ppm resulting to the coupling between the phosphorous with the protons of the methylene moiety.

2.4. (Benzene-1,3,5-triyltris(methylene))triphosphonic acid (H_6bmt)

2.4.1. Synthesis

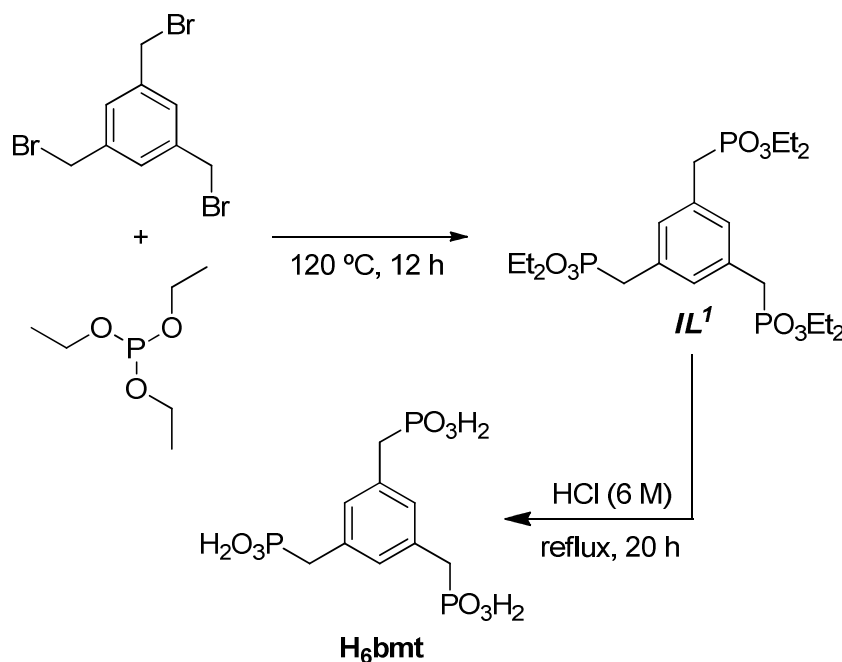
The synthesis and structural characterization of the tripodal (benzene-1,3,5-triyltris(methylene))triphosphonic acid (H_6bmt), as well as its phosphohexaethyl ester derivative, has been previously reported in several works.^{4,6-8,26,39-41} Its use has been focused for the preparation of mesostructured organosilica hybrids, to assembly to fullerene (C_{60}), as organic unities for the synthesis of dendrimers and, only once, for the synthesis of a MOF material.

Michaelis-Arbusov reaction

Based on the literature, our first attempts were based on the preparation of some reaction mixtures composed of the commercially available 1,3,5-tris(bromomethyl)-benzene and triethyl phosphite in dry toluene or xylene. The solutions were refluxed, under constant magnetic stirring, during large periods of time (ranging from 18 h to 3 days). Although we isolated the desired organic molecule (II^I , see scheme 2.5), reactions were very slow and II^I was obtained in low yields.

The synthetic procedure was modified to a Michaelis–Arbusov reaction: mixture composed of 1,3,5-tris-(bromomethyl)benzene⁴² with triethyl phosphite (acting as reactant and solvent).^{26,41} The reaction occurred at 120 °C during 12 h (see Experimental Section for further details). Upon completion of the reaction, the excess of triethyl phosphite was removed by distillation under reduced pressure (*Caution!* triethyl phosphite has an extremely unpleasant smell and it is harmful; it should be, therefore, always handled inside a fume hood). The intermediate compound II^I [hexaethyl(benzene-1,3,5-triyltris-

(methylene)tris(phosphonate)] was purified by flash column chromatography and isolated as a colorless oil in a very good yield (88%).



Scheme 2.5 - Synthetic route to (benzene-1,3,5-triyltris(methylene))triphosphonic acid (**H₆bmt**).

Acid hydrolysis

The second step, in order to isolate **H₆bmt**, was based on an acid hydrolysis reaction: **IL¹** was treated with an aqueous solution of HCl for 20 h at reflux. The resulting solution was washed with dichloromethane and **H₆bmt** was immediately isolated as a white crystalline solid, being washed with acetone. **H₆bmt** was obtained in 92% yield.

2.4.2. Structural Elucidation

The intermediate [hexaethyl(benzene-1,3,5-triyltris(methylene))tris(phosphonate)] (**IL¹**) and the desired (benzene-1,3,5-triyltris(methylene))triphosphonic acid (**H₆bmt**) organic compounds were both characterized by NMR spectroscopy using CDCl₃ and DMSO-*d*₆, respectively. **IL¹** and **H₆bmt** were investigated by TOF MS ES⁺ and TOF MS ES⁻ mass spectrometry, respectively. ¹H NMR spectrum of **IL¹** comprises at δ 1.22 ppm a signal representing one triplet ($J(^1\text{H}-^1\text{H}) = 7.1\text{ Hz}$) corresponding to the protons of the methyl (–CH₃) group (Figure 2.4). At δ 3.08 ppm appears one doublet ($J(^1\text{H}-^{31}\text{P}) = 22.1\text{ Hz}$) attributed to the protons of the methylene group identified as –CH₂–P and the resonances of the two protons of the other methylene group, identified as –O–CH₂ is located at δ 4.00 ppm as a double quartet ($J(^1\text{H}-^1\text{H}) = 7.2\text{ Hz}$ and $J(^1\text{H}-^{31}\text{P}) = 7.9\text{ Hz}$). Regarding to the aromatic of the spectrum we highlight a double triplet ($^4J(^1\text{H}-^1\text{H}) = ^4J(^1\text{H}-^{31}\text{P}) = 2.4\text{ Hz}$) at δ 7.10 ppm corresponding to the resonance of the three aromatic

protons. In the ^{13}C NMR spectrum of **IL**¹ the resonance of the carbon belonging the methyl group ($-\text{CH}_3$) is located in the δ 16.2–16.3 ppm range. The carbon of the $-\text{CH}_2-\text{P}$ moiety appears as a doublet ($J(^{13}\text{C}-^{31}\text{P}) = 138.0$ Hz) at 33.3 ppm and the signal comprised in the δ 62.0–62.1 ppm range is attributed to the carbon belonging to $-\text{O}-\text{CH}_2$. The aromatic carbons identified as $-\text{CH}$ and $-\text{C}-\text{CH}_2$ appear at δ 129.7 and 131.9–132.1 ppm as a double triplet ($^3J(^{13}\text{C}-^{31}\text{P}) = 5.8$ Hz and $^5J(^{13}\text{C}-^{31}\text{P}) = 5.2$ Hz) and a multiplet, respectively. In the TOF MS ES⁺ spectrum of **IL**¹ are located two peaks at m/z 529.2 ($\text{M} + \text{H}$)⁺ and 551.1 ($\text{M} + \text{Na}$)⁺.

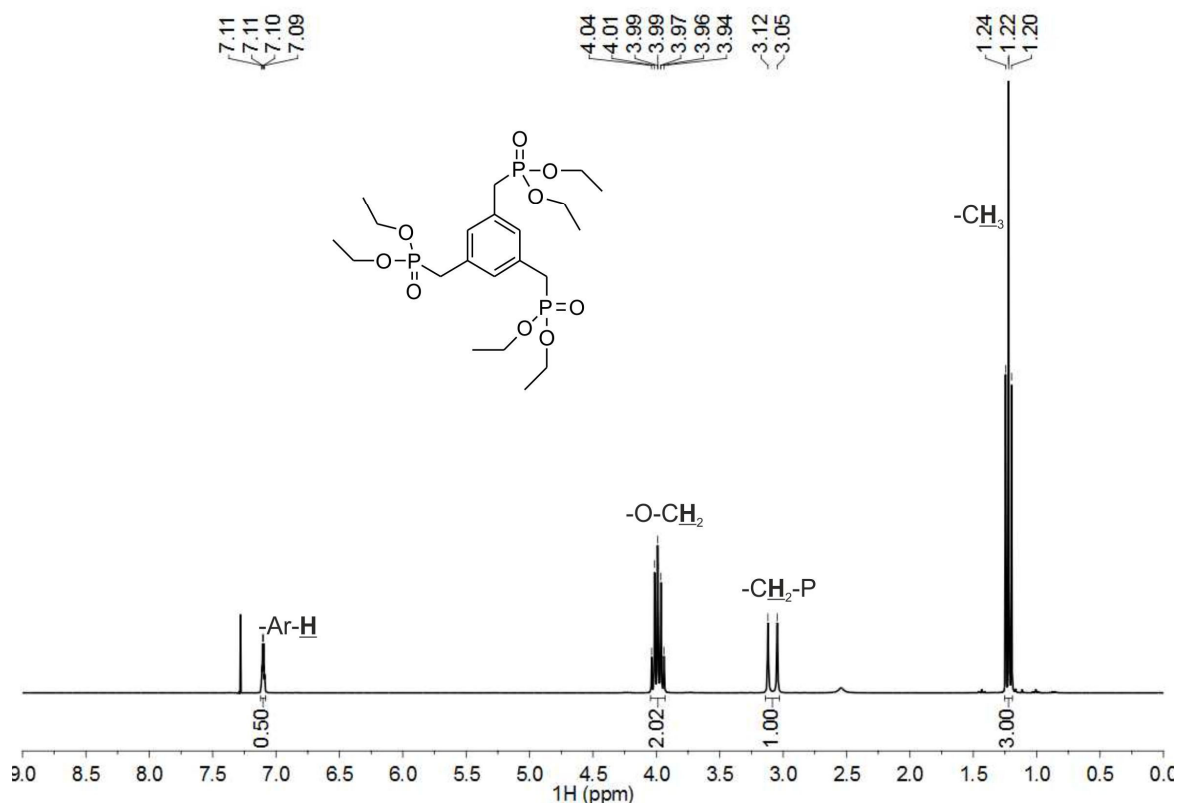


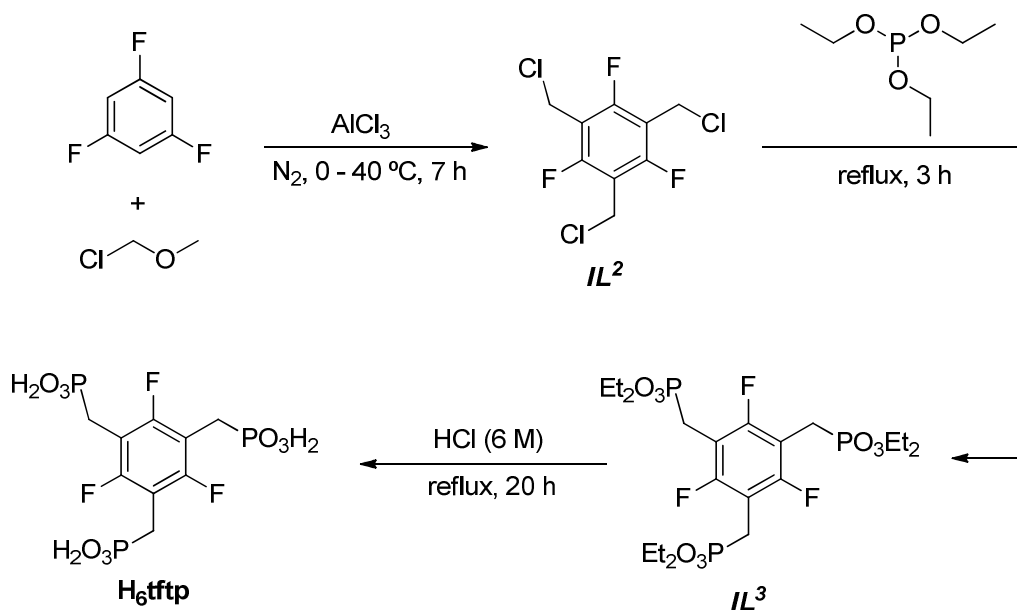
Figure 2.4 – ^1H NMR spectrum of the intermediate compound [hexaethyl(benzene-1,3,5-triyltris(methylene))tris(phosphonate)] (**IL**¹).

The ^1H NMR spectrum of **H₆bmt** is composed of a signal at δ 2.87 ppm as a doublet ($J(^1\text{H}-^{31}\text{P}) = 21.8$ Hz) attributed to the methylene group, and another doublet ($J(^1\text{H}-^1\text{H}) = 1.95$ Hz), in the aromatic region, at δ 7.01 ppm belonging to the three aromatic protons. The ^{13}C NMR spectrum presents a doublet ($J(^{13}\text{C}-^{31}\text{P}) = 132.6$ Hz) at δ 35.2 ppm attributed to the carbon of the $-\text{CH}_2$ moiety. The aromatic carbons $-\text{CH}$ and $-\text{C}-\text{CH}_2$ are located at δ 129.0 and 133.5 ppm, respectively. As described above for **H₄pmd**, the ^{31}P NMR spectrum of the organic ligand **H₆bmt** has a signal at δ 22.5 ppm as a triplet ($J(^{31}\text{P}-^1\text{H}) = 21.2$ Hz) corresponding to phosphorous. In the TOF MS ES⁻ spectrum of **H₆bmt** we can observe one peak at m/z 359.0 ($\text{M} - \text{H}$)⁻.

2.5. ((2,4,6-Trifluorobenzene-1,3,5-triyl)tris(methylene))triphosphonic acid (H_6tftp)

2.5.1. Synthesis

The tripodal organic linker ((2,4,6-trifluorobenzene-1,3,5-triyl)tris(methylene))triphosphonic acid (H_6tftp , Scheme 2.6) was, to the best of our knowledge, firstly prepared by our research group. Its synthesis involves three step reactions: i) chloromethylation; ii) Michaelis-Arbusov; and iii) acid hydrolysis.



Scheme 2.6 - Synthetic route of ((2,4,6-trifluorobenzene-1,3,5-triyl)tris(methylene))triphosphonic acid (H_6tftp).

Chloromethylation

The preparation of the intermediate compound 1,3,5-tris(chloromethyl)-2,4,6-trifluorobenzene (IL^2) was, the most challenging reaction step in order to prepare H_6tftp . The synthesis of IL^2 was attempted by preparing an reaction mixture composed of 1,3,5-trifluorobenzene, chloromethyl methyl ether (3.2, 4 or 6 eq.), carbon disulfide (CS_2) or dichloromethane (as solvent) in the presence of anhydrous aluminium chloride ($AlCl_3$; 1, 4 or 6 eq.). Reactions were performed at different temperatures (ambient or refluxing) varying the period of time (from 5 to 18 h), because the conversion of the starting material occurred very slowly. The reactions were quenched using a mixture of water/ice, and $NaHCO_3$ was added to neutralize the resulting mixture. The organic products were extracted with dichloromethane and the desired IL^2 intermediate was purified by flash column chromatography using petroleum ether / dichloromethane (4:1) as eluent. The desired organic molecule IL^2 was obtained in very low yields (10 – 20%).

Aiming at the production of IL^2 in large amounts, to some modifications in the synthetic protocol described above were made. A mixture of 1,3,5-trifluorobenzene and chloromethyl methyl ether (18 eq.) in the presence of 18 eq. of anhydrous $AlCl_3$ (slowly added to the reaction at 0 °C during approximately 10 min and, consequent, formation of an orange precipitate) was prepared in a two neck round-bottom flask, under nitrogen pressure (see Figure 2.5). The temperature was increased for 40 °C and the reaction occurred for approximately 7 h (see Experimental Section for further details). After that, the resulting mixture, having the desired compound as well as some secondary products, was quenched with a mixture of water/ice and neutralized with $NaHCO_3$. The organic products were recovered after extraction with dichloromethane and purified by flash column chromatography using petroleum ether/dichloromethane (4:1) as eluent. The intermediate IL^2 was isolated in 71% yield.

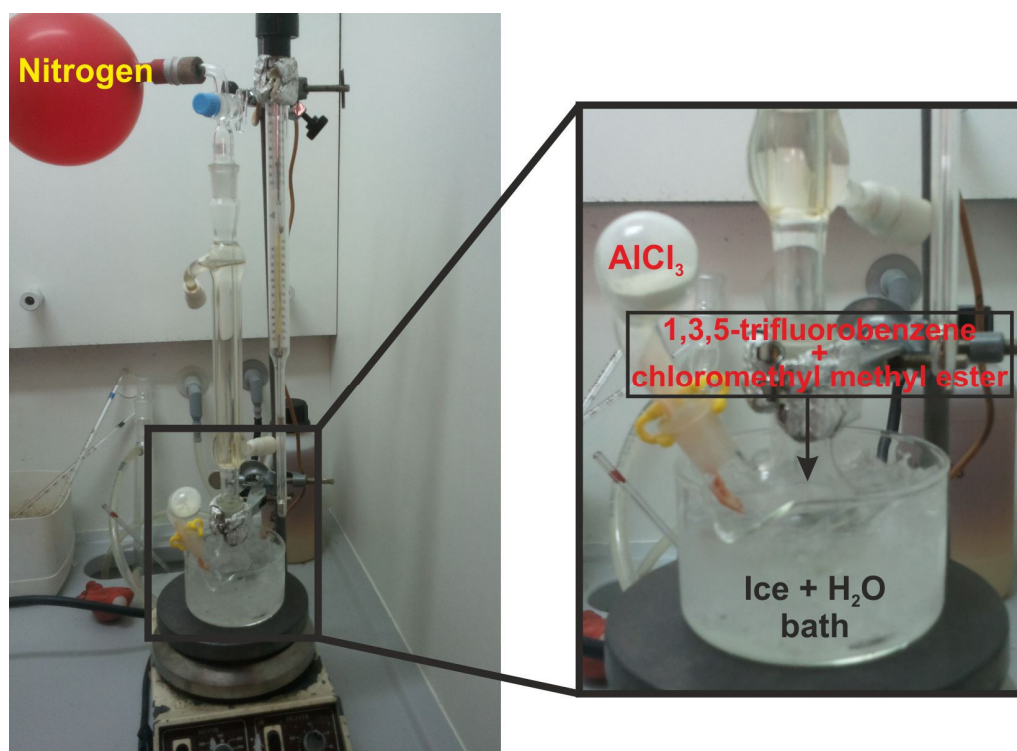


Figure 2.5 – Representation of the synthetic instrumentation towards the preparation of the intermediate compound IL^2 .

Michaelis-Arbusov reaction

To isolate IL^3 a Michaelis-Arbusov reaction was employed by refluxing a mixture of IL^2 and triethyl phosphite for approximately 3 h. The excess of triethyl phosphite was distilled under reduced pressure and IL^3 , [hexaethyl((2,4,6-trifluorobenzene-1,3,5-triyl)tris(methylene))tris(phosphonate)], was isolated as a white powder in 75% yield after being purified by flash column chromatography.

Acid hydrolysis

The last step consisted in an acid hydrolysis where an aqueous solution of HCl (6 M) was added to IL^3 and the reaction mixture refluxed for 20 h. The target compound H_6tftp was isolated as a white crystalline powder in quantitative yields (*ca.* 98%).

2.5.2. Structural Elucidation

The organic linker ((2,4,6-trifluorobenzene-1,3,5-triyl)tris(methylene))triphosphonic acid (H_6tftp) as well as their intermediate compounds 1,3,5-tris(chloromethyl)-2,4,6-trifluorobenzene (IL^2) and hexaethyl((2,4,6-trifluorobenzene-1,3,5-triyl)tris(methylene))tris(phosphonate) (IL^3) were obtained as crystalline compounds, allowing us to solve their crystal structure by single-crystal X-ray diffraction (Figures 2.6 - 2.8). All compounds were also characterized by NMR spectroscopy, being dissolve in $CDCl_3$ (IL^2 and IL^3) and $DMSO-d_6$ (H_6tftp), and mass spectrometry.

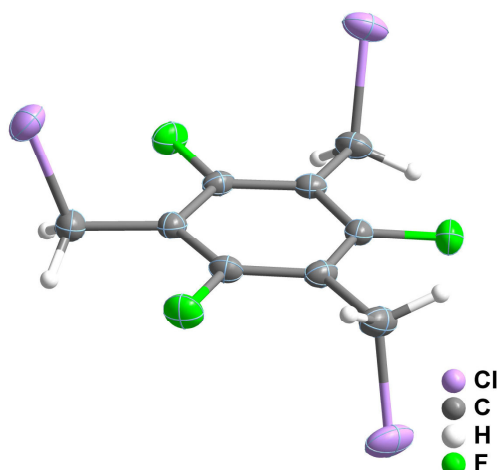


Figure 2.6 - Molecular structure of 1,3,5-tris(chloromethyl)-2,4,6-trifluorobenzene (IL^2) showing the atomic labeling scheme for all non-hydrogen atoms. Displacement ellipsoids are drawn at the 50% probability level.

The 1H NMR spectrum of IL^2 has just one signal at δ 4.64 ppm as a singlet, being attributed to the resonance of six protons of the methylene groups. Slightly more complicated is the ^{13}C NMR spectrum which has a multiplet between δ 31.8 and 31.9 ppm corresponding to the carbons of the methylene groups. The aromatic carbons of $-C-CH_2$ appear at δ 111.0-111.5 ppm range and, finally, the aromatic carbons $-C-F$ present their resonances at δ 159.5 ppm as a double triplet ($J(^{13}C-^{19}F) = 258.1$ Hz and $^3J(^{13}C-^{19}F) = 10.4$ Hz). In the ^{19}F NMR spectrum we highlight the resonance at δ -138.1 ppm as a singlet attributed to the three fluorine atoms.

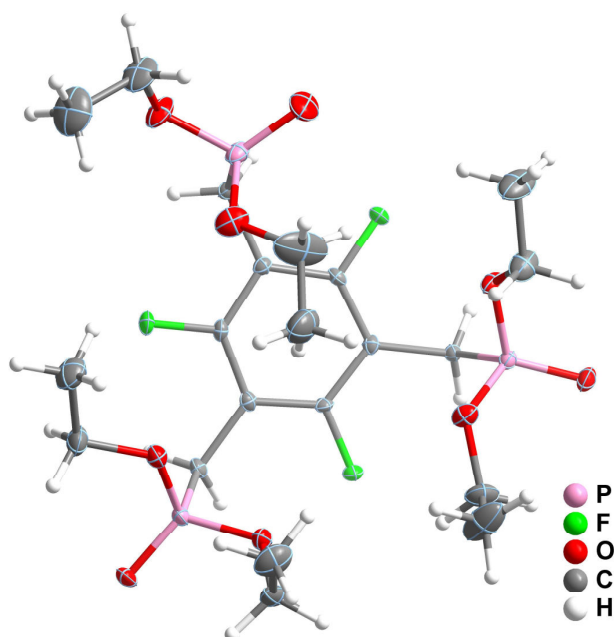


Figure 2.7 - Molecular structure of hexaethyl((2,4,6-trifluorobenzene-1,3,5-triyl)tris(methylene))tris(phosphonate) (II^3) showing the atomic labeling scheme for all non-hydrogen atoms. Displacement ellipsoids are drawn at the 30% probability level.

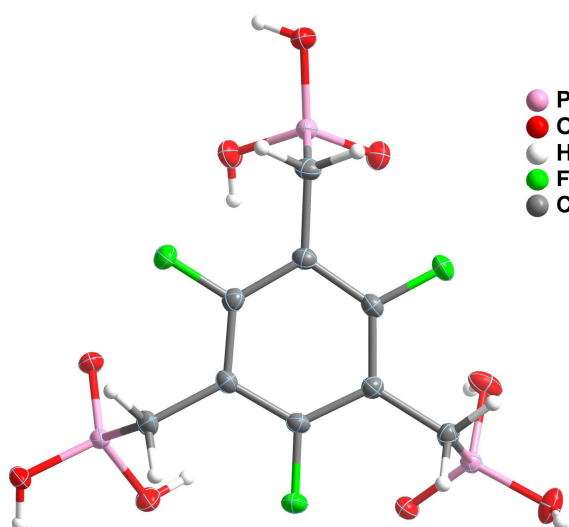


Figure 2.8 - Molecular structure of ((2,4,6-trifluorobenzene-1,3,5-triyl)tris(methylene))-triphosphonic acid (H_6tftp) showing the atomic labeling scheme for all non-hydrogen atoms. Displacement ellipsoids are drawn at the 50% probability level.

The 1H NMR spectrum of II^3 presents in the aliphatic region three well-resolved signals (Figure 2.9): i) a triplet ($J(^1H-^1H) = 7.07$ Hz) situated at δ 1.29 ppm corresponding to the resonance of the $-CH_3$ group; ii) at δ 3.19 ppm appears the resonance of the protons

of the methylene group in $-\text{CH}_2-\text{P}$ as a doublet ($J(^1\text{H}-^{31}\text{P}) = 21.4$ Hz); and iii) the resonance signal of the other methylene group $-\text{O}-\text{CH}_2$ emerge at δ 4.09 ppm as a double quartet ($J(^1\text{H}-^1\text{H}) = 7.07$ Hz and $J(^1\text{H}-^{31}\text{P}) = 7.3$ Hz).

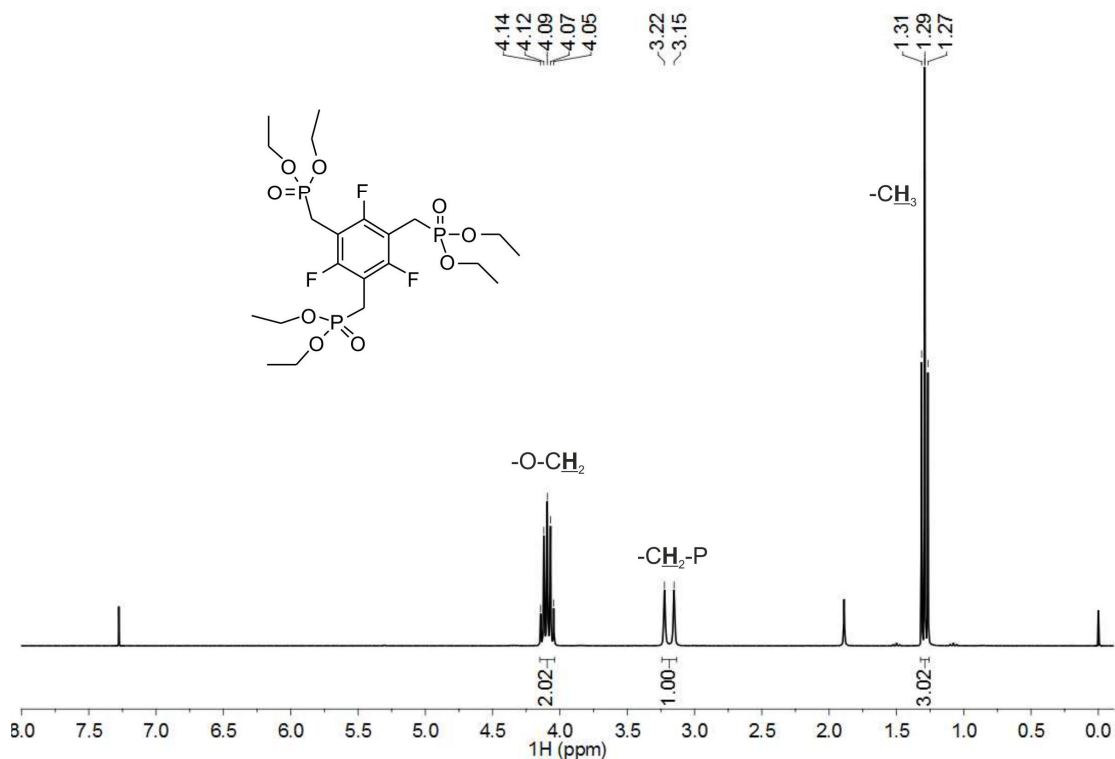


Figure 2.9 - ^1H NMR spectrum of the intermediate compound hexaethyl((2,4,6-trifluorobenzene-1,3,5-triyl)tris(methylene))tris(phosphonate) (IL^3).

The ^{13}C NMR spectrum of IL^3 has a signal between δ 16.3-16.4 ppm corresponding to the carbon of $-\text{CH}_3$ group. The aliphatic region shows the resonances of the carbons belonging to $-\text{CH}_2-\text{P}$ and $-\text{O}-\text{CH}_2$ at δ 21.0 [doublet ($J(^{13}\text{C}-^{31}\text{P}) = 143.2$ Hz)] and 62.3-62.4 ppm, respectively. The aromatic carbons $-\text{C}-\text{CH}_2$ are located between δ 104.7 and 105.3 ppm. At δ 156.3, 156.4 and 159.7 appears the resonances of the aromatic carbons $-\text{C}-\text{F}$. In the ^{19}F NMR spectrum there is a resonance signal centered as a quartet ($J(^{19}\text{F}-^{31}\text{P}) = 5.6$ Hz) at δ -138.7 ppm attributed to the fluorine atoms presented in the aromatic ring. The TOF MS ES^+ show two peaks at m/z 583.2 ($\text{M}+\text{H}$) $^+$ and 605.2 ($\text{M}+\text{Na}$) $^+$.

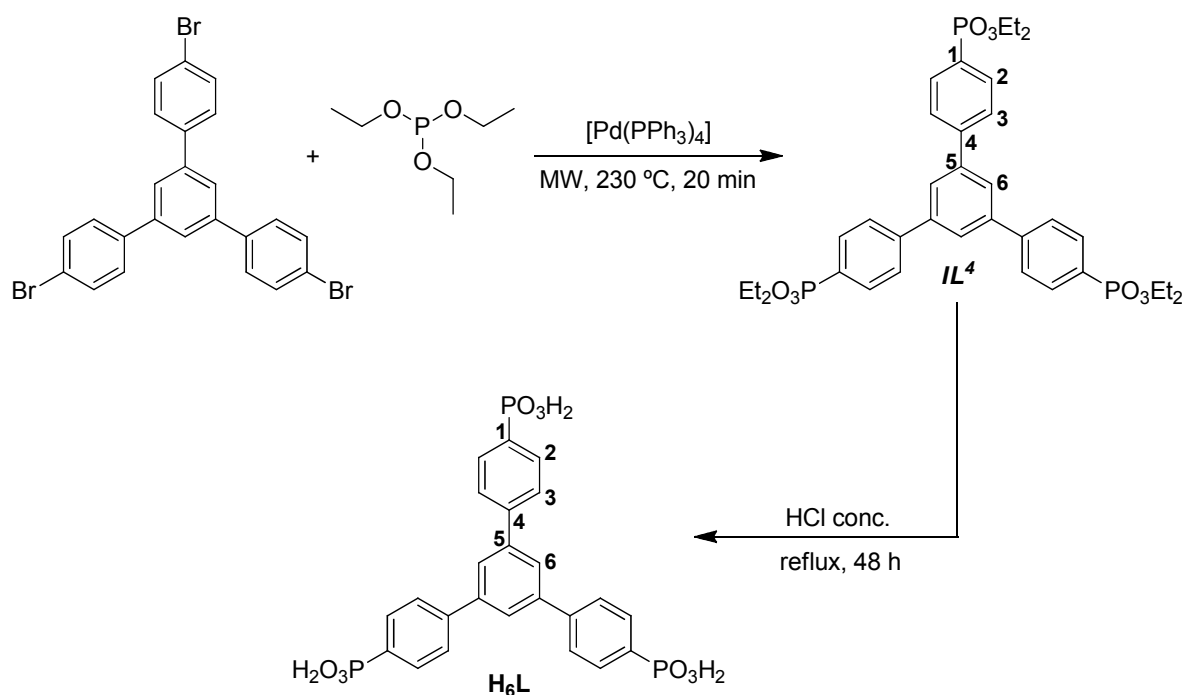
From the ^1H NMR spectrum of H_6tftp only can be inferred information about the protons belonging to the methylene group which are represented as a doublet ($J(^1\text{H}-^{31}\text{P}) = 20.9$ Hz) centered at δ 2.93 ppm. The ^{13}C NMR spectrum of H_6tftp shows in the aliphatic zone a signal as a doublet ($J(^{13}\text{C}-^{31}\text{P}) = 135.7$ Hz) at δ 23.0 ppm corresponding to the carbon $-\text{CH}_2-\text{P}$. In the aromatic region the carbons of $-\text{C}-\text{CH}_2-\text{P}$ (δ 105.8-106.2 ppm) and of $-\text{C}-\text{F}$ (between δ 155.5 and 155.8, and between δ 158.9 and 159.1) appear. In the ^{19}F NMR spectrum of H_6tftp it appears only a signal as a quartet ($J(^{19}\text{F}-^{31}\text{P}) = 5.6$ Hz) centered at δ -139.5 ppm attributed to the fluorine atoms. The phosphorous atoms present in the structure of H_6tftp were identified at δ 19.4 ppm as a triplet ($J(^{31}\text{P}-^1\text{H}) = 20.4$ Hz). The

TOF MS ES⁻ spectrum has three peaks at m/z 197.4 (M-2H-F)²⁻, 413.1 (M-H)⁻ and 451.0 (M-2H+K)⁻.

2.6. Large tripodal phosphonate ligand H_6L

2.6.1. Synthesis

Aiming at the preparation of three-dimensional robust and highly porous MOFs, a large tripodal H_6L phosphonate-based organic linker was prepared (Scheme 2.7). The presence of four aromatic rings is expected to originate more efficient photoluminescent materials owing to the promotion of an effective *antenna effect*. Additionally, highly porous MOFs should be isolated.



Scheme 2.7 - Synthetic route to the large tripodal phosphonate ligand H_6L .

The synthesis of H_6L has been previously reported for some research groups who used slight different methodologies and different reaction conditions.^{24-25,43} The most complex step is, undoubtedly, the isolation of its hexaalkyl ester intermediate. This step involves a Michaelis-Arbusov reaction catalyzed by $NiCl_2$, $NiBr_2$ or $[Pd(PPh_3)_4]$ taking from 1 to 6 days to be completed and, normally, high temperatures are required. Nevertheless, the intermediate compound of H_6L is isolated in high yields (80-90%). The second, and final, step towards the isolation of H_6L is based on an acid hydrolysis,

refluxing an aqueous solution of concentrated HCl during some hours. The desired compound is obtained from very high to quantitative yields.

Pd-catalyzed Cross-coupling reaction

Commercially available 1,3,5-tris(4-bromo phenyl)benzene and [Pd(PPh₃)₄] were added in a round-bottom flask containing triethyl phosphite. The resulting reaction mixture was refluxed, under N₂ atmosphere, on a sand bath for approximately 48 h. After cooling to ambient temperature, the resulting dark solution was placed under reduced pressure in order to remove the excess of triethyl phosphite. The resulting residue was purified by flash column chromatography using dichloromethane/methanol (97%/3%) as eluent. The phosphohexaethyl ester intermediate **IL**⁴ organic molecule was obtained as a yellow and viscous oil, becoming a powder, in 53% yield, when dried under vacuum.

The quest for faster synthetic approaches and better reaction yields, led to the use of the microwave-assisted approach to isolate the intermediate hexaethyl ester of H₆L. Experiments were performed in an Ethos SYNTH microwave labstation (Milestone Inc.) apparatus, by using glassware setup for atmospheric-pressure reactions (temperature measured with a fiber-optic probe). A reaction mixture composed of 1,3,5-tris(4-bromophenyl)benzene, [Pd(PPh₃)₄] and triethyl phosphite were added to a two-neck flask fitted with a reflux condenser and a temperature probe. The reaction mixture, under N₂ atmosphere, was irradiated using different powers (400, 500, 600, 700 and 800 W). Nevertheless, even using 800 W of power, the desired temperature was not achieved. Therefore, a weflon bar was placed into the reaction medium and in this way it was possible to reflux the reaction mixture [triethyl phosphite (used as reagent and solvent) does not absorb very well the microwave irradiation, becoming the heating process very difficult or, even, impossible in order to reach the desired temperature]. During our attempts the reaction time was also varied (ranging from 1 to 6 h). However, controlling, frequently, the reaction by TLC it was observed that almost all starting reagent was not converted.

Other microwave-assisted equipment was tested: CEM Focused Microwave Synthesis System Discover S-Class apparatus. After some experiments, this equipment was selected as the best choice for the preparation of the hexaethyl ester intermediate of H₆L (**IL**⁴). The first step involved a Pd-catalyzed cross-coupling reaction (Scheme 2.7). A reaction mixture composed of 1,3,5-tris(4-bromophenyl)benzene, [Pd(PPh₃)₄] and triethyl phosphite was prepared inside a 10 mL IntelliVent microwave reactor and refluxed, using a weflon bar (see Experimental Section for further details). When the reaction was completed, the excess of triethyl phosphite was distilled under reduced pressure and the hexaethyl ester intermediate **IL**⁴ was purified by flash column chromatography using a mixture of dichloromethane/methanol (97%:3%) as eluent. The obtained oily residue was washed with petroleum ether in an ultrasonic bath affording the target compound as a white powder in 83% yield.

Acid hydrolysis

The second reaction step was based on an acid hydrolysis. The reaction started by preparing a mixture composed of an aqueous solution of HCl (6 M) and the intermediate IL^4 compound and kept it under reflux for 2 days. After characterization by NMR spectroscopy, the NMR spectra suggest us that the hydrolysis was incomplete.

Then, the intermediate IL^4 compound was mixed with an aqueous solution of concentrated HCl and the mixture was refluxed for 2 days, under constant magnetic stirring (Scheme 2.7). The reaction was stopped after the formation of a brownish viscous residue. The resulting mixture was washed with dichloromethane (to extract some organic impurities or secondary less polar compounds) and the brownish viscous residue was dissolved with methanol. After distillation of methanol, we obtained again a brownish viscous residue which was redissolved in methanol, adding then dry toluene and dry hexane (1:1). This procedure aims at a more efficient drying of the desired compound. It afforded the formation of a yellowish foam which was dissolved in a small amount of dry methanol giving raise H_6L as a white powder in a 93% yield (see Experimental Section for further details).

2.6.2. Structural Elucidation

The intermediate IL^4 compound and the desired large tripodal organic linker H_6L , obtained as crystalline compounds, allowed us to solve their crystal structure by single-crystal X-ray diffraction (Figures 2.10 and 2.11). Both compounds were also characterized by NMR spectroscopy and mass spectrometry.

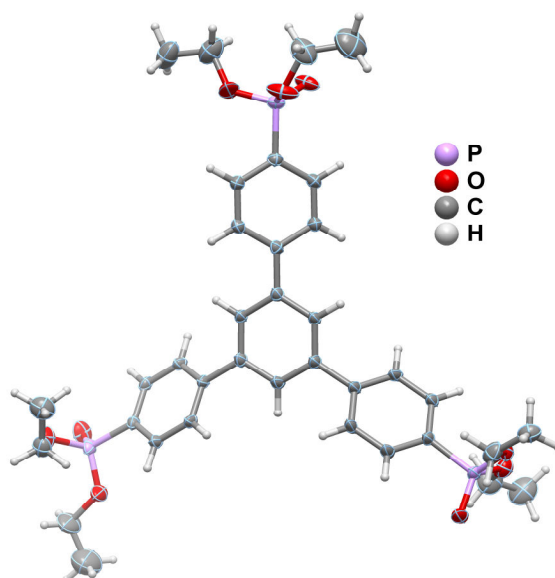


Figure 2.10 - Molecular structure of the intermediate molecule IL^4 . Displacement ellipsoids are drawn at the 30% probability level.

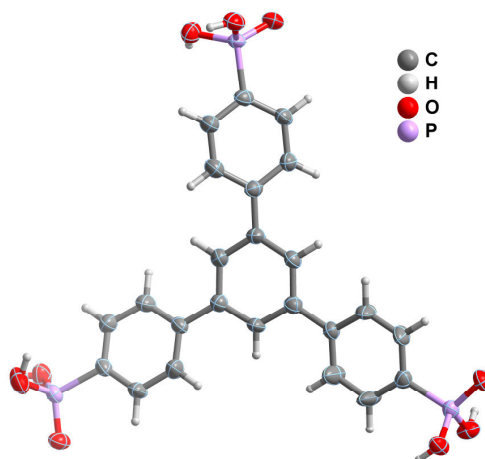


Figure 2.11 - Molecular structure of the large tripodal **H₆L** organic linker. Displacement ellipsoids are drawn at the 80% probability level.

The ^1H NMR spectrum of **IL⁴** shows, in the aliphatic region, a resonance signal as a triplet ($J(^1\text{H}-^1\text{H}) = 7.1$ Hz) centered at δ 1.36 ppm attributed to the protons of the methyl groups. Between δ 4.12 and 4.21 ppm there is a multiplet corresponding to the protons of the methylene moieties. In the aromatic region it is possible to observe: i) between δ 7.77 and 7.81 ppm a multiplet belonging to the resonance of the H3 protons; ii) a singlet at δ 7.83 ppm attributed to the three H6 aromatic protons located in the central ring; and iii) another multiplet between δ 7.91 and 7.98 ppm corresponding to H2 protons (Figure 2.12). The ^{13}C NMR spectrum provides several signals belonging to the **IL⁴** intermediate molecule. At δ 16.3 ppm there is the signal of the methyl groups as a doublet ($J(^{13}\text{C}-^{31}\text{P}) = 6.3$ Hz) and at δ 62.2 ppm the resonance of the methylene groups also as a doublet ($J(^{13}\text{C}-^{31}\text{P}) = 5.5$ Hz). At higher chemical shifts the spectrum has several and very close peaks, being difficult their assignment: 126.1, 126.9, 127.3 (d, $J(^{13}\text{C}-^{31}\text{P}) = 15.2$ Hz), 132.4 (d, $J(^{13}\text{C}-^{31}\text{P}) = 10.2$ Hz), 141.6 and 144.4 ($J(^{13}\text{C}-^{31}\text{P}) = 3.0$ Hz). In the TOF MS ES⁺ spectrum we can observe two peaks of **IL⁴** at m/z : 715.2 (M+H)⁺ and 737.2 (M+Na)⁺.

The ^1H NMR spectrum only provides, as expected, resonance signals of the H₆L organic linker in the aromatic region. Therefore, between δ 7.78 and 7.85 ppm it is possible to find the resonances of the H3 protons as a multiplet. The H2 protons are located, as a multiplet, between δ 7.97 and 8.10 ppm (being the last peak overlapped). The remaining resonance appears as a singlet at δ 8.01 ppm corresponding to the H6 protons. As mentioned in the description of the ^1H NMR spectrum, in the ^{13}C NMR spectrum of H₆L it is only observed resonance signals in the aromatic region: 125.2, 127.0 (d, $J(^{13}\text{C}-^{31}\text{P}) = 14.3$ Hz), 131.2 (d, $J(^{13}\text{C}-^{31}\text{P}) = 10.0$ Hz), 132.1, 134.5, 141.1 and 142.2 (d, $J(^{13}\text{C}-^{31}\text{P}) = 2.8$ Hz). The ^{31}P NMR spectrum of H₆L possesses only a resonance as a multiplet between δ 13.7 and 14.0. After analysis of the high-resolution ESI mass spectrum it is possible to observe one peak at m/z 547.0464 (M+H)⁺, which identifies the protonated form of the H₆L organic ligand.

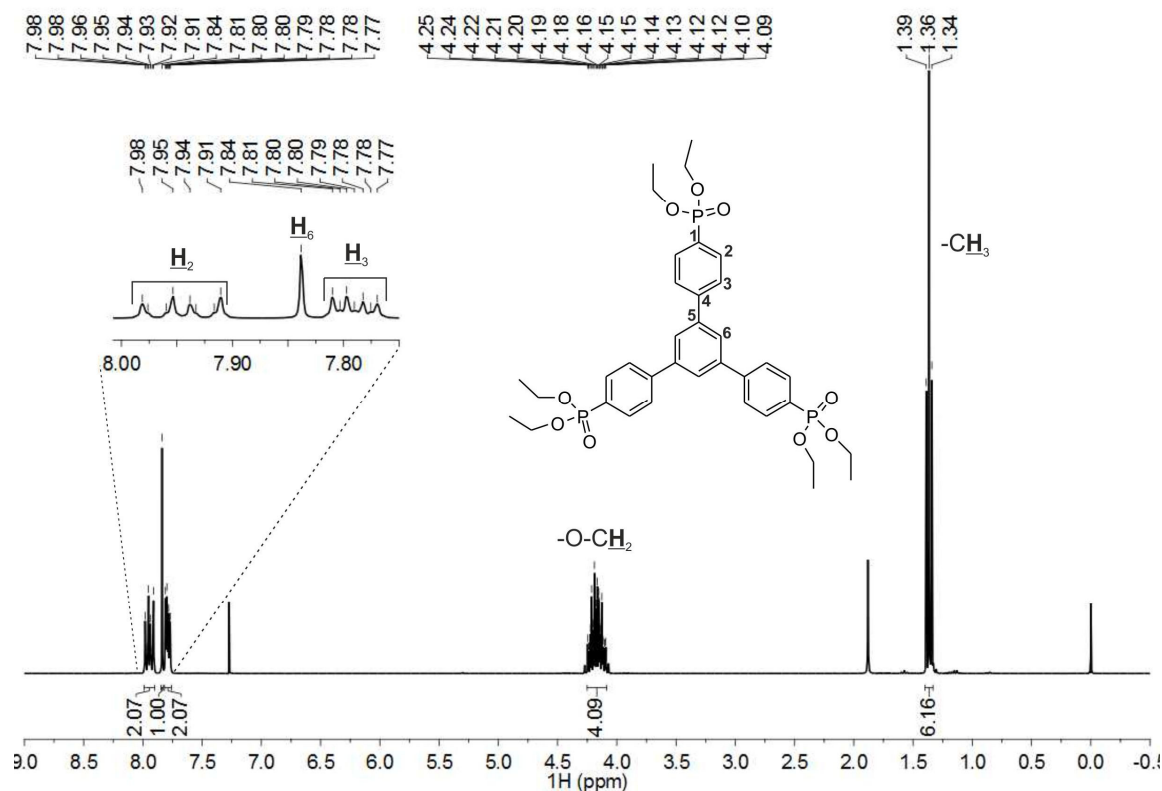


Figure 2.12 - ^1H NMR spectrum of the intermediate compound II^4 .

2.7. Results and Discussion

In this chapter it was documented in detail the synthetic procedures to prepare four different phosphonic acid organic linkers to be used for the preparation of multidimensional MOFs. The organic ligand 1,4-phenylenebis-(methylene)diphosphonic acid (H_4pmd) was isolated *via* an acid hydrolysis using an aqueous solution of HCl (6 M). The work-up of the reaction was simple, being only performed a liquid-liquid extraction using dichloromethane in order to remove some nonpolar impurities. After evaporation of the solvent, under reduced pressure, and washing with acetone, the desired compound was obtained in quantitative yields (96%).

More complex was the synthesis of the tripodal organic compound (benzene-1,3,5-triyltris(methylene))tri-phosphonic acid (H_6bmt). Its preparation started with a Michaelis-Arbusov reaction by preparing a reaction mixture containing 1,3,5-tris-(bromomethyl)benzene with triethyl phosphite. The latter reagent was added in excess acting as reactant and solvent. After purification the intermediate [hexaethyl(benzene-1,3,5-triyltris-(methylene))tris(phosphonate)] (II^1) compound was obtained, as a colorless oil, in 88% yield. After optimization of the reaction conditions, the synthetic route became quite simple and II^1 can be prepared in large amounts in period of time not so long. The second step, in order to isolate the desired H_6bmt organic ligand, consists, as for H_4pmd , in an acid hydrolysis using an aqueous solution of HCl (6 M). The work-up, washing and

drying process to obtain **H₆bmt** was very similar as for **H₄pmd**, and the resulting compound was obtained in 92% yield.

The preparation of the fluorinated tripodal ((2,4,6-trifluorobenzene-1,3,5-triyl)tris(methylene))triphosphonic acid (**H₆tftp**) linker comprised a three-step reaction: i) chloromethylation reaction; ii) Michaelis-Arbusov reaction; and iii) acid hydrolysis. The chloromethylation method is a kind of Friedel-Crafts reaction, consisting in an aromatic electrophilic substitution using aluminium chloride (AlCl₃) as catalyst. This reaction started with the preparation of a reactive mixture composed of 1,3,5-trifluorobenzene, chloromethyl methyl ether (used in excess displaying the role of reactant and solvent) and AlCl₃. This reaction required care: i) the constant use of gloves and laboratory glasses; ii) the handling of AlCl₃ (explosive when in contact with water and in humid atmospheres, this reactant become highly acid), and chloromethyl methyl ether (it has toxicity and carcinogenic features) always inside a hood fume. The chloromethylation reaction employed to prepare the intermediate compound 1,3,5-tris(chloromethyl)-2,4,6-trifluorobenzene (**IL²**) afforded several secondary products. The intermediate **IL²** compound (purified by flash column chromatography) was obtained in 71% yield. The synthetic methodologies to isolate hexaethyl((2,4,6-trifluorobenzene-1,3,5-triyl)tris(methylene))tris(phosphonate) (**IL³**) and **H₆tftp** consists in a Michaelis-Arbusov reaction and an acid hydrolysis, respectively. The procedures to perform both reactions were very similar to that described for **H₆bmt**. The intermediate **IL³** and the desired **H₆tftp** were obtained in 75% and 98% yields, respectively.

The fourth organic linker prepared during this work was the large tripodal **H₆L**. Its synthesis comprises a Pd-catalyzed cross-coupling reaction and an acid hydrolysis. At the beginning the intermediate compound **IL⁴**, prepared from a reactive mixture composed of 1,3,5-tris(4-bromophenyl)benzene, [Pd(PPh₃)₄] and triethyl phosphite, using conventional heating methods, was isolated in low reaction yields and the reaction took large periods of time. Nevertheless, changing this method for a simpler and economical-friendly approach, in this case microwave-assisted synthesis, **IL⁴** was obtained in a faster way and in much higher yields (83%). The employed high temperatures, the pressure (100 psi) generated inside the reactor seems to be the key reaction parameter to prepare **IL⁴** in a quickly way and in large amounts. The second step was based on an acid hydrolysis. The procedure to perform this reaction suffers some modifications when compared for that to obtain **H₄pmd**, **H₆bmt** and **H₆tftp**. The hydrolysis of **IL⁴** was carried out using concentrated HCl (12 M) instead an aqueous solution of HCl (6 M) and the period of time required was longer (2 days). This fact may be attributed to the increase of the non-polarity of the intermediated phosphohexaethyl ester **IL⁴**, once this has four aromatic rings instead of one as **H₄pmd**, **H₆bmt** and **H₆tftp**. The work-up of the final reaction mixture was performed in similar fashion to those of previous organic linkers. To isolate the large tripodal **H₆L** as white powder it was needed to use a particular drying procedure (a mixture of dried hexane and dried toluene). **H₆L** was obtained in a high reaction yield (93%).

Regarding all the employed synthetic routes reported in this chapter, one can conclude that they are good choices to isolate phosphohexaethyl ester intermediates and

the corresponding phosphonic acid organic linkers in short periods of time and with high reaction yields:

- i) the Michaelis-Arbusov method, a nucleophilic substitution (S_N2) reaction, is a very simple and efficient alternative to prepare phosphohexaethyl ester intermediates, which does not represent any risk for the human health. The use of triethyl phosphite as solvent and reactant at the same time, allows the synthesis of those intermediate compounds in a fast way, high yields and without the formation of more secondary products than when using other organic solvents (i.e., toluene or xylene). This method also allows the scale-up of the reaction in order to obtain the desired organic molecules in large amounts. The unique inconvenient resides in the distillation, under reduced pressure, of triethyl phosphite (being this procedure performed inside a hood fume using a quite complex system), and the need of high temperatures to carry out the reaction;
- ii) the Pd-catalyzed cross-coupling reaction showed is a good choice for the reaction between an aryl halide and triethyl phosphite. Compared with the Michaelis-Arbusov methodology, which does not need the use of any catalyst to isolate phosphohexaethyl ester intermediates, the reaction of aryl halide with trialkyl phosphite only occurs if we use a catalyst (in this case, the Pd-based catalyst $[Pd(PPh_3)_4]$). As for the previous described method, high temperatures are needed. Despite the high reaction temperature, it is not enough to isolate the desired compound in high yields and for short periods of time. This fact was detected when the reaction mixture was refluxed, containing the appropriate aryl halide, triethyl phosphite and $[Pd(PPh_3)_4]$, using conventional heating processes. Therefore, performing the Pd-catalyzed cross-coupling reaction using the simpler and less energy-consuming microwave-assisted approach, the desired phosphohexaethyl ester intermediate was quickly (much faster than by using conventional heating) isolated in high yields. Despite the high temperature employed, the generated pressure inside the reactor played an important role in the synthesis of the desired compound. In addition, the scale-up of this reaction seems to be not very complex if a bigger reactor (as for instance, with 35 mL of capacity) is used, and a restricted control of the pressure generated inside the reactor to prevent accidents (i.e., explosion). The inconvenient of this reaction follow the same line of the Michaelis-Arbusov method: the distillation of triethyl phosphite, under reduced pressure, inside of a hood fume and the need of high temperatures to perform the reaction;
- iii) Conventional acid hydrolysis proved to be a very efficient approach toward the hydrolysis of large amounts of phosphohexaethyl ester intermediate in order to produce the desired acid phosphonic organic linkers. The use of this type of reaction is very simple since it is only needed to mix the phosphohexaethyl ester compound with an aqueous solution of HCl. While an aqueous solution of HCl (6 M) is enough to hydrolyze all the phosphodiethyl ester groups of the intermediate

organic molecules with only an aromatic ring, for the compound with four aromatic rings the use of concentrated HCl is fundamental.

The structures of all intermediate compounds (IL^1 , IL^2 , IL^3 and IL^4) and the desired organic linkers (H_4pmd , H_6bmt , H_6tftp and H_6L) were unequivocally studied and characterized using standard liquid-state techniques (NMR spectroscopy and mass spectrometry). The crystal structure of the intermediate compounds IL^2 , IL^3 , IL^4 and the phosphonic acid H_6tftp and H_6L organic linkers were unveiled by using single-crystal X-ray diffraction studies. The crystal structure of IL^2 , IL^3 and H_6tftp were, for the best of our knowledge, firstly reported by our research group.⁴⁴

2.8. References

- (1) Toy, A. D. F.; Walsh, E. D. *Phosphorous Chemistry in Everyday Living*; 2nd ed.; American Chemical Society: Washington, D. C., 1987.
- (2) Barton, D.; Ollis, W. D.; Stoddart, J. F. *Comprehensive Organic Chemistry: the synthesis and reactions of organic compounds*; Oxford: Pergamon, 1979.
- (3) Kosolapoff, G. M.; Maier, L. *Organic Phosphorous Compounds*; John Wiley and Sons, Inc., Publishers, New York, N. Y., 1976; Vol. 7.
- (4) Clearfield, A.; Demadis, K. *Metal Phosphonate Chemistry: from Synthesis to Applications*; RSC Publishing, 2012.
- (5) Karlin, K. D. *Progress in Inorganic Chemistry*; John Wiley and Sons, Inc., Hoboken, New Jersey, 2012; Vol. 57.
- (6) Wainwright, P.; Maddaford, A.; Zhang, X.; Billington, H.; Leese, D.; Glen, R.; Pryde, D. C.; Middleton, D. S.; Stephenson, P. T.; Sutton, S.; *Nucleos Nucleot Nucl*, **2013**, *32*, 477-492.
- (7) Nicholson, J. W.; Singh, G.; *Biomaterials*, **1996**, *17*, 2023-2030.
- (8) Rajsiki, S. R.; Williams, R. M.; *Chem. Rev.*, **1998**, *98*, 2723-2795.
- (9) Alberti, G.; Costantino, U.; Allulli, S.; Tomassini, N.; *J. Inorg. Nucl. Chem.*, **1978**, *40*, 1113-1117.
- (10) Clearfield, A.; *Curr. Opin. Solid State Mater. Sci.*, **2002**, *6*, 495-506.
- (11) Seki, M.; Kondo, K.; Iwasaki, T.; *J. Chem. Soc., Perkin Trans.*, **1996**, 3-5.
- (12) Kurti, L.; Czako, B. *Strategic Applications of Named Reactions in Organica Synthesis*; Elsevier, 2005.
- (13) Eymery, F.; Iorga, B.; Savignac, P.; *Tetrahedron*, **1999**, *55*, 13109-13150.
- (14) Meier, H.; Lehmann, M.; *Angew. Chem. Int. Ed.*, **1998**, *37*, 643-645.
- (15) Diez-Barra, E.; Garcia-Martinez, J. C.; Merino, S.; del Rey, R.; Rodriguez-Lopez, J.; Sanchez-Verdu, P.; Tejada, J.; *J. Org. Chem.*, **2001**, *66*, 5664-5670.
- (16) Mizoshita, N.; Ikai, M.; Tani, T.; Inagaki, S.; *J. Am. Chem. Soc.*, **2009**, *131*, 14225-14227.
- (17) Murugavel, R.; Singh, M. P.; *New J. Chem.*, **2010**, *34*, 1846-1854.
- (18) Ranasinghe, M. I.; Murphy, P.; Lu, Z. K.; Huang, S. P. D.; Twieg, R. J.; Goodson, T.; *Chem. Phys. Lett.*, **2004**, *383*, 411-417.
- (19) Wang, Z. K.; Heising, J. M.; Clearfield, A.; *J. Am. Chem. Soc.*, **2003**, *125*, 10375-10383.
- (20) Fawcett, J.; Platt, A. W. G.; Vickers, S.; *Polyhedron*, **2003**, *22*, 1431-1435.
- (21) Clearfield, A.; *J. Alloy Compd.*, **2006**, *418*, 128-138.
- (22) Denmark, S. E.; Sweis, R. F.; *J. Am. Chem. Soc.*, **2004**, *126*, 4876-4882.
- (23) Kotha, S.; Lahiri, K.; Kashinath, D.; *Tetrahedron*, **2002**, *58*, 9633-9695.
- (24) Beckmann, J.; Ruttiger, R.; Schwich, T.; *Cryst. Growth Des.*, **2008**, *8*, 3271-3276.

- (25) Vaidhyanathan, R.; Mahmoudkhani, A. H.; Shimizu, G. K. H.; *Can. J. Chem.*, **2009**, *87*, 247-253.
- (26) Santos, J. S. D.; Montouillout, V.; Fayon, F.; Fernandez, C.; Delain-Bioton, L.; Villemin, D.; Jaffres, P. A.; *New J. Chem.*, **2004**, *28*, 1244-1249.
- (27) Gomez-Alcantara, M. M.; Cabeza, A.; Martinez-Lara, M.; Aranda, M. A. G.; Suau, R.; Bhuvanesh, N.; Clearfield, A.; *Inorg. Chem.*, **2004**, *43*, 5283-5293.
- (28) Paz, F. A. A.; Klinowski, J.; *J. Phys. Org. Chem.*, **2003**, *16*, 772-782.
- (29) Rocha, J.; Paz, F. A. A.; Shi, F. N.; Ananias, D.; Silva, N. J. O.; Carlos, L. D.; Trindade, T.; *Eur. J. Inorg. Chem.*, **2011**, 2035-2044.
- (30) Shi, F. N.; Paz, F. A. A.; Girginova, P.; Rocha, J.; Amaral, V. S.; Klinowski, J.; Trindade, T.; *J. Mol. Struct.*, **2006**, *789*, 200-208.
- (31) Shi, F. N.; Paz, F. A. A.; Girginova, P. I.; Mafra, L.; Amaral, V. S.; Rocha, J.; Makal, A.; Wozniak, K.; Klinowski, J.; Trindade, T.; *J. Mol. Struct.*, **2005**, *754*, 51-60.
- (32) Paz, F. A. A.; Rocha, J.; Klinowski, J.; Trindade, T.; Shi, F. N.; Mafra, L.; *Prog. Solid State Chem.*, **2005**, *33*, 113-125.
- (33) Paz, F. A. A.; Shi, F. N.; Klinowski, J.; Rocha, J.; Trindade, T.; *Eur. J. Inorg. Chem.*, **2004**, 2759-2768.
- (34) Cunha-Silva, L.; Ananias, D.; Carlos, L. D.; Paz, F. A. A.; Rocha, J.; *Zeitschrift Fur Kristallographie*, **2009**, *224*, 261-272.
- (35) Cunha-Silva, L.; Lima, S.; Ananias, D.; Silva, P.; Mafra, L.; Carlos, L. D.; Pillinger, M.; Valente, A. A.; Paz, F. A. A.; Rocha, J.; *J. Mater. Chem.*, **2009**, *19*, 2618-2632.
- (36) Silva, P.; Vieira, F.; Gomes, A. C.; Ananias, D.; Fernandes, J. A.; Bruno, S. M.; Soares, R.; Valente, A. A.; Rocha, J.; Paz, F. A. A.; *J. Am. Chem. Soc.*, **2011**, *133*, 15120-15138.
- (37) Cunha-Silva, L.; Mafra, L.; Ananias, D.; Carlos, L. D.; Rocha, J.; Paz, F. A. A.; *Chem. Mater.*, **2007**, *19*, 3527-3538.
- (38) Shi, F. N.; Trindade, T.; Rocha, J.; Paz, F. A. A.; *Cryst. Growth Des.*, **2008**, *8*, 3917-3920.
- (39) Gagnon, K. J.; Perry, H. P.; Clearfield, A.; *Chem. Rev.*, **2012**, *112*, 1034-1054.
- (40) Shimizu, G. K. H.; Vaidhyanathan, R.; Taylor, J. M.; *Chem. Soc. Rev.*, **2009**, *38*, 1430-1449.
- (41) Winter, A.; Friebe, C.; Hager, M. D.; Schubert, U. S.; *Eur. J. Org. Chem.*, **2009**, 801-809.
- (42) Fernandes, J. A.; Vilela, S. M. F.; Ribeiro-Claro, P. J. A.; Almeida Paz, F. A.; *Acta Crystallogr., Sect. C: Cryst. Struct. Commun.*, **2011**, *67*, O198-O200.
- (43) Ouellette, W.; Wang, G. B.; Liu, H. X.; Yee, G. T.; O'Connor, C. J.; Zubieta, J.; *Inorg. Chem.*, **2009**, *48*, 953-963.
- (44) Vilela, S. M. F.; Fernandes, J. A.; Ananias, D.; Carlos, L. D.; Rocha, J.; Tomé, J. P. C.; Paz, F. A. A.; *CrystEngComm*, **2013**, DOI: 10.1039/c1033ce41482e.

Chapter 3

1D and 3D MOFs from the Self-Assembly of Lanthanides with 1,4-Phenylenebis(methylene)diphosphonic acid

3.1. Initial Considerations

This chapter gives particular attention to the synthesis of several 1D and 3D MOFs using the bipodal phosphonate-based organic linker 1,4-phenylenebis(methylene)-diphosphonic acid (**H₄pmd**).

The structure of **H₄pmd** (Scheme 2.4) contains an 1,4-disubstituted aromatic ring with two methylenephosphonic acid groups, with the $-\text{CH}_2$ moieties grant it some flexibility. This organic linker has been widely employed in the preparation of inorganic-organic hybrid materials. The studies have been focused in the self-assembly of structures, typically under hydro(solvo)thermal conditions, which vary from 1D to 3D networks by combining residues of **H₄pmd**¹⁻² with, mainly, transition metals (Ni^{2+} , Mn^{2+} , Cd^{2+} , Co^{2+} , Zn^{2+} and Cu^{2+})³⁻⁹ and *p*-block (Ga^{3+} , Sn^{2+} and Pb^{2+})¹⁰⁻¹². To the best of our knowledge, our research group reported the synthesis of the first multidimensional MOFs combining the bipodal organic molecule **H₄pmd** with lanthanides: i) two isotypical 3D materials [$\text{Ce}(\text{Hpmd})(\text{H}_2\text{O})$] and [$\text{Pr}(\text{Hpmd})(\text{H}_2\text{O})$];¹³ recently, ii) five different Lanthanum-based MOFs, being one 1D ($[\text{La}_2(\text{H}_2\text{pmd})_3(\text{H}_2\text{O})_{12}]$) and four 3D ($[\text{La}_2(\text{H}_2\text{pmd})(\text{pmd})(\text{H}_2\text{O})_2]$, $[\text{La}(\text{H}_3\text{pmd})(\text{H}_2\text{pmd})(\text{H}_2\text{O})]$, $[\text{La}_2(\text{H}_2\text{pmd})_3(\text{H}_2\text{O})_2]$ and $[\text{La}_2(\text{H}_2\text{pmd})(\text{pmd})(\text{H}_2\text{O})_4]$).¹⁴

In this chapter it is described the preparation of several Lanthanide-Organic Frameworks from the self-assembly of **H₄pmd** with lanthanides. On the one hand, a family of isotypical compounds, formulated as $[\text{Ln}(\text{Hpmd})(\text{H}_2\text{O})]$ [where $\text{Ln}^{3+} = \text{Eu}^{3+}$ (**1**), Gd^{3+} (**2**) and Tb^{3+} (**3**)], was isolated by using three different approaches: i) conventional hydrothermal synthesis starting from the hydrolyzed ligand; ii) a rapid “five-second” method based on microwave-assisted synthesis (MWAS); and iii) the ultrasonic method, a novel heating approach in this field of research, allowing a drastic reduction of the required temperature to ambient temperature, which, at the same time, clearly promoted the formation of nano-sized crystallites (average length between 100 and 200 nm from visual inspection of SEM pictures). On the other hand, five novel MOF structures were discovered by employing the MWAS approach and a *bench* procedure coined as one-pot method. Large crystals of $[\text{La}_2(\text{H}_2\text{pmd})_3(\text{H}_2\text{O})_{12}]$ (**4**) and $[\text{La}_2(\text{H}_2\text{pmd})(\text{pmd})(\text{H}_2\text{O})_2]$ (**5**), formulated on the basis of single-crystal X-ray diffraction studies, were directly isolated from the reaction vials via filtration from the reaction products of both MWAS and the one-pot approaches. Small crystals of $[\text{La}(\text{H}_3\text{pmd})(\text{H}_2\text{pmd})(\text{H}_2\text{O})]$ (**6**) were found as impurities in some MWAS experiments. Samples from the one-pot reactions yielded crystals of $[\text{La}_2(\text{H}_2\text{pmd})_3(\text{H}_2\text{O})_2]$ (**7**) and powders of $[\text{La}_2(\text{H}_2\text{pmd})(\text{pmd})(\text{H}_2\text{O})_4]$ (**8**).

The crystalline structure of all materials were unveiled by single-crystal or powder X-ray diffraction and characterized by using standard solid-state techniques (thermogravimetry, vibrational spectroscopy (FT-IR and FT-Raman), elemental analysis, solid-state NMR and electron microscopy (SEM and EDS)). It is also discussed in detail the methodologies and rationale used to obtain the different compounds while comparing the structural features, purity, crystallinity, morphology and particle size of the obtaining materials.

3.2. From Micro- to Nano-Sized Lanthanide-Biphosphonate Coordination Polymers

3.2.1. Synthesis

3.2.1.1. Synthetic strategy

The hydro-ionothermal synthetic approach previously reported by our group led to the direct isolation of [Ce(Hpmd)(H₂O)] and [Pr(Hpmd)(H₂O)] from the self-assembly of lanthanide centers with tetraethyl-*p*-xylylenebisphosphonate (texbp) in aqueous ionic medium.¹³ For identical composition of the reactive mixtures we described in that report that conventional hydrothermal synthesis failed to produce the desired compounds. More recent (unpublished) laboratorial work further showed that the same strategy was i) poorly reproducible for other lanthanide centers, and that ii) even the use of microwave-assisted hydro-ionothermal synthesis did not promote the self-assembly of the primary building units (PBUs). Thus, experimental data strongly suggested that a crucial step for the self-assembly of the 3D MOF network resided in the ability of texbp to hydrolyze in solution the phosphoryl groups: in our original report we focused that i) the addition of water was necessary for the reaction and also that, in some cases, ii) the phosphonic acid molecule could be directly isolated as a by-product (thus supporting the assumption of *in situ* hydrolysis). In order to expand the series of this material to the remaining lanthanide centers we used instead the hydrolyzed molecule, 1,4-phenylenebis(methylene)diphosphonic acid (**H₄pmd**). Because the resulting [Ln(Hpmd)(H₂O)] [where Ln³⁺ = Eu³⁺ (**1**), Gd³⁺ (**2**) and Tb³⁺ (**3**)] materials were isolated using less mild reaction conditions (180 °C for 72 h), we employed different synthetic methods (microwave- and ultrasound-assisted synthesis) to prepare the desired materials in a simple and faster way, at mild conditions and as isolated nanoparticles.

3.2.1.2. Conventional Hydrothermal Synthesis

Hydro(solvo)thermal synthesis is the most used synthetic approach used to obtain MOFs as large single-crystals. Here, it is reported the synthesis of isotypical 3D MOFs, formulated as [Ln(Hpmd)(H₂O)] [where Ln³⁺ = Eu³⁺ (**1**), Gd³⁺ (**2**) and Tb³⁺ (**3**)], sharing identical crystal structures, isolated from the self-assembly between the bipodal **H₄pmd** organic linker with the respective lanthanide(III) chloride hydrates, under typical hydrothermal conditions (180 °C for 72 h; see sub-section 8.10.1.1 in the Experimental Section for further details).

Opposite to expected, the resulting materials were isolated as microcrystalline powders. Therefore, and after several attempts, the isolation of [Ln(Hpmd)(H₂O)] materials as single-crystals was not possible. Consequently, phase identification only could be performed from full Rietveld refinement (see sub-section 8.10.1.1 in the Experimental Section for further detailed information on crystal and structure refinement). Figure 3.1

shows the final Rietveld plot for compound **1** and scanning electron microscopy (SEM) images illustrating the morphologic features. A careful analysis of this set of data and subsequent comparison with the previously reported $[\text{Ce}(\text{Hpmd})(\text{H}_2\text{O})]$ and $[\text{Pr}(\text{Hpmd})(\text{H}_2\text{O})]$ materials lead us to conclude that all compounds have the same crystal structure.¹³

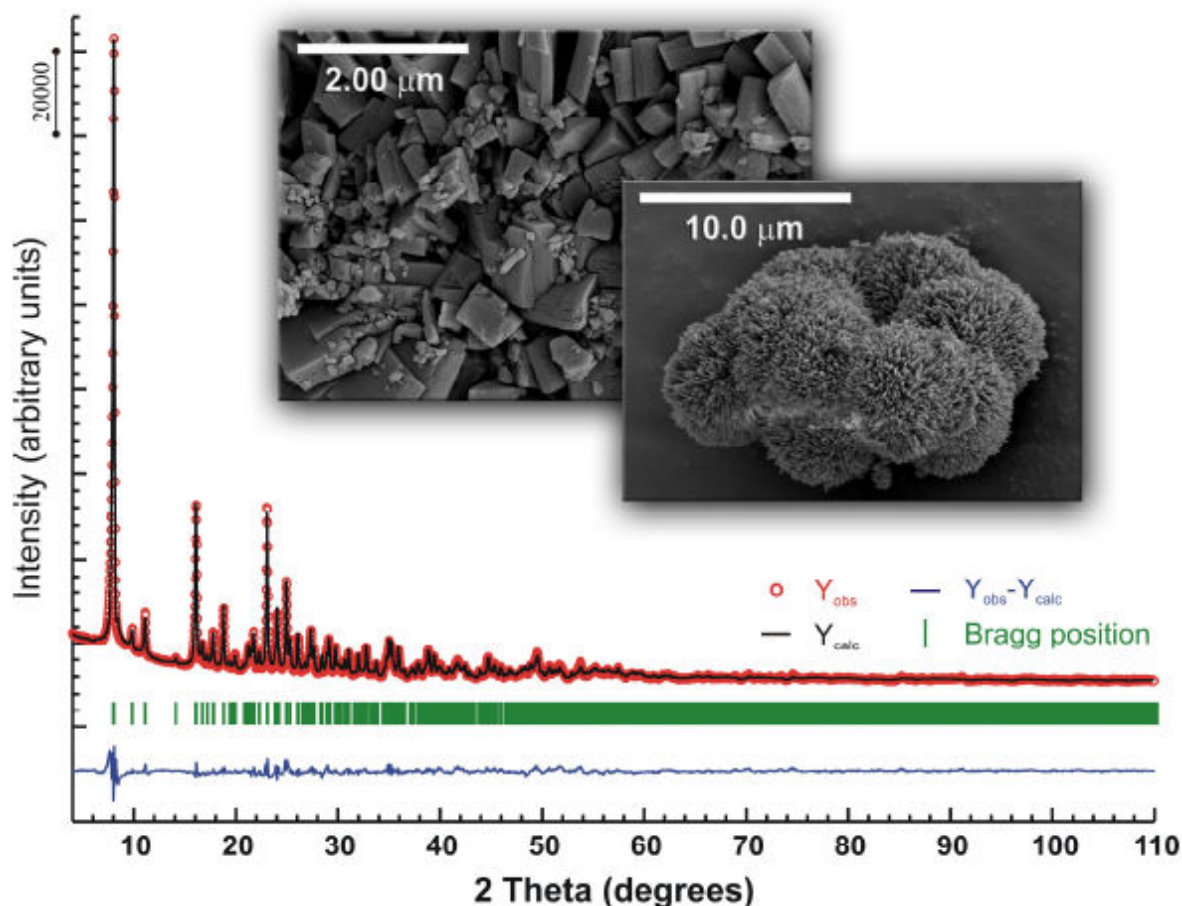


Figure 3.1 - Final Rietveld plot (laboratory powder X-ray diffraction data) of $[\text{Eu}(\text{Hpmd})(\text{H}_2\text{O})]$ (**1**). Observed data points are indicated as red circles, the best-fit profile (upper trace) and the difference pattern (lower trace) are drawn as solid black and blue lines, respectively. Green vertical bars indicate the angular positions of the allowed Bragg reflections. Refinement details are given in Experimental Section. Inset: SEM images of compound **1**.

Figure 3.2 depicts the powder X-ray diffraction patterns of compounds **2** and **3** and their respective SEM images. These compounds share identical crystal structures with **1**, as described above, and also have very similar crystal morphologies.

Comparing with the hydro-ionothermal synthetic approach, we found that the conventional hydrothermal method employing the previously synthesized H_4pmd molecule and the same reaction conditions (temperature of 180 °C and 3 days of reaction), is significantly more reproducible and controllable. This leads to the desired materials as highly microcrystalline phases with relatively uniform crystal size (Figure 3.2).

3.2.1.3. Microwave-Assisted Hydrothermal Synthesis

In order to prepare $[\text{Ln}(\text{Hpmd})(\text{H}_2\text{O})]$ materials in a simple and fast way, the Microwave-Assisted Synthesis (MWAS) method was employed. This not so common approach, when compared with the conventional hydrothermal approach, has been used for the preparation of crystalline multidimensional MOFs. Our group has been adopting this synthetic method because it promotes faster and more efficient preparations of functional hybrid materials.¹⁴⁻¹⁵ The possibility of preparing large amounts of $[\text{Eu}(\text{Hpmd})(\text{H}_2\text{O})]$ (**1**) and $[\text{Tb}(\text{Hpmd})(\text{H}_2\text{O})]$ (**3**) through the use of the microwave-assisted heating was investigated.

To find the best reaction conditions it was necessary to optimize the synthesis. Fixing the power at 50 W, other reaction parameters were tested, such as: i) temperature (40, 50, 60, 70, 90, 120 and 150 °C) and ii) reaction time (5 s, 10 s, 30 s, 1 min and 5 min) (see sub-section 8.10.1.2 in the Experimental Section for further synthetic details). It was found, after analyzing the powder X-ray diffraction patterns, that the desired materials can be readily isolated as phase-pure, in very good yields, at 40 °C with just 5 seconds of reaction time.

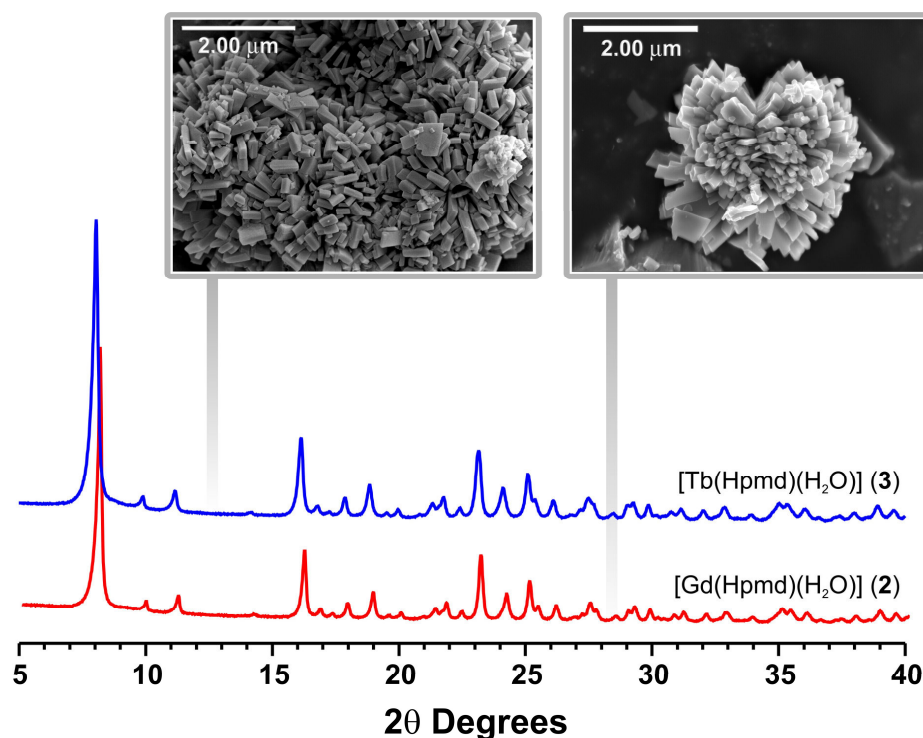


Figure 3.2 - Powder X-ray diffraction patterns and SEM images of the $[\text{Ln}(\text{Hpmd})(\text{H}_2\text{O})]$ [where $\text{Ln}^{3+} = \text{Gd}^{3+}$ (**2**) and Tb^{3+} (**3**)] materials.

After a careful examination of the SEM images obtained for **1**, it is very interesting to observe that this compound exhibits an almost homogeneous morphology and crystal size distribution both in severe (150 °C and 5 min of reaction) and in soft (60 °C and 1 min

of reaction) reaction conditions (Figure 3.3). Aiming to investigate the possibility to further decrease the crystal size of compound **3**, we reduced both the temperature and the total time of the microwave irradiation (Figure 3.4). By reducing this latter parameter a slight reduction of the average crystal size was observed (Figure 3.4 top and middle). Crystal size could be further decreased by also reducing the temperature to 50 °C (Figure 3.4 bottom). Noteworthy, and as mentioned above, compound **3** could also be isolated at 40 °C but for this case the average crystal size is relatively identical to that obtained at 50 °C (data not shown).

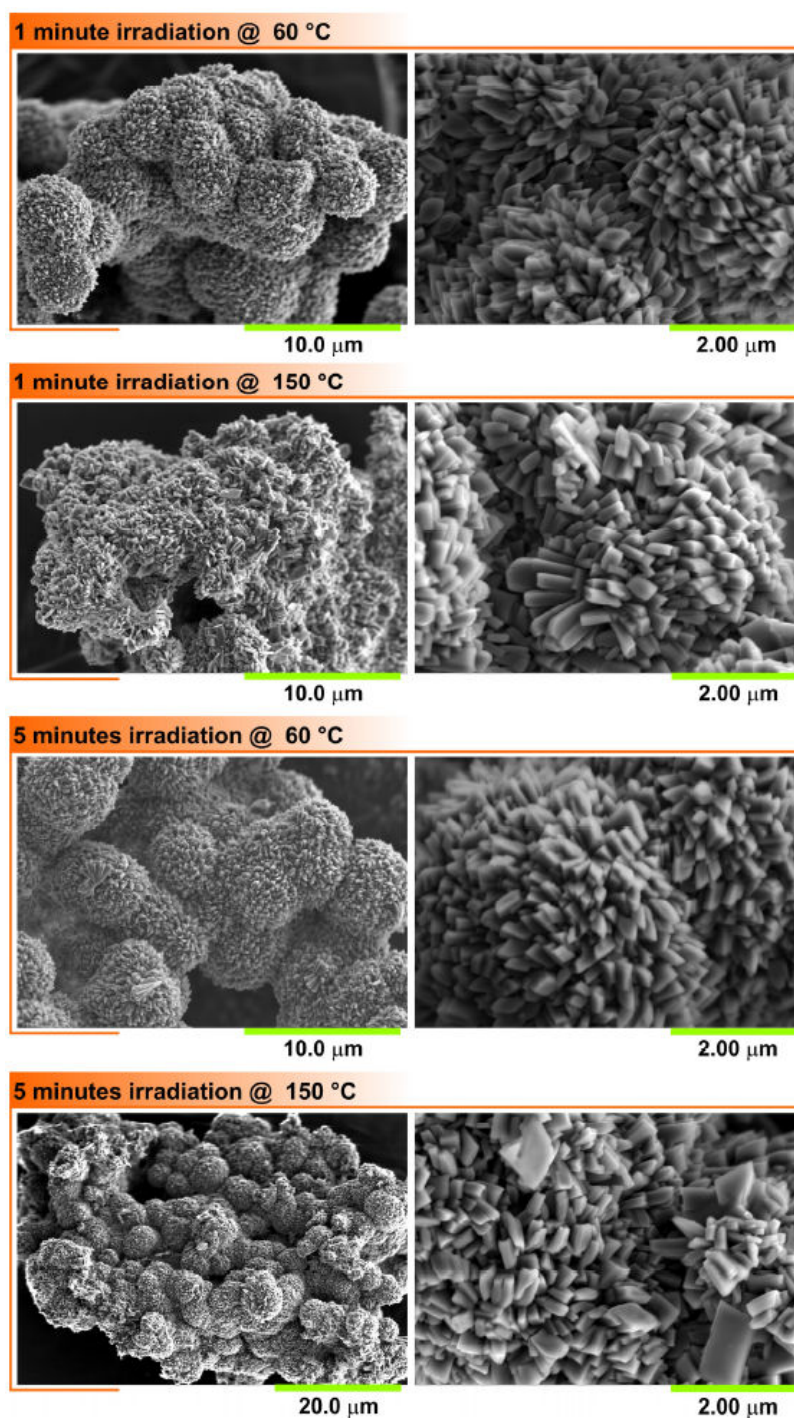


Figure 3.3 - SEM images of material [Eu(Hpmd)(H₂O)] (**1**) prepared using microwave heating (power 50 W).

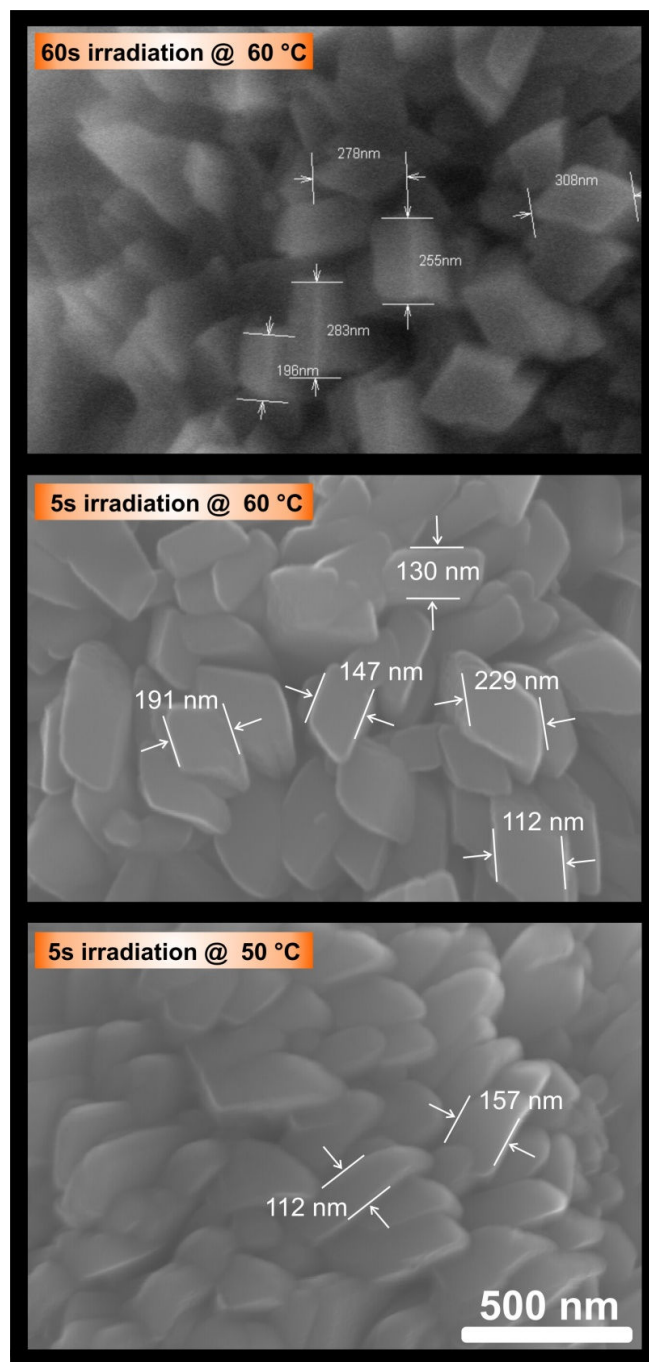


Figure 3.4 - SEM pictures of compound $[\text{Tb}(\text{Hpmd})(\text{H}_2\text{O})]$ (**3**) prepared using microwave heating at 60 and 50 °C for total irradiation times of 60 and 5 seconds. The scale bar (corresponding to 500 nm) is identical to all pictures.

3.2.1.4. $[\text{Ln}(\text{Hpmd})(\text{H}_2\text{O})]$ materials as isolated nanoparticles

In the previous subsection it was described the formation of aggregates of nanoparticles of compound $[\text{Tb}(\text{Hpmd})(\text{H}_2\text{O})]$ (**3**) under microwave irradiation. Since the preparation of $[\text{Ln}(\text{Hpmd})(\text{H}_2\text{O})]$ [where $\text{Ln}^{3+} = \text{Eu}^{3+}$ (**1**) and Tb^{3+} (**3**)] materials as isolated

nanoparticles was the goal, several attempts using different methodologies were performed:

i) Reverse microemulsion under constant conventional or mechanical stirring: a solution composed of Triton X-100, 1-octanol, cyclohexane, TEOS (tetraethyl orthosilicate), the organic ligand **H₄pmd** and EuCl₃·6H₂O was added to another containing Triton X-100, 1-octanol, cyclohexane and NH₃. The resulting reaction mixture was stirred in a conventional stirring plate or in a mechanical stirring equipment at ambient temperature during different periods of time (from 1 to 2 days). After reacting, acetone was added occurring the formation of a precipitate which was recovered by decantation and, then, by centrifugation. The precipitate was washed with water, ethanol and water again. This methodology was based on a published work with some modifications.¹⁶ In that work, the authors reported the preparation of lanthanide-containing polyoxometalates (POMs) in isolated silica nanoparticles. Employing this procedure we were, unfortunately, unable to obtain [Ln(Hpmd)(H₂O)] [where Ln³⁺ = Eu³⁺ (**1**) and Tb³⁺ (**3**)] materials in isolated silica nanoparticles. Additionally, analyzing the resulting materials by powder X-ray diffraction (PXRD) it was observed that the resulting precipitate has a PXRD pattern with a completely different profile (being also poorly crystalline) than the PXRD patterns (data not shown) of compounds **1** and **3**.

ii) Reverse microemulsion under ultrasonication: the experimental procedure to prepare the final reaction mixture was very similar to that described above. The differences reside in the replacement of the stirring methods by ultrasonication and the use of shorter reaction times (5 min, 30 min, 1 h and 4h) and temperature (ambient, 60 and 70 °C). The resulting precipitates presented different crystalline structures than the desired materials and the encapsulation with silica did not occur.

After all the previous attempts, and following some published reports it was decided to employ the ultrasonic-assisted synthesis method without the use of surfactants and silica. Ultrasound irradiation arises as an alternative synthetic technique known to be used in the preparation of nanoparticles,¹⁷⁻¹⁹ MOFs²⁰⁻²³ and, in particular, nanoscale MOFs.²⁴⁻²⁷

As for the microwave-assisted approach, the optimization of some reaction parameters in order to prepare isolated nanoparticles of **1** and **3** was performed. Therefore, optimization was based on the variation of: i) temperature (ambient temperature, 60 and 70 °C), ii) time of ultrasonic irradiation (1, 3, 5, 10, 20 and 30 minutes), and iii) (Ln³⁺:H₄pmd:H₂O) molar ratio (1:1:600, 1:1:1200, 1:1:1800, 1:1:3600 and 1:1:7200). After optimization, some important conclusions can be inferred from the collected data:

i) phase-pure **1** was only isolated when the reaction temperature was near the ambient temperature. Higher temperatures lead to the formation of secondary phases (left column in Figure 3.5);

- ii) below 3 minutes of ultrasonic irradiation the reaction product was systematically poorly crystalline and probably contaminated with an unidentified phase. For longer irradiation times, **1** was isolated as a phase-pure compound with particle morphology independent of the time (middle column in Figure 3.5);
- iii) while a $\text{Ln}^{3+}:\text{H}_4\text{pmd}:\text{H}_2\text{O}$ molar ratios of 1:1:600 (reaction condition used for conventional hydrothermal and microwave-assisted synthesis) and 1:1:1200 produce distinct phase from the aimed material, higher diluted solutions yield always the desired phase-pure materials (right column in Figure 3.5).

In short, it was found that the optimal conditions to prepare isolated nanoparticles of **1** and **3** are the following: 5 minutes of ultrasonic irradiation at ambient temperature with a 1:1:7200 molar ratio (see sub-section 8.10.1.3 in the Experimental Section for further reaction details). Nano-sized crystallites prepared under ultrasonic irradiation have been subjected to a myriad of comparative characterization studies with microcrystalline bulk materials so to unequivocally prove the structural resemblance between the isolated materials (Figure 3.6). For example, the highly sensitive photoluminescence studies of compound **1** showed that the Eu^{3+} cation shares the same local coordination environment in both the isolated nano-crystals (prepared under ultrasonic irradiation) and in the bulk microcrystalline material.

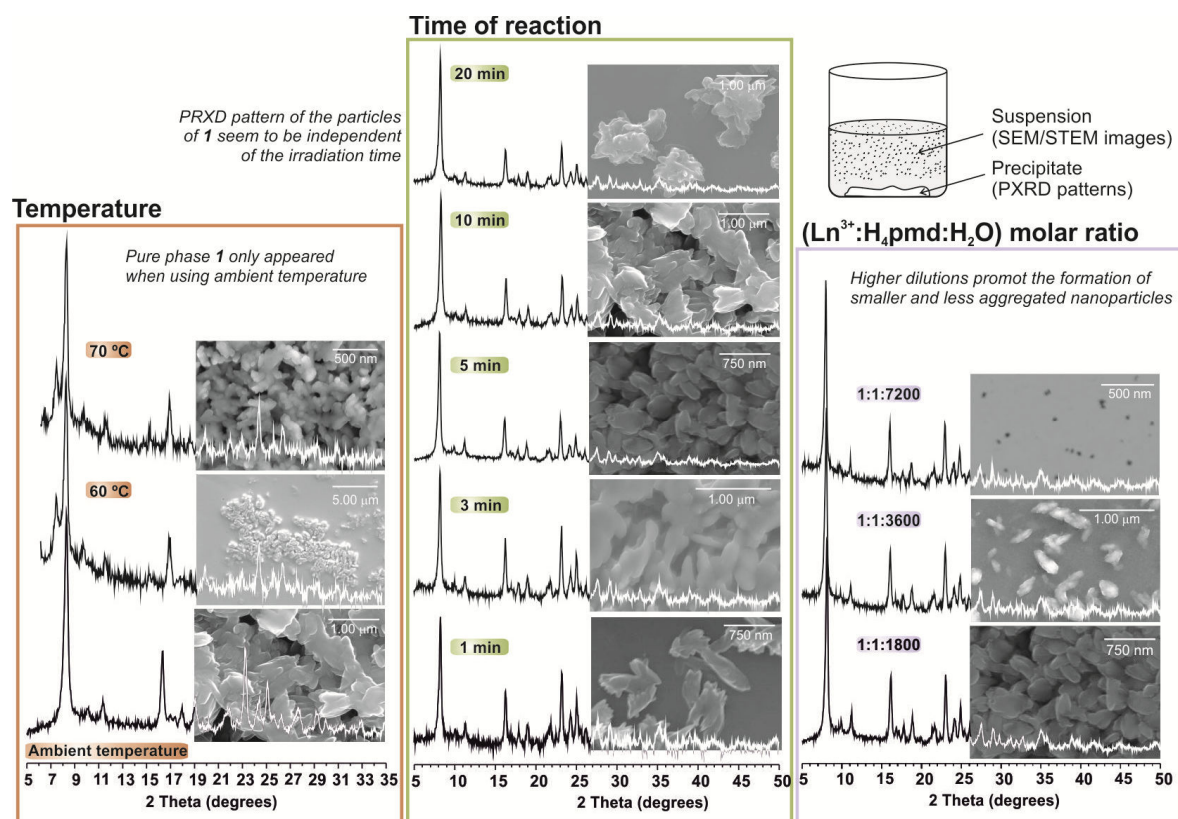


Figure 3.5 – Optimization of the reaction parameters to prepare isolated nanoparticles of compound **1**.

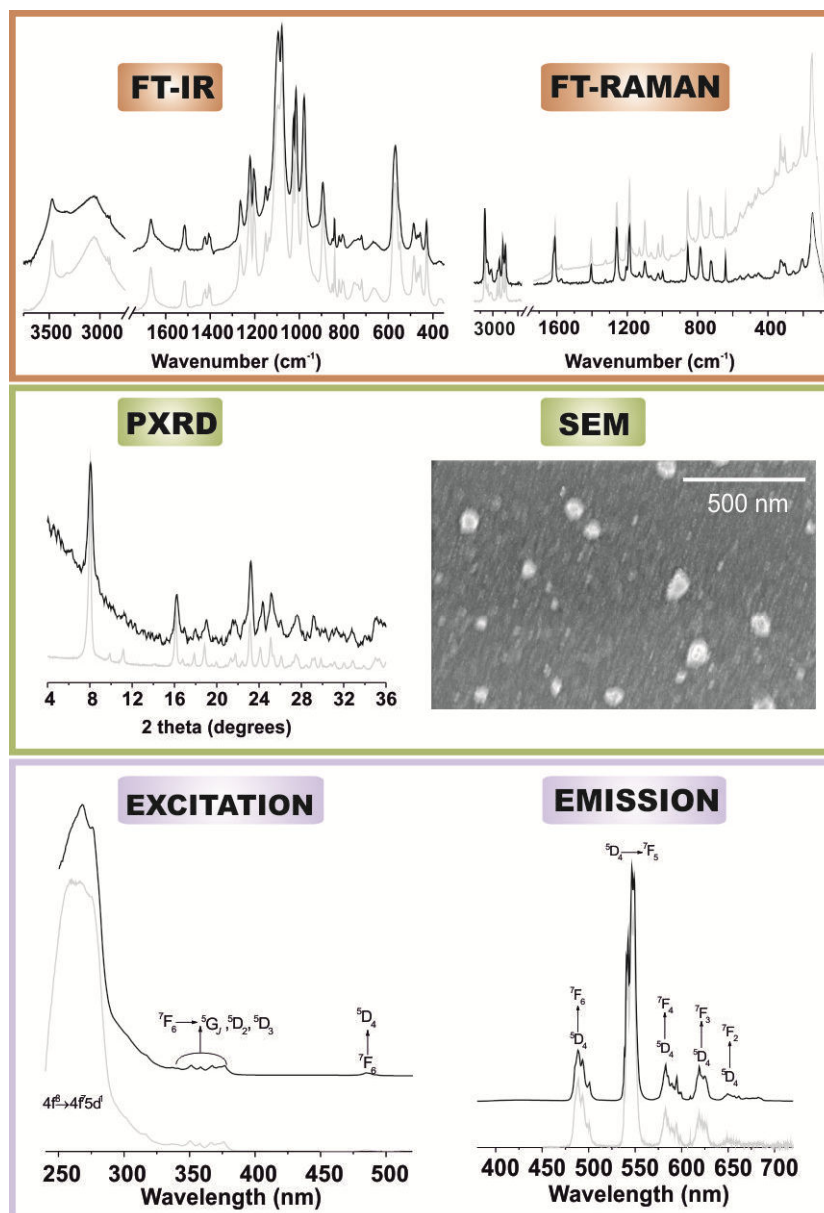


Figure 3.6 – Characterization of compound **1**. Comparison between nanoparticles of **1** (black) and the original material (grey).

3.2.2. Crystal Structure Description

[Ln(Hpmd)(H₂O)] compounds [where Ln³⁺ = Eu³⁺ (**1**), Gd³⁺ (**2**) and Tb³⁺ (**3**)] share identical crystal structures with [Ce(Hpmd)(H₂O)] and [Pr(Hpmd)(H₂O)].¹³ In this section we shall only focus on structure **1** with the structural features described in the following paragraphs being valid for all remaining compounds of the series.

Compound **1** has a single Eu³⁺ site which is coordinated to one water molecule and to five phosphonate groups, overall describing a {EuO₇} seven-coordinated environment whose geometry resembles a significantly distorted monocapped trigonal prism (Figure 3.7). O(4) and O(5) belong to the same phosphonate group which *O,O*-chelates to the

metallic centre via a bite angle of $56.76(5)^\circ$ (see Table A.1.1 in the appendices for further details), in good agreement with the value reported for the Ce^{3+} and Pr^{3+} analogues. This seven-coordination environment can also be described as derived from a highly distorted octahedron, in which one of the apical positions is occupied by this chelating moiety [$\text{Eu}(1)-\text{C}_{\text{g},\text{O}(4)/\text{O}(5)}$ of $2.274(1) \text{ \AA}$], having the *cis* and *trans* octahedral angles in the *ca.* $73.00-99.83^\circ$ and $156.82-174.00^\circ$ ranges, respectively.

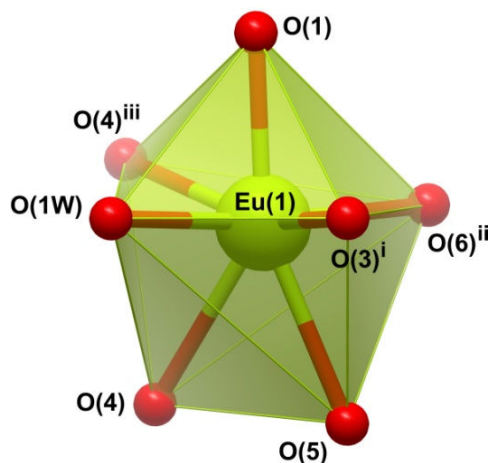


Figure 3.7 - Schematic representation of the distorted $\{\text{EuO}_7\}$ mon capped trigonal prismatic coordination polyhedra present in $[\text{Eu}(\text{Hpmd})(\text{H}_2\text{O})]$ (**1**). For selected bond lengths (in \AA) and angles (in degrees) see Table A.1.1. Symmetry transformations used to generate equivalent atoms: (i) $2-x, 1-y, -z$; (ii) $3-x, -y, -z$; (iii) $2-x, -y, -z$.

The material contains two independent phosphonate moieties, each belonging to a distinct organic ligand located at a crystallographic inversion center. The fully deprotonated phosphonate moiety is that *O,O*-chelated to Eu^{3+} , and promotes the formation of lanthanide dimers having a $\text{Eu}\cdots\text{Eu}$ intermetallic distance of *ca.* 4.05 \AA (Figure 3.8). The same terminal group also connects adjacent dimers along the $[010]$ direction of the unit cell (closest $\text{Eu}\cdots\text{Eu}$ distance of *ca.* 5.11 \AA), leading to the formation of a one-dimensional (1D) zigzag array as depicted in Figure 3.9a. Noteworthy, the registered intermetallic distances are smaller than those reported by us for the Ce^{3+} and Pr^{3+} analogue compounds, agreeing well with the expected contraction of the lanthanide radii. Bridges between 1D arrays are ensured by strong $\text{O}-\text{H}\cdots\text{O}$ hydrogen bonds (green dashed lines in Figure 3.8a) involving the hydrogenophosphonate and the coordinated water molecule (*i.e.*, donor groups): on the one hand, the coordinated water molecule is engaged in two interactions with neighboring (hydrogeno)phosphonate moieties ($\text{O}\cdots\text{O}$ distances of about 2.64 and 2.77 \AA); on the other, the same hydrogenophosphonate which accepts the hydrogen from the coordinated water donates its proton to the neighbouring phosphonate group ($\text{O}\cdots\text{O}$ distance of about 2.88 \AA). Noteworthy, this arrangement of supramolecular interactions promotes structural cohesion within the inorganic lanthanide (hydrogeno)phosphonate layer (Figure 3.8c). Indeed, upon heating, it was not observed a discrete release of the coordinated water molecule without structural modification.

Instead, the sudden release of water (at high temperatures) is concomitant with the collapse of the framework (see following section), thus providing additional evidence for structural importance of these interactions.

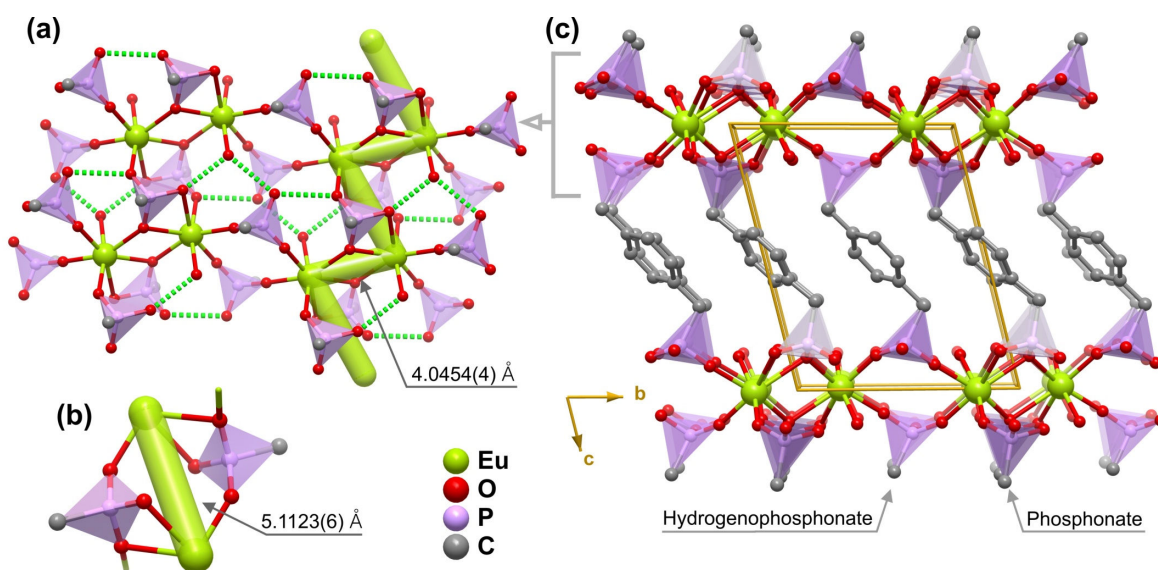


Figure 3.8- (a) and (b) Schematic representation of the inorganic europium(III) phosphonate layer showing the hydrogen bonds (green dashed lines) connecting the coordinated water molecule and the (hydrogeno)phosphonate moieties. The zigzag green chain depicts the alternation between the short and the long Eu...Eu intermetallic distances due to the different coordination modes of the chelating phosphonate moieties. (c) Perspective view along the [100] direction of the unit cell of the crystal packing of $[\text{Eu}(\text{Hpmd})(\text{H}_2\text{O})]$ (**1**). The location of the phosphonate or hydrogenophosphonate inside each layer is indicated.

3.2.3. Thermogravimetry and Variable Temperature Powder X-ray Diffraction Studies

The thermal behavior of $[\text{Ln}(\text{Hpmd})(\text{H}_2\text{O})]$ materials has been investigated between ambient temperature and *ca.* 800 °C (see tabulated data in the Experimental Section for further details). Even though the decomposition pathway seems to have different kinetics according to the lanthanide centre, overall the processes are relatively similar (see Figure A.1.1 in the appendices for further details). For the particular case of **1**, as clearly evidenced by the *in situ* variable-temperature powder X-ray diffraction studies (Figure 3.9a), the framework is thermally robust up to *ca.* 260 °C with no visible modifications (peak presence or intensity) being noticeable in the diffractograms. This was further confirmed using vibrational spectroscopy (data not shown): the FT-IR spectrum of a portion of **3** placed inside an oven at 230 °C for 3.5 hours is completely identical to that of the as-prepared material. It is noted that up to *ca.* 260 °C the weight loss is negligible (Figure 3.9b) and may be attributed, mainly, to the release of adsorbed water molecules.

At higher temperatures (above *ca.* 290 °C) there is an abrupt weight loss up to *ca.* 450 °C, globally corresponding to *ca.* 6.5% in mass, which clearly exceeds the expected value for the complete release of the stoichiometric amount of coordinated water molecules (4.15%). It is, thus, feasible to assume that above 290 °C there is, in a first stage, a complete release of these water molecules with the framework retaining its crystallinity (up to *ca.* 350-365 °C); in a second stage, the extra weight loss may be attributed to the partial dehydration of the material from the protonated P–OH groups, with this process ultimately leading to the concomitant collapse of the framework (as clearly shown in the variable-temperature powder X-ray diffraction studies).

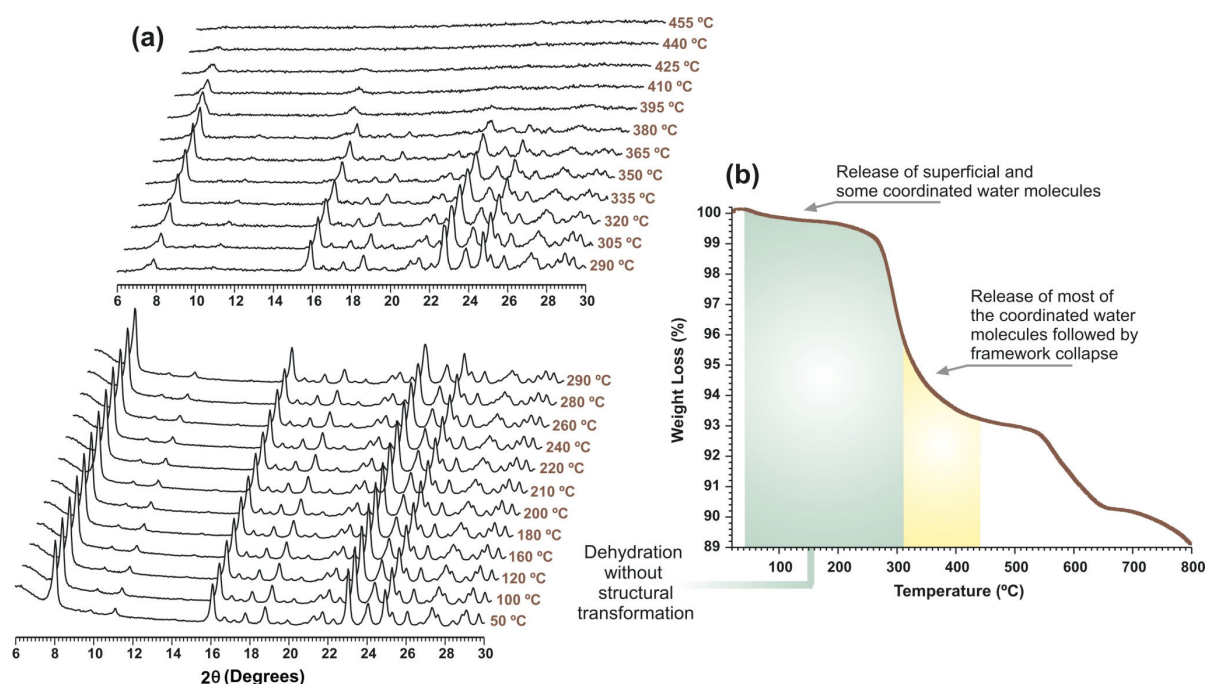


Figure 3.9 – Representation of the (a) variable-temperature powder X-ray diffraction patterns and (b) the thermogram of [Eu(Hpmd)(H₂O)] (1) material.

3.2.4. Vibrational Spectroscopy Studies

The vibration modes of the [Ln(Hpmd)(H₂O)] materials reported in this chapter were fully studied. A reliable assignment of the vibrational spectra of the compounds requires the support from computational calculated data. In Figures A.1.2 and A.1.3 (in the Appendices) are represented the FT-IR and Raman spectra of compounds 1-3. Experimental and calculated data for compound 3 are given in Tables A.1.2 and A.1.3 in the Appendices.

The FT-IR and Raman spectra of the four materials are very similar with the exception of a handful of bands. These differences are summarized in Table 3.1. The typical lanthanide contraction along the series can explain the observed differences, which is accompanied by variations in bonding forces and lengths. In the FT-Raman spectra the

most prominent difference between the spectra concerns the combination of $\rho(\text{PO}_3) + \rho(\text{CH}_2)$ vibrational modes varying from 345 to 350 cm^{-1} from **1** to **3** (calcd. 343 cm^{-1}).

Table 3.1 - Main differences in the FT-IR spectra of materials **1-3** and their respective assignments (in cm^{-1}).^a

Assignment	Calculated	1	2	3
$\delta(\text{H}_2\text{O})$	1605	1662(<i>w</i>)	1664(<i>w</i>)	1666(<i>w</i>)
$\gamma(\text{CH}) + \rho(\text{CH}_2)$	881	866(<i>sh</i>)	<i>Not visible</i>	<i>Not visible</i>
$\gamma(\text{CH})$	746	<i>Not visible</i>	<i>Not visible</i>	752(<i>w,br</i>)
$\tau(\text{H}_2\text{O})$	648	645(<i>w</i>)	657(<i>w</i>)	664(<i>w</i>)
$\tau(\text{PO}_3) + \rho(\text{CH}_2)$	367	350(<i>w</i>)	358(<i>w</i>)	363(<i>w</i>)

^a Footnotes: *w* – weak; *sh* – shoulder; *br* – broad.

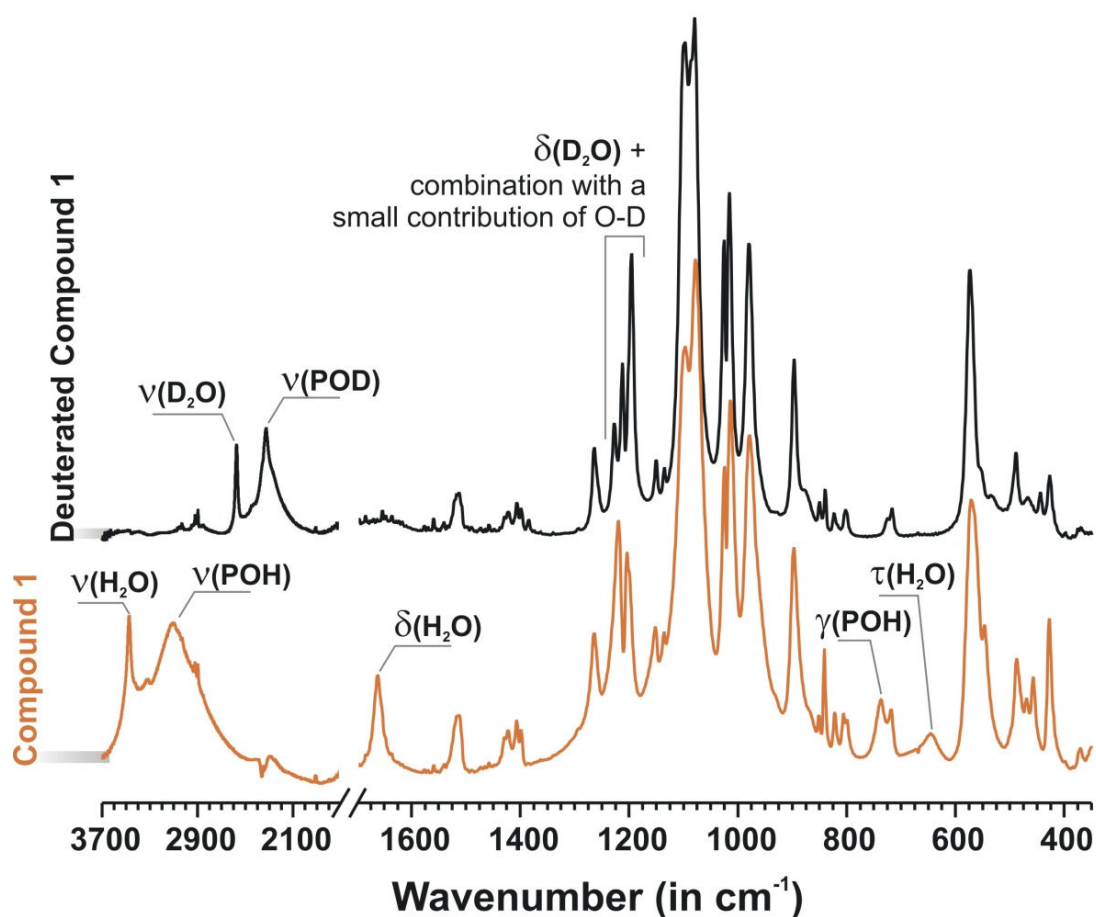


Figure 3.10 - Comparison between the FT-IR spectra of compound **1** and its deuterated form (**1_D**). The most significant modifications in the bands are emphasized. For a full description of the modifications upon deuteration see Table 3.2.

In order to unequivocally confirm the assignment performed by the theoretical calculations, compound **1** was also prepared in D₂O (**1_D**). A number of modifications are clearly visible in the spectra (Figure 3.10). Upon deuteration, some vibrations related to the O–H normal modes are absent. For example, $\nu(\text{POH})$ is absent with the concomitant appearance of $\nu(\text{POD})$ (Figure 3.10 and Table 3.2). Other vibrations are also affected by deuteration, because the O–D is a small contributor; for example $\delta(\text{POH}) + \omega(\text{CH}_2)$ at 1220 cm⁻¹ is shifted. Noteworthy, this study allowed us to identify two important vibrations related to water below 1800 cm⁻¹. In particular, the twisting mode vibration [$\tau(\text{H}_2\text{O})$] at about 660 cm⁻¹ arises from coordination to the metal centre. Below 600 cm⁻¹ the spectrum was widely affected by the deuteration. This is due to the appearance of new bands for the $\gamma(\text{POD})$ and $\tau(\text{D}_2\text{O})$ vibrations, the change of unobserved bands of **1** corresponding to the vibrations of coordinated water, and to other combination vibrations which have a small contribution of the O-D vibration modes.

Table 3.2 - Main differences above 600 cm⁻¹ in the FT-IR spectra of **1** and **1_D** and their respective assignments (in cm⁻¹).

Calculated (for 1)	1	1_D
3606 + 3791	3474 $\nu(\text{H}_2\text{O})$	2574 $\nu(\text{D}_2\text{O})$
3438	3104 $\nu(\text{POH})$	2297 $\nu(\text{POD})$
1605	1663 $\delta(\text{H}_2\text{O})$	1212 or 1196 $\delta(\text{D}_2\text{O})$
1215	1220 $\delta(\text{POH}) + \omega(\text{CH}_2)$	1212 or 1196 $\delta(\text{POD}) + \omega(\text{CH}_2)$
707	737 $\gamma(\text{POH})$	553 or 535 $\gamma(\text{POD})$
648	645 $\tau(\text{H}_2\text{O})$	468 or 444 $\tau(\text{D}_2\text{O})$

ν – stretching; δ – in-plane deformation; ω – wagging; γ – out-of-plane deformation; τ – twisting

3.2.5. Photoluminescence

The presence of optically active metallic centers (*i.e.*, Eu³⁺ and Tb³⁺) in the structure of MOFs allows the conversion of UV radiation into visible light. In the next paragraphs, it is reported the photoluminescent properties of the [Eu(Hpmd)(H₂O)] (**1**), as well as its deuterated form [Eu(Hpmd)(D₂O)] (**1_D**), and the [Tb(Hpmd)(H₂O)] (**3**) materials.

Figure 3.11a displays the 300 K excitation spectra of compounds **1** and **1_D**, monitored within the Eu³⁺ ⁵D₀ → ⁷F₂ transition. The broad UV band (*ca.* 240-340 nm) is attributed to the π - π^* transitions associated with the organic linkers, which is also present in the same wavelength range in the 11 K excitation spectrum of [Gd(Hpmd)(H₂O)] (**2**)

monitored at 445 nm (Figure 3.11b). The spectra are dominated by a series of sharp lines assigned to the ${}^7F_{0,1} \rightarrow {}^5D_{0-4}$, 5L_6 , ${}^5G_{2-6}$, ${}^5H_{3-7}$ and ${}^5F_{1-5}$ Eu^{3+} intra- $4f^6$ transitions. The 300 K excitation spectrum of **3** (Figure 3.11b) is dominated by a similar intense broad band centered at about 266 nm arising from the $\pi \rightarrow \pi^*$ electronic transition associated with the organic moiety, which matches satisfactorily with the excitation profile of **2** recorded at 11 K (Figure 3.11b). The intra- $4f^8$ transition between the 7F_6 ground state and the ${}^5D_{4-0}$ and 5G_J excited states of Tb^{3+} are noticeable weaker. This demonstrates that the H_4pmd is a more suitable ligand to sensitize the Tb^{3+} cations than the Eu^{3+} ones via an energy transfer process, the so-called *antenna effect*. In this context, while Tb^{3+} is reasonably activated by the indirect ligand excitation, a direct excitation is more effective for the Eu^{3+} emission.

As expected the emission spectra of compounds **1** and **1D** at 300 K present a very similar profile (Figure 3.12a). They present, however, distinct emission features as discussed in more detail below. The emission spectra exhibit a series of narrow lines ascribed to the Eu^{3+} ${}^5D_0 \rightarrow {}^7F_{0-4}$ transitions; the ${}^5D_0 \rightarrow {}^7F_{5,6}$ transitions are not experimentally detected. The 11 K emission spectra (Figure 3.12b for **1D**) permit to unravel the local-field splitting of the ${}^7F_{1,2}$ levels into 4 and, at least, 7 Stark components, respectively. These observations are apparently contradictory to the crystallographic studies which call for the presence of a single Ln^{3+} site (maximum of 3 and 5 Stark components for the ${}^7F_{1,2}$ levels, respectively).

The detection of a single non-degenerated ${}^5D_0 \rightarrow {}^7F_0$ transition and the identical time-resolved emission spectra profile for very distinct initial delays and integration times, suggest, however, that the low intensity supplementary emission lines should be attributed to vibronic emission. In fact, the energy difference relatively to the ${}^5D_0 \rightarrow {}^7F_0$ transition match well with vibrations observed by FT-IR and FT-Raman studies, namely those at *ca.* 428 and 1025 cm^{-1} most likely assigned to $\tau(\text{PO}_3)$ and $\nu(\text{PO}_3)$ vibronic modes (Tables A.1.2 and A.1.3 in the appendices). Because the phosphonate groups compose the second coordination sphere of the Eu^{3+} ions, a vibronic coupling between both species can be expected. Considering this, Eu^{3+} emission spectroscopy suggests the presence of a single Eu^{3+} local site without inversion centre (higher intensity for the ${}^5D_0 \rightarrow {}^7F_2$ transition). Moreover, the integrated intensity ratio between the ${}^5D_0 \rightarrow {}^7F_2$ and ${}^5D_0 \rightarrow {}^7F_1$ transitions, $I_{({}^5D_0 \rightarrow {}^7F_2)} / I_{({}^5D_0 \rightarrow {}^7F_1)}$, is for **1** *ca.* 3.29, which is significantly higher than the 0.68 value reported for a centrosymmetric Eu^{3+} emitting center.²⁸ As described from the crystallographic studies the seven-coordinated environment of Eu^{3+} resembles a highly distorted $\{\text{EuO}_7\}$ monocapped trigonal prism. Thus, the point group of Eu^{3+} is C_1 , which agrees well with the information derived from the Eu^{3+} emission spectroscopy.

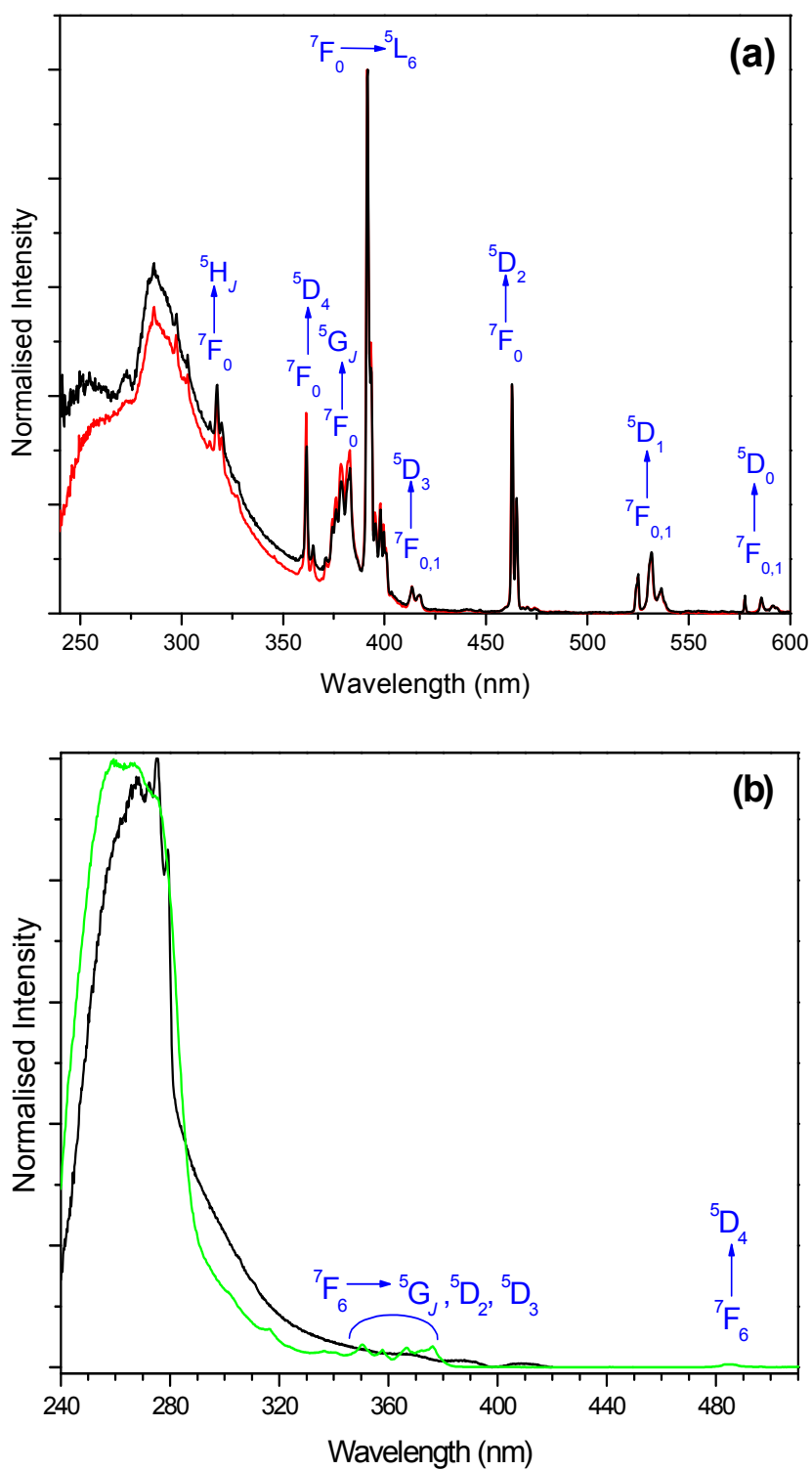


Figure 3.11 - (a) Excitation spectra of [Eu(Hpmd)(H₂O)] (**1**) (black line) and [Eu(Dpmd)(D₂O)] (**1_D**) (red line) acquired at 300 K, while monitoring the emission at 609.4 nm. (b) Excitation spectra of [Tb(Hpmd)(H₂O)] (**3**) (green line) at 300 K and of [Gd(Hpmd)(H₂O)] (**2**) (black line) at 11 K, while monitoring the emission at 545 and 445 nm, respectively.

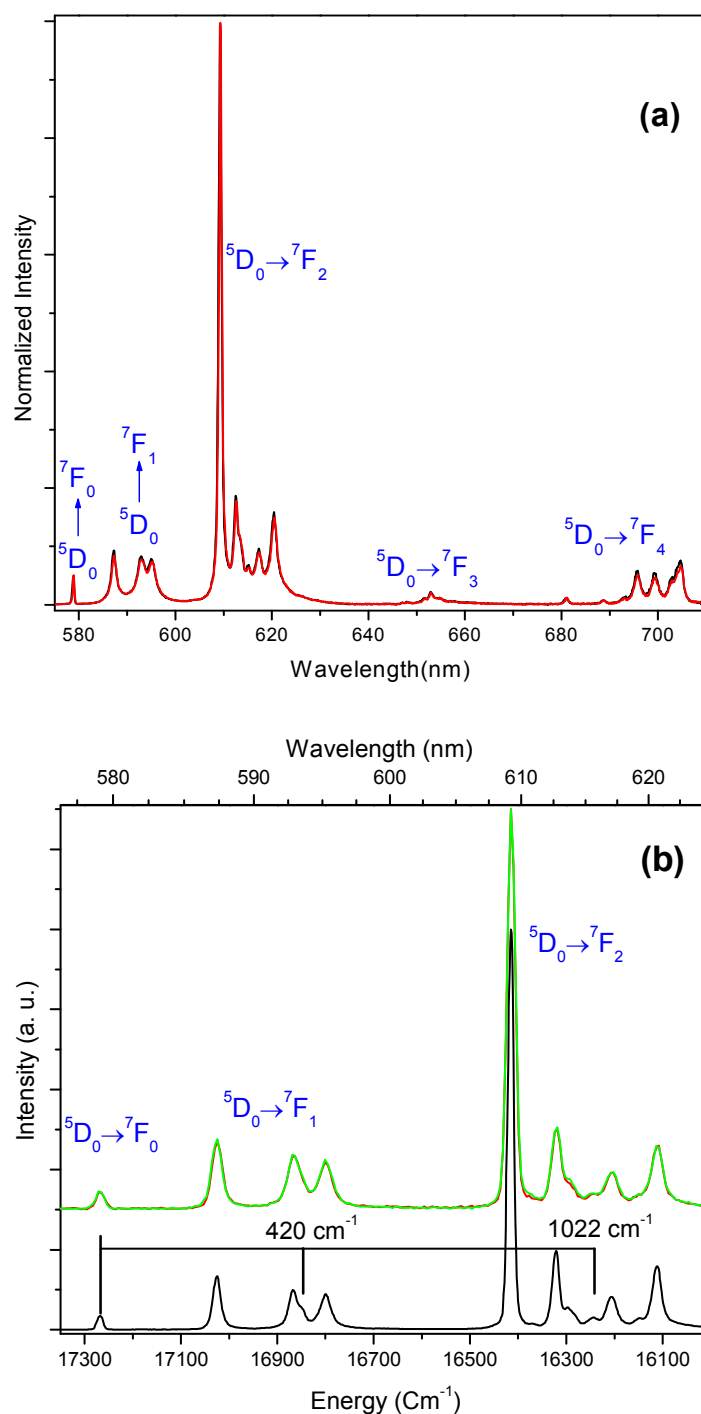


Figure 3.12 - (a) Emission spectra of [Eu(Hpmd)(H₂O)] (**1**) (black line) and [Eu(Dpmd)(D₂O)] (**1_D**) (red line) acquired at 300 K. **(b)** Partial emission spectrum of **1_D** at 11 K in stationary state (black line) identifying possible emission vibronic lines, and the corresponding time-resolved emission spectra (red line - initial delay 0.05 ms and integration time of 0.2 ms; green line - initial delay 3 ms and integration time of 10 ms). Note that the time-resolved emission spectra were acquired with a lower resolution relatively to the steady-state emission mode, and both were not corrected for detection and optical spectral response of the spectrofluorimeter. All spectra were acquired with the excitation fixed at 392 nm.

The 5D_0 decay time was measured for **1** and **1_D** while monitoring the strongest 7F_2 Stark component. Experimental data are well described by single-exponential functions for both cases (exemplified in Figure 3.13 for the data collected at 300 K), yielding lifetimes of 0.58 ± 0.01 and 1.98 ± 0.01 ms at 300 K, and of 0.66 ± 0.01 and 2.24 ± 0.01 ms at 11 K for **1** and **1_D**, respectively. This is further proof of the presence of a unique Eu^{3+} crystallographic site and clearly demonstrates the improvement of the decay time (*ca.* 3.4 times) with the substitution of the coordinated water molecule by a deuterated one, leading to the suppression of emission quenching through the coupling of the Eu^{3+} excited states with the vibrational states of the O–H oscillators. Note that, the temperature quenching effect is negligible when compared to that arising from the O–H groups.

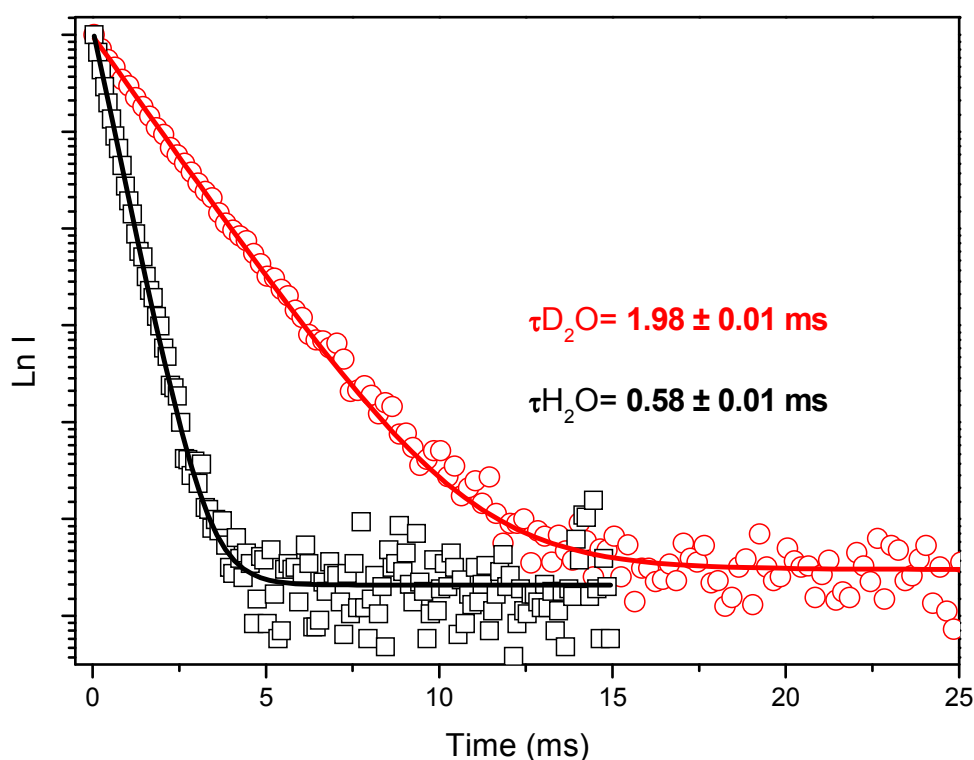


Figure 3.13 - 5D_0 decay curves of $[\text{Eu}(\text{Hpmd})(\text{H}_2\text{O})]$ (**1**) (black line) and $[\text{Eu}(\text{Dpmd})(\text{D}_2\text{O})]$ (**1_D**) (red line), acquired at 300 K and fitted with single exponential decay functions. Emission was monitored at 609.4 nm and the excitation was performed at 392 nm.

Based on the emission spectra, 5D_0 lifetimes and empirical radiative and non-radiative transition rates, and assuming that only non-radiative and radiative processes are involved in the depopulation of the 5D_0 state, the 5D_0 quantum efficiency, q^{29-33} was determined for **1** and **1_D**, establishing the effect of the coordinated water molecule on the reduction of the emission efficiency. The number of coordinated water molecules was also evaluated.³⁴ This data, including the absolute emission quantum yield (measured experimentally), are collected in Table 3.3 for both compounds.

Table 3.3 - Experimental 5D_0 lifetime, τ , radiative, k_r , and non-radiative, k_{nr} , transition rates, 5D_0 quantum efficiency calculated for an excitation wavelength of 392 nm, q , absolute emission quantum yield (for 392 nm and 288 nm excitation wavelengths), η , and the estimated number of water molecules, n_w , for compounds **1** and **1D**. The data have been obtained at room temperature (300 K).

Compound	τ [ms]	k_r [s^{-1}]	k_{nr} [s^{-1}]	q [%]	η [%] (392)	η [%] (288)	n_w
1	0.58±0.01	277	1435	16	4	2	1.0±0.1
1D	1.98±0.01	274	231	54	45	7	

Because of the resemblances between the emission spectra (Figure 3.12), compounds **1** and **1D** also have very similar 5D_0 radiative transition rates. The huge increase observed in the 5D_0 lifetime for the deuterated form is mainly due to the drastic decrease of the non-radiative transition rate, promoted by the suppression of the O–H oscillators. Therefore, the 5D_0 quantum efficiency increases strongly from 16% to 54%. The absolute emission quantum yield measured at 392 nm (direct excitation of Eu^{3+}) of **1D** has a magnified increase from 4% to 45%. These results demonstrate the strong quenching effect of the O–H groups on the photoluminescence of **1**. Also, the relative low absolute emission quantum yield value measured at 288 nm demonstrates the inefficient energy transfer pathway from the ligand moieties to Eu^{3+} . The 5D_0 quantum efficiency (q) and the quantum yield (η) are related by:³⁵⁻³⁸

$$\eta = k q$$

where the rate k accounts for all processes involved in the sensitization efficiency, defined as the efficacy with which energy is transferred from the feeding level (in this case essentially the intra-4f 5L_6 level) onto the 5D_0 emitting state. In the present example $k=0.83$ for **1D**, which indicates that *ca.* 17% of the absorbed light at 392 nm (that essentially corresponds to 5L_6 absorption, Figure 9) is lost in non-radiative processes before reaching the 5D_0 emitting state. The estimation of the number of coordinated water molecules, *ca.* 1.0, is in good agreement with the performed crystallographic studies.

The emission spectrum of **3** (Figure 3.14) acquired at ambient temperature markedly shows an intense green emission associated with the $^5D_4 \rightarrow ^7F_J$ transitions typical of Tb^{3+} . The $^5D_4 \rightarrow ^7F_5$ transition centered at *ca.* 544 nm is the strongest corresponding to *ca.* 57% of the integrated emission spectrum. The absence of transitions between the second excited state (5D_3 level) indicates an efficient relaxation process from the 5D_3 to 5D_4 levels, most likely due to resonant energy transfer between adjacent Tb^{3+} ions which are at an short intermetallic distance of *ca.* 3.99 Å, favourable to the occurrence of this mechanism controlled by electric dipole interaction. As discussed above, the relative efficient energy transference from the antenna ligand to the emitting 5D_4 Tb^{3+} excited level was ultimately confirmed by measuring an absolute emission quantum yield of *ca.* 14%, which is significantly higher than the values obtained for **1** and **1D** under similar excitation.

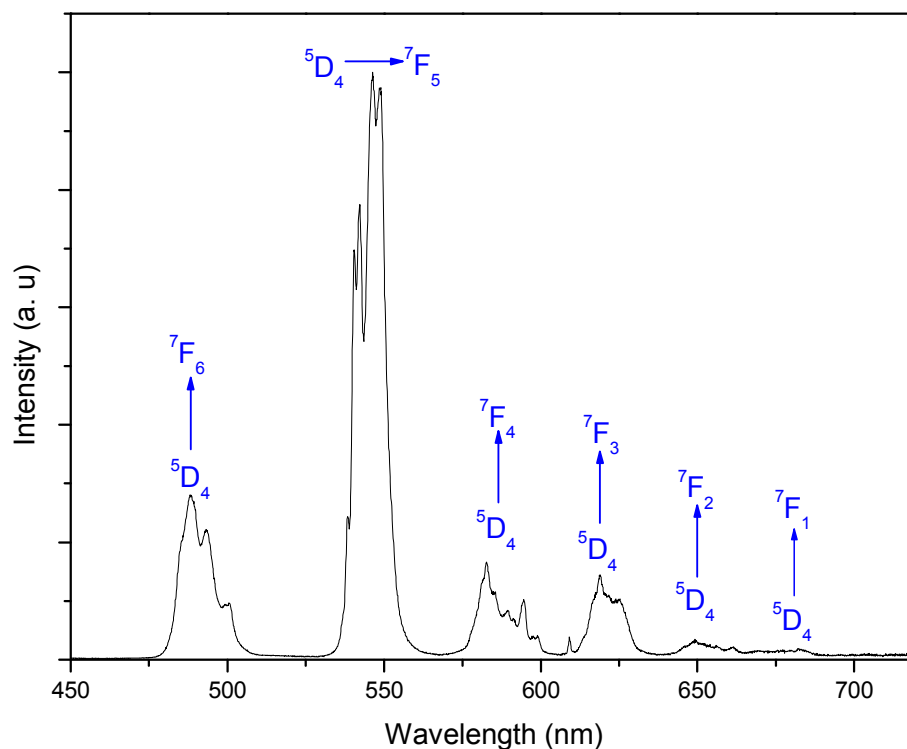
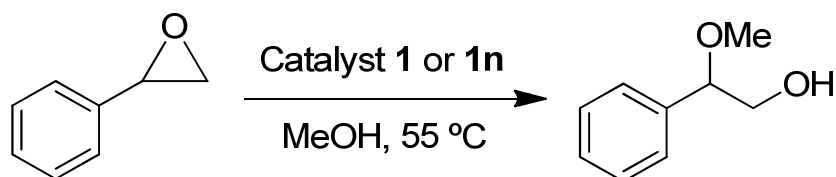


Figure 3.14 - Ambient temperature emission spectra of [Tb(Hpmd)(H₂O)] (**3**) excited at 275 nm.

3.2.6. Heterogeneous Catalysis

The catalytic performances of the microcrystalline bulk [Eu(Hpmd)(H₂O)] (**1**) and the nanocrystalline [Eu(Hpmd)(H₂O)]_{nano} (**1n**) materials were investigated in the ring-opening reaction of styrene oxide (PhEtO) with methanol, at 55 °C (Scheme 3.1). The reaction of PhEtO in the presence of **1** was very sluggish giving 2-methoxy-2-phenylethanol (MeOPhEtOH) as the only product formed in 7% / 11% yield at 24 h / 48 h reaction. It is noted that similar results were observed without adding the catalyst, suggesting that **1** does not exhibit significant catalytic activity (Table 3.4). After a 48 h-batch run the solid material was recovered and characterized by PXRD and SEM. SEM images of the recovered solid reveal some morphological changes: bundles (*ca.* 15 μm wide) of very fine needles turned into micro-sized aggregates of irregular morphology. Powder X-ray diffraction studies reveal, nevertheless, that the crystal structure of **1** remained unchanged under the used reaction conditions (Figure 3.15).



Scheme 3.1 - Reaction of styrene oxide with methanol, catalyzed for **1** or **1n**, to produce 2-methoxy-2-phenylethanol.

Table 3.4 - Ring opening of styrene oxide with methanol, at 55 °C. ^a

Catalyst	Reaction time (h)	Conversion of PhEtO (%)	Selectivity to MeOPhEtOH (%)
None	4/24/48	2/10/15	100
1	4/24/48	2/7/10	100/100/100
1n	4/24/48	30/93/100	100/100/100
EuCl ₃ ·6H ₂ O	4/24/48	58/87/91	75/81/79
H ₄ pmd	1	100	100

^a Reaction conditions: PhEtO (0.18 mmol), catalyst (7.5 mg **1**, or 0.018 mmol of EuCl₃·6H₂O or H₄pmd, methanol (0.43 mL), 55 °C.

The reaction of PhEtO with methanol in the presence of **1n** gives MeOPhEtOH in quantitative yield within 48 h reaction, at 55 °C (Table 3.4). These results are far superior to those observed for **1**. Opposite to that, **1n** exhibits excellent regioselectivity to the formation of the β-alkoxy alcohol product. According to the literature, the alcoholysis of PhEtO may be favored by the presence of free coordination positions at Lewis acid sites for the activation of the PhOEt molecules and the subsequent nucleophilic attack of (heteroatom-based nucleophile) methanol at the benzylic carbon atom of the epoxide ring.³⁹⁻⁴⁰ The SEM images of the recovered solid **1n** show that this material remained nanocrystalline (*ca.* 100 nm), forming aggregates of *ca.* 5-10 μm in diameter. Reducing the crystallites size of **1** down to the nano-scale increases the surface area, which expectedly enhances the number of accessible active sites, explaining the enhanced catalytic activity of **1n** in comparison to **1**. It is also possible that the active sites correspond to structural defects, in which case the reduction of crystallite sizes would expectedly enhance the number of external defect sites and consequently the catalytic activity.

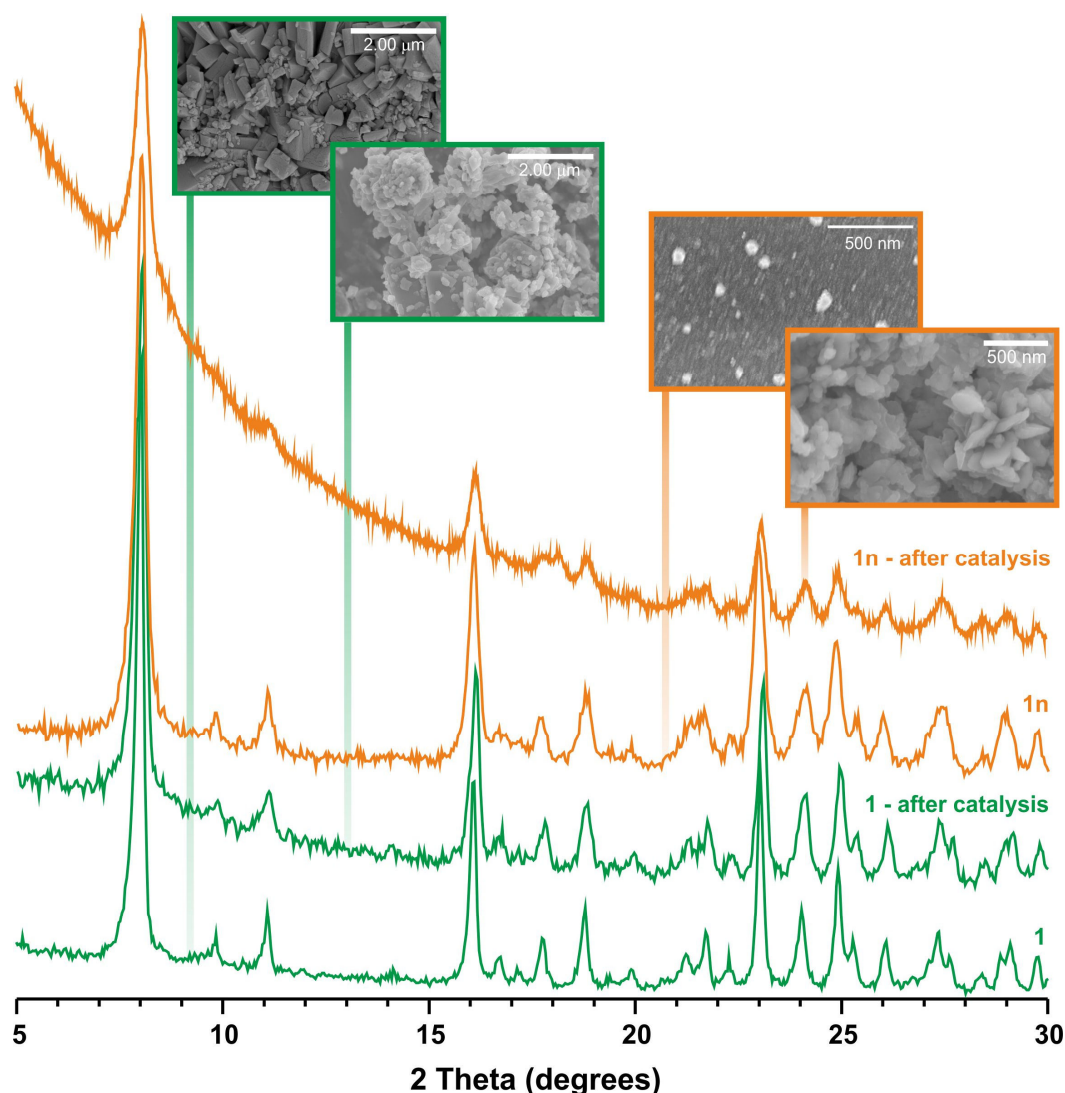


Figure 3.15 – Powder X-ray diffraction and SEM of the bulk [Eu(Hpmd)(H₂O)] (**1**) and nano [Eu(Hpmd)(H₂O)] (**1n**) materials before and after catalytic studies.

For comparative purposes the precursors **H₄pmd** organic linker and EuCl₃·6H₂O were tested as (homogeneous) catalysts in the methanolysis of PhEtO, under similar reaction conditions (using molar equivalent amounts to those of ligand and lanthanide, respectively, in the loaded **1n** catalyst). In the case of **H₄pmd**, MeOPhEtOH is formed in quantitative yield within 1 h reaction, indicating that it is a quite active and selective Brønsted acid organocatalyst (Table 3.4). Using EuCl₃·6H₂O MeOPhEtOH is formed in 79% selectivity at 91% conversion, reached at 48 h reaction, indicating that this precursor is less selective than that observed for **1n**. Based on these results we may postulate that the active sites in **1n** may be of the type Brønsted acid and/or coordinatively unsaturated Lewis acid sites, which would inherently correspond to structural defect sites.

3.3. Lanthanum-Biphosphonate Coordination Polymers Isolated by Microwave-Assisted and One-Pot Synthesis

3.3.1. Synthesis

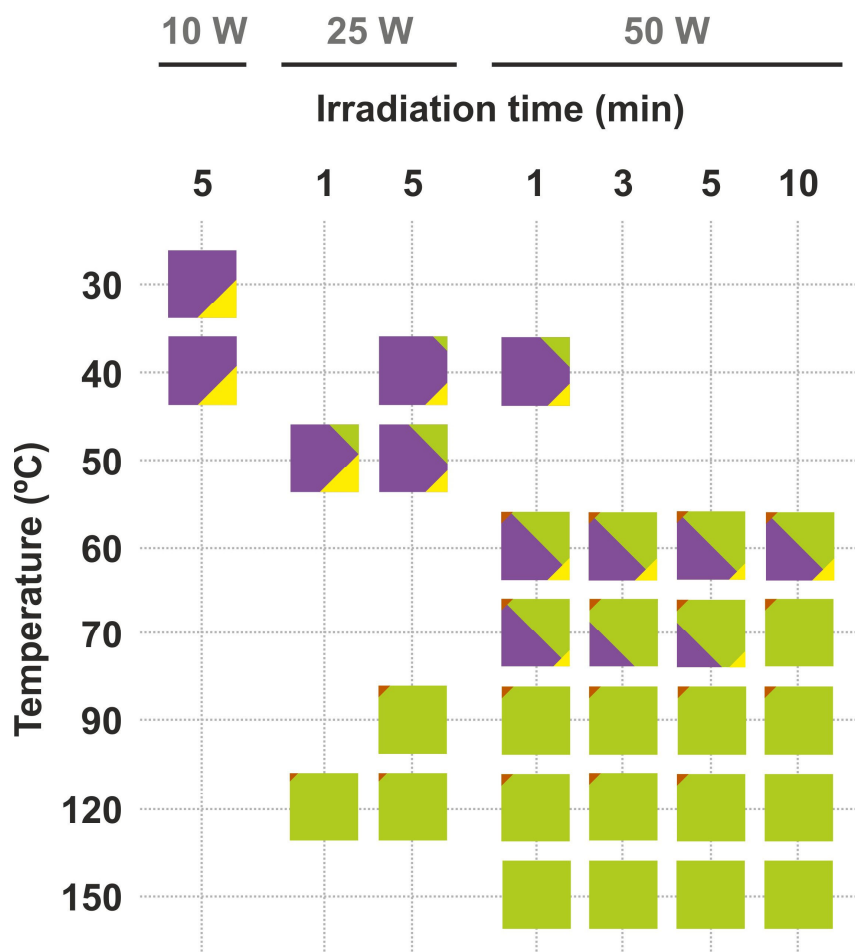
3.3.1.1. Synthetic strategy

Microwave-Assisted Synthesis (MWAS) and one-pot method have distinct principles and a direct transposition of the experimental conditions from one method to another is difficult. While MWAS permits the reduction of reaction time and the possibility to control the morphology of the materials,^{15,41} the one-pot method usually allows growing of crystals for single-crystal X-ray diffraction studies while maintaining small reaction times.⁴²⁻⁴³ A systematic variation of the experimental conditions is, thus, pertinent in order to obtain (i) phase-pure and (ii) highly crystalline materials while (iii) exhibiting uniform crystal habit and size distribution. In order to quickly screen the achieved products in terms of purity and morphology, a combination of X-ray diffraction (powder and single-crystal) and Scanning Electron Microscopy (SEM) was used. Replication of the synthetic conditions was also performed to test the reproducibility of the present reactive system and the results are summarized in the following sub-sections.

3.3.1.2. Microwave-assisted synthesis

Hydrothermal synthesis has been routinely employed as a daily synthetic approach of MOFs. In this context, phase-pure $[\text{La}_2(\text{H}_2\text{pmd})(\text{pmd})(\text{H}_2\text{O})_2]$ (**5**) was first isolated under typical hydrothermal conditions, using convection heating at 180 °C during 72 h (see sub-section 8.10.2.1 in the Experimental Section for further details). The crystals obtained presented a plate-like morphology having dozens of micrometers.

Considering that mild and faster conditions are usually preferred, we first transposed the preparation of the aforementioned material to MWAS. The presence of three distinct phases, as identified by PXRD, was unequivocally confirmed while inspecting the influence of the reaction parameters on the purity and crystal habit (see Scheme 3.2). Microwave heating was found to be an efficient method to prepare different phases by solely changing the reaction temperature: $[\text{La}_2(\text{H}_2\text{pmd})_3(\text{H}_2\text{O})_{12}]$ (**4**) is formed at low temperatures (below 40 °C); $[\text{La}_2(\text{H}_2\text{pmd})(\text{pmd})(\text{H}_2\text{O})_2]$ (**5**) is mainly obtained at high temperatures, typically above 90 °C, in line with the results of the static hydrothermal conditions. For a mid-range temperature, mixtures of both compounds were always observed alongside with the presence of a small amount of $[\text{La}(\text{H}_3\text{pmd})(\text{H}_2\text{pmd})(\text{H}_2\text{O})]$ (**6**). Unreacted organic ligand may be found in all prepared materials (except for high temperatures). Nevertheless, it does not represent an experimental hindrance because it is easily removed from the final product by washing with distilled water. We note that grinding the reactant prior to the synthetic procedure can drastically reduce the presence of unreacted ligand.



Scheme 3.2 – Optimization of the microwave-assisted hydrothermal synthesis of $[\text{La}_2(\text{H}_2\text{pmd})_3(\text{H}_2\text{O})_{12}]$ (**4**) and $[\text{La}_2(\text{H}_2\text{pmd})(\text{pmd})(\text{H}_2\text{O})_2]$ (**5**). Legend: ■ – phase-pure **4**; ■ – phase-pure **5**; ■ – $[\text{La}(\text{H}_3\text{pmd})(\text{H}_2\text{pmd})(\text{H}_2\text{O})]$ (**6**); ■ – indicates the presence of unreacted organic linker which can be easily removed by washing the products with distilled water. The metal-to-ligand molar ratio used in all synthesis is of *ca.* 1:1.

The reaction time does not seem to have a significant influence in the preparation of **5**. The same does not happen for the employed irradiation power. A strict control of the reaction temperature is, thus, crucial. It is also noted that using this experimental setup, power input may have a great influence in the outcome because it is difficult to maintain stable low temperatures while using high irradiation power and *vice-versa*.

Besides **4** and **5**, the optimization stage also revealed the presence of minor quantities of compound **6** as impurity. Optimization of the experimental conditions to isolate phase-pure **6** proved unsuccessful. Nevertheless, from the obtained physical mixtures and taking into account the considerable differences in particle size and morphology, it was possible to manually isolate a crystal representative of each phase. These crystals allowed a full structural characterization using single-crystal X-ray diffraction studies (see tabulated data in Experimental Section).

3.3.1.3. One-Pot Synthesis

The one-pot methodology is substantially different from MWAS: milder temperatures are typically used alongside with no (autogenous) pressure. For each pair of temperature/time, the metal-to-ligand molar ratios were varied at the proportions of *ca.* 1:1 and 1:2. A second 1:1 trial was performed but diluted to the double, hereafter defined as 1:1*. As in MWAS, phase-pure products $[\text{La}_2(\text{H}_2\text{pmd})_3(\text{H}_2\text{O})_{12}]$ (**4**) and $[\text{La}_2(\text{H}_2\text{pmd})(\text{pmd})(\text{H}_2\text{O})_2]$ (**5**) may be readily obtained under various reaction conditions. Additionally, two new compounds were found, namely $[\text{La}_2(\text{H}_2\text{pmd})_3(\text{H}_2\text{O})_2]$ (**7**) and $[\text{La}_2(\text{H}_2\text{pmd})(\text{pmd})(\text{H}_2\text{O})_4]$ (**8**). All the materials are crystalline and show particle size in the micrometer range, as observed for the samples prepared by MWAS.

It is noted that this method has the drawback of introducing some randomness in the prediction of the phases to be obtained (Scheme 3.3). In opposition to MWAS, where a clear evolution of a phase into the other with increasing temperature (the most significant reaction parameter) is observed, in the one-pot method the same logical behavior is not present.

As for MWAS, the reaction time does not seem to have a strong influence on the obtained compound and the most important parameter is, once again, the temperature. Above ambient temperature the composition of the reactive mixtures is also a factor to be considered. In spite of a handful of exceptions at 40 °C, some conclusions can be inferred:

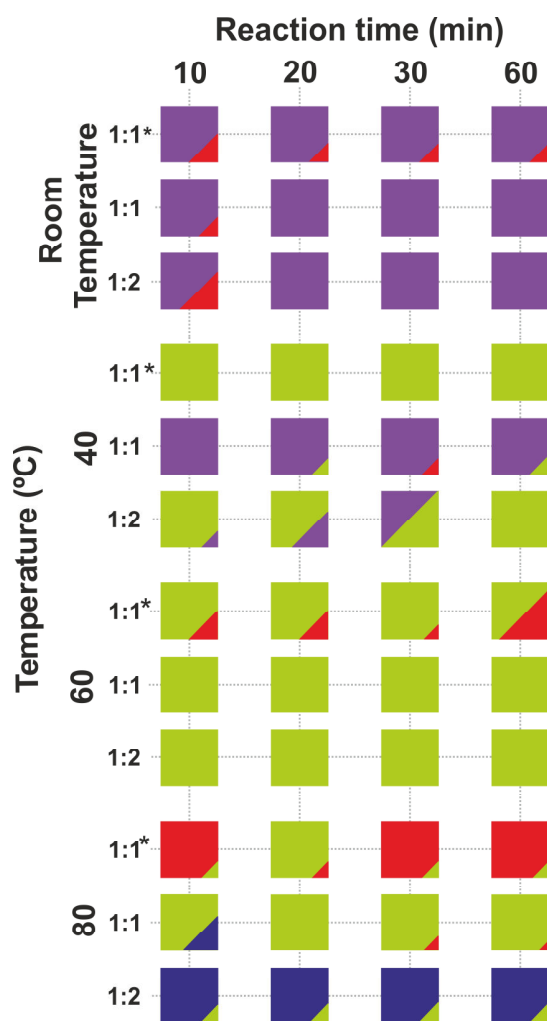
i) Compound **4** predominates at ambient temperature, whereas compound **5** is formed especially at high temperatures (Scheme 3.3);

ii) In general, compound **8** appears essentially in the 1:1* trials; at 80 °C this compound is even the major product;

iii) Higher temperatures and ligand-to-metal molar ratios favor the appearance of compound **7**;

iv) Compounds **7** and **8** can only be prepared (but not isolated as phase-pure) at high temperatures (80 °C).

In short, we can assume that **4** is the kinetic compound because it is formed at milder conditions. On the other hand, **5** seems to be the thermodynamic phase. A higher quantity of H_4pmd favors the formation of **7** due to its 1:1.5 La: H_2pmd stoichiometry, with this tendency being enhanced at higher temperatures.



Scheme 3.3 – Optimization of the one-pot synthesis conditions for $[\text{La}_2(\text{H}_2\text{pmd})_3(\text{H}_2\text{O})_{12}]$ (**4**) and $[\text{La}_2(\text{H}_2\text{pmd})(\text{pmd})(\text{H}_2\text{O})_2]$ (**5**). Legend: ■ – phase-pure **4**; ■ – phase-pure **5**; ■ – $[\text{La}_2(\text{H}_2\text{pmd})_3(\text{H}_2\text{O})_2]$ (**7**); ■ – $[\text{La}_2(\text{H}_2\text{pmd})(\text{pmd})(\text{H}_2\text{O})_4]$ (**8**). * refers to a concentration of metal and ligand half of those used for the other syntheses. The ratio is represented as metal-to-ligand molar ratio. Phase **4** is predominant at ambient temperature and **5** is formed preferentially at higher temperatures. These two compounds can be isolated as phase-pure in a variety of experimental conditions. Compounds **7** and **8** are mostly formed, as main products, at high temperatures (80 °C) and could not be isolated as phase-pure.

3.3.2. Crystal Morphology

Crystal morphology varies according to the obtained phase for the two heating methods. Crystals of $[\text{La}_2(\text{H}_2\text{pmd})_3(\text{H}_2\text{O})_{12}]$ (**4**) exhibit needle-like morphology for all tested reaction conditions, with individual crystallites being stacked into large aggregates with varying shape and size. This was also observed for compound $[\text{La}_2(\text{H}_2\text{pmd})(\text{pmd})(\text{H}_2\text{O})_2]$ (**5**), with the exception of the crystallite habit, which are in this case plates.

Comparing the two methods, MWAS originates needles of **4** with lengths typically smaller than those obtained by the one-pot methodology. On the other hand, the plate-like crystallites of **5** have similar sizes for the two approaches. Concerning crystallite size, when MWAS is employed, the size of needles of **4** is generally smaller than the plate-like crystallites of **5**. In opposition, it is not possible to unequivocally determine the relation in size of crystallites of the two compounds for the one-pot method.

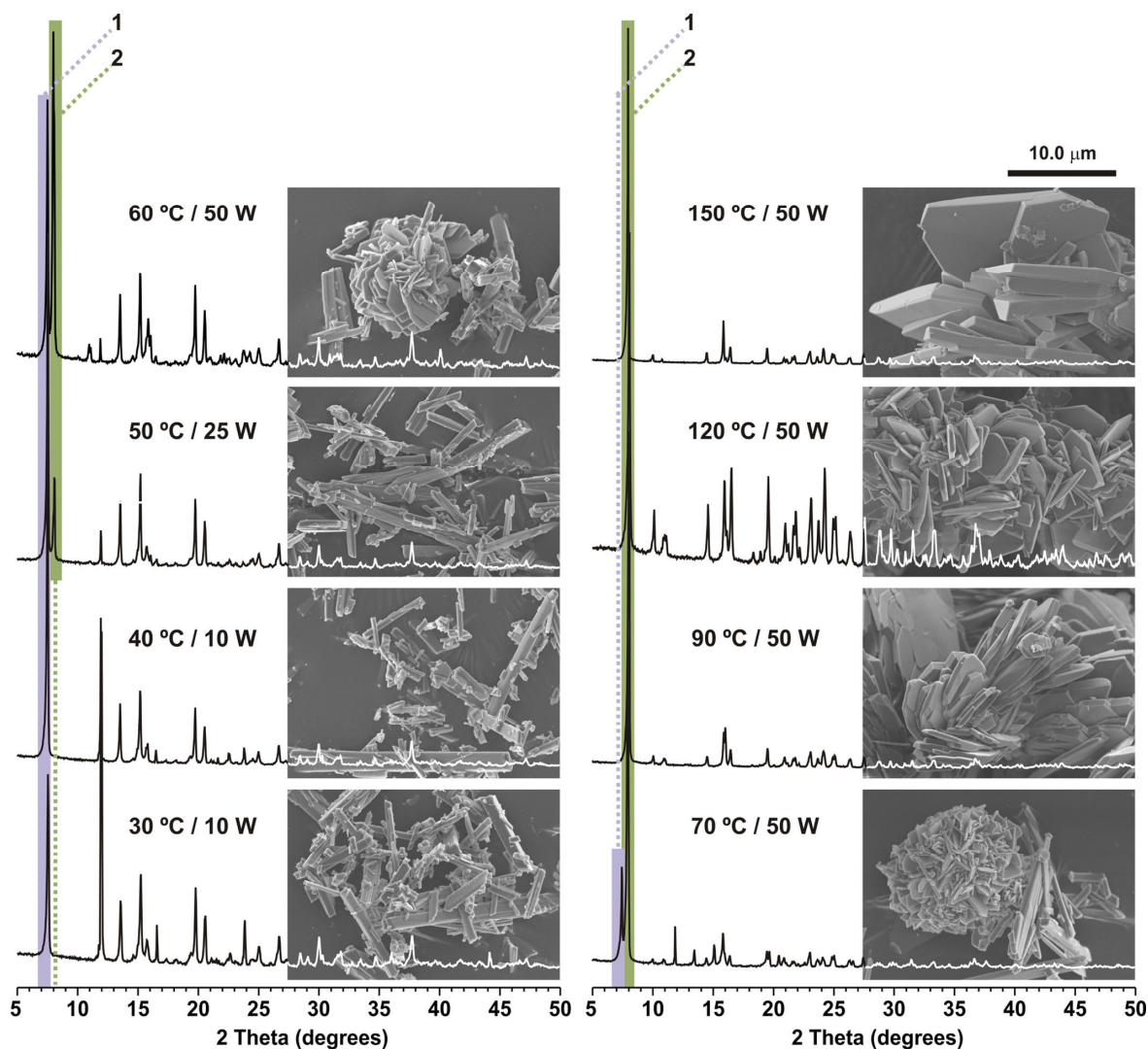


Figure 3.16 – Powder X-ray diffraction patterns and SEM images of bulk materials prepared using MWAS at different temperatures during 5 minutes of reaction: phase-pure **4**, as needle-like crystals, is isolated at low temperatures (30 and 40 °C) while phase-pure **5**, comprising plate-like crystals, at 150 °C (please note: at 90 and 120 °C compound **5** is contaminated with small amounts of **6**). Intermediate temperatures (50, 60 and 70 °C) promote the preparation of mixtures comprised of both phases **4** and **5**.

Because the temperature is of crucial importance to isolate phase-pure products it is, thus, pertinent to look into more detail to the variation of the average particle size and thickness when this parameter is changed. For MWAS, at lower temperatures (*e.g.*, 30 and

40 °C) and irradiation power (10 W) phase-pure **4** is obtained (after removing the excess of the organic linker) with particle size ranging from few to tens of micrometers. At 50, 60 and 70 °C mixtures of **4** and **5** are isolated (for irradiation powers of 25 and 50 W). Crystals of phase-pure **5** begin to appear at 50 °C becoming predominant above 70 °C, as observed from the combined PXRD and SEM studies given in Figure 3.16. In this case it is not possible to conclude on a trend for the variation of the average crystal size. Only at 150 °C a significant increase in the crystallite size is observed. However, the emergence of $[\text{La}(\text{H}_3\text{pmd})(\text{H}_2\text{pmd})(\text{H}_2\text{O})]$ (**6**) in the reactions performed at 90 and 120 °C may, somehow, inhibit crystal growth. Hence only at 150 °C there is no interference of contaminant species (*i.e.*, free organic ligand or compound **6**) and, therefore, the increase in particle size is clearly noticeable.

For the materials obtained at 150 °C, but using different microwave irradiation periods, it seems that reaction time does not have a significant role in the final particle morphology and size (Figure 3.17).

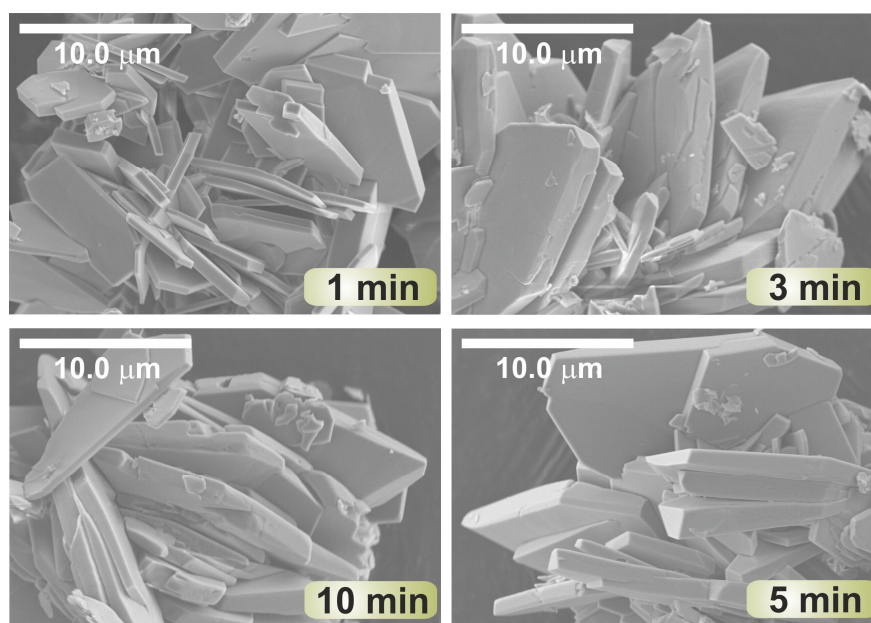


Figure 3.17 – SEM images of phase-pure $[\text{La}_2(\text{H}_2\text{pmd})(\text{pmd})(\text{H}_2\text{O})_2]$ (**4**) prepared under microwave irradiation at 150 °C using different reaction periods. Despite the variation of reaction time (from 1 to 10 min), significant variations in crystallite habit are not observable: particle size and plate-like morphology remain approximately identical.

When using the one-pot method and for a metal-to-ligand molar ratio of *ca.* 1:1, at mild temperatures in which compound **4** is predominant (ambient temperature and 40 °C), the increase of the reaction time decreases, in general, the length of the needles. Furthermore, the difference in size for these two temperatures is negligible. For higher temperatures (60 and 80 °C) plate-like crystallites of **5** are observed, and the reaction time does not affect the particle size. The raise in temperature increases aggregation of particles

and the distribution size for all sample ranges from few micrometers (*ca.* 2-3 μm) to dozens of micrometers (*ca.* 20-30 μm) (Figure 3.18).

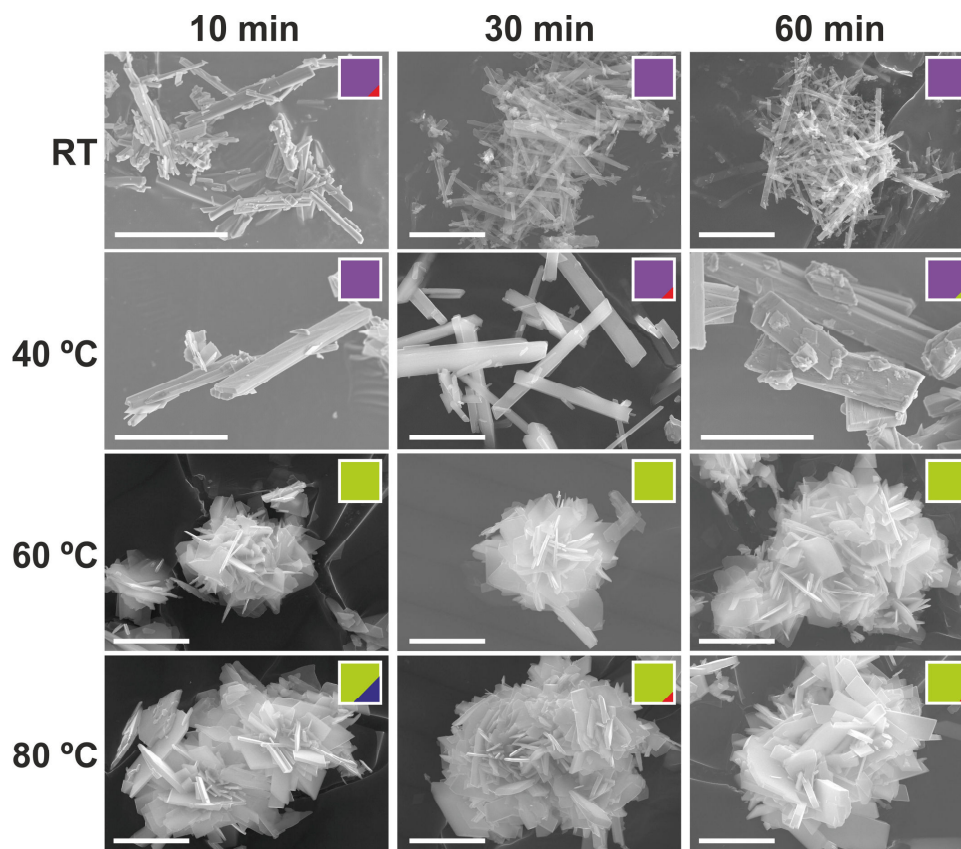


Figure 3.18 – SEM pictures of the materials obtained using the one-pot method when a *ca.* 1:1 metal-to-ligand molar ratio is employed, depicting the variation of temperature and reaction time. Variation in temperature produces changes in particle morphology and size. Despite the variation in the reaction time significant modifications are not observable: particle size and morphology remain approximately identical at the same temperature. The white bars represent 10 μm . Legend: ■ – phase-pure $[\text{La}_2(\text{H}_2\text{pmd})_3(\text{H}_2\text{O})_{12}]$ (**4**); ■ – phase-pure $[\text{La}_2(\text{H}_2\text{pmd})(\text{pmd})(\text{H}_2\text{O})_2]$ (**5**); ■ – $[\text{La}_2(\text{H}_2\text{pmd})_3(\text{H}_2\text{O})_2]$ (**7**); ■ – $[\text{La}_2(\text{H}_2\text{pmd})(\text{pmd})(\text{H}_2\text{O})_4]$ (**8**).

3.3.3. Crystal Structure Description

In this subsection will not be describe in detailed the crystal structure of each isolated material. Due to the variety of compounds herein obtained using two different synthetic methods, the main objective is based on the comparison of those products concerning their purity, crystallinity, morphology and particle size. Therefore, in this subsection it is only discussed their general structural features. While compounds **4** to **7** were characterized by single-crystal X-ray diffraction, compound **8** was identified by *ab initio* powder X-ray diffraction studies. For a detailed description on collection of data and crystal structure resolution of **4-8** see sub-section 8.10.2.3 in the Experimental Section and the published work reporting these data.¹⁴

As mentioned above, the present crystallographic description has comparative purposes. Therefore, to have more insights about crystal data (i.e., selected bond lengths, angles and hydrogen bonding geometry) see Tables A.2.1- A.2.9 in the Appendices.

Five different crystal structures, namely $[\text{La}_2(\text{H}_2\text{pmd})_3(\text{H}_2\text{O})_{12}]$ (**4**), $[\text{La}_2(\text{H}_2\text{pmd})(\text{pmd})(\text{H}_2\text{O})_2]$ (**5**), $[\text{La}(\text{H}_3\text{pmd})(\text{H}_2\text{pmd})(\text{H}_2\text{O})]$ (**6**), $[\text{La}_2(\text{H}_2\text{pmd})_3(\text{H}_2\text{O})_2]$ (**7**) and $[\text{La}_2(\text{H}_2\text{pmd})(\text{pmd})(\text{H}_2\text{O})_4]$ (**8**) [where **H₄pmd** = 1,4-phenylenebis(methylene)diphosphonic acid), were unveiled in the course of this work. As it is shown by the formulae, all compounds appear in three different La : H_{4-x}pmd^x ratios: 1 : 1 for **5** and **8**; 1 : 1.5 for **4** and **7**; 1 : 2 for **6**. Except for compounds **4** and **8**, which have higher contents of water molecules per metal center (6 and 2, respectively), compounds typically have a sole water molecule per metal center.

The coordination number of the La³⁺ metal centers also varies and is related to the kind and hapticity of the coordinated ligands. In **4** the coordination geometry around the nonacoordinated metal center resembles a tricapped trigonal prism formed by the coordination to six water molecules and three crystallographic independent κ^1 -O-hydrogenophosphonato moieties (Figure 3.19). The coordination number of nine is only possible given the presence of a large number of small water ligands and a low number of bulk **H₄pmd** residues. In compound **5**, La³⁺ is octacoordinated to five phosphonic residues, being two of them O,O'-chelating, and to one water molecule. If we consider the chelating phosphonates as single coordination sites, the geometry around the metal center can be seen as a highly distorted octahedron (Figure 3.20). The H_{4-x}pmd^x residues appear in two different protonation degrees and hapticities, being one of the type μ_2 -O, μ_2 -O', κ^1 -O''-phosphonate and the other of the type μ_2 -O,O'-hydrogenophosphonate.

In **6** and **7**, the metal center is heptacoordinated to six non-chelating phosphonic residues and to one water molecule. The large number of bulky ligands prevented chelation, reducing in this way the coordination number to a considerably low number for the La³⁺ cation. Remarkably, while in **6** the metal center is almost rotosymmetric with the coordination environment resembling a distorted pentagonal bipyramid, in **7** the metal center resembles a monocapped trigonal prism (Figures 3.21 and 3.22). The refinement of the crystal structure of **6** did not permit a clear determination of the protonation sites. Excluding the assignment of protonation degree, it is possible to say there are two different hapticities for the phosphonate moiety residues, being one μ_2 -O,O' and another κ^1 -O. In **7** all the ligand moieties act as μ_2 -O,O'-hydrogenophosphonates. In compound **8** the metal center is octacoordinated. As it happens with compounds **6** and **7**, the metal center is, in **8**, coordinated to six organic residues, which, given their large volume, prevent chelation.

However, the high number of organic ligands does not limit the number of water molecules, and in this case the metal center is connected to two water molecules. The coordination geometry around the metal center resembles a square antiprism (Figure 3.23). Given that the model of the crystal structure of **8** was obtained by *ab initio* solution (Figure 3.24) from powder X-ray data a clear determination of the proton sites was not possible. Excluding the location of the protons, the organic ligands appear as two centrosymmetric

phosphonic residues comprising a μ_3-O, O', O'' -coordination of the two crystallographically independent phosphonic residues.

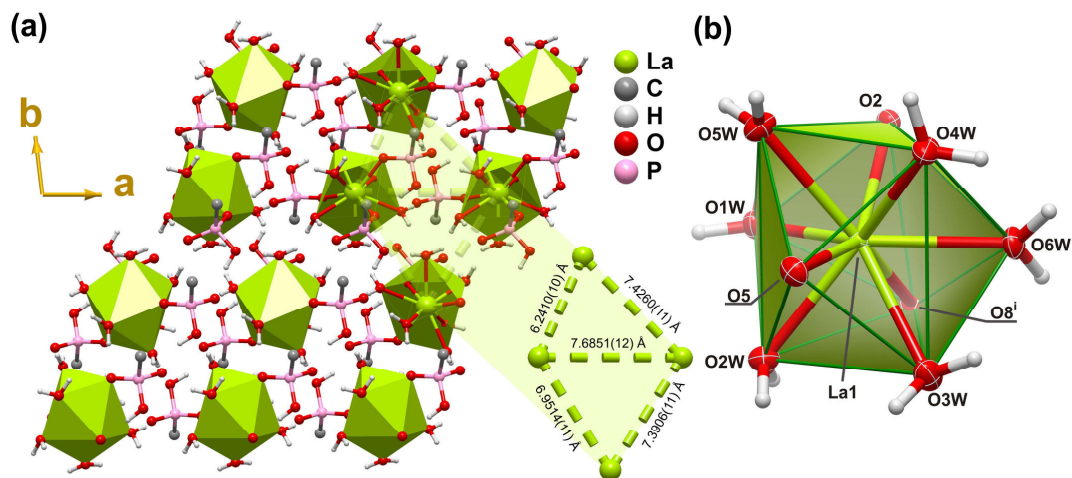


Figure 3.19 – (a) Schematic representation of the inorganic layer of $[\text{La}_2(\text{H}_2\text{pmd})_3(\text{H}_2\text{O})_{12}]$ (**4**) perpendicular to the c axis of the unit cell. The $\{\text{LaO}_9\}$ cores are represented as green polyhedra. Please note: because phosphonate groups do not act as bridges between La^{3+} cations the $\text{La}\cdots\text{La}$ intermetallic distances are represented by dashed green lines in an offset fashion. (b) Coordination environment around the metallic center of **4** showing all non-hydrogen atoms as displacement ellipsoids drawn at the 70% probability level and hydrogen atoms as small spheres with arbitrary radius. For selected bond lengths and angles see Table A.2.1 (in appendix A.2.1). Symmetry code used to generate equivalent atoms: (i) $x, y, -1+z$.

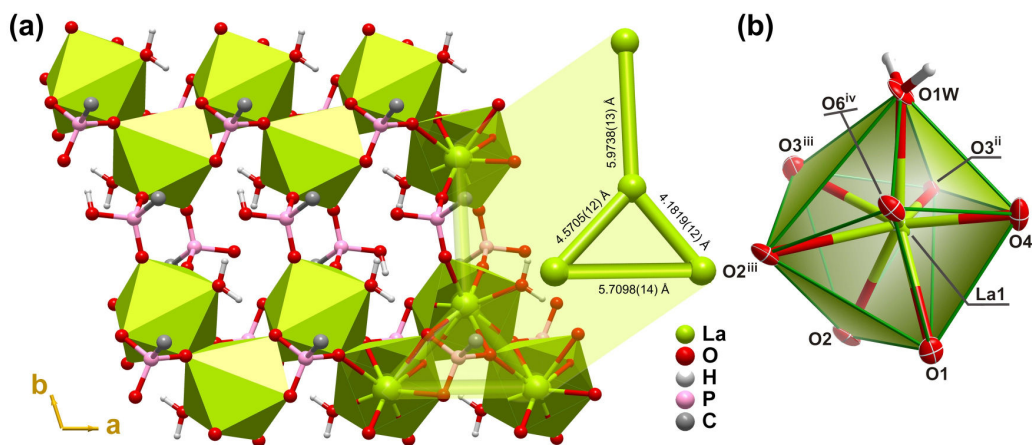


Figure 3.20 – (a) Schematic representation of the inorganic layer of $[\text{La}_2(\text{H}_2\text{pmd})(\text{pmd})(\text{H}_2\text{O})_2]$ (**5**) perpendicular to the c axis of the unit cell. The $\{\text{LaO}_8\}$ cores are represented as green polyhedra. Please note: $\text{La}\cdots\text{La}$ intermetallic distances imposed by bridging phosphonate groups are represented by green lines. (b) Coordination environment around metallic center of **5** showing all non-hydrogen atoms as displacement ellipsoids drawn at the 70% probability level and hydrogen atoms as small spheres with arbitrary radius. For selected bond lengths and angles see Table A.2.3 (in appendix A.2.1). Symmetry codes used to generate equivalent atoms: (ii) $-1+x, y, z$; (iii) $2-x, 2-y, -z$; (iv) $1-x, 1-y, -z$.

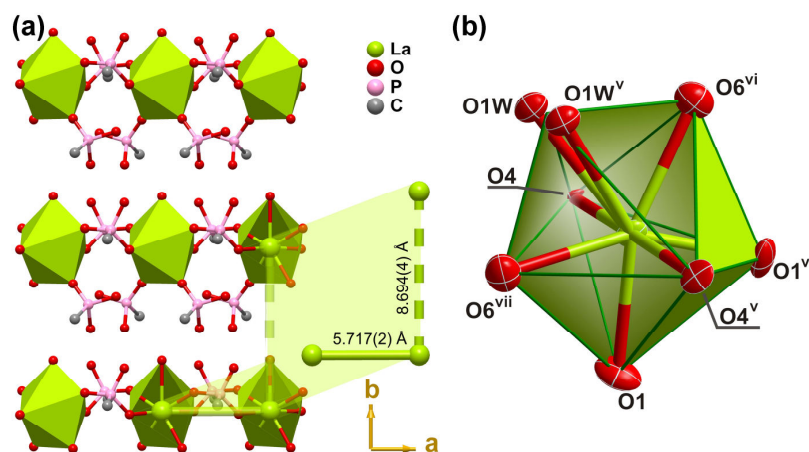


Figure 3.21 – (a) Schematic representation of the inorganic layer of $[\text{La}(\text{H}_3\text{pmd})(\text{H}_2\text{pmd})(\text{H}_2\text{O})]$ (**6**) perpendicular to the c axis of the unit cell. The $\{\text{LaO}_7\}$ cores are represented as green polyhedra. The water molecule bonded to the metal center is disordered over two symmetry-related positions with half occupancy for each. Please note: $\text{La}\cdots\text{La}$ intermetallic distances are represented as filled or dashed green lines in the presence or otherwise, respectively, of phosphonate bridges between metallic center. (b) Coordination environment around metallic center of **6** showing all non-hydrogen atoms as displacement ellipsoids drawn at the 70% probability level and hydrogen atoms as small spheres with arbitrary radius. For selected bond lengths and angles see Table A.2.5 (in appendix A.2.1). Symmetry codes used to generate equivalent atoms: (v) $\frac{1}{2}-x, y, \frac{1}{2}-z$; (vi) $-\frac{1}{2}-x, y, \frac{1}{2}-z$; (vii) $1+x, y, z$.

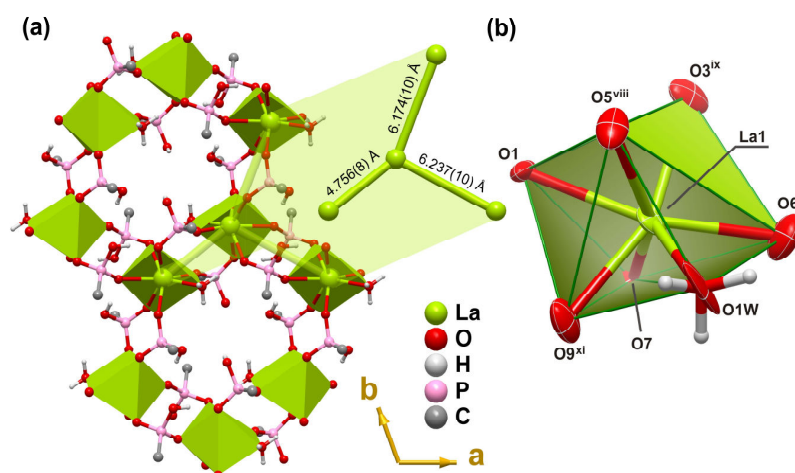


Figure 3.22 – (a) Schematic representation of the inorganic layer of $[\text{La}_2(\text{H}_2\text{pmd})_3(\text{H}_2\text{O})_2]$ (**7**) perpendicular to the c axis of the unit cell. The $\{\text{LaO}_7\}$ cores are represented as green polyhedra. Please note: $\text{La}\cdots\text{La}$ intermetallic distances imposed by bridging phosphonate groups are represented by green lines. (b) Coordination environment around metallic center of **7** showing all non-hydrogen atoms as displacement ellipsoids drawn at the 50% probability level and hydrogen atoms as small spheres with arbitrary radius. One of the hydrogen atoms attached to O1W is disordered over two positions with half occupancy for each. For selected bond lengths and angles see Table A.2.6 (in appendix A.2.1). Symmetry codes used to generate equivalent atoms: (viii) $2-x, 1-y, 2-z$; (ix) $2-x, 1-y, 1-z$; (x) $1+x, y, -1+z$; (xi) $2-x, -y, 1-z$.

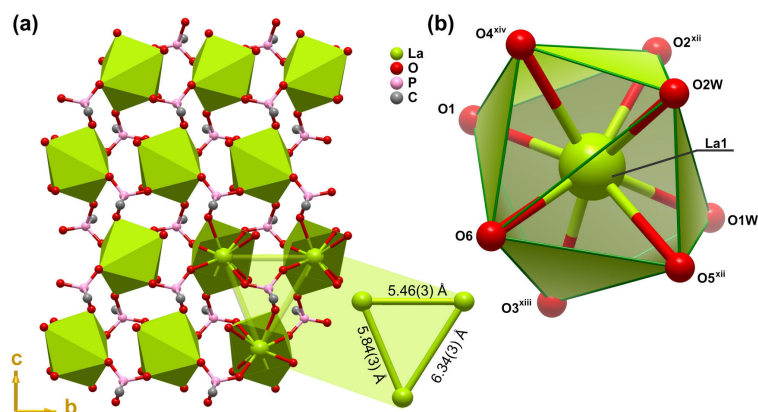


Figure 3.23 – (a) Schematic representation of the inorganic layer of $[\text{La}_2(\text{H}_2\text{pmd})(\text{pmd})(\text{H}_2\text{O})_4]$ (**8**) perpendicular to the a axis of the unit cell. The $\{\text{LaO}_8\}$ cores are represented as green polyhedra. Please note: $\text{La}\cdots\text{La}$ intermetallic distances imposed by bridging phosphonate groups are represented by green lines. (b) Coordination environment around metallic center of **8** showing all atoms as small spheres with arbitrary radius. For selected bond lengths and angles see Table A.2.8 (in appendix A.2.1). Symmetry codes used to generate equivalent atoms: (xii) $x, 1+y, z$; (xiii) $x, -1/2-y, -1/2+z$; (xiv) $x, -1/2-y, 1/2+z$.

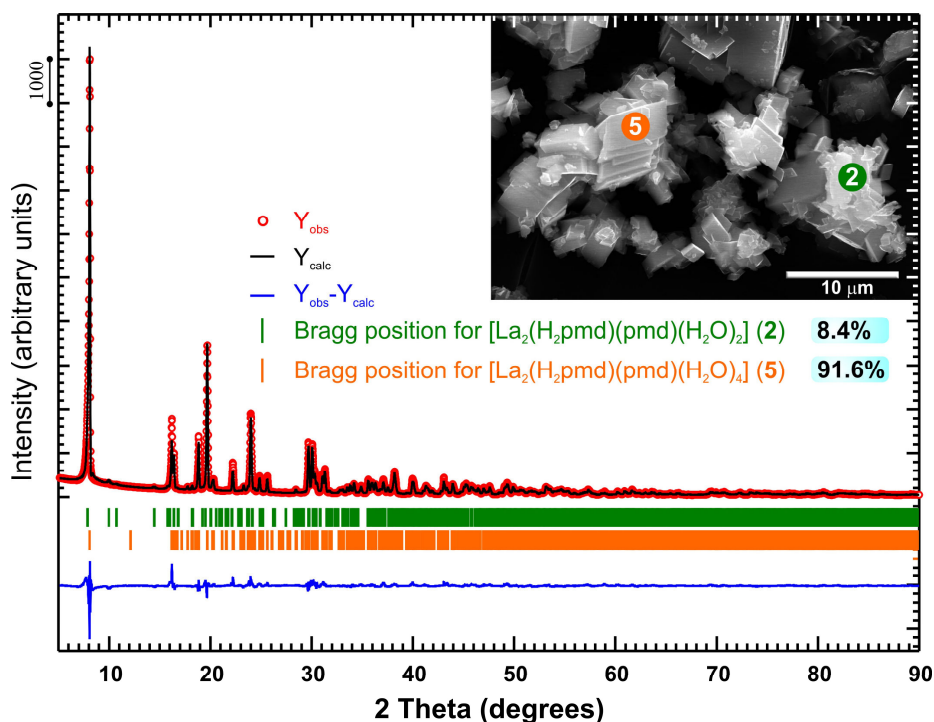


Figure 3.24 – Final Rietveld plot (powder X-ray diffraction data) of a mixture of $[\text{La}_2(\text{H}_2\text{pmd})(\text{pmd})(\text{H}_2\text{O})_2]$ (**5**) and $[\text{La}_2(\text{H}_2\text{pmd})(\text{pmd})(\text{H}_2\text{O})_4]$ (**8**) (8.4% and 91.6%, respectively, from total integrated intensity). Observed data points are indicated as red circles, the best-fit profile (upper trace) and the difference pattern (lower trace) are drawn as solid black and blue lines, respectively. Green and orange vertical bars indicate the angular positions of the allowed Bragg reflections for **5** and **8**, respectively. Refinement details are given in Experimental Section. Inset: SEM image of a representative portion of the studied material (physical mixture of compounds **5** and **8**) showing the plate-like crystal habit of compound **5** and the block-type for compound **8**.

Given its high number of water ligands, compound **4** is a 1D polymer, in which two metallic coordination polyhedra alternate with three bridging $\text{H}_2\text{pmd}^{2-}$ ligands (Figure 3.25). The remaining compounds are 3D structures. In spite of having different stoichiometries, coordination numbers and dimensionalities, the crystal packing of the five compounds is based on the alternation of inorganic layers, containing the $\{\text{LaO}_n\}$ polyhedra, with organic layers comprising the organic linkers.

In compounds **5-7** the lanthanide phosphonate layers are disposed perpendicular to the c axis while in **8** it is along the a axis (Figures 3.26 and 3.27, respectively). Along the inorganic layer, the geometrical arrangement of $\{\text{LaO}_n\}$ polyhedra and their connection with the phosphonate residues is different for the five structures.

In **4** the 1D polymer shows two non-directly bonded metal centers at 6.2410(10) Å from each other, which are arranged in a slightly distorted close hexagonal packing [other $\text{La}\cdots\text{La}$ distances range between 6.9514(11) and 7.6851(12) Å] (Figures 3.19 and 3.26). Only in **5** there is connection between the $\{\text{LaO}_8\}$ polyhedra forming a zigzag chain parallel to the a -axis of the unit cell, with the $\text{La}\cdots\text{La}$ intermetallic distances being of 4.1819(12) and 4.5705(12) Å (Figures 3.20 and 3.26). While the $\mu_2\text{-O}$, $\mu_2\text{-O}'$, $\kappa^1\text{-O}''$ -phosphonate moiety is embedded in this chain, contributing for its stability, the $\mu_2\text{-O,O}'$ -hydrogenophosphanate moiety acts as interconnection between chains giving the 2D aspect to the inorganic layer.

In **6**, the isolated $\{\text{LaO}_7\}$ polyhedra are arranged in the inorganic layer in a rectangular grid with the $\text{La}\cdots\text{La}$ distances being 5.717(2) and 8.694(4) Å. In this compound the inorganic layers are disposed in an ABAB \cdots fashion, where each vertex of the grid is aligned with the center of the layer immediately above and below, instead of being completely aligned along the c -axis as it happens with the remaining four compounds (Figures 3.21 and 3.26). In **7** the $\{\text{LaO}_7\}$ polyhedra are arranged in the inorganic layer in an elongated open hexagonal packing with the hole centered in the unit cell coordinates ($\frac{1}{2}$, 0, $\frac{1}{2}$). This is a hydrophilic hole toward which the coordinated water molecules and the hydroxyl groups from $\text{H}_2\text{pmd}^{2-}$ are directed. The distances between vertices of the hexagonal pattern (the metal centers) range from 4.756(8) to 6.237(10) Å (Figures 3.22 and 3.26).

In **8** the $\{\text{LaO}_8\}$ polyhedra are arranged in a hexagonal fashion along the inorganic layer with $\text{La}\cdots\text{La}$ distances ranging from *ca.* 5.46 to 6.34 Å (Figures 3.23 and 3.27). The two crystallographically independent phosphonate residues are distributed in alternate layers along the a axis, *i.e.*, between each three consecutive inorganic layers. The first pair is connected by the ligand containing atoms P1, and the other is connected by the ligand containing atom P2, or *vice-versa*.

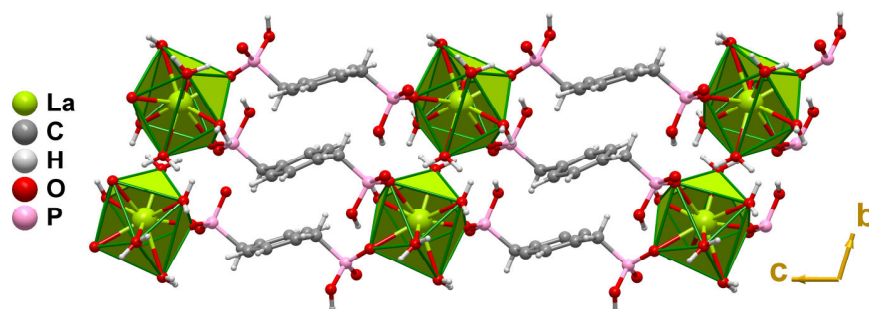


Figure 3.25 – Schematic representation of a portion of the 1D polymer present in compound $[\text{La}_2(\text{H}_2\text{pmd})_3(\text{H}_2\text{O})_{12}]$ (**4**), viewed in perspective along $[100]$ direction of the unit cell. The 1D polymer is formed by the alternation between two metallic coordination polyhedra and three bridging $\text{H}_2\text{pmd}^{2-}$ ligands.

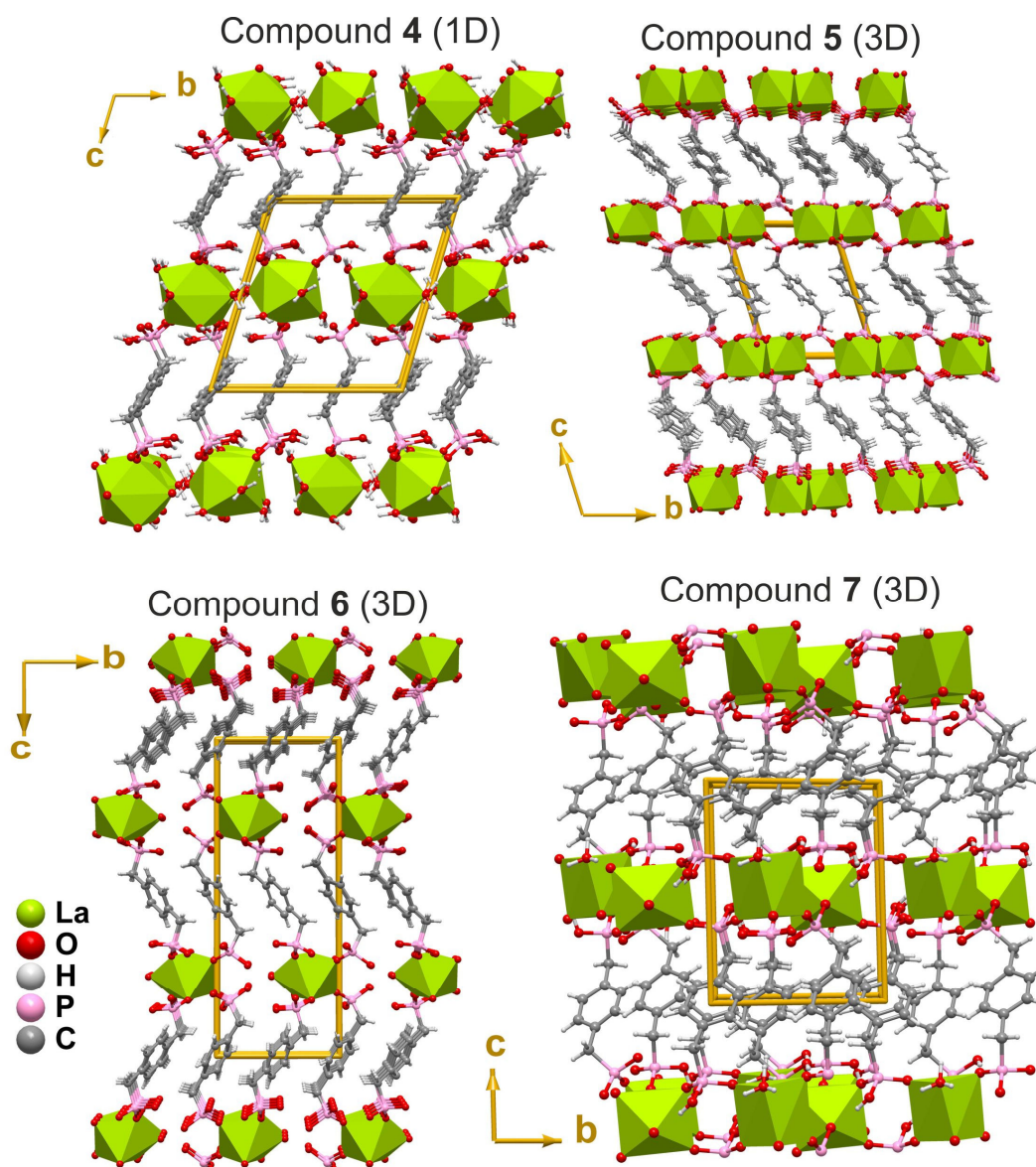


Figure 3.26 – Crystal packing of compounds **4** to **7** viewed in perspective along $[100]$ direction of the unit cell.

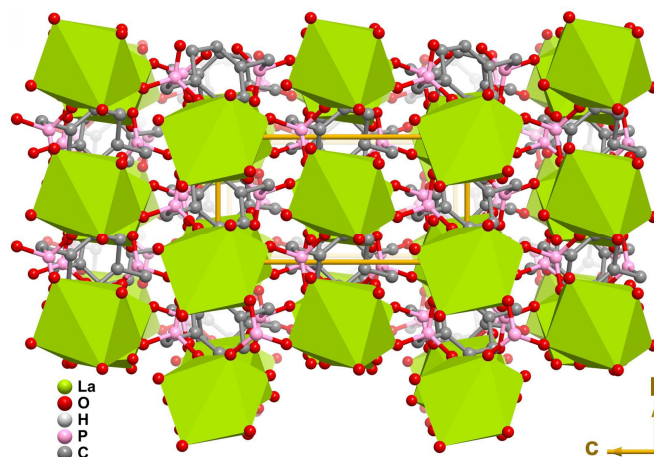


Figure 3.27 – Mixed ball-and-stick and polyhedral crystal packing of compound $[\text{La}_2(\text{H}_2\text{pmd})(\text{pmd})(\text{H}_2\text{O})_4]$ (**8**) viewed in perspective along $[100]$ direction of the unit cell.

3.3.4. Thermogravimetric Studies of Phase-Pure Materials 4 and 5

The thermal stability of the bulk (phase-pure) materials **4** and **5** were investigated between ambient temperature and *ca.* 800 °C (Figure 3.28), providing additional structural information on their hydration level. As shown in Figure 3.28, the thermograms of the two materials are strikingly distinct reflecting the different chemical composition of the compounds.

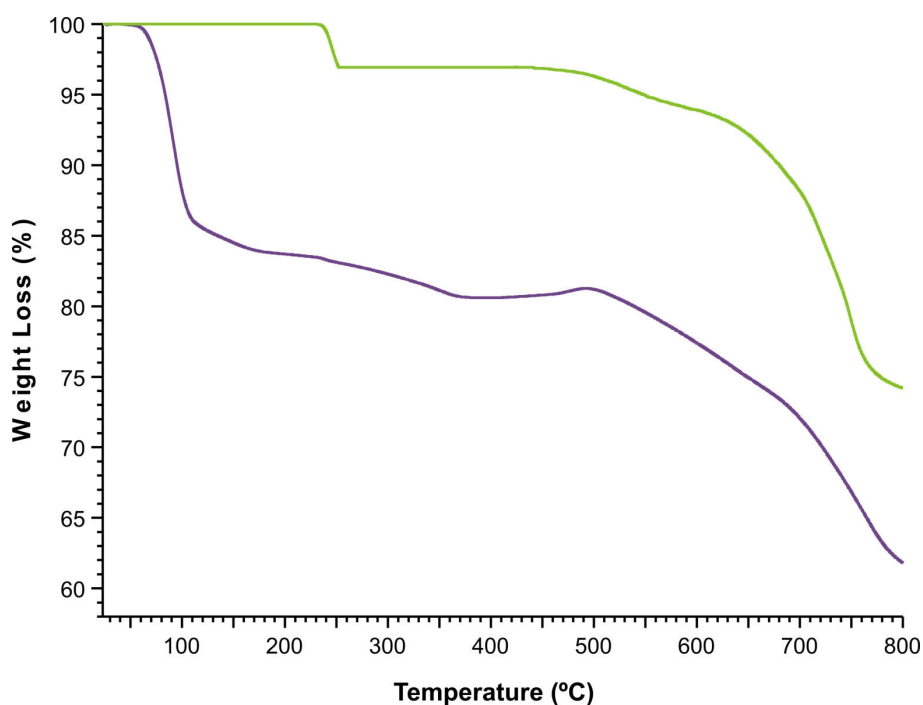


Figure 3.28 – Thermograms of compounds $[\text{La}_2(\text{H}_2\text{pmd})_3(\text{H}_2\text{O})_{12}]$ (**4**) and $[\text{La}_2(\text{H}_2\text{pmd})(\text{pmd})(\text{H}_2\text{O})_2]$ (**5**).
Legend: ■ – phase-pure 4; ■ – phase-pure 5.

For **4**, three main weight losses are observed. In the 45-130 °C temperature range the compound loses approximately 15.4% of the total weight, which agrees well with the release of eleven water molecules per formula unit. This weight loss is slightly smaller than the calculated value of about 17.2% corresponding to the twelve water molecules (based on the crystallographic studies). However, and as observed for **5**, these correspond to subsequent weight losses, increasing the difficulty to determine where each loss begins and finishes. In that sense, and looking to the slow decrease in weight above 130 °C we believe that both values (observed and calculated) are in good agreement. The latter two weight losses, corresponding to a total of *ca.* 3.1% and *ca.* 19.4%, were observed in the temperature ranges between 200-400 °C and 490-800 °C, respectively. It is, thus, feasible to assume that they may be attributed to the overlap of the release of the remaining water molecules and, lately, to the full decomposition of the organic components and concomitant collapse of the crystalline network.

For **5**, the framework is thermally robust up to *ca.* 230 °C, after which a weight loss corresponding to *ca.* 3.1% in mass is observed, mainly attributed to the release of coordinated water molecules (calculated value of *ca.* 4.3% for one molecule per La³⁺ cation). Therefore, it is possible to infer that not all water molecules are released at this temperature, being most likely liberated gradually afterwards. At higher temperatures (above *ca.* 450 °C) there are two subsequent weight losses, globally corresponding to *ca.* 4.1% (in 450-640 °C range) and *ca.* 18.5% (in 640-800 °C range), respectively. It is feasible to assume that the former weight loss may be attributed to partial dehydration of the material from the protonated P–OH groups, leading to the release of approximately one water molecule per La³⁺ cation (calculated value of *ca.* 4.3%). The latter weight loss could arise from the decomposition of the organic component of the framework.

3.3.5. FT-IR Spectroscopy

FT-IR spectroscopy studies clearly support the structural features unveiled by the X-ray diffraction studies. Figure 3.29 depicts selected regions in the spectra of phase-pure compounds **4** and **5**. Relevant differences in some spectral regions are noticeable despite their overall identical profiles, with most of these diagnostic bands being assigned to vibrational modes of coordinated water molecules. Such differences provide important information concerning the different coordination modes of the H_{4-x}pmd^{x-} residues and the chemical environment of the water molecules in the compound.

The typical $\nu(\text{O-H})$ stretching vibrational modes of the coordinated water molecules appear in the 3600-3200 cm⁻¹ range. Although below 2500 cm⁻¹ the spectra of the two compounds share striking similarities, in the 3600-3200 cm⁻¹ range, which corresponds to the vibrations assigned to the coordinated water molecules, there are notable differences: while for **4** a large number of bands are scattered in a vast interval between *ca.* 3600 and 2600 cm⁻¹, for **5** two strong bands are located at 3470 and 3395 cm⁻¹. This observation is in a clear agreement with the donor···acceptor distances shown in Tables A.2.2 and A.2.4 in the appendices: a wider interval of D···A distances was

observed for **4** (from *ca.* 2.71 to 3.30 Å) than for **5** (from *ca.* 2.82 to 2.91 Å). Large internuclear D···A distances imply weaker hydrogen bonds that, ultimately, correspond to stronger O–H vibrations that appear at higher wavenumbers. We note that the registered wavenumbers are also affected by the D–H···A interaction angle, but in this case the variation intervals reproduce the same general trend than that described for the distances. Thus, the narrow and strong band located at 3588 cm⁻¹ for **4** is attributed to a water molecule with, at least, one proton involved in weak hydrogen bonding interactions. This could be assigned either to O1W (with very short D–H···A angles in a bifurcated hydrogen bond) or to O6W (which corresponds to the largest D···A distance). In both materials there is also a band characteristic of the coordinated water molecules at *ca.* 1600 cm⁻¹. Again, the relationship between the observed intervals of internuclear D···A distances and the D–H···A interaction angle with the variation wavenumbers is observed: the band(s) for **4** is (are) considerably larger, clearly corresponding to at least two distinct environments for water, in agreement with the structural information described above.

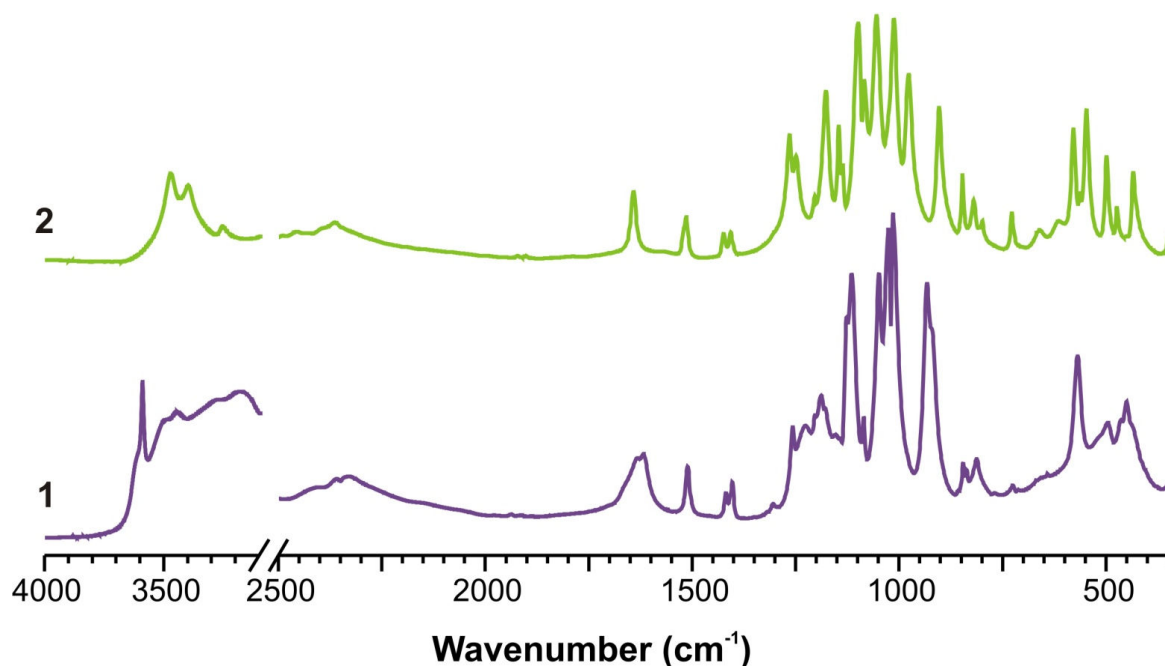


Figure 3.29 – FT-IR spectra of compounds [La₂(H₂pmd)₃(H₂O)₁₂] (**4**) and [La₂(H₂pmd)(pmd)(H₂O)₂] (**5**).

Legend: ■ – phase-pure **4**; ■ – phase-pure **5**.

The PO–H stretching modes were observed at *ca.* 2300 cm⁻¹ as medium intensity bands. The medium intensity peaks between 1700-1500 cm⁻¹ are attributed to the ν(C=CH–) deformation vibration in 1,4-disubstituted benzene rings. The two peaks at *ca.* 1400 cm⁻¹ with medium intensity are attributed to the –CH₂– deformation modes from the P–CH₂– groups. The vibrational modes ν_s(P=O), ν_s(P–O) and ν_s(P–C) appear between 1200-1100 cm⁻¹ (strong intensity), 1050-900 cm⁻¹ (strong intensity) and 800-600 cm⁻¹ (medium intensity), respectively.⁴⁴

3.3.6. Solid-State Nuclear Magnetic Resonance (NMR)

The presence of the diamagnetic La^{3+} rare-earth cation in compounds $[\text{La}_2(\text{H}_2\text{pmd})_3(\text{H}_2\text{O})_{12}]$ (**4**) and $[\text{La}_2(\text{H}_2\text{pmd})(\text{pmd})(\text{H}_2\text{O})_2]$ (**5**) permits the study of the bulk compounds using solid-state NMR, ultimately providing additional information on both the purity of the materials and further information on the composition of the asymmetric units.

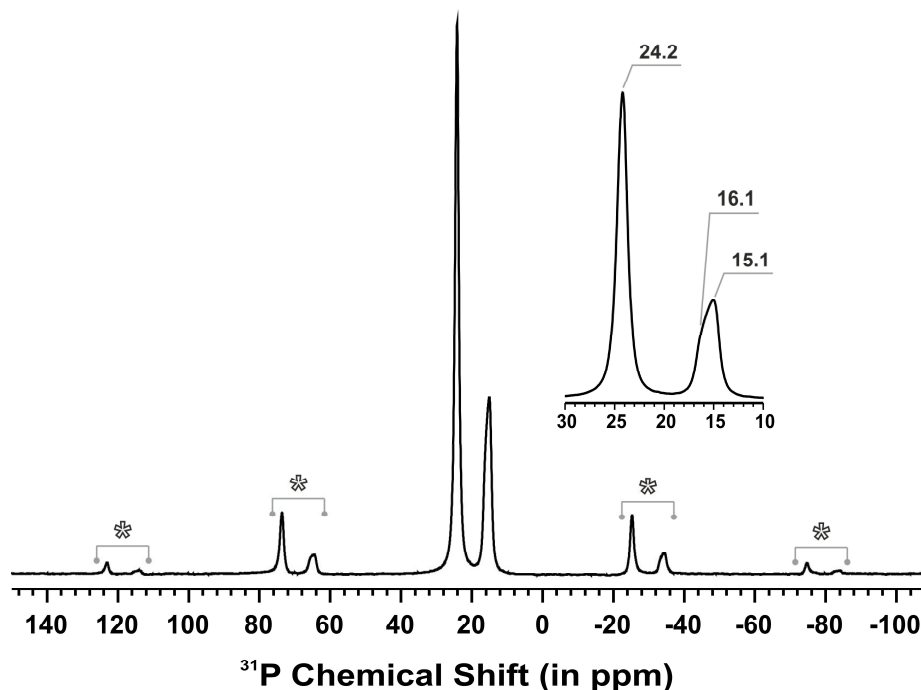


Figure 3.30 – ^{31}P HPDEC MAS spectrum of $[\text{La}_2(\text{H}_2\text{pmd})_3(\text{H}_2\text{O})_{12}]$ (**4**). Spinning sidebands are denoted using an asterisk. Peak deconvolution and integration throughout the entire spectral range (*i.e.*, including the spinning sidebands) gives a ratio of *ca.* 0.54 : 0.52 : 2.00 for the isotropic resonances at *ca.* 15.1, 16.1 and 24.2 ppm, respectively.

The isotropic region of the ^{31}P MAS spectra show two well-resolved resonances as depicted in Figures 3.30 and 3.31 for **4** and **5**, respectively. For compound **4**, the less deshielded peak is, nevertheless, composed of two resonances peaking at *ca.* 16.1 and 15.1 ppm while that at 24.2 ppm is well resolved. Peak deconvolution and integration including the spinning sidebands yields a ratio of *ca.* 2.00 : 0.52 : 0.52 for these resonances, which add up to a total of 3 sites for compound **4**. The splitting of one resonance may be attributed to some structural disorder associated with the phosphonate groups, ultimately leading to slightly distinct chemical environments. Nevertheless, for **4**, the $^{13}\text{C}\{^1\text{H}\}$ CP MAS spectrum (Figure A.2.2 in the Appendices) clearly shows two distinct spectral regions: the 20-50 ppm spectral range (peaks at 34.1 and 35.4 ppm) is attributed to the $-\text{CH}_2-$ groups; the aromatic carbon atoms from the ring appear instead in the 120-140 ppm window (peaks at 129.6, 131.3, 131.9 and 133.6 ppm). In addition, the ^1H MAS spectrum (Figure A.2.1 in the Appendices) is clearly dominated by an intense and narrow resonance

at ca. 4.61 ppm attributed to water molecules that are highly mobile in the crystal structure of **4**. It is also possible to discern in the ^1H MAS spectrum the signal arising from the $-\text{CH}_2-$ groups (at ca. 1.25 ppm) and a broad band containing both the aromatic protons and those associated with the protonated phosphonate moieties.

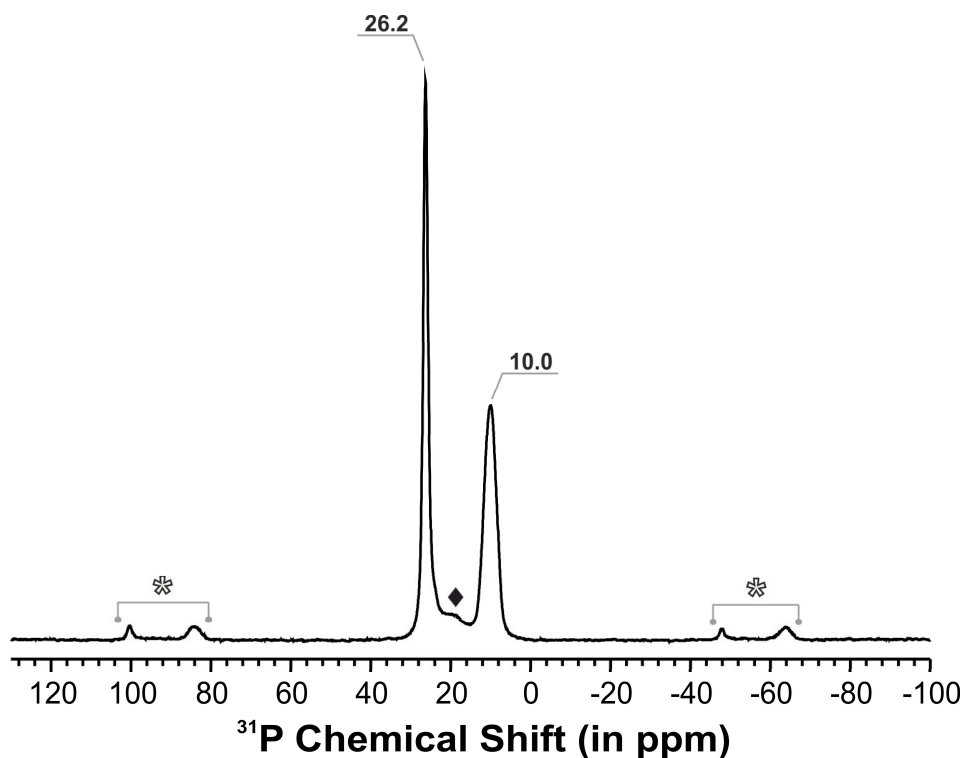


Figure 3.31 – ^{31}P HPDEC MAS spectrum of $[\text{La}_2(\text{H}_2\text{pmd})(\text{pmd})(\text{H}_2\text{O})_2]$ (**5**). Spinning sidebands are denoted using an asterisk. Peak deconvolution and integration throughout the entire spectral range (*i.e.*, including the spinning sidebands) gives a ratio of ca. 1.00 : 1.12 for the isotropic resonances at ca. 26.2 and 10.0 ppm. A small impurity present in **5** is identified by a diamond symbol (◆).

Compound **5** is considerably more crystalline and this fact is also noticeable in the corresponding solid-state NMR spectra. Indeed, the ^1H MAS spectrum (Figure A.2.3 in the Appendices) is much more resolved than that of compound **4**, being possible to see the resonances arising from the $-\text{CH}_2-$ groups (at ca. 1.05 ppm), the water molecules (at ca. 3.27 ppm), the aromatic ring (broad band peaking at ca. 6.42 ppm) and those of the considerably deshielded $-\text{POH}$ moieties (at ca. 11.1 ppm). As in **4**, peak deconvolution and integration including the spinning sidebands in the ^{31}P MAS spectrum (Figure 3.31) yields a ratio of ca. 1.00 : 1.12 for the resonances peaking at ca. 26.2 and 10.0 ppm, agreeing well with the expected two sites with equal occupancy present in the crystalline structure. The $^{13}\text{C}\{^1\text{H}\}$ CP MAS spectrum (Figure A.2.4 in the Appendices) is concordant with that of compound **4**, exhibiting two clear spectral regions found at ca. 25-50 (for the methylene groups) and 120-140 ppm (for the aromatic carbon atoms). It is important to emphasize

that in the former region one can clearly observe two resonances peaking at *ca.* 39.0 and 34.6 ppm exhibiting spin multiplets arising from $^1J_{C,P}$ coupling.⁴⁵

3.4. Results and Discussion

Several multidimensional MOFs were successfully isolated combining the bipodal 1,4-phenylenebis(methylene)diphosphonic acid (**H₄pmd**) organic linker with some lanthanide centers: i) isotypical 3D [Ln(Hpmd)(H₂O)] [where Ln³⁺ = Eu³⁺ (**1**), Gd³⁺ (**2**) and Tb³⁺ (**3**)] materials; and ii) five different Lanthanum-based MOFs, being one 1D ([La₂(H₂pmd)₃(H₂O)₁₂] (**4**) and four 3D ([La₂(H₂pmd)(pmd)(H₂O)₂] (**5**), [La(H₃pmd)(H₂pmd)(H₂O)] (**6**), [La₂(H₂pmd)₃(H₂O)₂] (**7**) and [La₂(H₂pmd)(pmd)(H₂O)₄] (**8**). The crystalline structures of all materials were carefully investigated and fully characterized by using several solid-state techniques (X-ray diffraction (single-crystal or powder), vibrational spectroscopy (FT-IR and FT-Raman), electron microscopy (SEM and EDS), solid-state NMR, thermogravimetric and elemental analysis).

Compounds **1-3** were prepared under conventional hydrothermal conditions, however, and opposite to expected, this methodology did not afford the desired materials as large single-crystals. Therefore, **1-3** were isolated as microcrystalline powders and their crystalline structures were unveiled by powder X-ray diffraction. These materials share similar architecture to the previously reported [Ce(Hpmd)(H₂O)] and [Pr(Hpmd)(H₂O)].¹³ Hydrothermal synthesis, using the hydrolyzed **H₄pmd**, showed to be a more efficient and reproducible approach than the hydro-ionothermal synthesis which involved the combination of lanthanide centers with the phosphoryl ester organic ligand tetraethyl-*p*-xylylenebisphosphonate in aqueous ionic medium. Nevertheless, conventional hydrothermal synthesis required the employment of high temperatures (180 °C) and large periods of times (72 h). These reaction conditions are not attractive for industry mainly if it is intended to scale-up the materials. Having this in mind, the preparation of **1-3** was carried out by using a simpler and faster synthetic approach (MWAS). Remarkably, compounds **1-3** can be isolated at 40 °C with just 5 seconds of reaction. It was also demonstrated that by varying the heating procedure and other synthetic parameters it is possible to control crystallite size: while the conventional hydrothermal approach produces typically micro-sized crystals, MWAS or ultrasounds-assisted synthesis (USAS), a recent synthetic approach in the MOFs field, can isolate **1-3** as nano-sized materials. USAS further permits the preparation of the nano-crystals in an isolated fashion.

Compounds **1-3** were investigated regarding their vibration modes. The preparation of the deuterated compound **1_D** allowed to elucidate the elusive vibrational modes of confined (and coordinated) water molecules. Indeed, the combined experimental/theoretical study identified most of the bands in the spectra including, for example, the rarely-reported twisting vibration of water at about 665 cm⁻¹.

Variable-temperature powder X-ray diffraction and thermogravimetry studies showed that the materials are thermally robust up to *ca.* 290 °C: the release of the

coordinated water molecule above this temperature is immediately followed by a collapse of the framework. Materials can, in this way, be employed in a robust fashion below this temperature without compromising structural integrity and crystallinity. For example, the catalytic activity of compound **1** was tested in the methanolysis of styrene oxide, under solvent-free conditions at 55 °C. It was discovered that the crystallite size of **1** plays a determinant role in this catalytic system: while microcrystalline **1** does not possess significant catalytic activity, the nano-sized counterpart **1n** exhibits relatively high catalytic activity and excellent selectivity to 2-methoxy-2-phenylethanol (100% yield within 48 h reaction). Reduction of the crystallite size promotes an increase of the total surface area, which expectedly enhances the number of accessible active sites of **1n**. Studies using the primary building blocks of **1** (*i.e.*, ligand and metal source) permitted to conclude that these active sites of **1n** should be of the Brønsted acid type and/or coordinatively unsaturated Lewis acid sites, which would inherently correspond to structural defect sites.

The photoluminescent properties of compounds **1** and **3** have been further investigated. Photoluminescent studies showed that the organic ligand is a suitable sensitizer of Tb³⁺ (absolute quantum yield as *ca.* 14%) via the energy transfer process called *antenna effect*, leading to the isolation of an intense green-emitting material. We have further shown that the coordinated water molecule to Eu³⁺ quenches significantly the photoluminescence of **1**: while at 300 and 11 K this compound exhibits lifetimes of 0.58±0.01 and 0.66±0.01 ms, respectively, these values are boosted for its deuterated form (**1D**) to 1.98±0.01 and 2.24±0.01 ms, respectively.

Compounds [La₂(H₂pmd)₃(H₂O)₁₂] (**4**) and [La₂(H₂pmd)(pmd)(H₂O)₂] (**5**), a 1D and a 3D structures, respectively, were successfully isolated as phase-pure compounds using both synthetic approaches MWAS and a *bench* procedure coined as one-pot method and their crystalline structures were solved by single-crystal X-ray diffraction. Crystals of [La(H₃pmd)(H₂pmd)(H₂O)] (**6**) and [La₂(H₂pmd)₃(H₂O)₂] (**7**) (obtained using microwave irradiation and from the one-pot approach, respectively) were manually harvested from physical mixtures, ultimately allowing their full structural elucidation using also single-crystal X-ray diffraction studies. Compound [La₂(H₂pmd)(pmd)(H₂O)₄] (**8**), also obtained in one-pot approach, could only be isolated as a microcrystalline powder and its crystal structure was determined instead by powder X-ray diffraction studies.

It was found that mild synthetic conditions are the optimal conditions for both synthetic methods so to promote the formation of the low dimensional compound **4**, whereas the use of a higher temperature favored the formation of the 3D network **5**. In that sense, we may look to **4** as the kinetic compound while **5** seems to be the thermodynamic one. Investigations on the modification of the particle size and shape promoted by variation of the reaction temperature and time, revealed that **4** crystallizes preferentially as aggregates of needle-like crystals while **5** crystallizes as plate-like particles. Furthermore, we concluded that there is no direct relationship between the variations of those parameters and the final average particle size.

Compound **6** could only be isolated as a residual product in MWAS and, despite all the efforts, it was not possible to successfully isolate it as a phase-pure material. Likewise, the appearance of **7** and **8** (synthesized using the one-pot approach) was promoted by the use of high values of temperature (typically above 80 °C). Compound **7** was favoured by the use of higher ligand-to-metal proportion and its formation at higher temperatures could be related with its 1:1.5 La:H₄pmd stoichiometry in the reactive gel.

MWAS, as mentioned above, and the one-pot methodologies have considerable advantages over typical solvo(hydro)thermal synthesis. In terms of reaction time, and as an attempt to solve the typical problem of using long reaction periods in the latter case, we were able to drastically decrease the typical 3 days initially used to prepare compound **5** to just a single minute of reaction under microwave irradiation or, alternatively, to 10 minutes using the one-pot methodology. Noteworthy, this drastic reduction in the reaction time has a direct and huge influence in the total energy consumed to prepare the MOF compound. For instance, considering the above reaction periods and power input/output values associated with each of the three synthetic methods, we were able to estimate the energy consumption, which ranged from *ca.* 340 000 kJ (3 days of hydrothermal conditions), to *ca.* 18.0 kJ (for 1 min in MWAS) and to *ca.* 8.6 kJ (for 10 min in one-pot). Therefore, these two alternative synthetic approaches to the typical hydrothermal reaction allow, on one hand, to prove the phase diagram of one given system for other architectures and, on the other hand, may also be considered for a possible implementation of the synthesis of MOFs at an industrial scale as they are cost efficient.

3.5. References

- (1) Allen, F. H.; Motherwell, W. D. S.; *Acta Cryst. B*, **2002**, *58*, 407-422.
- (2) Allen, F. H.; *Acta Cryst. B*, **2002**, *58*, 380-388.
- (3) Jones, S.; Liu, H.; Schmidtke, K.; O'Connor, C. C.; Zubieta, J.; *Inorg. Chem. Commun.*, **2010**, *13*, 298-301.
- (4) Konar, S.; Zon, J.; Prosvirin, A. V.; Dunbar, K. R.; Clearfield, A.; *Inorg. Chem.*, **2007**, *46*, 5229-5236.
- (5) Li, H.; Zhu, G.-S.; Guo, X.-D.; Sun, F.-X.; Ren, H.; Chen, Y.; Qiu, S.-L.; *Eur. J. Inorg. Chem.*, **2006**, 4123-4128.
- (6) Stock, N.; Bein, T.; *J. Solid State Chem.*, **2002**, *167*, 330-336.
- (7) Sun, Y.-Q.; Hu, J.; Zhang, H.-H.; Chen, Y.-P.; *J. Solid State Chem.*, **2012**, *186*, 189-194.
- (8) Tripuramallu, B. K.; Kishore, R.; Das, S. K.; *Polyhedron*, **2010**, *29*, 2985-2990.
- (9) Xu, X.; Wang, P.; Hao, R.; Gan, M.; Sun, F.; Zhu, G.-s.; *Solid State Sci.*, **2009**, *11*, 68-71.
- (10) Harvey, H. G.; Herve, A. C.; Hailes, H. C.; Attfield, M. P.; *Chem. Mater.*, **2004**, *16*, 3756-3766.
- (11) Irran, E.; Bein, T.; Stock, N.; *J. Solid State Chem.*, **2003**, *173*, 293-298.
- (12) Stock, N.; Guillou, N.; Bein, T.; Férey, G.; *Solid State Sci.*, **2003**, *5*, 629-634.
- (13) Shi, F. N.; Trindade, T.; Rocha, J.; Paz, F. A. A.; *Cryst. Growth Des.*, **2008**, *8*, 3917-3920.
- (14) Vilela, S. M. F.; Mendes, R. F.; Silva, P.; Fernandes, J. A.; Tome, J. P. C.; Paz, F. A. A.; *Cryst. Growth Des.*, **2013**, *13*, 543-560.
- (15) Silva, P.; Valente, A. A.; Rocha, J.; Paz, F. A. A.; *Cryst. Growth Des.*, **2010**, *10*, 2025-2028.
- (16) Granadeiro, C. M.; Ferreira, R. A. S.; Soares-Santos, P. C. R.; Carlos, L. D.; Trindade, T.; Nogueira, H. I. S.; *J. Mater. Chem.*, **2010**, *20*, 3313-3318.
- (17) Nemamcha, A.; Rehspringer, J. L.; Khatmi, D.; *J. Phys. Chem. B*, **2006**, *110*, 383-387.
- (18) Xia, H. S.; Wang, Q.; *Chem. Mater.*, **2002**, *14*, 2158-2165.
- (19) Mousavi-Kamazani, M.; Salavati-Niasari, M.; Ramezani, M.; *J. Cluster Sci.*, **2013**, *24*, 927-934.
- (20) Jung, D. W.; Yang, D. A.; Kim, J.; Ahn, W. S.; *Dalton Trans.*, **2010**, *39*, 2883-2887.
- (21) Khan, N. A.; Jhung, S. H.; *Bull. Korean Chem. Soc.*, **2009**, *30*, 2921-2926.
- (22) Son, W. J.; Kim, J.; Ahn, W. S.; *Chem. Commun.*, **2008**, 6336-6338.
- (23) Tahmasian, A.; Morsali, A.; *Inorg. Chim. Acta*, **2012**, *387*, 327-331.

- (24) Shaabani, B.; Mirtamizdoust, B.; Viterbo, D.; Croce, G.; Hammud, H.; Hojati-Lalemi, P.; Khandar, A.; *Z. Anorg. Allg. Chem.*, **2011**, *637*, 713-719.
- (25) Sadeghzadeh, H.; Morsali, A.; *J. Inorg. Organom. Polym. Mater.*, **2010**, *20*, 733-738.
- (26) Haque, E.; Khan, N. A.; Park, J. H.; Jhung, S. H.; *Chem.-Eur. J.*, **2010**, *16*, 1046-1052.
- (27) Flugel, E. A.; Ranft, A.; Haase, F.; Lotsch, B. V.; *J. Mater. Chem.*, **2012**, *22*, 10119-10133.
- (28) Klink, S. I.; Grave, L.; Reinhoudt, D. N.; van Veggel, F. C. J. M.; Werts, M. H. V.; Geurts, F. A. J.; Hofstraat, J. W.; *J. Phys. Chem. A*, **2000**, *104*, 5457-5468.
- (29) Werts, M. H. V.; Jukes, R. T. F.; Verhoeven, J. W.; *Phys. Chem. Chem. Phys.*, **2002**, *4*, 1542-1548.
- (30) Carlos, L. D.; Messaddeq, Y.; Brito, H. F.; Ferreira, R. A. S.; Bermudez, V. D.; Ribeiro, S. J. L.; *Adv. Mater. (Weinheim, Ger.)*, **2000**, *12*, 594-598.
- (31) Malta, O. L.; Brito, H. F.; Menezes, J. F. S.; Silva, F.; Alves, S.; Farias, F. S.; deAndrade, A. V. M.; *J. Lumin.*, **1997**, *75*, 255-268.
- (32) Malta, O. L.; dosSantos, M. A. C.; Thompson, L. C.; Ito, N. K.; *J. Lumin.*, **1996**, *69*, 77-84.
- (33) Hazenkamp, M. F.; Blasse, G.; *Chem. Mater.*, **1990**, *2*, 105-110.
- (34) Supkowski, R. M.; Horrocks, W. D.; *Inorg. Chim. Acta*, **2002**, *340*, 44-48.
- (35) Bunzli, J. C. G.; Chauvin, A. S.; Kim, H. K.; Deiters, E.; Eliseeva, S. V.; *Coord. Chem. Rev.*, **2010**, *254*, 2623-2633.
- (36) Bunzli, J. C. G.; *Chem. Rev.*, **2010**, *110*, 2729-2755.
- (37) Barbosa, A. J.; Maia, L. J. Q.; Montanari, B.; Goncalves, R. R.; Messaddeq, Y.; Ferreira, R. A. S.; Carlos, L. D.; Ribeiro, S. J. L.; *Langmuir*, **2010**, *26*, 14170-14176.
- (38) Carlos, L. D.; Ferreira, R. A. S.; Bermudez, V. D.; Ribeiro, S. J. L.; *Adv. Mater. (Weinheim, Ger.)*, **2009**, *21*, 509-534.
- (39) Dhakshinamoorthy, A.; Alvaro, M.; Garcia, H.; *Chem.-Eur. J.*, **2010**, *16*, 8530-8536.
- (40) Kumar, G.; Singh, A. P.; Gupta, R.; *Eur. J. Inorg. Chem.*, **2010**, 5103-5112.
- (41) Silva, P.; Vieira, F.; Gomes, A. C.; Ananias, D.; Fernandes, J. A.; Bruno, S. M.; Soares, R.; Valente, A. A.; Rocha, J.; Paz, F. A. A.; *J. Am. Chem. Soc.*, **2011**, *133*, 15120-15138.
- (42) Cho, W.; Lee, H. J.; Oh, M.; *J. Am. Chem. Soc.*, **2008**, *130*, 16943-16946.
- (43) Tachikawa, T.; Choi, J. R.; Fujitsuka, M.; Majima, T.; *J. Phys. Chem. C*, **2008**, *112*, 14090-14101.
- (44) Socrates, G. *Infrared and Raman Characteristic Group Frequencies: Tables and Charts*; 2nd ed.; John Wiley & Sons Ltd: Baffins Lane, Chichester, 1994.
- (45) Ben Akacha, A.; Barkallah, S.; Zantour, H.; *Magn. Reson. Chem.*, **1999**, *37*, 916-920.

Chapter 4

**From 1D to 3D Functional MOFs based on
(Benzene-1,3,5-triyltris-(methylene))triphosphonic Acid**

4.1. Initial Considerations

This Chapter describes three families of MOFs with different dimensionalities (*i.e.*, 1D, 2D and 3D) prepared from the self-assembly between a tripodal phosphonate-based organic ligand and lanthanide metallic centers. The preparation of these materials was achieved by using both conventional hydrothermal synthesis and microwave-assisted synthesis (MWAS).

(Benzene-1,3,5-triyltris(methylene))triphosphonic acid (**H₆bmt**, Scheme 2.5) also has some degree of more flexibility due to the presence of three pendant $-\text{CH}_2-$ moieties. Structural rigidity arises from the presence of the central benzene ring. Compared with the previously described **H₄pmd** organic ligand, **H₆bmt** has one more phosphonic acid group which provides it more coordinative sites and the possibility to isolate different multidimensional structures. The crystal structure of **H₆bmt** was reported for the first time by Jaffrès and collaborators.¹ Since then this organic molecule have been scarcely employed in either the synthesis of coordination-based complexes or in traditional crystal engineering approaches: i) in 2010 the group of Clearfield reported the preparation of a dimeric complex of Cu^{2+} , formulated as $[\text{Cu}_2(\text{H}_4\text{bmt})_2(4,4'\text{-bpy})(\text{H}_2\text{O})_2]$, using **H₆bmt** and 4,4'-bipyridine (4,4'-bpy) under solvothermal conditions;² ii) one year later Yang *et al.* prepared the 3D open-framework $[\text{Cu}_3(\text{bmt})(\text{H}_2\text{O})_{3,6}]\cdot\text{H}_2\text{O}$ from a reactive mixture composed of **H₆bmt** and $\text{CuCl}_2\cdot 2\text{H}_2\text{O}$ in water;³ iii) more recently, Tang and collaborators reported eight new transition metal trisphosphonate complexes, one 2D layered structure, formulated as $[\text{Cu}_2(\text{H}_3\text{bmt})_2(\text{H}_2\text{O})_2][\text{H}_2\text{dpe}][\text{H}_2\text{O}]_4$, produced by using **H₆bmt** and seven from the self-assembly of its analogue (2,4,6-trimethylbenzene-1,3,5-triyltris(methylene))triphosphonic acid organic molecule.⁴ To the present data **H₆bmt** was used with lanthanide cations only by the MOF research group working at the University of Aveiro.⁵⁻⁶

It is described the preparation of three distinct families of multidimensional MOFs produced from the self-assembly of the tripodal **H₆bmt** with non-radioactive lanthanide cations (all with the exception of Lu^{3+}):

- i) 1D $[\text{Ln}(\text{H}_4\text{bmt})(\text{H}_5\text{bmt})(\text{H}_2\text{O})_2]\cdot 3\text{H}_2\text{O}$ materials [where $\text{Ln}^{3+} = \text{La}^{3+}$ (**9**), $(\text{La}_{0.97}\text{Eu}_{0.03})^{3+}$ (**10**) and $(\text{La}_{0.97}\text{Tb}_{0.03})^{3+}$ (**11**)] isolated by hydrothermal MWAS;⁵
- ii) 2D layered $[\text{Ln}_2(\text{H}_3\text{bmt})_2]\cdot\text{H}_2\text{O}$ materials [where $\text{Ln}^{3+} = \text{Eu}^{3+}$ (**12**), Gd^{3+} (**13**), Tb^{3+} (**14**), Dy^{3+} (**15**), Ho^{3+} (**16**), Er^{3+} (**17**), Tm^{3+} (**18**) and Yb^{3+} (**19**)] prepared under conventional hydrothermal conditions;
- iii) 3D $[\text{Ln}_2(\text{H}_3\text{bmt})_2(\text{H}_2\text{O})_2]\cdot\text{H}_2\text{O}$ materials [where $\text{Ln}^{3+} = \text{La}^{3+}$ (**20**), Ce^{3+} (**21**), Pr^{3+} (**22**), Nd^{3+} (**23**), $(\text{La}_{0.95}\text{Eu}_{0.05})^{3+}$ (**24**) and $(\text{La}_{0.95}\text{Tb}_{0.05})^{3+}$ (**25**)] isolated under hydrothermal conditions and also by employing the MWAS approach.⁶

The crystal structures of the isotypical families of the 1D and 3D compounds were unveiled by single-crystal X-ray, while the 2D materials, isolated as microcrystalline powders, were investigated using powder X-ray diffraction studies. All

materials were fully characterized by standard solid-state techniques (FT-IR, electron microscopy (SEM and EDS), solid-state NMR, thermogravimetric and elemental analysis).

The catalytic behavior of the **9** and **20** was evaluated in the ring-opening reaction of styrene oxide with methanol. Both compounds showed excellent regioselectivity, recyclability and structural stability in consecutive catalytic runs. Nevertheless, the catalytic activity of **9** (conversion of 100% of styrene oxide in 30 min) is notably outstanding compared with that of compound **20** (conversion of 80% of styrene oxide in 24 h).

The photoluminescent properties of the 1D materials **10** and **11**, and of the 3D materials **24** and **25** is described in detail. The Tb³⁺-based compounds **11** and **25** showed to be highly efficient light converting materials exhibiting absolute emission quantum yields of 44 and 46%, respectively. Removing under vacuum all the water molecules (coordinated and of crystallization) from the crystalline structure of **24** promotes a remarkable increase of the quantum efficiency from *ca.* 15 to 54%.

4.2. Microwave-Assisted Synthesis of 1D Lanthanide-Organic Frameworks

4.2.1. Microwave-Assisted Hydrothermal Synthesis

Two different lanthanum-based materials, formulated as [La(H₄bmt)(H₅bmt)(H₂O)₂] \cdot 3H₂O (**9**) and [La₂(H₃bmt)₂(H₂O)₂] \cdot H₂O (**20**), have been isolated while reacting the tripodal organic ligand **H₆bmt** with lanthanum chloride under microwave irradiation (see sub-section 8.11.1.1 in the Experimental Section for further details). Compound **20** was firstly prepared under conventional hydrothermal conditions and further details are described in Section 4.4.

Aiming at the preparation of new phase-pure materials (in this case **9** and **20**), the reaction time and temperature in MWAS conditions were systematically varied (Figure 4.1). The 1D compound **9** is readily isolated at low temperatures, mainly at 40 and 60 °C. Increasing both the reaction time and temperature, compound **20** starts to prevail as the main product. The latter material is, however, obtained as phase-pure only at 150 °C. Mixtures of both compounds are isolated at 90, 100, and 120 °C, with **20** dominating at higher reaction times (15 and 20 minutes).

Crystal morphology of **9** and **20** was investigated using scanning electron microscopy (SEM): while **9** is composed of aggregates of particles with poorly defined morphology, **20** is instead composed of spherical aggregates with sizes in the range of tens of micrometers (Figure 4.2). The reaction temperature seems to have an important role in the crystal morphology and size of compound **9**: at 40 °C this compound is mostly composed of aggregates of small and irregular particles; increasing the

temperature for 60 and 90 °C crystal growth is boosted, affording better-defined particles. Crystals of **20** begin to appear at 100 °C (for periods of time of 5 minutes), becoming predominant at 120 °C. In the 100-150 °C temperature range changes in the crystal size and morphology of **20** are not easily discerned.

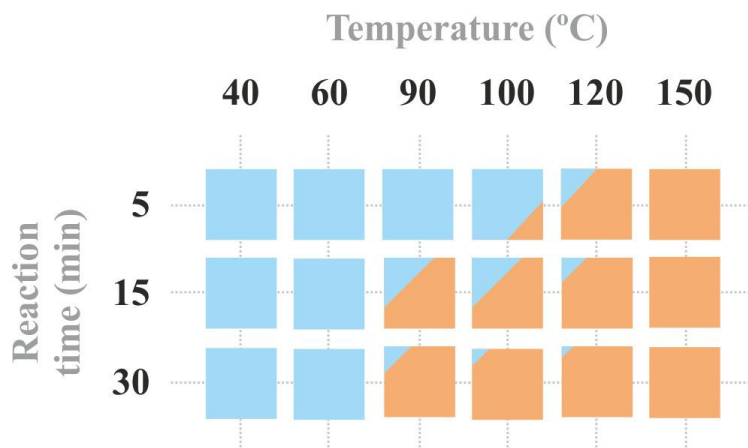


Figure 4.1 - Microwave-assisted hydrothermal synthesis optimization of the reaction temperature and time to obtain $[\text{La}(\text{H}_4\text{bmt})(\text{H}_5\text{bmt})(\text{H}_2\text{O})_2] \cdot 3\text{H}_2\text{O}$ (**9**) (light blue) and $[\text{La}_2(\text{H}_3\text{bmt})_2(\text{H}_2\text{O})_2] \cdot \text{H}_2\text{O}$ (**20**) (light orange) materials.

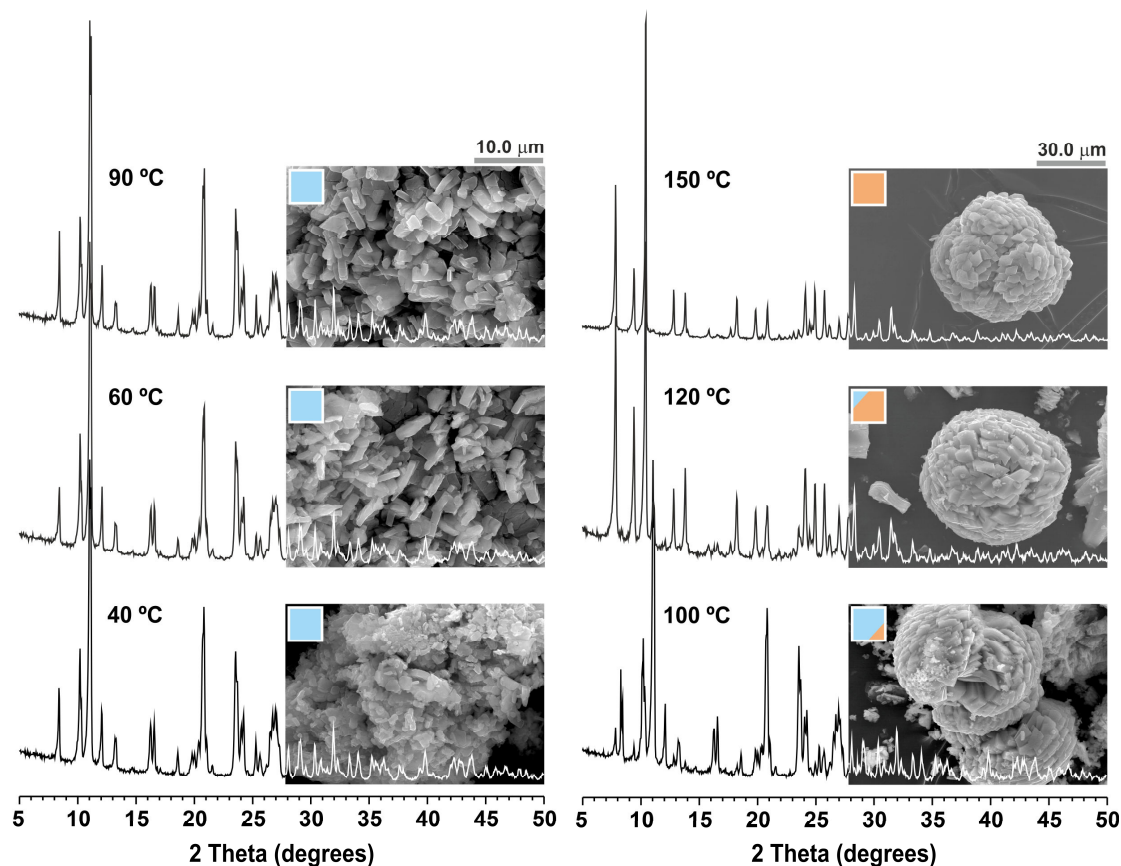


Figure 4.2 - PXRD patterns and SEM images of $[\text{La}(\text{H}_4\text{bmt})(\text{H}_5\text{bmt})(\text{H}_2\text{O})_2] \cdot 3\text{H}_2\text{O}$ (**9**) (light blue) and $[\text{La}_2(\text{H}_3\text{bmt})_2(\text{H}_2\text{O})_2] \cdot \text{H}_2\text{O}$ (**20**) (light orange) prepared under microwave irradiation at different temperatures for 5 minutes of reaction time.

The preparation of optically-active materials with stoichiometric amounts of distinct lanthanides was performed using the optimal conditions discovered for **9** while including 3% of Eu^{3+} or Tb^{3+} in the reactive mixtures: $[(\text{La}_{0.97}\text{Eu}_{0.03})(\text{H}_4\text{bmt})(\text{H}_5\text{bmt})(\text{H}_2\text{O})_2]\cdot 3\text{H}_2\text{O}$ (**10**) and $[(\text{La}_{0.97}\text{Tb}_{0.03})(\text{H}_4\text{bmt})(\text{H}_5\text{bmt})(\text{H}_2\text{O})_2]\cdot 3\text{H}_2\text{O}$ (**11**) were obtained at 60 °C using 5 minutes of irradiation. Phase purity of all materials and rare-earth distribution were unequivocally confirmed using several solid-state techniques, including powder X-ray diffraction (see Figure B.1.1 in the Appendices for further details).

4.2.2. Crystal Structure of $[\text{La}(\text{H}_4\text{bmt})(\text{H}_5\text{bmt})(\text{H}_2\text{O})_2]\cdot 3\text{H}_2\text{O}$

The crystal structure of **9** was unequivocally determined from single-crystal X-ray diffraction studies at 100 K in the monoclinic centrosymmetric space group $P2_1/m$, with the asymmetric unit comprising a whole residue of H_6bmt , half of a La^{3+} metal centre, and five halves of crystallographically independent water molecules. The structure is made up by a single La^{3+} ion located on the crystallographic mirror plane, being coordinated to four symmetry-related organic ligands and two water molecules (which are also located on the mirror plane). The overall coordination environment, $\{\text{LaO}_8\}$, resembles a slightly distorted square antiprism (Figure 4.3). The La–O distances are 2.665(5) and 2.713(5) Å for the coordinated water molecules and range between 2.406(3) to 2.488(3) Å for the connections to the four symmetry-equivalent organic ligands composing the coordination sphere. The quadrangular and triangular faces of the square antiprism show angles in the 77.80(15)-101.62(13)° and 42.04(7)-74.96(10)° ranges, respectively. The phosphonic acid residues are all located on the same side of the medium plane defined by the carbon atoms of the organic ligand [largest deviation of 0.064(4) Å for C5].

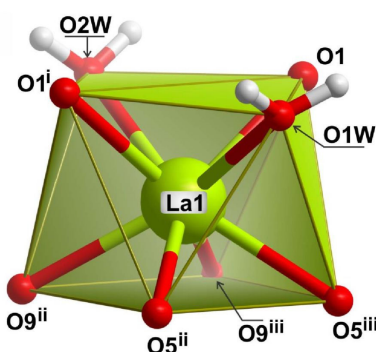


Figure 4.3 - Distorted $\{\text{LaO}_8\}$ square antiprismatic coordination environment of the crystallographically independent La^{3+} cation present in $[\text{La}(\text{H}_4\text{bmt})(\text{H}_5\text{bmt})(\text{H}_2\text{O})_2]$ (**9**). Symmetry codes: (i) $x, 1.5-y, z$; (ii) $-x, 1-y, -z$; (iii) $-x, \frac{1}{2}+y, -z$. For selected bond lengths and angles see Table B.1.1 in the Appendices.

The connectivity of ligands and metal centres results in a neutral one-dimensional $\infty^1[\text{La}(\text{H}_4\text{bmt})(\text{H}_5\text{bmt})(\text{H}_2\text{O})_2]$ coordination polymer running parallel to the [010] direction of the unit cell (Figure 4.4b). Each pair of consecutive metal centres along the polymer is bridged by two organic ligands related by inversion symmetry. The forces that contribute for the packing of individual polymers are strong π - π interactions [distance between centromers of 3.535(3) Å] and a complex network of hydrogen bonds of various strengths (Table 4.1) involving coordinated and uncoordinated water molecules and various PO-H groups from the organic linker (Figure 4.4a).

Table 4.1 Supramolecular contacts present in compound $[\text{La}(\text{H}_4\text{bmt})(\text{H}_5\text{bmt})(\text{H}_2\text{O})_2]\cdot 3\text{H}_2\text{O}$ (**9**). Distances are given in Å and interaction angles in degrees.^a

D-H...A	d(D...A)	<(DHA)
O2-H2Z...O3 ⁱⁱ	2.554(4)	166
O3-H3Z...O7 ⁱⁱ	2.540(4)	156
O4-H4Z...O2 ⁱⁱ	2.703(4)	157
O6-H6Z...O6 ^{iv}	2.580(7)	156
O8-H8Z...O3W ^v	2.609(5)	177
O1W-H1X...O8 ^{vi}	3.038(5)	148
O2W-H2X...O6 ^{vii}	2.838(5)	127
O3W-H3X...O2W ^{vii}	2.752(7)	174
O3W-H3Y...O4W	2.551(8)	152
O4W-H4X...O5W ^{iv}	2.701(11)	157
O4W-H4Y...O5	2.957(8)	171
O5W-H5X...O6 ^{viii}	3.155(11)	143
O5W-H5Y...O9	3.079(11)	161

^a Symmetry transformations used to generate equivalent atoms:

(ii) $-x, 1-y, -z$; (iv) $x, \frac{1}{2}-y, z$; (v) $x, y, -1+z$; (vi) $1-x, 1-y, -z$;

(vii) $-x, 1-y, 1-z$; (viii) $1+x, y, z$.

In order to balance the metal charge the ligand loses an average number of 1.5 protons. While the phosphonic residue centred in P1 is neutral, that centred in P3 is monodeprotonated. Two symmetry-related and adjacent O6 atoms (bonded to P2) share a single proton, giving an average half of a proton for each donor atom.

All water molecules show half occupation, given their location on the mirror plane (O1W to O3W) or because of symmetry disorder due to the proximity to it (O4W and O5W). These molecules are involved in two types of hydrogen bond assemblies,

namely a one-dimensional array (Figure 4.5a) and a discrete chain (Figure 4.5b). The polymeric array runs across the mirror plane, parallel to the [100] direction of the unit cell. It comprises two rings (O2W···O6···O6 and O1W···O8···O3W···O8) and a discrete chain (O5···O4W···O5W···O9), with graph sets motifs $R_3^2(6)$, $R_4^3(8)$, $D_3^3(6)$, respectively.⁷ Alternatively, a polymeric chain with the graph set motif $C_7^5(12)$ can be observed by choosing a suitable path in the array (Figure 4.5a). In the independent discrete chain atoms O2, O3, O4 and O7 from adjacent phosphonic moieties are engaged in strong hydrogen bonds located inside the boundaries of the one-dimensional $\infty^1[\text{La}(\text{H}_4\text{bmt})(\text{H}_5\text{bmt})(\text{H}_2\text{O})_2]$ polymer corresponding to a centrosymmetric $R_2^2(8)$ ring.

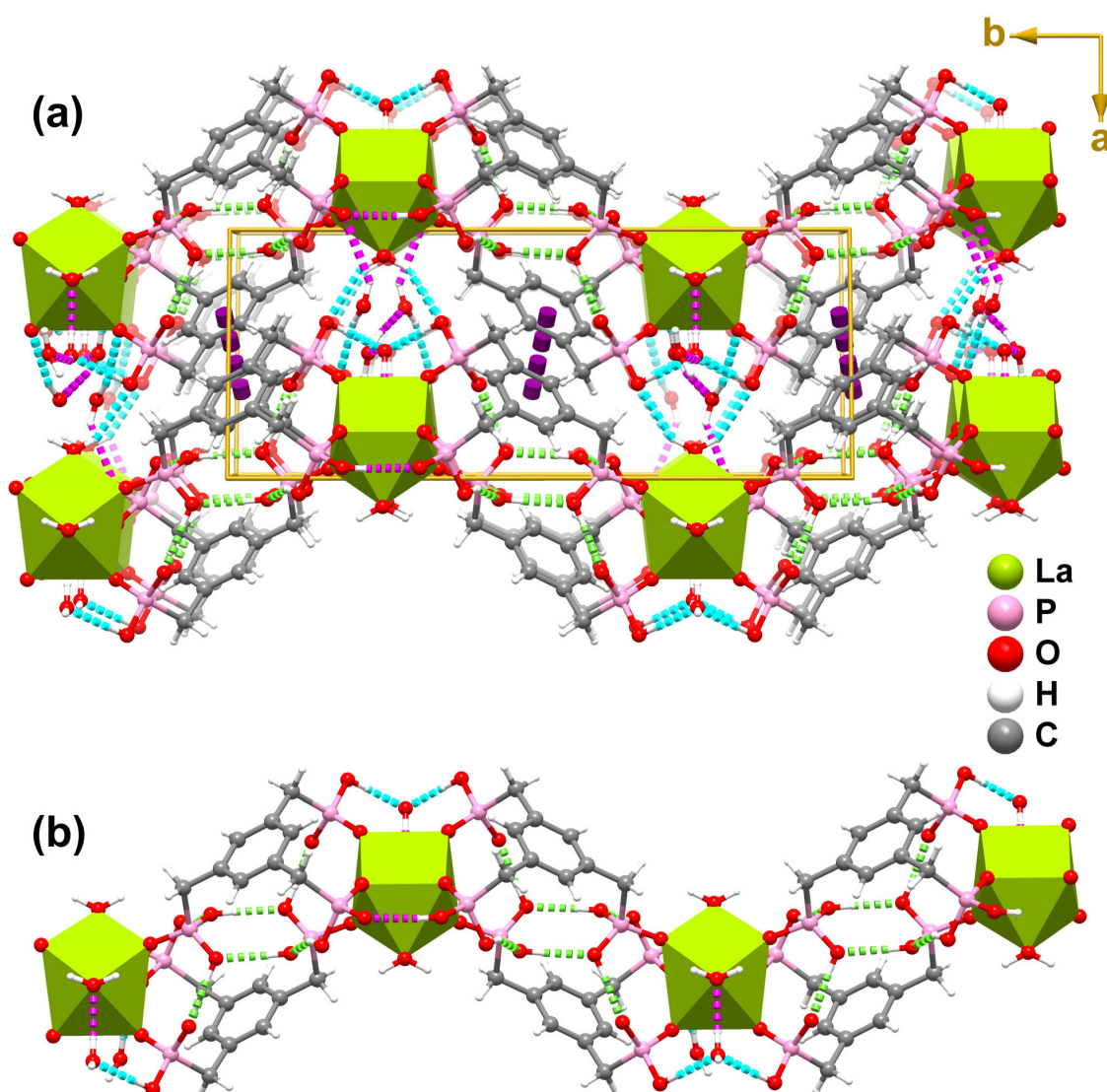


Figure 4.4 - Mixed ball-and-stick and polyhedral schematic representation of the (a) crystal packing of $[\text{La}(\text{H}_4\text{bmt})(\text{H}_5\text{bmt})(\text{H}_2\text{O})_2] \cdot 3\text{H}_2\text{O}$ (9), and of the neutral (b) one-dimensional $\infty^1[\text{La}(\text{H}_4\text{bmt})(\text{H}_5\text{bmt})(\text{H}_2\text{O})_2]$ polymer. The two representations are viewed in perspective along the [001] direction of the unit cell. The coordination environment around the metal centre is shown as green polyhedra. Hydrogen bonds are depicted as dashed lines (colour codes is explained in Figure 5.5). π - π interactions are represented as dashed violet lines.

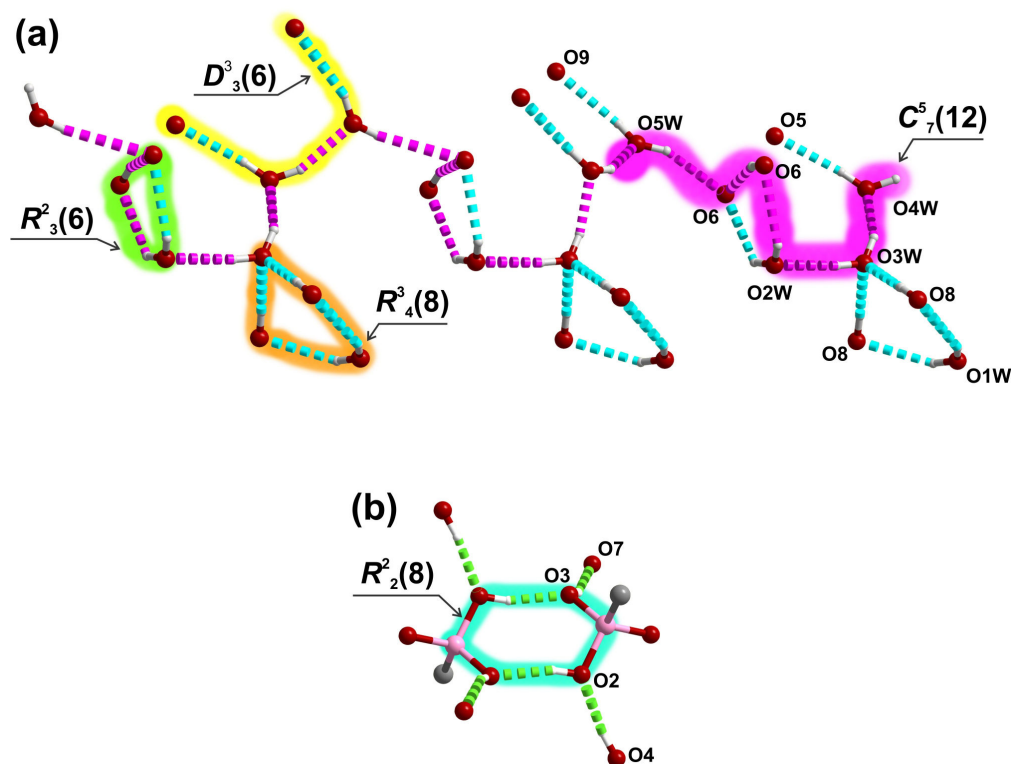


Figure 4.5 - Hydrogen bonding sub-networks in the crystal structure of compound $[\text{La}(\text{H}_4\text{bmt})(\text{H}_5\text{bmt})(\text{H}_2\text{O})_2] \cdot 3\text{H}_2\text{O}$ (**9**). **(a)** Complex 1D network running parallel to the $[100]$ axis of the unit cell. A polymeric chain with graph set motif $\text{C}^5_7(12)$ runs along the network (dashed pink lines, with the composing unit highlighted also in pink; the remaining bonds are represented by dashed blue lines). Alternatively, the same network can be fragmented into the graph set motifs $\text{D}^3_3(6)$ (highlighted in yellow), $\text{R}^3_4(8)$ (highlighted in orange) and $\text{R}^2_3(6)$ (highlighted in green). Because the water molecules O4W and O5W are distributed in pairs of close, and geometrically equivalent, sites only one molecule of each pair is represented in the scheme for the sake of clarity. *Please note:* different selection of molecules changes dramatically the geometry of the $\text{D}^3_3(6)$ chain. Additionally, the position of the proton shared by two geometrically equivalent O6 atoms also rules the geometry of the $\text{R}^2_3(6)$ ring. **(b)** Discrete centrosymmetric $\text{R}^2_2(8)$ ring with four lateral O–H \cdots O hydrogen bonds. Symmetry codes used to generate equivalent atoms have been omitted for the sake of clarity.

4.2.3. Thermogravimetry and Thermodiffractometry

The thermal stability of bulk $[\text{Ln}(\text{H}_4\text{bmt})(\text{H}_5\text{bmt})(\text{H}_2\text{O})_2] \cdot 3\text{H}_2\text{O}$ materials [where $\text{Ln}^{3+} = \text{La}^{3+}$ (**9**), $(\text{La}_{0.97}\text{Eu}_{0.03})^{3+}$ (**10**) and $(\text{La}_{0.97}\text{Tb}_{0.03})^{3+}$ (**11**)] was investigated between ambient temperature and *ca.* 800 °C. Thermograms show a relatively similar thermal stability for all compounds (Figure B.1.2 in the Appendices). In order to evaluate the effect of increasing temperature in the crystal structure VTPXRD studies have been performed for **9** in the 30-500 °C range (Figure 4.6 – *top right*). In the following paragraphs we shall focus the discussion on the thermal behavior of compound **9**, being assumed that this behavior is similar for the remaining members of the isotypical series.

Between ambient temperature and *ca.* 184 °C, two consecutive weight losses are markedly visible (Figure 4.6 – *bottom left*): three water molecules are released in the first step (*ca.* 5.9% weight loss; calculated *ca.* 5.7%), while the second step agrees well with the liberation of two of such moieties (*ca.* 3.5% weight loss; calculated *ca.* 3.8%). These results are in perfect agreement with the crystallographic studies which determined for the empirical formula of **9** the presence of three disordered water molecules housed within the small crystal channels, and two additional ones coordinated to the rare-earth cations. Moreover, the two markedly distinct environments for these moieties fully justify the temperature ranges in which they are released.

Thermodiffraction studies show that the structure of compound **9** remains unaltered up to *ca.* 60 °C (Figure 4.6 – *top right*). Between this temperature and *ca.* 120 °C a new crystalline phase is obtained, most likely corresponding to the phase without the disordered lattice water molecules of crystallization (see above). The liberation of the coordinated water molecules induces a new sudden structural modification which prevails in the *ca.* 120-200 °C temperature range.

A third weight loss, corresponding to a total of *ca.* 5.1%, occurs between *ca.* 230 and 350 °C. According to our previous studies on lanthanide polyphosphonates,⁸ at this temperature range the organic ligand may begin to deteriorate leading to the formation of pyrophosphonates with the consequent release of water molecules (in this case the observed weight loss is equivalent to almost three water molecules). To prove this hypothesis, compound **9** was calcined at 350 °C and the resulting residue was analyzed by FT-IR so to identify the typical $\nu(\text{P-O-P})$ stretching vibration of pyrophosphonates, which normally appears in the 930-915 cm^{-1} range.⁹ The results were inconclusive due to the existence of other vibrational modes in this spectral region overlapping of the $\nu(\text{P-O-P})$ vibration. We note, however, that thermodiffraction reveal two more phase transformations in the *ca.* 230-350 °C temperature range, both leading to crystalline phases.

After the formation of an amorphous residue at *ca.* 450 °C, there is a markedly visible weight increase of *ca.* 1.5 % at around *ca.* 500 °C, which can be attributed to an oxidation of the organic component, in particular the oxidation of the phosphonate P-C bond to a P-O moiety. This assumption is further supported by a direct comparison between the thermograms of compound **9** performed under air and nitrogen atmospheres (Figure B.1.3 in the Appendices): when using N_2 there is no weight increase at *ca.* 500 °C. It is important to emphasize that up to this temperature (*ca.* 500 °C) the thermal behaviour in air and nitrogen of compound **9** is almost identical, ultimately indicating that the thermal stability of the material, alongside with its phase transformations due to the release of water molecules and most likely the formation of the pyrophosphonates, is independent of the atmosphere. The presence (or absence) of an oxidative atmosphere only starts to be important when the organic ligand begins to decompose: indeed, in air the decomposition is much faster than in nitrogen as depicted in Figure B.1.3 (in the Appendices).

After the decomposition of the organic ligand, which occurs above *ca.* 700 °C, powder X-ray diffraction studies (PDF4+ 2012 release ICDD database) showed that the residue was composed of lanthanum catenatriphosphate (LaP_3O_9 , ICDD 00-033-0717), which further evolved (at *ca.* 900 °C) to a mixture composed of LaP_3O_9 and monazite (LaPO_4 , ICDD 01-071-6745).

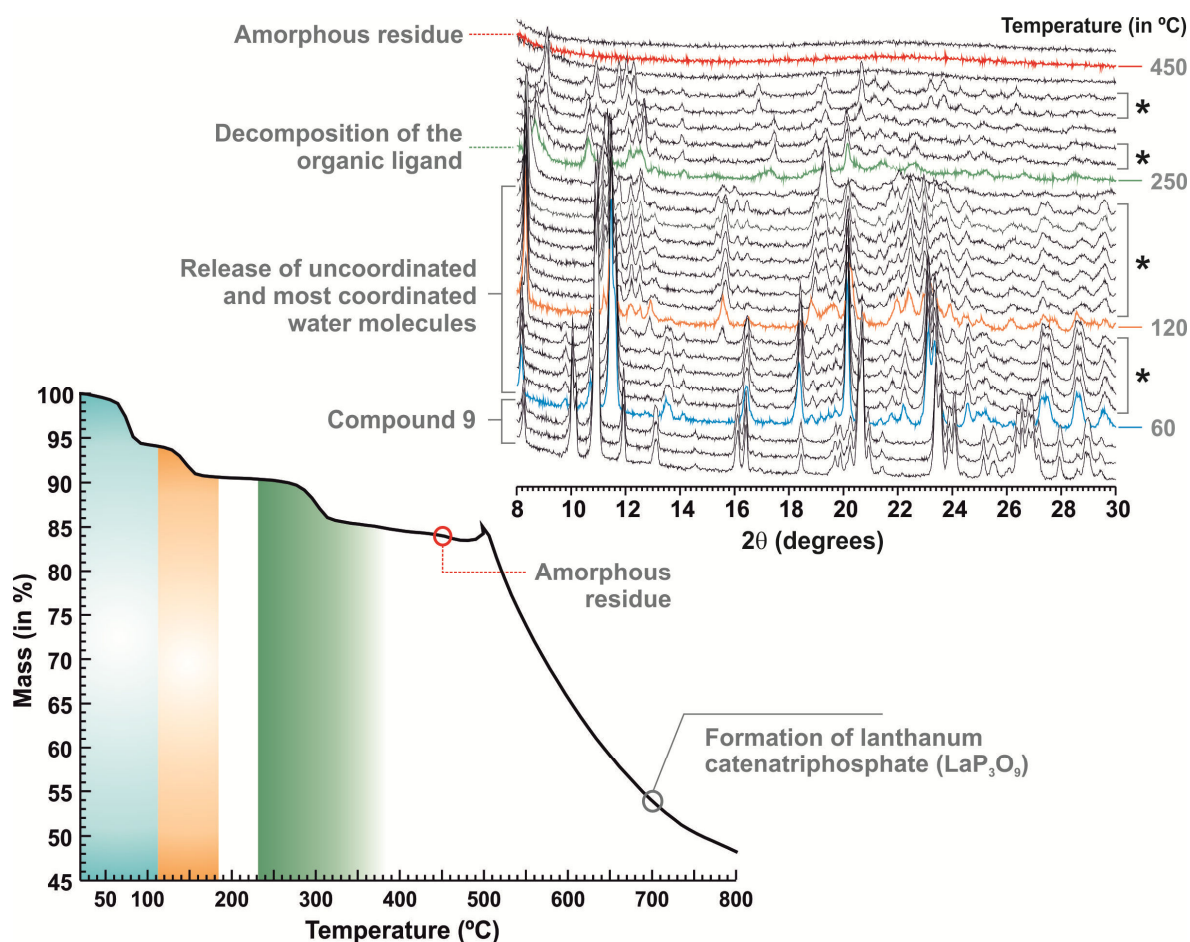


Figure 4.6 - Thermogram and VTPXRD studies of $[\text{La}(\text{H}_4\text{bmt})(\text{H}_5\text{bmt})(\text{H}_2\text{O})_2]\cdot 3\text{H}_2\text{O}$ (**9**). Phase transformations promoted by temperature increase are depicted using an asterisk (*). All studies have been performed in air.

4.2.4. FT-IR Spectroscopic Studies

The FT-IR spectra (Figure 4.7) of the isotypical $[\text{Ln}(\text{H}_4\text{bmt})(\text{H}_5\text{bmt})(\text{H}_2\text{O})_2]\cdot 3\text{H}_2\text{O}$ materials [where $\text{Ln}^{3+} = \text{La}^{3+}$ (**9**), $(\text{La}_{0.97}\text{Eu}_{0.03})^{3+}$ (**10**) and $(\text{La}_{0.97}\text{Tb}_{0.03})^{3+}$ (**11**)] exhibit a number of bands which are diagnostic of the structural features of the materials. This subsection discusses only the spectral features of compound **9**, being the conclusions also valid for **10** and **11**.

The material contains in its crystal structure several types of water molecules with very distinct crystallographic environment. This structural feature is markedly

visible in the FT-IR spectrum, particularly in the 3750-2100 cm^{-1} spectral range which is dominated by the O–H vibrational modes of water molecules. The two sharp bands of medium intensity located at *ca.* 3629 and 3546 cm^{-1} correspond to the $\nu(\text{O-H})$ stretching vibrational modes of coordinated water molecules. The same features are observed for the lattice water molecules of crystallization with the occurrence of two weak broad bands centered at around 3338 and 3225 cm^{-1} . These assignments were unequivocally confirmed from analyses on the dehydrated material: after thermal treatment at *ca.* 190 $^{\circ}\text{C}$ (data not shown) the broad bands associated with the lattice water molecules of crystallization completely disappear, and those of the coordinated moieties (sharp bands) are almost extinguished (*please note:* according to the thermogravimetric studies at this temperature the release of all water molecules may not be complete; this data is in good agreement with the performed thermogravimetric studies).

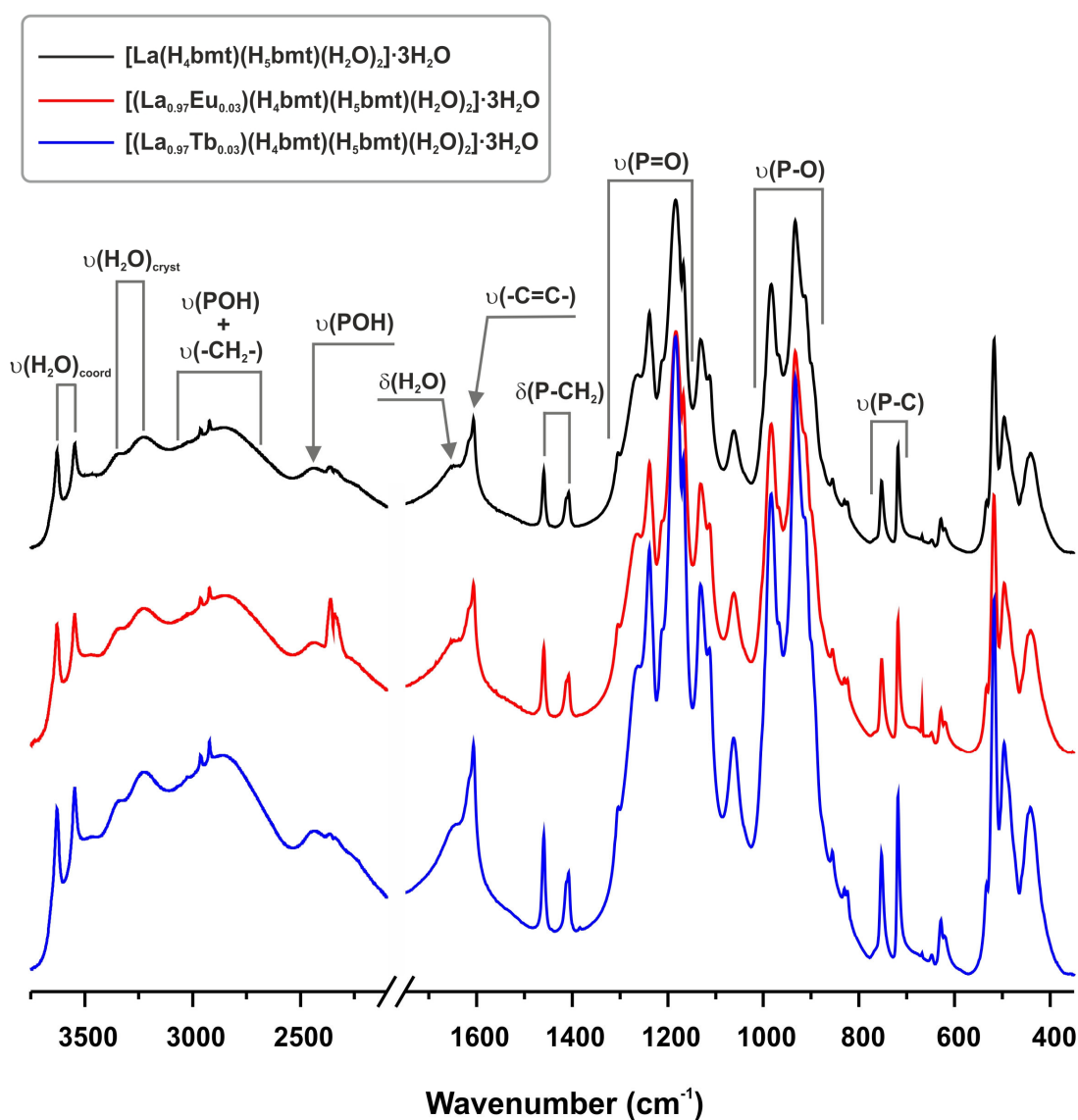


Figure 4.7 - FT-IR spectra of the $[\text{Ln}(\text{H}_4\text{bmt})(\text{H}_5\text{bmt})(\text{H}_2\text{O})_2]\cdot 3\text{H}_2\text{O}$ materials [where $\text{Ln}^{3+} = \text{La}^{3+}$ (**9**), $(\text{La}_{0.97}\text{Eu}_{0.03})^{3+}$ (**10**) and $(\text{La}_{0.97}\text{Tb}_{0.03})^{3+}$ (**11**)].

The presence of two bands for each type of water molecule agrees well with the crystallographic studies that show that there are two levels of strength for the hydrogen bonding interactions involving such moieties: for example, for the coordinated O1W and O2W water molecules it is possible to see that the latter is engaged in stronger interactions than the former based solely on the inter-nuclear distances between donor and acceptor (Table 4.1); regarding the water molecules of crystallization (O3W, O4W and O5W), the hydrogen bonding network is composed of strong connections (internuclear distances ranging from *ca.* 2.55 to 2.75 Å) and weaker interactions (distances in the *ca.* 2.96-3.16 Å – see Table 4.1). As a consequence, the O–H bonds for these molecules have overall two levels of strength that are ultimately reflected into different bands in the FT-IR spectrum. In this wide spectral region the typical $\nu(\text{O–H})$ and $\nu(\text{C–H})$ stretching vibrational modes of PO–H and –CH₂– are also found: between *ca.* 3085 and 2715 cm⁻¹ for both groups, and at around 2437 cm⁻¹ for PO–H in which the hydrogen atom is probably involved in hydrogen-bonding interactions.

Below *ca.* 1750 cm⁻¹ the FT-IR spectrum of **9** is complex with a large number of medium-to-very strong vibration bands arising from the organic ligand. Based in the literature,⁹ at *ca.* 1648 cm⁻¹ one observes the in-plane deformation of water molecules, followed of the medium intensity band at *ca.* 1606 cm⁻¹ attributed to the typical $\nu(\text{–C=C–})$ stretching vibrations of the aromatic ring. At *ca.* 1459, 1412 and 1407 cm⁻¹ the –CH₂– deformation vibrational modes from the P–CH₂ groups are visible. Additionally, two sets of vibration bands in the 1350-1150 cm⁻¹ and 1025-915 cm⁻¹ ranges include the $\nu(\text{P=O})$ and $\nu(\text{P–O})$ modes, respectively. The $\nu(\text{P–C})$ stretching vibrational modes are found at *ca.* 753 and 718 cm⁻¹.

4.2.5. Solid-State NMR: [La(H₄bmt)(H₅bmt)(H₂O)₂] \cdot 3H₂O

In order to get a better insight into the phase purity and composition of the asymmetric unit, solid-state NMR studies have been performed on the diamagnetic [La(H₄bmt)(H₅bmt)(H₂O)₂] \cdot 3H₂O (**9**) material. The ³¹P MAS spectrum of **9** shows, in the isotropic region, three well-resolved sharp resonances centered at *ca.* 17.0, 22.1 and 26.7 ppm (Figure 4.8). This information agrees well with the presence of three crystallographically distinct phosphorus sites. Peak deconvolution and integration, including the spinning sidebands, provides a ratio of *ca.* 1.00 : 0.92 : 0.94 for each resonance, respectively.

The ¹³C{¹H} CP MAS spectrum (Figure B.1.4 in the Appendices) is composed of two distinct spectral regions. The *ca.* 20-45 ppm range comprises two resonances at *ca.* 32.5 (shoulder) and 34.2 ppm, attributed to the –CH₂– groups of the organic ligand. In the 120-140 ppm spectral region the resonances of the aromatic carbon atoms appear peaking at *ca.* 128.3, 128.9, 132.1 and 133.7 ppm. In summary, data from the ³¹P MAS spectrum is unequivocal strongly indicating the presence in the asymmetric unit of only one organic molecule, in good agreement with the crystallographic studies.

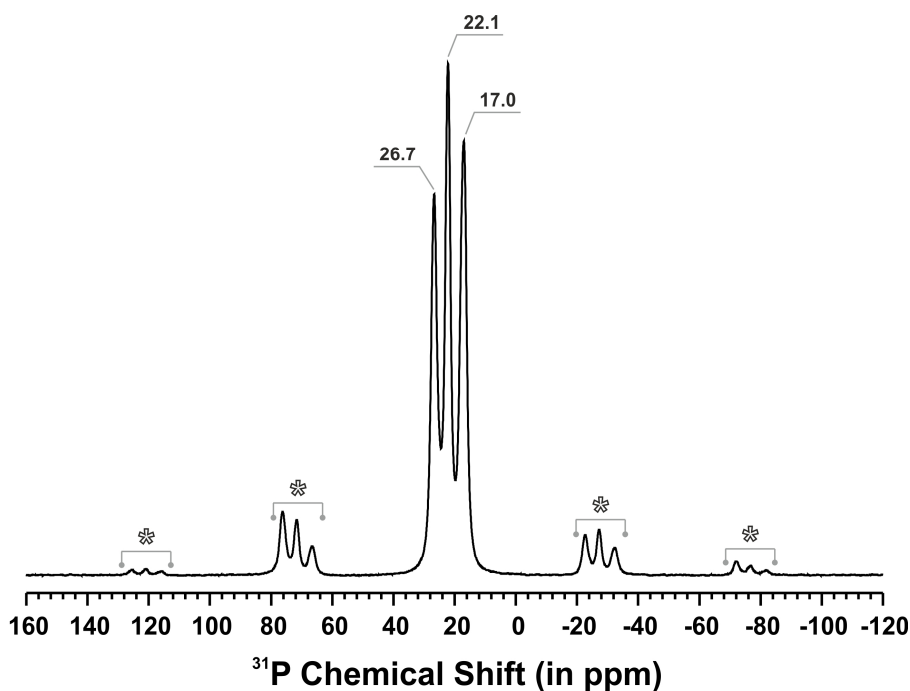


Figure 4.8 - ^{31}P HPDEC MAS spectrum of $[\text{La}(\text{H}_4\text{bmt})(\text{H}_5\text{bmt})(\text{H}_2\text{O})_2]\cdot 3\text{H}_2\text{O}$ (**9**). Spinning sidebands are denoted using an asterisk. Peak deconvolution and integration throughout the entire spectral range (*i.e.*, including the spinning sidebands) gives a ratio of *ca.* 1.00 : 0.92 : 0.94 for the isotropic resonances peaking at *ca.* 17.0, 22.1 and 26.7 ppm, respectively.

4.2.6. Photoluminescence

The excitation spectra of the stoichiometric mixed-lanthanide materials $[(\text{La}_{0.97}\text{Eu}_{0.03})(\text{H}_4\text{bmt})(\text{H}_5\text{bmt})(\text{H}_2\text{O})_2]\cdot 3\text{H}_2\text{O}$ (**10**) and $[(\text{La}_{0.97}\text{Tb}_{0.03})(\text{H}_4\text{bmt})(\text{H}_5\text{bmt})(\text{H}_2\text{O})_2]\cdot 3\text{H}_2\text{O}$ (**11**), recorded at ambient temperature while monitoring within the Eu^{3+} $^5\text{D}_0 \rightarrow ^7\text{F}_2$ and Tb^{3+} $^5\text{D}_4 \rightarrow ^7\text{F}_5$ transitions (Figure 4.9), are dominated by a broad UV band (240-288 nm) attributed to $\pi\text{-}\pi^*$ transitions. In the emission spectra of **10** and **11** recorded at ambient temperature (excited at 276 nm; Figure 4.10) the sharp lines are assigned to transitions between the first excited non-degenerate $^5\text{D}_0$ state and the $^7\text{F}_{0-4}$ levels of the fundamental Eu^{3+} septet and to the first excited state $^5\text{D}_4$ and the $^7\text{F}_{6-0}$ levels of Tb^{3+} , respectively for **10** and **11**. The local-field splitting of the Eu^{3+} $^7\text{F}_{1,2}$ levels into three and clearly less than five Stark components, respectively, and the predominance of the $^5\text{D}_0 \rightarrow ^7\text{F}_2$ transition relatively to the $^5\text{D}_0 \rightarrow ^7\text{F}_1$ (Figure 4.10), indicates the presence of a single low-symmetry Eu^{3+} environment in the structure, as supported by the crystal structure determination.

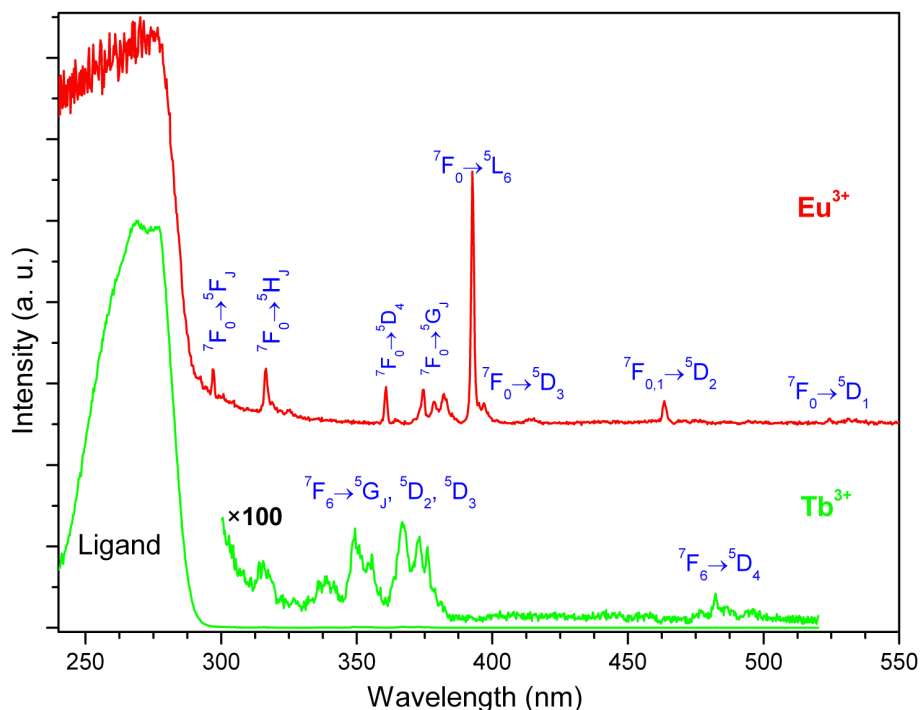


Figure 4.9 - Ambient temperature excitation spectra of $[(La_{0.97}Eu_{0.03})(H_4bmt)(H_5bmt)-(H_2O)_2] \cdot 3H_2O$ (**10**) (red) and $[(La_{0.97}Tb_{0.03})(H_4bmt)(H_5bmt)(H_2O)_2] \cdot 3H_2O$ (**11**) (green) monitoring the emission at 611.4 and 544 nm, respectively.

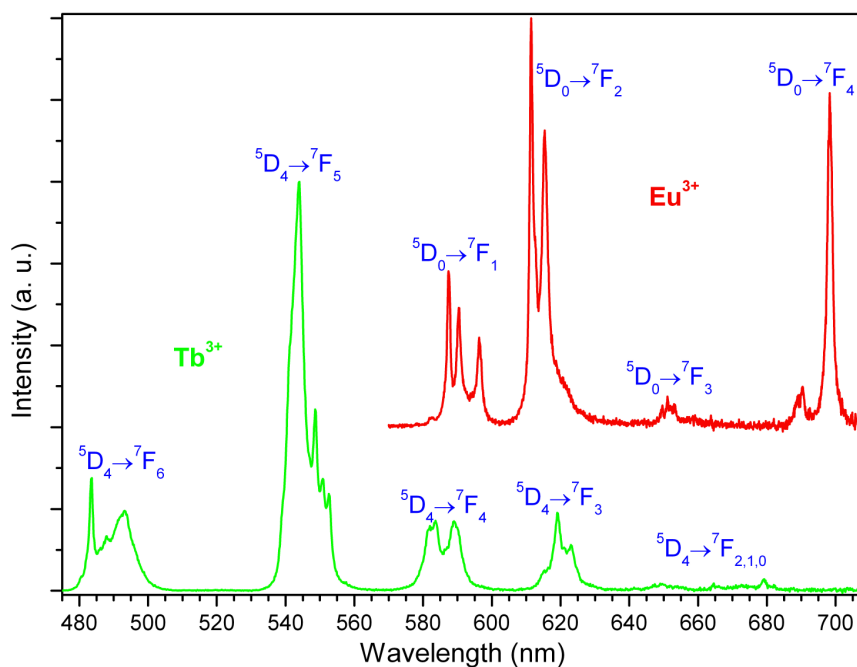


Figure 4.10 - Ambient temperature emission spectra of $[(La_{0.97}Eu_{0.03})(H_4bmt)(H_5bmt)-(H_2O)_2] \cdot 3H_2O$ (**10**) (red) and $[(La_{0.97}Tb_{0.03})(H_4bmt)(H_5bmt)(H_2O)_2] \cdot 3H_2O$ (**11**) (green), excited at 276 nm.

The ambient temperature 5D_0 and 5D_4 lifetimes of Eu^{3+} and Tb^{3+} of **10** and **11** were determined by monitoring the emission decay curves within the maximum of the $^5D_0 \rightarrow ^7F_2$ and $^5D_4 \rightarrow ^7F_5$ transitions, using an excitation at 393 and 376 nm, respectively (Figure 4.11). Decay curves were fitted by single exponential functions, with lifetimes of 0.37 ± 0.01 and 1.52 ± 0.01 ms for **10** and **11**, respectively.

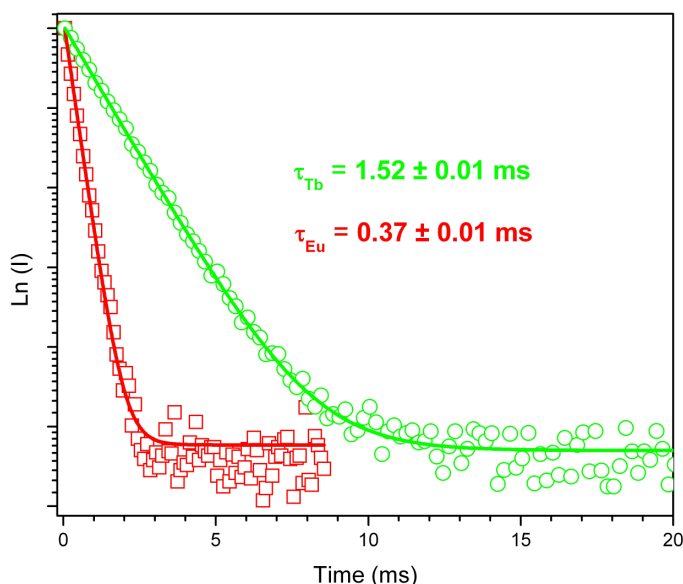


Figure 4.11 - 5D_0 and 5D_4 decay curves of $[(\text{La}_{0.97}\text{Eu}_{0.03})(\text{H}_4\text{bmt})(\text{H}_5\text{bmt})(\text{H}_2\text{O})_2] \cdot 3\text{H}_2\text{O}$ (**10**) (red) and $[(\text{La}_{0.97}\text{Tb}_{0.03})(\text{H}_4\text{bmt})(\text{H}_5\text{bmt})(\text{H}_2\text{O})_2] \cdot 3\text{H}_2\text{O}$ (**11**) (green), acquired at ambient temperature, while monitoring the emission at 614 and 543.5 nm, respectively, and fitted with single exponential decay functions. The excitation was performed at 393 and 376 nm, respectively.

Based on the emission spectra, 5D_0 lifetimes and empirical radiative and non-radiative transition rates, assuming that only non-radiative and radiative processes are involved in the depopulation of the 5D_0 state, the 5D_0 quantum efficiency, q ,¹⁰⁻¹⁴ has been determined for **10**. The number of water molecules (n_w) coordinated to Eu^{3+} and Tb^{3+} may be determined using the empirical formulae of Horrocks and Kimura, respectively.¹⁵⁻¹⁶ Data for **10** and **11**, including the absolute emission quantum yield (η , measured experimentally), are collected in Table 4.2.

Compound **10** has a relative low quantum efficiency (8%). The measured absolute emission quantum yield reaches a maximum of 5% at 393 nm. In contrast, compound **11** reaches a relative high absolute emission quantum yield of 44% at 276 nm excitation. The high absolute emission quantum yield reached for the Tb^{3+} emission is presumably due to a good superposition between the interconfigurational $4f^75d^1$ excited states of Tb^{3+} , namely the high spin states commonly positioned at around 280 nm, with the emitting $S_1 \rightarrow S_0$ transition of the ligand (zero-phonon level at *ca.* 277 nm).⁶

Table 4.2 - Experimental 5D_0 lifetime, τ , radiative, k_r , and non-radiative, k_{nr} , transition rates, 5D_0 quantum efficiency, q , absolute emission quantum yield, η , and the estimated number of water molecules, n_w , for $[(La_{0.97}Eu_{0.03})(H_4bmt)(H_5bmt)(H_2O)_2] \cdot 3H_2O$ (**10**). The experimental 5D_4 lifetime, τ , absolute emission quantum yield, ϕ , and the estimated number of water molecules, n_w , are also given for $[(La_{0.97}Tb_{0.03})(H_4bmt)(H_5bmt)(H_2O)_2] \cdot 3H_2O$ (**11**). Data have been collected at ambient temperature and pressure (298 K).

Compound	τ [ms]	k_r [s^{-1}]	k_{nr} [s^{-1}]	q [%]	η [%] ($\lambda_{Exc.}$; nm)	n_w
10	0.37±0.01	229	2681	8	1 (276) / 5 (393)	2.4
11	1.52±0.01	-	-	-	44 (276) / 1 (376)	1.6

4.2.7. Heterogeneous catalysis

The catalytic performance of $[La(H_4bmt)(H_5bmt)(H_2O)_2] \cdot 3H_2O$ (**9**) was explored in the methanolysis of styrene oxide (PhEtO) (see Scheme 3.1 in Chapter 3). The catalytic reaction at 55 °C gave 2-methoxy-2-phenylethanol (MeOPhEtOH) in quantitative yield within 30 min reaction (Table 4.3), while without a catalyst no reaction occurred. The catalytic stability of **9** was investigated by reusing the washed-dried catalyst: slightly decrease in the PhEtO conversion and MeOPhEtOH yield at 30 min reaction were observed for four consecutive batch runs. These differences are less pronounced when comparing the results for 1h reaction (Figure 4.12).

Table 4.3 - Reaction of PhEtO with methanol to MeOPhEtOH in the presence of **9** or of corresponding synthetic precursors as catalysts.^a

Catalyst	initialCatalyst amount	Temp. ^b (°C)	Reaction time	MeOPhEtOH yield (%)
9	20 g ₍₉₎ L ^{-1 c}	55	30 min	100
9	3.3 g ₍₉₎ L ⁻¹	55	30 min / 1 h	95 / 100
9	20 g ₍₉₎ L ⁻¹	35	30 min / 1 h	96 / 100
9	3.3 g ₍₉₎ L ⁻¹	35	1 h / 6 h	40 / 100
H₆bmt	3.5 mM ^d	35	30 min / 1 h	99 / 100
LaCl ₃ ·7H ₂ O	3.5 mM ^d	35	3 h	4 ^e

^a Reaction conditions: 0.4 M PhEtO, 800 rpm. ^b Reaction temperature. ^c Catalyst bulk density of **9** expressed as initial mass of solid per volume of reaction mixture.

^d Initial concentration of precursor which was completely dissolved (homogeneous catalyst).

^e Conversion was 4%.

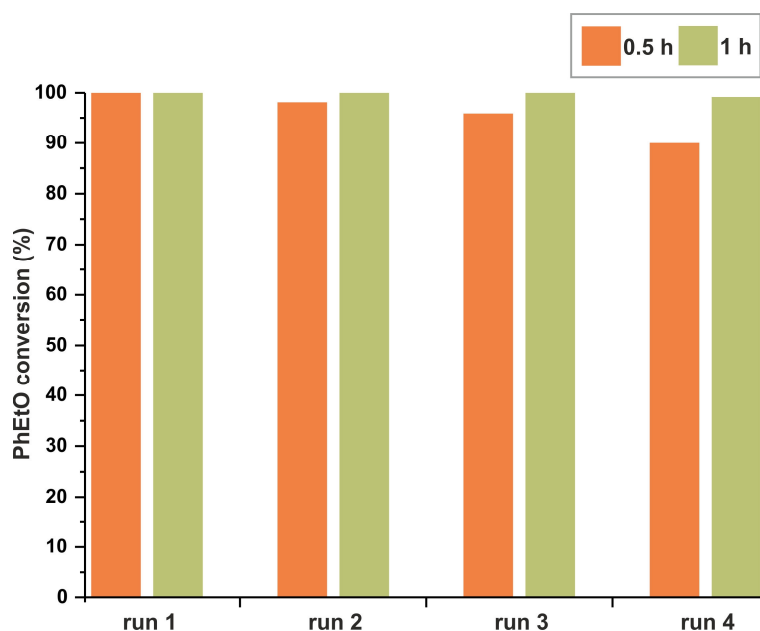


Figure 4.12 - Reaction of styrene oxide (PhEtO) with methanol to afford 2-methoxy-2-phenylethanol in the presence of the heterogeneous catalyst $[\text{La}(\text{H}_4\text{bmt})(\text{H}_3\text{bmt})(\text{H}_2\text{O})_2] \cdot 3\text{H}_2\text{O}$ (**9**) in four consecutive batch runs. Reaction conditions: 0.4 M PhEtO, 20 $\text{g}_{(9)} \text{L}^{-1}$, 1 h, 55 °C, 800 rpm.

The structural and morphological features of **9** after each catalytic batch run were studied by PXRD and electron microscopy (Figure 4.13). Despite a decrease in the crystal size of catalyst **9** recovered after first catalytic run (maintaining in the subsequent batch runs), the structure of **9** was preserved without visible modifications. The morphological changes may lead to the observed slight catalyst deactivation, possibly due to the destruction of some active sites. Nevertheless, the catalytic performance of **9** in recycling runs was fairly good without catalyst regeneration steps.

A six-fold decrease in the catalyst bulk density (from 20 to 3.3 $\text{g}_{(9)} \text{L}^{-1}$) led to comparably outstanding catalytic results: 95%/100% MeOPhEtOH at 30 min/1 h reaction, 55 °C (Table 4.2). Furthermore, at approximately ambient temperature (35 °C) and using a catalyst bulk density of 20 $\text{g}_{(9)} \text{L}^{-1}$, quantitative MeOPhEtOH yield was reached at 1 h reaction. Decreasing the catalyst bulk density from 20 to 3.3 $\text{g}_{(9)} \text{L}^{-1}$ at 35 °C resulted in a slower reaction; nevertheless, after 6 h reaction, 100% MeOPhEtOH yield was reached (Table 4.2). The leaching tests for **9** (fresh) and for the catalyst recovered after a 6 h-batch run at 35 °C led to <2% conversion which is minor compared to that observed in the presence of **9** (100% conversion, Table 4.3) indicating that the catalytic reaction is heterogeneous in nature.

In order to get insights into the type of active sites responsible for the catalytic activity of **9**, the reaction of PhEtO was carried out in the presence of catalytic amounts of the corresponding ligand and lanthanide precursors, namely **H₆bmt** and $\text{LaCl}_3 \cdot 7\text{H}_2\text{O}$ (used in equivalent amounts to those corresponding to 3.3 $\text{g}_{(9)} \text{L}^{-1}$). The reaction of PhEtO was very sluggish in the presence of $\text{LaCl}_3 \cdot 7\text{H}_2\text{O}$ (4% conversion at 3 h reaction,

35 °C). In contrast, the **H₆bmt** ligand precursor led to 100% MeOPhEtOH yield at 1 h reaction. These results suggest that Brønsted acidity renders the epoxide more susceptible to nucleophilic attack by the alcohol than Lewis acidity, leading to faster alcoholysis of the epoxide.

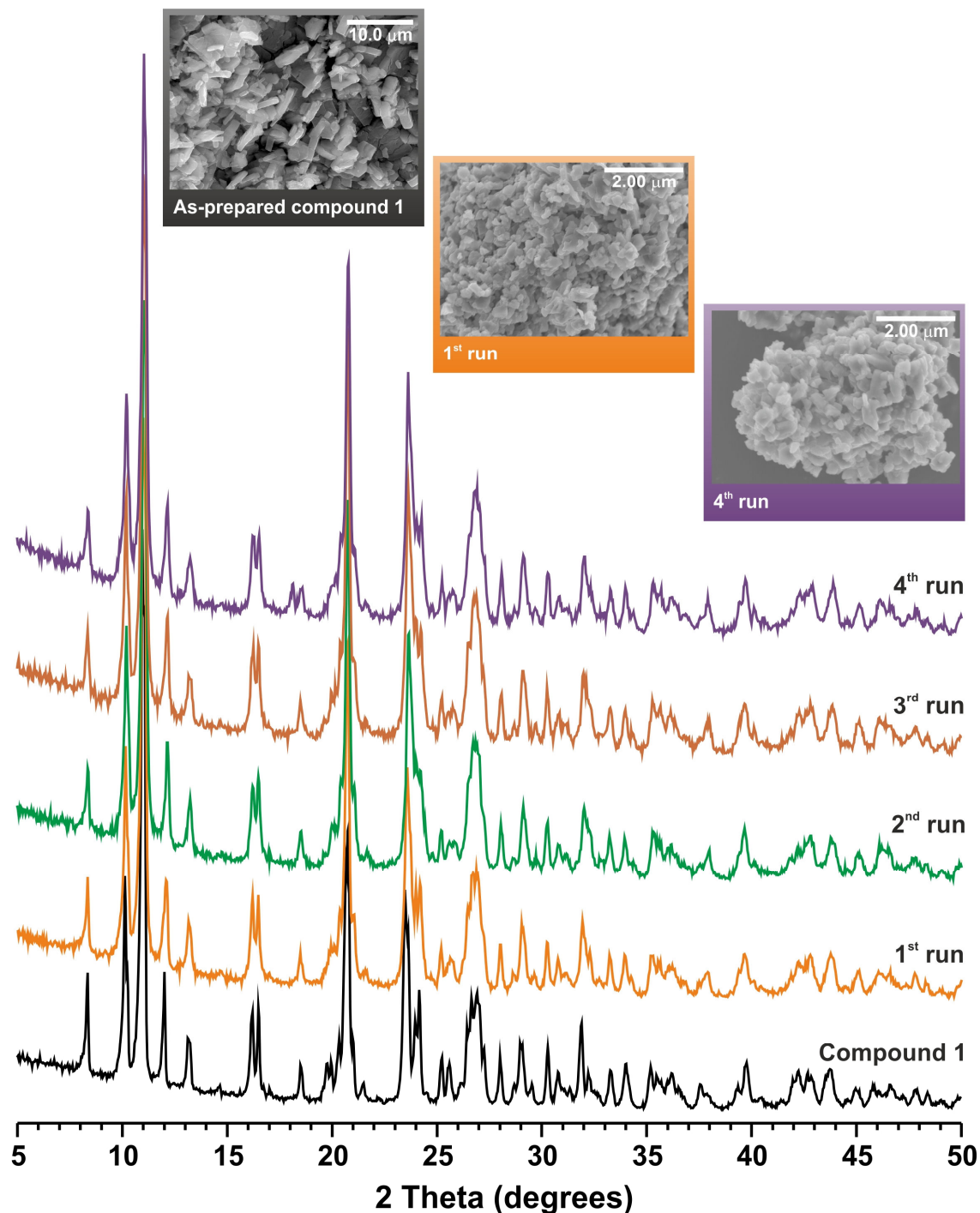


Figure 4.13 - PXRD patterns and SEM images of the as-prepared $[\text{La}(\text{H}_4\text{bmt})(\text{H}_5\text{bmt})(\text{H}_2\text{O})_2] \cdot 3\text{H}_2\text{O}$ (**9**) material and after consecutive batch runs (up to four) in the reaction of styrene oxide with methanol.

4.3. Hydrothermal Synthesis of Layered 2D Lanthanide-Organic Frameworks

4.3.1. Hydrothermal Synthesis

The transformation of mixtures composed of **H₆bmt** with the respective lanthanide chloride salts under hydrothermal conditions led to the isolation of a new family of layered 2D Lanthanide-Organic Frameworks, formulated as $[\text{Ln}_2(\text{H}_3\text{bmt})_2]\cdot\text{H}_2\text{O}$ [where $\text{Ln}^{3+} = \text{Eu}^{3+}$ (**12**), Gd^{3+} (**13**), Tb^{3+} (**14**), Dy^{3+} (**15**), Ho^{3+} (**16**), Er^{3+} (**17**), Tm^{3+} (**18**) and Yb^{3+} (**19**)] (see sub-section 8.11.2.1 in the Experimental Section for further details on the synthesis).

Because the 2D $[\text{Ln}_2(\text{H}_3\text{bmt})_2]\cdot\text{H}_2\text{O}$ materials are solely composed of microcrystalline powders, phase identification and crystal solution were performed from Rietveld refinement studies using laboratory powder X-ray diffraction data. Figure 4.14 shows the final Rietveld plot of the $[\text{Eu}_2(\text{H}_3\text{bmt})_2]\cdot\text{H}_2\text{O}$ (**12**) material.

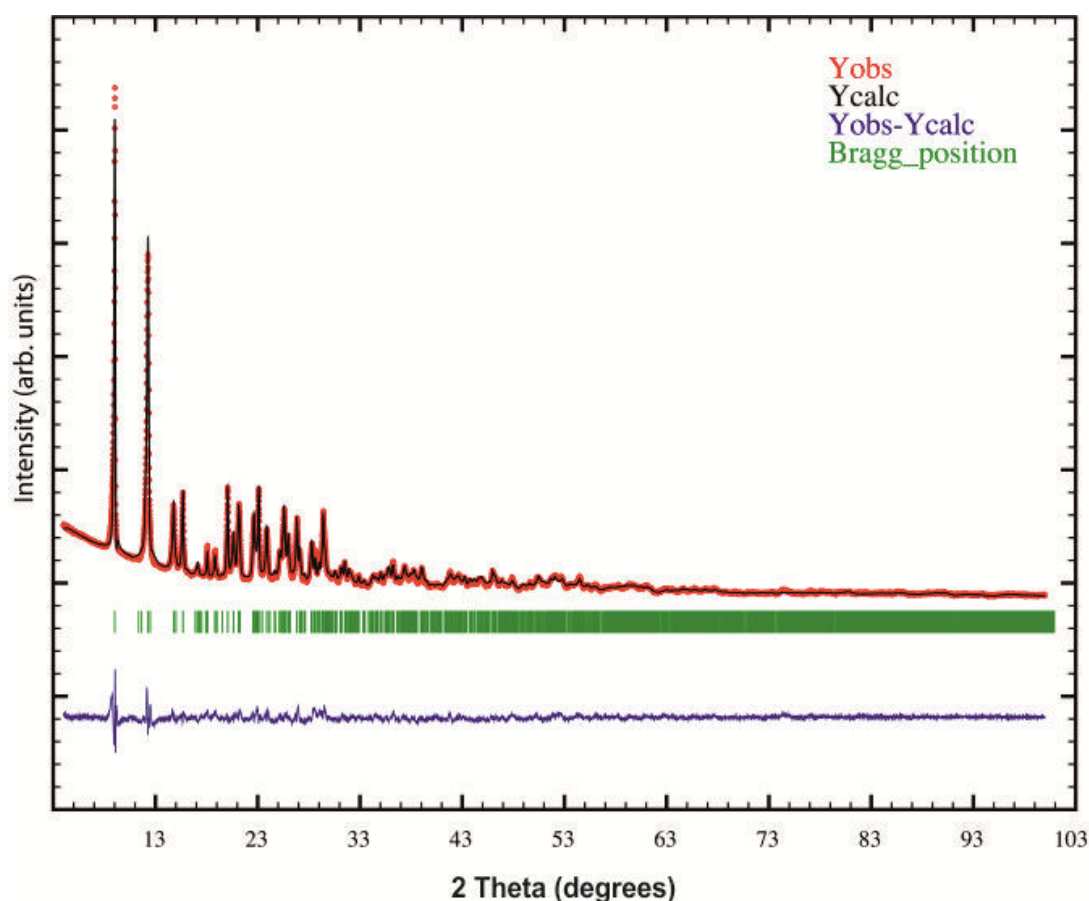


Figure 4.14 – Rietveld plot (laboratory powder X-ray diffraction data) of $[\text{Eu}_2(\text{H}_3\text{bmt})_2]\cdot\text{H}_2\text{O}$ (**12**) material. Observed data points are indicated as red circles, the best-fit profile (upper trace) and the difference pattern (lower trace) are drawn as solid black and blue lines, respectively. Green vertical bars indicate the angular positions of the allowed Bragg reflections.

Rietveld studies of the bulk **12** material are only preliminary at this stage. A more unequivocal and detailed study is in progress using high-resolution synchrotron data collected both at ID31 (ESRF, Grenoble, France) and at I11 (DLS, Oxford, United Kingdom). The remaining materials belonging to the $[\text{Ln}_2(\text{H}_3\text{bmt})_2]\cdot\text{H}_2\text{O}$ series were characterized by PXRD which allowed to confirm the structural similarities between all compounds (Figure 4.15). The inclusion of different lanthanide centers affects, nevertheless, the collected PXRD patterns: going from Eu^{3+} to Yb^{3+} there is an average increase of the full-width-at-half-maximum (FWHM) of the diffraction peaks. This behavior is characteristic of materials with decreasing size of the crystallites (Figure 4.15).

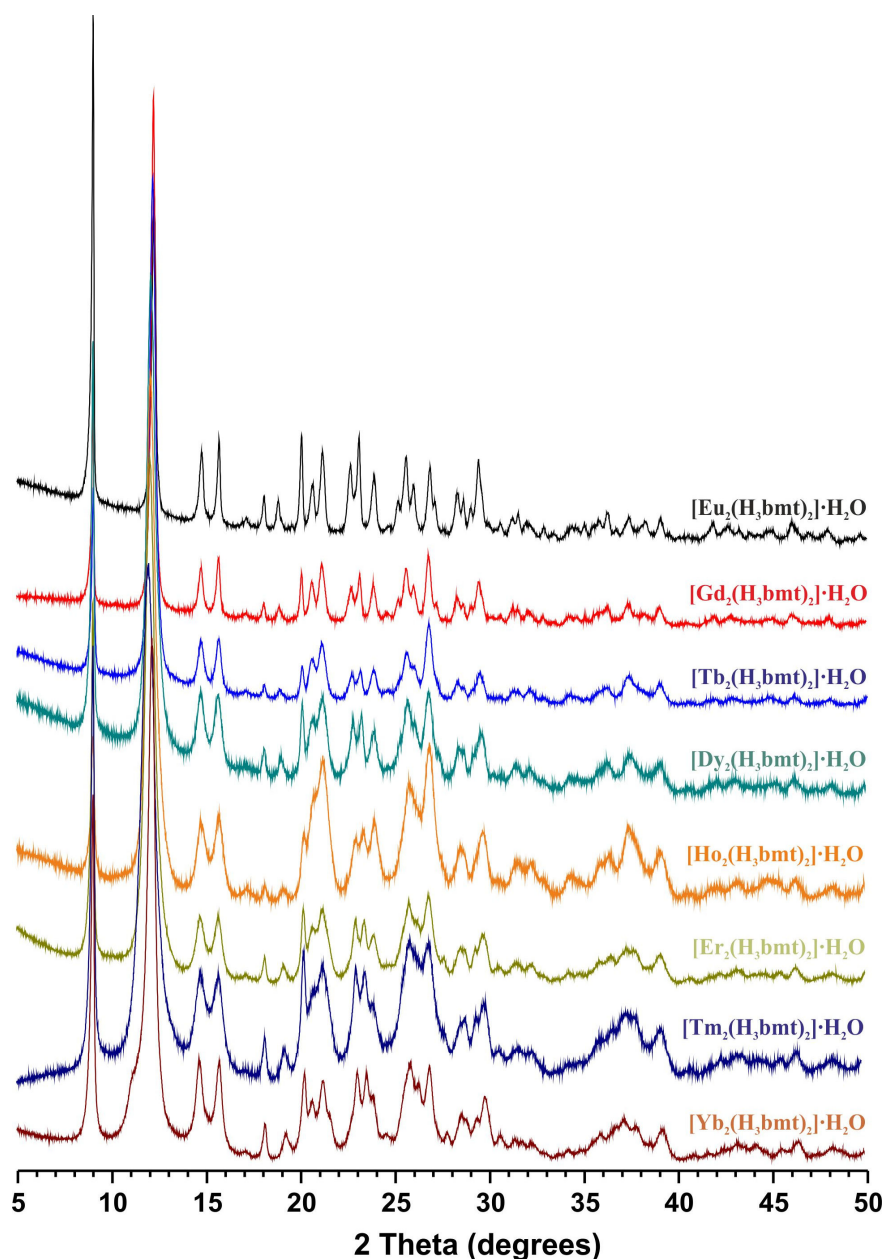


Figure 4.15 – PXRD patterns of the 2D $[\text{Ln}_2(\text{H}_3\text{bmt})_2]\cdot\text{H}_2\text{O}$ materials [where $\text{Ln}^{3+} = \text{Eu}^{3+}$ (**12**), Gd^{3+} (**13**), Tb^{3+} (**14**), Dy^{3+} (**15**), Ho^{3+} (**16**), Er^{3+} (**17**), Tm^{3+} (**18**) and Yb^{3+} (**19**)].

SEM studies performed on the bulk $[\text{Ln}_2(\text{H}_3\text{bmt})_2]\cdot\text{H}_2\text{O}$ materials so to analyze crystal morphology further support the aforementioned assumption (Figure 4.16). Despite the morphological differences between the compounds, it is noteworthy a clear decrease in the average particle size of the compounds. Indeed, compounds containing in their structure lanthanide centers with lower atomic number (*i.e.*, larger ionic radius), as for instance Eu^{3+} and Gd^{3+} , are composed of larger particles. Using Yb^{3+} , the last element of the lanthanide series, as the metal center a isotypical material is obtained but, in this case, formed of much smaller crystallites. Because the reaction conditions to prepare all $[\text{Ln}_2(\text{H}_3\text{bmt})_2]\cdot\text{H}_2\text{O}$ materials were identical (see sub-section 8.10.2.1 in the of the Experimental Section for further details), these results clearly suggest that the decrease of the average particle size is due to the decrease of the ionic radius of the employed lanthanide center.

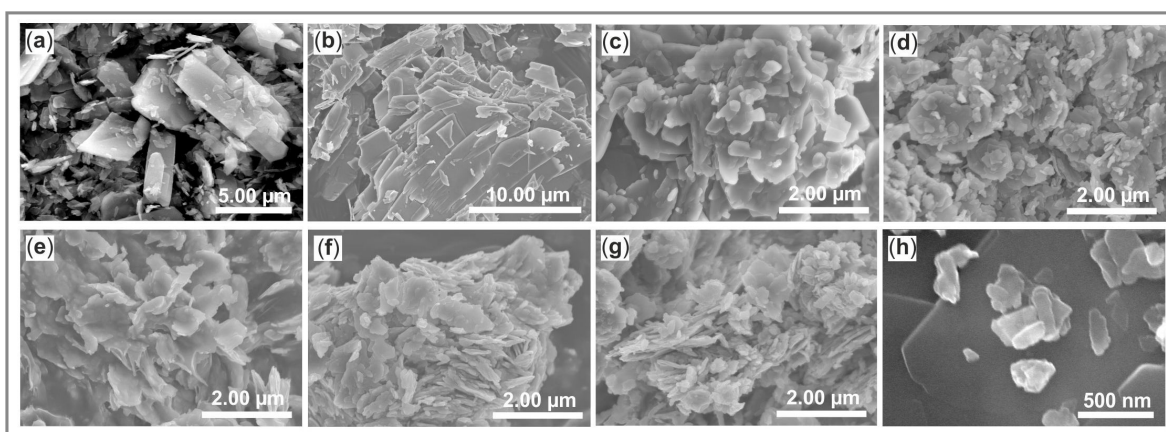


Figure 4.16 – SEM images of the 2D $[\text{Ln}_2(\text{H}_3\text{bmt})_2]\cdot\text{H}_2\text{O}$ materials [where $\text{Ln}^{3+} = \text{Eu}^{3+}$ (a), Gd^{3+} (b), Tb^{3+} (c), Dy^{3+} (d), Ho^{3+} (e), Er^{3+} (f), Tm^{3+} (g) and Yb^{3+} (h)].

4.3.2. Crystal Structure Description of $[\text{Eu}_2(\text{H}_3\text{pmt})_2]\cdot\text{H}_2\text{O}$

Preliminary powder X-ray diffraction studies provide insight on the crystal structure of the novel 2D $[\text{Eu}_2(\text{H}_3\text{bmt})_2]\cdot\text{H}_2\text{O}$ (**12**) material. Compound **12** crystallizes in the monoclinic $P2_1/n$ space group, with the asymmetric unit comprising a single Eu^{3+} metallic center, one $\text{H}_3\text{bmt}^{3-}$ bridging organic linker and half of one water molecule of crystallization. The coordination sphere of Eu^{3+} center is composed of six phosphonate groups describing a distorted octahedral coordination geometry as depicted in Figure 4.17. The metallic center is, thus, coordinated to a total of six oxygen atoms, $\{\text{EuO}_6\}$, all connected to the metallic center by way of a *syn*-bridging coordination mode.

Compound **12** contains a two-dimensional $\infty^2[\text{Eu}_2(\text{H}_3\text{bmt})_2]$ network placed on the *ab* plane of the unit cell (Figure 4.18a). Hydrogen bonding between individual $\infty^2[\text{Eu}_2(\text{H}_3\text{bmt})_2]$ layers leads to the formation of a compact structure as described in Figure 4.18b.

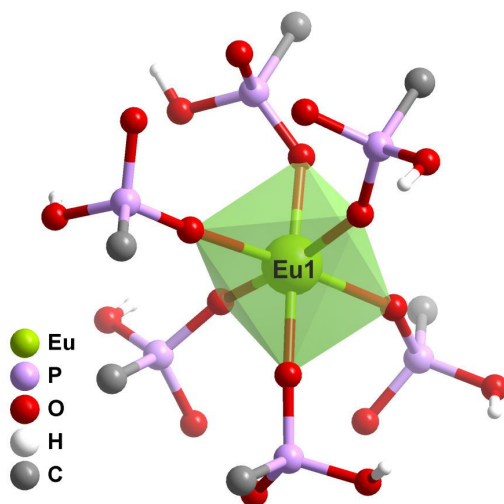


Figure 4.17 – Mixed ball-and-stick and polyhedral representation of the coordination environment of the Eu^{3+} metallic center present in $[\text{Eu}_2(\text{H}_3\text{bmt})_2]\cdot\text{H}_2\text{O}$ (**12**).

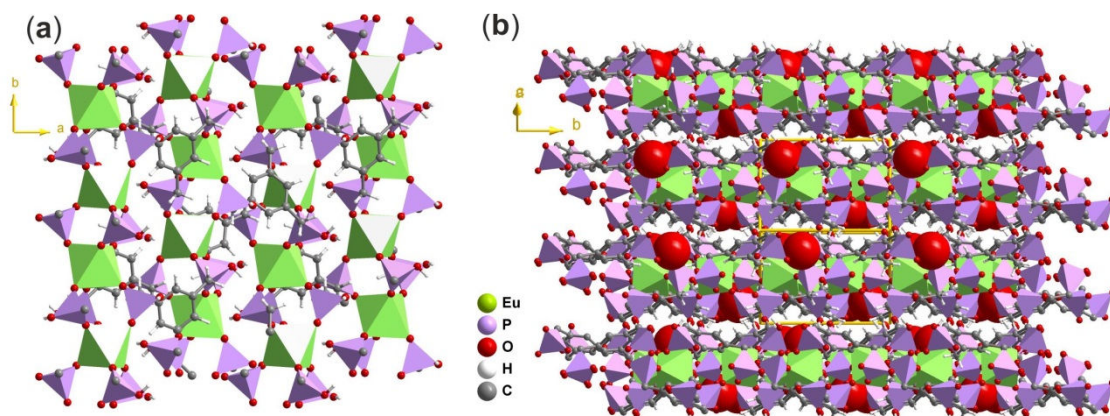


Figure 4.18 – (a) View along the [001] direction of the unit cell of the two-dimensional $\infty^2[\text{Eu}_2(\text{H}_3\text{bmt})_2]$ MOF present in the crystal structure of compound **12**. (b) Crystal packing of **12** viewed in perspective along the [00-1] direction of the unit cell. $\{\text{LaO}_6\}$ octahedra and $\{\text{PO}_3\text{C}\}$ tetrahedra are represented in green and purple, respectively. Water molecules of crystallization are represented in space-filling mode.

4.3.3. Thermogravimetry and Thermodiffraction

The thermal stability of the 2D layered $[\text{Ln}_2(\text{H}_3\text{bmt})_2]\cdot\text{H}_2\text{O}$ materials [where $\text{Ln}^{3+} = \text{Eu}^{3+}$ (**12**), Gd^{3+} (**13**), Tb^{3+} (**14**), Dy^{3+} (**15**), Ho^{3+} (**16**), Er^{3+} (**17**), Tm^{3+} (**18**) and Yb^{3+} (**19**)] were studied from ambient temperature to 800 °C. Thermograms show slightly different weight loss profiles for each materials (Figure B.2.1 in the Appendices). The decomposition pathways observed for compounds that have lanthanide centers with higher atomic numbers (as for instance Yb^{3+}) are less defined than those for compounds possessing lanthanides with lower atomic numbers. This fact may be attributed to the decrease of the particle size: as mentioned in section 4.3.1

(supported by the SEM images) the Yb^{3+} material is mainly composed of nanoparticles. As a consequence, the overall thermal stability of these compounds is lower, leading to thermal decompositions also at lower temperatures. Nevertheless, despite these differences, the thermal decomposition of all materials occurs in the same general way.

In order to evaluate the effect of increasing temperature in the crystal structure VTPXRD studies have been performed for **12** in the 30-510 °C range (Figure 4.19 – right). The discussion is solely focused on the thermal behavior of compound **12**, being assumed that this behavior is similar for the remaining members of the isotypical series.

VTPXRD patterns show that compound **12** is thermally robust up to *ca.* 370 °C. From the thermogram of **12** (Figure 4.19 – left), the first weight loss occurs in the *ca.* 163-255 °C range corresponding to the release of the water molecules of crystallization: noteworthy, the observed weight loss of 1.3% is slightly lower than the expected one (1.7%). At higher temperature there is a second decomposition of 4.9%. The various protonated P-OH moieties may be at the genesis of a dehydration process that occurs from *ca.* 255 to 532 °C leading to this additional loss of water. Indeed, VTPXRD studies show a significant modification in the structure (mainly, loss of crystallinity) of **12** within this temperature range. The structure of compound **12** starts to decompose above this temperature.

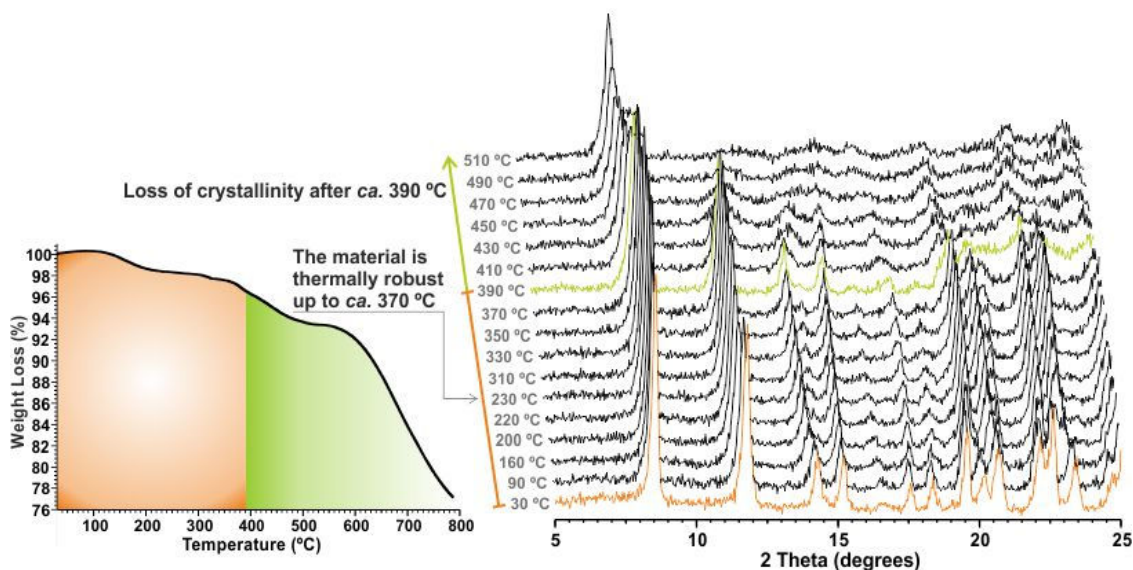


Figure 4.19 - Thermogram and VTPXRD studies of the $[\text{Eu}_2(\text{H}_3\text{bmt})_2]$ (**12**) material.

4.3.4. FT-IR Spectroscopic Studies

FT-IR spectra of the 2D $[\text{Ln}_2(\text{H}_3\text{bmt})_2] \cdot \text{H}_2\text{O}$ materials [where $\text{Ln}^{3+} = \text{Eu}^{3+}$ (**12**), Gd^{3+} (**13**), Tb^{3+} (**14**), Dy^{3+} (**15**), Ho^{3+} (**16**), Er^{3+} (**17**), Tm^{3+} (**18**) and Yb^{3+} (**19**)] were collected so to further investigate some structural details previously described (Figure 4.20 and Figure B.2.2 in the Appendices). Figure 4.20 depicts selected spectral regions emphasizing a number of vibrational bands of the most structurally-relevant functional

groups present in **12**. Due to the very similar spectral profiles, only compound **12** will be described with more detail in the following paragraphs, being the conclusions also valid for the remaining materials.

The FT-IR spectrum of **12** is dominated by two spectral regions. In the *ca.* 3750-2500 cm^{-1} range it is possible to observe the typical $\nu(\text{POH})$ vibrational mode of strong intensity centered at *ca.* 3607 cm^{-1} . At *ca.* 3397 cm^{-1} the $\nu(\text{O-H})$ stretching vibrations of the water molecules of crystallization and a broad band in the *ca.* 3328-2865 cm^{-1} spectral range belonging to the $\nu(\text{POH})$ and $\nu(\text{C-H})$ stretching vibrations of the $-\text{CH}_2-$ groups also appear in this region.

Below 1800 cm^{-1} the FT-IR spectrum of **12** is complex with a large number of weak-to-very strong bands.⁹ At *ca.* 1615 and 1605 cm^{-1} the typical $\delta(\text{H}_2\text{O})$ and $\nu(-\text{C}=\text{C}-)$ in-plane deformations are markedly visible. Two bands of medium intensity peaking at *ca.* 1460 and 1410 cm^{-1} are attributed to the $-\text{CH}_2-$ deformation vibrational modes from the P-CH_2 groups. Additionally, three vibrational bands are also visible in the FT-IR spectrum: i) the $\nu(\text{P}=\text{O})$ appear in the 1176-1035 cm^{-1} range; ii) the $\nu(\text{P-O})$ mode is identified at *ca.* 931 cm^{-1} as a vibration band with very strong intensity; iii) the $\nu(\text{P-C})$ stretching vibrational modes appear as weak bands centered at *ca.* 771 and 756 cm^{-1} .

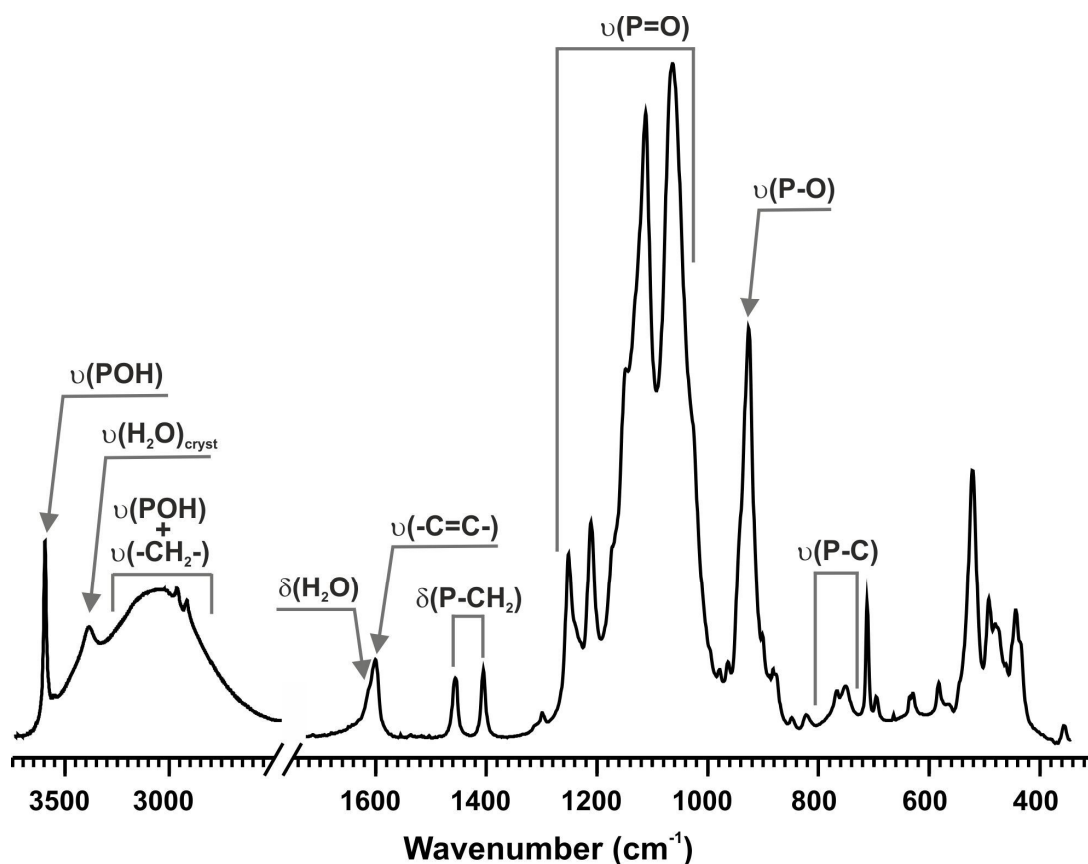


Figure 4.20 - FT-IR spectra of the layered $[\text{Eu}_2(\text{H}_3\text{bmt})_2]\cdot\text{H}_2\text{O}$ (**12**) material.

4.4. Conventional Hydrothermal Synthesis of 3D Lanthanide-Organic Frameworks

4.4.1. Hydrothermal Synthesis

The reaction between the tripodal organic ligand **H₆bmt** and lanthanide (III) chloride hydrates afforded $[\text{Ln}_2(\text{H}_3\text{bmt})_2(\text{H}_2\text{O})_2] \cdot \text{H}_2\text{O}$ materials as large single crystals [where $\text{Ln}^{3+} = \text{La}^{3+}$ (**20**), Ce^{3+} (**21**), Pr^{3+} (**22**), Nd^{3+} (**23**), $(\text{La}_{0.95}\text{Eu}_{0.05})^{3+}$ (**24**) and $(\text{La}_{0.95}\text{Tb}_{0.05})^{3+}$ (**25**)]. Synthesis occurred under typical hydrothermal conditions at a temperature of 180 °C, under autogeneous pressure, over a period of 3 days (see subsection 8.11.3.1 in the Experimental Section for further details). The structural features of these materials could, therefore, be readily unveiled using single-crystal X-ray diffraction studies as described in the following subsection. Independently of the lanthanide (or mixture of lanthanides for the optically-active materials **24** and **25**), these conditions were highly reproducible, systematically yielding crystalline products of the desired phases. Phase purity and homogeneity of the bulk samples **20** to **25** have been confirmed also by PXRD (Figure 4.21).

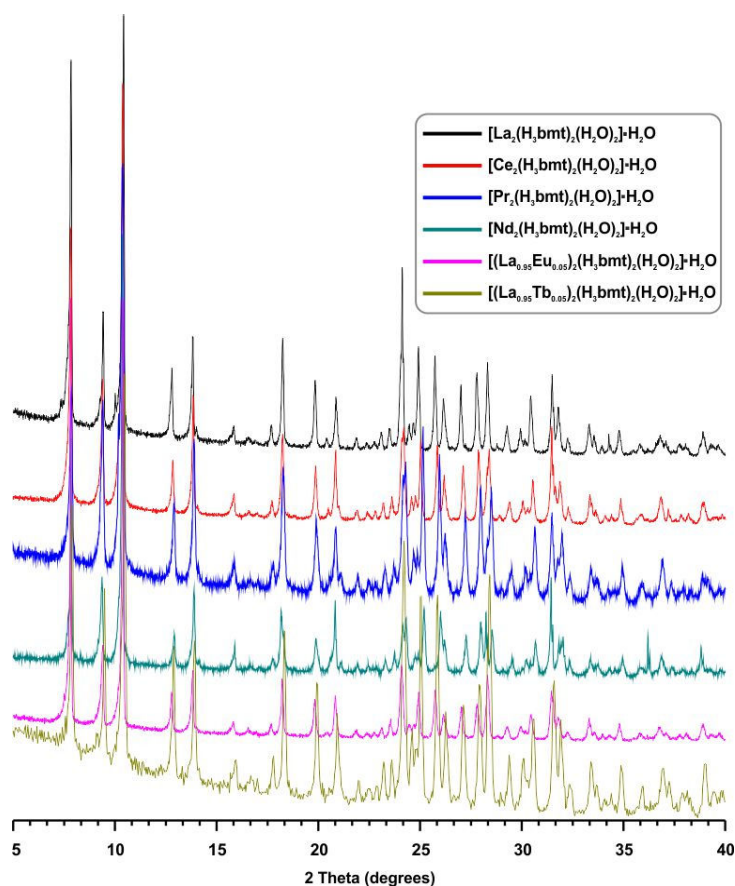


Figure 4.20 – PXRD patterns of the $[\text{Ln}_2(\text{H}_3\text{bmt})_2(\text{H}_2\text{O})_2] \cdot \text{H}_2\text{O}$ materials [where $\text{Ln}^{3+} = \text{La}^{3+}$ (**20**), Ce^{3+} (**21**), Pr^{3+} (**22**), Nd^{3+} (**23**), $(\text{La}_{0.95}\text{Eu}_{0.05})^{3+}$ (**24**) and $(\text{La}_{0.95}\text{Tb}_{0.05})^{3+}$ (**25**)].

Aiming to investigate if milder conditions could be employed, the preparation of **20** was further tested at 100 °C for reactions times ranging from 1 to 3 days, also under conventional hydrothermal conditions. Results suggest that the desired pure-phase could be readily isolated under all the tested conditions as large single crystals (Figure 4.22). Additionally, and as described in the sub-section 4.2.1, MWAS also proved to be an excellent alternative to prepare **20** with large particles. This method brings the additional advantage of drastically reducing the preparation time from 1 day to only 5 minutes.

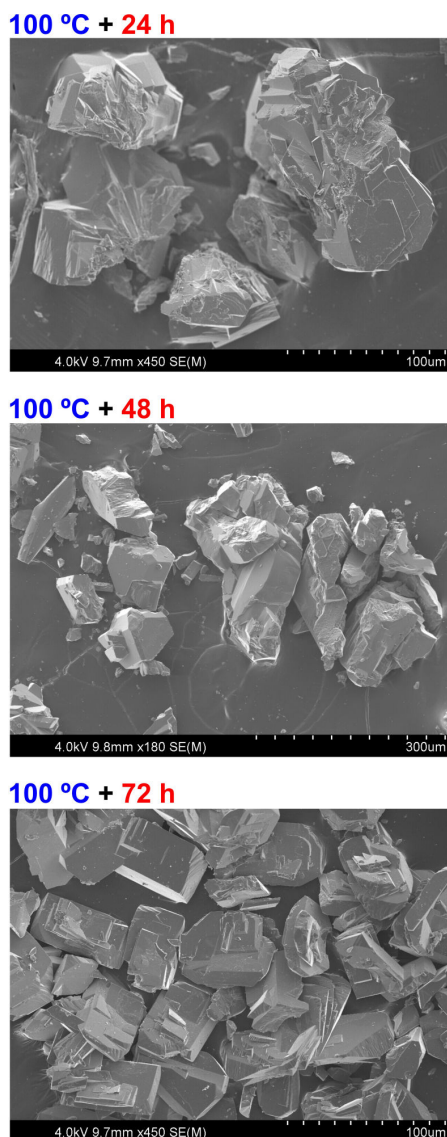


Figure 4.22 - SEM images emphasizing the crystal morphology of the $[\text{La}_2(\text{H}_3\text{bmt})_2(\text{H}_2\text{O})_2]\cdot\text{H}_2\text{O}$ (**20**) material prepared at mild temperatures (100 °C) and over different periods of time.

Optically-active materials containing Eu^{3+} and Tb^{3+} embedded into La^{3+} matrices, were isolated as bulk microcrystalline materials by including in the reactive gels 5% of Eu^{3+} or Tb^{3+} salts (in mol; see sub-section 8.11.3.1 in the Experimental

Section for details). We note that this methodology of preparing optically-active materials permits, on the one hand, to guarantee that the framework structure is not altered due to the known lanthanide contraction effect and, on the other, that Eu^{3+} and Tb^{3+} cations are statistically diluted in the networks so to prevent self-quenching effects.

4.4.2. Crystal Structure of $[\text{La}_2(\text{H}_3\text{bmt})_2(\text{H}_2\text{O})_2]\cdot\text{H}_2\text{O}$

Large single-crystals of $[\text{Ln}_2(\text{H}_3\text{bmt})_2(\text{H}_2\text{O})_2]\cdot\text{H}_2\text{O}$ materials [where $\text{Ln}^{3+} = \text{La}^{3+}$ (**20**), Ce^{3+} (**21**), Pr^{3+} (**22**), Nd^{3+} (**23**)] were directly harvested from the reaction vessels and their crystal structure determined in the centrosymmetric monoclinic $C2/c$ space group using single-crystal X-ray diffraction (see sub-section 8.11.3.1 in the Experimental Section for further details). The crystal structure of the dehydrated material of **20** ($[\text{La}(\text{H}_3\text{bmt})]$, **20-dehyd**) was also unequivocally unveiled from single-crystal X-ray diffraction. The structural details in the following paragraphs will be, therefore, solely based on the La^{3+} materials (as-prepared and dehydrated), and are assumed to be valid for the remaining members of the series.

The asymmetric units of **20** and **20-dehyd** are composed of a single crystallographically independent La^{3+} centre and one entire molecular unit of the deprotonated $\text{H}_3\text{bmt}^{3-}$ organic linker. These crystallographic details are in good agreement with the structural features derived from both the solid-state NMR studies and the detailed photoluminescence investigations (see following sub-sections). In **20**, the La^{3+} center is eight-coordinated, $\{\text{LaO}_8\}$, to a total of six phosphonate groups (from six symmetry-related $\text{H}_3\text{bmt}^{3-}$ anionic ligands) and one disordered water molecule (over two distinct locations - O1W and O2W - with 50% of rate of occupancy for each), with the overall coordination polyhedron resembling a highly distorted capped pentagonal bipyramid. The removal of the coordinated water molecule to yield **20-dehyd** (by heating above 100 °C with or without high vacuum), leads to a seven-coordination environment, $\{\text{LaO}_7\}$, with the overall geometry now resembling a simple distorted pentagonal bipyramid (the capping position was occupied by the solvent molecule - see Figures 4.23a and 4.23b).

This seamless transformation is concomitantly accompanied by only small adjustments in the geometrical parameters of the coordination polyhedra, as clearly registered by the tabulated La–O distances and O–La–O angles given in Tables B.3.1 and B.3.2, respectively, in the Appendices. These small modifications are attributed to the intrinsic need to accommodate the extra coordinative position left vacant by the liberation of the coordinated solvent molecule. The La–O bond lengths are, therefore, found in the 2.3365(18)-2.6908(17) Å and 2.3293(14)-2.6459(12) Å ranges for **20** and **20-dehyd**, respectively. As expected, the reduction in the coordination number of La^{3+} also leads to a reduction of all bond lengths. It is further noted that the longest La–O bond lengths registered for both structures [2.6908(17) and 2.6029(16) Å for **20**; 2.6459(12) and 2.6012(12) Å for **20-dehyd** - see Table B.3.1 in the Appendices] are directly associated with the P2 phosphonate group which has a pivotal role in the

structure architectures: besides being the sole phosphonate group which is *O,O*-chelated to La^{3+} (bite angles of $55.44(5)$ and $55.80(4)^\circ$ for **20** and **20-dehyd**, respectively; see Figures 4.23a and 4.23b), it further establishes physical connections between three adjacent metallic centres, leading to the formation of a one-dimensional zigzag lanthanum oxide chain running parallel to the [010] direction of the unit cell, assembled from edge-sharing of $\{\text{LaO}_8\}$ or $\{\text{LaO}_7\}$ polyhedra (Figures 4.23c, 4.23d and 4.24).

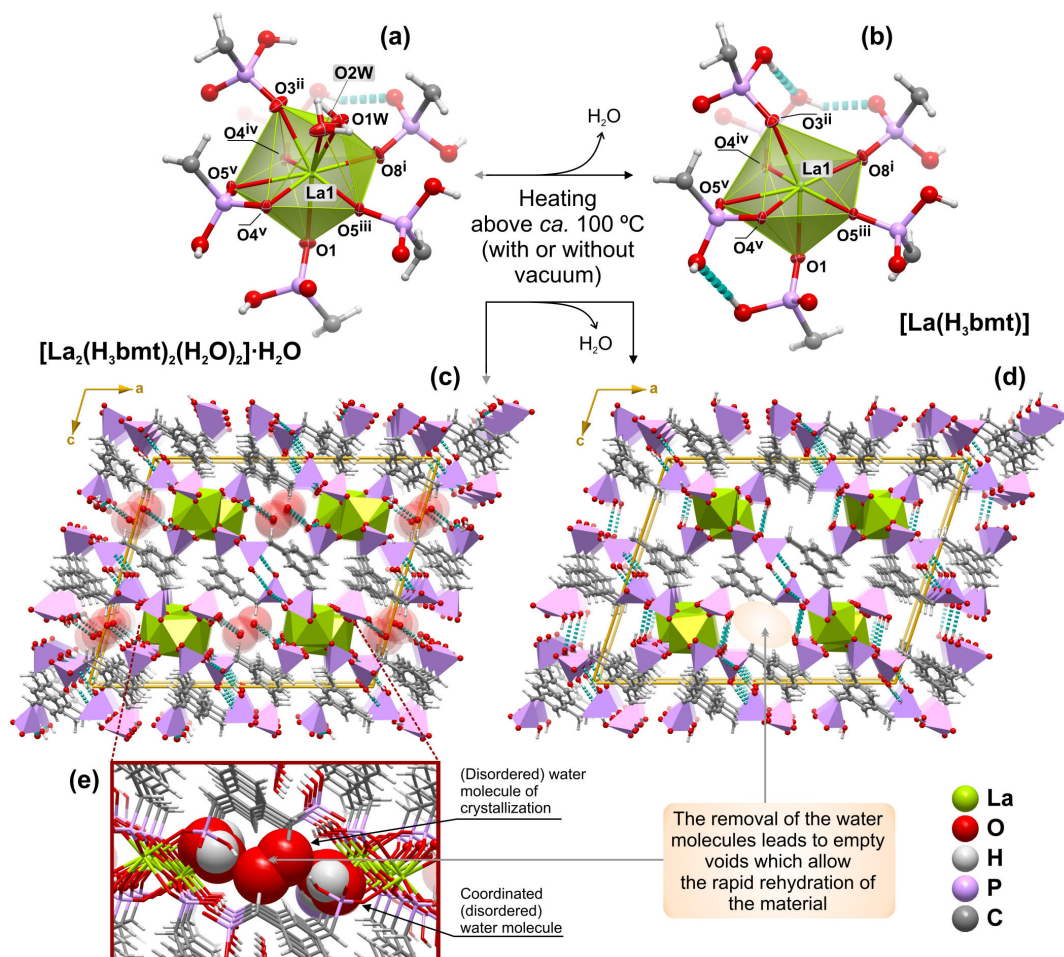


Figure 4.23 - Side by side comparison between the La^{3+} coordination environments and crystal packing features of $[\text{La}_2(\text{H}_3\text{bmt})_2(\text{H}_2\text{O})_2]\cdot\text{H}_2\text{O}$ (**20**) and $[\text{La}(\text{H}_3\text{bmt})]$ (**20-dehyd**). **(a)** and **(b)** Distorted $\{\text{LaO}_8\}$ and $\{\text{LaO}_7\}$ capped and simple pentagonal bipyramidal coordination environments present in compounds **20** and **20-dehyd**, respectively, emphasizing the location of the coordinated water molecule in the former material and the slight modifications in the local environment induced by its release. For selected bond lengths (in Å) and angles (in degrees) see Tables B.3.1 and B.3.2 in the Appendices. Symmetry transformations used to generate equivalent atoms: (i) $-\frac{1}{2}+x, -\frac{1}{2}+y, z$; (ii) $\frac{1}{2}-x, -\frac{1}{2}+y, \frac{1}{2}-z$; (iii) $\frac{1}{2}-x, 2.5-y, -z$; (iv) $\frac{1}{2}-x, 1.5-y, -z$; (v) $x, 2-y, \frac{1}{2}+z$. **(c)** and **(d)** Crystal packing of **20** and **20-dehyd** viewed in perspective along the [010] direction of the unit cell. The disordered water molecules of crystallization and those coordinated to the La^{3+} in **20** are depicted in space-filling mode (zoom perspective in **(e)**) so to better illustrate the presence of framework apertures which facilitate the removal of these moieties upon heating of the material. Hydrogen bonding interactions are shown as dashed dark green lines. For details on the geometry of the represented $\text{O}-\text{H}\cdots\text{O}$ interactions see Table B.3.3 in the Appendices.

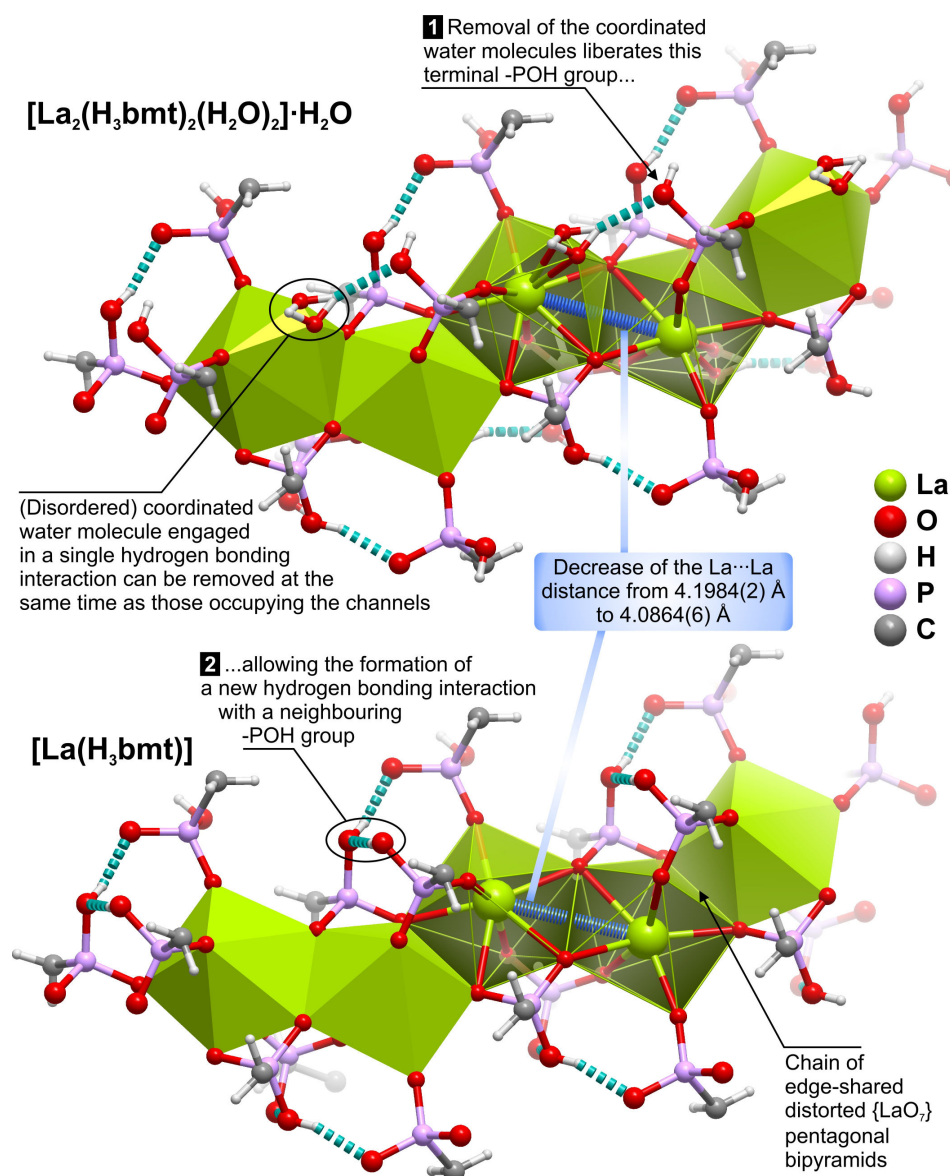


Figure 4.24 - Fragments of the crystal structures of $[\text{La}_2(\text{H}_3\text{bmt})_2(\text{H}_2\text{O})_2] \cdot \text{H}_2\text{O}$ (**20**) and $[\text{La}(\text{H}_3\text{bmt})]$ (**20-dehyd**) showing the lanthanum oxide chains formed by the edge-sharing of either $\{\text{LaO}_8\}$ or $\{\text{LaO}_7\}$ polyhedra. The representation depicts how the release of the coordinated water molecules in **20** affects the hydrogen bonding network present in the crystal structures and the inter-lanthanide distance across the zigzag chains.

The typical zeolitic-type behaviour observed for the $[\text{Ln}_2(\text{H}_3\text{bmt})_2(\text{H}_2\text{O})_2] \cdot \text{H}_2\text{O}$ materials concerning the water molecules can be rationalized taking solely into consideration the structural features of the networks. Both the coordinated and crystallization water molecules are located in hydrophilic cavities in the structure, distributed in a parallel fashion to the aforementioned lanthanum oxide chains which, under high temperatures or high vacuum, constitute an effective escape route for the solvent molecules (Figures 4.23c, 4.23d and 4.23e). This process motivates a structural modification of the lanthanum oxide chains. On the one hand, the observed intermetallic

La \cdots La distance is reduced by *ca.* 3% from 4.1984(2) Å to 4.0864(6) Å. On the other hand, the absence of the water molecules (coordinated and in the cavities), which are engaged in O–H \cdots O hydrogen bonds with the neighbouring P1 phosphonate group (Table B.3.3), induces a modification of the hydrogen bonding network: the P1–O2–H2 moiety becomes free to rotate and establish a new interaction with the neighbouring O,O-chelated P2 phosphonate group (Figure 4.24).

4.4.3. Thermogravimetry and Thermodiffraction

Bulk [Ln₂(H₃bmt)₂(H₂O)₂] \cdot H₂O materials [where Ln³⁺ = La³⁺ (**20**), Ce³⁺ (**21**), Pr³⁺ (**22**), Nd³⁺ (**23**), (La_{0.95}Eu_{0.05})³⁺ (**24**) and (La_{0.95}Tb_{0.05})³⁺ (**25**)] exhibit similar thermal stabilities with increasing temperature (thermogram for **20** given in Figure 4.25; thermograms for **21-25** are provided in Figure B.3.1 in the Appendices). In order to fully understand the structural modifications of the materials with temperature, thermodiffraction between ambient temperature and *ca.* 600 °C was performed for [La₂(H₃bmt)₂(H₂O)₂] \cdot H₂O (**20**) (Figure 4.25). We note that the results and conclusions described in the following paragraphs have only been experimentally derived for the La³⁺-based material (**20**). It is, however, feasible to assume that all members of this series should behave in a very similar fashion as, for example, concluded from the photoluminescent studies on the mixed-lanthanide materials.

Between ambient temperature and *ca.* 265 °C, **20** releases a total of 4.9% of its weight in a clear two-step fashion (peaks at 69 and 162 °C). This loss agrees well with the release of the total amount of water molecules described by the empirical formula (for 3 water molecules a theoretical weight loss of *ca.* 5.2% is estimated). As found from the crystallographic studies (see above), the structures house a total of one disordered water molecule which is readily released in a very early stage: between ambient temperature and *ca.* 130 °C there is a continuous weight loss of 1.4% corresponding to the liberation of the solvent of crystallization (calculated of *ca.* 1.7%). From the thermodiffraction studies one notes that this release induces very small modifications in the crystal structure. The second stage of solvent liberation corresponds to those that are coordinated to the La³⁺ centers (see structural details below), occurring between *ca.* 130 and 265 °C (weight loss observed 3.5%, calculated 3.4%): above *ca.* 130 °C the PXRD patterns clearly show a progressive structural modification of the material up to the *in situ* formation of the completely dehydrated form, [La(H₃bmt)] (**20-dehyd**). This framework remains structurally stable over a temperature window of about 150 °C. At *ca.* 420 °C thermal decomposition (most probably due to oxidation of the organic component) settles in, leading to the formation of an amorphous residue (Figure 4.25).

It is worth noting that the complete dehydration of **20** could be achieved by either increasing the temperature (as described above), or by placing the material under a high vacuum (as ascertained from the photoluminescence studies for the mixed-lanthanide material with Eu³⁺ - see subsection 4.4.5). The completely dehydrated

materials could readily revert to their original form with exposure to air. We note that this typical zeolitic behaviour was tested *in situ* for a number of cycles with little, or no loss, of overall crystallinity. This structural robustness was of crucial importance to isolate the completely dehydrated material and unveil its crystal structure from single-crystal X-ray diffraction studies (see above).

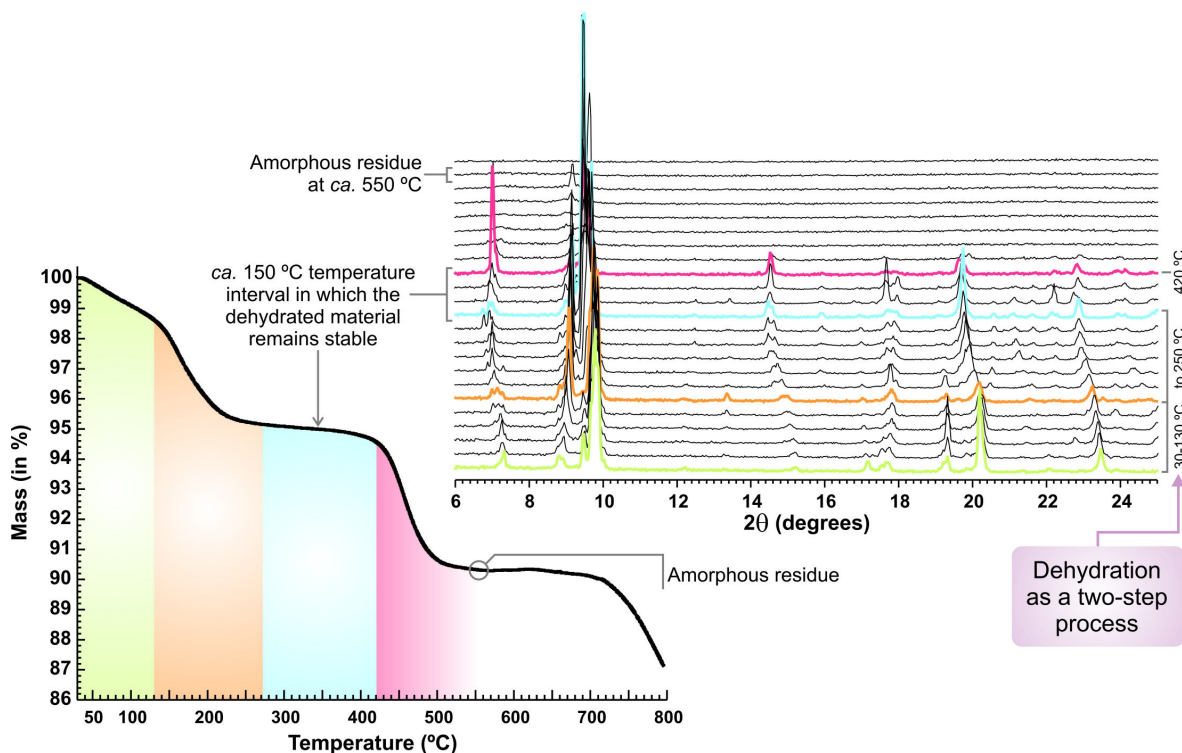


Figure 4.25 - Thermogram and variable temperature powder X-ray diffraction study of $[\text{La}_2(\text{H}_3\text{bmt})_2(\text{H}_2\text{O})_2]\cdot\text{H}_2\text{O}$ (**20**).

4.4.4. Solid-State NMR and FT-IR Spectroscopy Studies

The ^{31}P MAS spectrum of **20** shows the presence of three well-resolved isotropic resonances peaking at 15.3, 19.7 and 23.4 ppm (Figure 4.26). In addition, peak deconvolution and integration including the spinning sidebands yields a ratio of *ca.* 1.00 : 1.04 : 1.01 for these resonances. The $^{13}\text{C}\{^1\text{H}\}$ CP MAS spectrum (Figure B.3.2 in the Appendices) clearly shows two distinct spectral regions: the 29-41 ppm spectral range (peaks at: 35.4 ppm and 36.8 ppm - shoulder) is attributed to the $-\text{CH}_2-$ groups, with its deficiency of spectral resolution being simultaneously attributed to very similar chemical environments (for the three expected groups) and to the likely existence of spin multiplets arising from $^1J_{\text{C,P}}$ coupling (usually in the 5-90 Hz range);¹⁷ the aromatic carbon atoms from the ring appear in the 124-139 ppm window (peaks at: 129.4, 130.1, 133.1 and 135.7 ppm). This bulk technique clearly supports the existence of a single crystallographically unique $\text{H}_3\text{bmt}^{3-}$ organic PBU in the asymmetric unit. Additionally,

and based on the performed photoluminescence studies (see dedicated section below), the material should also contain a single independent lanthanide center. These results are in perfect agreement with the performed crystallographic studies, also indicating phase purity and homogeneity.

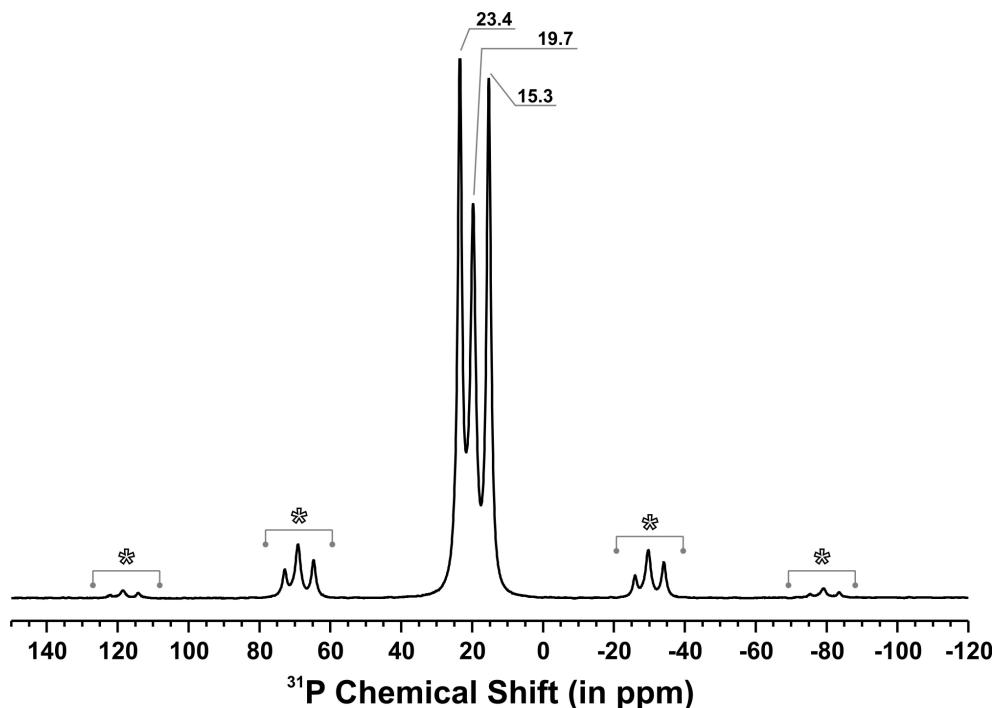


Figure 4.26 - ^{31}P HPDEC MAS spectrum of $[\text{La}_2(\text{H}_3\text{bmt})_2(\text{H}_2\text{O})_2]\cdot\text{H}_2\text{O}$ (**20**). Spinning sidebands are depicted by an asterisk. Peak deconvolution and integration throughout the entire spectral range (*i.e.*, including the spinning sidebands) gives a ratio of *ca.* 1.00 : 1.04 : 1.01 for the isotropic resonances at *ca.* 15.3, 19.7 and 23.4 ppm, respectively, which is in perfect agreement with the crystal structure determination of the same material.

As also ascertained by PXRD studies, vibrational FT-IR spectroscopy studies clearly support that bulk materials **20** to **25** are indeed isotypical (see Figure 4.27 for compound **20** and Figure B.3.3 in the Appendices for the remaining compounds **21-25**). Figure 4.27 shows the two most relevant regions of the spectra providing tentative assignments for the most diagnostic vibrational bands of compound **20**. Those present in the $3750\text{-}2500\text{ cm}^{-1}$ region arise mainly from stretching vibrations of O–H groups (from water molecules, both coordinated and of crystallization, and the PO–H groups) and –CH₂– groups. Between $350\text{ and }1700\text{ cm}^{-1}$ the spectra are significantly more complex being dominated by the vibrational modes associated with coordinated phosphonate groups, aromatic ring vibrations and the in-plane deformation of water molecules (peaking around *ca.* 1600 cm^{-1}).⁹

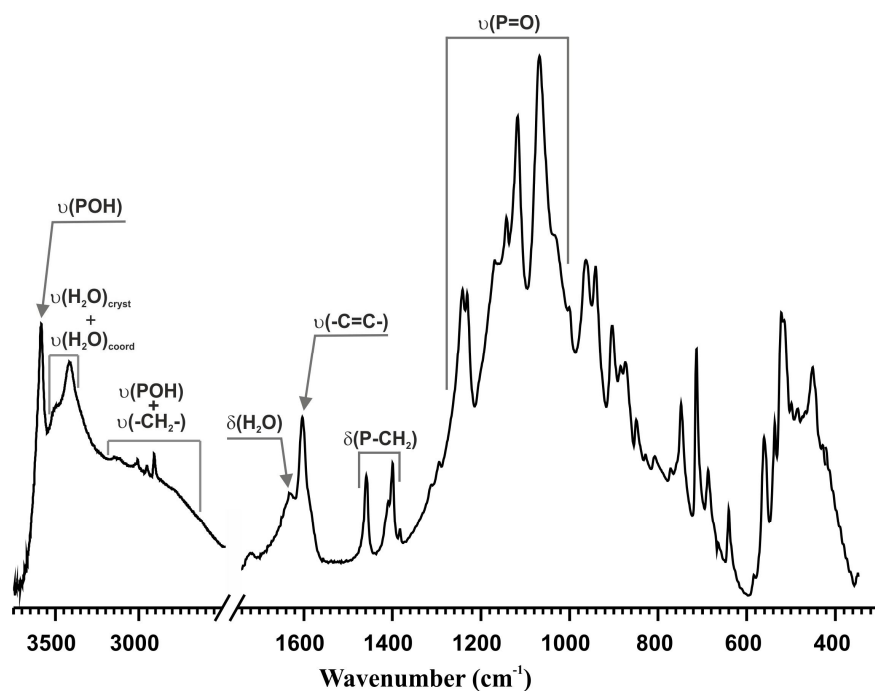


Figure 4.27 - FT-IR spectrum of the $[\text{La}_2(\text{H}_3\text{bmt})_2(\text{H}_2\text{O})_2]\cdot\text{H}_2\text{O}$ material (**20**).

4.4.5. Photoluminescence

The inclusion of optically-active lanthanide centers (such as Eu^{3+} and Tb^{3+}) into the La^{3+} matrix of compound **20** leads to the formation of new materials capable of converting UV radiation into visible light at ambient temperature as depicted in Figure 4.28 for $[(\text{La}_{0.95}\text{Eu}_{0.05})_2(\text{H}_3\text{bmt})_2(\text{H}_2\text{O})_2]\cdot\text{H}_2\text{O}$ (**24**) and $[(\text{La}_{0.95}\text{Tb}_{0.05})_2(\text{H}_3\text{bmt})_2]\cdot\text{H}_2\text{O}$ (**25**). The excitation and emission spectra, and the $^5\text{D}_4$ decay curves of **25** and its dehydrated form, $[(\text{La}_{0.95}\text{Tb}_{0.05})(\text{H}_3\text{bmt})]$ (**25-dehyd**), are provided in Figure B.3.4 in the Appendices. The following paragraphs focus the discussion only on the Eu^{3+} -containing compounds. It is also briefly discussed the photoluminescence properties of compound $[\text{La}_2(\text{H}_3\text{bmt})_2(\text{H}_2\text{O})_2]\cdot\text{H}_2\text{O}$ (**24**), which are characteristic of its organic PBUs and can only be discerned at low temperature.

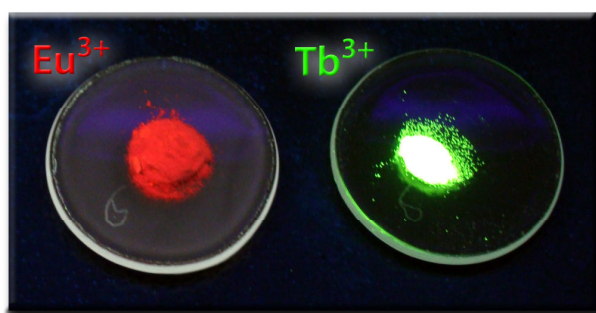


Figure 4.28 - Visible emission of the $[(\text{La}_{0.95}\text{Eu}_{0.05})_2(\text{H}_3\text{bmt})_2(\text{H}_2\text{O})_2]\cdot\text{H}_2\text{O}$ (**24**) and $[(\text{La}_{0.95}\text{Tb}_{0.05})_2(\text{H}_3\text{bmt})_2(\text{H}_2\text{O})_2]\cdot\text{H}_2\text{O}$ (**25**) materials when irradiated using a laboratory UV lamp ($\lambda = 254 \text{ nm}$).

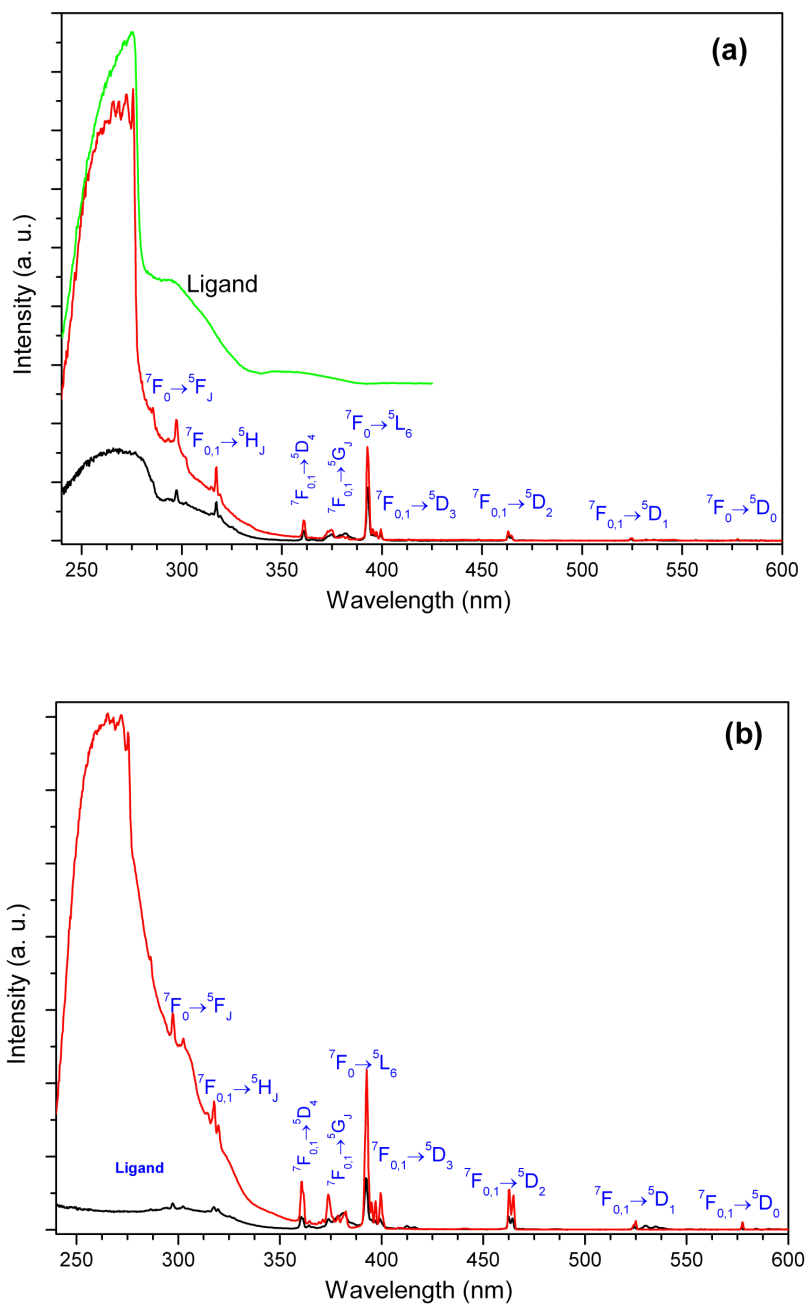


Figure 4.29 - (a) Excitation spectrum of $[\text{La}_2(\text{H}_3\text{bmt})_2(\text{H}_2\text{O})_2] \cdot \text{H}_2\text{O}$ (20) at 11 K (green line) while monitoring the emission at 445 nm, and excitation spectra of $[(\text{La}_{0.95}\text{Eu}_{0.05})_2(\text{H}_3\text{bmt})_2(\text{H}_2\text{O})_2] \cdot \text{H}_2\text{O}$ (24) at 298 (black line) and 11 K (red line) while monitoring the Eu^{3+} emission at 611.4 nm. (b) Excitation spectra of $[(\text{La}_{0.95}\text{Eu}_{0.05})(\text{H}_3\text{bmt})]$ (24-dehyd) at 298 (black line) and 11 K (red line) while monitoring the emission at 612.2 nm.

The excitation spectra of $[(\text{La}_{0.95}\text{Eu}_{0.05})_2(\text{H}_3\text{bmt})_2(\text{H}_2\text{O})_2] \cdot \text{H}_2\text{O}$ (24) was recorded at 298 and 11 K while monitoring within the $\text{Eu}^{3+} {}^5\text{D}_0 \rightarrow {}^7\text{F}_2$ transition (Figure 4.29a). Both spectra are dominated by two broad UV bands (240-288 and 288-340 nm) which may be attributed to $\pi\text{-}\pi^*$ transitions of the organic PBUs. This attribution was

confirmed recording at 11 K the excitation spectrum of **20** while monitoring the phosphorescence emission at 445 nm (Figure 4.29a). The sharp lines are assigned to the ${}^7F_{0,1} \rightarrow {}^5D_{1-4}$, 5L_6 , ${}^5G_{2-6}$, ${}^5H_{3-7}$ and ${}^5F_{1-5}$ Eu^{3+} intra- $4f^6$ transitions. A similar band assignment of the excitation spectra can be performed for the fully dehydrated form of **24**, $[(\text{La}_{0.95}\text{Eu}_{0.05})(\text{H}_3\text{bmt})]$ (**24-dehyd**) (Figure 4.29b), prepared *in situ* from the dehydration of **24** at *ca.* 450 K and under a high vacuum (*ca.* 5×10^{-6} mbar). For this latter material the intensity of the UV broad bands are significantly more distinct and the Eu^{3+} intra- $4f^6$ transitions are more noticeable, in particular the ${}^7F_0 \rightarrow {}^5D_0$ transition which is almost absent in **24**.

The emission spectra of **24** and **24-dehyd** recorded at 298 and 11 K (excited at 393 nm) are provided in Figures 4.30a and 4.30b, respectively. The sharp lines are assigned to transitions between the first excited non-degenerate 5D_0 state and the ${}^7F_{0-4}$ levels of the fundamental Eu^{3+} septet. Except for ${}^5D_0 \rightarrow {}^7F_1$, which has a predominant magnetic-dipole character independent of the Eu^{3+} crystal site, the observed transitions are mainly of electric-dipole nature. The presence of one single line for the ${}^5D_0 \rightarrow {}^7F_0$ transition and the local-field splitting of the ${}^7F_{1,2}$ levels into three and a maximum of five Stark components, respectively, and the predominance of the ${}^5D_0 \rightarrow {}^7F_2$ transition relatively to the ${}^5D_0 \rightarrow {}^7F_1$, indicates the presence of a single low-symmetry Eu^{3+} environment without inversion symmetry in both structures, as supported by the crystal structure determination (see dedicated section for details). Eu^{3+} emission is highly sensitive to small modifications on the first coordination sphere of the metal, such as the variation of the number and type of coordinated moieties. Thus, the reversible transformation of **24** into **24-dehyd**, due to the release and subsequent absorption of water molecules, can easily be accompanied by photoluminescence (Figures 4.30c and 4.30d). Under the employed experimental conditions (high vacuum), the structural change on the first coordination sphere of Eu^{3+} starts at *ca.* 350 K and is nearly complete at 400 K (Figure 4.30c). The starting form can be regenerated with subsequent exposure of the dehydrated material to air under normal ambient conditions (Figure 4.30d). We note that these temperatures are slightly distinct, but still very comparable, to those observed both in the TGA measurements and in the thermodiffraction studies (see sub-section 4.4.3). We attribute the small differences to the fact that the photoluminescence studies have been performed under vacuum, which greatly facilitates the release of all water molecules.

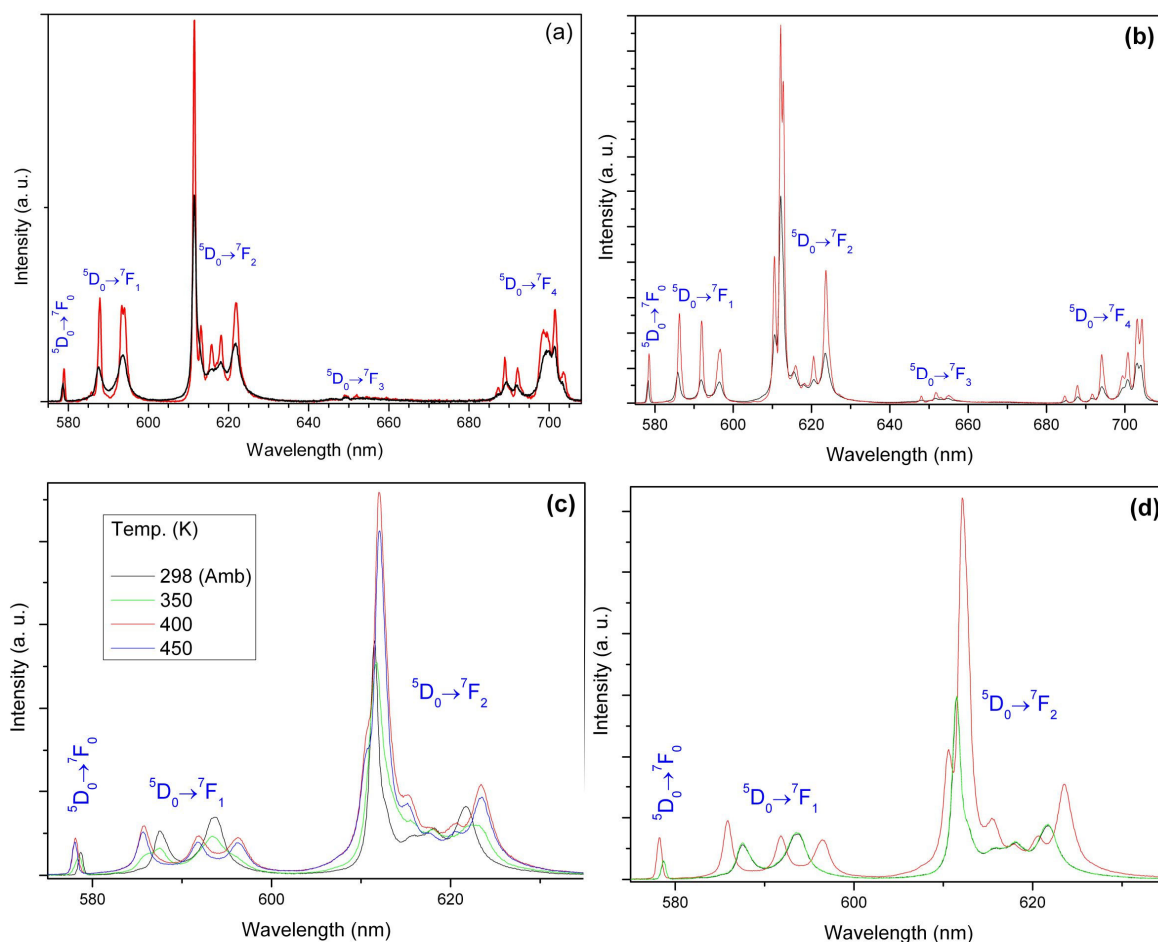


Figure 4.30 - (a and b) Emission spectra of $[(La_{0.95}Eu_{0.05})_2(H_3bmt)_2(H_2O)_2] \cdot H_2O$ (**24**) and $[(La_{0.95}Eu_{0.05})(H_3bmt)]$ (**24-dehyd**), respectively, at 298 (black line) and 11 K (red line). (c) Partial emission spectra of **24** as a function of temperature and vacuum ($\lambda_{exc} = 393$ nm): the spectrum at 298 K was recorded at ambient pressure (1 bar) and the spectra at 350, 400 and 450 K were recorded with a vacuum of *ca.* 5×10^{-6} mbar. (d) Partial emission spectra of **24** and **24-dehyd** with $\lambda_{exc} = 393$ nm (ambient temperature - 298 K): black line, **24** at ambient pressure; red line, **24** after dehydration at 450 K under a vacuum of 5×10^{-6} mbar; green line after dehydration at 450 K followed by rehydration over a period of one day at ambient conditions (temperature and pressure). *Please note*: the green and black lines are nearly perfectly overlapped.

Dehydration of **24** is accompanied by a boost in the emission efficiency of the material with a *ca.* 1.7 fold increase in the integrated emission intensity (Figure 4.30d). The ratio between the integrated intensities of the ${}^5D_0 \rightarrow {}^7F_2$ and ${}^5D_0 \rightarrow {}^7F_1$ transitions, $I_{({}^5D_0 \rightarrow {}^7F_2)} / I_{({}^5D_0 \rightarrow {}^7F_1)}$, known as the asymmetric ratio, was calculated at *ca.* 2.5 and 4.0 for **24** and **24-dehyd**, respectively. These values point to a slightly more distorted environment of the Eu^{3+} coordination polyhedron in the dehydrated material (*please note*: a low value indicates a lower distortion of local environment for Eu^{3+} , approaching to the ideal case of an inversion center). This result agrees well with the crystallographic studies: while the release of the coordinated water molecule does not

imply a considerable rearrangement of the coordination polyhedron of Eu^{3+} , it nevertheless leads to a more asymmetric environment as the bond angles to the apical positions of the pentagonal bipyramid become larger than those between the equatorially-connected atoms.

The ambient temperature (298 K) $^5\text{D}_0$ lifetime of Eu^{3+} of **24** and **24-dehyd** were determined by monitoring the emission decay curves within the maximum of the $^5\text{D}_0 \rightarrow ^7\text{F}_2$ transition, using an excitation at *ca.* 393 nm (Figure 4.31). The decay curves were fitted by single exponential functions, yielding lifetimes of 0.60 ± 0.01 and 1.60 ± 0.01 ms for **24** and **24-dehyd**, respectively. This indicates the presence of a unique Eu^{3+} crystallographic site and clearly demonstrates the improvement of the decay time (*ca.* 2.7 times) with the removal of the coordinated water molecules due to the suppression of emission quenching through the coupling of the Eu^{3+} excited states with the vibrational states of the O–H oscillators.

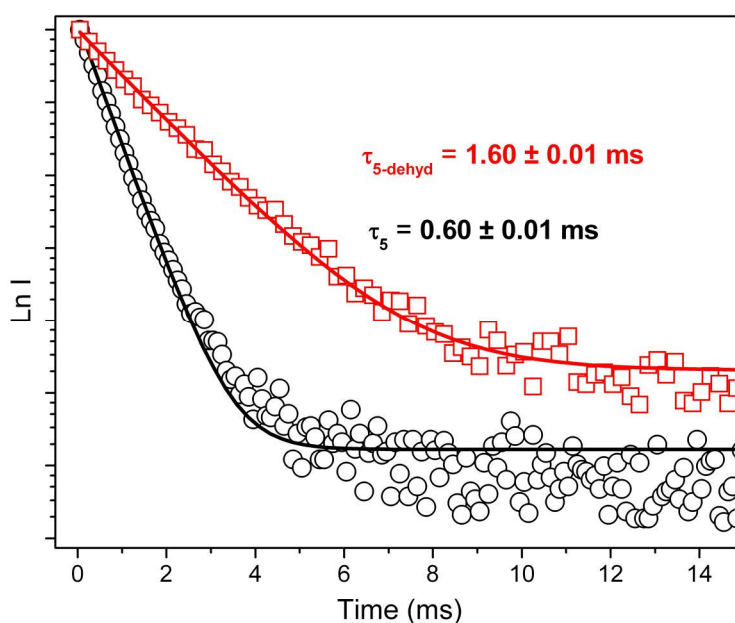


Figure 4.31 - $^5\text{D}_0$ decay curves of $[(\text{La}_{0.95}\text{Eu}_{0.05})_2(\text{H}_3\text{bmt})_2(\text{H}_2\text{O})_2] \cdot \text{H}_2\text{O}$ (**24**) (black) and $[(\text{La}_{0.95}\text{Eu}_{0.05})(\text{H}_3\text{bmt})]$ (**24-dehyd**) (red), acquired at 298 K while monitoring the emission at 611.5 and 612.1 nm, respectively. Curves were fitted by using single exponential decay functions. The excitation was performed at 393 nm.

Compounds **25** and **25-dehyd** have similar excitation spectra at ambient temperature (298 K), being dominated by the broad UV band ranging from 240 to 288 nm and attributed to the ligand excited states (Figure B.3.4 in the Appendices). The Tb^{3+} intra- $4f^8$ transitions can be readily visualized after a magnification of the spectra. The enhancement of the broad UV band on the Tb^{3+} -containing compounds when compared with the Eu^{3+} -based materials may be explained by a more efficient energy transfer from the ligands to the Tb^{3+} cations, promoted by the superposition with the interconfigurational $4f^7 5d^1$ excited states of Tb^{3+} in this region of the spectrum.¹⁸ The

impact of the dehydration process of **25** into **25-dehyd** has also been studied: although in a smaller magnitude with respect to measurable effects, the emission spectra and 5D_4 decay curves recorded at 298 K yield comparable results to those discussed above for **24** and **24-dehyd** (Figures B.3.5 and B.3.6 in the Appendices).

Based on the emission spectra, 5D_0 lifetimes and empirical radiative and non-radiative transition rates, and assuming that only non-radiative and radiative processes are involved in the depopulation of the 5D_0 state, the 5D_0 quantum efficiency, q ,¹⁰⁻¹³ has been determined for **24** and **24-dehyd**. As for compound **1**, the number of water molecules (n_w) coordinated to Eu^{3+} and Tb^{3+} may be determined using the empirical formula of Kimura & Kato,¹⁶ also in agreement with the formula of Horrocks.¹⁵ Data, including the absolute emission quantum yield (measured experimentally), are collected in Table 4.4 for compounds **24**, **24-dehyd** and **25**.

Table 4.4 - Experimental 5D_0 lifetime, τ , radiative, k_r , and non-radiative, k_{nr} , transition rates, 5D_0 quantum efficiency, q , absolute emission quantum yield, η , and the estimated number of water molecules, n_w , for $[(La_{0.95}Eu_{0.05})_2(H_3bmt)_2(H_2O)_2] \cdot H_2O$ (**24**) and $[(La_{0.95}Eu_{0.05})(H_3bmt)]$ (**25-dehyd**). The experimental 5D_4 lifetime, τ , absolute emission quantum yield, η , and the estimated number of water molecules, n_w , are also given for $[(La_{0.95}Tb_{0.05})_2(H_3bmt)_2(H_2O)_2] \cdot H_2O$ (**25**). Data have been obtained at ambient temperature (298 K).

Compound	τ [ms]	k_r [s^{-1}]	K_{nr} [s^{-1}]	q [%]	η [%] ($\lambda_{Exc.}$; nm)	n_w
24	0.60±0.01	248	1418	15	4 (280) / 1 (393)	1.12
24-dehyd	1.60±0.01	337	288	54	—	-0.02
25	1.63±0.01	—	—	—	46 (280) / 3 (376)	1.45

As expected, **24-dehyd** has a relative high quantum efficiency (54%) when compared to the as-prepared material (15%). This occurs because of a relatively low non-radiative transition rate promoted by the suppression of the O–H oscillators associated with the coordinated water molecules, and the concomitant increment of the radiative transition rate. The measured maximum absolute emission quantum yield of **24** (4% at 280 nm) is, nevertheless, far from the calculated quantum efficiency indicating that part of the absorbing light into the ligand excited levels relaxes non-radiatively and not reaching the 5D_0 emitting state. In contrast, compound **25** reaches a relatively high absolute emission quantum yield (46% at 280 nm excitation). The high absolute emission quantum yield observed for **25** must then be interpreted by a good balance between absorption, energy transfer and emission rates. Note that, as the dehydrated materials readily rehydrate at normal ambient conditions it was not possible to measure their corresponding absolute emission quantum yields.

4.4.6. Heterogeneous catalysis

The catalytic performance of $[\text{La}_2(\text{H}_3\text{bmt})_2(\text{H}_2\text{O})_2]\cdot\text{H}_2\text{O}$ (**20**) was investigated in the ring-opening reaction of styrene oxide (PhEtO) with methanol at 55 °C (see Scheme 3.1 in Chapter 3). The only reaction product is 2-methoxy-2-phenylethanol (MeOPhEtOH), which was formed in 80% yield after 24 h of reaction. Noteworthy, in the absence of the heterogeneous catalyst (but under similar reaction conditions) the conversion at 24 h was only *ca.* 10%. These results clearly show that **20** exhibits activity and excellent regioselectivity in the methanolysis of PhEtO to the β -alkoxy alcohol product.

For comparative purposes the PBUs (organic linker and the lanthanide precursor) were also tested under similar reaction conditions as (homogeneous) catalysts (using amounts equivalent to those in the loaded MOF catalyst) in the methanolysis of PhEtO. In the case of the ligand **H₆bmt**, MeOPhEtOH was formed in quantitative yields within 1 h of reaction, indicating that the organic PBU is a highly active and selective homogeneous Brønsted acid organocatalyst (Table 4.5). When the lanthanide precursor ($\text{LaCl}_3\cdot 7\text{H}_2\text{O}$) was employed as the catalyst, MeOPhEtOH was produced in 71% yield at 24 h reaction (93% selectivity).

Table 4.5 - Ring-opening reaction of styrene oxide with methanol at 55 °C.^a

Catalyst	Reaction Time (h)	Conversion ^b (%)	Selectivity ^c (%)
none	24	10	100
H₆bmt	1	100	100
$\text{LaCl}_3\cdot 7\text{H}_2\text{O}$	4 / 24	27 / 71	93 / 93
20	4 / 24	10 / 80	100

^a Reaction conditions: PhEtO (0.41 mmol), catalyst (20 mg), alcohol (1 mL).

^b Conversion of PhEtO.

^c Selectivity to MeOPhEtOH.

The recyclability of the catalyst **20** was investigated for three consecutive batch runs in the reaction of PhEtO with methanol at 55 °C. Prior to reuse, the solid catalyst was separated from the reaction mixture by centrifugation, washed with *n*-hexane and dried overnight at ambient temperature. In all runs MeOPhEtOH was always the only reaction product and no decrease in catalytic activity was observed (Figure 4.32). On the contrary, it was observed an increase in the reaction rate from the first to subsequent runs, most likely due to an increase in the number of effective active sites. Structural

integrity of the catalyst after the first and the third runs was investigated using PXRD and electron microscopy (Figure 4.33). These studies clearly show that despite the large crystals of the as-prepared catalyst **20** were fragmented during the catalytic process (which may result in an enhanced amount of effective active sites) leading to a small loss of overall crystallinity, the framework of the material remained intact.

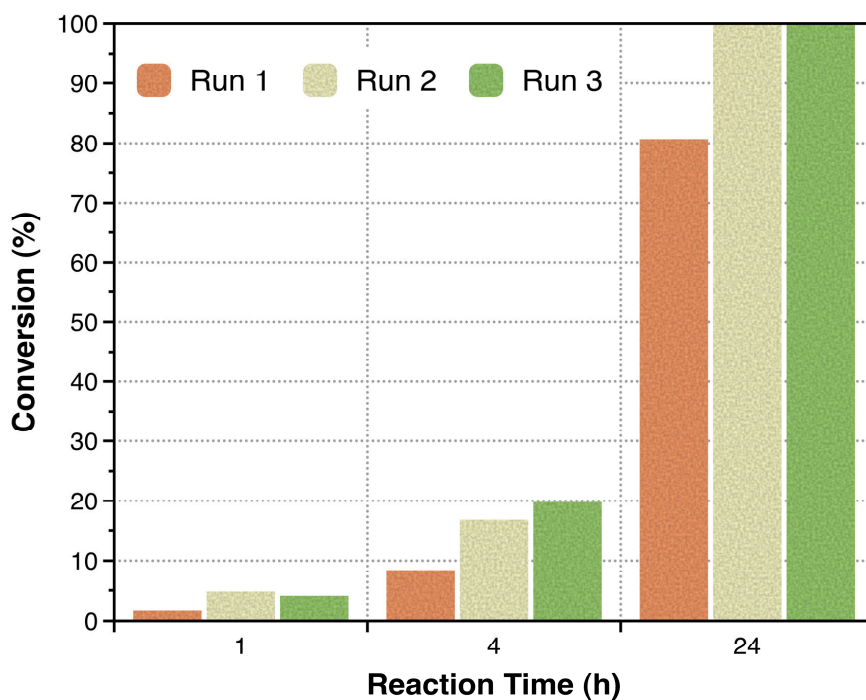


Figure 4.32 - Catalytic performance of compound $[\text{La}_2(\text{H}_3\text{bmt})_2(\text{H}_2\text{O})_2] \cdot \text{H}_2\text{O}$ (**20**) in three consecutive batch runs of the reaction of styrene oxide using methanol at 55 °C.

In order to get a better insight on the hetero/homogeneous nature of the catalytic reaction a leaching test was performed for **20** which consisted in filtering the used catalyst (through a 0.20 μm nylon GVS membrane) after 4 h reaction, at 55 °C, and leaving the reaction solution under magnetic stirring for further 20 h. The ratio of the increment in conversion in the period of time 4-24 h of the leaching test to that for the reaction without catalyst is equal to 1, indicating that the catalytic reaction is heterogeneous in nature.

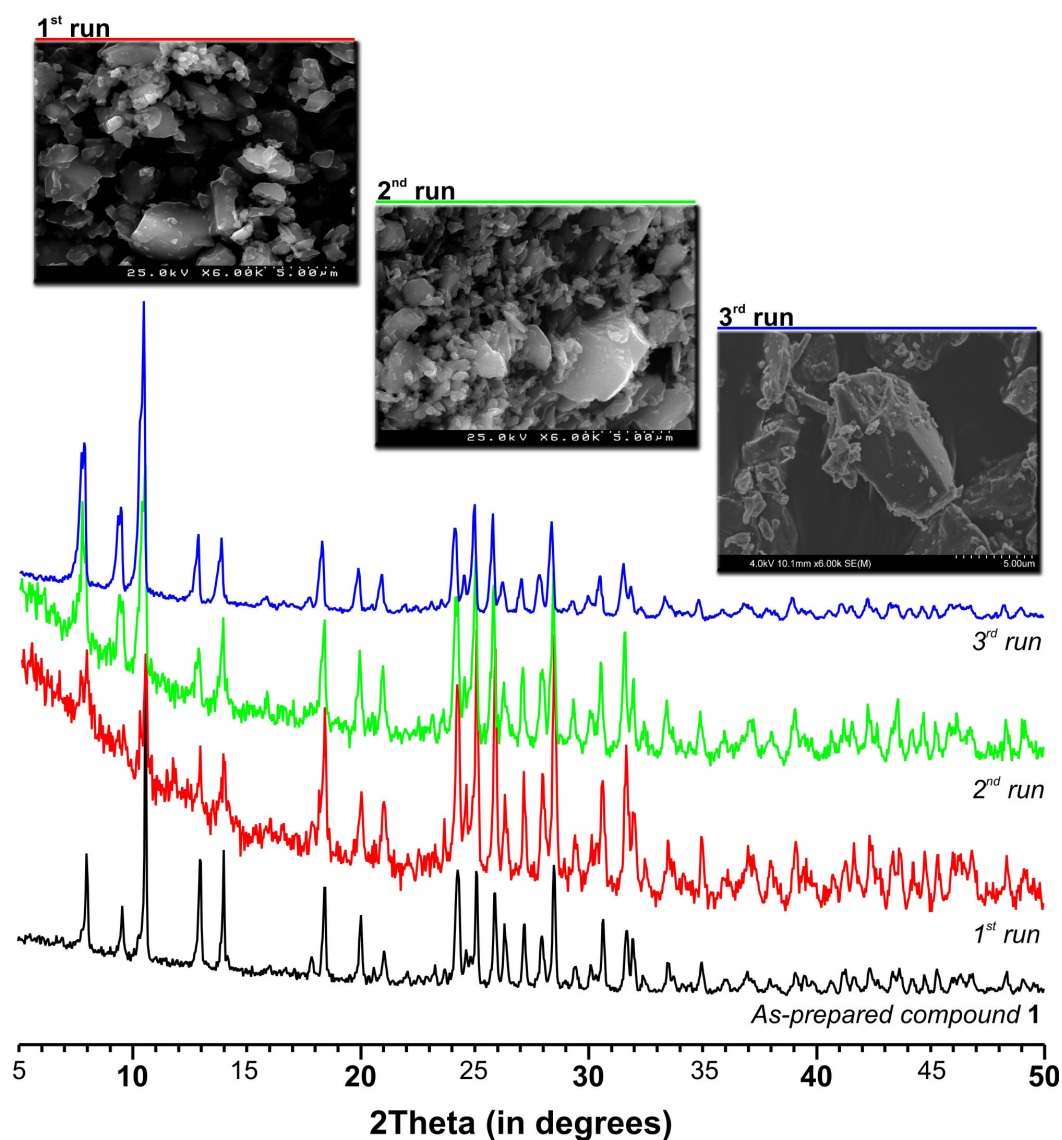


Figure 4.33 - SEM images and PXRDs of the recovered $[\text{La}_2(\text{H}_3\text{bmt})_2(\text{H}_2\text{O})_2]\cdot\text{H}_2\text{O}$ (**20**) catalyst after each batch run. Results indicate that the crystal structure of the material remains unaltered throughout the catalytic tests. For comparative purposes the PXRD pattern of the bulk material **20** is also depicted. *Please note*: the distinct signal-to-noise ratios of the PXRD patterns are a consequence of distinct acquisition periods.

4.5. Results and Discussion

The self-assembly between the tripodal organic ligand **H₆bmt** and lanthanide cations, with the exception of lutetium, successfully produced three different families of multidimensional MOFs:

- i) 1D $[\text{Ln}(\text{H}_4\text{bmt})(\text{H}_5\text{bmt})(\text{H}_2\text{O})_2]\cdot 3\text{H}_2\text{O}$ materials [where $\text{Ln}^{3+} = \text{La}^{3+}$ (**9**), $(\text{La}_{0.97}\text{Eu}_{0.03})^{3+}$ (**10**) and $(\text{La}_{0.97}\text{Tb}_{0.03})^{3+}$ (**11**)];

- ii) 2D layered $[\text{Ln}_2(\text{H}_3\text{bmt})_2]\cdot\text{H}_2\text{O}$ materials [where $\text{Ln}^{3+} = \text{Eu}^{3+}$ (**12**), Gd^{3+} (**13**), Tb^{3+} (**14**), Dy^{3+} (**15**), Ho^{3+} (**16**), Er^{3+} (**17**), Tm^{3+} (**18**) and Yb^{3+} (**19**)];
- iii) 3D $[\text{Ln}_2(\text{H}_3\text{dmt})_2(\text{H}_2\text{O})_2]\cdot\text{H}_2\text{O}$ materials [where $\text{Ln}^{3+} = \text{La}^{3+}$ (**20**), Ce^{3+} (**21**), Pr^{3+} (**22**), Nd^{3+} (**23**), $(\text{La}_{0.95}\text{Eu}_{0.05})^{3+}$ (**24**) and $(\text{La}_{0.95}\text{Tb}_{0.05})^{3+}$ (**25**)].

The crystalline structure of all compounds were unveiled by single-crystal or powder X-ray diffraction studies, and bulk materials were fully characterized using standard solid-state techniques (FT-IR, electron microscopy, solid-state NMR, thermogravimetric and elemental analysis).

Conventional hydrothermal synthesis (180 °C for 72 h) was found to be an efficient synthetic approach for the isolation of the 2D and 3D families of materials as microcrystalline powders or large single-crystals, respectively. It was discovered that temperatures as low as 100 °C also seem to lead to the isolation of the 3D MOFs, with large particle size and in periods of time varying between 1 and 3 days. The MWAS approach was ideal to isolate isotypical 1D compounds at mild reaction conditions (40 °C for 5 minutes). Remarkably, under microwave irradiation, compound **20** could also be prepared. Nevertheless, in this situation the employed temperature was found to be a crucial parameter in the self-assembly process: for 5 minutes of reaction time, phase-pure materials can only be isolated for temperatures greater than 150 °C. These results clearly indicate that by systematically investigating the synthesis of these isotypical systems of LnOFs it might be possible to derive optimal conditions to isolate them in the shortest possible period of time. Moreover, and based on investigations in the use of microwave irradiation performed by the MOF research group at the University of Aveiro,¹⁹ it might even be possible to either control the crystal morphology or size, or even both, or even find new functional materials. The studies led to the conclusion that these materials can indeed be isolated under very mild conditions, with this fact clearly constituting an attractive option for eventual large-scale preparations (reduced energy consumption and operation costs).

From single-crystal X-ray diffraction studies, it was found that $[\text{Ln}_2(\text{H}_3\text{bmt})_2(\text{H}_2\text{O})_2]\cdot\text{H}_2\text{O}$ materials are 3D MOFs, built-up on a single crystallographically independent lanthanide center, trapping solvent water molecules (both of crystallization and coordinated to the lanthanide center). As expected, the anionic $\text{H}_3\text{bmt}^{3-}$ linker was found to be a rather robust organic PBU, leading to materials which exhibit a typical zeolitic behaviour: by heating or applying a high vacuum, all water molecules could be reversibly removed from the structures; this process was shown to occur without loss of crystallinity or considerable structural modifications. These features are supported by VT-XRD studies, which showed that the release of both coordinated and uncoordinated water molecules only induces very small modifications in the crystal structure of the $[\text{Ln}_2(\text{H}_3\text{bmt})_2(\text{H}_2\text{O})_2]\cdot\text{H}_2\text{O}$ materials. The dehydrated form of these compounds maintains the stability and thermal robustness up to around 400 °C. A drastic different behaviour was described for the 1D $[\text{Ln}(\text{H}_4\text{bmt})(\text{H}_3\text{bmt})(\text{H}_2\text{O})_2]\cdot 3\text{H}_2\text{O}$ materials that exhibited comparatively very poor

thermal stability. The release of the five water molecules (two coordinated and three of crystallization) promotes structural modifications. Although not completely solved at this stage, the structure of the 2D layered $[\text{Ln}_2(\text{H}_3\text{bmt})_2]\cdot\text{H}_2\text{O}$ materials showed remarkable thermal stability up to *ca.* 370 °C. For this family of materials, dehydration did not lead to structural modifications.

Another interesting feature found in the $[\text{Ln}_2(\text{H}_3\text{bmt})_2]\cdot\text{H}_2\text{O}$ materials is related to their particle sizes. The inclusion of lanthanide cations with higher atomic numbers (*i.e.*, smaller ionic radii) led to a drastic reduction in the average particle size, being this effect more noticeable in the Yb^{3+} -based compound. In the literature some reports have described that the lanthanide contraction may affect the geometry and the overall architecture of the materials.²⁰⁻²² Nevertheless, to present it seems that this system constitutes the first time for which this effect of the lanthanide contraction in the particle size is fully described. The properties of $[\text{Ln}_2(\text{H}_3\text{bmt})_2]\cdot\text{H}_2\text{O}$ materials are currently unexplored. However, as described for compound **1n** (reported in Chapter 3) the decrease of the crystal size in the materials may lead to an improvement in their catalytic behavior.

The zeolitic behaviour described for the $[\text{Ln}_2(\text{H}_3\text{bmt})_2(\text{H}_2\text{O})_2]\cdot\text{H}_2\text{O}$ materials has important consequences in the observed photoluminescent properties. Firstly, the removal of the water molecules for the Eu^{3+} -based material leads to a concomitant increase of the quantum efficiency from *ca.* 15% (for the as-prepared compound) to *ca.* 54%. Secondly, the Tb^{3+} compound shows the remarkable absolute emission quantum yield of *ca.* 46% (at 280 nm excitation) reflecting a good balance between absorption, energy transfer and emission rates. Similar behaviour was found for the Tb^{3+} -based material **11** showing an absolute quantum yield of 44%. Conversely, the Eu^{3+} -based material **10** has an absolute quantum yield of only 5%.

The catalytic performance of the La^{3+} -based materials **9** and **20** were tested in the ring-opening reaction of styrene oxide with methanol. Results suggest that: i) both materials act as truly heterogeneous catalysts; ii) excellent regioselectivity towards 2-methoxy-2-phenylethanol is observed, with this compound being always the sole reaction product; iii) catalysts can be recycled by simple and efficient regeneration processes; iv) the activity of **20** increases with the catalytic runs without a significant loss of crystallinity or modification of the crystal structure. Noteworthy, compound **9** showed an outstanding catalytic activity compared to **20**. While **9** converts 100% of styrene oxide in only 30 min, **20** takes 24 h to convert 80%. This remarkable activity is related with the active sites of **9** that are likely of Brønsted-type (associated with its organic component). It is worth mentioning that the very active organocatalyst **H₆bmt** ligand catalyses in an homogeneous fashion, posing significant experimental drawbacks which can be overcome by using the heterogeneous catalyst **9**.

4.6. References

- (1) Jaffres, P. A.; Villemin, D.; Montouillout, V.; Fernandez, C.; Chardon, J.; Santos, J. S. D.; *Mol. Cryst. Liq. Cryst.*, **2002**, *389*, 87-95.
- (2) Zon, J.; Kong, D. Y.; Gagnon, K.; Perry, H.; Holliness, L.; Clearfield, A.; *Dalton Trans.*, **2010**, *39*, 11008-11018.
- (3) Yang, C. I.; Song, Y. T.; Yeh, Y. J.; Liu, Y. H.; Tseng, T. W.; Lu, K. L.; *CrystEngComm*, **2011**, *13*, 2678-2686.
- (4) Tang, S. F.; Pan, X. B.; Lv, X. X.; Yan, S. H.; Xu, X. R.; Li, L. J.; Zhao, X. B.; *CrystEngComm*, **2013**, *15*, 1860-1873.
- (5) Vilela, S. M. F.; Firmino, A. D. G.; Mendes, R. F.; Fernandes, J. A.; Ananias, D.; Valente, A. A.; Ott, H.; Carlos, L. D.; Rocha, J.; Tomé, J. P. C.; Almeida Paz, F. A.; *Chem. Commun.*, **2013**, *49*, 6400-6402.
- (6) Vilela, S. M. F.; Ananias, D.; Gomes, A. C.; Valente, A. A.; Carlos, L. D.; Cavaleiro, J. A. S.; Rocha, J.; Tomé, J. P. C.; Almeida Paz, F. A.; *J. Mater. Chem.*, **2012**, *22*, 18354-18371.
- (7) Grell, J.; Bernstein, J.; Tinhofer, G.; *Acta Cryst. B*, **1999**, *55*, 1030-1043.
- (8) Silva, P.; Vieira, F.; Gomes, A. C.; Ananias, D.; Fernandes, J. A.; Bruno, S. M.; Soares, R.; Valente, A. A.; Rocha, J.; Paz, F. A. A.; *J. Am. Chem. Soc.*, **2011**, *133*, 15120-15138.
- (9) Socrates, G. *Infrared and Raman Characteristic Group Frequencies: Tables and Charts*; 2nd ed.; John Wiley & Sons Ltd: Baffins Lane, Chichester, 1994.
- (10) Werts, M. H. V.; Jukes, R. T. F.; Verhoeven, J. W.; *Phys. Chem. Chem. Phys.*, **2002**, *4*, 1542-1548.
- (11) Carlos, L. D.; Messaddeq, Y.; Brito, H. F.; Ferreira, R. A. S.; Bermudez, V. D.; Ribeiro, S. J. L.; *Adv. Mater.*, **2000**, *12*, 594-598.
- (12) Malta, O. L.; Brito, H. F.; Menezes, J. F. S.; Silva, F.; Alves, S.; Farias, F. S.; de Andrade, A. V. M.; *J. Lumin.*, **1997**, *75*, 255-268.
- (13) Malta, O. L.; dos Santos, M. A. C.; Thompson, L. C.; Ito, N. K.; *J. Lumin.*, **1996**, *69*, 77-84.
- (14) Hazenkamp, M. F.; Blasse, G.; *Chem. Mater.*, **1990**, *2*, 105-110.
- (15) Supkowski, R. M.; Horrocks, W. D.; *Inorg. Chim. Acta*, **2002**, *340*, 44-48.
- (16) Kimura, T.; Kato, Y.; *J. Alloys Compd.*, **1995**, *225*, 284-287.
- (17) Ben Akacha, A.; Barkallah, S.; Zantour, H.; *Magn. Reson. Chem.*, **1999**, *37*, 916-920.
- (18) Ananias, D.; Kostova, M.; Paz, F. A. A.; Ferreira, A.; Carlos, L. D.; Klinowski, J.; Rocha, J.; *J. Am. Chem. Soc.*, **2004**, *126*, 10410-10417.
- (19) Klinowski, J.; Paz, F. A. A.; Silva, P.; Rocha, J.; *Dalton Trans.*, **2011**, *40*, 321-330.
- (20) Sun, X. L.; Shen, B. X.; Zang, S. Q.; Du, C. X.; *CrystEngComm*, **2013**, *15*, 5910-5918.

- (21) Gao, J. Y.; Xiong, X. H.; Chen, C. J.; Xie, W. P.; Ran, X. R.; Yue, S. T.; Liu, Y. L.; Cai, Y. P.; *Inorg. Chem. Commun.*, **2013**, *31*, 5-12.
- (22) He, Z.; Gao, E. Q.; Wang, Z. M.; Yan, C. H.; Kurmoo, M.; *Inorg. Chem.*, **2005**, *44*, 862-874.

Chapter 5

Layered Lanthanide-Organic Frameworks Based on ((2,4,6-Trifluorobenzene-1,3,5-triyl)tris-(methylene))triphosphonic acid

5.1. Initial Considerations

Although not very common, perfluorinated or partially fluorinated organic linkers in which the hydrogen atoms are replaced by fluorine or $-\text{CF}_3$ groups have already been used in the preparation of functional MOFs.¹⁻⁹ Compared with non-fluorinated, fluorinated MOFs have shown to enhance the hydrophobicity, increase structural stability in water or moisture atmospheres, and even to improve the photoluminescent properties.^{7,10-11} Additionally, the presence of fluorine atoms as constituent of the organic molecules may lead to the formation of $\text{F}\cdots\text{F}$ interactions, helping in the stabilization of the resulting networks.^{5,12}

Fully or partially fluorinated MOFs have been studied, mainly, as potential materials for application in adsorption processes,^{3,8-9} and luminescent devices.¹³⁻¹⁴ The research group of Omary reported the synthesis of totally fluorinated MOFs, coined as FMOF-1 and FMOF-2, from the combination of Ag^+ with 3,5-bis(trifluoromethyl)-1,2,4-triazolate.^{10,15-16} The hydrophobic character of FMOF-1 is the main responsible for the observed efficient selective adsorption ability of aliphatic and aromatic oil components (benzene, toluene, *p*-xylene, cyclohexane and *n*-hexane), while preventing the entrance of water molecules in their pores. In 2006 Chen *et al.* isolated two Er^{3+} -organic frameworks, $[\text{Er}_2(\text{bdc})_3(\text{DMF})_2(\text{H}_2\text{O})_2]\cdot\text{H}_2\text{O}$ and $[\text{Er}_2(\text{bdc-F}_4)_3(\text{DMF})(\text{H}_2\text{O})]\cdot\text{DMF}$, by using the organic linkers 1,4-benzenedicarboxylate (H_2bdc) and its fluorinated analogue 2,3,5,6-tetrafluoro-1,4-benzenedicarboxylate ($\text{H}_2\text{bdc-F}_4$), respectively.¹⁴ In this comparative study the authors showed that the replacement of the C-H fluorescence quencher by C-F groups improves significantly (approximately three times) the near-infrared luminescence properties. Noteworthy, the use of fluorinated organic molecules does not, however, ensure just by itself an improvement in the desired properties of the resulting material. A striking example concerns the work reported by Banerjee's group on a handful of fluorinated and non-fluorinated MOFs. The results showed that it is difficult to evaluate the influence of the fluorination on the H_2 and CO_2 adsorption.¹⁻²

Optically-active lanthanide- (or mixed-lanthanide)-based compounds have found potential applications in the fabrication of sensing devices.¹⁷⁻¹⁹ As described in Chapters 3 and 4, the MOF research group at the University of Aveiro has been interested in the preparation of luminescent Lanthanide-Organic Frameworks (LnOFs). Following this line of research, a novel fluorinated tripodal organic ligand ((2,4,6-trifluorobenzene-1,3,5-triyl)tris(methylene)triphosphonic acid (**H₆tftp**) was designed and prepared in a simple three-step reaction procedure (Scheme 2.6). This molecule is a structural analogue of (benzene-1,3,5-triyl)tris(methylene)triphosphonic acid (**H₆bmt**) whose MOF structures were described in Chapter 2. **H₆tftp** was self-assembled with lanthanide cations under hydrothermal conditions to produce a new family of isotypical LnOFs, formulated as $[\text{Ln}(\text{H}_3\text{tftp})(\text{H}_2\text{O})]$ [where $\text{Ln}^{3+} = \text{La}^{3+}$ (**26**), $(\text{La}_{0.95}\text{Eu}_{0.05})^{3+}$ (**27**), $(\text{La}_{0.95}\text{Tb}_{0.05})^{3+}$ (**28**).²⁰ The crystal structure of **26**, isolated as large single-crystals, was unveiled by single-crystal X-ray diffraction and consists of neutral $\infty^2[\text{La}(\text{H}_3\text{tftp})(\text{H}_2\text{O})]$ layers. All materials were fully characterized by standard solid-state techniques (powder X-ray diffraction, FT-IR, electron

microscopy (SEM and EDS), solid-state NMR, thermogravimetric and elemental analysis). The photoluminescent properties of the compounds **27** and **28** were investigated.

5.2. Strategy

The presence of O-H, C-H and/or N-H groups (usually belonging to solvents molecules, such as water and the most common organic solvents, or organic linkers) in the close proximity of lanthanide centers quench their photoluminescence properties through non-radiative processes.^{14,21-23} An alternative option to circumvent this limitation would be to suppress the presence of such oscillator groups. Reduction/elimination of the quenching effect can also be achieved from the deuteration of O-H (as described in Chapter 3) and C-H groups, or by replacing C-H for C-F bonds in the organic molecules. Having in mind this idea, the trifluorinated **H₆tftp** organic molecule was designed and prepared.

Due to the structure similarity between **H₆tftp** and **H₆bmt** it is aimed at the preparation of MOFs sharing the same crystalline structure of the 1D, 2D or 3D compounds reported in Chapter 4. It is also suggested a comparative study of the photoluminescent properties between the optically-active MOF materials isolated by using **H₆tftp** and **H₆bmt**.

5.3. Synthesis

5.3.1. Hydrothermal Synthesis of isotypical [Ln(H₃tftp)(H₂O)] materials

The self-assembly between the new tripodal organic ligand **H₆tftp** and lanthanide (III) chloride hydrates, under hydrothermal conditions (180 °C for 72 h), afforded a new family of MOF structures composed of three isotypical materials formulated as [Ln(H₃tftp)(H₂O)] [where Ln³⁺ = La³⁺ (**26**), (La_{0.95}Eu_{0.05})³⁺ (**27**) and (La_{0.95}Tb_{0.05})³⁺ (**28**)] (see sub-section 8.12.1 in the Experimental Section for further details). Compound **26** was the only one that could be isolated with suitable particle size to be investigated by single-crystal X-ray diffraction. Phase identification of the mixed-lanthanide materials **27** and **28** as microcrystalline powders was performed using powder X-ray diffraction.

Figure 5.1 shows the PXRD patterns and SEM images of all materials. PXRD patterns indicate that compounds are crystalline and share the same crystalline phase. Concerning morphology it is clear that all compounds have the same crystal habit based on block-like crystals. A notable feature stands out: compound **26** possesses crystalline block-like particles with sizes in the tens of micrometers; the inclusion of 5% of Eu³⁺ or Tb³⁺ leads to a reduction of the average particle size of **27** and **28**, with this feature being significantly more evident in the latter material.

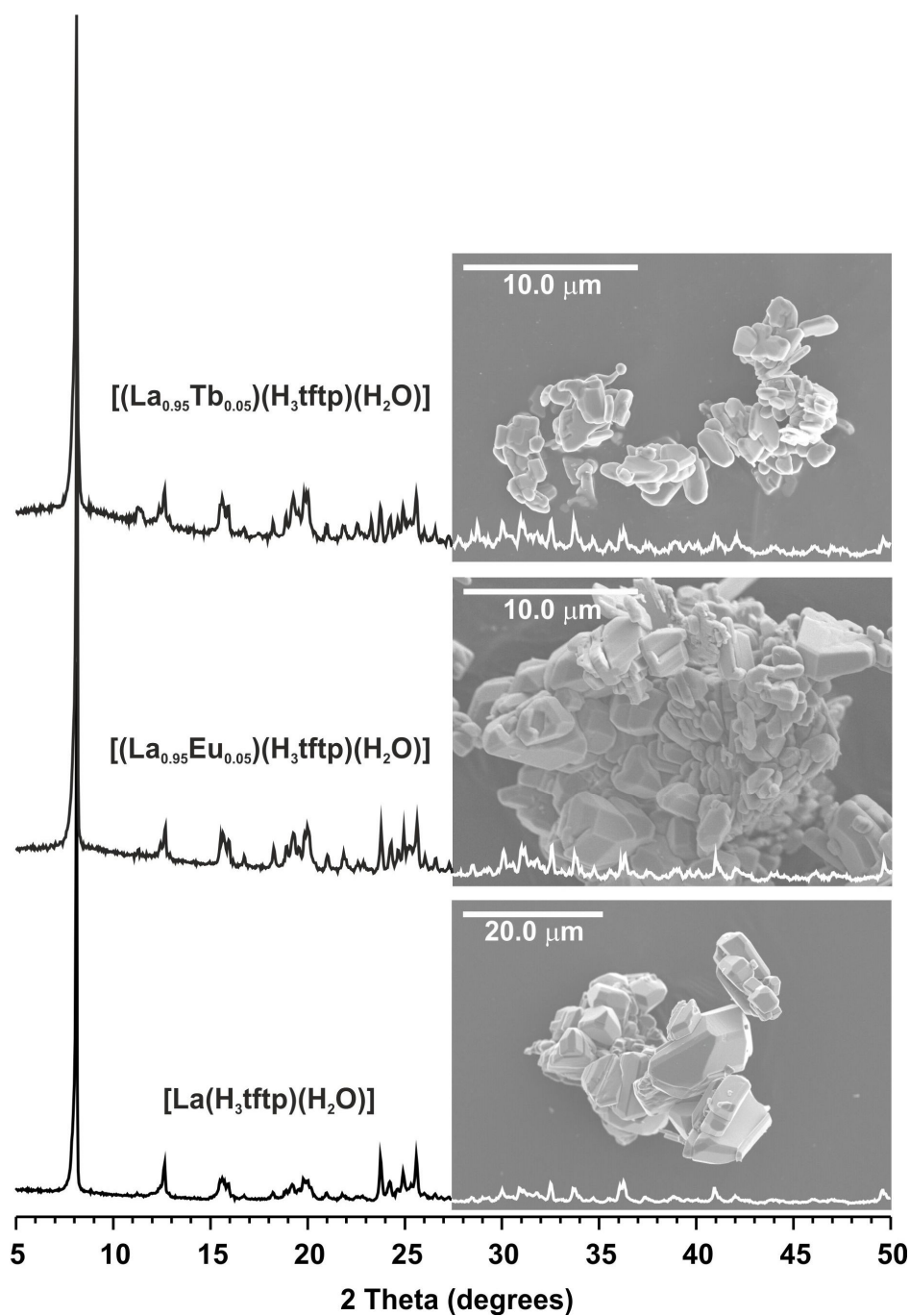


Figure 5.1 - PXRD patterns and SEM images of compounds **26**, **27** and **28** prepared (under hydrothermal conditions) at 180 °C for 72 h.

In addition, the use of stoichiometric amounts of different lanthanides in the initial reactive mixtures leads to isotypical materials having a random distribution of the metallic centers throughout the framework. This evidence is supported from EDS mapping studies for the mixed-lanthanide materials **27** and **28** (Figures 5.2 and 5.3).

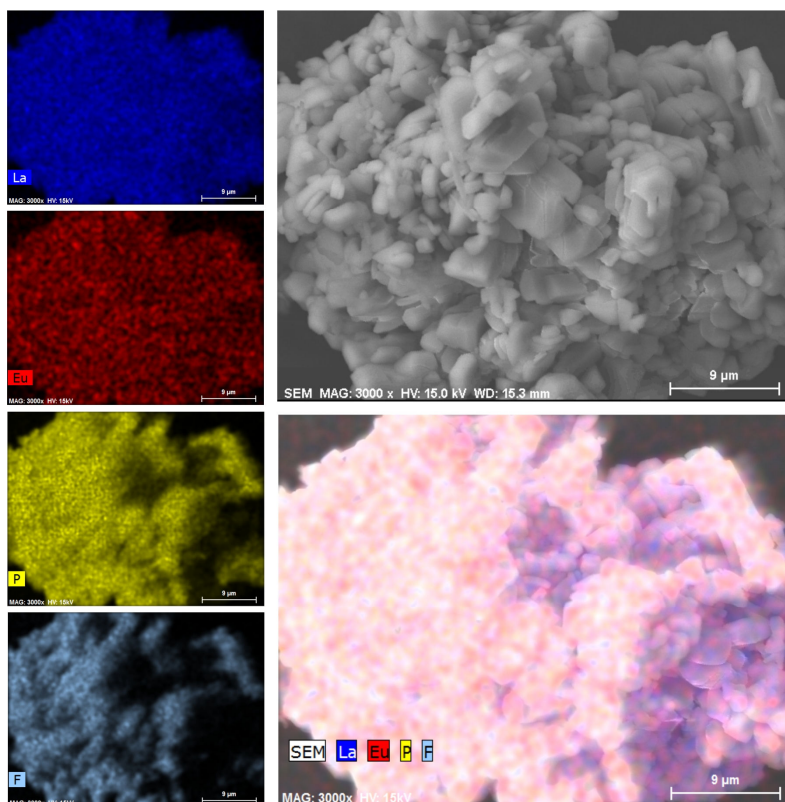


Figure 5.2 - Electron microscopy EDS mapping studies of a portion of the mixed-lanthanide material $[(\text{La}_{0.95}\text{Eu}_{0.05})(\text{H}_3\text{tftp})(\text{H}_2\text{O})]$ (**27**).

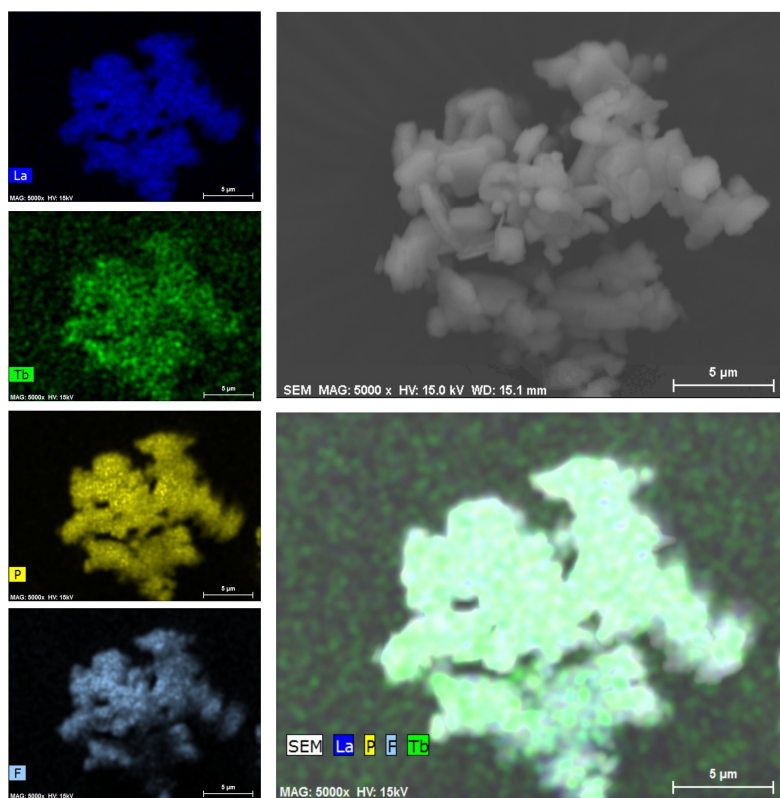


Figure 5.3 - Electron microscopy EDS mapping studies of a portion of the mixed-lanthanide material $[(\text{La}_{0.95}\text{Tb}_{0.05})(\text{H}_3\text{tftp})(\text{H}_2\text{O})]$ (**28**).

5.3.2. Isolation of large single-crystals of isotypical [Ln(H₃tftp)(H₂O)] materials

The procedure to isolate compound **26** as large single-crystals is similar to that described in the previous sub-section with slight modifications. Reactive mixtures composed of the new tripodal organic ligand **H₆tftp** and LaCl₃·7H₂O in distilled water were prepared. A few drops of an aqueous solution of HCl (6 M) were added. The reaction mixture was kept at 180 °C during 72 h (see dedicated Experimental Section for further details).

The isolated material was characterized by PXRD, unequivocally confirming that this material share the same crystalline phase with compound **26**, and electron microscopy. Figure 5.4 shows a SEM image of compound **26** evidencing the presence of large single crystals. The addition of some drops of HCl (6 M) led to a substantial increase (from approximately 20 to *ca.* 100 μm) of the particle size of **26**.

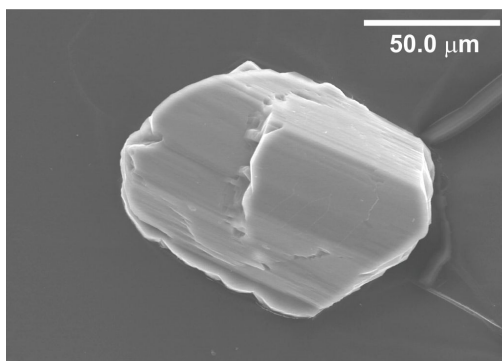


Figure 5.4 - SEM image of compound **26** prepared from a reactive mixture to which a few drops of an aqueous solution of HCl (6 M) were added.

5.4. Crystal Structure Description of [La(H₃tftp)(H₂O)]

The self-assembly between the tripodal trifluorinated **H₆tftp** organic ligand and LaCl₃·7H₂O under hydrothermal conditions produced compound [La(H₃tftp)(H₂O)] (**26**). Large crystals were directly harvested from the reaction vessels and studied by single-crystal X-ray diffraction. Compound **26** crystallizes in the centrosymmetric triclinic *P*₁ space group (see sub-section 8.12.1 in the Experimental Section for further details). The asymmetric unit is composed of two La³⁺ metal centers, two whole (H₃tftp)³⁻ residues and two coordinated water molecules.

The two crystallographically independent La³⁺ metal centers are heptacoordinated, {LaO₇}, to one water molecule and six independent phosphonate groups from four H₃tftp³⁻ residues. All phosphonate groups bear an uncoordinated –OH moiety with the two other oxygen atoms being connected to La³⁺ metal centers in a typical μ₂-O,O' bridging mode. The La–O bond lengths to phosphonate groups range from 2.361(6) to 2.595(7) Å and the

La–O_{water} distances are 2.591(6) and 2.593(6) Å. The O–La–O angles composing the coordination spheres were found in the 73.3(2)–161.5(2)° range (see Figure 5.5 and Table C.1.1 in the Appendices for additional geometrical details). The overall coordination environment of the metal centers resembles a monocapped trigonal prism, with the trigonal and quadrangular internal angles found in the 43.4(2)–91.7(3)° and 76.7(2)–100.6(2)° ranges, respectively (Fig. 2).

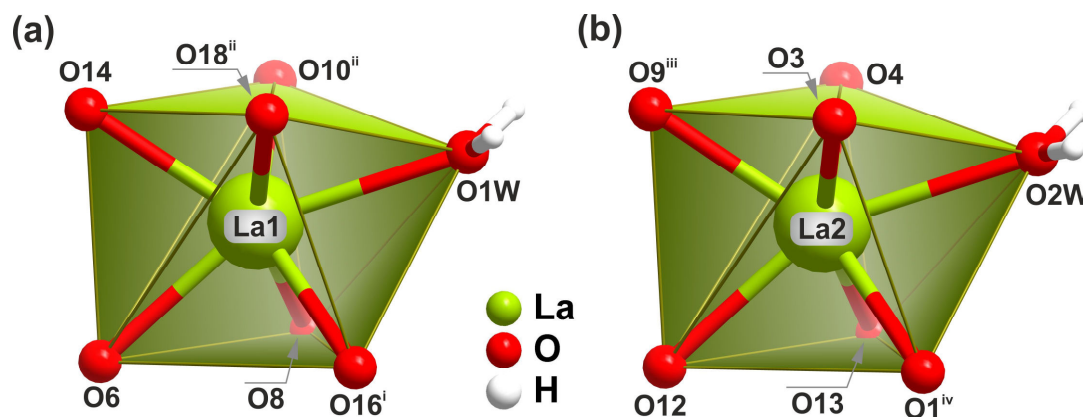


Figure 5.5 - Polyhedral representation of the $\{LaO_7\}$ distorted monocapped trigonal prismatic coordination environments of the two crystallographically independent La^{3+} centers present in **26**: (a) La1 and (b) La2. For selected bond lengths and angles see Table C.1.1 in the Appendices.

As shown in Figure 5.6 the crystallographically independent pairs of metal centers and organic residues are highly superimposable. Moreover, the calculated root mean squares (rms) of 0.005 and 0.04 Å for the coordination spheres of the lanthanum atoms and the organic residues, respectively, are comparable with the experimental error of the atomic positions (for instance, the average C–C bond precision is 0.0133 Å). This fact could, in principle, indicate problems in the determination of cell parameters and/or the space group of compound **26**. Nevertheless attempts to find better cell parameters or space groups always produced the crystallographic data displayed in the sub-section 8.12.1 (in the Experimental Section) as the best choice. Additionally, the presence of six ^{31}P resonances in the solid-state NMR spectrum of **26**, and the existence of nine Stark components in the $^5D_0 \rightarrow ^7F_2$ transition at 14 K (see dedicated sections for further details) for the isotypical compound **27**, agree well with the current proposal for the structural model of this series of materials.

The combination between the H_3tftp^{3-} organic residues and La^{3+} metal centers originates a two-dimensional $\infty^2[La(H_3tftp)(H_2O)]$ neutral coordination polymer placed on the ac lattice plane of the unit cell (Figure 5.7). Despite the hydrophobic aromatic rings of H_3tftp^{3-} being located in the walls of the polymeric layers, they are not engaged in π - π stacking interactions. Weak supramolecular $F \cdots F$ interactions are present within the hydrophobic wall (see legend of Figure 5.7 for additional details), with all C–F \cdots F angles being comprised in the 139.6(6)–142.0(6)° range. The similarity between these values and

their interaction angle allows to classify unequivocally these interactions as of type I, ultimately considering them as of weak nature. Indeed, for the F \cdots F interactions being considered strong (type II), the C–F \cdots F angles should be markedly distinct with values of approximately 90 and 180°. ²⁴ Instead, the fluorine atoms are engaged in intramolecular C–H \cdots F interactions (not shown).

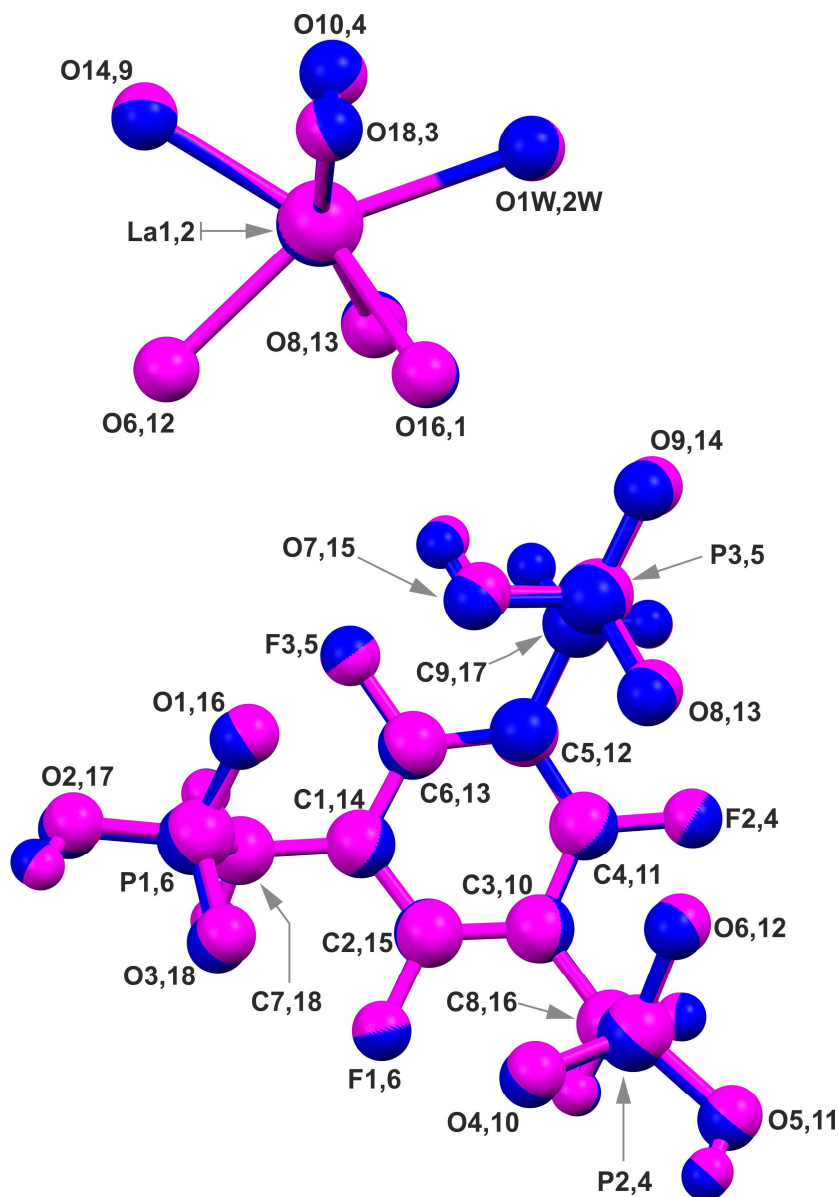


Figure 5.6 - Structure overlay of the (a) two coordination environments around the La³⁺ metallic centres, La1 in blue and La2 in pink, and of the (b) two crystallographic independent residues of **H₆tftp** (H₃tftp³⁻). The organic ligand comprising the P1 to P3 atoms is depicted in blue and the organic ligand containing the P4 to P6 atoms is represented in pink. The first and second numbers appearing in the atom labels correspond to the blue and pink entities, respectively. Symmetry transformations used to generate equivalent atoms for the La³⁺ coordination spheres were omitted for clarity. The geometric coordinates of the atoms were adjusted using the “structure overlay” command in the software package Mercury CSD 3.1. The rms values were calculated as *ca.* 0.005 and 0.04 Å for the metal centers and organic linkers, respectively.

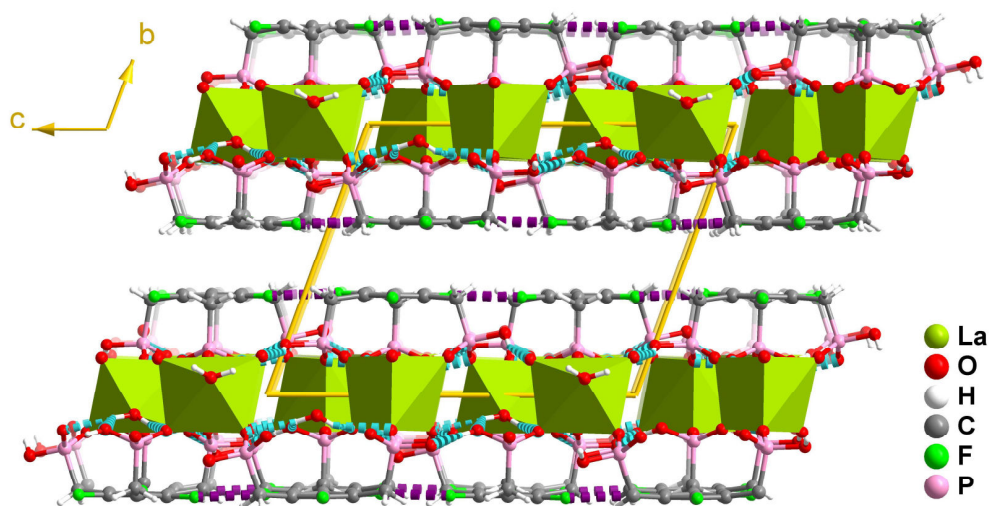


Figure 5.7 - Crystal packing of **26** viewed in perspective along of the [100] direction of the unit cell. The coordination environments around the metal centers are shown as green polyhedra. Hydrogen bonds are represented as dashed blue lines (for geometrical details about the hydrogen bonding geometry see Table C.1.2 in the Appendices). F \cdots F interactions are depicted as dashed violet lines: F3 \cdots F4 2.848(9) Å and F2 \cdots F5 2.864(9) Å; interaction angles C–F3 \cdots F4–C -177.8(1)° and C–F2 \cdots F5–C -178.3(1)°; \angle (C–F \cdots F) ranging from 139.6(6) to 142.0(6)°.

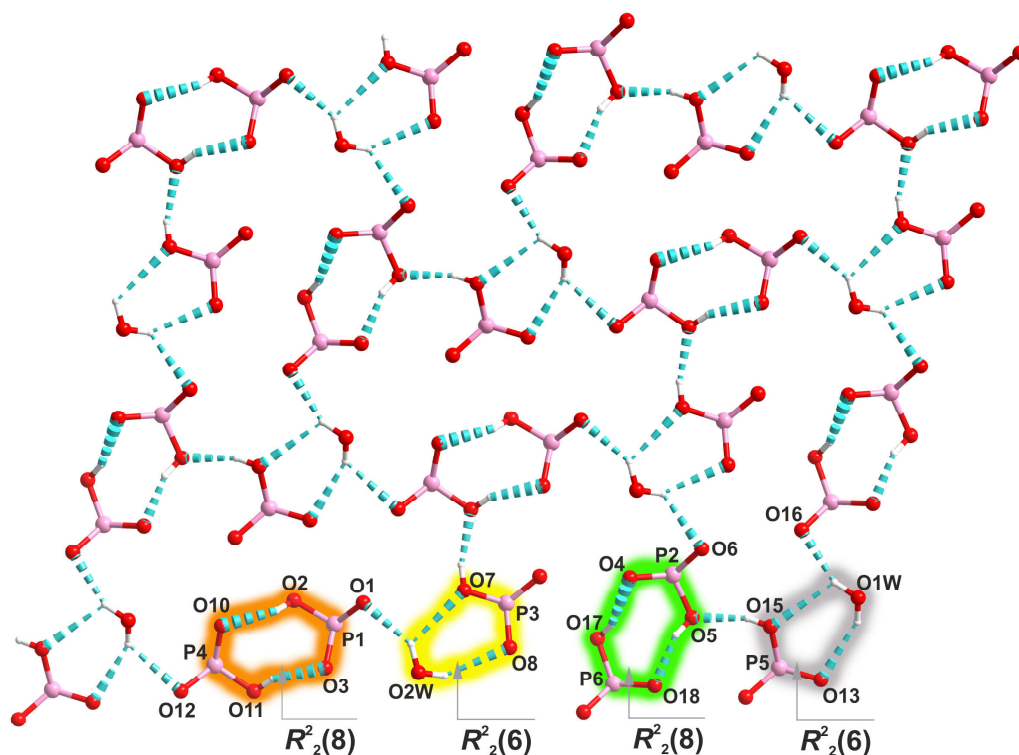


Figure 5.8 - Schematic representation of the hydrogen bonding network present in the crystal structure of **26** emphasizing the presence of four different rings with graph set motifs of $R_2^2(6)$ (highlighted in yellow and gray) and $R_2^2(8)$ (highlighted in orange and green). Symmetry codes used to generate equivalent atoms have been omitted for clarity. For geometrical details on the represented hydrogen bonds see Table C.1.2 in the Appendices.

All phosphonate groups point to the interlamellar space forming a lanthanum oxide layer and an intricate hydrogen bond network as depicted in Figure 5.8. All oxygen atoms of this network are located within a layer with thickness of *ca.* 1.8 Å, also parallel to the *ac* lattice plane. Two pairs of rings with graph set motifs $R^2_2(6)$ and $R^2_2(8)$ are the most remarkable features of this network. The $R^2_2(8)$ set motifs are formed by two hydrogenophosphonate groups (with O···O distances ranging from 2.568(9) to 2.692(9) Å and O–H···O interaction angles between *ca.* 153 and 161°). The $R^2_2(6)$ graph set motifs comprise one hydrogenophosphonate group and one water molecule (with internuclear O···O distances ranging from 3.109(8) to 3.154(9) Å and O–H···O interaction angles between 113 and 143°; for further geometrical details see Table C.1.3 in the Appendices). The most significant packing forces between layers are weak van der Waals interactions. This structural feature can be related with the low crystal robustness of **26** and further explains the great difficulty of finding suitable single-crystals for X-ray diffraction studies.

5.5. Thermogravimetry and Variable Temperature Powder X-ray Diffraction Studies

The thermal stability of the isotypical materials **26**, **27** and **28** was investigated between ambient temperature and *ca.* 800 °C. The thermograms of the three materials exhibit slight different profiles (Figure C.1.1 in the Appendices), with this fact being attributed to the decrease of the average particle size of compounds **27** and **28** (see SEM images in Figure 5.1): materials with smaller average particle size are expected to have a higher surface area, being ultimately thermally less stable, hence leading to distinct overall thermal behaviors. The decomposition behavior of **27** and **28** start at lower temperatures than that registered for **26**. This is more evident for compound **28** (corresponding to the smallest average particle size). In spite of these differences the thermal decomposition of materials **26-28** occurs in a rather similar fashion as depicted in Figure C.1.1 (in the Appendices).

In order to understand the temperature effect in the crystal structure itself, VTPRXD studies on bulk **26** were performed between *ca.* 30 to 700 °C. Compound **26** is thermally stable from ambient temperature to approximately 200 °C. In this temperature range no weight loss is observed (Figure 5.9 – *bottom left*), with the crystal structure remaining intact (Figure 5.9 – *top right*). The first weight loss occurs between *ca.* 207 and 357 °C, being attributed to the release of the coordinated water molecules and the beginning of the material deterioration. As observed from the VTPRXD patterns a dramatic loss of crystallinity occurs during the first weight loss. After this temperature, several weight losses are observed leading to the formation of an amorphous residue at approximately 450 °C. At *ca.* 700 °C a residue composed of a mixture of lanthanum catenatriphosphate (LaP₃O₉, ICDD 00-033-0717) and monazite (LaPO₄, ICDD 01-071-

6745) was identified by powder X-ray diffraction studies (PDF4+ 2012 release ICDD database).

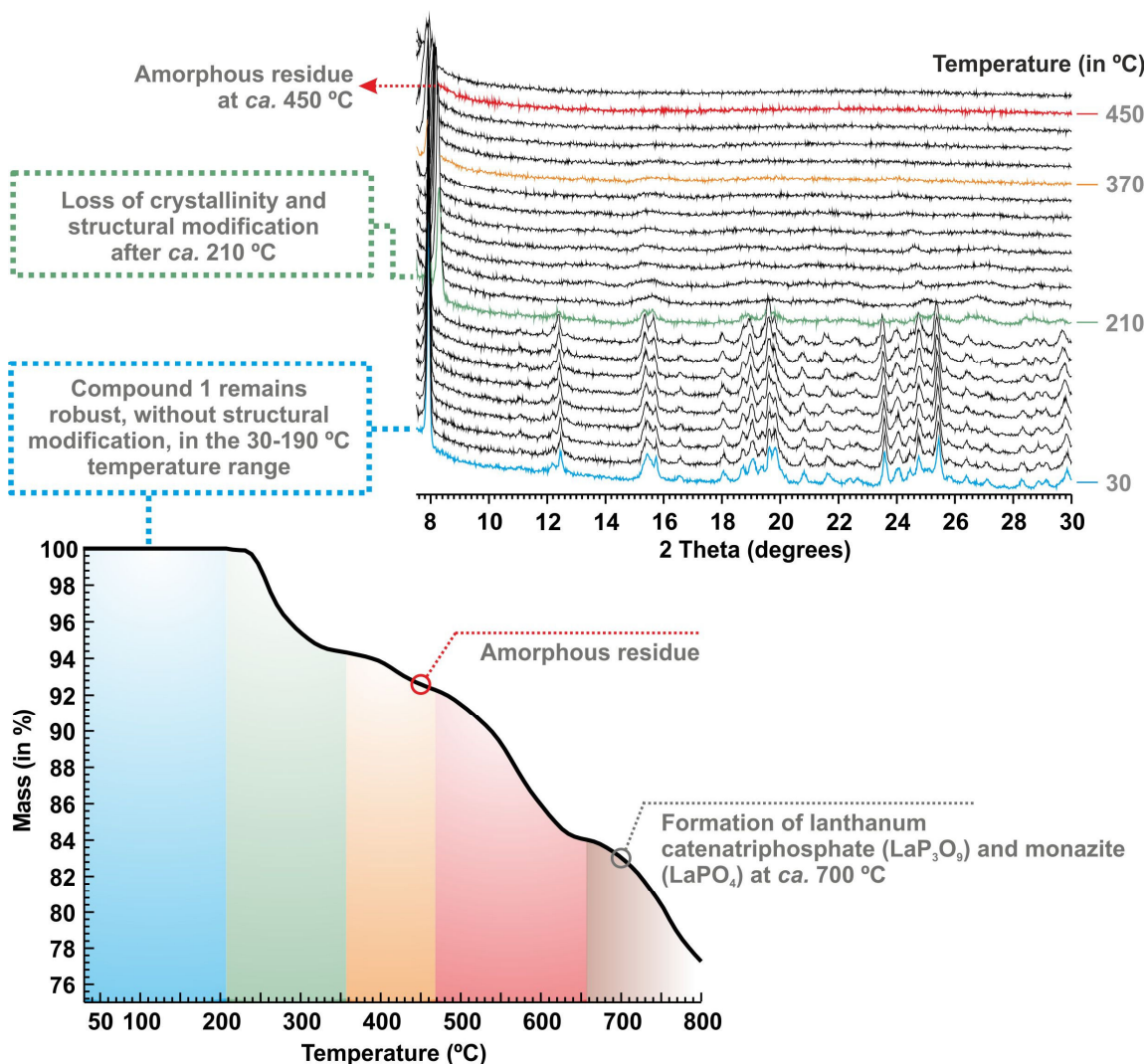


Figure 5.9 - Thermogram and VTPXRD studies for compound $[\text{La}(\text{H}_3\text{tftp})(\text{H}_2\text{O})]$ (**26**).

5.6. Solid-State NMR and FT-IR Spectroscopic Studies

To gain more insight on the composition of the asymmetric unit and phase purity of the bulk materials, solid-state NMR studies were performed on bulk material **26** containing the La^{3+} diamagnetic metallic center. The ^{31}P MAS spectrum exhibits, in the isotropic region, two well-resolved resonances. After deconvolution, six peaks centered at *ca.* 8.4, 9.6, 10.6, 11.8, 16.9 and 17.0 ppm were found (Figure 5.10), agreeing well with the presence of six crystallographic distinct phosphorus sites. Peak deconvolution and integration, including the spinning sidebands, provides a ratio of *ca.* 1.00 : 1.00 : 1.00 : 1.00 : 1.00 : 1.00.

The $^{13}\text{C}\{^1\text{H}\}$ CP MAS spectrum (Figure C.1.2 in the Appendices) contains three distinct spectral regions: the $-\text{CH}_2-$ groups appear as a broad peak centered at *ca.* 23.2 ppm; the aromatic C–C and C–F moieties appear in the 100–115 ppm (peaks at *ca.* 106.0 and 108.6 ppm) and 150–170 ppm (peaks at *ca.* 156.8, 157.8, 159.3 and 160.2 ppm) spectral ranges, respectively. These data are consistent with the performed crystallographic studies, agreeing particularly well with the presence of two organic ligands in the asymmetric unit of **26**.

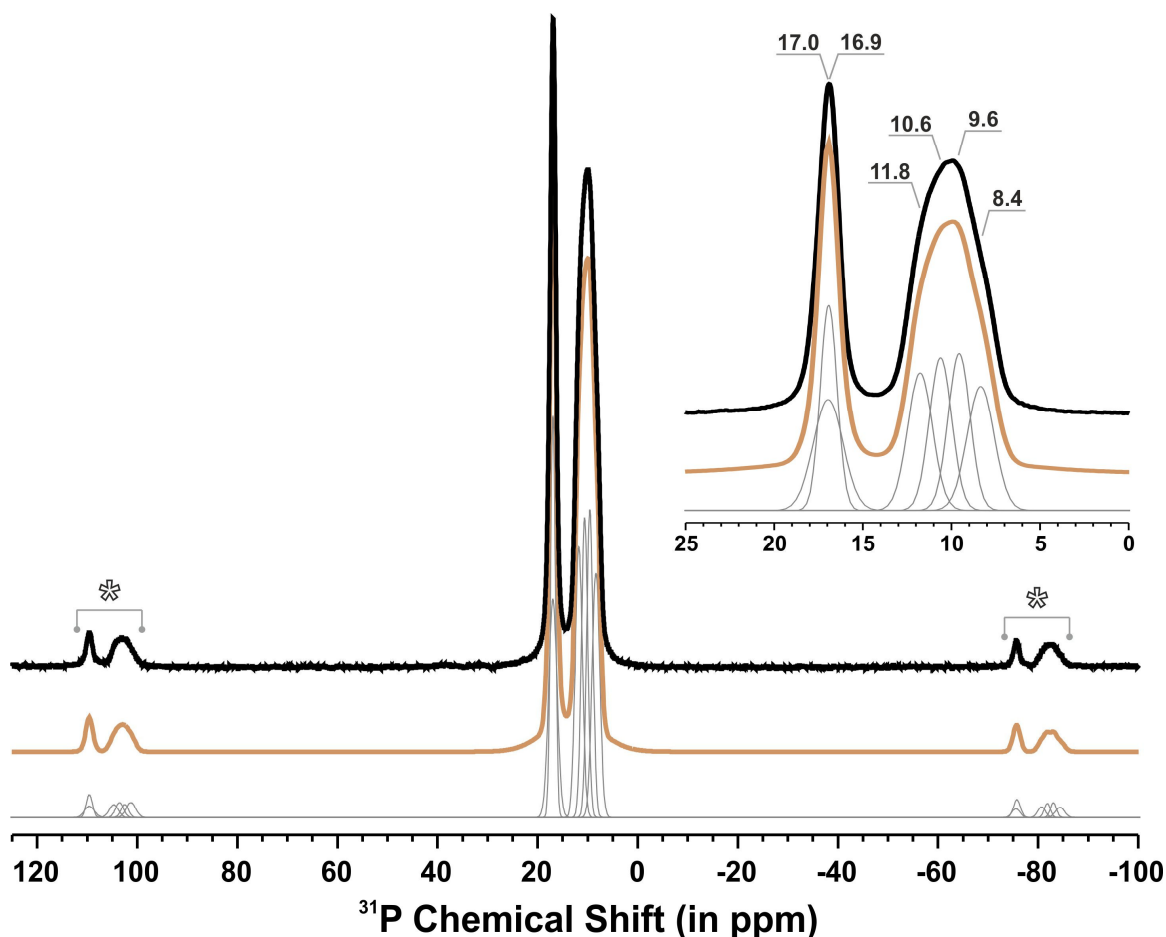


Figure 5.10 - Experimental (black) and deconvoluted (light brown) ^{31}P HPDEC MAS spectra of compound **26**. Spinning sidebands are denoted using an asterisk. Peak deconvolution and integration throughout the entire spectral range (*i.e.*, including the spinning sidebands) gives a ratio of *ca.* 1.00 : 1.00 : 1.00 : 1.00 : 1.00 : 1.00 for the isotropic resonances peaking at *ca.* 8.4, 9.6, 10.6, 11.8, 16.9 and 17.0 ppm, respectively. The grey lines represent the individual fits for the single resonances.

FT-IR spectroscopy studies (Figure 5.11) indicate that the bulk materials **26**, **27** and **28** are indeed isotypical. Thus, in the following paragraphs only the spectral features for compound **26** will be discussed, being assumed that identical considerations are valid for the remaining materials **27** and **28**.

The FT-IR spectrum of **26** is mainly composed of two relevant spectral regions. In the $3750\text{--}2500\text{ cm}^{-1}$ range one can observe: (i) the typical $\nu(\text{O-H})$ stretching vibrational

modes of the coordinated water molecules (at *ca.* 3493 and 3446 cm^{-1}) and of the PO–H groups (at *ca.* 3213 cm^{-1}); and (ii) a weak and sharp band observed at *ca.* 2941 cm^{-1} attributed to the $\nu(\text{C–H})$ stretching vibration of the $-\text{CH}_2-$ groups.

Below 1800 cm^{-1} the FT-IR spectrum of **26** is complex with a large number of medium-to-very strong vibration bands.²⁵ At *ca.* 1673, 1625 and 1602 cm^{-1} it is possible to observe the $\delta(\text{H}_2\text{O})$ and $\nu(-\text{C}=\text{C}-)$ in-plane deformations. The very intense peak at around *ca.* 1470 cm^{-1} is attributed to a $\nu(-\text{C}=\text{C}-)$ stretching vibration mode of the aromatic ring, being frequently observed with the presence of electron acceptors connected to the aromatic rings. Two medium intensity bands peaking at *ca.* 1420 and 1409 cm^{-1} belong to the $-\text{CH}_2-$ deformation vibrational modes from the P– CH_2 groups. Additionally, the $\nu(\text{P}=\text{O})$ and $\nu(\text{C–F})$ modes appear in the 1350–1050 cm^{-1} range, followed of a set of vibration bands between 1040 and 900 cm^{-1} attributed to the $\nu(\text{P–O})$ modes. The $\nu(\text{P–C})$ stretching vibrations are centered at *ca.* 763 and 745 cm^{-1} .²⁵

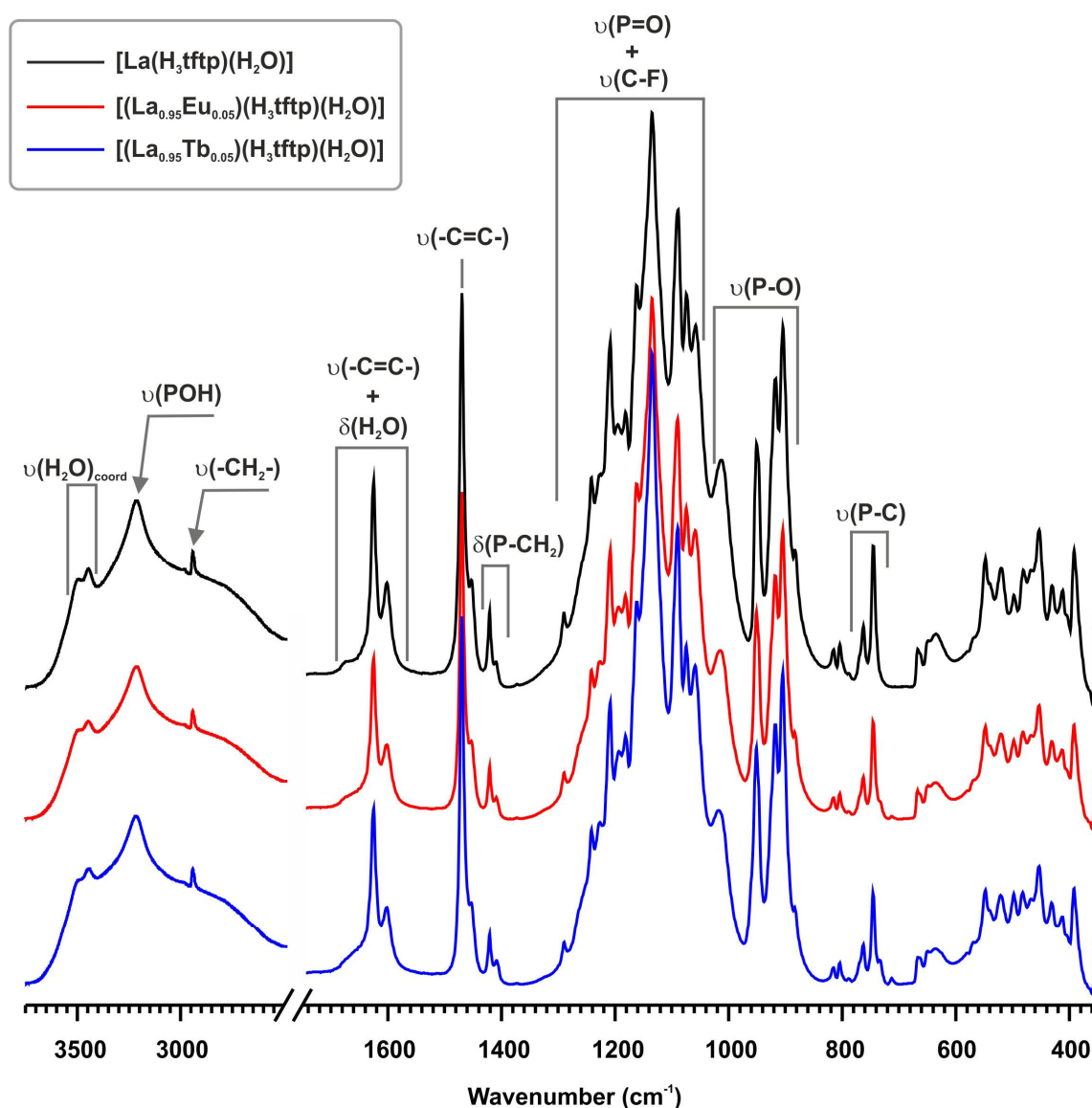


Figure 5.11 - FT-IR spectra of the isotypical series of the materials [La(H₃tftp)(H₂O)] (**26**), [(La_{0.95}Eu_{0.05})(H₃tftp)(H₂O)] (**27**) and [(La_{0.95}Tb_{0.05})(H₃tftp)(H₂O)] (**28**).

5.7. Photoluminescence

The photoluminescence properties of the isotypical mixed-lanthanide compounds $[(\text{La}_{0.95}\text{Eu}_{0.05})(\text{H}_3\text{tftp})(\text{H}_2\text{O})]$ (**27**) and $[(\text{La}_{0.95}\text{Tb}_{0.05})(\text{H}_3\text{tftp})(\text{H}_2\text{O})]$ (**28**) were investigated both at ambient and low temperature and compared with the starting **H₆tftp** ligand and the former compound $[\text{La}(\text{H}_3\text{tftp})(\text{H}_2\text{O})]$ (**26**). The excitation spectra of **27** and **28**, while monitoring the emission at 616 and 542 nm within the $\text{Eu}^{3+} \ ^5\text{D}_0 \rightarrow \ ^7\text{F}_2$ and $\text{Tb}^{3+} \ ^5\text{D}_4 \rightarrow \ ^7\text{F}_5$ transitions, respectively, are shown in Figure 5.12. Spectra are dominated by a broad UV band (240-280 nm) which may be attributed to the $\pi\text{-}\pi^*$ transitions associated with the organic linkers. This assignment was further confirmed by monitoring the singlet UV emission at 330 nm in both the **H₆tftp** ligand and compound **26** (Figure 5.12). The excitation of **26** is slightly red shifted relatively to that of **H₆tftp** and resembles the UV broad band observed for **27** and **28**. The additional sharp extra lines in the spectra of **27** and **28** were identified as the intra- $4f^6$ transitions $^7\text{F}_0 \rightarrow \ ^5\text{D}_{1-4}$, $^5\text{L}_6$, $^5\text{G}_{2-6}$, $^5\text{H}_{3-7}$ and $^5\text{F}_{1-5}$ of Eu^{3+} , and as the intra- $4f^8$ transitions $^7\text{F}_6 \rightarrow \ ^5\text{D}_{2-4}$ and $^5\text{G}_J$ of Tb^{3+} .

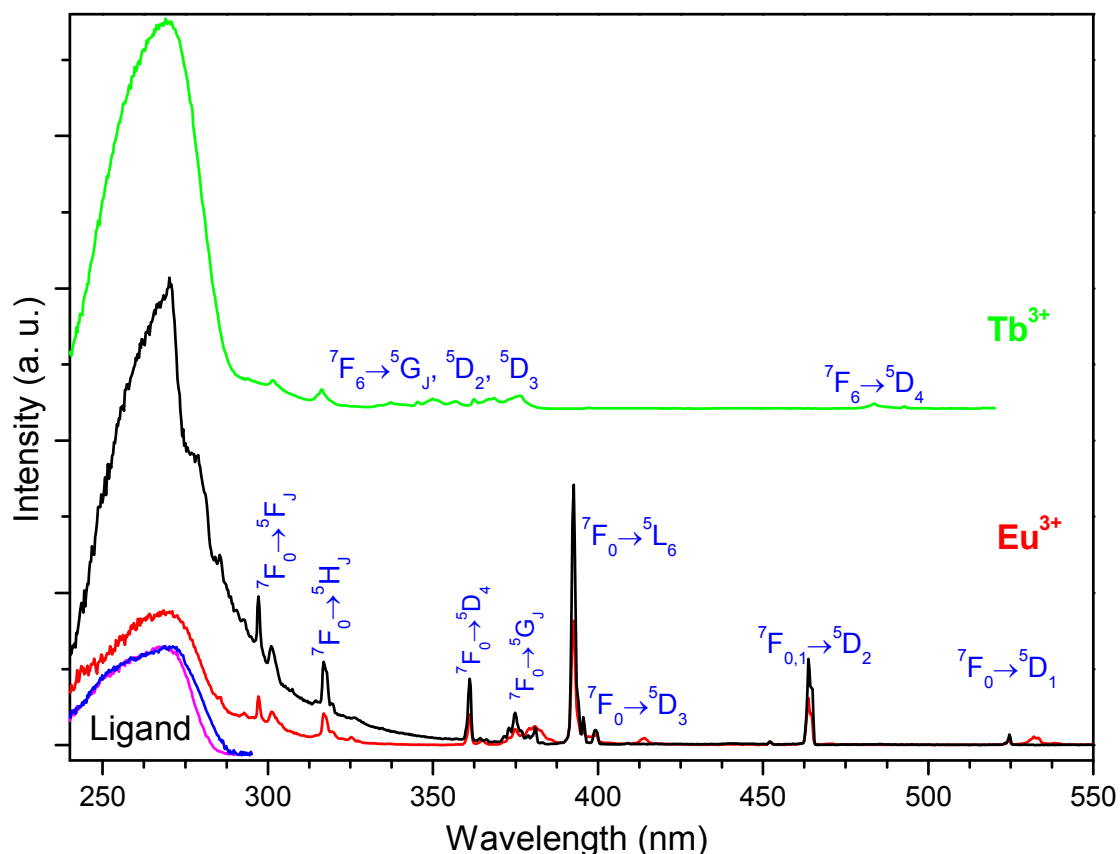


Figure 5.12 - Excitation spectra of compound **27** at ambient temperature (red line) and at 14 K (black line), and of compound **28** at ambient temperature (green line). Emission was monitored at 616 and 542 nm for the Eu^{3+} - and Tb^{3+} -based materials, respectively. The ambient temperature excitation spectra of the **H₆tftp** ligand (magenta line) and of the compound **26** (blue line), while detecting the emission fluorescence at 330 nm, are provided for comparative purposes.

The emission spectra of compounds **27** and **28**, recorded at ambient temperature (using an excitation wavelength of 270 nm), are shown in Figure 5.13. The sharp lines are assigned to the transitions between the first excited non-degenerate 5D_0 state and the $^7F_{0-4}$ levels of the fundamental Eu^{3+} septet, and between the first excited state 5D_4 and the $^7F_{6-0}$ levels of Tb^{3+} for **27** and **28**, respectively. The emission spectrum of **27** shows a predominance of the $^5D_0 \rightarrow ^7F_2$ transition comparatively to the $^5D_0 \rightarrow ^7F_1$. The identification of, at least, nine Stark components in this spectrum for the $^5D_0 \rightarrow ^7F_2$ transition at 14 K (inset in Figure 5.13) clearly indicates the presence of at least two low-symmetry Eu^{3+} environments in the crystal structure. This feature agrees well with the performed crystallographic studies (see dedicated section for further details).

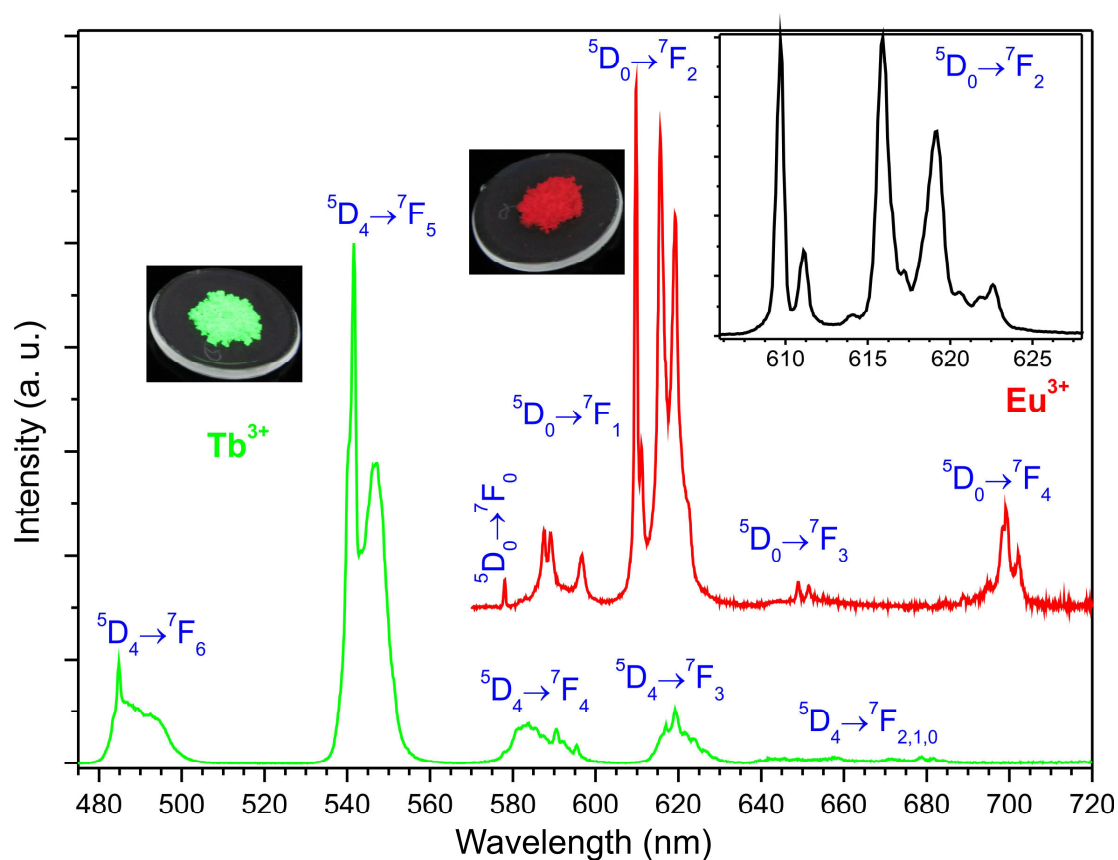


Figure 5.13 - Emission spectra of **27** (red line) and **28** (green line) at ambient temperature while using an excitation wavelength of 270 nm. The inset shows a magnification of the $\text{Eu}^{3+} ^5D_0 \rightarrow ^7F_2$ transition recorded at 14 K.

The ambient temperature 5D_0 and 5D_4 lifetimes of Eu^{3+} - and Tb^{3+} -based materials were determined by monitoring the emission decay curves within the maximum of the $^5D_0 \rightarrow ^7F_2$ and $^5D_4 \rightarrow ^7F_5$ transitions, using an excitation at 393 and 376 nm, respectively (Figure 5.14). Both decay curves can be well fitted by single exponential functions, yielding lifetimes of 0.51 ± 0.01 and 1.26 ± 0.01 ms for **27** and **28**, respectively. For distinct excitation and/or the emission detection wavelengths identical lifetimes values were systematically obtained.

Considering the presence of the two distinct Ln^{3+} environments in the crystal structures, the determination of single exponential decay curves arises as a further indication of the strong similarity between the two crystallographically independent Ln^{3+} sites in terms of the emission decay lifetime. Note that, based on crystallographic studies, both Ln^{3+} metal centers have the same coordinated elements on the first sphere (seven oxygen atoms: six belonging to six independent phosphonate groups and one belonging to a water molecule) with very similar Ln–O distances (see Table C.1.1 in the Appendices for further details). At 14 K the $^5\text{D}_0$ decay curve of **27** has also a single exponential behaviour independently of the excitation and emission wavelengths, yielding a lifetime of 0.56 ± 0.01 ms (data not shown). Noteworthy, the calculated lifetime is not dependent of the emission wavelength detection.

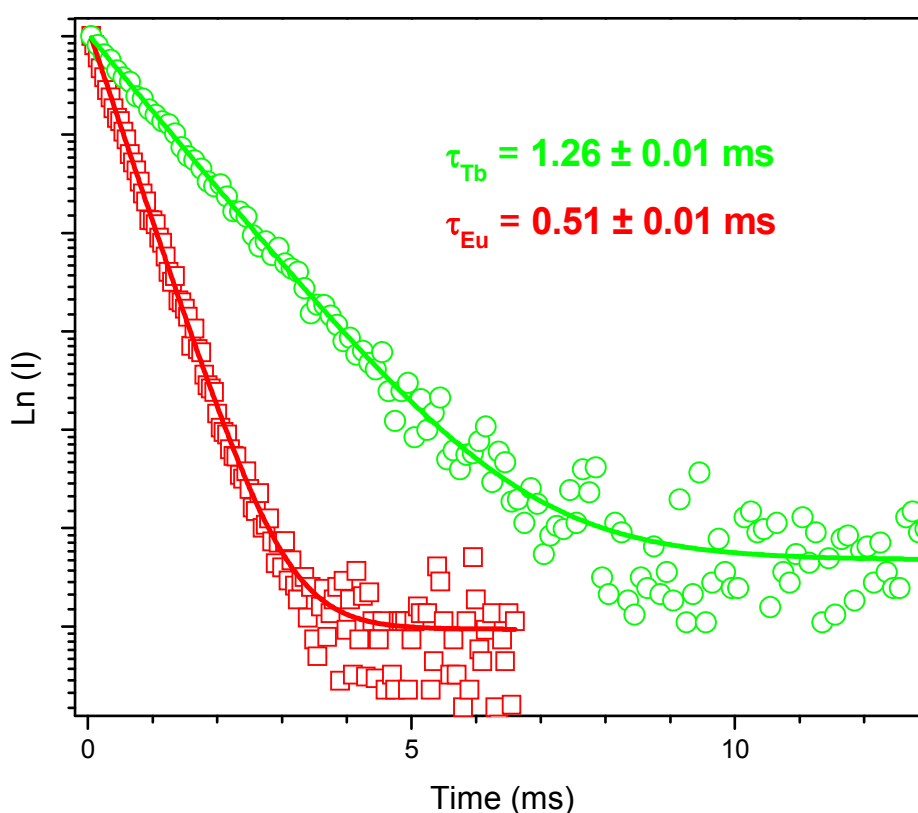


Figure 5.14 - $^5\text{D}_0$ and $^5\text{D}_4$ decay curves of the mixed-lanthanide $[(\text{La}_{0.95}\text{Eu}_{0.05})(\text{H}_3\text{tftp})(\text{H}_2\text{O})]$ (**27**) (red line) and $[(\text{La}_{0.95}\text{Tb}_{0.05})(\text{H}_3\text{tftp})(\text{H}_2\text{O})]$ (**28**) (green line) materials acquired at ambient temperature (298 K), while monitoring the emission at 610 and 542 nm, respectively. Data have been fitted with single exponential decay functions. The excitation was performed at 393 and 376 nm for **27** and **28**, respectively.

The measured absolute emission quantum yields, *ca.* 1% at 270 nm and 12% at 393 nm for **27**, and *ca.* 7% at 270 nm and 4% at 376 nm for **28**, are relatively low. The low emission performance of the mixed-lanthanide Ln^{3+} -based light emitters is certainly the result of the combination of two main factors: (i) the presence of one water molecule in the first coordination sphere of the crystallographically independent Ln^{3+} cations, and (ii) an

inefficient ligand-to-Ln³⁺ energy transfer mechanism. The latter assumption is further supported by the observation of the singlet ligand emission in the UV spectral region for compound **27**, under 270 nm excitation at ambient temperature (Figure 5.15). The UV emission broad band has a very short lifetime, less than 10 μ s, which is below the range of the used phosphorimeter. A similar UV emission band was also detected for the Tb³⁺-based material **28** (data not shown).

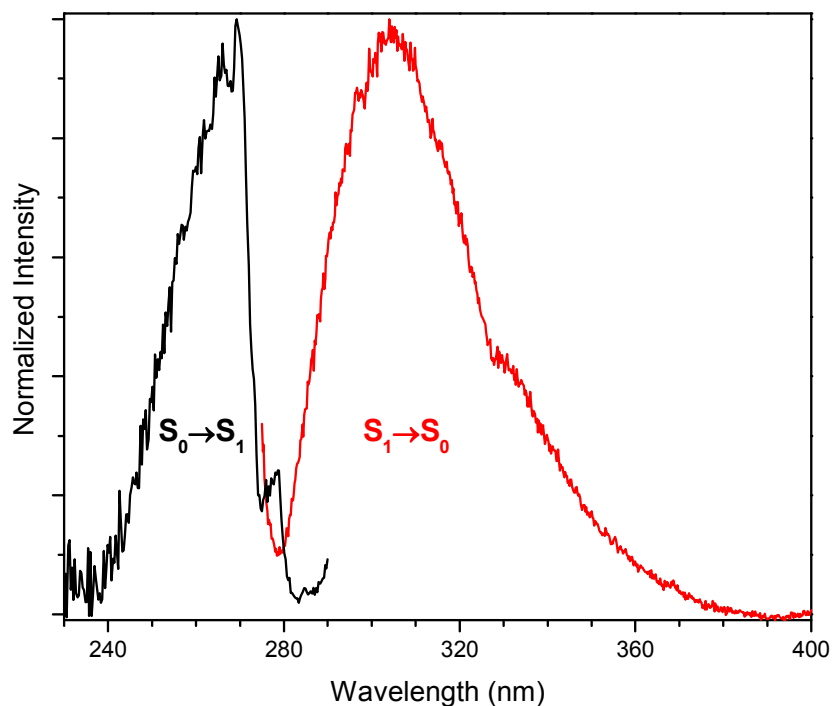


Figure 5.15 - Excitation and emission spectra of the mixed-lanthanide material **27** recorded at ambient temperature. For the excitation spectrum the emission was detected at 300 nm (black line) while for the emission spectrum (red line) the excitation was fixed at 270 nm.

5.8. Results and Discussion

In this Chapter a family of new isotypical layered MOFs was reported: compounds [La(H₃tftp)(H₂O)] (**26**), [(La_{0.95}Eu_{0.05})(H₃tftp)(H₂O)] (**27**) and [(La_{0.95}Tb_{0.05})(H₃tftp)(H₂O)] (**28**) were prepared from the reaction between lanthanide chloride hydrated salts with the novel organic ligand **H₆tftp** under hydrothermal conditions. All materials were characterized by using in tandem several standard solid-state techniques.

The use of conventional hydrothermal synthesis with the same synthetic conditions (temperature, 180 °C; time, 3 days; water as reaction medium) as for 2D and 3D LnOFs **12-25** previously reported in Chapter 4, led to a distinct architecture. The two-dimensional ∞^2 [La(H₃tftp)(H₂O)] neutral coordination polymer (isolated when **H₆tftp** was used) has a completely different crystalline structure than the 2D and 3D materials, prepared when the non-fluorinated **H₆bmt** organic ligand was employed. The 2D material

∞ [La(H₃tftp)(H₂O)] has the hydrophobic aromatic rings pointing to the interlamellar space, and the phosphonate groups and metal centers forming an internal inorganic sheet.

Regarding to the thermal stability, the fluorinated compound **26** suffered a drastic loss of crystallinity upon release of the coordinated water molecules (from approximately 200 °C), contrasting with the thermal behaviors of the 2D materials **12-19** (thermally robust up to approximately 400 °C) and 3D materials **20-25** (showing very small structural modifications after the dehydration process). The structure of the 1D materials **9-11** suffers some structural alterations during the release of the coordinated and crystallization water molecules, however, it remains crystalline.

As mentioned in Chapter 1 and observed in Chapters 3 and 4, one of the major challenges resides in the preparation of phosphonate-based MOFs with large particle sizes. For the material described in this Chapter, the addition of small amounts of an aqueous solution of HCl (6 M) to the reactive mixtures led to the isolation of compound **26** as large single-crystals suitable for single-crystal X-ray diffraction studies.

Mixed-lanthanide materials with stoichiometric amounts of optically-active lanthanides have been studied with results unequivocally showing that the presence of the O–H vibrations of the coordinated water molecules, composing the first coordination sphere, quench the photoluminescence of compounds **27** and **28**. In addition, it was demonstrated that for the materials reported in this Chapter the ligand-to-metal charge transfer mechanism is poorly efficient, with the combination of these two factors leading to low absolute emission quantum yields. In this way it is pertinent that future work is devoted to investigate alternative synthetic ways to produce new LnOF materials using the novel organic ligand **H₆tftp** but without water molecules in the first coordination sphere of the metallic center. In this way, it is envisaged that more efficient photoluminescent materials could be isolated, aiming at their use for the construction of sensing devices. Besides changing the reaction parameters (such as temperature, reaction time, solvent, among others), the present studies clearly show that future work could be focused on the use of other heating methods such as microwave heating and one-pot reactions. These approaches could have the advantage of allowing a faster and low energy-consuming synthetic process (two attractive features to industrial processes and for scaling up).

The materials reported in this chapter constitute the first example in which a fluorinated phosphonate organic ligand has been used for the preparation of multidimensional MOFs with lanthanide cations. Despite of this, and based on the conclusions summarized above, the main objective of this work was not achieved: even though the sole difference between **H₆tftp** and **H₆bmt** is the replacement of hydrogen of the aromatic ring by fluorine atoms, isotypical functional MOF materials sharing the same crystalline structure of the previously reported architectures **12-25** based on residues of **H₆bmt** could not be isolated. In this way, the photoluminescence of the two families of materials could not be straightforwardly compared, and the influence of the C-F groups instead the C-H bonds in the final properties could not be assessed.

5.9. References

- (1) Pachfule, P.; Chen, Y. F.; Jiang, J. W.; Banerjee, R.; *Chem.-Eur. J.*, **2012**, *18*, 688-694.
- (2) Pachfule, P.; Chen, Y. F.; Sahoo, S. C.; Jiang, J. W.; Banerjee, R.; *Chem. Mater.*, **2011**, *23*, 2908-2916.
- (3) Hulvey, Z.; Sava, D. A.; Eckert, J.; Cheetham, A. K.; *Inorg. Chem.*, **2011**, *50*, 403-405.
- (4) Hulvey, Z.; Falcao, E. H. L.; Eckert, J.; Cheetham, A. K.; *J. Mater. Chem.*, **2009**, *19*, 4307-4309.
- (5) Zhang, Z. H.; Chen, S. C.; Mi, J. L.; He, M. Y.; Chen, Q.; Du, M.; *Chem. Commun.*, **2010**, *46*, 8427-8429.
- (6) Xue, D. X.; Cairns, A. J.; Belmabkhout, Y.; Wojtas, L.; Liu, Y. L.; Alkordi, M. H.; Eddaoudi, M.; *J. Am. Chem. Soc.*, **2013**, *135*, 7660-7667.
- (7) Serre, C.; *Angew. Chem., Int. Ed.*, **2012**, *51*, 6048-6050.
- (8) Fernandez, C. A.; Thallapally, P. K.; Motkuri, R. K.; Nune, S. K.; Sumrak, J. C.; Tian, J.; Liu, J.; *Cryst. Growth Des.*, **2010**, *10*, 1037-1039.
- (9) Biswas, S.; Remy, T.; Couck, S.; Denysenko, D.; Rampelberg, G.; Denayer, J. F. M.; Volkmer, D.; Detavernier, C.; Van Der Voort, P.; *Phys. Chem. Chem. Phys.*, **2013**, *15*, 3552-3561.
- (10) Yang, C.; Kaipa, U.; Mather, Q. Z.; Wang, X. P.; Nesterov, V.; Venero, A. F.; Omary, M. A.; *J. Am. Chem. Soc.*, **2011**, *133*, 18094-18097.
- (11) Wu, T. J.; Shen, L. J.; Luebbers, M.; Hu, C. H.; Chen, Q. M.; Ni, Z.; Masel, R. I.; *Chem. Commun.*, **2010**, *46*, 6120-6122.
- (12) Pachfule, P.; Dey, C.; Panda, T.; Banerjee, R.; *CrystEngComm*, **2010**, *12*, 1600-1609.
- (13) Harbuzaru, B. V.; Corma, A.; Rey, F.; Atienzar, P.; Jordá, J. L.; Garcia, H.; Ananias, D.; Carlos, L. D.; Rocha, J.; *Angew. Chem., Int. Ed.*, **2008**, *47*, 1080-1083.
- (14) Chen, B. L.; Yang, Y.; Zapata, F.; Qian, G. D.; Luo, Y. S.; Zhang, J. H.; Lobkovsky, E. B.; *Inorg. Chem.*, **2006**, *45*, 8882-8886.
- (15) Yang, C.; Wang, X. P.; Omary, M. A.; *Angew. Chem., Int. Ed.*, **2009**, *48*, 2500-2505.
- (16) Yang, C.; Wang, X. P.; Omary, M. A.; *J. Am. Chem. Soc.*, **2007**, *129*, 15454-15455.
- (17) Bunzli, J. C. G.; Eliseeva, S. V.; *Chemical Science*, **2013**, *4*, 1939-1949.
- (18) Bunzli, J. C. G.; Piguet, C.; *Chem. Soc. Rev.*, **2005**, *34*, 1048-1077.
- (19) Eliseeva, S. V.; Bunzli, J. C. G.; *New J. Chem.*, **2011**, *35*, 1165-1176.
- (20) Vilela, S.; Fernandes, J. A.; Ananias, D.; Carlos, L. A. D.; Rocha, J.; Tome, J.; Almeida Paz, F. A.; *CrystEngComm*, **2013**, DOI:10.1039/C1033CE41482E.
- (21) Sabitha, G.; Babu, R. S.; Rajkumar, M.; Reddy, C. S.; Yadav, J. S.; *Tetrahedron Lett.*, **2001**, *42*, 3955-3958.

- (22) Glover, P. B.; Bassett, A. P.; Nockemann, P.; Kariuki, B. M.; Van Deun, R.; Pikramenou, Z.; *Chem.-Eur. J.*, **2007**, *13*, 6308-6320.
- (23) Hasegawa, Y.; Ohkubo, T.; Sogabe, K.; Kawamura, Y.; Wada, Y.; Nakashima, N.; Yanagida, S.; *Angew. Chem., Int. Ed.*, **2000**, *39*, 357-360.
- (24) Samai, S.; Biradha, K.; *Crystengcomm*, **2009**, *11*, 482-492.
- (25) Socrates, G. *Infrared and Raman Characteristic Group Frequencies: Tables and Charts*; 2nd ed.; John Wiley & Sons Ltd: Baffins Lane, Chichester, 1994.

Chapter 6

Porous Yttrium-Triphosphonate MOF: Synthesis and Properties

6.1. Initial Considerations

As mentioned in Chapter 1, the quest for porosity in MOFs is the most required feature from worldwide researchers. The design and synthesis of rigid, large and multipodal O- and N-donor organic PBUs to combine with metallic centers seems to have a strong influence in the porosity and architecture of the desired material. Keeping this in mind, several research groups have prepared different organic linkers with these requirements. In this context, MOFs assembled from very large bi-, tri- or tetrapodal organic molecules in their structure, conferring them high porosity, have been reported over the years. As also described in Chapter 1, the 3D MOF materials reported until now have pores with diameters varying from few to dozens of angstroms (IRMOF-74-XI with pore diameter of 100 \AA)¹ and world records in surface areas (*e.g.*, NU-110 with a BET surface area of $7140 \text{ m}^2\text{g}^{-1}$)¹⁻² when compared with other common porous materials (*i.e.*, zeolites or active carbons). This feature in conjugation with other functionalities have conferred to this type of materials the ability to store high quantities of gases (*i.e.*, H_2 and CH_4) to be used as clean energy and to retain, from mixture of gases, the non-environmentally friendly CO_2 , while retaining their crystalline structure.

To evaluate the porosity of a given MOF it is normally performed static adsorption experiments using N_2 (at 77 K), Ar (at 77 K) and CO_2 (at 195 or 273 K). The obtained data allow us to have insights about some physical features of MOFs, such as: i) accessibility of gases to the framework; ii) gravimetric or volumetric adsorption capacity to retain gases; iii) specific surface area; iv) adsorption enthalpies and v) network stability (*i.e.*, permanent porosity) after evacuation of the guest solvent molecules.³ The latter feature provides information to know if the network collapses or preserve its crystalline integrity after the releasing of the solvent molecules. This process is performed under vacuum at high temperatures to include guest molecules of interest (*e.g.*, H_2 , N_2 , CO_2 or CH_4). Figure 6.1 depicts the adsorption/sorption process which may occur in a porous MOFs. The adsorption process occurs, normally, after the activation (*i.e.*, desolvation), under heating, of the porous MOF. This procedure leads to the availability of all adsorption sites capable to adsorb the gases of interest. Then, heating the material, while passing an inert gas flux, allows the sorption process with the consequent release of the gas molecules.

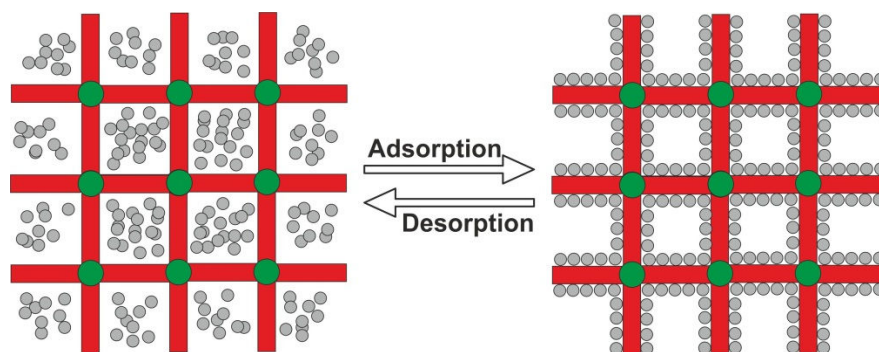


Figure 6.1 – Representation of the adsorption/desorption process which occur in the porous MOFs.

The parameters mentioned above are determined from the measurement of the typical experimental adsorption isotherms using the small noble gas Ar and/or small molecules such as N_2 and CO_2 (at the condensation temperature of the corresponding gas). The adsorption of a given substance in a material is measured according to the quantity of a gas adsorbed at a certain temperature in function of the gas pressure in equilibrium with the solid material. There are different types of adsorption isotherms (Figure 6.2):³⁻⁷

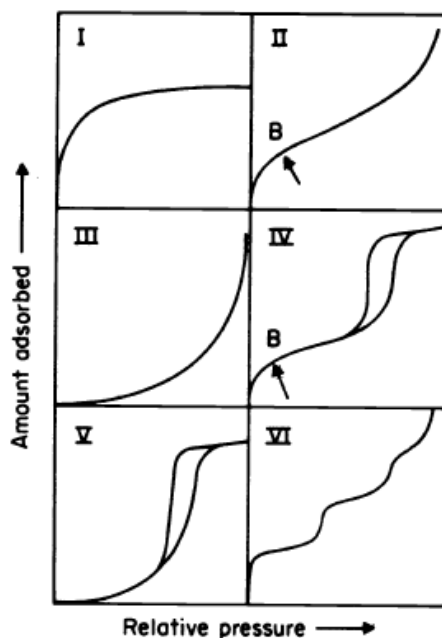


Figure 6.2 – Representation of the six different types of adsorption isotherms. Reproduced from reference 4.

- i) Type I: correspond to the adsorption in microporous materials (*i.e.*, MOFs, zeolites and active carbons). The majority of the micropores are filled at low relative pressures (below than 0.1);
- ii) Type II: is related with the multilayer adsorption and reflects the statistical thickness of the N_2 adsorbed by the material (typical for the adsorption of N_2 on macroporous compounds, as for instance, SiO_2 and Al_2O_3). The monolayer coverage is, then, followed by coverage of multilayers;
- iii) Type III: common associated to both non-porous and microporous compounds. Existence of weak gas-solid interactions (*e.g.*, adsorption of H_2O molecules on noble metals or carbons). The weak interaction between adsorbate and adsorbent leads to low uptake at low relative pressures and high uptake at higher relative pressures;
- iv) Type IV: associated to multilayer adsorption and pore condensation in mesoporous materials, as for instance silica and alumina (*e.g.*, adsorption of N_2 on MCM-41 type material (mesostructured silica)). The presence of a hysteresis loop is very

often associated to the existence of mesopores. However, higher uptakes only occur at high relative pressures.

- v) Type V: as for the adsorption isotherm type III, this corresponds also to weak gas-solid interactions (*e.g.*, adsorption of H₂O molecules on noble metals). It may be attributed to microporous or mesoporous materials;
- vi) Type VI: typical for homogeneous multilayered and non-porous adsorbents (as for instance, adsorption of Kr on graphite).

Adsorption isotherms only provide information about the texture of the porous materials and their affinity to gases of interest. Nevertheless, if it is necessary to evaluate the potential of a porous MOF for gas separation processes it is required other more advanced studies. In the front line of this research is the group of Navarro who have prepared MOFs capable to capture nerve agents (*i.e.*, sarin and mustard gas analogues)⁸⁻⁹ and harmful volatile organic compounds (benzene, cyclohexane and thiophene)¹⁰, incorporated and released the non-conventional [Ru(*p*-cymene)Cl₂(pta)] RAPTA-C metallodrug,¹¹ and studied the ability of pyrazolate-based MOFs towards the separation of CO₂ from binary (CO₂/N₂ and CO₂/CH₄)¹²⁻¹⁴ and ternary (CO₂/CH₄/C₂H₂)¹² gas mixtures. These investigations allowed to gain insights about the potential of their porous pyrazolate-based MOFs to be used in gas separation processes, mainly, to capture CO₂.

Gas separation measurements are performed using two advanced methods:¹²

- i) Pulse gas chromatographic experiments to evaluate the possible application of a given MOF on gas separation purification. This methodology allows to determine the capacity of a porous MOF to retain gases into their structure. Gases having higher affinity with the structure of a material are retained during longer periods of time. This is a preliminary qualitative test before quantitative measurements. Usually it is used a mixture of several gases (*e.g.*, H₂, CH₄, C₂H₂, CO₂, C₂H₄, C₂H₆, C₃H₆ and C₃H₈) and an inert carrier gas (*e.g.*, He). The experiments are carried out at different temperatures (273, 298, 303, 323 K and if necessary higher temperatures). The resulted data consist in a chromatogram showing the retention time of each gas (Figure 6.3);
- ii) Gas separation breakthrough studies. This is a quantitative method and it is performed after a first screening using the previous methodology. This approach is adequate for the bulk separation of gases. As mentioned above, it is required a binary (*e.g.*, CO₂/CH₄) or ternary (CO₂/CH₄/C₂H₂) mixture of gases using, as for instance, He as diluting gas in order to avoid pressure drops in the column. The used experimental temperature may be the same as for pulse gas chromatographic experiments. Gases with affinity for the structure of a porous MOF are more retained, while gases with lower affinity are rapidly released. The obtained data allow us to determine the quantity of a given gas into the structure of a porous MOF at different temperatures. Figure 6.4 depicts typical breakthrough curves.

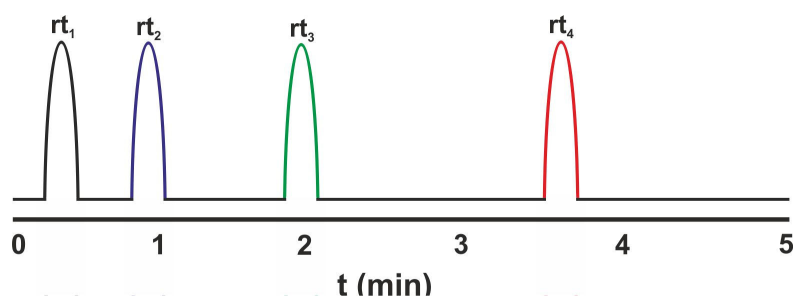


Figure 6.3 – Representation of pulse gas chromatogram curves exemplifying the gas separation process according to the affinity between the porous MOF material and the gases of interest. The gas of the reference curve (*e.g.*, H_2) is represented in black and the curves in blue, green and red correspond to the different gases using on the measurement, as for instance, CH_4 , C_2H_2 and CO_2 , respectively. In these experiments it is always used an inert carrier gas (generally He). rt_n (where $n = 1, 2, 3$ and 4) is attributed to the retention time of each gas.

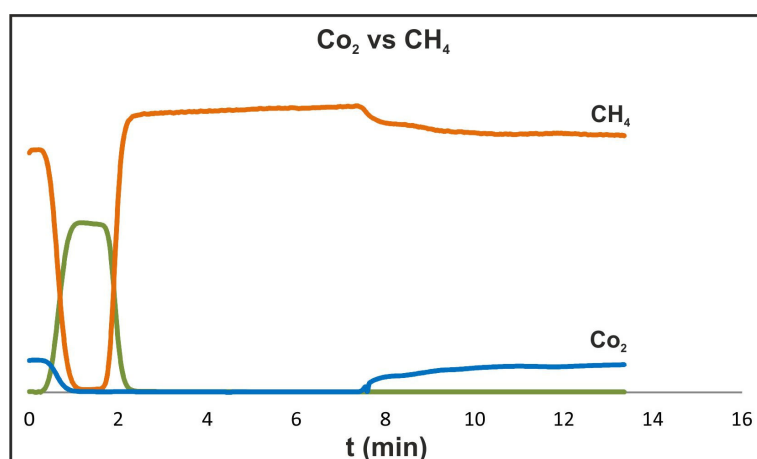


Figure 6.4 – Example of a CO_2/CH_4 breakthrough experiment: because CO_2 has more affinity with the porous MOF material, it is retained into its structure during longer periods of time than CH_4 , which does not interact with the material. In these experiments the inert carrier gas (generally He) is always used.

This Chapter describes the preparation of a porous Yttrium-Organic Framework based on a large tripodal phosphonate-organic ligand, termed as H_6L . To the best of knowledge there are only three works reporting the organic ligand H_6L : i) Beckmann *et al.* reported, for the first time, the synthesis and structural elucidation of this molecule as a potential organic PBUs to employ in supramolecular chemistry;¹⁵ ii) one year later, in 2009, the research group led by Shimizu reported the preparation of a microporous interpenetrated alkaline-earth phosphonate material, termed as $[Sr_2(H_2L)(CH_3OH)(H_2O)_4]$.¹⁶ This MOF material showed some affinity to CO_2 , however, it also exhibited weak capacity to retain high quantity of this gas; iii) in the same year, Ouellette and co-workers reported the synthesis of a 2D oxovanadium-arylphosphonate structure, formulated as $[V_3O_3(OH)(H_3L)_2] \cdot 7.5H_2O$, being to date the first example of a mixed-valence compound having core.¹⁷

H₆L is an analogue of the 4,4',4''-benzene-1,3,5-triyltribenzoic acid (BTB) organic linker (Figure 6.5). The latter was employed with Zn²⁺ cations for the self-assembly of the well-known highly porous MOF-177 (cage diameter of 14.4 Å).¹⁸ Both **H₆L** and BTB possess the phosphonic and carboxylic acids, respectively, located in order to confer them a planar triangular geometry. The geometry of both organic linkers and the fact that they large and relatively rigid structure confer them good properties to be used as organic PBUs for the preparation of 3D porous MOFs.

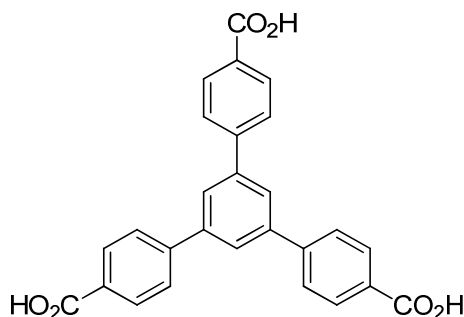


Figure 6.5 – Molecular structure of the 4,4',4''-benzene-1,3,5-triyltribenzoic acid (BTB) organic linker.

This chapter describes the synthesis of the family of isotypical porous MOFs, formulated as [RE(H₃L)]·xH₂O·yMeOH [where RE³⁺ = Y³⁺ (**29**); (Y_{0.95}Eu_{0.05})³⁺ (**30**) and (Y_{0.95}Tb_{0.05})³⁺ (**31**)] from the self-assembly of **H₆L** with respective rare-earth cations, under hydro(solvo)thermal conditions. The preparation of this novel materials can be performed employing distinct synthetic methodologies: i) conventional solvothermal synthesis; ii) slow diffusion; iii) the *bench* “one-pot” approach; and iv) ionothermal synthesis. In addition to all these four methodologies to produce compound **29** as a crystalline material, its preparation as large crystals suitable for single-crystal X-ray diffraction studies was only possible by using the solvothermal synthesis while adding HCl (6 M) to the reaction mixtures.

The crystalline structure of **29** was unveiled by single-crystal X-ray diffraction and all materials were characterized by standard solid-state techniques (powder X-ray diffraction, FT-IR, electron microscopy (SEM and EDS), thermogravimetric and elemental analysis). The adsorption properties of the porous compound **29** were investigated. This compound, with a specific BET surface area of 719 m² g⁻¹, has the ability to retain CO₂ (1.89 mmol g⁻¹) into their structure from a binary mixture of CO₂/N₂. This MOF can also separate small amounts of C₃H₈, almost pure, from a binary C₃H₈/C₃H₆ mixture. Aiming to improve the selective adsorption capacity of **29** towards CO₂, it was prepared the ion-exchanged [Y(H₃L)]·xSolvent_K (**32**) material. After adsorption studies, it was possible to conclude that **32** has the ability to retain CO₂ into their network at higher temperatures, which was not observed for **29**. This is probably due to the inclusion of K⁺ cations into the porous structure of the as-prepared material **29**. Additionally, compound **32** showed to be able to separate C₂H₂, during a short period of time, from a ternary gas mixture composed

of $N_2/C_2H_2/CO_2$. Preliminary photoluminescent properties of compounds **30** and **31** were investigated.

6.2. Synthesis

6.2.1. Synthetic strategy

Aiming at the preparation of compound **29** as large single-crystals for X-ray diffraction studies, it was tested a set of synthetic methodologies: i) conventional solvothermal synthesis; ii) slow diffusion; iii) the *bench* “one-pot” approach; and iv) ionothermal synthesis. All the four approaches employed led to **29** as a microcrystalline white powder. Isolation of large crystals of **29** was only achieved under solvothermal conditions while adding HCl (6 M).

Conventional solvothermal synthesis

A reactive mixture composed of H_6L and $YCl_3 \cdot 6H_2O$, with an overall 1:4 ($H_6L:Y^{3+}$) molar ratio, in a mixture of $H_2O/MeOH$ (v/v 7:3) was prepared and kept at 140 °C for 48 h. After reacting, the desired compound **29** was isolated as microcrystalline white powder. Figure 6.6 shows the PXRD pattern and the morphological features (small rod-like particles with an average size of approximately 1-2 μm) of **29**. The mixed rare-earth materials with 5% of Eu^{3+} (**30**) or 5% of Tb^{3+} (**31**) dispersed in a Y^{3+} matrix were prepared following the same procedure for **29** while adjusting the desired amounts of the lanthanide chloride salts.

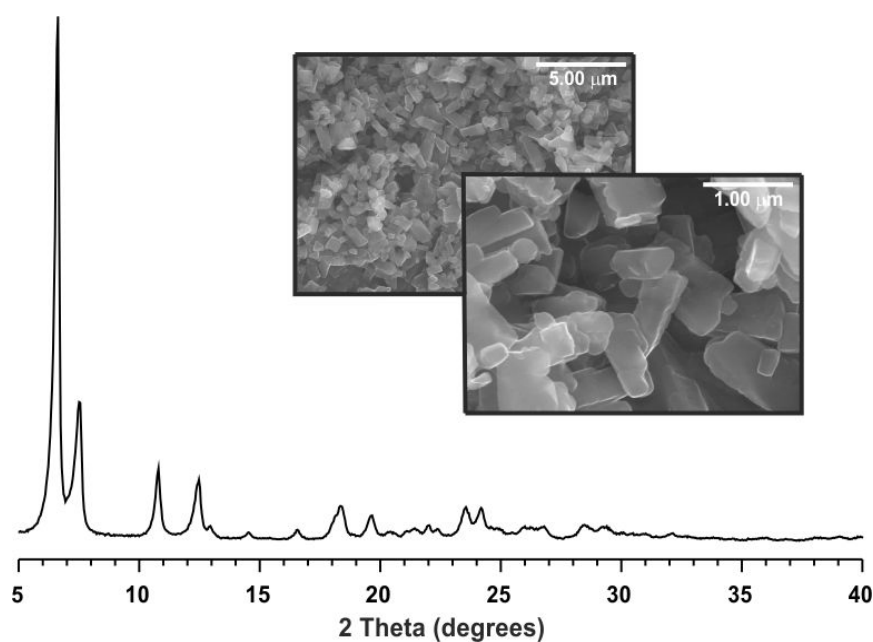


Figure 6.6 – PXRD and SEM images of $[Y(H_3pptd)] \cdot xH_2O \cdot yMeOH$ (**29**) isolated under solvothermal conditions.

Because **29** did not have large enough particle size to be studied using single-crystal XRD, the optimization of various reaction parameters took place:

- Temperature: 100, 140 and 180 °C;
- Heating/cooling temperature ramps: i) 1 h (from ambient temperature to 140 °C) → 24 h (isothermal at 140 °C) → 48 h (cooling to 30 °C); ii) 1 h (from ambient temperature to 140 °C) → 48 h (isothermal at 14 °C) → 72 h (cooling to 30 °C); iii) 1 h (from ambient temperature to 140 °C) → 120 h (isothermal at 14 °C) → 96 h (cooling to 30 °C); iv) 48 h (from ambient temperature to 140 °C) → 24 h (isothermal at 14 °C) → 48 h (cooling to 30 °C); and v) 24 h (from ambient temperature to 140 °C) → 48 h (isothermal at 14 °C) → 72 h (cooling to 30 °C). Figure 6.7 depicts an example of a heating/cooling temperature program used in the optimization process to isolate **29** as single-crystals;

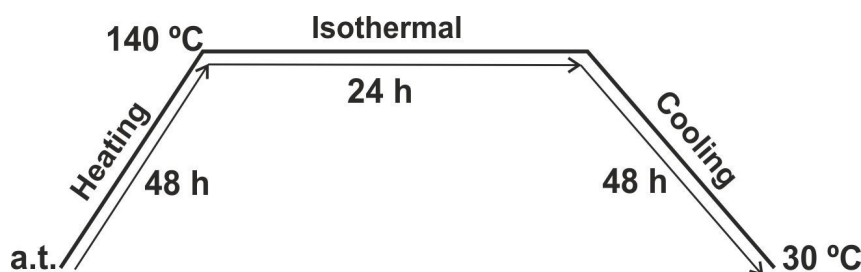


Figure 6.7 – Schematic representation of a heating/cooling temperature program used in the optimization process to isolate **29** as single-crystals: a.t. means ambient temperature.

- Reaction time: 2, 3, 5, 10, 15, 20 and 30 days;
- Solvent: H₂O, H₂O/MeOH (v/v 7:3), H₂O/MeOH (v/v 1:3), H₂O/MeOH (v/v 1:4), H₂O/MeOH (v/v 1:9), H₂O/MeOH (v/v 7:3) and few drops of HF or HBF₄;
- Metal source: YCl₃·6H₂O and YNO₃·xH₂O;
- (Ligand : Metal) molar ratio: 1:2, 1:4, 1:12 (**H₆L**:Y³⁺).

After varying all these synthetic parameters, it was still not possible to isolate compound **29** as large single-crystals.

Ionothermal synthesis

Reactive mixtures composed of **H₆L** and YCl₃·6H₂O were prepared in 1-butyl-3-methylimidazolium chloride [BMIm]Cl, 1-ethyl-3-methylimidazolium chloride [EMIm]Cl or in a eutectic mixture containing choline chloride and urea. Besides the use of different ionic liquids and a eutectic mixture, other reaction parameters were varied: i) temperature (140 and 150 °C); ii) reaction time (48, 72 and 98 h); and iii) **H₆L**:Y³⁺ molar ratio (1:2 and 1:4).

The ionothermal synthetic approach afforded compound **29**, however, once again, as a microcrystalline white powder (Figure 6.8). Morphologically, the particle size and shape of **29** are very similar when compared to those particles obtained by hydro(solvo)thermal synthesis.

One-pot synthesis

As reported in Chapter 3, one-pot synthesis has been a viable alternative to isolate MOF materials with large particle size, being known as a simple and low-energy consumption method. Therefore, reactive mixtures containing **H₆L** and $\text{YCl}_3 \cdot 6\text{H}_2\text{O}$, with an overall (**H₆L**: Y^{3+}) molar ratio of 1:4, in $\text{H}_2\text{O}/\text{MeOH}$ (v/v 7:3) or [EMIm]Cl were prepared. The resulting solution was kept under constant magnetic stirring. The reaction time (2, 24, 48 and 72 h) and temperature (ambient temperature, 60 and 100 °C) were varied.

Such as for the previous synthetic procedure, the preparation of compound **29** as single-crystals was unsuccessful. Nevertheless, this method showed to be a very good alternative to isolate **29** as a microcrystalline powder, in milder reaction conditions. The distribution of particle size is not however very homogeneous and the morphology is not regular and well-defined (Figure 6.8). Additionally, “one-pot” synthesis seems to be able to isolate **29** in large amounts (*i.e.*, in the gram-scale) in a simple way under mild conditions.

Slow diffusion

This method is very slow, unattractive for industry and affords small quantities of the desired materials. Nevertheless, slow diffusion synthesis is, probably, the best alternative to grow crystals. Some attempts were performed to isolate single-crystals of **29** using this approach:

- i) an aqueous solution of $\text{YCl}_3 \cdot 6\text{H}_2\text{O}$ was layered with other containing **H₆L** and MeOH. The reaction occurred at ambient temperature during 20 days;
- ii) an aqueous solution of $\text{YCl}_3 \cdot 6\text{H}_2\text{O}$ was layered with 1-octanol; a third layer containing **H₆L** and MeOH was added. The reaction was kept at ambient temperature for 30 days;
- iii) a solution composed of $\text{YCl}_3 \cdot 6\text{H}_2\text{O}$ and [EMIm]Cl was layered with H_2O , and then another solution containing **H₆L** and MeOH (third layer) was added. The reaction was kept at ambient temperature for 20 days.

Within all these three attempts, compound **29** was again isolated as a microcrystalline white powder. Concerning morphology, this synthetic method afforded larger particles (with some of them reaching approximately 20 μm) with needle-like shape (Figure 6.8). Unfortunately, **29** was still not composed of crystals with enough size for single-crystal XRD studies.

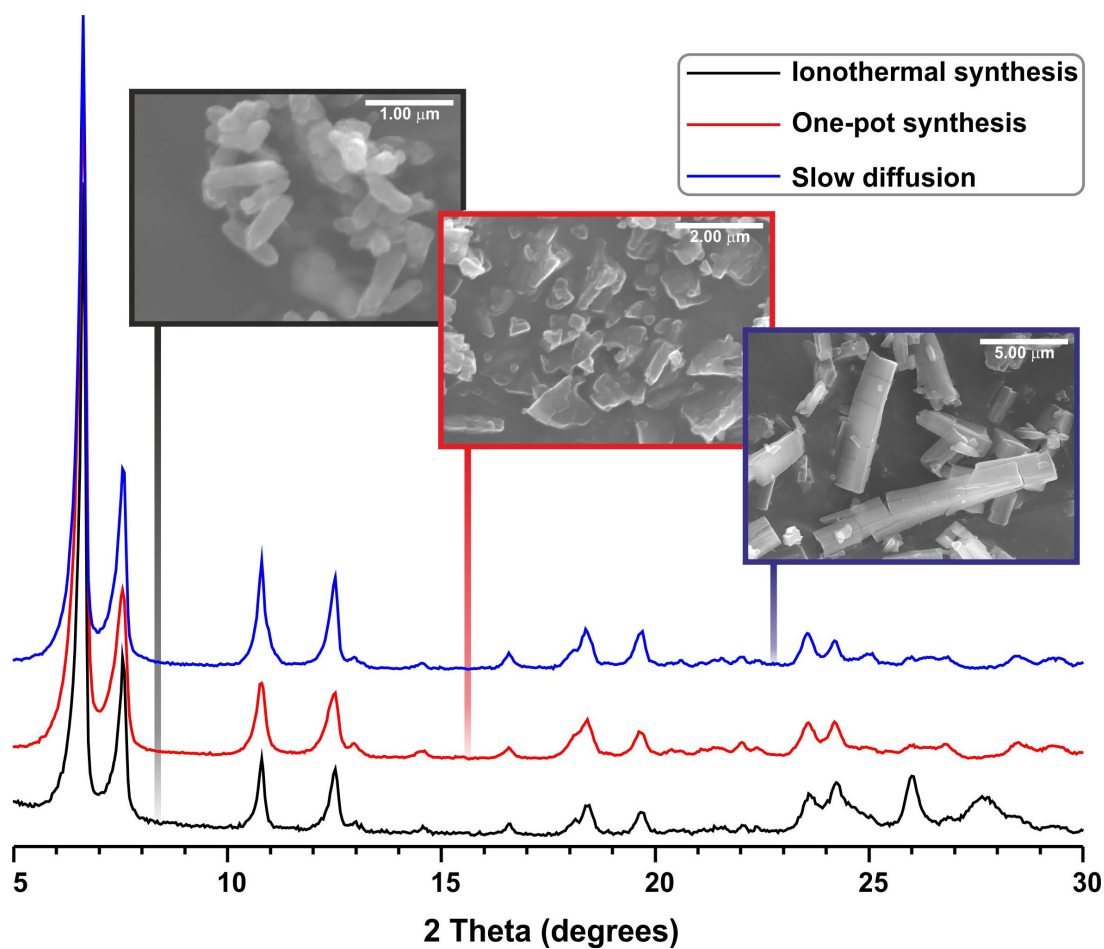


Figure 6.8 – PXRD and SEM images of compound **9** prepared by using different synthetic approaches: ionothermal synthesis (black), one-pot synthesis (red) and slow diffusion (blue).

Preparation of compound $[Y(H_3L)] \cdot xH_2O \cdot yMeOH$ as large single-crystals

A solution of $YCl_3 \cdot 6H_2O$ dissolved in distilled water was added to a solution composed of the large tripodal organic ligand **H₆L** and HCl (6 M) (0.25, 0.5, 1, 3 or 5 mL) in $H_2O/MeOH$. The resulting reactive reaction mixtures were kept according to the following temperature program: 48 h (from ambient temperature to 140 °C), 24 h (isothermal at 140 °C) and 48 h (cooling to 30 °C) (see sub-section 8.13.1 in the Experimental Section for further details).

The addition of higher amounts of HCl (6 M) to the reaction mixtures led to a considerable increase in the particle size of compound **29**, while the crystalline structure remained intact. The exception was for the reaction where it was used 5 mL of HCl (6 M) which afforded a mixture of the crystalline phase of **29** with a secondary one (Figure 6.9). This method allowed, thus, the isolation of large single-crystals (note the presence of particles with sizes higher than 100 μm) for the desired XRD studies. Compound **29** comprises needle-like particles which break when submitted to high vacuum during the SEM analysis. This is, probably, due to the release of the solvent molecules from the crystalline structure.

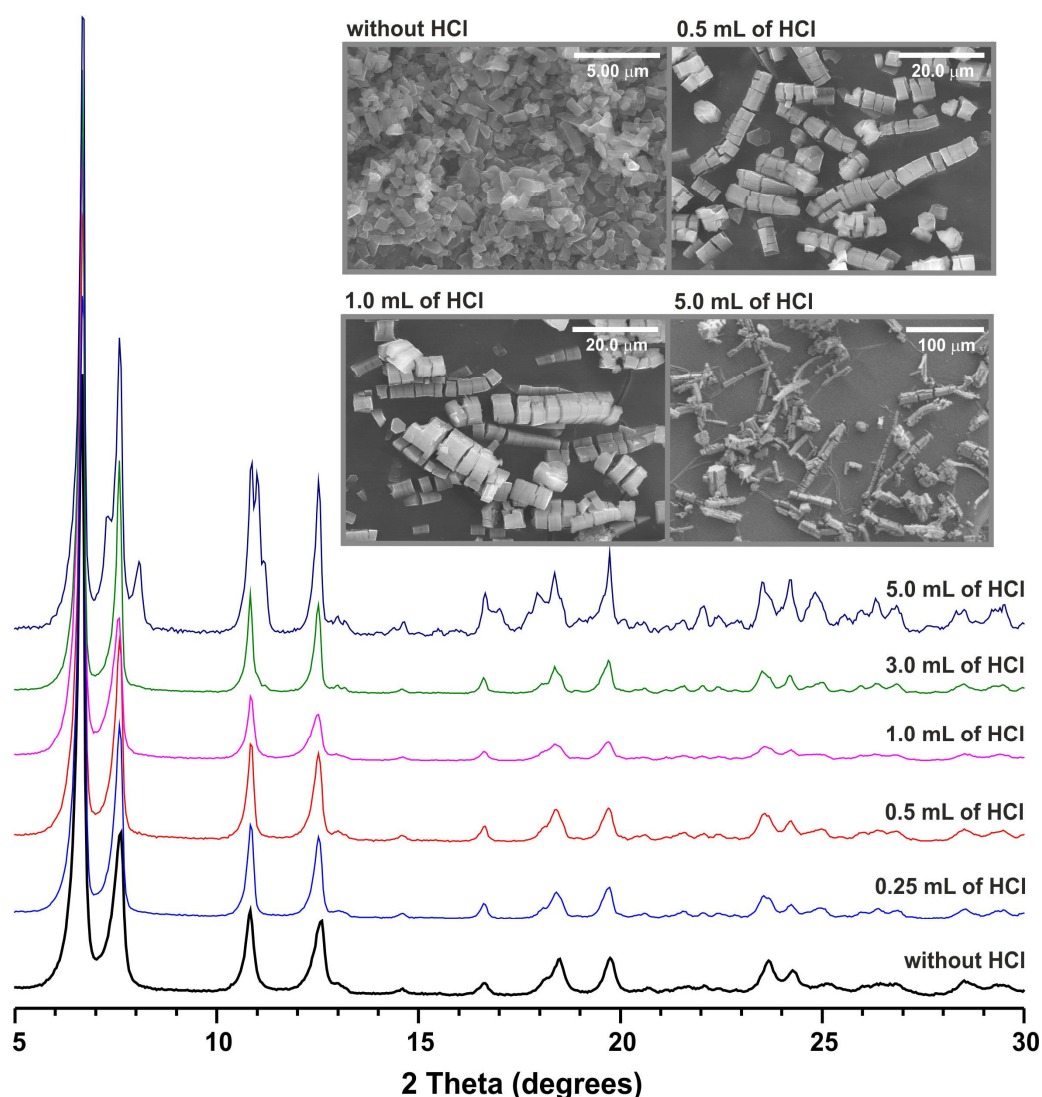


Figure 6.9 – PXRD and SEM images of compound **29** prepared while adding different amounts of HCl (6M): it is visible the effect of HCl (6 M) in the particle size of **29**. Higher amounts lead to the formation of larger particles with needle-like shape.

6.3. Crystal Structure Description of the Porous Material

$[Y(H_3L)] \cdot xH_2O \cdot yMeOH$

The structural details reported in this section come from a preliminary elucidation of the crystal structure of **29**, with further crystallographic studies being needed, specially to investigate the behaviour of the solvent molecules in the channels.

Large needle-like crystals of **29** were directly harvested from the reaction vessels. This compound crystallizes in the orthorhombic $Pna2_1$ space group. The asymmetric unit of **29** comprises a single crystallographically independent Y^{3+} metallic center, an organic ligand moiety and several (being not exactly determined yet) solvent molecules (water and methanol). The connection of the Y^{3+} metal center to six oxygen atoms, belonging all to

six phosphonate groups of different organic ligands, leads to the formation of a $\{YO_6\}$ six-coordinated distorted octahedra (Figure 6.10).

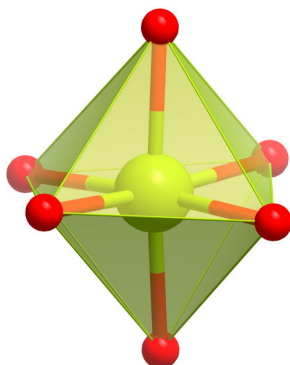


Figure 6.10 – Schematic representation of the distorted $\{YO_6\}$ coordination octahedron present in the material **29**: the yttrium metallic center and the oxygen atoms composing the polyhedra are represented as lime and red spheres, respectively.

The arrangement between the phosphonate-based organic ligands and the Y^{3+} cations leads to the formation of a 3D structure comprising one-dimensional channels, with distorted hexagonal geometry, running along of the $[100]$ direction of the unit cell (Figure 6.11). Because the refinement of the crystalline structure of **29** is still not completed, the solvent molecules filling the channels of **29** are not represented. Another crystallographic feature that stands out is the presence of 1D hydrogenophosphonate yttrium chains running along of the $[100]$ direction of the unit cell.

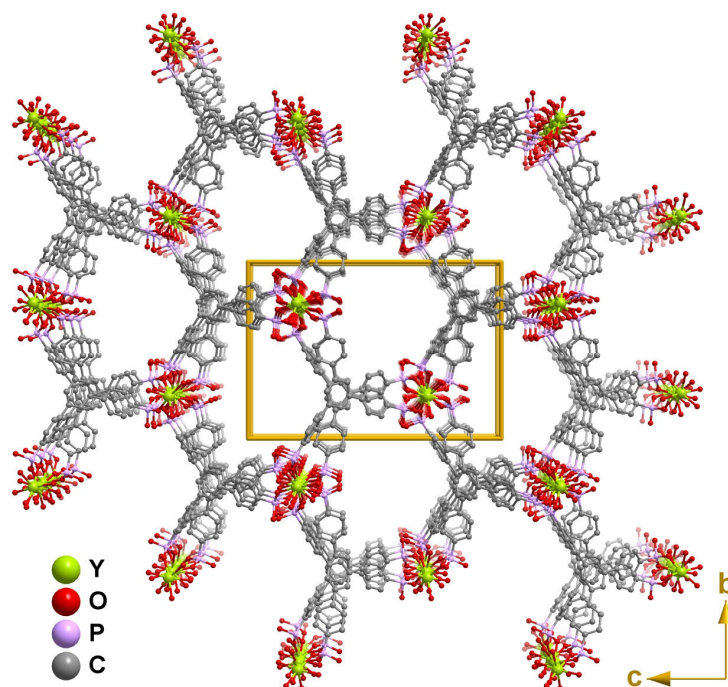


Figure 6.11 – Crystal packing of the porous material **29** viewed in perspective along the $[100]$ direction of the unit cell. Solvent molecules were omitted for clarity.

6.4. Thermogravimetry and Variable Temperature Powder X-ray Diffraction Studies

The thermal behavior of compound **29** was investigated between ambient temperature and *ca.* 800 °C from thermogravimetric analysis (Figure 6.12 – *bottom left*). Additionally, to gain insight into the structure modifications that occur in the crystal structure of **29**, VTPXRD studies (in the 30-600 °C temperature range) were also performed (Figure 6.12 – *top right*).

From the thermogravimetric curve of **29** it is possible to observe that the first weight loss occurs below *ca.* 100 °C (precisely, between ambient temperature and *ca.* 82 °C). This step corresponds to a weight loss of *ca.* 22.7% and it is attributed to the release of all the solvent molecules contained into the framework of **29**. VTPXRD studies show, at *ca.* 50 °C, a structural modification in the crystalline structure of **29** due to this first weight loss process. This may be endorsed to contraction of the network of the porous material during the release of the water and methanol molecules. Noteworthy, the new desolvated structure is highly robust until approximately *ca.* 400 °C being not visible any additional weight loss or structural modification.

After *ca.* 376 °C, two weight losses of 21.7 and 5.2% are observed. These are related with the decomposition of the organic components leading to a drastic loss of crystallinity and, consequently, to the formation of an amorphous residue at *ca.* 560 °C.

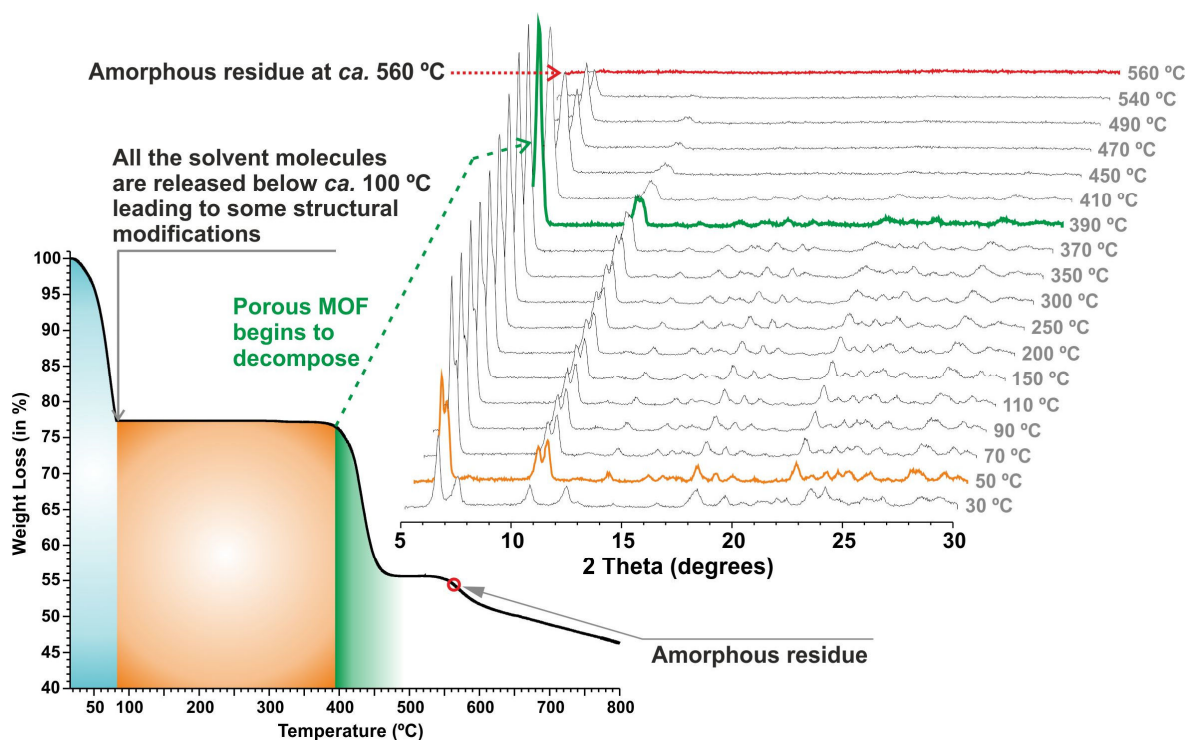


Figure 6.12 – Thermogram (*below left*) and variable-temperature powder X-ray diffraction patterns (*top right*) of the porous material **29**.

6.5. FT-IR Spectroscopy

The FT-IR spectrum of the porous material **29** (Figure 6.13) exhibits diagnostic bands of the various structural features described above. As previously mentioned, **29** has solvent molecules (water and methanol) of crystallization in their channel structure. The FT-IR spectrum exhibits a very broad band in the *ca.* 3723-2555 cm^{-1} spectral range, attributed to the overlap of the typical $\nu(\text{H}_2\text{O})_{\text{cryst}}$, $\nu(\text{CH}_3\text{O-H})_{\text{cryst}}$, $\nu(\text{POH})$ and $\nu(-\text{CH}_2-)$ stretching vibrational modes.

Below 1800 cm^{-1} the FT-IR spectrum of **29** is quite complex, exhibiting a large number of weak-to-very strong vibrational bands attributed, mainly, to the large **H₆L** organic ligand. Based on the literature¹⁹ the typical in-plane deformation of water molecules appears at *ca.* 1632 cm^{-1} as a vibration band of medium intensity, followed of three medium weak bands centred at *ca.* 1600, 1557 and 1503 cm^{-1} , respectively, attributed to the $\nu(-\text{C}=\text{C}-)$ stretching vibration modes of the aromatic rings. Additionally, the typical $\nu(\text{P}=\text{O})$ stretching vibrations, with very strong intensity, are present at *ca.* 1144 and 1075 cm^{-1} . At *ca.* 925 and 829 cm^{-1} the $\nu(\text{P}-\text{O})$ vibration modes appear as bands of strong intensity.

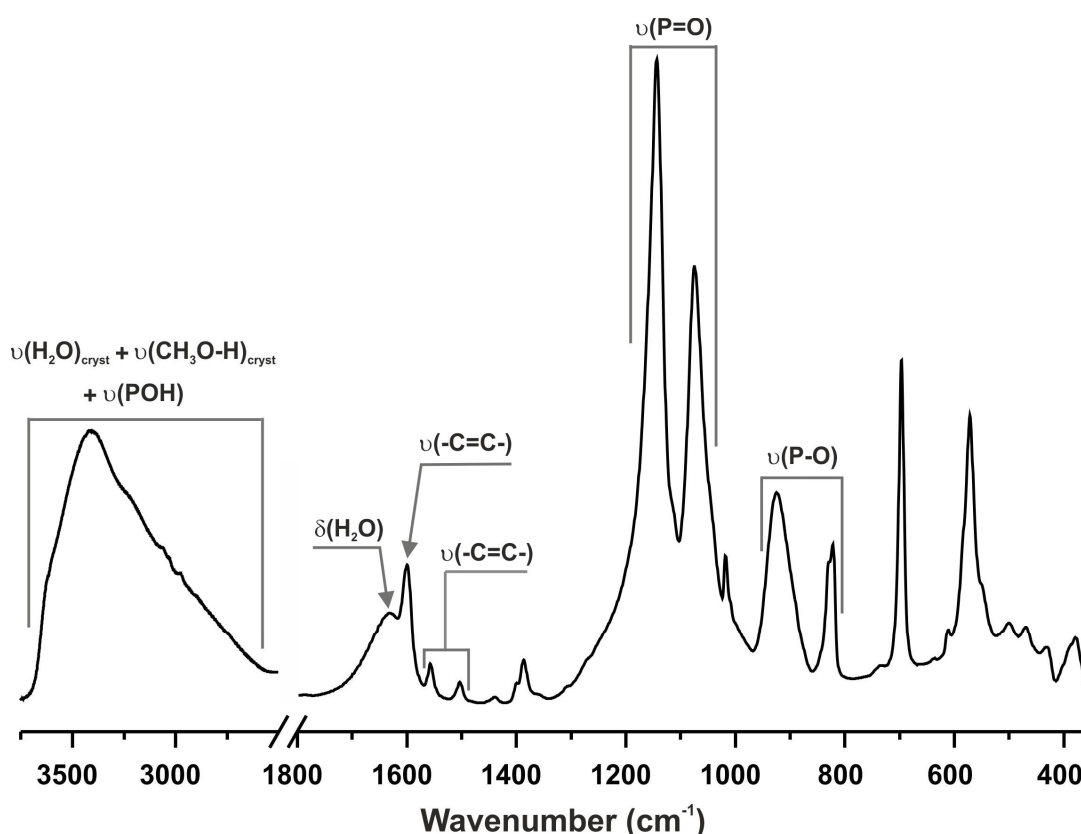


Figure 6.13 – FT-IR spectrum of the porous material **29**.

6.6. Adsorption Properties

As mentioned in Chapter 1, in the last years several scientific research groups have dedicated great efforts in the preparation of porous MOFs envisaging their application in the sequestration, separation and purification of gases with industrial and environmental interest. The selective adsorption capacity of the porous material toward some gases (CO_2 , C_2H_2 , C_3H_8 and C_3H_6) was, thus, investigated. The selective adsorption of propane, propylene, acetylene and carbon dioxide over as, for instance nitrogen and methane may be related with some differences in their physical properties, such as kinetic diameter, polarizability (α), quadrupole moment (θ) and dipole moment (μ).²⁰

The first step of these studies started with the acquisition of the conventional single component adsorption isotherms in order to study the porous nature of the materials, followed by more complex and advanced studies such as pulse gas chromatography and gas separation breakthrough studies.

6.6.1. Static adsorption experiments

In order to evaluate the accessibility of guest molecules into the porous framework of compound **29**, the N_2 at 77 K and CO_2 at 195 K adsorption isotherms were collected (Figure 6.14). Both N_2 and CO_2 adsorption isotherms display type-I behavior, being characteristic of crystalline microporous materials. Material **29** possesses specific BET surface areas of 104 and 719 $\text{m}^2 \text{g}^{-1}$ measured from the N_2 and CO_2 adsorption isotherms, respectively.

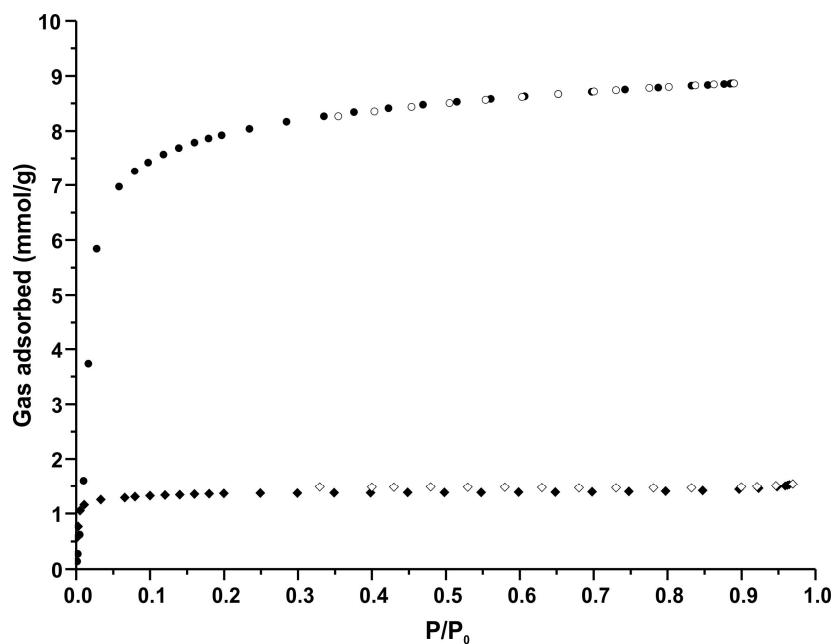


Figure 6.14 – N_2 (diamond) and CO_2 (circle) adsorption isotherms measured at 77 and 195 K, respectively. The filled and empty symbols represent adsorption and desorption processes, respectively.

Compound **29** has much higher adsorption capacity for CO₂ than for N₂. This fact may be associated with kinetic reasons, avoiding the diffusion of N₂ molecules into the porous framework. At higher adsorption temperatures, in this case 195 K, the CO₂ molecules have larger kinetic energy, contrasting with the lower one to N₂ at 77 K. Therefore, CO₂ molecules are able to enter into the pores of the material and, consequently, there is no diffusion limitation. As a consequence of that the adsorption values are more reasonable. The diffusion limitations of N₂ molecules at 77 K are not an uncommon result, being typical of ultramicroporous materials with pore size < 0.5 nm.²¹⁻²²

6.6.2. Pulse gas chromatography experiments

The potential application of the porous material **29** in gas purification processes was investigated. A chromatographic column was constructed and then packed with **29** (Figure 6.15). The pulse gas chromatography experiments have been performed in the 273-403 K temperature range using two different gas mixtures: i) C₂H₂/CO₂/H₂; and ii) C₃H₆/C₃H₈/H₂. Each experiment consisted in the injection, at 1 bar, of the previously mentioned equimolecular gas mixtures (0.6 mL) on the home-made chromatographic column, packed with the porous materials (previously activated at 423 K for 4 h), at different temperatures (273-403 K). The separation gas performance has been examined by means of a mass spectrometer gas analysis system. During the experiments a constant inert He flow (20 mL min⁻¹) was used as the carrier gas. The interaction between H₂ and the studied materials is almost negligible, being used as reference value for the column dead volume. Figure 6.16 depicts the instrumentation used to perform the gas separation measurements.

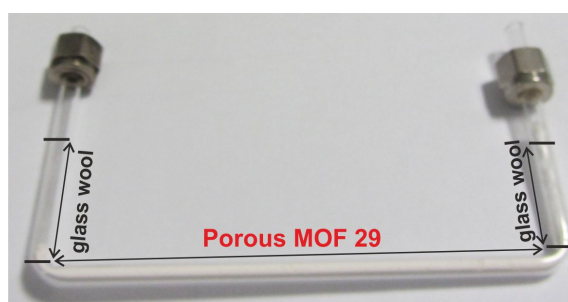


Figure 6.15 – Picture of the home-made chromatographic column packed with the porous material **29** to use in the gas adsorption measurements. The glass wool is used to avoid the escape of **29** when the gas fluxes are flowed.

Pulse gas chromatograms for an equimolar mixture of C₃H₈/C₃H₆/H₂ collected at different temperatures using **29** show that this material can retain C₃H₈ and C₃H₆, mainly at lower temperatures (see Figure D.1.1 in the Appendices for further details). At higher temperatures (*i.e.*, 363 and 403 K) both C₃H₈ and C₃H₆ are retained into the structure of **29** during short periods of time. Decreasing the experimental temperature, the tested gases are retained during longer periods of time leading to a peak enlargement of the

chromatograms. Nevertheless, it is well visible that C_3H_6 has higher affinity with the porous structure of **29**, remaining retained during longer periods of time than C_3H_8 .

Regarding the experimental measurements toward the separation process of CO_2 and C_2H_2 , the results suggest that compound **29** allows considerably interactions with both gases (see Figure D.1.2 in the Appendices for further details). It is nevertheless possible to observe that **29** has more affinity for C_2H_2 , being this gas retained, mainly, at lower temperatures (*e.g.*, 273 K) for longer periods of time than CO_2 (Figure 6.17).



Figure 6.16 – Schematic representation of the instrumentation used for the separation tests: (*top*) overview of the equipment composed of flux gas controllers, a gas chromatograph and a mass spectrometer; (*bottom left*) flux gas controllers for different gases of interest; and (*bottom right*) view of the home-made chromatographic column packed with **29** inside of the thermostated GC oven.

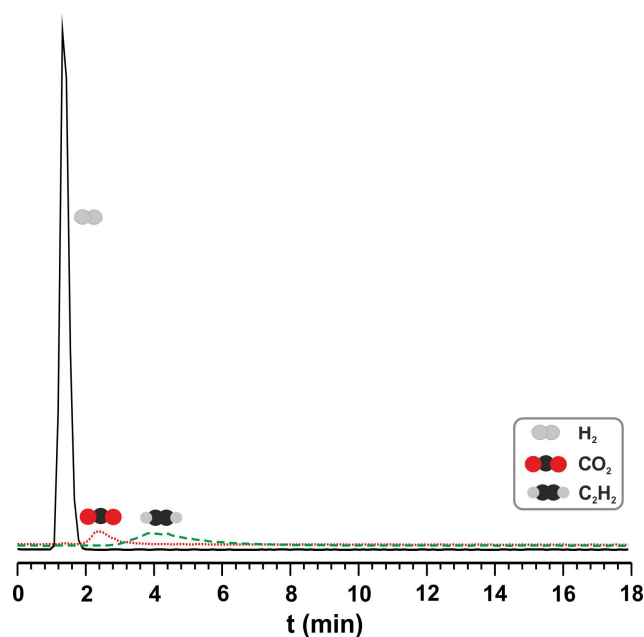


Figure 6.17 – Pulse gas chromatograms for an equimolar mixture of $CO_2/C_2H_2/H_2$ collected at 273 K using material **29**.

6.6.3. Gas separation breakthrough studies

Breakthrough curves were measured to evaluate the performance of the porous material **29** in the bulk separation of gas mixtures. These experiments were performed using the home-made chromatographic columns described in the previous section, packed with the porous material **29**. Before flowing the desired gas mixtures the column was activated at 423 K for approximately 4 h under a pure He flow (20 mL min^{-1}).

The first experiment used two gas mixtures, $\text{C}_3\text{H}_8/\text{N}_2$ ($10 \text{ mL min}^{-1} : 10 \text{ mL min}^{-1}$) and $\text{C}_3\text{H}_6/\text{N}_2$ ($10 \text{ mL min}^{-1} : 10 \text{ mL min}^{-1}$), to evaluate the performance of **29** in the retention of propane and propylene at 273 and 296 K (see Figures 6.18 and D.1.3 in the Appendices). Figure 6.18 displays the $\text{C}_3\text{H}_8/\text{N}_2$ and $\text{C}_3\text{H}_6/\text{N}_2$ breakthrough experiments at 273 K for **29**. The results show that N_2 is not retained into the porous network of **29**, while C_3H_8 and C_3H_6 have strong interactions with the framework, being C_3H_6 more retained (Table 6.1). These results are in agreement with the pulse gas chromatography studies, because also in those experiments it is possible to observe that C_3H_6 has stronger interactions with **29** than C_3H_8 .

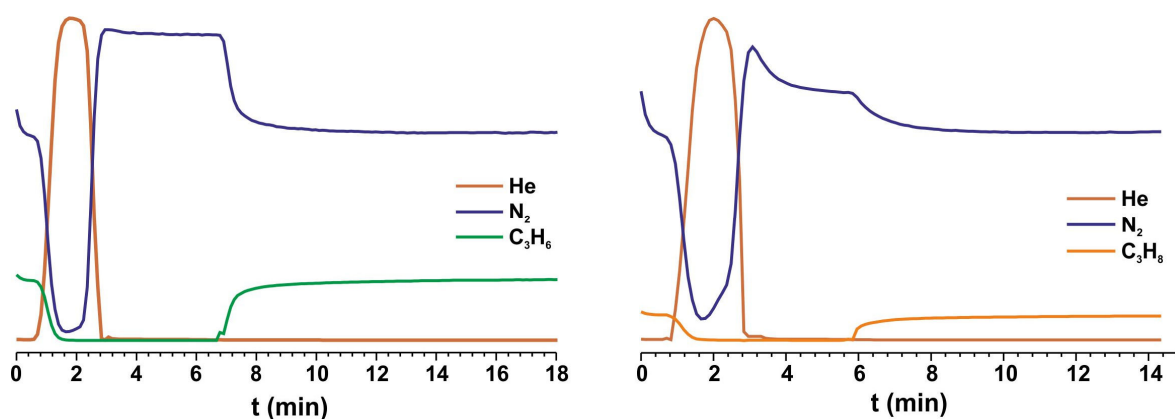


Figure 6.18 – (left) $\text{C}_3\text{H}_6/\text{N}_2$ and (right) $\text{C}_3\text{H}_8/\text{N}_2$ breakthrough curves measured at 273 K for the porous material **29**.

In the second experiments, mixtures of N_2 (17 mL min^{-1}) and CO_2 (3 mL min^{-1}), simulating the emission of a flue gas from a power plant, were flowed through **29**, at 273 and 298 K. The obtained breakthrough curves revealed that CO_2 is selectively retained while N_2 flew through the materials (Figure 6.19). The breakthrough curve for **29**, measured at 273 K, shows that CO_2 is retained into the porous structure of this material during 5.92 min. This result means that 1.89 mmol of CO_2 is retained per gram of compound **29**. At higher temperatures (*i.e.*, 298 K) it is observed a drastic decrease in the adsorption capacity of **29** towards CO_2 . All data are summarized in Table 6.1.

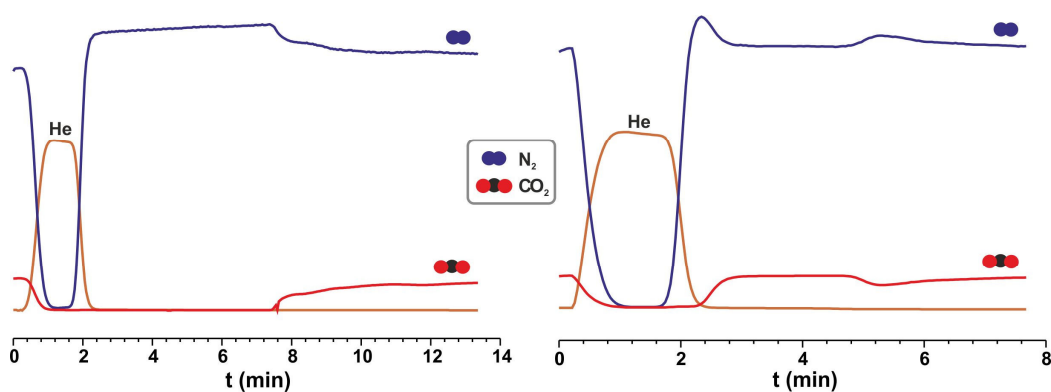


Figure 6.19 - CO_2/N_2 breakthrough curves measured at (left) 273 and (right) 298 K for the porous material **29**.

Table 6.1 - Amount of propylene, propane and carbon dioxide (mmol g^{-1}) retained from $\text{C}_3\text{H}_6/\text{N}_2$, $\text{C}_3\text{H}_8/\text{N}_2$ and CO_2/N_2 breakthrough curves measured at different temperatures for the porous material **29**.

Adsorbate	273 K	296 K	298 K
C_3H_6	4.47	4.03	-
C_3H_8	3.13	2.59	-
CO_2	1.89	-	0.18

A complex ternary gas mixture, $\text{CH}_4/\text{CO}_2/\text{C}_2\text{H}_2$ ($14 \text{ mL min}^{-1} : 3 \text{ mL min}^{-1} : 3 \text{ mL min}^{-1}$), was also tested to assess, qualitatively, the interaction of these gases with compound **29** at 273 K. From the breakthrough curves (Figure 6.20) is possible to observe that CH_4 was not retained into the framework. The interactions between CO_2 and C_2H_2 with the porous material **29** are very similar, being these gases more retained than CH_4 . Because CO_2 and C_2H_2 are released practically at the same time, it seems that the separation between these two gases is not possible under the applied conditions.

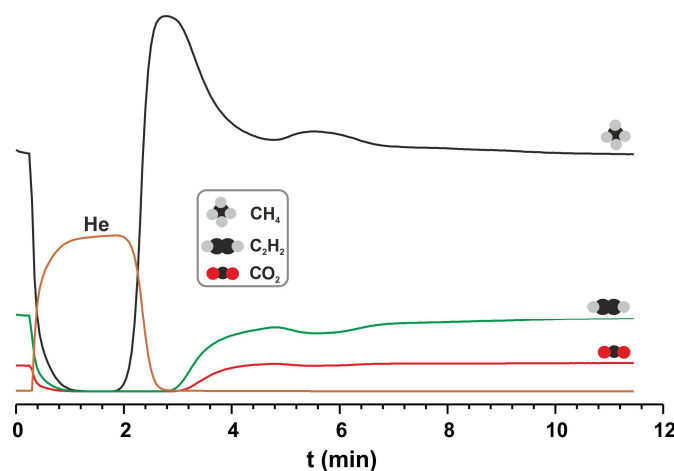


Figure 6.20 – $\text{CH}_4/\text{CO}_2/\text{C}_2\text{H}_2$ breakthrough curves measured at 273 K for the porous material **29**.

Finally, it was collected other breakthrough curves flowing through the compound **29** a gas mixture composed of He (10 mL min^{-1}), C_3H_8 (10 mL min^{-1}) and C_3H_6 (10 mL min^{-1}) at 273 and 297 K. He was used as diluting gas since both C_3H_8 and C_3H_6 are strong interacting adsorbents. As expected, based in previous breakthrough experiments, C_3H_8 and C_3H_6 have strong interaction with the framework of **29**. Although both gases are jointly retained, C_3H_6 has stronger interaction with **29** (Figure 6.21). Therefore, during a certain period of time (between 3.98 and 5.17 min) the porous material **29** is able to separate propane from propylene which is of industrial interest.

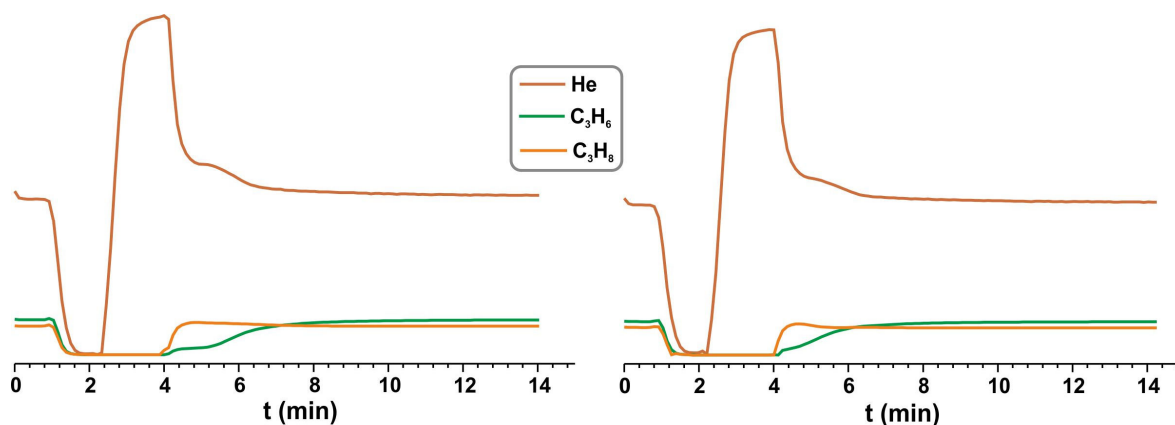


Figure 6.21 – $\text{C}_3\text{H}_6/\text{C}_3\text{H}_8/\text{He}$ breakthrough curves measured at 273 (left) and 297 K (right) for the porous material **29**.

6.6.4. Preparation and adsorption properties of the ion-exchanged $[\text{K}_x\text{Y}(\text{H}_{3-x}\text{L})]\cdot y\text{Solvent}$

In order to improve the adsorption properties of the porous material **29**, mainly in the retention of CO_2 , several ion-exchange experiments were performed. Ethanolic solutions of KOH (0.5, 0.25, 0.05 and 0.025 M) were prepared. After optimization, it was found that the best conditions for the ion-exchange reaction consisted in the use of more diluted solutions of KOH, once the more concentrated ones afford amorphous or poorly crystalline materials. Therefore, reaction mixtures containing 0.025 g of **29**, KOH (0.05 M) in 5 mL of ethanol was prepared and then, ultrasonicated for approximately 5 min. The resulting suspension was stirred at ambient temperature during 24 h. After that, the final compound, formulated as $[\text{K}_x\text{Y}(\text{H}_{3-x}\text{L})]\cdot y\text{Solvent}$ (**32**) was recovered by vacuum filtration and air-dried at ambient temperature.

After characterization by powder X-ray diffraction (PXRD), it was observed that material **32** has a different PXRD pattern than the starting material **29** (Figure 6.22). These differences may be, probably, related with some distortion in the framework of **29** promoted by the inclusion of K^+ . Because the ion-exchanged material **32** was isolated as powders, its crystalline structure remains unknown.

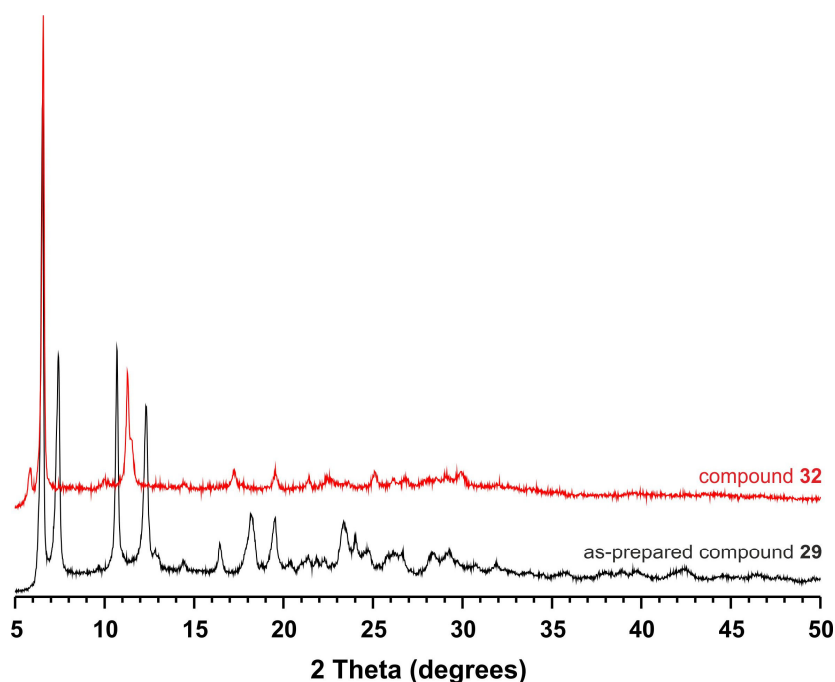


Figure 6.22 - PXRD patterns of the as-prepared material **29** and of the ion-exchanged material **32**.

Gas separation breakthrough studies

Preliminary adsorption tests were performed for the ion-exchanged material **32**. Measurements were very similar to those for material **29**: a chromatographic column was packed with **32**, being then activated at 443 K for approximately 4 h under a pure He flow (20 mL min^{-1}).

The performance of **32** in the bulk separation of a mixture of gases was evaluated. A mixture composed of N_2 (17 mL min^{-1}) and CO_2 (3 mL min^{-1}) was flowed through material **32** at 273, 297 and 323 K (Figure 6.23). Results show that, as expected, N_2 is not retained in the column. However, different behavior is visible for CO_2 which interacts strongly with **32**. Although the amount of carbon dioxide (1.53 mmol g^{-1}) retained at 273 K is lower than that observed, under the same conditions, for **29** (1.89 mmol g^{-1}), at higher temperatures (297 and 323 K) compound **32** is capable to adsorb larger amounts of this gas (Table 6.2). This improvement is, probably, related with the presence of K^+ cations in the framework of the **32**.

Table 6.2 - Comparison of the amount of CO_2 (mmol g^{-1}) retained in dynamic conditions from the CO_2/N_2 breakthrough experiments at different temperatures for material **29** and **32**.

Material	273 K	297 K	323 K
29	1.89	0.18	-
32	1.53	0.82	0.33

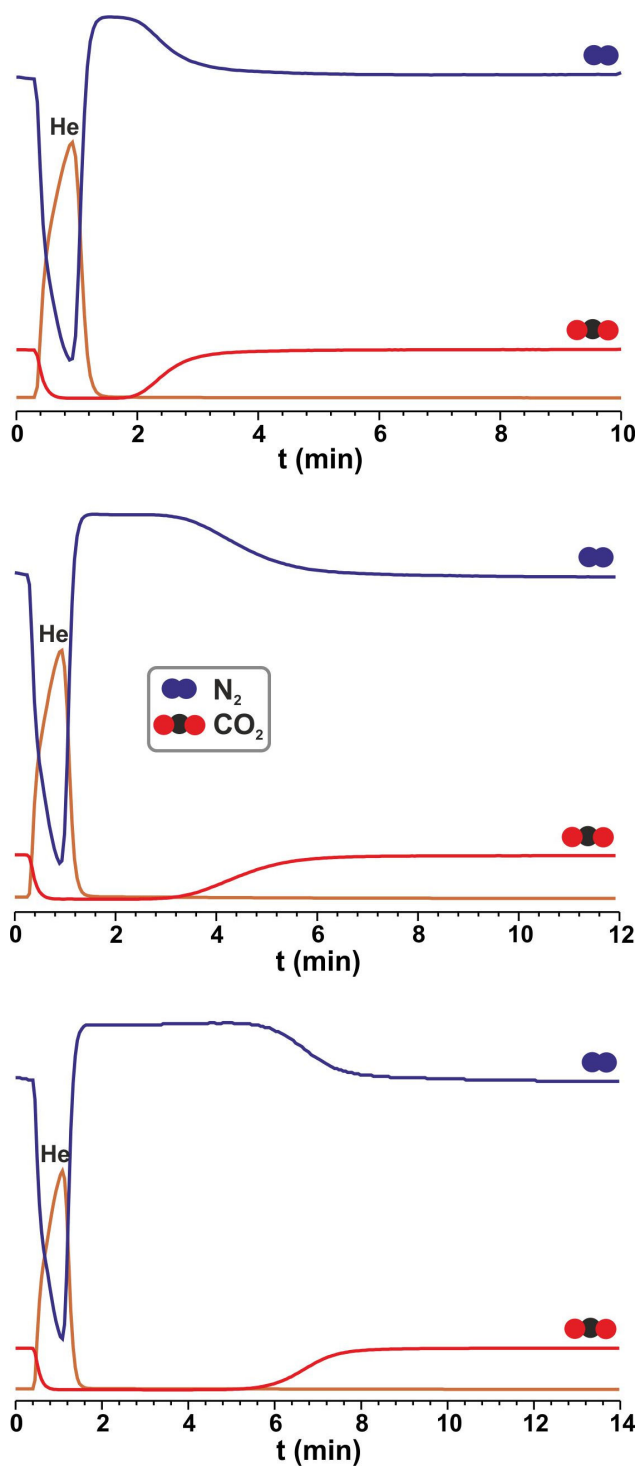


Figure 6.23 – N₂/CO₂ breakthrough curves measured at (bottom) 273, (middle) 297 and (top) 323 K for porous material **32**.

The last measurement was based on the use a complex ternary gas mixture containing N₂ (14 mL min⁻¹), CO₂ (3 mL min⁻¹) and C₂H₂ (3 mL min⁻¹), at 273 K, in order to evaluate, qualitatively, the interaction of material **32** with the last two gases. As for the previous experiments, N₂ is not retained in the column. Nevertheless, C₂H₂ and CO₂ have strong interaction with **32**, being the latter gas more retained (Figure 6.24).

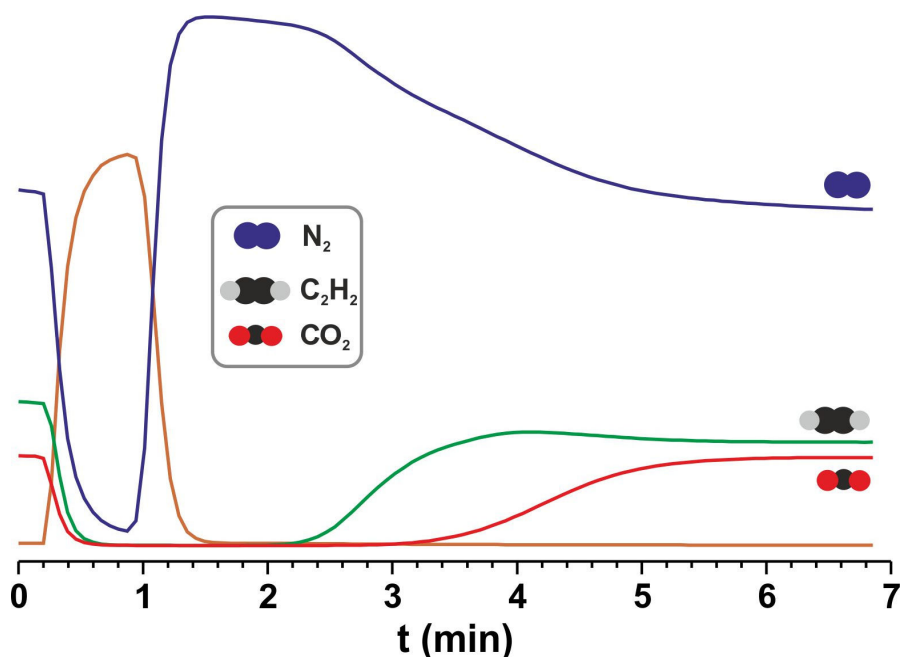


Figure 6.24 – $\text{N}_2/\text{CO}_2/\text{C}_2\text{H}_2$ breakthrough curves measured at 273 K for porous material **32**.

6.7. Stability Studies under Constant CO_2 Flow

In this section it will be described the stability and robustness of the porous material **29**, after desolvation, under a constant CO_2 flow measured at different temperatures and flow pressures.

Compound **29** was packed in a quartz capillary ($\Phi = 0.5$ mm) and placed in a home-made sample holder (Figure 6.25). A constant He flow was passed through the material while heated from 303 to 375 K (heating ramp of 6 K/h). The latter temperature was kept for 1h30min (while using a constant He flow) to achieve the complete desolvation of **29**. After dehydration, the temperature was cooled down to 303 K (cooling ramp of 2 K/h) and the gas flux was replaced from He to CO_2 . After stabilization the flux of CO_2 (during approximately 45 min), the pressure was increased for 1, 2, 3, 4 and 5 bar, remaining constant for 25 min at each pressure level. Then, the CO_2 flow pressure was allowed to decrease to 1 bar and the temperature cooled down to 273 K (cooling ramp of 2 K/h). The CO_2 flow pressure was manipulated in a quite similar way to that used for the measurements performed at 303 K. Finally, the desolvated form of **29** was maintained at 273 K, under a small and constant CO_2 flow for approximately 8 h. In all the experience steps, powder X-ray diffraction patterns were collected with intervals of 5 s. All these investigations were performed in the beamline ID11 of the European Synchrotron Radiation Facility (ESRF) (Grenoble, France).

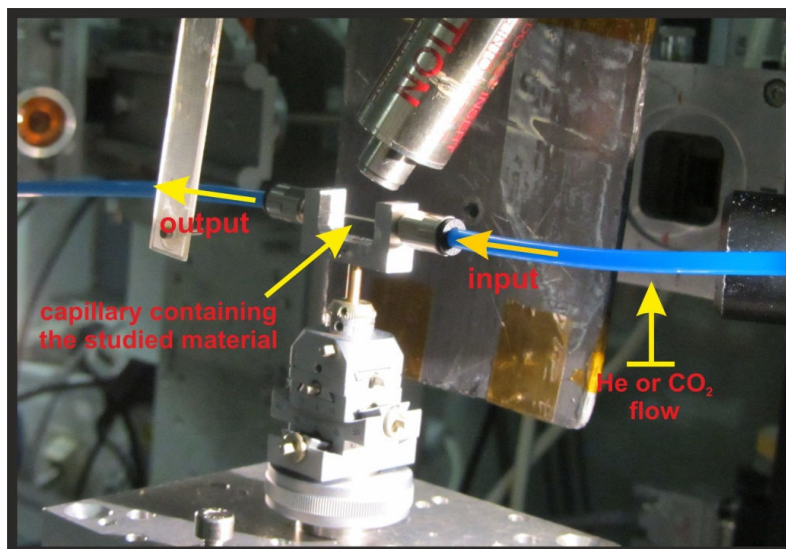


Figure 6.25 - Schematic representation of the instrumentation used for the high-resolution powder X-ray diffraction studies.

The stability and robustness of the porous material **29** regarding its desolvation process and exposure to a constant CO₂ flow was studied by high-resolution synchrotron powder X-ray diffraction. Studies started, as mentioned above, with the desolvation of **29** using a constant He flow while increasing the temperature from 303 to 375 K. During this process it was observed a structural modification promoted by the release of the solvent molecules. The new phase remained stable for a long period of time and it seems to be more crystalline than the original one (Figure 6.26).

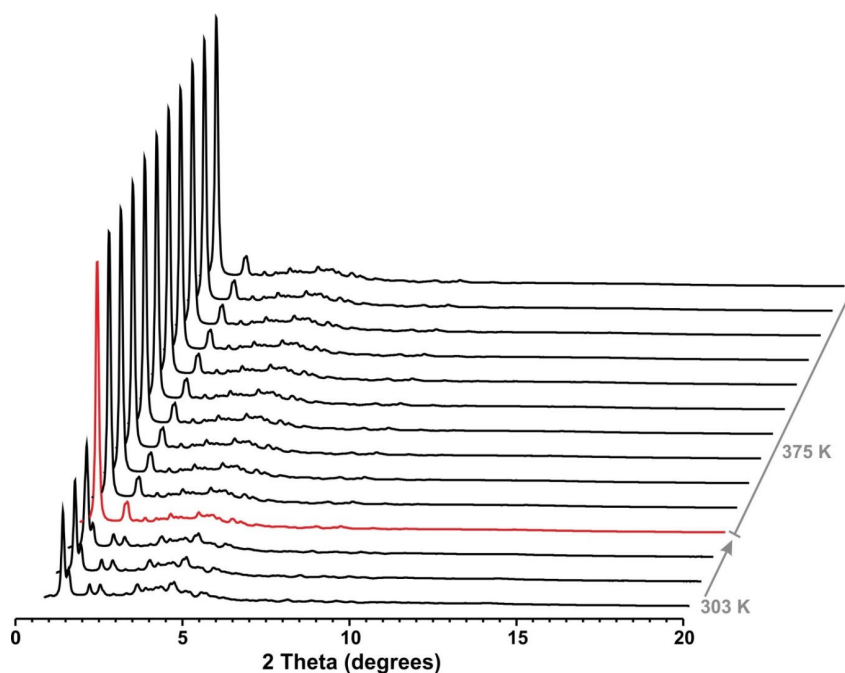


Figure 6.26 - PXRD patterns collected ($\lambda = 0.2954$ nm) after dehydration process of the porous material **29**.

After the desolvation step, the experimental temperature was decreased to 303 K. Figure 6.27 shows a small decrease in the crystallinity of the studied material (mainly observed in the first peak) during the cooling process, however, the crystalline structure remains the same. The flow of He was replaced for CO₂ in order to evaluate if the accommodation of this gas induces some structural modification in the desolvated form of **29**. Therefore, these measurements were initialized by allowing the passage of a small CO₂ flow through the capillary containing the material. Pressure was increased for 1, 2, 3, 4, 5 bar and, finally, decreased for 1 bar. Despite some variation in the crystallinity of the material, promoted by the variation of the pressure, its structure remained robust and stable (Figure 6.28).

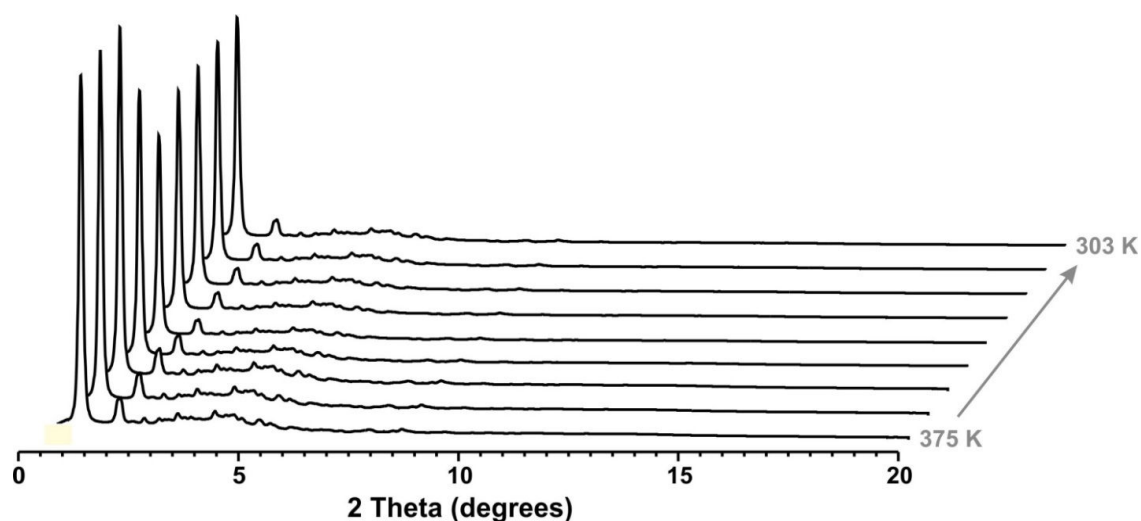


Figure 6.27 - PXRD patterns of the desolvated form of **29** collected ($\lambda = 0.2954$ nm) when the experimental temperature was decreased from 375 to 303 K.

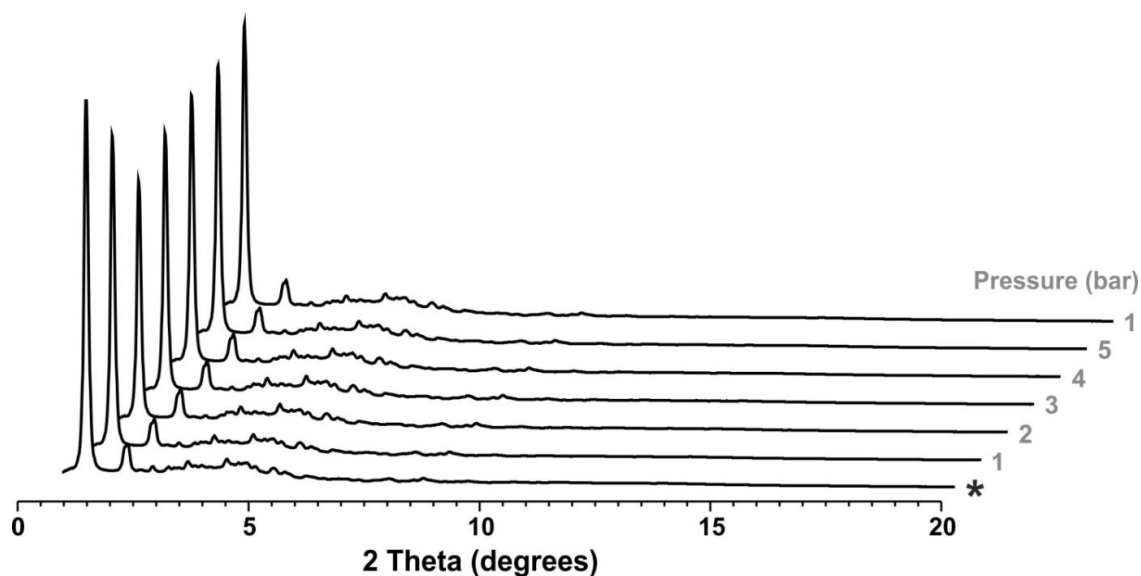


Figure 6.28 - PXRD patterns collected ($\lambda = 0.2954$ nm) for the desolvated form of **29** at 303 K by using different CO₂ flow pressures. The PXRD pattern of the desolvated **29**, collected before the pressure studies, is denoted with an asterisk (*).

Decreasing the temperature for 273 K it is not detected, once again, any structural alteration (Figure 6.29). The effect of different pressures in the desolvated material **29** it was evaluated at that temperature. As describe above for the measurements performed at 303 K the structure of the material does not suffer any modification (Figure 6.30).

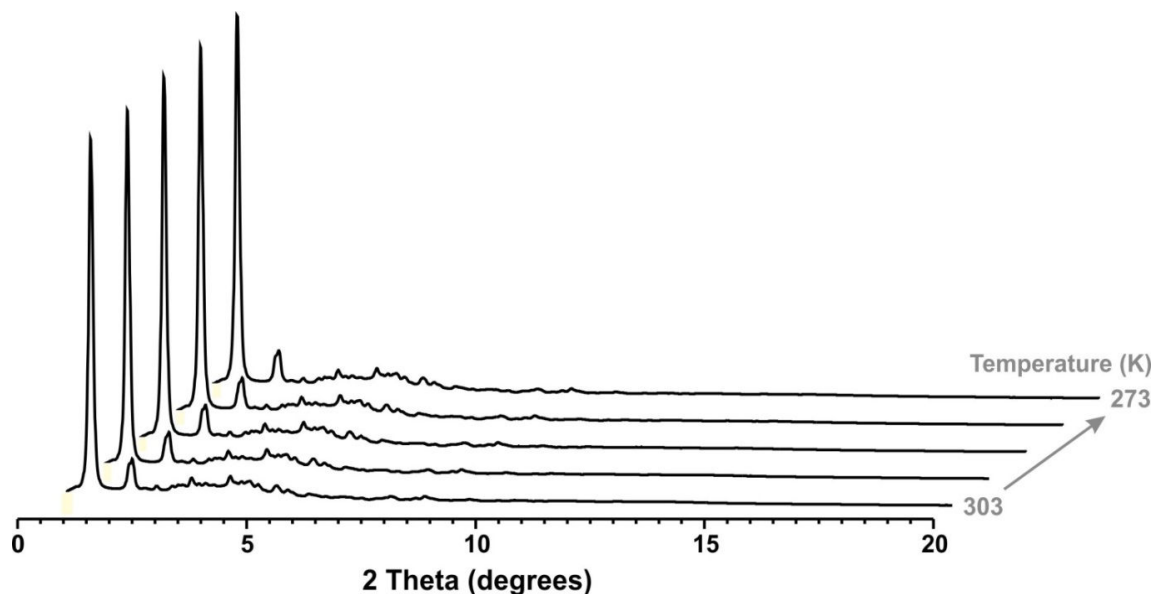


Figure 6.29 - PXRD patterns of the desolvated material **29** collected ($\lambda = 0.2954$ nm) when the experimental temperature was decreased from 303 to 273 K.

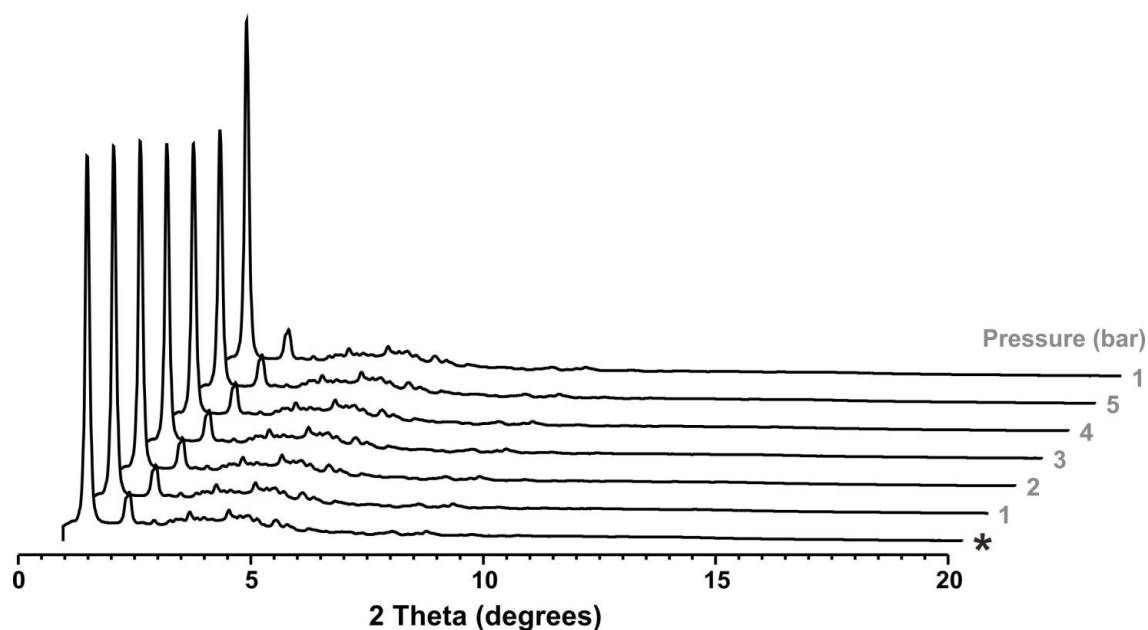


Figure 6.30 - PXRD patterns collected ($\lambda = 0.2954$ nm) for the desolvated material **29** at 273 K by using different CO₂ flow pressures. The PXRD pattern of desolvated **29**, collected before the pressure studies, is denoted with an asterisk (*).

6.8. Photoluminescence Studies

The photoluminescent properties of the mixed-rare earths materials **30** and **31** were investigated. The excitation spectra of the both compounds (at ambient pressure and under a vacuum of *ca.* 10^{-5} mbar) were recorded while monitoring within the strongest Eu^{3+} $^5\text{D}_0 \rightarrow ^7\text{F}_2$ and Tb^{3+} $^5\text{D}_4 \rightarrow ^7\text{F}_5$ emission transitions, respectively (Figure 6.31). The spectra are dominated by a broad UV band composed by two main components attributable to the excited states of the organic ligand moieties. This attribution was confirmed recording the excitation spectra of **30** (under vacuum, Figure 6.31) monitoring their fluorescence emission at 385 nm (discussed below). The typical intra- $4f^6$ and $4f^8$ transitions of Eu^{3+} and Tb^{3+} , respectively, cannot be properly recognized on the corresponding excitation spectrum, indicating an efficient sensitization of Eu^{3+} and Tb^{3+} , via the excited states of the ligand comparatively to their direct excitation.

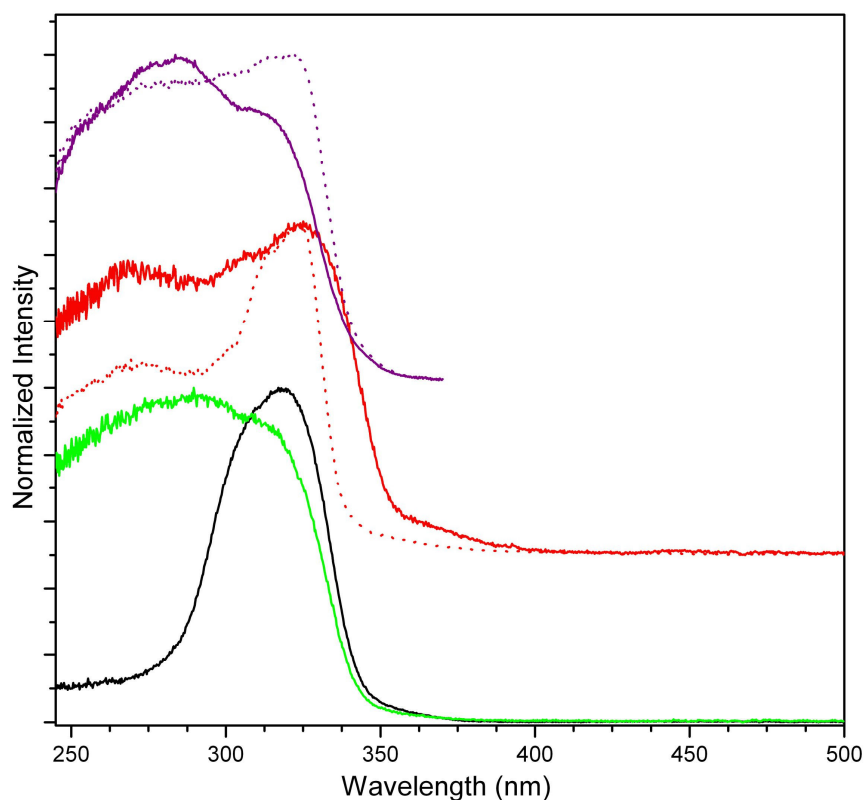


Figure 6.31 - Excitation spectra of **31** ($\lambda_{\text{Em.}} = 549.5$ nm, green) and **30** ($\lambda_{\text{Em.}} = 609.3$ nm, black) at ambient pressure and under vacuum ($\lambda_{\text{Em.}} = 611.4$ nm, red; $\lambda_{\text{Em.}} = 385$, purple) while monitoring the emission of the Tb^{3+} and Eu^{3+} ions, and of the ligand, respectively. The spectra have been recorded at ambient temperature (solid lines) and at 12 K (dotted lines).

The emission spectra of **30** and **31**, recorded at ambient conditions (297 K) and with excitation at 320 nm, are provided in Figure 6.32. The sharp emission lines of **30** and **31** are assigned to the $^5\text{D}_0 \rightarrow ^7\text{F}_{0-4}$ and $^5\text{D}_4 \rightarrow ^7\text{F}_{6-3}$ transitions, respectively, which originates

a red and green emitted light. Although, after instantaneous exposure (under ambient conditions) to the excited UV light, the visible emissions are relatively bright, their intensities quickly decrease becoming negligible in the time range. Thus, it is necessary to record a complete emission spectra (ca. 10 minutes) due to, most probably, an effective photobleaching of the compounds. Because of that, the emission spectra are uncorrected and are only presented to elucidate the emission capability of the Tb^{3+} and Eu^{3+} . It is noticeable a loss of the emission intensities on the high wavelength region for both spectra. In the other hand, as observed for **30** (Figure 6.32 on top), the samples under vacuum (ca. 10^{-3} mbar) undergo a phase transformation (evidenced by the changes observed on the Eu^{3+} emission lines) and their emissions became stable. This demonstrates that the application of a vacuum is able to remove the solvent molecules (water and methanol) located into the channels promoting the phase transition, which should be the responsible for the photobleaching activation observed at ambient pressure. This is in agreement with VTPXRD investigations, where it was possible to observe structural modifications after the release of the solvent molecules.

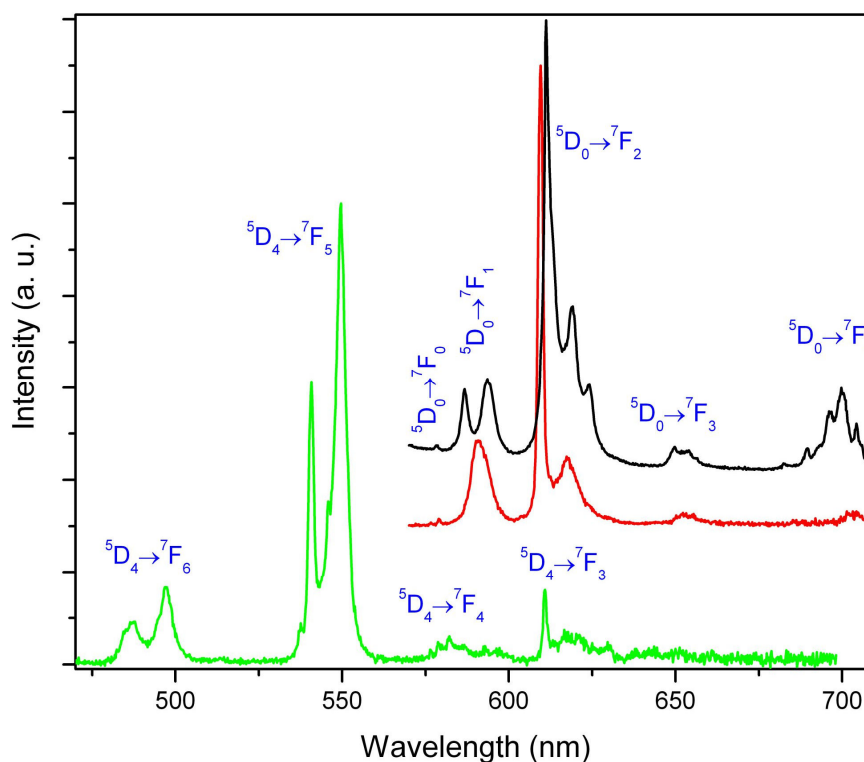


Figure 6.32 - Ambient temperature emission spectra of **31** (green line) and **30** at ambient pressure (red line) and under vacuum (black line) with excitation at 320 nm.

Encompass the effective sensitization of the Tb^{3+} and Eu^{3+} emitter ions by the ligand moieties mentioned above, the concentration of the optical active Ln^{3+} ions used in the present case is not enough to receive all the UV light absorbed by the ligands and to eliminate the intrinsic photoluminescence of the ligands in UV and visible region. In fact,

as can be seen in Figure 6.33, the complete emission spectra of **30** under vacuum in the UV/Vis region is characterized by the predominance of a strong UV band on the 340-440 nm range, which at 12 K has a structured profile. Considering the results of the time-resolved emission spectra depicted in Figure 6.33, this band should be attributed to the superposition of the $S_1 \rightarrow S_0$ fluorescence of the ligand (evidenced with the very short live detection conditions) and to a most probably emission of their phosphonate groups, which has some similarities with the emission of norbornene derived phosphonates recently presented by Bhattacharya *et al.*²³ Note that the residual emission band obtained in the 340-440 nm spectral region, applying an initial delay of 1 ms, cannot be attributed to the common ligand fluorescence, and in the present situation it has the exact same profile as the emission band collected in the stationary state mode. Because of that, it can be speculated the possible function of the phosphonate groups as optical active elements which can be also sensitized by the pure organic part of the ligand moiety. An additional emission in the region of 450 to 550 nm is also observed at 12 K which, based on their long lifetime characteristics and their temperature dependence, is attributed to the ligand triplet phosphorescence emission, probably conjugated with the phosphonate groups. More detailed and comprehensive studies are needed to complete discern the role of the phosphonate groups on these promising optical active systems.

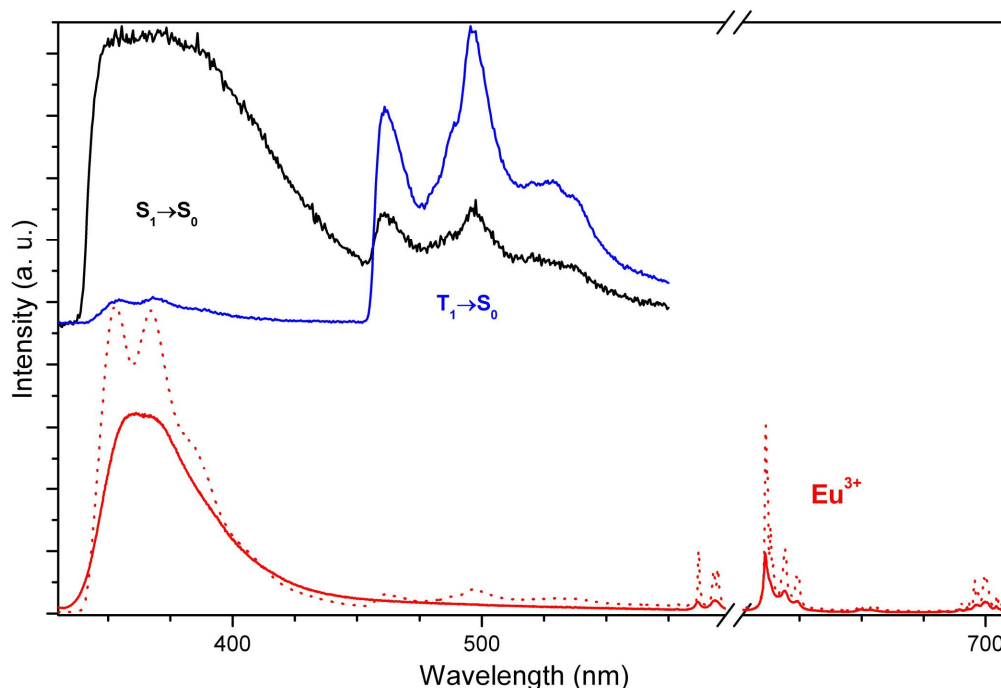


Figure 6.33 - Stationary state UV/Vis emission spectra of **30** under vacuum recorded at 297 K (solid red line) and at 12 K (dotted red line) with the excitation at 300 nm, and corresponding time-resolved emission spectra (black line, initial delay 0.01 ms and integration time of 1 ms; blue line, initial delay 1 ms and integration time of 30 ms) recorded at 12 K. The break in the graph signalizes the second order excitation position.

6.9. Results and Discussion

This chapter summarized the synthesis and application of a family of isotypical porous MOFs, termed as $[\text{RE}(\text{H}_3\text{L})]\cdot x\text{H}_2\text{O}\cdot y\text{MeOH}$ [where $\text{RE}^{3+} = \text{Y}^{3+}$ (**29**); $(\text{Y}_{0.95}\text{Eu}_{0.05})^{3+}$ (**30**) and $(\text{Y}_{0.95}\text{Tb}_{0.05})^{3+}$ (**31**)]. These compounds were typically prepared as microcrystalline powders. Isolation of large crystals suitable for single-crystal X-ray diffraction studies was a hard task. The material **29** may be prepared by using several synthetic methods under very distinct reaction conditions: i) conventional solvothermal synthesis (140 °C for 48 h); ii) *bench* “one-pot” synthesis (60 °C for 24 h); iii) slow diffusion (ambient temperature for approximately 3 weeks); and iv) ionothermal synthesis using the ionic liquid $[\text{EMIm}]\text{Cl}$ (140 °C for 72 h). Figure 6.34 summarizes the employed synthetic approaches and the corresponding reaction conditions.

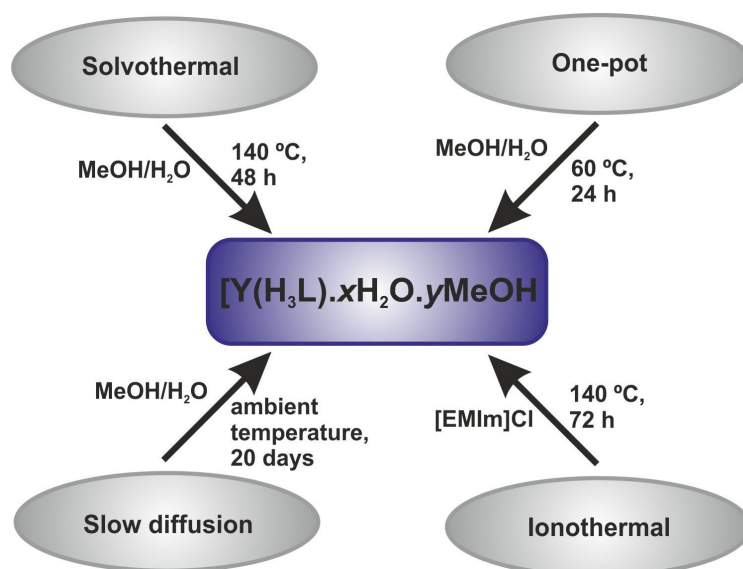


Figure 6.34 – Schematic representation of the synthetic approaches and reaction conditions used to isolate compound **29**.

Despite the several attempts and efforts, isolation of **29** as large particles was unsuccessful. Nevertheless, using conventional solvothermal conditions and adding different amounts of HCl (6 M) to the reactive mixtures single-crystals were isolated. Thus, it is possible to conclude that this step is the key factor to improve crystallinity. Moreover the increase of the amount of HCl (6 M), until certain point, in the reaction mixtures leads to a substantial increase of the particle size.

The *bench* “one-pot” approach exhibited itself, once again, as an excellent alternative to prepare large amounts (*i.e.*, in the gram-scale) of desired MOF **29** at milder reaction conditions during acceptable periods of time. This methodology has in this way a handful of attractive features which make it a strong synthetic alternative to large scale synthesis: it allows the preparation of MOFs in a very simple way with low energy-consumption.

From thermal analyses, it was possible to observe that the crystalline structure of compound **29** suffers some modifications when submitted to thermal treatment. Although the structure of **29** is still not completely elucidated, preliminary studies indicated that this porous material has its channels filled of solvent molecules (water and methanol) of crystallization. Therefore, the release of these molecules occurs easily from low temperatures (the solvent molecules are released below *ca.* 100 °C). This fact may induce a rearrangement, as for instance a possible contraction, in the network of **29**. Nevertheless, it is noteworthy to observe that the new desolvated material is robust being stable up to approximately 400 °C. This is an uncommon feature, which mechanically appears nevertheless more often in phosphonate-based MOFs than, for instance, in carboxylate-based ones. In this context, this robustness provides this material the possibility to be applied in areas which require more severe conditions (*e.g.*, higher temperatures and activation of the pores).

The selective adsorption properties of compound **29** were studied. From the conventional single component adsorption isotherms it was observed that this material is able to incorporate significant amounts of CO₂ molecules into its structure. Regarding to N₂, compound **29** presents some diffusion problems toward this gas. This behavior appears as typical of ultramicroporous materials with pore size < 0.5 nm. Additionally, the performance of **29** in gas separation processes, using binary (*i.e.*, C₃H₆/C₃H₈ and CO₂/N₂) and ternary (*i.e.*, CH₄/CO₂/C₂H₂ and N₂/CO₂/C₂H₂) mixtures of gases, was evaluated by employing advanced measurements: pulse gas chromatography and gas separation breakthrough measurements. After these tests, the results suggest that the desolvated form of compound **29**:

- i) has the ability to retain higher amounts of propylene (4.47 mmol g⁻¹ at 273 K and 4.03 mmol g⁻¹ at 296 K) than propane (3.13 mmol g⁻¹ at 273 K and 2.59 mmol g⁻¹ at 296 K);
- ii) is able to separate to nearly 100% of purity propane from a mixture composed of C₃H₆/C₃H₈ during a certain period of time;
- iii) shows the capacity to selectively adsorb CO₂ (polar gas) over the N₂ (non-polar);
- iv) has high affinity for acetylene (observed from the pulse gas chromatographic measurements) over CO₂; the separation of these gases was not, nevertheless, achieved using a mixture composed of CO₂/C₂H₂.

Propylene-propane separation processes, using porous MOFs, have been tested by several scientists because this field is of great scientific and industrial interest.^{20,24-29} In the reported MOFs the higher affinity to propylene over propane is related to the presence of the C=C bond: the π^* orbital interacts typically with the electron density of the metal cations, leading to strong interactions with this gas over propane.^{20,28,30-32}

The CO₂/C₂H₂ separation is also of significant industrial interest. Acetylene is an important molecule which has been used as starting material, as for instance, for the production of chemical products.³³ However, opposite to C₃H₆/C₃H₈ separation, the

selective separation between C_2H_2 over CO_2 was, unfortunately, not achieved with **29**. This fact may be due to the similarity existing between the nature of them, as for instance, their sublimation points, critical temperatures and molecular size.³⁴ In order to improve the selective CO_2/C_2H_2 separation it was prepared the ion-exchanged compound **32** using **29** as starting material. Results suggest that **32** has higher capacity to adsorb CO_2 , mainly at higher temperatures. Performing a preliminary breakthrough measurement it was possible to observe that this new material exhibits the ability to retain CO_2 while C_2H_2 is firstly released. Thus, the purification of acetylene (of approximately 100%) using a CO_2/C_2H_2 gas mixture was achieved during a certain period of time (for approximately 1 minute). The improvement in the separation process may be attributed to the introduction of the K^+ cations into the framework of **29**. These sites may allow the coordination with CO_2 molecules, improving their affinity with the material. This behavior leads to a later release of CO_2 from the porous structure of **32**, allowing first the release of C_2H_2 , which has not strong affinity with the material. Additionally, the selectively adsorption of CO_2 over C_2H_2 may be further improved if, as for instance, two chromatographic columns packed with **32**, instead one, can be used.

To the best of knowledge, only two reports describe the adsorption capacity of phosphonate-based MOFs toward some gases (*i.e.*, CO_2 , CO and CH_4). In 2008, Wright's group reported that a porous MOF, termed Ni-STA-12, had the ability to uptake ten times CO_2 (2.5 mmol g^{-1}) than CH_4 at 304 K from 0 to 1 bar.³⁵ Latter, in 2012, the same research group performed some breakthrough tests using a family of STA-12 porous materials (having Mg, Mn, Fe, Co or Ni as metallic centers).³⁶ The STA-12(Ni) material exhibited CO_2 selective adsorption over CH_4 and CO. This material showed selectivities to CO_2 of 6.5 (at 1 bar) and 24.4 (at 5 bar) at 303 K using a CO_2/CH_4 (1:1) gas mixture. The latter work is the unique example reported in the literature describing gas separation breakthrough studies using a phosphonate-based MOF for the selective adsorption of CO_2 over other gases. The work reported in this chapter constitutes the first time a phosphonate-based MOF has been used for C_3H_6/C_3H_8 , CO_2/N_2 , $CH_4/CO_2/C_2H_2$ and $N_2/CO_2/C_2H_2$ separation processes.

The effect of the desolvation process of the porous material **29** as well as the influence of different CO_2 flow pressures was investigated by high-resolution synchrotron powder X-ray diffraction (performed in ESRF). These experiments aimed to gain insight on the stability and robustness of the crystalline structure of this compound. These involved different two main tasks: i) evacuation of the solvent molecules of the studied material using a He flow; and ii) variation of the CO_2 flow pressures (1, 2, 3, 4 and 5 bar) at 273 and 303 K. The obtained data suggest that it occurs some structural modifications in **29** after its desolvation process, affording a new desolvated material still more crystalline. These observations agree to those collecting in the VTPXRD studies. Nevertheless, it was concluded that this new phase is highly robust and stable when different CO_2 flow pressures were tested at different temperatures (273 and 303 K).

The photoluminescent properties of compounds **30** and **31** were investigated. Eu^{3+} - and Tb^{3+} -based materials emitted relatively intense red and green light, respectively.

Nevertheless, these intensities decrease very quickly and it was not possible to collect a complete emission spectra in the time range needed. This fact may be related to an effective photobleaching resulting from the instability and possible degradation of the tested compounds. As mentioned above, the release of the solvent molecules (water and methanol), even at low temperatures, of **29** led to structural modifications. This may justify the difficulty in collecting the photoluminescence data. These results are only some preliminary studies and it is necessary to investigate in more details these properties.

6.10. References

- (1) Furukawa, H.; Cordova, K. E.; O'Keeffe, M.; Yaghi, O. M.; *Science*, **2013**, *341*, 974-986.
- (2) Farha, O. K.; Eryazici, I.; Jeong, N. C.; Hauser, B. G.; Wilmer, C. E.; Sarjeant, A. A.; Snurr, R. Q.; Nguyen, S. T.; Yazaydin, A. O.; Hupp, J. T.; *J. Am. Chem. Soc.*, **2012**, *134*, 15016-15021.
- (3) van Bekkum, H.; Flanigen, E. M.; Jacobs, P. A.; Jansen, J. C. *Introduction to Zeolite Science and Practice*; Elsevier, 2001.
- (4) Sing, K. S. W.; Everett, D. H.; Haul, R. A. W.; Moscou, L.; Pierotti, R. A.; Rouquerol, J.; Siemieniewska, T.; *Pure Appl. Chem.*, **1985**, *57*, 603-619.
- (5) Dunne, J. A.; Rao, M.; Sircar, S.; Gorte, R. J.; Myers, A. L.; *Langmuir*, **1996**, *12*, 5896-5904.
- (6) Dunne, J. A.; Mariwals, R.; Rao, M.; Sircar, S.; Gorte, R. J.; Myers, A. L.; *Langmuir*, **1996**, *12*, 5888-5895.
- (7) Kratschmer, W.; Rathousky, J.; Zukal, A.; *Carbon*, **1999**, *37*, 301-305.
- (8) Montoro, C.; Linares, F.; Procopio, E. Q.; Senkowska, I.; Kaskel, S.; Galli, S.; Masciocchi, N.; Barea, E.; Navarro, J. A. R.; *J. Am. Chem. Soc.*, **2011**, *133*, 11888-11891.
- (9) Padial, N. M.; Procopio, E. Q.; Montoro, C.; Lopez, E.; Oltra, J. E.; Colombo, V.; Maspero, A.; Masciocchi, N.; Galli, S.; Senkowska, I.; Kaskel, S.; Barea, E.; Navarro, J. A. R.; *Angew. Chem., Int. Ed.*, **2013**, *52*, 8290-8294.
- (10) Galli, S.; Masciocchi, N.; Colombo, V.; Maspero, A.; Palmisano, G.; Lopez-Garzon, F. J.; Domingo-Garcia, M.; Fernandez-Morales, I.; Barea, E.; Navarro, J. A. R.; *Chem. Mater.*, **2010**, *22*, 1664-1672.
- (11) Procopio, E. Q.; Rojas, S.; Padial, N. M.; Galli, S.; Masciocchi, N.; Linares, F.; Miguel, D.; Oltra, J. E.; Navarro, J. A. R.; Barea, E.; *Chem. Commun.*, **2011**, *47*, 11751-11753.
- (12) Colombo, V.; Montoro, C.; Maspero, A.; Palmisano, G.; Masciocchi, N.; Galli, S.; Barea, E.; Navarro, J. A. R.; *J. Am. Chem. Soc.*, **2012**, *134*, 12830-12843.
- (13) Procopio, E. Q.; Linares, F.; Montoro, C.; Colombo, V.; Maspero, A.; Barea, E.; Navarro, J. A. R.; *Angew. Chem., Int. Ed.*, **2010**, *49*, 7308-7311.
- (14) Barea, E.; Tagliabue, G.; Wang, W. G.; Perez-Mendoza, M.; Mendez-Linan, L.; Lopez-Garzon, F. J.; Galli, S.; Masciocchi, N.; Navarro, J. A. R.; *Chem.-Eur. J.*, **2010**, *16*, 931-937.
- (15) Beckmann, J.; Ruttinger, R.; Schwich, T.; *Cryst. Growth Des.*, **2008**, *8*, 3271-3276.
- (16) Vaidhyanathan, R.; Mahmoudkhani, A. H.; Shimizu, G. K. H.; *Can. J. Chem.*, **2009**, *87*, 247-253.
- (17) Ouellette, W.; Wang, G. B.; Liu, H. X.; Yee, G. T.; O'Connor, C. J.; Zubieta, J.; *Inorg. Chem.*, **2009**, *48*, 953-963.
- (18) Chae, H. K.; Siberio-Perez, D. Y.; Kim, J.; Go, Y.; Eddaoudi, M.; Matzger, A. J.; Yaghi, O. M.; *Nature*, **2004**, *427*, 523-527.

- (19) Socrates, G. *Infrared and Raman Characteristic Group Frequencies: Tables and Charts*; 2nd ed.; John Wiley & Sons Ltd: Baffins Lane, Chichester, 1994.
- (20) Geier, S. J.; Mason, J. A.; Bloch, E. D.; Queen, W. L.; Hudson, M. R.; Brown, C. M.; Long, J. R.; *Chem. Sci.*, **2013**, *4*, 2054-2061.
- (21) Lozano-Castello, D.; Cazorla-Amoros, D.; Linares-Solano, A.; *Carbon*, **2004**, *42*, 1233-1242.
- (22) Navarro, J. A. R.; Barea, E.; Rodriguez-Dieguez, A.; Salas, J. M.; Ania, C. O.; Parra, J. B.; Masciocchi, N.; Galli, S.; Sironi, A.; *J. Am. Chem. Soc.*, **2008**, *130*, 3978-3984.
- (23) Bhattacharya, S.; Rao, V. N.; Sarkar, S.; Shunmugam, R.; *Nanoscale*, **2012**, *4*, 6962-6966.
- (24) Kwon, H. T.; Jeong, H. K.; *Chem. Commun.*, **2013**, *49*, 3854-3856.
- (25) Bao, Z. B.; Alnemrat, S.; Yu, L.; Vasiliev, I.; Ren, Q. L.; Lu, X. Y.; Deng, S. G.; *Langmuir*, **2011**, *27*, 13554-13562.
- (26) Plaza, M. G.; Ribeiro, A. M.; Ferreira, A.; Santos, J. C.; Lee, U. H.; Chang, J. S.; Loureiro, J. M.; Rodrigues, A. E.; *Sep. Purif. Technol.*, **2012**, *90*, 109-119.
- (27) Plaza, M. G.; Ferreira, A. F. P.; Santos, J. C.; Ribeiro, A. M.; Muller, U.; Trukhan, N.; Loureiro, J. M.; Rodrigues, A. E.; *Microporous Mesoporous Mater.*, **2012**, *157*, 101-111.
- (28) Yoon, J. W.; Seo, Y. K.; Hwang, Y. K.; Chang, J. S.; Leclerc, H.; Wuttke, S.; Bazin, P.; Vimont, A.; Daturi, M.; Bloch, E.; Llewellyn, P. L.; Serre, C.; Horcajada, P.; Greneche, J. M.; Rodrigues, A. E.; Ferey, G.; *Angew. Chem., Int. Ed.*, **2010**, *49*, 5949-5952.
- (29) Lee, C. Y.; Bae, Y. S.; Jeong, N. C.; Farha, O. K.; Sarjeant, A. A.; Stern, C. L.; Nickias, P.; Snurr, R. Q.; Hupp, J. T.; Nguyen, S. T.; *J. Am. Chem. Soc.*, **2011**, *133*, 5228-5231.
- (30) Wuttke, S.; Bazin, P.; Vimont, A.; Serre, C.; Seo, Y. K.; Hwang, Y. K.; Chang, J. S.; Ferey, G.; Daturi, M.; *Chem.-Eur. J.*, **2012**, *18*, 11959-11967.
- (31) Bloch, E. D.; Queen, W. L.; Krishna, R.; Zadrozny, J. M.; Brown, C. M.; Long, J. R.; *Science*, **2012**, *335*, 1606-1610.
- (32) Plaza, M. G.; Ribeiro, A. M.; Ferreira, A.; Santos, J. C.; Hwang, Y. K.; Seo, Y. K.; Lee, U. H.; Chang, J. S.; Loureiro, J. M.; Rodrigues, A. E.; *Microporous Mesoporous Mater.*, **2012**, *153*, 178-190.
- (33) Hou, X. J.; He, P.; Li, H. Q.; Wang, X. R.; *J. Phys. Chem. C*, **2013**, *117*, 2824-2834.
- (34) Zhang, Z. J.; Xiang, S. C.; Chen, B. L.; *CrystEngComm*, **2011**, *13*, 5983-5992.
- (35) Miller, S. R.; Pearce, G. M.; Wright, P. A.; Bonino, F.; Chavan, S.; Bordiga, S.; Margiolaki, I.; Guillou, N.; Feerey, G.; Bourrelly, S.; Llewellyn, P. L.; *J. Am. Chem. Soc.*, **2008**, *130*, 15967-15981.
- (36) Wharmby, M. T.; Pearce, G. M.; Mowat, J. P. S.; Griffin, J. M.; Ashbrook, S. E.; Wright, P. A.; Schilling, L. H.; Lieb, A.; Stock, N.; Chavan, S.; Bordiga, S.; Garcia, E.; Pirngruber, G. D.; Vreeke, M.; Gora, L.; *Microporous Mesoporous Mater.*, **2012**, *157*, 3-17.

Chapter 7

General Conclusions

For this PhD project it was proposed as the main objective the preparation of functional and multidimensional MOF materials from the self-assembly of rare-earth cations with new phosphonate-based organic ligands designed and isolated in large amounts. Efforts were directed and focused toward the optimization of the ideal reaction conditions as well as the choice of the best synthetic approaches to isolate both organic linkers and multidimensional MOFs in high yields and, at the same time, with a high level of purity.

The preparation of the phosphonate-based organic ligands **H₄pmd**, **H₆bmt**, **H₆tftp** and **H₆L** involved the strict optimization of several reaction conditions (*e.g.*, reaction time, temperature and solvents). Synthetic approaches used the conventional heating synthetic methods or microwave heating which permitted the use of mild reaction conditions and a drastic reduction of the total reaction time (as observed for the preparation of the large tripodal **H₆L** organic ligand). This latter approach afforded the expected organic molecules in higher yields and in a fast, clean and safe way. These prepared multipodal linkers showed to be suitable organic PBUs to employ (together with several rare-earth cations) for the preparation of various and structurally distinct functional multidimensional MOFs. Single-crystal X-ray diffraction in tandem with the standard liquid-state NMR spectroscopy and mass spectrometry proved to be useful tools to unequivocally unveil and characterize the structure of all organic ligands.

The structural properties of the organic ligands arises, undoubtedly, as crucial factor in the preparation of multidimensional MOFs, mainly concerning their final architecture. The use of the more flexible bipodal **H₄pmd** and tripodal **H₆bmt** and **H₆tftp** molecules led to the preparation of 1D to 3D relatively dense MOF materials. Conversely, the large and rigid **H₆L** ligand directed the isolation of the porous $[Y(H_3L)] \cdot xH_2O \cdot yMeOH$ (**29**) material. The results found in this thesis come in line with those of several reports published in the literature, in which porous, or highly porous MOF materials have been isolated by using rigid and, very often, very large organic ligands. The presence of the methylene $-CH_2-$ moiety in the former ligands embodies the former organic PBUs with some degree of flexibility, resulting instead in the preparation of more dense MOFs.

The isolation of the several multidimensional MOFs was achieved by employing distinct synthetic approaches: i) conventional hydro(solvo)thermal synthesis; ii) synthesis using microwave or ultrasound irradiation; iii) *bench* “one-pot” synthesis; iv) ionothermal synthesis. The hydro(solvo)thermal synthesis showed, as expected, to be a good choice to isolate large single-crystals suitable for X-ray diffraction studies. Nevertheless, the preparation of the $[Ln(Hpmd)(H_2O)]$ (**1-3**) and $[Ln_2(H_3bmt)_2] \cdot H_2O$ (**12-19**) materials with large particle size it was not achieved.

Due to the general harsh reaction conditions (high temperatures) and long periods of time needed to prepare MOFs using the conventional hydro(solvo)thermal approach, other simpler, faster, cleaner and with low energy-consumption synthetic methodologies were investigated. MWAS and the *bench* “one-pot” approaches emerged as good alternatives. Owing the easy close control of various reaction parameters (*i.e.*, reaction time and temperature, power and pressure), MWAS allowed the preparation of different

architectures using the same organic and inorganic PBUs: i) the self-assembly between **H₄pmd** and La³⁺ cations produce the 1D [La₂(H₂pmd)₃(H₂O)₁₂] (**4**) and the 3D [La₂(H₂pmd)(pmd)(H₂O)₂] (**5**) materials while varying the temperature and the irradiation time; ii) a similar behaviour was observed in the preparation of the phase-pure 1D [La(H₄bmt)(H₅bmt)(H₂O)₂] \cdot 3H₂O (**9**) and 3D [La₂(H₃bmt)₂(H₂O)₂] \cdot H₂O (**20**) from reaction mixtures composed of **H₆bmt** and La³⁺ cations in distilled water. Additionally, MWAS also permits a drastic reduction of the reaction time and temperature of the preparation of MOF materials usually synthesized using conventional hydrothermal synthesis: the isotypical [Ln(Hpmd)(H₂O)] materials [where Ln³⁺ = Eu³⁺ (**1**), Gd³⁺ (**2**) and Tb³⁺ (**3**)] were isolated in very good yields, at 40 °C under just 5 seconds of reaction time, while standard hydrothermal conditions required 180 °C and a period of 72 h. MWAS exhibited also good reproducibility, the possibility to prepare MOF materials with homogeneous crystal morphology and different particle sizes (ranging from nano- to micro-sized particles), while maintaining their crystal structure.

The *bench* “one-pot” approach permitted the isolation of phase-pure 1D [La₂(H₂pmd)₃(H₂O)₁₂] (**4**) and 2D [La₂(H₂pmd)(pmd)(H₂O)₂] (**5**) materials, and also the 3D [La₂(H₂pmd)₃(H₂O)₂] (**7**) and [La₂(H₂pmd)(pmd)(H₂O)₄] (**8**) compounds. This latter material was, however, contaminated with other crystalline phases. “One-pot” synthesis also allowed the preparation of the porous MOF **29** at milder reaction conditions (60 °C for 24 h) when compared with the conventional solvothermal method (140 °C for 48 h). In short, the *bench* “one-pot” and MWAS approaches exhibited themselves as potential and suitable synthetic alternatives to prepare MOFs in a simple and usually faster way with low-energy consumption.

As mentioned in Chapter 1 the preparation of phosphonate-based MOFs is usually not straightforward, mainly because the synthesis usually leads to microcrystalline powders, many of the times composed of mixtures of phases. In addition, the final structure of this type of materials is also less predictable than when carboxylate or N-donor organic ligands are employed in the self-assembly process with, for example, transition metals. This occurs mainly because the phosphonate organic linkers have several coordination modes (as demonstrated abundantly in the various MOF structures reported in this thesis) which allied with the typical high coordination numbers of lanthanides boost the occurrence of supramolecular isomerism. In Chapters 5 and 6 the addition of controlled amounts of an aqueous solution of HCl (6 M) promoted the isolation of phosphonate-based MOFs as large single crystals, ultimately avoiding the production of only microcrystalline powders.

The photoluminescent properties of the optically-active Eu³⁺-based materials [Eu(Hpmd)(H₂O)] (**1**), [(La_{0.97}Eu_{0.03})(H₄bmt)(H₅bmt)(H₂O)₂] \cdot 3H₂O (**10**), [(La_{0.95}Eu_{0.05})₂(H₃bmt)₂(H₂O)₂] \cdot H₂O (**24**) and [(La_{0.95}Eu_{0.05})(H₃tftp)(H₂O)] (**27**), and the Tb³⁺-based materials [Tb(Hpmd)(H₂O)] (**3**) [(La_{0.97}Tb_{0.03})(H₄bmt)(H₅bmt)(H₂O)₂] \cdot 3H₂O (**11**), [(La_{0.95}Tb_{0.05})₂(H₃bmt)₂(H₂O)₂] \cdot H₂O (**25**) and [(La_{0.95}Tb_{0.05})(H₃tftp)(H₂O)] (**28**) were investigated. On the one hand, the Tb³⁺-based materials exhibited always higher absolute quantum yields than their Eu³⁺ analogue materials. This demonstrates that the organic

ligands employed are suitable sensitizers of Tb^{3+} via the energy transfer process called *antenna effect*, leading to the isolation of intense green-emitting materials. On the other hand, the suppression of the O–H quenchers, as mentioned in Chapter 1, by deuteration or dehydration processes improved significantly the photoluminescent properties of some Eu^{3+} -based materials. The effect of the replacement of the C–H quenchers by C–F moieties in the photoluminescent properties of the fluorinated MOFs reported in this thesis did not lead to conclusive results.

The heterogeneous catalytic activity of the $[\text{Eu}(\text{Hpmd})(\text{H}_2\text{O})]$ (**1**), $[\text{La}(\text{H}_4\text{bmt})(\text{H}_3\text{bmt})(\text{H}_2\text{O})_2]\cdot 3\text{H}_2\text{O}$ (**9**) and $[\text{La}_2(\text{H}_3\text{bmt})_2(\text{H}_2\text{O})_2]\cdot \text{H}_2\text{O}$ (**20**) materials in the ring-opening reaction of styrene oxide (PhEtO) with methanol was investigated. Compounds **1**, **9** and **20** showed to be truly heterogeneous catalysts and to exhibit excellent regioselectivity towards 2-methoxy-2-phenylethanol, which is always the sole reaction product. Compounds **9** and **20** can be recycled by simple and efficient regeneration processes. A comparative study between the catalyst **1** and its nanocrystalline form **1n** revealed that the latter exhibited much higher catalytic activity than **1** toward the conversion of PhEtO. This is, probably, related with the small particle size of **1n** compared with the microcrystalline phase. The catalytic activity of **20** increases from the first to the second and third catalytic runs promoted by the breaking of larger crystals into smaller ones. This feature may lead to an increase in the number of effective active sites and, consequently, increases the catalytic performance of the material, coming in line with that observed for **1n**. To summarize, it was found that **9** has higher catalytic activity (conversion of 100% of PhEtO toward the product 2-methoxy-2-phenylethanol at 55 °C in only 30 min) than **1**, **1n** and **20**. This outstanding catalytic activity is related with the amount of the active sites of **9** that are likely to be of Brønsted type.

A search in the literature reveals that some copper and iron-containing MOFs used as catalysts in the same reaction have relatively high PhEtO conversions reached at shorter reaction times and lower reaction temperatures. Nevertheless, for these transition-metal MOFs selectivity toward MeOPhEtOH was always less than 100%.¹⁻² Layered $[\text{La}(\text{H}_3\text{nmp})]$ led to 76% yield.³ 2D or 3D $[\text{La}(L)]$ led to 100% yield at 4 h.³ The nano-sized HKUST-1 led to 90% of conversion at 40 °C for 2.5h.⁴ Compound **9** represents, until now, the most outstanding catalytic activity in the ring-opening reaction of PhEtO with methanol.

The performance of the porous MOF **29** was investigated in gas separation processes. This compound, after activation (desolvation), exhibited the capacity to separate propane over propylene, although not with 100% of purity, during a certain period of time. The separation of acetylene over carbon dioxide was not achieved. However, after some preliminary screening tests concerning the preparation of the ion-exchanged material $[\text{Y}(\text{H}_3\text{L})]\cdot x\text{Solvent}_K$ (**32**) it was observed that acetylene was indeed separated (with almost 100% of purity) over carbon dioxide. The inclusion of the K^+ cations into the framework of **29** led to a higher ability of this compound to retain CO_2 .

References

- (1) Dhakshinamoorthy, A.; Alvaro, M.; Garcia, H.; *Chem.-Eur. J.*, **2010**, *16*, 8530-8536.
- (2) Jiang, D.; Mallat, T.; Krumeich, F.; Baiker, A.; *J. Catal.*, **2008**, *257*, 390-395.
- (3) Silva, P.; Vieira, F.; Gomes, A. C.; Ananias, D.; Fernandes, J. A.; Bruno, S. M.; Soares, R.; Valente, A. A.; Rocha, J.; Paz, F. A. A.; *J. Am. Chem. Soc.*, **2011**, *133*, 15120-15138.
- (4) Wee, L. H.; Lohe, M. R.; Janssens, N.; Kaskel, S.; Martens, J. A.; *J. Mater. Chem.*, **2012**, *22*, 13742-13746.

Chapter 8

Experimental Section

8.1. General Characterization Methods

SEM (Scanning Electron Microscopy) images were acquired using either a Hitachi S4100 field emission gun tungsten filament instrument working at 25 kV or a high-resolution Hitachi SU-70 working at 4 kV. Samples were prepared by deposition on aluminium sample holders followed by carbon coating using an Emitech K950X carbon evaporator. EDS (Energy Dispersive X-ray Spectroscopy) data and SEM mapping images were recorded using the same microscope, Hitachi SU-70, working at 15 kV and using a Bruker Quantax 400 or a Sprit 1.9 EDS microanalysis system.

Thermogravimetric analyses (TGA) were carried out using a Shimadzu TGA 50, from ambient temperature to *ca.* 800 °C, with a heating rate of 5 °C/min under a continuous stream of air at a flow rate of 20 mL min⁻¹.

Fourier Transform Infrared (FT-IR) spectra (in the range 3750-350 cm⁻¹) were recorded as KBr pellets (typically 2 mg of the sample were mixed in a mortar with *ca.* 200 mg of KBr) using a Bruker Tensor 27 spectrometer by averaging 200 scans at a maximum resolution of 2 cm⁻¹.

Elemental analyses for C and H were performed with a Truspec Micro CHNS 630-200-200 elemental analyzer at the Department of Chemistry, University of Aveiro. Analysis Parameters: sample amount between 1 and 2 mg; combustion furnace temperature = 1075 °C; afterburner temperature = 850 °C. Detection method: carbon - infrared absorption, hydrogen - infrared absorption. Analysis time = 4 minutes. Required gasses: carrier - helium, combustion – oxygen, pneumatic – compressed air.

Routine Powder X-Ray Diffraction (PXRD) data for all materials were collected at ambient temperature on an X'Pert MPD Philips diffractometer (Cu K_{α1,2} X-radiation, λ₁ = 1.540598 Å; λ₂ = 1.544426 Å), equipped with an X'Celerator detector and a flat-plate sample holder in a Bragg-Brentano para-focusing optics configuration (45 kV, 40 mA). Intensity data were collected by the step-counting method (step 0.04°), in continuous mode, in the *ca.* 5 ≤ 2θ ≤ 50° range.

¹³C CP MAS and ¹H or ³¹P HPDEC MAS spectra were recorded at 9.4 T on a Bruker Avance 400 wide-bore spectrometer (DSX model) on a 4 mm BL cross-polarization magic-angle spinning (CPMAS) VTN probe at 100.6 and 161.9 MHz, respectively. For the ¹³C{¹H} CP MAS spectra the Hartmann-Hahn (HH) “sideband” matching condition $\nu_1^{13C} = \nu_1^{1H} + n\nu_R$ ($n = \pm 1$) was carefully matched by calibrating the ¹H and the ¹³C *rf* field strengths; recycle delay: 3 s; contact time: 2 ms; ν_R = 15 kHz. For the ³¹P HPDEC spectra a 90° single pulse excitation of 3.5 μs was employed; recycle delay: 60 s; ν_R = 15 kHz. Chemical shifts are quoted in parts per million (ppm) with respect to TMS for ¹H and ¹³C nuclei, and to an 85% H₃PO₄ solution for the ³¹P nucleus.

¹H, ¹³C, ³¹P and ¹⁹F liquid NMR spectra were recorded with a Bruker AVANCE 300 spectrometer at 300.13, 75.47, 121.49 and 282.40 MHz, respectively. Deuterated chloroform (CDCl₃) or dimethylsulfoxide-*d*₆ (DMSO-*d*₆) were used as solvents. Tetramethylsilane, H₃PO₄ (85%) or hexafluorobenzene were used as internal references. Chemical shifts (δ) are quoted in ppm and the coupling constants (*J*) in Hz.

Mass spectra were collected using a Micromass Q-TOF2 equipment. Dichloromethane, water or methanol were used as solvent to dissolve the organic ligands as well as their precursors. The employed concentration was 1 mg mL⁻¹. Samples were diluted in methanol to a concentration of 2 μ L (sample)/200 μ L (methanol).

8.2. Reagents and Solvents

Chemicals were readily available from commercial sources and were used as received without further purification: lanthanide (III) chloride hydrates LnCl₃·xH₂O (where Ln³⁺ = La³⁺, Ce³⁺, Pr³⁺, Nd³⁺, Eu³⁺, Gd³⁺, Tb³⁺, Dy³⁺, Ho³⁺, Er³⁺, Tm³⁺, Yb³⁺, 99.9%, Sigma-Aldrich); tetraethyl 1,4-phenylenebis(methylene)bisphosphonate (C₁₆H₂₈O₆P₂, >95%, TCI Europe); 1,3,5-tris(bromomethyl)benzene (C₉H₉Br₃, 97%, Sigma-Aldrich); 1,3,5-trifluorobenzene (C₆H₃F₃, 98%, Alfa Aesar); chloromethyl methyl ether (C₂H₅ClO, technical grade, Sigma-Aldrich); triethyl phosphite [(C₂H₅O)₃P, 98%, Sigma-Aldrich]; 1,3,5-Tris(4-bromophenyl)benzene (C₂₄H₁₅Br₃, 97%, Sigma-Aldrich); tetrakis(triphenylphosphine)palladium(0) [(C₁₈H₁₅P₃)₄Pd, 99%, Sigma-Aldrich]; aluminium chloride (AlCl₃, >98%, Merck); sodium hydrogen carbonate (NaHCO₃, 99%, Panreac); hydrochloric acid (HCl, 37%, Panreac); dichloromethane (CH₂Cl₂, pure, Sigma-Aldrich); methanol (CH₃OH, >99.8%, Fluka); *n*-hexane (>99%, Sigma-Aldrich); dimethyl sulfoxide-*d*₆ (DMSO-*d*₆, 99.99%, Euriso-top); deuterated chloroform (CDCl₃, 99.99%, Euriso-top); potassium bromide (KBr, for infra-red spectroscopy, BDH SpectroSol); sodium hydroxide (NaOH, \geq 98%, Sigma-Aldrich); potassium hydroxide (KOH, 85% *p.a.*, Riedel-de Haën).

8.3. Single-Crystal X-ray Diffraction Studies

Single crystals of the organic molecules **IL**², **IL**³, **IL**⁴, **H₆tftp** and **H₆L**, and the materials **4**, **5**, **6**, **7**, **9**, **20**, **21**, **22**, **23**, **26** and **29** were manually harvested from the reaction vessel and immediately immersed in highly viscous FOMBLIN Y perfluoropolyether vacuum oil (LVAC 140/13, Sigma-Aldrich) to avoid degradation caused by the evaporation of the solvent. Crystals were mounted on Hampton Research CryoLoops with the help of a Stemi 2000 stereomicroscope equipped with Carl Zeiss lenses.¹ The selection of a suitable single-crystal for analysis was a challenging task because they frequently presented cracks. Because of this, several data sets were collected, and the crystal model herein presented corresponds to the best solution that could be found. Data were collected on a Bruker X8 Kappa APEX II CCD area-detector diffractometer (Mo K α graphite-monochromated radiation, λ = 0.71073 Å) controlled by the APEX2 software package² and equipped with an Oxford Cryosystems Series 700 cryostream monitored remotely using the software interface Cryopad.³ Images were processed using the software package SAINT+,⁴ and data were corrected for absorption by the multiscan semi-empirical method

implemented in SADABS.⁵ The structure was solved using the Patterson synthesis algorithm implemented in SHELXS-97,^{6, 7} which allowed the immediate location of the two crystallographically independent La³⁺ centres and most of the heaviest atoms belonging to the organic linkers. The remaining non-hydrogen atoms were located from difference Fourier maps calculated from successive full-matrix least-squares refinement cycles on F^2 using SHELXL-97.^{7, 8} All the non-hydrogen atoms were successfully refined by assuming anisotropic displacement parameters.

8.4. Structural Determination: Laboratory Powder X-ray Diffraction

Conventional powder X-ray diffraction data for the bulk materials **1**, **2**, **3**, **8** and **12**, suitable for structural refinements were collected at ambient temperature on a X'Pert MPD Philips diffractometer (Cu K _{α 1,2} X-radiation, $\lambda_1 = 1.540598$ Å and $\lambda_2 = 1.544426$ Å), equipped with a X'Celerator detector and a flat-plate sample holder in a Bragg-Brentano para-focusing optics configuration (40 kV, 50 mA). Intensity data were collected by the step-counting method (step 0.02°), in continuous mode, in the *ca.* $4 \leq 2\theta \leq 110^\circ$ range.

Powder patterns were readily indexed with DICVOL04,⁹ thus unequivocally confirming the assumed structural similarities with compounds [Ce(Hpmd)(H₂O)] and [Pr(Hpmd)(H₂O)] previously reported by the MOF research group at the University of Aveiro.¹⁰ Rietveld structural refinements¹¹ using as starting premise the atomic coordinates of the aforementioned structures were performed with FullProf.2k.^{12, 13} Background was corrected using fixed points throughout the entire angular range determined by the linear interpolation between consecutive (and manually selected) breakpoints in the powder pattern. Cauchy profile functions, along with two asymmetry correction parameters, were selected to generate the line shapes of the simulated diffraction peaks. The angular dependence of the full-width-at-half-maximum (FWHM) of individual reflections was also taken into account by employing a Caglioti function correction.¹⁴

8.5. Variable-Temperature Powder X-ray Diffraction

Variable-temperature powder X-ray diffraction data for [La(H₃tftp)(H₂O)] (**1**) were collected on a D8 Advance Bruker diffractometer (Cu K _{α 1,2} X-radiation, $\lambda_1 = 1.540598$ Å; $\lambda_2 = 1.544426$ Å) under air atmosphere, equipped with a LynxEye detector, curved graphite-monochromated radiation, a flat-plate low background Si wafer (911 oriented) as sample holder in a Bragg-Brentano para-focusing optics configuration (40 kV, 50 mA), and a high-temperature Anton Parr HTK1200 chamber. Intensity data were collected in the step mode (0.02°) in the range *ca.* $5 \leq 2\theta \leq 50^\circ$. Data were collected between ambient temperature and 1000 °C.

8.6. Photoluminescence Spectroscopy

Emission and excitation spectra were recorded on a Fluorolog-2® Horiba Scientific (Model FL3-2T) spectroscopy, with a modular double grating excitation spectrometer (fitted with a 1200 grooves/mm grating blazed at 330 nm) and a TRIAX 320 single emission monochromator (fitted with a 1200 grooves/mm grating blazed at 500 nm, reciprocal linear density of $2.6 \text{ nm} \cdot \text{mm}^{-1}$), coupled to a R928 Hamamatsu photomultiplier, using the front face acquisition mode. The excitation source was a 450 W Xe arc lamp. Emission spectra were corrected for detection and optical spectral response of the spectrofluorimeter and the excitation spectra were corrected for the spectral distribution of the lamp intensity using a photodiode reference detector. Time-resolved measurements have been carried out using a 1934D3 phosphorimeter coupled to the Fluorolog®-3, and a Xe-Hg flash lamp (6 μs /pulse half width and 20-30 μs tail) was used as the excitation source. The variable temperature measurements were performed using a helium-closed cycle cryostat with vacuum system measuring $\sim 5 \times 10^{-6}$ mbar and a Lakeshore 330 auto-tuning temperature controller with a resistance heater. The temperature can be adjusted from 11 to 450 K.

The absolute emission quantum yields were measured at ambient temperature using a quantum yield measurement system C9920-02 from Hamamatsu with a 150 W Xenon lamp coupled to a monochromator for wavelength discrimination, an integrating sphere as sample chamber and a multi-channel analyzer for signal detection. Three measurements were made for each sample so that the average value is reported. The method is accurate to within 10%.

8.7. Heterogeneous Catalysis

A 5 mL borosilicate batch reactor, equipped with a magnetic stirrer (800 rpm) and a valve for sampling, was charged with the catalysts **1**, **1n**, **9** and **20** (or with the organic ligands **H₄pmd** or **H₆bmt**, or lanthanide precursors $\text{EuCl}_3 \cdot 6\text{H}_2\text{O}$ and $\text{LaCl}_3 \cdot 7\text{H}_2\text{O}$), 1.5 mL of methanol and 0.4 M of styrene oxide (PhEtO). The reaction was carried out under atmospheric air, with the batch reactor immersed in an external thermostated oil bath (35 or 55 °C). Prior to reuse, the solid catalyst was separated from the reaction mixture by centrifugation, washed with methanol and dried at 55 °C (under atmospheric air). Leaching tests were carried out by heating a suspension of the catalyst (fresh or used) in methanol for 1 h at 35 or 55 °C (under agitation), subsequently filtering the solid at 35 or 55 °C through a 0.20 μm PVDF w/ GMF Whatman membrane, and finally adding PhEtO to the filtrate and monitoring the reaction of PhEtO at 35 or 55 °C, under agitation.

The progress of the catalytic reactions was monitored using a Varian 3900 GC equipped with a capillary column (SPB-5, 20 m \times 0.25 mm) and a flame ionization detector (using mesitylene as an internal standard). The identification of the reaction

product was carried out by GC-MS (Trace GC 2000 Series (Thermo Quest CE Instruments) - DSQ II (Thermo Scientific)), using He as the carrier gas.

8.8. Adsorption Studies

8.8.1. Gas Adsorption Measurements

Conventional adsorption isotherms were measured using a Micromeritics Tristar 3000 volumetric instrument under continuous adsorption conditions. Brunauer–Emmet–Teller (BET) were carried out to determine the total specific surface areas for the N₂ and CO₂ isotherms at 77 and 195 K, respectively. In addition, CO₂ isotherms at 195 K were measured to evaluate the micropore region by means of the Dubinin–Radushkevich equation. Prior to measurement, the powdered material **29** was outgassed to 10⁻⁶ Torr and heated at 423 K for 7 h.

8.8.2. Variable-Temperature Pulse Gas Chromatography

Gas-phase adsorption at zero coverage surface was studied using the pulse chromatographic technique, employing a gas chromatograph (Varian 450-GC) equipped with a home-made chromatographic column, with 0.4 cm internal diameter and 29 cm of length. The columns was packed with *ca.* 0.543 g of the powdered material **29**. For the activation of the materials, a He flow (20 mL min⁻¹) was passed through the column at 423 K during approximately 4 h. Later, 0.6 mL of equimolecular gas mixtures of C₂H₂/CO₂/H₂ and C₃H₆/C₃H₈/H₂ were injected at 1 bar on a He flow (20 mL min⁻¹). The separation performance of the chromatographic column was then examined at different temperatures (273–403 K) by means of a mass spectrometer gas analysis system (Pfeiffer Vacocon), detecting ion peaks at *m/z* 44 (CO₂ and C₃H₈), 42 (C₃H₆), 26 (C₂H₂), 4 (He) and 2 (H₂). The dead volume of the system was calculated using the retention time of hydrogen as a reference.

8.8.3. Breakthrough Experiments for Gas Separation

The chromatographic column, prepared as detailed in the section above, was activated under a pure He flow (20 mL min⁻¹) at 423 K during approximately 4 h and then used for evaluating the N₂/CO₂, N₂/C₃H₈, N₂/C₃H₆, C₃H₈/C₃H₆, CH₄/CO₂/C₂H₂ and N₂/CO₂/C₂H₂ separation performances of the material **29**. The desired gas mixture (20 mL min⁻¹) was prepared via mass flow controllers. For instance, N₂/CO₂ (0.85:0.15) mixtures were prepared to simulate the emission of flue gas from a power plant employing 3 mL min⁻¹ of CO₂ and 17 mL min⁻¹ of N₂ flows, and the breakthrough experiments were carried out at different temperatures (273–323 K) by step changes from He to N₂/CO₂ flow mixtures. The relative amounts of gases passing through the column were monitored on a mass spectrometer gas analysis system (Pfeiffer Vacocon) detecting ion peaks at *m/z* 44 (CO₂ and C₃H₈), 42 (C₃H₆), 26 (C₂H₂), 4 (He) and 2 (H₂).

8.9. Synthesis of Bi- and Tripodal Phosphonate Organic Ligands

8.9.1. 1,4-Phenylenebis(methylene)diphosphonic acid (H₄pmd)

Tetraethyl 1,4-phenylenebis(methylene)bisphosphonate (500 mg, 1.32 mmol) was added to an aqueous solution of HCl (30 mL, 6 M). The reaction mixture was kept under constant magnetic stirring and heated to reflux. The evolution of the reaction was controlled by TLC and stopped after approximately 20 h, when the hydrolysis was complete. Impurities were successfully eliminated via a liquid/liquid extraction with dichloromethane. Water was then removed under reduced pressure, and the final compound, 1,4-phenylenebis(methylene)diphosphonic acid (H₄pmd), was obtained in quantitative amounts (yield of about 96%).

¹H NMR (300.13 MHz, DMSO-*d*₆) δ (in ppm): 2.91 (d, 4H, $J(^1\text{H}-^{31}\text{P}) = 19.9$ Hz, CH₂) and 7.15 (s, 4H, Ar-H).

¹³C NMR (75.47 MHz, DMSO-*d*₆) δ (in ppm): 35.0 (d, $J(^{13}\text{C}-^{31}\text{P}) = 132.6$ Hz, CH₂), 129.4 (Ar-CH) and 131.8 (Ar-C).

³¹P NMR (121.49 MHz, DMSO-*d*₆) δ (in ppm): 21.7 (t, $J(^{31}\text{P}-^1\text{H}) = 22.2$ Hz, PO₃H₂).

8.9.2. (Benzene-1,3,5-triyltris(methylene))triphosphonic acid (H₆bmt)

A mixture of 1,3,5-tris(bromomethyl)benzene (0.3 g, 0.84 mmol) and triethyl phosphite (5 mL) was allowed to react under nitrogen atmosphere and at 120 °C for approximately 12 h. After cooling to ambient temperature the excess of triethyl phosphite was removed by distillation under reduced pressure. The resulting orange oil residue was dissolved in dichloromethane and the intermediate **IL**^I was purified by flash column chromatography using a mixture of dichloromethane and methanol (95 : 5) as eluent. **IL**^I was isolated as a colorless oil in 88% yield. Intermediate **IL**^I (0.47 g, 0.89 mmol) was transferred into an aqueous solution of HCl (30 mL, 6 M) and the reaction mixture was then refluxed for approximately 20 h under continuous magnetic stirring. The reaction product was washed with dichloromethane and the aqueous phase was distilled under reduced pressure. The resulting compound, (benzene-1,3,5-triyltris(methylene))-triphosphonic acid (H₆bmt), was recovered as a white solid by vacuum filtration and was washed with copious amounts of acetone. Yield: 92%.

IL^I: ¹H NMR (300.13 MHz, CDCl₃) δ (in ppm): 1.22 (t, 18H, $J(^1\text{H}-^1\text{H}) = 7.1$ Hz, CH₃), 3.08 (d, 6H, $J(^1\text{H}-^{31}\text{P}) = 22.1$ Hz, CH₂PO₃Et₂), 4.00 (dq, 12H, $J(^1\text{H}-^1\text{H}) = 7.2$ Hz and $J(^1\text{H}-^{31}\text{P}) = 7.9$ Hz, CH₂CH₃) and 7.10 (dt, 3H, $^4J(^1\text{H}-^1\text{H}) = ^4J(^1\text{H}-^{31}\text{P}) = 2.4$ Hz, Ar-H).

^{13}C NMR (75.47 MHz, CDCl_3) δ (in ppm): 16.2–16.3 (CH_3), 33.3 (d, $J(^{13}\text{C}-^{31}\text{P}) = 138.0$ Hz, $\text{CH}_2\text{PO}_3\text{Et}_2$), 62.0–62.1 (CH_2CH_3), 129.7 (dt, $^3J(^{13}\text{C}-^{31}\text{P}) = 5.8$ Hz and $^5J(^{13}\text{C}-^{31}\text{P}) = 5.2$ Hz, Ar-CH) and 131.9–132.1 (Ar-C).

MS (TOF MS ES^+) m/z : 529.2 ($\text{M} + \text{H}^+$) and 551.1 ($\text{M} + \text{Na}^+$).

H₆bmt: ^1H NMR (300.13 MHz, DMSO-d_6) δ (in ppm): 2.87 (d, 6H, $J(^1\text{H}-^{31}\text{P}) = 21.8$ Hz, CH_2) and 7.01 (d, 3H, $J(^1\text{H}-^1\text{H}) = 1.95$ Hz, Ar-H).

^{13}C NMR (75.47 MHz, DMSO-d_6) δ (in ppm): 35.2 (d, $J(^{13}\text{C}-^{31}\text{P}) = 132.6$ Hz, CH_2), 129.0 (Ar-CH) and 133.5 (Ar-C).

^{31}P NMR (121.49 MHz, DMSO-d_6) δ (in ppm): 22.5 (t, $J(^{31}\text{P}-^1\text{H}) = 21.2$ Hz, PO_3H_2).

MS (TOF MS ES^-) m/z : 359.0 ($\text{M} - \text{H}^-$).

8.9.3. ((2,4,6-Trifluorobenzene-1,3,5-triyl)tris(methylene))triphosphonic acid (**H₆tftp**)

To a mixture of 1,3,5-trifluorobenzene (0.60 g, 4.54 mmol) and chloromethyl methyl ether (6.58 g, 81.7 mmol, 18 eq.), anhydrous AlCl_3 (10.90 g, 81.7 mmol, 18 eq.) was slowly added for about 10 min, under nitrogen atmosphere and at 0 °C. This step was accompanied with the formation of an orange precipitate. The mixture was stirred at 0 °C for 10 min and then at 40 °C for approximately 7 h. The final dark brown solution was poured onto ice and stirred overnight. A liquid/liquid extraction was performed using dichloromethane. The organic phase was then neutralized with a saturated solution of NaHCO_3 and dried over anhydrous NaSO_4 . Dichloromethane was distilled under reduced pressure and the final oily residue was purified by flash column chromatography using petroleum ether / dichloromethane (4:1) as eluent. The target compound, 1,3,5-tris(chloromethyl)-2,4,6-trifluorobenzene (**IL²**), was obtained as a microcrystalline white powder in 71% yield (0.90 g).

A mixture of **IL²** (0.94 g, 3.40 mmol) and triethyl phosphite (15 mL) was refluxed under nitrogen atmosphere for approximately 3 h. After cooling to ambient temperature, the excess of triethyl phosphite was distilled under reduced pressure (*Caution!* triethyl phosphite has an extremely unpleasant smell and it is harmful; it should be, therefore, always handled inside a fume hood). The resulting oily residue was dissolved in dichloromethane and the desired compound, hexaethyl((2,4,6-trifluorobenzene-1,3,5-triyl)tris(methylene))tris(phosphonate) (**IL³**), was purified by flash column chromatography using a mixture of dichloromethane / methanol (95%:5%) as eluent. **IL³** was isolated as a microcrystalline white powder in 75% yield (1.49 g).

To **IL³** (1.70 g, 2.92 mmol) an aqueous solution of HCl (110 mL, 6M) was added, and the resulting reaction mixture was refluxed for approximately 20 h under continuous magnetic stirring. The reaction product was washed with dichloromethane and the aqueous phase was distilled under reduced pressure. The desired compound, ((2,4,6-trifluorobenzene-1,3,5-triyl)tris(methylene))triphosphonic acid (**H₆tftp**), was recovered as

a microcrystalline white crystalline powder (98% yield, 1.18 g) by vacuum filtration and washed with abundant amounts acetone.

***IL*²**: ¹H NMR (300.13 MHz, CDCl₃) δ (in ppm): 4.64 (s, 6H, CH₂).

¹³C NMR (75.47 MHz, CDCl₃) δ (in ppm): 31.8-31.9 (CH₂), 111.0-111.5 (Ar-C) and 159.5 (dt, $J(^{13}\text{C}-^{19}\text{F}) = 258.1$ Hz and $^3J(^{13}\text{C}-^{19}\text{F}) = 10.4$ Hz, Ar-CF).

¹⁹F NMR (282.40 MHz, CDCl₃) δ (in ppm): -138.1 (s, 3F, ArF).

Crystal data for *IL*²: C₉H₆Cl₃F₃, MW=277.49 g mol⁻¹, colourless block (0.13×0.11×0.08 mm³), orthorhombic, space group *P*2₁2₁2₁, *a*=8.1025(3) Å, *b*=8.7996(3) Å, *c*=14.9510(6) Å, α=90°, β=90°, γ=90(4)°, *V*=1065.99(7) Å³, *Z*=4, *D*_c=1.729 g cm⁻³, μ(Mo-Kα)=0.861 mm⁻¹, 18734 reflections were collected in the range 3.58° ≤ θ ≤ 33.08°, index ranges -12 ≤ *h* ≤ 11, -10 ≤ *k* ≤ 13, -22 ≤ *l* ≤ 22, of which 4042 were independent (*R*_{int}=0.0279), completeness to θ=33.08°=99.8%, final *R*1 ($[I > 2\sigma(I)]$)=0.0314, w*R*2 ($[I > 2\sigma(I)]$)=0.0671, *R*1 (all data)=0.0399, w*R*2 (all data)=0.0717.

***IL*³**: ¹H NMR (300.13 MHz, CDCl₃) δ (in ppm): 1.29 (t, 18H, $J(^1\text{H}-^1\text{H}) = 7.07$ Hz, CH₃), 3.19 (d, 6H, $J(^1\text{H}-^{31}\text{P}) = 21.4$ Hz, CH₂PO₃Et₂), 4.09 (dq, 12H, $J(^1\text{H}-^1\text{H}) = 7.07$ Hz and $J(^1\text{H}-^{31}\text{P}) = 7.3$ Hz, CH₂CH₃).

¹³C NMR (75.47 MHz, CDCl₃) δ (in ppm): 16.3-16.4 (CH₃), 21.0 (d, $J(^{13}\text{C}-^{31}\text{P}) = 143.2$ Hz, CH₂), 62.3-62.4 (CH₂CH₃), 104.7-105.3 (Ar-C), 156.3, 156.4 and 159.7 (Ar-CF).

¹⁹F NMR (282.40 MHz, CDCl₃) δ (in ppm): -138.7 (q, $J(^{19}\text{F}-^{31}\text{P}) = 5.6$ Hz, 3F, ArF).

MS (TOF MS ES⁺) *m/z*: 583.2 (M+H)⁺ and 605.2 (M+Na)⁺.

Crystal data for *IL*³: C₂₁H₃₆F₃O₉P₃, MW=582.41 g mol⁻¹, colourless plate (0.09×0.04×0.02 mm³), triclinic, space group *P* $\bar{1}$, *a*=10.3141(6) Å, *b*=10.5339(6) Å, *c*=15.0122(10) Å, α=69.566(3)°, β=71.856(3)°, γ=69.669(3)°, *V*=1399.25(15) Å³, *Z*=2, *D*_c=1.382 g cm⁻³, μ(Mo-Kα)=0.277 mm⁻¹, 24278 reflections were collected in the range 3.69° ≤ θ ≤ 29.13°, index ranges -14 ≤ *h* ≤ 12, -14 ≤ *k* ≤ 14, -20 ≤ *l* ≤ 20, of which 7427 were independent (*R*_{int}=0.0505), completeness to θ=29.13°=98.6%, final *R*1 ($[I > 2\sigma(I)]$)=0.0520, w*R*2 ($[I > 2\sigma(I)]$)=0.1122, *R*1 (all data)=0.1017, w*R*2 (all data)=0.1298.

H₆tfoot: ¹H NMR (300.13 MHz, DMSO-*d*₆) δ (in ppm): 2.93 (d, 6H, $J(^1\text{H}-^{31}\text{P}) = 20.9$ Hz, CH₂).

¹³C NMR (75.47 MHz, DMSO-*d*₆) δ (in ppm): 23.0 (d, $J(^{13}\text{C}-^{31}\text{P}) = 135.7$ Hz, CH₂), 105.8-106.2 (Ar-C) and 155.5-155.8 and 158.9-159.1 (Ar-CF).

¹⁹F NMR (282.40 MHz, DMSO-*d*₆) δ (in ppm): -139.5 (q, $J(^{19}\text{F}-^{31}\text{P}) = 5.6$ Hz, 3F, ArF).

³¹P NMR (121.49 MHz, DMSO-*d*₆) δ (in ppm): 19.4 (t, $J(^{31}\text{P}-^1\text{H}) = 20.4$ Hz, PO₃H₂).

MS (TOF MS ES⁻) *m/z*: 197.4 (M-2H-F)²⁻, 413.1 (M-H)⁻ and 451.0 (M-2H+K)⁻.

Crystal data for H₆tfoot: C₉H₁₆F₃O₁₁P₃, MW=450.13 g mol⁻¹, colourless block (0.12×0.09×0.05 mm³), monoclinic, space group *P*2₁/*c*, *a*=9.7829(5) Å, *b*=9.9524(5) Å, *c*=17.0510(9) Å, α=90.00°, β=100.424(2)°, γ=90.00°, *V*=1632.74(15) Å³, *Z*=4, *D*_c=1.831 g cm⁻³, μ(Mo-Kα)=0.455 mm⁻¹, 68711 reflections were collected in the range 3.57° ≤ θ ≤ 33.14°, index ranges -15 ≤ *h* ≤ 14, -15 ≤ *k* ≤ 15, -26 ≤ *l* ≤ 26, of which 68711

were independent ($R_{\text{int}}=0.0309$), completeness to $\theta=33.14^\circ=99.6\%$, final $R1$ ($[I > 2\sigma(I)]$)=0.0345, $wR2$ ($[I > 2\sigma(I)]$)=0.0924, $R1$ (all data)=0.0449, $wR2$ (all data)=0.0997.

8.9.4. Large tripodal phosphonate ligand H_6L

A mixture of 1,3,5-tris(4-bromophenyl)benzene (300 mg, 0.552 mmol), $[Pd(PPh_3)_4]$ (20 mg, 0.017 mmol) and triethyl phosphite (2 mL, 11.7 mmol) was prepared inside a 10 mL IntelliVent microwave reactor. The reaction mixture was kept inside a CEM Focused Microwave Synthesis System Discover S-Class equipment, under constant magnetic stirring (controlled by the microwave equipment), employing an irradiation power of 120 W for 20 min. The initial reaction temperature was 230 °C (achieved by using a weflon stirring bar), starting to decrease when the pressure inside the reactor reached 100 psi (limit value selected). The close control of the temperature inside the reactor was ensured with a constant flow of air (*ca.* 20-30 psi of pressure). After the reaction, the excess of triethyl phosphite was removed under reduced pressure and the crude product was purified by flash column chromatography using dichloromethane/methanol (97%:3%) as eluent. The resulting yellowish and viscous oily residue was washed with petroleum ether in an ultrasonic bath and the target organic intermediate IL^4 was obtained, as a white powder, in 83% yield.

The IL^4 intermediate (1.30 g, 1.82 mmol) was added to an aqueous solution of concentrated HCl (50 mL, 12 M) and the resulting reaction mixture was refluxed, under constant magnetic stirring, for approximately 48 h. The reaction was completed with the precipitation of a brownish viscous residue (*Attention!* During the reaction occurs the formation of an intermediate white precipitate being then dissolved). After cooling to ambient temperature, the reaction mixture was washed with dichloromethane and the resulting residue was dissolved in methanol, being then distilled under reduced pressure. The resulting brownish viscous residue was redissolved with dried methanol and a mixture of dried toluene and dried hexane (1:1) was added. The solvents were distilled under reduced pressure. The resulting residue was dried under vacuum affording a yellowish foam, which was dissolved in a small amount of dried methanol (2-3 mL) occurring then the precipitation of the desired H_6L compound as a white powder (yield of 93%).

IL^4 : 1H NMR (300.13 MHz, $CDCl_3$) δ (in ppm): 1.36 (t, 18 H, $J(^1H-^1H) = 7.1$ Hz, CH_3), 4.12-4.21 (m, 12 H, CH_2), 7.77-7.81 (m, 6 H, H3), 7.83 (s, 3 H, H6) and 7.91-7.98 (m, 6 H, H2).

^{13}C NMR (75.47 MHz, $CDCl_3$) δ (in ppm): 16.3 (d, $J(^{13}C-^{31}P) = 6.3$ Hz, CH_3), 62.2 (d, $J(^{13}C-^{31}P) = 5.5$ Hz, CH_2), 126.1, 126.9, 127.3 (d, $J(^{13}C-^{31}P) = 15.2$ Hz), 132.4 (d, $J(^{13}C-^{31}P) = 10.2$ Hz), 141.6 and 144.4 ($J(^{13}C-^{31}P) = 3.0$ Hz).

MS (TOF MS ES^+) m/z : 715.2 ($M+H$) $^+$ and 737.2 ($M+Na$) $^+$.

Crystal data for IL^4 : $C_{36}H_{47}O_{10}P_3$, $MW=732.65$ g mol $^{-1}$, colourless plate (0.12×0.08×0.05 mm 3), monoclinic, space group $P2_1/c$, $a=11.2203(10)$ Å, $b=14.5145(13)$ Å, $c=23.220(2)$ Å,

$\alpha=90.00^\circ$, $\beta=96.497(4)^\circ$, $\gamma=90.00^\circ$, $V=3757.2(6) \text{ \AA}^3$, $Z=4$, $D_c=1.295 \text{ g cm}^{-3}$, $\mu(\text{Mo-K}\alpha)=0.213 \text{ mm}^{-1}$, 57874 reflections were collected in the range $3.52^\circ \leq \theta \leq 25.34^\circ$, index ranges $-13 \leq h \leq 13$, $-17 \leq k \leq 17$, $-27 \leq l \leq 23$, of which 6850 were independent ($R_{\text{int}}=0.0430$), completeness to $\theta=25.34^\circ=99.5\%$, final $R1$ ($[I>2\sigma(I)]$)=0.0809, $wR2$ ($[I>2\sigma(I)]$)=0.2306, $R1$ (all data)=0.1027, $wR2$ (all data)=0.2541.

H₆L: ¹H NMR (300.13 MHz, DMSO-*d*₆) δ (in ppm): 7.78-7.85 (m, 6H, H3), 7.97-8.01 (overlapped) (m, 6H, H2) and 8.01 (s, 3H, H6).

¹³C NMR (75.47 MHz, DMSO-*d*₆) δ (in ppm): 125.2, 127.0 (d, $J(^{13}\text{C}-^{31}\text{P}) = 14.3 \text{ Hz}$), 131.2 (d, $J(^{13}\text{C}-^{31}\text{P}) = 10.0 \text{ Hz}$), 132.1, 134.5, 141.1 and 142.2 (d, $J(^{13}\text{C}-^{31}\text{P}) = 2.8 \text{ Hz}$).

³¹P NMR (121.49 MHz, DMSO-*d*₆) δ (in ppm): 13.7-14.0 (m, PO₃H₂).

HR-MS (ESI) m/z : 547.0464 (M+H)⁺.

Crystal data for H₆L: C₂₇H₃₃O₁₂P₃, MW=642.44 g mol⁻¹, colourless needle (0.11×0.04×0.03 mm³), monoclinic, space group *Cc*, $a=16.1261(8) \text{ \AA}$, $b=24.9525(13) \text{ \AA}$, $c=7.5650(4) \text{ \AA}$, $\alpha=90.00^\circ$, $\beta=104.358(3)^\circ$, $\gamma=90.00^\circ$, $V=2949.0(3) \text{ \AA}^3$, $Z=4$, $D_c=1.447 \text{ g cm}^{-3}$, $\mu(\text{Mo-K}\alpha)=0.265 \text{ mm}^{-1}$, 16071 reflections were collected in the range $3.69^\circ \leq \theta \leq 29.13^\circ$, index ranges $-21 \leq h \leq 22$, $-28 \leq k \leq 34$, $-10 \leq l \leq 10$, of which 7706 were independent ($R_{\text{int}}=0.0318$), completeness to $\theta=29.13^\circ=99.6\%$, final $R1$ ($[I>2\sigma(I)]$)=0.0391, $wR2$ ($[I>2\sigma(I)]$)=0.0797, $R1$ (all data)=0.0509, $wR2$ (all data)=0.0851.

8.10. 1D and 3D MOFs from the Self-Assembly of Lanthanides with 1,4-Phenylenebis(methylene)diphosphonic acid

8.10.1. From Micro- to Nano-Sized Lanthanide-Biphosphonate Coordination Polymers

8.10.1.1. Conventional Hydrothermal Synthesis

Reactive mixtures of the corresponding lanthanide (III) chloride hydrates [(LnCl₃·*x*H₂O, Ln³⁺ = Eu³⁺ (**1**), Gd³⁺ (**2**) and Tb³⁺ (**3**)], or their mixtures, with 0.2954 g **H₄pmd** in distilled water (*ca.* 12 mL) and having a molar ratio of approximately 1 : 1 : 600 (Ln³⁺ : H₄pmd : H₂O), were kept under constant magnetic stirring in open air and at ambient temperature for approximately 30 min. The isolated homogenous suspensions were transferred to Teflon-lined Parr Instrument reaction vessels and then placed inside a MMM Venticell oven. Reactions took place at 180 °C over a period of 72h, after which time the oven was turned off and the samples cooled slowly to ambient temperature (while inside the oven). After that, the reactions were recovered by vacuum filtration, washed with abundant amounts of distilled water and dried at room temperature. The final product was a white crystalline material.

The deuterated material [Eu(Hpmd)(D₂O)] (**1_D**) was prepared by using the same procedure that for compounds **1-3**, with slight modifications. Deuterium oxide, D₂O, was

used as solvent instead distilled water and, after reaction, **1D** was washed with D₂O instead, once again, distilled water.

Elemental analyses. Calcd (%) for **1**: C 22.2; H 2.56. Found: C 22.2; H 2.91. Calcd (%) for **2**: C 21.9; H 2.53. Found: C 21.7; H 2.67. Calcd (%) for **3**: C 21.8; H 2.52. Found: C 21.3; H 2.65.

Thermogravimetric analysis (TGA) data (weight losses in %) and derivative thermogravimetric peaks (DTG; in italics inside the parentheses). **1**: 150-450 °C -6.5% (290 °C); 450-700 °C -3.1% (564 °C). **2**: 195-515 °C -6.5% (300 °C); 515-700 °C -1.1% (645 °C). **3**: 180-490 °C -10.9% (295 °C); 490-725 °C -4.5% (675 °C).

Powder X-ray diffraction data for **1**: C₈H₁₁EuO₇P₂, MW=433.07 g mol⁻¹, Triclinic, space group *P* $\bar{1}$, *a*=5.6110(4) Å, *b*=9.3974(6) Å, *c*=11.4933(8) Å, α =75.069(3)°, β =81.651(3)°, γ =80.964(4)°, *V*=574.80(7) Å³, *Z*=2, *D*_c=2.502 g cm⁻³, Profile function: Cauchy, Caglioti law parameters (*U* = 0.28(2), *V* = -0.188(7) and *W* = 0.0442(7), asymmetric parameters [up to 20° 2 θ = 0.0291(1) and 0.0179(3)], zero shift [2 θ] = 0.021(1), 1590 independent reflections, 1 global refined parameter, 13 profiles refinement parameters, 36 intensity-dependent refinement parameters, *R*_p = 2.09, *R*_{wp} = 2.91, *R*_{exp} = 0.84.

2: C₈H₁₁GdO₇P₂, MW=438.36 g mol⁻¹, Triclinic, space group *P* $\bar{1}$, *a*=5.6010(4) Å, *b*=9.3849(7) Å, *c*=11.4837(8) Å, α =75.205(4)°, β =81.625(4)°, γ =81.120(4)°, *V*=573.06(7) Å³, *Z*=2, *D*_c=2.502 g cm⁻³, Profile function: Cauchy, Caglioti law parameters (*U* = 0.36(2), *V* = -0.230(8) and *W* = 0.0483(8), asymmetric parameters [up to 20° 2 θ = -0.230(8) and 0.020(2)], zero shift [2 θ] = 0.020(12), 1518 independent reflections, 1 global refined parameter, 13 profiles refinement parameters, 36 intensity-dependent refinement parameters, *R*_p = 1.80, *R*_{wp} = 2.56, *R*_{exp} = 0.76.

3: C₈H₁₁TbO₇P₂, MW=440.03 g mol⁻¹, Triclinic, space group *P* $\bar{1}$, *a*=5.5882(5) Å, *b*=9.3484(8) Å, *c*=11.4594(10) Å, α =75.325(4)°, β =81.698(4)°, γ =81.177(5)°, *V*=568.76(8) Å³, *Z*=2, *D*_c=2.569 g cm⁻³, Profile function: Cauchy, Caglioti law parameters (*U* = 0.49(9), *V* = -0.33(1) and *W* = 0.070(1), asymmetric parameters [up to 20° 2 θ = 0.029(1) and 0.0148(3)], zero shift [2 θ] = -0.004(2), 1511 independent reflections, 1 global refined parameter, 13 profiles refinement parameters, 36 intensity-dependent refinement parameters, *R*_p = 2.22, *R*_{wp} = 2.96, *R*_{exp} = 0.74.

8.10.1.2. Microwave-Assisted Hydrothermal Synthesis

A mixture containing 0.2034 g of EuCl₃·6H₂O (or TbCl₃·6H₂O) and 0.1477 g of **H₄pmd** was prepared at ambient temperature in distilled water (*ca.* 6 mL), with an overall molar ratio of *ca.* 1 : 1 : 600 (Eu³⁺ : H₄pmd : H₂O), directly inside a 10 mL IntelliVent microwave reactor. The reaction mixture was kept under constant magnetic stirring throughout the synthesis which occurred inside a CEM Focused Microwave Synthesis System Discover S-Class equipment. A constant flow of air (*ca.* 10 psi of pressure) ensured a close control of the temperature inside the reactor. Parameters varied during the reaction: temperature (40, 50, 60, 70, 90, 120 and 150 °C) and irradiation (50 W power) time (5 s, 30 s, 1 min and 5 min). The final product was recovered by vacuum filtration,

washed with abundant amounts of distilled water and then air-dried at ambient temperature.

8.10.1.3. [Ln(Hpmd)(H₂O)] materials as isolated nanoparticles

Mixtures of respective lanthanide (III) chloride hydrate (LnCl₃·xH₂O, Ln³⁺ = Eu³⁺ or Tb³⁺), with **H₄pmd** in distilled water (*ca.* 6 mL), were kept under magnetic stirring at ambient temperature for approximately 1 min. The resulting homogeneous reactive mixtures were submitted to ultrasound irradiation. The supernatant suspension was separated by decantation and the solid product was recovered by vacuum filtration. Both the suspension and the recovered solid were the subject to further characterization in order to confirm the presence of either [Eu(Hpmd)(H₂O)] (**1**) or [Tb(Hpmd)(H₂O)] (**2**).

The following experimental conditions were systematically varied in order to optimize the synthetic conditions aiming at isolating separated nano-particles:

- (i) Temperature: ambient temperature, 60 and 70°C;
- (ii) Reaction time (ultra-sound irradiation): 1, 3, 4, 5, 6, 7, 10, 20 or 30 min;
- (iii) Composition of the reactive mixtures: Ln³⁺ : H₄pmd : H₂O molar ratios of about 1 : 1 : 600, 1 : 1 : 1200, 1 : 1 : 1800, 1 : 1 : 3600 or 1 : 1 : 7200.

Isolated nanoparticles of **1** were obtained when the reaction was performed at ambient temperature, during 5 minutes of ultrasonic irradiation with a molar ratio of the reactive mixture of about 1 : 1 : 7200. Identical nanoparticles of compound **2** were isolated using similar experimental conditions.

8.10.1.4. Theoretical Calculations

Ab initio calculations were performed using the G03w package¹⁵ on the multiprocessor cluster Flamingo belonging to CICECO, University of Aveiro. Partial optimized geometries, harmonic vibrational frequencies and intensities were obtained at the B3LYP level using the Los Alamos Effective Core Potentials plus double-zeta basis set (LanL2DZ option of G03). The basis set for phosphorus was extended with a *d* function.

We have observed from the crystallographic studies that the structural and vibrational features remain constant for the investigated lanthanides. Assuming that the lanthanum-based compound is isostructural, and because this metal is more convenient due to the absence of *f* electrons, the crystal structure of the praseodymium-based compound was used as a model with the praseodymium atoms being substituted by lanthanum.¹⁰

The whole framework was divided in three independent model structures corresponding to the phosphonate, hydrogenophosphonate and water ligands. Each one of these moieties, and the respective metal center, were allowed to be optimized inside a box of fixed atoms. Each model structure was further divided into layers: one layer corresponds to one of the ligands and the metal, and was set free in the optimization; the other layer is composed by the neighboring atoms up to a distance of about 2 Å from those of the central layer. These layers were built from the real crystallographic data, using the Diamond software package.¹⁶ The partial optimization, with the internal layer free and the other

layers fixed, led to fragments very similar analogous in the crystal structure. The theoretical spectrum of the structure was obtained by adding the three fractional spectra.

8.10.2. Lanthanum-Biphosphonate Coordination Polymers Isolated by Microwave-Assisted and One-Pot Synthesis

8.10.2.1. Microwave-assisted synthesis

Mixtures of **H₄pmd** (0.1477g, 0.55 mmol) and water (*ca.* 6 mL) were stirred at ambient temperature inside a 10 mL IntelliVent microwave reactor for *ca.* 5 min. LaCl₃·7H₂O (0.2061 g, 0.55 mmol) was then added obtaining an overall molar ratio of *ca.* 1:1:600 (La³⁺:H₄pmd:H₂O) for the reactive mixture. The resulting homogeneous suspension was placed inside a CEM Focused Microwave™ Synthesis System Discover S-Class equipment and was kept under constant magnetic stirring (controlled by the microwave equipment). A constant flow of air (*ca.* 20-30 psi of pressure) ensured a close control of the temperature inside the reactor.

Synthetic conditions were investigated by systematically varying the experimental parameters: (i) temperature (30, 35, 40, 50, 60, 70, 90, 120 and 150 °C); (ii) power (10, 25 and 50 W); (iii) irradiation time (1, 3, 5 and 10 min).

After reacting, a white precipitate was obtained, and the final product was recovered by vacuum filtration, followed by washing with abundant amounts of distilled water, and then air-dried.

8.10.2.2. One-Pot Synthesis

For a typical metal:ligand molar ratio of 1:1, a mixture containing *ca.* 0.1 mmol of an aqueous LaCl₃·xH₂O solution (5 mL of *ca.* 20 mmol/L solution) and *ca.* 5 mL of an aqueous solution of **H₄pmd** (0.0254 g, 0.0954 mmol) was homogenized in a round-bottom flask with constant magnetic stirring. The resulting solution was heated to the desired temperature and kept stirring during the required time, leading to the formation of a white precipitate. After cooling, the obtained solid product was centrifuged for 20 min at 3500 rpm, using a SIGMA 2-5 equipment, or filtrated under vacuum, washed with copious amounts of distilled water and ethanol, and allowed to air dry at room temperature.

As performed for the microwave-assisted approach, a systematic variation of the experimental conditions was performed by changing the following parameters: (i) La³⁺:H₄pmd molar ratios (1:1, 1:2 and 2:1); (ii) temperature (room temperature, 40, 60 and 80 °C); (iii) reaction time (10, 20, 30 and 60 min).

8.10.2.3. Characterization data for the isolated phase-pure MOFs 4 and 5 and for compounds 6, 7 and 8.

[La₂(H₂pmd)₃(H₂O)₁₂] (4)

Elemental analyses. Calcd (%): C 22.41, H 4.23. Found: C 22.45, H 4.24.

Thermogravimetric analysis (TGA) data (weight losses in %) and derivative thermogravimetric peaks (DTG; in italics inside the parentheses): 25-270 °C -3.1% (246 °C); 450-640 °C -4.1%; 640-800 °C -18.5%.

Selected FT-IR data (cm^{-1}): $\nu(\text{POH}) = 2230$ *w*, $\nu(\text{Ph}) = 1511$ *m*, $\delta(\text{CH}) = 1403$ *w*, $\delta(\text{POH}) = 1257$ *vs* and 1014 *s*, $\nu(\text{PO}) = 1152$ *vs*, $\rho(\text{CH}_2) + \gamma(\text{CH}) = 769$ *m*, $\gamma(\text{Ph}) + \nu(\text{PO}_3) = 566$ *vs*.

Crystal data: $\text{C}_{24}\text{H}_{54}\text{La}_2\text{O}_{30}\text{P}_6$, $\text{MW}=1286.31$ g mol^{-1} , colourless needle ($0.09 \times 0.02 \times 0.02$ mm^3), Triclinic, space group $P\bar{1}$, $a=7.6851(11)$ Å, $b=11.6395(16)$ Å, $c=12.7044(19)$ Å, $\alpha=105.665(7)^\circ$, $\beta=102.544(7)^\circ$, $\gamma=93.172(6)^\circ$, $V=1060.2(3)$ Å³, $Z=1$, $D_c=2.015$ g cm^{-3} , $\mu(\text{Mo-K}\alpha)=2.315$ mm^{-1} , 28682 reflections were collected in the range $3.56^\circ \leq \theta \leq 29.13^\circ$, index ranges $-10 \leq h \leq 10$, $-15 \leq k \leq 15$, $-17 \leq l \leq 17$, of which 5655 were independent ($R_{\text{int}}=0.0335$), completeness to $\theta=29.06^\circ=98.9\%$, final $R1$ ($[I>2\sigma(I)]$)=0.0261, $wR2$ ($[I>2\sigma(I)]$)=0.0657, $R1$ (all data)=0.0310, $wR2$ (all data)=0.0671.

[La₂(H₂pmd)(pmd)(H₂O)₂] (5)

Elemental analyses. Calcd (%): C 22.88, H 2.64. Found: C 22.85, H 2.74.

Thermogravimetric analysis (TGA) data (weight losses in %) and derivative thermogravimetric peaks (DTG; in italics inside the parentheses): 45-130 °C -15.4% (91 °C); 200-400 °C -3.1%; 490-800 °C -19.4%.

Selected FT-IR data (cm^{-1}): $\nu(\text{POH}) = 2363$ *w*, $\nu(\text{Ph}) = 1515$ *m*, $\delta(\text{CH}) = 1407$ *w*, $\delta(\text{POH}) = 1248$ *vs* and 976 *s*, $\nu(\text{PO}) = 1136$ *vs*, $\rho(\text{CH}_2) + \gamma(\text{CH}) = 798$ *m*, $\gamma(\text{Ph}) + \nu(\text{PO}_3) = 563$ *vs*.

Crystal data: $\text{C}_8\text{H}_{11}\text{LaO}_7\text{P}_2$, $\text{MW}=420.02$ g mol^{-1} , colourless plate ($0.09 \times 0.02 \times 0.02$ mm^3), Triclinic, space group $P\bar{1}$, $a=5.7098(9)$ Å, $b=9.6259(14)$ Å, $c=11.822(2)$ Å, $\alpha=104.874(11)^\circ$, $\beta=96.054(11)^\circ$, $\gamma=105.347(10)^\circ$, $V=595.02(16)$ Å³, $Z=2$, $D_c=2.344$ g cm^{-3} , $\mu(\text{Mo-K}\alpha)=3.881$ mm^{-1} , 8322 reflections were collected in the range $3.63^\circ \leq \theta \leq 29.06^\circ$, index ranges $-6 \leq h \leq 7$, $-13 \leq k \leq 13$, $-15 \leq l \leq 15$, of which 2965 were independent ($R_{\text{int}}=0.1007$), completeness to $\theta=29.06^\circ=93.4\%$, final $R1$ ($[I>2\sigma(I)]$)=0.0654, $wR2$ ($[I>2\sigma(I)]$)=0.1242, $R1$ (all data)=0.1382, $wR2$ (all data)=0.1451.

Crystal data for [La(H₃pmd)(H₂pmd)(H₂O)] (6): $\text{C}_{16}\text{H}_{23}\text{LaO}_{13}\text{P}_4$, $\text{MW}=686.13$ g mol^{-1} , colourless plate ($0.09 \times 0.02 \times 0.02$ mm^3), Monoclinic, space group $P 2/n$, $a=5.717(2)$ Å, $b=8.694(3)$ Å, $c=22.649(8)$ Å, $\alpha=90.00^\circ$, $\beta=94.384(16)^\circ$, $\gamma=90.00^\circ$, $V=1122.6(7)$ Å³, $Z=2$, $D_c=2.030$ g cm^{-3} , $\mu(\text{Mo-K}\alpha)=2.256$ mm^{-1} , 11489 reflections were collected in the range $3.58^\circ \leq \theta \leq 25.34^\circ$, index ranges $-6 \leq h \leq 6$, $-10 \leq k \leq 10$, $-27 \leq l \leq 26$, of which 2019 were independent ($R_{\text{int}}=0.11212$), completeness to $\theta=25.34^\circ=97.7\%$, final $R1$ ($[I>2\sigma(I)]$)=0.1443, $wR2$ ($[I>2\sigma(I)]$)=0.3267, $R1$ (all data)=0.1684, $wR2$ (all data)=0.3368.

Crystal data for [La₂(H₂pmd)₃(H₂O)₂] (7): $\text{C}_{12}\text{H}_{17}\text{LaO}_{10}\text{P}_3$, $\text{MW}=553.08$ g mol^{-1} , colourless needle ($0.02 \times 0.01 \times 0.01$ mm^3), Triclinic, space group $P\bar{1}$, $a=9.232(15)$ Å, $b=9.263(15)$ Å, $c=11.124(18)$ Å, $\alpha=90.15(5)^\circ$, $\beta=93.08(5)^\circ$, $\gamma=110.77(5)^\circ$, $V=888(2)$ Å³, $Z=2$, $D_c=2.069$ g cm^{-3} , $\mu(\text{Mo-K}\alpha)=2.726$ mm^{-1} , 7165 reflections were collected in the range $3.67^\circ \leq \theta \leq 25.34^\circ$, index ranges $-11 \leq h \leq 11$, $-8 \leq k \leq 11$, $-13 \leq l \leq 13$, of which 3123

were independent ($R_{\text{int}}=0.2430$), completeness to $\theta=25.34^\circ=96.3\%$, final $R1$ ($[I>2\sigma(I)]$)=0.0982, $wR2$ ($[I>2\sigma(I)]$)=0.1943, $R1$ (all data)=0.2594, $wR2$ (all data)=0.2636.

Crystal data and structure refinement details for the physical mixture of $[\text{La}_2(\text{H}_2\text{pmd})(\text{pmd})(\text{H}_2\text{O})_2]$ (5) and $[\text{La}_2(\text{H}_2\text{pmd})(\text{pmd})(\text{H}_2\text{O})_4]$ (8): $[\text{La}_2(\text{H}_2\text{pmd})(\text{pmd})(\text{H}_2\text{O})_4]$ (8): $\text{C}_8\text{H}_5\text{LaO}_8\text{P}_2$, $\text{MW}=429.97 \text{ g mol}^{-1}$, Monoclinic, space group $P2_1/c$, $a=21.9799(7) \text{ \AA}$, $b=5.4581(2) \text{ \AA}$, $c=10.8462(3) \text{ \AA}$, $\beta=94.285(2)^\circ$, $V=1297.57(7) \text{ \AA}^3$, $Z=4$, $D_c=2.201 \text{ g cm}^{-3}$, Profile function: Pseudo-Voigt [$\eta = 0.407(9)$], Caglioti law parameters ($U = 0.016(4)$, $V = -0.002(3)$ and $W = 0.0157(3)$), asymmetric parameters [up to $2\theta = 0.0413(4)$ and $-0.0758(7)$], zero shift [2θ] = $-0.0758(7)$, 2214 (5: 1097; 8: 1117) independent reflections, 1 global refined parameter, 14 profiles refinement parameters, 62 intensity-dependent refinement parameters, $R_p = 7.14$, $R_{wp} = 9.23$, $R_{\text{exp}} = 1.59$.

8.11. From 1D to 3D Functional MOFs based on (Benzene-1,3,5-triyltris(methylene))triphosphonic Acid

8.11.1. Microwave-Assisted Synthesis of 1D Lanthanide-Organic Frameworks

8.11.1.1. Microwave-Assisted Hydrothermal Synthesis

A reactive mixture composed of 0.0666 g of **H₆bmt** and 0.1374 g of $\text{LaCl}_3 \cdot 7\text{H}_2\text{O}$ in *ca.* 6 mL of distilled water, with a molar ratio of *ca.* 2 : 1: 1800 ($\text{La}^{3+} : \text{H}_6\text{bmt} : \text{H}_2\text{O}$), was prepared at ambient temperature inside a 10 mL IntelliVent microwave reactor. Reactions took place inside a CEM Focused Microwave Synthesis System Discover S-Class equipment, under constant magnetic stirring (controlled by the microwave equipment) by employing an irradiation power of 50 W. A constant flow of air (*ca.* 20-30 psi of pressure) ensured a close control of the temperature inside the reactor.

Synthetic conditions were investigated by systematically varying the experimental parameters: (i) temperature (40, 60, 90, 100, 120 and 150 °C) and (ii) irradiation time (1, 15 and 30 min).

The resulting products, $[\text{La}(\text{H}_4\text{bmt})(\text{H}_5\text{bmt})(\text{H}_2\text{O})_2] \cdot 3\text{H}_2\text{O}$ (**9**) and the known $[\text{La}_2(\text{H}_3\text{bmt})_2(\text{H}_2\text{O})_2] \cdot \text{H}_2\text{O}$ (**20**), as white powders, were recovered by vacuum filtration, washed with copious amounts of distilled water and then air-dried at ambient temperature.

Isotypical materials containing stoichiometric amounts of optical centers, 3% of Eu^{3+} (**10**) and 3% of Tb^{3+} (**11**), were prepared using a similar procedure to that described above (at 60 °C for 5 minutes) using the required amounts of the corresponding lanthanide chloride salts.

Elemental CH composition (%). Calcd for **9**: C 22.83; H 3.94. Found: C 22.60; H 3.95. Calcd for **10**: C 22.82; H 3.94. Found: C 22.53; H 3.81. Calcd for **11**: C 22.82; H 3.94. Found: C 22.69; H 3.83.

Thermogravimetric analysis (TGA) data (weight losses in %) and derivative thermogravimetric peaks (DTG; in italics inside the parentheses); **9**: 22-111 °C -5.9% (73 °C); 111-184 °C -3.5% (146 °C); 231-351 °C -5.1% (301 °C). **10**: 27-112 °C -5.5% (72 °C); 112-183 °C -3.4% (143 °C); 230-341 °C -4.4% (294 °C). **11**: 34-106 °C -5.6% (74 °C); 106-181 °C -3.0% (145 °C); 240-342 °C -5.2% (295 °C).

Selected FT-IR data (in cm^{-1} ; from KBr pellets); **9**: $\nu(\text{H}_2\text{O})_{\text{coord}} = 3629$ *m* and 3546 *m*; $\nu(\text{H}_2\text{O})_{\text{cryst}} = 3338$ *w* and 3225 *w*; $\nu(\text{POH})$ and $\nu(-\text{CH}_2-)$ = 3085-2715 *w*; $\nu(\text{POH}) = 2437$ *w*; $\delta(\text{H}_2\text{O}) = 1648$ *w*; $\nu(-\text{C}=\text{C}-) = 1606$ *m*; $\delta(\text{P}-\text{CH}_2) = 1459$ *m*, 1412 *m* and 1407 *m*; $\nu(\text{P}=\text{O}) = 1350$ -1150 *m-vs*; $\nu(\text{P}-\text{O}) = 1025$ -915 *vs*; $\nu(\text{P}-\text{C}) = 753$ *m* and 718 *m*. **10**: $\nu(\text{H}_2\text{O})_{\text{coord}} = 3629$ *m* and 3546 *m*; $\nu(\text{H}_2\text{O})_{\text{cryst}} = 3338$ *w* and 3225 *w*; $\nu(\text{POH})$ and $\nu(-\text{CH}_2-)$ = 3087-2713 *w*; $\nu(\text{POH}) = 2435$ *w*; $\delta(\text{H}_2\text{O}) = 1647$ *w*; $\nu(-\text{C}=\text{C}-) = 1607$ *m*; $\delta(\text{P}-\text{CH}_2) = 1459$ *m*, 1412 *m* and 1407 *m*; $\nu(\text{P}=\text{O}) = 1350$ -1150 *m-vs*; $\nu(\text{P}-\text{O}) = 1025$ -915 *vs*; $\nu(\text{P}-\text{C}) = 753$ *m* and 718 *m*. **11**: $\nu(\text{H}_2\text{O})_{\text{coord}} = 3628$ *m* and 3546 *m*; $\nu(\text{H}_2\text{O})_{\text{cryst}} = 3338$ *w* and 3224 *w*; $\nu(\text{POH})$ and $\nu(-\text{CH}_2-)$ = 3092-2717 *w*; $\nu(\text{POH}) = 2434$ *w*; $\delta(\text{H}_2\text{O}) = 1646$ *w*; $\nu(-\text{C}=\text{C}-) = 1607$ *m*; $\delta(\text{P}-\text{CH}_2) = 1459$ *m*, 1412 *m* and 1407 *m*; $\nu(\text{P}=\text{O}) = 1350$ -1150 *m-vs*; $\nu(\text{P}-\text{O}) = 1025$ -915 *vs*; $\nu(\text{P}-\text{C}) = 753$ *m* and 718 *m*.

Crystal data for 9: $\text{C}_{18}\text{H}_{37}\text{LaO}_{23}\text{P}_6$, MW=946.21 g mol^{-1} , colourless plate ($0.02 \times 0.01 \times 0.003$ mm^3), Monoclinic, space group $P2_1/m$, $a=8.9221(11)$ Å, $b=21.208(2)$ Å, $c=9.1060(10)$ Å, $\beta=107.921(3)^\circ$, $V=1639.5(3)$ Å³, $Z=2$, $D_c=1.917$ g cm^{-3} , $\mu(\text{Mo-K}\alpha)=1.688$ mm^{-1} , 11975 reflections were collected in the range $2.35^\circ \leq \theta \leq 25.35^\circ$, index ranges $-10 \leq h \leq 10$, $-25 \leq k \leq 25$, $-10 \leq l \leq 10$, of which 3054 were independent ($R_{\text{int}}=0.0642$), completeness to $\theta=25.35^\circ=98.8\%$, final $R1$ ($[I > 2\sigma(I)]$)=0.0425, $wR2$ ($[I > 2\sigma(I)]$)=0.0793, $R1$ (all data)=0.0705, $wR2$ (all data)=0.0861.

8.11.2. Hydrothermal Synthesis of Layered 2D Lanthanide-Organic Frameworks

8.11.2.1. Hydrothermal Synthesis

Mixtures of the respective lanthanide (III) chloride hydrate [$\text{LnCl}_3 \cdot n\text{H}_2\text{O}$, where $\text{Ln}^{3+} = \text{Eu}^{3+}$ (**12**), Gd^{3+} (**13**), Tb^{3+} (**14**), Dy^{3+} (**15**), Ho^{3+} (**16**), Er^{3+} (**17**), Tm^{3+} (**18**) and Yb^{3+} (**19**)] and **H₆bmt** were prepared in distilled water (*ca.* 6 mL) with a molar ratio of approximately 1:2:1800 ($\text{H}_6\text{pmt}:\text{Ln}^{3+}:\text{H}_2\text{O}$), respectively. The mixtures were kept under constant magnetic stirring for approximately 30 min. The resulting homogeneous suspension was then transferred to a Teflon-lined Parr Instrument autoclave and then placed inside a MMM Venticell oven, where remained at 180 °C for 72 h. Then, the resulting materials, as white crystalline powder, were recovered by vacuum filtration, washed with abundant amounts of distilled water and dried at ambient temperature.

Thermogravimetric analysis (TGA) data (weight losses in %) and derivative thermogravimetric peaks (DTG; in italics inside the parentheses); **12**: 163-255 °C -1.3%

(176 °C); 255-532 °C -4.9% (425 °C). **13**: 168-209 °C 0.9% (177 °C); 357-550 °C -4.1% (425 °C). **14**: 43-215 °C -2.4% (166 °C); 278-530 °C -4.6% (424 °C). **15**: 39-216 °C -2.6% (152 °C); 260-520 °C -4.8% (437 °C). **16**: 37-187 °C -1.3% (158 °C); 310-520 °C -3.7% (444 °C). **17**: 30-260 °C -2.4% (159 °C); 260-495 °C -3.9% (425 °C). **18**: 30-174 °C -2.5% (95 °C); 384-535 °C -4.0% (470 °C). **19**: 38-250 °C -3.2% (147 °C); 250-520 °C -5.3% (443 °C).

Selected FT-IR data (in cm^{-1} ; from KBr pellets); **12**: $\nu_{\text{asym}}(\text{O-H, water}) = 3607 m$, $\nu_{\text{asym}}(\text{O-H, water}) = 3397 w$, $\nu(\text{PO-H and CH } (-\text{CH}_2-)) = 3300\text{-}2850 w$, $\delta(\text{H}_2\text{O}) = 1605 m$, $\nu_{\text{sym}}(\text{P=O}) = 1116 \nu\text{s}$, $\nu_{\text{asym}}(\text{P-O}_{\text{coord}}) = 1068 \nu\text{s}$, $\nu_{\text{sym}}(\text{P-O}_{\text{coord}}) = 968 w$, $\nu_{\text{sym}}(\text{P-OH}) = 930 \nu\text{s}$. **13**: $\nu_{\text{asym}}(\text{O-H, water}) = 3607 m$, $\nu_{\text{asym}}(\text{O-H, water}) = 3397 w$, $\nu(\text{PO-H and CH } (-\text{CH}_2-)) = 3300\text{-}2850 w$, $\delta(\text{H}_2\text{O}) = 1605 m$, $\nu_{\text{sym}}(\text{P=O}) = 1120 \nu\text{s}$, $\nu_{\text{asym}}(\text{P-O}_{\text{coord}}) = 1069 \nu\text{s}$, $\nu_{\text{sym}}(\text{P-O}_{\text{coord}}) = 968 w$, $\nu_{\text{sym}}(\text{P-OH}) = 930 \nu\text{s}$. **14**: $\nu_{\text{asym}}(\text{O-H, water}) = 3607 m$, $\nu_{\text{asym}}(\text{O-H, water}) = 3403 w$, $\nu(\text{PO-H and CH } (-\text{CH}_2-)) = 3300\text{-}2850 w$, $\delta(\text{H}_2\text{O}) = 1605 m$, $\nu_{\text{sym}}(\text{P=O}) = 1121 \nu\text{s}$, $\nu_{\text{asym}}(\text{P-O}_{\text{coord}}) = 1069 \nu\text{s}$, $\nu_{\text{sym}}(\text{P-O}_{\text{coord}}) = 968 w$, $\nu_{\text{sym}}(\text{P-OH}) = 931 \nu\text{s}$. **15**: $\nu_{\text{asym}}(\text{O-H, water}) = 3606 m$, $\nu_{\text{asym}}(\text{O-H, water}) = 3397 w$, $\nu(\text{PO-H and CH } (-\text{CH}_2-)) = 3300\text{-}2850 w$, $\delta(\text{H}_2\text{O}) = 1605 m$, $\nu_{\text{sym}}(\text{P=O}) = 1121 \nu\text{s}$, $\nu_{\text{asym}}(\text{P-O}_{\text{coord}}) = 1070 \nu\text{s}$, $\nu_{\text{sym}}(\text{P-O}_{\text{coord}}) = 968 w$, $\nu_{\text{sym}}(\text{P-OH}) = 931 \nu\text{s}$. **16**: $\nu_{\text{asym}}(\text{O-H, water}) = 3607 m$, $\nu_{\text{asym}}(\text{O-H, water}) = 3397 w$, $\nu(\text{PO-H and CH } (-\text{CH}_2-)) = 3300\text{-}2850 w$, $\delta(\text{H}_2\text{O}) = 1605 m$, $\nu_{\text{sym}}(\text{P=O}) = 1124 \nu\text{s}$, $\nu_{\text{asym}}(\text{P-O}_{\text{coord}}) = 1072 \nu\text{s}$, $\nu_{\text{sym}}(\text{P-O}_{\text{coord}}) = 968 w$, $\nu_{\text{sym}}(\text{P-OH}) = 931 \nu\text{s}$. **17**: $\nu_{\text{asym}}(\text{O-H, water}) = 3606 m$, $\nu_{\text{asym}}(\text{O-H, water}) = 3397 w$, $\nu(\text{PO-H and CH } (-\text{CH}_2-)) = 3300\text{-}2850 w$, $\delta(\text{H}_2\text{O}) = 1605 m$, $\nu_{\text{sym}}(\text{P=O}) = 1128 \nu\text{s}$, $\nu_{\text{asym}}(\text{P-O}_{\text{coord}}) = 1073 \nu\text{s}$, $\nu_{\text{sym}}(\text{P-O}_{\text{coord}}) = 968 w$, $\nu_{\text{sym}}(\text{P-OH}) = 931 \nu\text{s}$. **18**: $\nu_{\text{asym}}(\text{O-H, water}) = 3605 m$, $\nu_{\text{asym}}(\text{O-H, water}) = 3405 w$, $\nu(\text{PO-H and CH } (-\text{CH}_2-)) = 3300\text{-}2850 w$, $\delta(\text{H}_2\text{O}) = 1605 m$, $\nu_{\text{sym}}(\text{P=O}) = 1128 \nu\text{s}$, $\nu_{\text{asym}}(\text{P-O}_{\text{coord}}) = 1074 \nu\text{s}$, $\nu_{\text{sym}}(\text{P-O}_{\text{coord}}) = 968 w$, $\nu_{\text{sym}}(\text{P-OH}) = 931 \nu\text{s}$. **19**: $\nu_{\text{asym}}(\text{O-H, water}) = 3604 m$, $\nu_{\text{asym}}(\text{O-H, water}) = 3406 w$, $\nu(\text{PO-H and CH } (-\text{CH}_2-)) = 3300\text{-}2850 w$, $\delta(\text{H}_2\text{O}) = 1605 m$, $\nu_{\text{sym}}(\text{P=O}) = 1132 \nu\text{s}$, $\nu_{\text{asym}}(\text{P-O}_{\text{coord}}) = 1076 \nu\text{s}$, $\nu_{\text{sym}}(\text{P-O}_{\text{coord}}) = 968 w$, $\nu_{\text{sym}}(\text{P-OH}) = 932 \nu\text{s}$.

8.11.3. Conventional Hydrothermal Synthesis of 3D Lanthanide-Organic Frameworks

8.11.3.1. Hydrothermal Synthesis

Mixtures of the respective lanthanide (III) chloride hydrates [$\text{LnCl}_3 \cdot n\text{H}_2\text{O}$, where $\text{Ln}^{3+} = \text{La}^{3+}$ (**20**), Ce^{3+} (**21**), Pr^{3+} (**22**), and Nd^{3+} (**23**)] and **H₆bmt** were prepared in distilled water (*ca.* 6 mL) with a molar ratio of approximately 1:2:1800 ($\text{H}_6\text{pmt}:\text{Ln}^{3+}:\text{H}_2\text{O}$), respectively (for **20**: 0.0666 g of **H₆bmt** were reacted with 0.1374 g of $\text{LaCl}_3 \cdot 7\text{H}_2\text{O}$). The mixtures were kept under constant magnetic stirring and atmospheric conditions for approximately 30 min. The resulting suspensions were transferred to Teflon-lined Parr Instrument autoclaves and placed inside a pre-heated MMM Venticell oven where they remained at 180 °C for a period of 72 h. After reacting, the vessels were allowed to cool slowly to ambient temperature and the resulting materials (typically white microcrystalline powders) were recovered by vacuum filtration, washed with abundant amounts of distilled water and air-dried at ambient temperature.

The mixed-lanthanide materials with 5% of Eu^{3+} (**24**) or 5% of Tb^{3+} (**25**) dispersed in a La^{3+} matrix were prepared following the aforementioned procedure while adjusting the amounts of the lanthanide chloride salts to the desired amounts.

Elemental CH composition (%). Calcd for **20**: C 20.70; H 2.89. Found: C 20.50; H 2.84. Calcd for **21**: C 20.60; H 2.88. Found: C 20.90; H 2.80. Calcd for **22**: C 20.60; H 2.88. Found: C 21.10; H 2.82. Calcd for **23**: C 20.50; H 2.86. Found: C 20.80; H 2.79. Calcd for **24**: C 20.60; H 2.89. Found: C 20.60; H 2.78. Calcd for **25**: C 20.60; H 2.89. Found: C 20.50; H 2.85.

Thermogravimetric analysis (TGA) data (weight losses in %) and derivative thermogravimetric peaks (DTG; in italics inside the parentheses). **20**: 38-130 °C -1.4% (69 °C); 130-265 °C -3.5% (162 °C); 350-565 °C -4.7% (458 °C). **21**: 31-106 °C -1.4% (50 °C); 106-270 °C -3.0% (159 °C); 366-521 °C -4.2% (472 °C). **22**: 35-107 °C -1.2% (51 °C); 107-280 °C -2.7% (154 °C); 417-560 °C -3.9% (477 °C). **23**: 32-99 °C -1.5% (54 °C); 99-270 °C -3.1% (148 °C); 360-578 °C -4.7% (486 °C). **24**: 44-121 °C -1.2% (53 °C); 121-263 °C -3.2% (162 °C); 373-555 °C -4.4% (465 °C). **25**: 50-142 °C -0.8% (63 °C); 142-267 °C -2.2% (157 °C); 441-506 °C -3.2% (471 °C).

Selected FT-IR data (in cm^{-1} ; from KBr pellets). **20**: $\nu(\text{H}_2\text{O})_{\text{coord}} = 3588m$; $\nu(\text{POH}) = 3420m$; $\nu(\text{H}_2\text{O})_{\text{cryst}}$ and $\nu(-\text{CH}_2-)$ = 3180-2820w; $\delta(\text{H}_2\text{O}) = 1605m$; $\delta(\text{POH}) = 1122vs$ and 1069vs. **21**: $\nu(\text{H}_2\text{O})_{\text{coord}} = 3588m$; $\nu(\text{POH}) = 3413m$; $\nu(\text{H}_2\text{O})_{\text{cryst}}$ and $\nu(-\text{CH}_2-)$ = 3190-2750w; $\delta(\text{H}_2\text{O}) = 1605m$; $\delta(\text{POH}) = 1119vs$ and 1069 vs. **22**: $\nu(\text{H}_2\text{O})_{\text{coord}} = 3589m$; $\nu(\text{POH}) = 3412m$; $\nu(\text{H}_2\text{O})_{\text{cryst}}$ and $\nu(-\text{CH}_2-)$ = 3190-2750w; $\delta(\text{H}_2\text{O}) = 1605m$; $\delta(\text{POH}) = 1120vs$ and 1067vs. **23**: $\nu(\text{H}_2\text{O})_{\text{coord}} = 3589m$; $\nu(\text{POH}) = 3410m$; $\nu(\text{H}_2\text{O})_{\text{cryst}}$ and $\nu(-\text{CH}_2-)$ = 3190-2750w; $\delta(\text{H}_2\text{O}) = 1605m$; $\delta(\text{POH}) = 1122vs$ and 1067 vs. **24**: $\nu(\text{H}_2\text{O})_{\text{coord}} = 3588m$; $\nu(\text{POH}) = 3414m$; $\nu(\text{H}_2\text{O})_{\text{cryst}}$ and $\nu(-\text{CH}_2-)$ = 3190-2750w; $\delta(\text{H}_2\text{O}) = 1605m$; $\delta(\text{POH}) = 1120 vs$ and 1069 vs. **25**: $\nu(\text{H}_2\text{O})_{\text{coord}} = 3589m$; $\nu(\text{POH}) = 3415m$; $\nu(\text{H}_2\text{O})_{\text{cryst}}$ and $\nu(-\text{CH}_2-)$ = 3190-2750w; $\delta(\text{H}_2\text{O}) = 1605m$; $\delta(\text{POH}) = 1119 vs$ and 1069 vs.

Crystal data for 20: $\text{C}_{18}\text{H}_{30}\text{La}_2\text{O}_{21}\text{P}_6$, MW=1046.06 g mol^{-1} , colourless prism ($0.12 \times 0.08 \times 0.04 \text{ mm}^3$), Monoclinic, space group $C2/c$, $a=23.5921(6) \text{ \AA}$, $b=7.2774(2) \text{ \AA}$, $c=19.7125(5) \text{ \AA}$, $\beta=106.1760(10)^\circ$, $V=3250.43(15) \text{ \AA}^3$, $Z=4$, $D_c=2.138 \text{ g cm}^{-3}$, $\mu(\text{Mo-K}\alpha)=2.974 \text{ mm}^{-1}$, 33829 reflections were collected in the range $3.60^\circ \leq \theta \leq 29.13^\circ$, index ranges $-32 \leq h \leq 32$, $-9 \leq k \leq 9$, $-26 \leq l \leq 26$, of which 4356 were independent ($R_{\text{int}}=0.0408$), completeness to $\theta=29.13^\circ=99.8\%$, final $R1$ ($[I>2\sigma(I)]$)=0.0226, $wR2$ ($[I>2\sigma(I)]$)=0.0501, $R1$ (all data)=0.0310, $wR2$ (all data)=0.0535.

Crystal data for 20-dehyd: $\text{C}_8\text{H}_{12}\text{LaO}_9\text{P}_3$, MW=496.01 g mol^{-1} , colourless prism ($0.11 \times 0.10 \times 0.07 \text{ mm}^3$), Monoclinic, space group $C2/c$, $a=24.757(4) \text{ \AA}$, $b=7.1588(13) \text{ \AA}$, $c=19.353(4) \text{ \AA}$, $\beta=108.455(7)^\circ$, $V=3253.6(10) \text{ \AA}^3$, $Z=8$, $D_c=2.025 \text{ g cm}^{-3}$, $\mu(\text{Mo-K}\alpha)=2.959 \text{ mm}^{-1}$, 49338 reflections were collected in the range $3.54^\circ \leq \theta \leq 33.13^\circ$, index ranges $-38 \leq h \leq 38$, $-10 \leq k \leq 11$, $-29 \leq l \leq 29$, of which 6180 were independent ($R_{\text{int}}=0.0233$), completeness to $\theta=33.13^\circ=99.9\%$, final $R1$ ($[I>2\sigma(I)]$)=0.0208, $wR2$ ($[I>2\sigma(I)]$)=0.0510, $R1$ (all data)=0.0229, $wR2$ (all data)=0.0520.

Crystal data for 21: $\text{C}_{18}\text{H}_{30}\text{Ce}_2\text{O}_{21}\text{P}_6$, MW=1048.48 g mol^{-1} , colourless prism ($0.08 \times 0.02 \times 0.01 \text{ mm}^3$), Monoclinic, space group $C2/c$, $a=23.3599(13) \text{ \AA}$, $b=7.2198(4) \text{ \AA}$,

$c=19.7793(11)$ Å, $\beta=106.034(2)^\circ$, $V=3206.6(10)$ Å³, $Z=4$, $D_c=2.172$ g cm⁻³, $\mu(\text{Mo-K}\alpha)=3.190$ mm⁻¹, 37494 reflections were collected in the range $3.63^\circ \leq \theta \leq 29.13^\circ$, index ranges $-31 \leq h \leq 31$, $-9 \leq k \leq 9$, $-27 \leq l \leq 25$, of which 4291 were independent ($R_{\text{int}}=0.0410$), completeness to $\theta=29.13^\circ=99.4\%$, final $R1$ ($[I>2\sigma(I)]$)=0.0226, $wR2$ ($[I>2\sigma(I)]$)=0.0462, $R1$ (all data)=0.0307, $wR2$ (all data)=0.0486.

Crystal data for 22: C₁₈H₃₀Pr₂O₂₁P₆, MW=1050.06 g mol⁻¹, colourless prism ($0.08 \times 0.06 \times 0.04$ mm³), Monoclinic, space group $C2/c$, $a=23.368(4)$ Å, $b=7.2040(11)$ Å, $c=19.745(3)$ Å, $\beta=106.262(7)^\circ$, $V=3190.9(9)$ Å³, $Z=4$, $D_c=2.186$ g cm⁻³, $\mu(\text{Mo-K}\alpha)=3.406$ mm⁻¹, 7961 reflections were collected in the range $3.51^\circ \leq \theta \leq 25.35^\circ$, index ranges $-27 \leq h \leq 28$, $-8 \leq k \leq 6$, $-23 \leq l \leq 23$, of which 2904 were independent ($R_{\text{int}}=0.0864$), completeness to $\theta=25.35^\circ=99.0\%$, final $R1$ ($[I>2\sigma(I)]$)=0.0497, $wR2$ ($[I>2\sigma(I)]$)=0.1043, $R1$ (all data)=0.0998, $wR2$ (all data)=0.1213.

Crystal data for 23: C₁₈H₃₀Nd₂O₂₁P₆, MW=1056.72 g mol⁻¹, colourless prism ($0.07 \times 0.01 \times 0.01$ mm³), Monoclinic, space group $C2/c$, $a=23.419(5)$ Å, $b=7.1793(16)$ Å, $c=19.697(4)$ Å, $\beta=106.605(14)^\circ$, $V=3172.8(12)$ Å³, $Z=4$, $D_c=2.212$ g cm⁻³, $\mu(\text{Mo-K}\alpha)=3.627$ mm⁻¹, 18869 reflections were collected in the range $3.52^\circ \leq \theta \leq 29.12^\circ$, index ranges $-27 \leq h \leq 32$, $-9 \leq k \leq 9$, $-26 \leq l \leq 26$, of which 4251 were independent ($R_{\text{int}}=0.1118$), completeness to $\theta=29.12^\circ=99.6\%$, final $R1$ ($[I>2\sigma(I)]$)=0.0466, $wR2$ ($[I>2\sigma(I)]$)=0.0703, $R1$ (all data)=0.0974, $wR2$ (all data)=0.0810.

8.12. Layered Lanthanide-Organic Frameworks Based on ((2,4,6-Trifluorobenzene-1,3,5-triyl)tris(methylene))triphosphonic acid

8.12.1. Hydrothermal Synthesis of isotypical [Ln(H₃tftp)(H₂O)] materials

A reactive mixture composed of 0.1374 g of LaCl₃·7H₂O and 0.0766 g of H₆tftp in distilled water (*ca.* 6 mL), with an overall molar ratio of approximately 1:2:1800 (H₆tftp:La³⁺:H₂O), was prepared. The mixture was kept under constant magnetic stirring for approximately 30 min at ambient temperature. The resulting homogeneous suspension was transferred to a Teflon-lined Parr Instrument autoclave and then placed inside a MMM Venticell oven where it remained at 180 °C for 72 h. The resulting [La(H₃tftp)(H₂O)] (**26**) material was recovered by vacuum filtration as white crystalline powder, being then washed with copious amounts of distilled water and then air-dried at ambient temperature.

The isotypical materials with 5% of Eu³⁺ (**27**) and Tb³⁺ (**28**) were prepared as described above for compound **26** while adjusting the amounts of the lanthanide chloride salts in the initial reactive mixture to the desired percentages.

Elemental CH composition (%). Calcd for **26**: C 19.02; H 1.96. Found: C 19.00; H 1.84. Calcd (%) for **27**: C 18.99; H 1.95. Found: C 18.99; H 1.86. Calcd (%) for **28**: C 18.99; H 1.95. Found: C 18.86; H 1.86.

Selected FT-IR data (in cm⁻¹; from KBr pellets). **26**: $\nu(\text{H}_2\text{O})_{\text{coord}} = 3493w$ and $3446w$; $\nu(\text{POH}) = 3213m$; $\nu(-\text{CH}_2-) = 2941w$; $\delta(\text{H}_2\text{O}) + \nu(-\text{C}=\text{C}-) = 1673w$, $1625s$ and

1602m; $\nu(-C=C-)$ = 1470vs; $\delta(P-CH_2)$ = 1420m and 1409m; $\nu(P=O)$ and $\nu(C-F)$ = 1350-1050m-vs; $\nu(P-O)$ = 1040-900vs; $\nu(P-C)$ = 763m and 745m. **27**: $\nu(H_2O)_{\text{coord}}$ = 3491w and 3446w; $\nu(POH)$ = 3214m; $\nu(-CH_2-)$ = 2941w; $\delta(H_2O) + \nu(-C=C-)$ = 1674w, 1625s and 1602m; $\nu(-C=C-)$ = 1470vs; $\delta(P-CH_2)$ = 1420m and 1410m; $\nu(P=O)$ and $\nu(C-F)$ = 1350-1050m-vs; $\nu(P-O)$ = 1040-900vs; $\nu(P-C)$ = 763m and 745m. **28**: $\nu(H_2O)_{\text{coord}}$ = 3489w and 3445w; $\nu(POH)$ = 3216m; $\nu(-CH_2-)$ = 2942w; $\delta(H_2O) + \nu(-C=C-)$ = 1660w, 1625s and 1602m; $\nu(-C=C-)$ = 1470vs; $\delta(P-CH_2)$ = 1420m and 1408m; $\nu(P=O)$ and $\nu(C-F)$ = 1350-1050m-vs; $\nu(P-O)$ = 1040-900vs; $\nu(P-C)$ = 763m and 745m.

Crystal data for 26: $C_{18}H_{22}F_6La_2O_{20}P_6$, MW=1136.00 g mol⁻¹, colourless plate (0.04×0.04×0.01 mm³), Triclinic, space group $P\bar{1}$, $a=9.4435(4)$ Å, $b=11.7657(5)$ Å, $c=14.9918(7)$ Å, $\alpha=110.335(2)^\circ$, $\beta=90.018(2)^\circ$, $\gamma=93.142(2)(4)^\circ$, $V=1559.23(12)$ Å³, $Z=2$, $D_c=2.420$ g cm⁻³, $\mu(\text{Mo-K}\alpha)=3.135$ mm⁻¹, 44212 reflections were collected in the range $3.54^\circ \leq \theta \leq 25.35^\circ$, index ranges $-11 \leq h \leq 11$, $-14 \leq k \leq 14$, $-18 \leq l \leq 17$, of which 5677 were independent ($R_{\text{int}}=0.0789$), completeness to $\theta=25.35^\circ=99.2\%$, final $R1$ ($[I > 2\sigma(I)]$)=0.0512, $wR2$ ($[I > 2\sigma(I)]$)=0.1148, $R1$ (all data)=0.0805, $wR2$ (all data)=0.1266.

8.13. Porous Yttrium-Triphosphonate MOF: Synthesis and Properties

8.13.1. Conventional Solvothermal Synthesis

A reactive mixture composed of 0.1111 g of $YCl_3 \cdot 6H_2O$ and 0.0766 g of **H₆L**, with an overall molar ratio of approximately 1:4 ($H_6L:Y^{3+}$), in a mixture of distilled water and methanol (7:3) was prepared. The mixture was kept under constant magnetic stirring for approximately 30 min at ambient temperature. The resulting homogeneous suspension was transferred to a Teflon-lined Parr Instrument autoclave and then placed inside a MMM Venticell oven where it remained at 140 °C for 48 h. The resulting $[Y(H_3L)] \cdot xH_2O \cdot yMeOH$ (**29**) material was recovered by vacuum filtration as white crystalline powder, being then washed with copious amounts of distilled water and then air-dried at ambient temperature.

The isotypal materials with 5% of Eu^{3+} (**30**) and Tb^{3+} (**31**) were prepared as described above for compound **26** while adjusting the amounts of the lanthanide chloride salts in the initial reactive mixture to the desired percentages.

Thermogravimetric analysis (TGA) data (weight losses in %) and derivative thermogravimetric peaks (DTG; in italics inside the parentheses) for **29**: 19-82 °C -22.7% (71 °C); 376-486 °C -21.7% (436 °C); 522-641 °C -5.2% (570 °C).

Selected FT-IR data (in cm⁻¹; from KBr pellets) for **29**: $\nu(H_2O)_{\text{cryst}} + \nu(CH_3O-H)_{\text{cryst}} + \nu(POH)$ = 3723-2555 s; $\delta(H_2O)$ = 1632 m; $\nu(-C=C-)$ = 1600 m, 1557 w and 1503 w; $\nu(P=O)$ = 1144 vs and 1075 vs; $\nu(P-O)$ = 925 s and 829 s.

Crystal data for 29: $C_{30}H_{30}F_6YO_{12}P_3$, MW=764.36 g mol⁻¹, Orthorhombic, space group $Pna2_1$, $a=9.835(3)$ Å, $b=16.634(5)$ Å, $c=23.500(8)$ Å, $V=3844.49(210)$ Å³, $Z=5$, $D_c=1.65064$ g cm⁻³.

8.13.2. Preparation of compound $[Y(H_3L)] \cdot xH_2O \cdot yMeOH$ as large single-crystals

A solution of $YCl_3 \cdot 6H_2O$ dissolved in 1 mL of distilled water was added to a solution composed of the large tripodal organic ligand **H₆L**, 1 mL of distilled water, 3 mL of methanol and 5 mL of an aqueous solution of HCl (6 M). The mixture was kept under constant magnetic stirring during approximately 1 min at ambient temperature. The resulting homogeneous suspension was transferred to a Teflon-lined Parr Instrument autoclave and then placed inside a MMM Venticell oven according to the following temperature program: 48 h (from ambient temperature to 140 °C), 24 h (isothermal at 140 °C) and 48 h (cooling to 30 °C). The resulting material **29** was recovered by vacuum filtration as large single-crystals, being then washed with copious amounts of distilled water and then air-dried at ambient temperature.

References

1. T. Kottke and D. Stalke, *J. Appl. Crystallogr.*, 1993, **26**, 615-619.
2. APEX2, *Data Collection Software Version 2.1-RC13*, Bruker AXS, Delft, The Netherlands, 2006.
3. Cryopad, *Remote monitoring and control, Version 1.451*, Oxford Cryosystems, Oxford, United Kingdom, 2006.
4. SAINT+, *Data Integration Engine v. 7.23a* ©, 1997-2005, Bruker AXS, Madison, Wisconsin, USA.
5. G. M. Sheldrick, *SADABS v.2.01*, Bruker/Siemens Area Detector Absorption Correction Program, 1998, Bruker AXS, Madison, Wisconsin, USA.
6. G. M. Sheldrick, *Acta Cryst. A*, 2008, **64**, 112-122.
7. G. M. Sheldrick, *SHELXS-97, Program for Crystal Structure Solution*, University of Göttingen, 1997.
8. G. M. Sheldrick, *SHELXL-97, Program for Crystal Structure Refinement*, University of Göttingen, 1997.
9. A. Boulouf and D. Louër, *J. Appl. Crystallogr.*, 2004, **37**, 724-731.
10. F. N. Shi, T. Trindade, J. Rocha and F. A. A. Paz, *Cryst. Growth Des.*, 2008, **8**, 3917-3920.
11. H. M. Rietveld, *J. Appl. Crystallogr.*, 1969, **2**, 65-71.
12. T. Roisnel and J. Rodriguez-Carvajal, *WinPLOTR [June 2005] - A Windows Tool for Powder Diffraction Pattern Analysis. Materials Science Forum, Proceedings of the Seventh European Powder Diffraction Conference (EPDIC 7)*, Ed. R. Delhez and E.J. Mittenmeijer 2000, 118-123.
13. J. Rodriguez-Carvajal, *FULLPROF - A Program for Rietveld Refinement and Pattern Matching Analysis, Abstract of the Satellite Meeting on Powder Diffraction of the XV Congress of the IUCR, Toulouse, France 1990*, 127.
14. G. Caglioti, A. Paoletti and F. P. Ricci, *Nucl. Instr.*, 1958, **3**, 223-228.
15. M. J. Frisch, G. W. Trucks, H. B. Schlegel, G. E. Scuseria, M. A. Robb, J. R. Cheeseman, J. J. A. Montgomery, T. Vreven, K. N. Kudin, J. C. Burant, J. M. Millam, S. S. Iyengar, J. Tomasi, V. Barone, B. Mennucci, M. Cossi, G. Scalmani, N. Rega, G. A. Petersson, H. Nakatsuji, M. Hada, M. Ehara, K. Toyota, R. Fukuda, J. Hasegawa, M. Ishida, T. Nakajima, Y. Honda, O. Kitao, H. Nakai, M. Klene, X. Li, J. E. Knox, H. P. Hratchian, J. B. Cross, C. Adamo, J. Jaramillo, R. Gomperts, R. E. Stratmann, O. Yazyev, A. J. Austin, R. Cammi, C. Pomelli, J. Ochterski, P. Y. Ayala, K. Morokuma, G. A. Voth, P. Salvador, J. J. Dannenberg, V. G. Zakrzewski, S. Dapprich, A. D. Daniels, M. C. Strain, J. Farkas, A. D. Malick, A. D. Rabuck, K. Raghavachari, J. B. Foresman, J. V. Ortiz, Q. Cui, A. G. Baboul, S. Clifford, J. Cioslowski, B. B. Stefanov, G. Liu, A. Liashenko, P. Piskorz, I. Komaromi, D. J. Martin, D. J. Fox, T. Keith, M. A. Al-Laham, C. Y. Peng, A. Nanayakkara, M. Challacombe, B. G. Gill, B. G. Johnson, W. Chen, M. W. Wong, C. Gonzalez and J. A. Pople, Revision D.02 ed.; Gaussian, I., Ed. Pittsburgh, PA, 2003.

16. K. Brandenburg, *DIAMOND, Version 3.2, Crystal Impact GbR, Bonn, Germany, 2006.*

Appendices

Appendix A

A.1. Chapter 3: From Micro- to Nano-Sized Lanthanide-Biphosphonate Coordination Polymers

A.1.1. Crystallographic Details

Table A.1.1 - Selected bond lengths (in Å) and angles (in degrees) for the Eu³⁺ coordination environment in [Eu(Hpmd)(H₂O)] (1).^a

Eu(1)–O(1W)	2.4010(17)	Eu(1)–O(4) ⁱⁱⁱ	2.4698(15)
Eu(1)–O(1)	2.1986(16)	Eu(1)–O(5)	2.5598(16)
Eu(1)–O(3) ⁱ	2.2356(15)	Eu(1)–O(6) ⁱⁱ	2.2448(17)
Eu(1)–O(4)	2.6100(16)		
O(1W)–Eu(1)–O(4) ⁱⁱⁱ	90.32(5)	O(3) ⁱ –Eu(1)–O(4) ⁱⁱⁱ	156.82(6)
O(1W)–Eu(1)–O(4)	79.07(5)	O(3) ⁱ –Eu(1)–O(5)	75.17(5)
O(1W)–Eu(1)–O(5)	102.32(5)	O(3) ⁱ –Eu(1)–O(6) ⁱⁱ	95.36(6)
O(1)–Eu(1)–O(1W)	83.59(6)	O(4) ⁱⁱⁱ –Eu(1)–O(4)	74.47(6)
O(1)–Eu(1)–O(3) ⁱ	83.54(6)	O(4) ⁱⁱⁱ –Eu(1)–O(5)	125.21(5)
O(1)–Eu(1)–O(4)	147.67(5)	O(5)–Eu(1)–O(4)	56.76(5)
O(1)–Eu(1)–O(4) ⁱⁱⁱ	78.60(6)	O(6) ⁱⁱ –Eu(1)–O(1W)	167.72(6)
O(1)–Eu(1)–O(5)	154.90(5)	O(6) ⁱⁱ –Eu(1)–O(4)	110.37(5)
O(1)–Eu(1)–O(6) ⁱⁱ	91.37(6)	O(6) ⁱⁱ –Eu(1)–O(4) ⁱⁱⁱ	99.68(6)
O(3) ⁱ –Eu(1)–O(1W)	72.99(6)	O(6) ⁱⁱ –Eu(1)–O(5)	77.77(6)
O(3) ⁱ –Eu(1)–O(4)	116.44(5)		

^a Symmetry transformations used to generate equivalent atoms: (i) 2-x, 1-y, -z; (ii) 3-x, -y, -z; (iii) 2-x, -y, -z.

A.1.2 - Chapter 3: Thermogravimetry

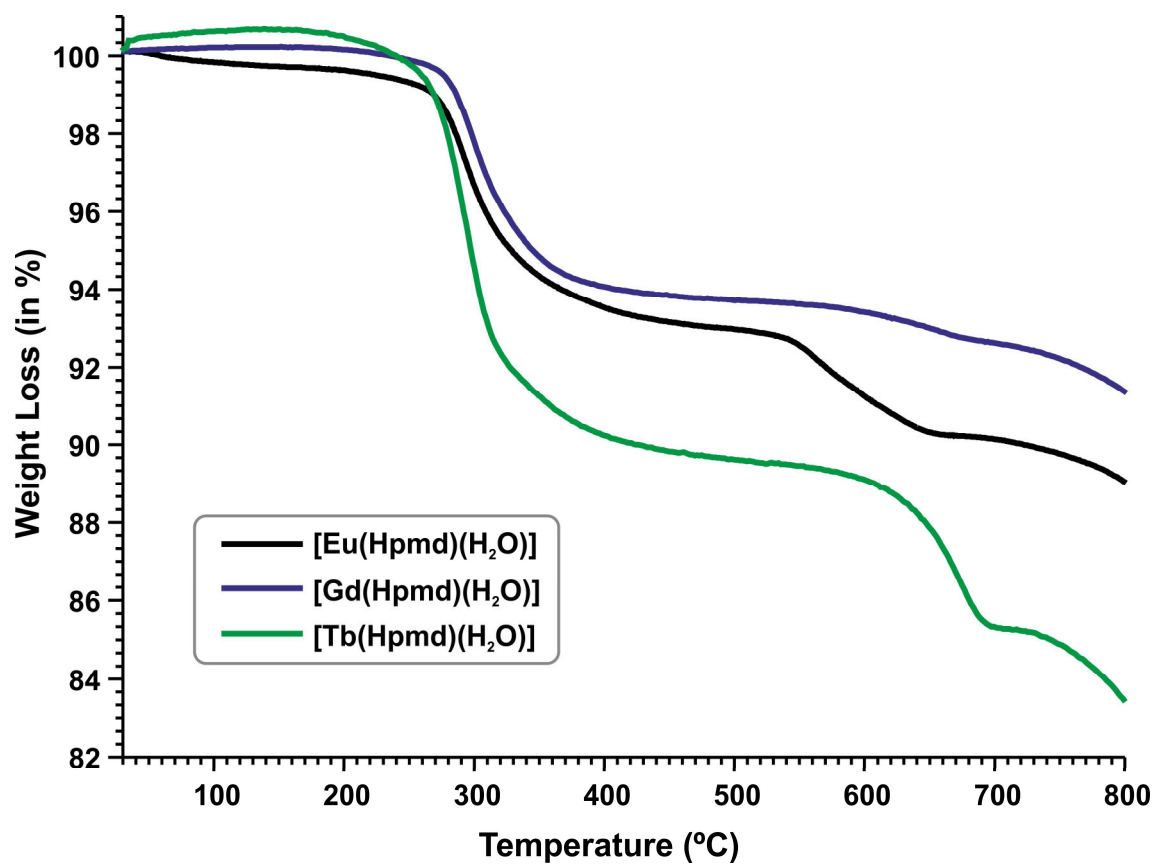


Figure A.1.1 - Thermograms of [LnHpmd)(H₂O)] materials between ambient temperature and 800 °C.

A.3 - Chapter 3: FT-IR and Raman studies

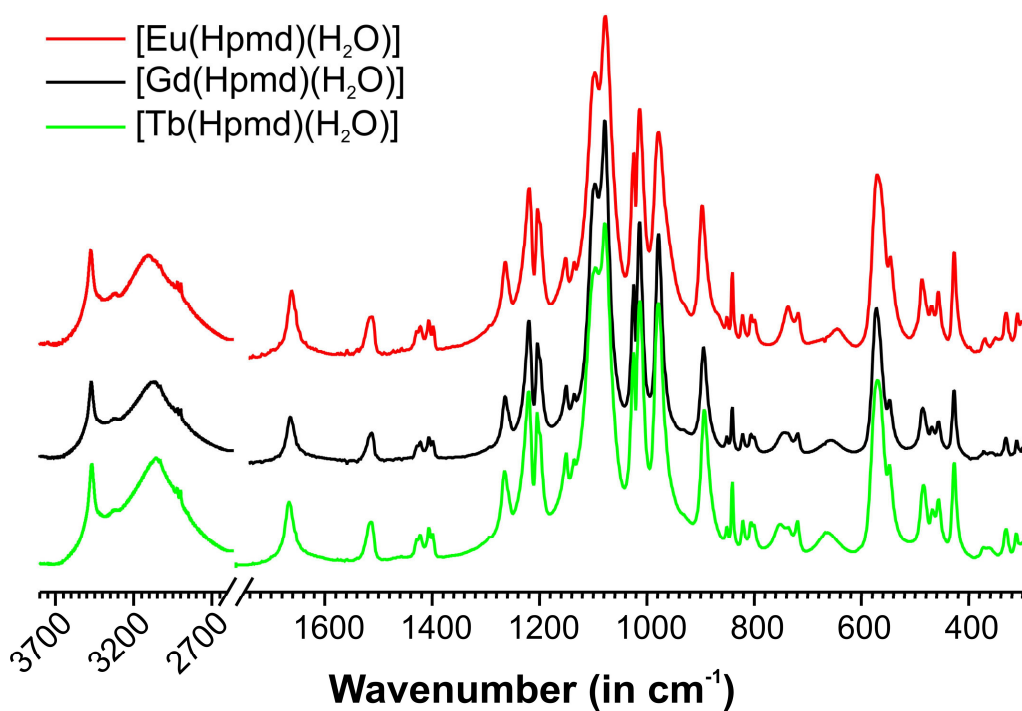


Figure A.1.2 – FT-IR spectra (in absorbance, arbitrary units) of [LnHpmd)(H₂O)] materials collected from KBr pellets.

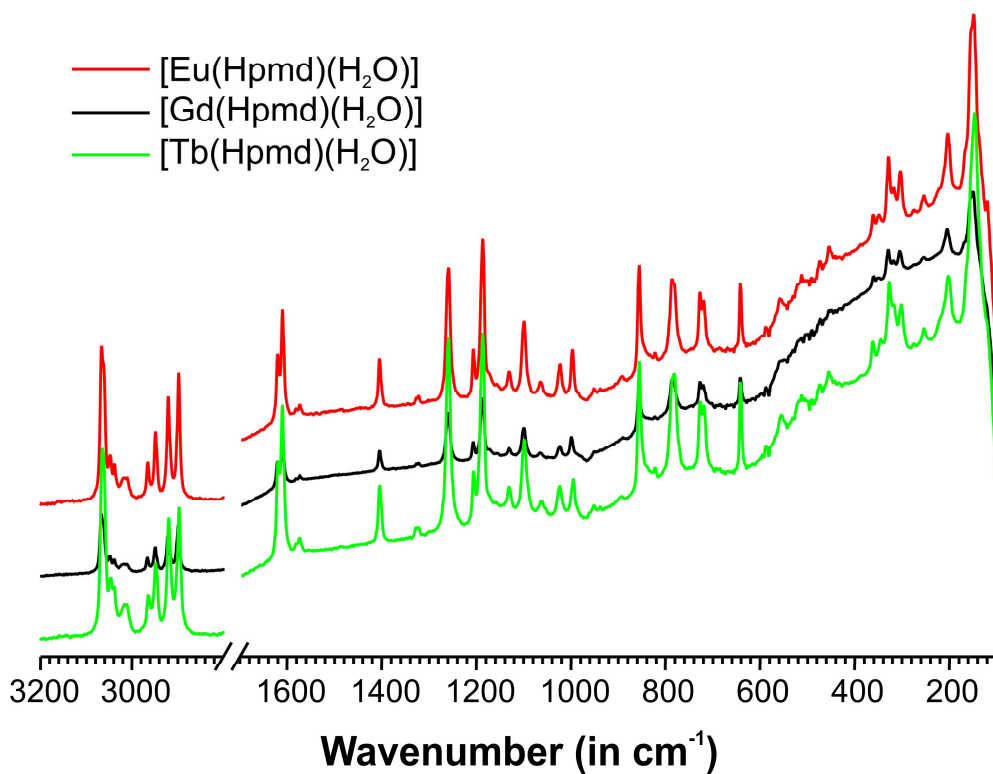


Figure A.1.3 – FT-Raman spectra (in absorbance, arbitrary units) of [LnHpmd)(H₂O)] materials. The spectra have a large fluorescence band below 2500 cm⁻¹.

Table A.1.2 - Comparison between the experimental and theoretical FT-IR bands for compound **3**.

<i>Experimental</i> ^a	<i>Calculated</i>	<i>Fragment</i> ^b	<i>Assignments</i>
363; 372	367	P	$\tau(\text{PO}_3) + \rho(\text{CH}_2)$
428 _m	410	H	$\tau(\text{PO}_3) + \rho(\text{CH}_2)$
	433	H	$\tau(\text{PO}_3) + \rho(\text{CH}_2)$
457	468	P	$\delta(\text{PO}_3) + \gamma(\text{Ph})$
469	478	H	$\delta(\text{PO}_3) + \gamma(\text{Ph})$
488	494	P	$\delta(\text{PO}_3) + \gamma(\text{Ph})$
	495	W	$\omega(\text{H}_2\text{O})$
548	531	P	$\delta(\text{PO}_3) + \gamma(\text{Ph})$
572 _m	573	P	$\delta(\text{PO}_3) + \gamma(\text{Ph})$
663	648	W	$\tau(\text{H}_2\text{O})$
737 ^c	707	H	$\gamma(\text{POH})$
718	723	P	$\gamma(\text{CH})$
752	746	H	$\gamma(\text{CH})$
799; 806	806	H	$\delta(\text{Ph})$
	839	P	$\rho(\text{CH}_2)$
822; 840	845	H	$\rho(\text{CH}_2)$
	866	H	$\rho(\text{CH}_2) + \gamma(\text{CH})$
897 _m	912	H	$\rho(\text{CH}_2) + \gamma(\text{CH})$
979 _s	959	P	$\nu(\text{PO}_3) + \nu(\text{PC})$
1014 _s ; 1025 _m	992	P	$\nu(\text{PO}_3) + \omega(\text{CH}_2)$
1078 _{vs}	1075	P	$\nu(\text{PO}_3) + \rho(\text{CH}_2)$
1097 _s	1075	H	$\nu(\text{PO}_3) + \tau(\text{CH}_2)$
1136	1116	H	$\tau(\text{CH}_2)$
1152	1146	H	$\delta(\text{POH})$
1219 _m ^c	1215	H	$\delta(\text{POH}) + \omega(\text{CH}_2)$
1203 _m	1247	H	$\delta(\text{CH}) + \omega(\text{CH}_2)$
1264	1289	H	$\delta(\text{CH}) + \omega(\text{CH}_2)$
1398	1462	H	$\delta(\text{CH}) + \tau(\text{CH}_2)$
1407	1464	P	$\delta(\text{CH}_2) + \nu(\text{Ph})$
1422	1487	P	$\delta(\text{CH}_2) + \nu(\text{Ph})$
1429	1492	H	$\delta(\text{CH}_2)$
1513	1560	H	$\nu(\text{Ph})$
1516	1564	P	$\nu(\text{Ph})$
1667	1605	W	$\delta(\text{H}_2\text{O})$
2900	3044	P	$\nu(\text{CH}_2)$
2922	3066	H	$\nu(\text{CH}_2)$
3054 _b	3438	H	$\nu(\text{POH})$
3468 _m	3606; 3791	W	$\nu(\text{H}_2\text{O})$

^a Peaks are weak unless they are assigned as *s* – strong, *b* - broad or *m* - medium.

^b P and H correspond to the phosphonate and hydrogenophosphonate ligands, respectively; W corresponds to the coordinated water.

^c Assignments based on calculated vibrational modes and comparison between deuterated and non-deuterated samples.

Table A.1.3 - Comparison between the experimental and theoretical FT-Raman bands for compound **3**.

<i>Experimental</i> ^a	<i>Calculated</i>	<i>Fragment</i> ^b	<i>Assignments</i>
318	321	P	$\gamma(\text{Ph}) + \rho(\text{PO}_3)$
329 _m	326	H	$\gamma(\text{Ph}) + \rho(\text{PO}_3)$
351	343	P	$\rho(\text{PO}_3) + \rho(\text{CH}_2)$
360	378	P	$\rho(\text{CH}_2) + \delta(\text{Ph})$
642 _m	658	H and P	$\delta(\text{Ph})$
711	713	H	$\gamma(\text{POH}) + \gamma(\text{Ph})$
720 _m	733	P	$\gamma(\text{Ph})$
727 _m	745	H	$\gamma(\text{POH}) + \gamma(\text{Ph})$
786 _m	783	P	$\gamma(\text{Ph}) + \nu(\text{PO}_3)$
	789	H	$\gamma(\text{POH}) + \gamma(\text{Ph})$
857 _s	873	P	$\delta(\text{Ph})$
	860	H	$\delta(\text{Ph})$
999	964	P	$\nu(\text{PO}_3)$
1024	991	P	$\nu(\text{PO}_3) + \gamma(\text{CH})$
1065	1075	P	$\nu(\text{PO}_3)$
1100 _m	1079	H	$\tau(\text{CH}_2)$
1131	1141 and 1153	H	$\tau(\text{CH}_2) + \delta(\text{POH})$
1186 _s	1213	H	$\omega(\text{CH}_2) + \delta(\text{POH})$
1207	1237 and 1241	H	$\delta(\text{CH}_2)$
1260 _s	1317	P	$\omega(\text{CH}_2) + \nu(\text{Ph})$
	1286	H	$\omega(\text{CH}_2) + \nu(\text{Ph})$
1405 _m	1481	P	$\delta(\text{CH}_2)$
	1491	H	$\delta(\text{CH}_2)$
1572	1605	W	$\delta(\text{H}_2\text{O})$
1581	1638	P	$\nu(\text{Ph})$
	1631	H	$\nu(\text{Ph})$
1610 _s	1677	H	$\nu(\text{Ph})$
1620	1686	P	$\nu(\text{Ph})$
2998 _m	3043	P	$\nu_s(\text{CH}_2)$
2921 _m	3066	H	$\nu_s(\text{CH}_2)$
2949	3114	P	$\nu_a(\text{CH}_2)$
2960	3127	H	$\nu_a(\text{CH}_2)$
3039	3189	P	$\nu(\text{CH})$
3048	3192	H	$\nu(\text{CH})$
3066 _s	3218	H and P	$\nu(\text{CH})$

^a Peaks are weak unless they are assigned as *s* - strong or *m* - medium.

^b P and H correspond to the phosphonate and hydrogenophosphonate ligands, respectively; W corresponds to the coordinated water. The 375-630 cm^{-1} range was affected by noise related to the fluorescence band.

A.2. Chapter 3: Lanthanum-Biphosphonate Coordination Polymers Isolated by Microwave-Assisted and One-Pot Synthesis

A.2.1. Crystallographic Details

Table A.2.1 - Selected bond lengths (in Å) and angles (in degrees) for the {LaO₉} coordination environment present in [La₂(H₂pmd)₃(H₂O)₁₂] (**4**).

La1–O5	2.404(2)
La1–O2	2.530(2)
La1–O8 ⁱ	2.549(2)
La1–O4W	2.562(3)
La1–O1W	2.573(3)
La1–O2W	2.575(3)
La1–O5W	2.597(3)
La1–O6W	2.601(2)
La1–O3W	2.730(3)
O5–La1–O2	139.86(8)
O5–La1–O8 ⁱ	141.64(8)
O2–La1–O8 ⁱ	77.57(8)
O5–La1–O4W	75.16(8)
O2–La1–O4W	81.34(8)
O8 ⁱ –La1–O4W	131.30(8)
O5–La1–O1W	109.43(8)
O2–La1–O1W	68.11(8)
O8 ⁱ –La1–O1W	71.88(8)
O4W–La1–O1W	136.86(8)
O5–La1–O2W	68.92(8)
O2–La1–O2W	131.48(8)
O8 ⁱ –La1–O2W	78.50(8)
O4W–La1–O2W	143.54(8)
O1W–La1–O2W	64.53(8)
O5–La1–O5W	71.62(9)
O2–La1–O5W	70.58(8)
O8 ⁱ –La1–O5W	136.09(8)
O4W–La1–O5W	72.94(9)
O1W–La1–O5W	68.65(8)
O2W–La1–O5W	100.69(8)
O5–La1–O6W	120.82(9)
O2–La1–O6W	77.48(8)
O8 ⁱ –La1–O6W	64.99(8)
O4W–La1–O6W	67.81(8)
O1W–La1–O6W	129.27(8)
O2W–La1–O6W	127.07(8)
O5W–La1–O6W	132.22(9)
O5–La1–O3W	72.26(8)
O2–La1–O3W	141.95(8)
O8 ⁱ –La1–O3W	78.27(8)
O4W–La1–O3W	93.19(9)
O1W–La1–O3W	129.62(8)
O2W–La1–O3W	70.44(8)
O5W–La1–O3W	143.54(8)
O6W–La1–O3W	65.77(8)

^a Symmetry operation used to generate equivalent atoms: (i) $x, y, -1+z$.

Table A.2.2 - Hydrogen bonding geometry (distances in Å and angles in degrees) for [La₂(H₂pmd)₃(H₂O)₁₂] (**4**).

D–H···A	<i>d</i> (D···A)	<(DHA)
O1–H1Z···O8 ⁱ	2.660(3)	172
O6–H6Z···O3 ^{xv}	2.598(4)	137
O7–H7Z···O4 ^{xvi}	2.575(4)	164
O1W–H1X···O3 ^{vii}	2.707(3)	161
O1W–H1Y···O2	2.858(3)	111
O1W–H1Y···O6 ^{xvii}	3.112(4)	116
O2W–H2X···O9 ^{xvi}	2.777(4)	164
O2W–H2Y···O9 ⁱ	2.723(3)	156
O3W–H3X···O7 ^{xviii}	2.974(4)	172
O3W–H3Y···O9 ^{xvi}	3.032(3)	134
O4W–H4X···O2 ^{xv}	2.891(4)	179
O4W–H4Y···O4 ⁱⁱ	2.738(4)	170
O5W–H5X···O3 ^{xv}	2.736(4)	153
O5W–H5Y···O6 ^{xvii}	3.203(4)	173
O6W–H6X···O4 ⁱⁱ	2.842(4)	153
O6W–H6Y···O3W ^{xix}	3.301(4)	172

^a Symmetry operations used to generate equivalent atoms:

(i) $x, y, -1+z$; (ii) $-1+x, y, z$; (vii) $1+x, y, z$; (xv) $-x, -y, 1-z$; (xvi) $-1+x, 1-y, 2-z$; (xvii) $1-x, -y, 1-z$; (xviii) $-x, 1-y, 2-z$; (xix) $-x, 1-y, 1-z$.

Table A.2.3 - Selected Bond Lengths (in Å) and angles (in degrees) for the {LaO₈} coordination environment present in [La₂(H₂pmd)(pmd)(H₂O)₂] (5).

La1–O4	2.334(7)
La1–O6 ^{iv}	2.368(6)
La1–O3 ⁱⁱ	2.518(6)
La1–O1	2.545(7)
La1–O1W	2.554(8)
La1–O3 ⁱⁱⁱ	2.577(6)
La1–O2 ⁱⁱⁱ	2.698(7)
La1–O2	2.715(7)
O4–La1–O6 ^{iv}	84.2(2)
O4–La1–O3 ⁱⁱ	81.4(2)
O6 ^{iv} –La1–O3 ⁱⁱⁱ	153.4(2)
O4–La1–O1	79.3(2)
O6 ^{iv} –La1–O1	87.3(2)
O3 ⁱⁱ –La1–O1	111.6(2)
O4–La1–O1W	83.7(2)
O6 ^{iv} –La1–O1W	77.2(2)
O3 ⁱⁱ –La1–O1W	79.0(2)
O1–La1–O1W	158.0(2)
O4–La1–O3 ⁱⁱⁱ	143.4(2)
O6 ^{iv} –La1–O3 ⁱⁱⁱ	112.2(2)
O3 ⁱⁱ –La1–O3 ⁱⁱⁱ	69.7(2)
O1–La1–O3 ⁱⁱⁱ	131.6(2)
O1W–La1–O3 ⁱⁱⁱ	69.5(2)
O4–La1–O2 ⁱⁱⁱ	158.3(2)
O6 ^{iv} –La1–O2 ⁱⁱⁱ	76.8(2)
O3 ⁱⁱ –La1–O2 ⁱⁱⁱ	120.2(2)
O1–La1–O2 ⁱⁱⁱ	89.3(2)
O1W–La1–O2 ⁱⁱⁱ	101.9(2)
O3 ⁱⁱⁱ –La1–O2 ⁱⁱⁱ	56.1(2)
O4–La1–O2	120.5(2)
O6 ^{iv} –La1–O2	124.7(2)
O3 ⁱⁱ –La1–O2	81.9(2)
O1–La1–O2	55.6(2)
O1W–La1–O2	146.3(2)
O3 ⁱⁱⁱ –La1–O2	77.9(2)
O2 ⁱⁱⁱ –La1–O2	64.8(2)

^a Symmetry operations used to generate equivalent atoms:

(ii) $-1+x, y, z$; (iii) $2-x, 2-y, -z$; (iv) $1-x, 1-y, -z$.

Table A.2.4 - Hydrogen bond geometry (distances in Å and angles in degrees) for [La₂(H₂pmd)(pmd)(H₂O)₂] (**5**).

D — H···A	<i>d</i> (D···A)	<(DHA)
O1W — H1X···O5 ^{xx}	2.913(10)	166
O1W — H1Y···O2 ^{xxi}	2.818(9)	155
O5 — H5Z···O1 ⁱⁱ	2.627(9)	156

^a Symmetry operations used to generate equivalent atoms:

(ii) $-1 + x, y, z$; (xx) $-x, 1-y, -z$; (xxi) $1-x, 2-y, -z$.

Table A.2.5 - Selected bond lengths (in Å) and angles (in degrees) for the {LaO₇} coordination environment present in [La(H₃pmd)(H₂pmd)(H₂O)] (6).

La1–O6 ^{vi}	2.417(18)
La1–O6 ^{vii}	2.417(18)
La1–O1	2.429(17)
La1–O4	2.462(16)
La1–O1W	2.78(3)
O6 ^{vi} –La1–O6 ^{vii}	127.8(9)
O6 ^{vi} –La1–O1	154.6(6)
O6 ^{vii} –La1–O1	77.2(6)
O1 ^v –La1–O1	78.3(9)
O6 ^{vi} –La1–O4	86.9(6)
O6 ^{vii} –La1–O4	94.6(6)
O1 ^v –La1–O4	90.5(6)
O1–La1–O4	86.8(6)
O1–La1–O4 ^v	90.4(6)
O4–La1–O4 ^v	176.5(7)
O6 ^{vi} –La1–O1W	64.7(8)
O6 ^{vii} –La1–O1W	64.1(8)
O1 ^v –La1–O1W	141.2(8)
O1–La1–O1W	138.1(8)
O4–La1–O1W	80.9(7)
O1W–La1–O1W ^v	21.7(13)

^a Symmetry operations used to generate equivalent atoms:

(v) $\frac{1}{2}-x, y, \frac{1}{2}-z$; (vi) $-\frac{1}{2}-x, y, \frac{1}{2}-z$; (vii) $1+x, y, -z$.

Table A.2.6 - Selected Bond Lengths (in Å) and angles (in degrees) for the {LaO₇} coordination environment present in [La₂(H₂pmd)₃(H₂O)₂] (7).

La1–O6 ^x	2.396(17)
La1–O7	2.398(15)
La1–O9 ^{xi}	2.418(16)
La1–O5 ^{viii}	2.503(15)
La1–O3 ^{ix}	2.505(15)
La1–O1	2.540(14)
La1–O1W	2.566(19)
O6 ^x –La1–O7	88.7(6)
O6 ^x –La1–O9 ^{xi}	124.8(6)
O7–La1–O9 ^{xi}	81.2(6)
O6 ^x –La1–O5 ^{viii}	116.0(5)
O7–La1–O5 ^{viii}	151.1(5)
O9 ^{xi} –La1–O5 ^{viii}	95.1(6)
O6 ^x –La1–O3 ^{ix}	78.1(6)
O7–La1–O3 ^{ix}	91.6(5)
O9 ^{xi} –La1–O3 ^{ix}	155.4(5)
O5 ^{viii} –La1–O3 ^{ix}	79.9(5)
O6 ^x –La1–O1	152.8(5)
O7–La1–O1	76.7(5)
O9 ^{xi} –La1–O1	76.0(5)
O5 ^{viii} –La1–O1	74.6(5)
O3 ^{ix} –La1–O1	79.5(5)
O6 ^x –La1–O1W	72.9(6)
O7–La1–O1W	125.4(6)
O9 ^{xi} –La1–O1W	69.9(5)
O5 ^{viii} –La1–O1W	78.8(6)
O3 ^{ix} –La1–O1W	131.3(5)
O1–La1–O1W	134.2(6)

^a Symmetry operations used to generate equivalent atoms:

(viii) 2-*x*, 1-*y*, 2-*z*; (ix) 2-*x*, 1-*y*, 1-*z*; (x) 1+*x*, *y*, -1+*z*; (xi) 2-*x*, -*y*, 1-*z*.

Table A.2.7 - Hydrogen bond geometry (distances in Å and angles in degrees) for [La₂(H₂pmd)₃(H₂O)₂] (7).

D — H···A	<i>d</i> (D···A)	<(DHA)
O1W — H1X···O3 ^{vii}	2.76(2)	176
O2 — H2Z···O5 ^{viii}	2.55(2)	172
O4 — H4Z···O8 ^{xxii}	2.81(2)	109
O8 — H8Z···O1	2.55(2)	172

^a Symmetry operations used to generate equivalent atoms:

(vii) 1+*x*, *y*, *z*; (viii) 2-*x*, 1-*y*, 2-*z*; (xxii) *x*, *y*, 1+*z*.

Table A.2.8 - Selected bond lengths (in Å) and angles (in degrees) for the {LaO₈} coordination environment present in [La₂(H₂pmd)(pmd)(H₂O)₄] (**8**).

La1–O1	2.60(3)
La1–O2 ^{xii}	2.62(3)
La1–O3 ^{xiii}	2.63(3)
La1–O4 ^{xiv}	2.62(3)
La1–O5 ^{xii}	2.66(3)
La1–O6	2.38(3)
La1–O1W	2.77(4)
La1–O2W	2.50(4)
O1–La1–O1W	107.9(11)
O1–La1–O2W	131.2(13)
O1–La1–O6	82.3(8)
O1–La1–O2 ^{xii}	78.7(8)
O1–La1–O5 ^{xii}	157.0(10)
O1–La1–O3 ^{xiii}	79.5(8)
O1–La1–O4 ^{xiv}	69.2(8)
O1W–La1–O2W	99.4(10)
O1W–La1–O6	132.4(12)
O1W–La1–O2 ^{xii}	65.9(10)
O1W–La1–O5 ^{xii}	74.1(10)
O1W–La1–O3 ^{xiii}	69.7(10)
O1W–La1–O4 ^{xiv}	146.7(11)
O2W–La1–O6	107.9(12)
O2 ^{xii} –La1–O2W	76.8(11)
O2W–La1–O5 ^{xii}	69.1(12)
O2W–La1–O3 ^{xiii}	149.0(13)
O2W–La1–O4 ^{xiv}	65.9(11)
O2 ^{xii} –La1–O6	157.5(10)
O5 ^{xii} –La1–O6	80.2(9)
O3 ^{xiii} –La1–O6	66.8(9)
O4 ^{xiv} –La1–O6	80.8(8)
O2 ^{xii} –La1–O5 ^{xii}	121.1(6)
O2 ^{xii} –La1–O3 ^{xiii}	120.5(11)
O2 ^{xii} –La1–O4 ^{xiv}	81.3(10)
O3 ^{xiii} –La1–O5 ^{xii}	79.9(10)
O4 ^{xiv} –La1–O5 ^{xii}	122.1(11)
O3 ^{xiii} –La1–O4 ^{xiv}	137.5(8)

^a Symmetry operations used to generate equivalent atoms:

(xii) $x, 1+y, z$; (xiii) $x, -\frac{1}{2}-y, -\frac{1}{2}+z$; (xiv) $x, -\frac{1}{2}-y, \frac{1}{2}+z$.

Table A.2.9 - Hydrogen bonding geometry (distances in Å and angles in degrees) for $[\text{La}_2(\text{H}_2\text{pmd})(\text{pmd})(\text{H}_2\text{O})_4]$ (**8**).

$\text{D}\cdots\text{A}$	$d(\text{D}\cdots\text{A})$
$\text{O3}\cdots\text{O4}^{\text{xiv}}$	2.39(4)
$\text{O1W}\cdots\text{O1}^{\text{xii}}$	2.60(4)
$\text{O1W}\cdots\text{O3}^{\text{xxi}}$	2.97(4)
$\text{O2W}\cdots\text{O5}^{\text{xiv}}$	2.60(5)
$\text{O2W}\cdots\text{O6}^{\text{xii}}$	3.02(4)

^a Symmetry operations used to generate equivalent atoms:

(xii) $x, 1+y, z$; (xiv) $x, -\frac{1}{2}-y, \frac{1}{2}+z$; (xxi) $x, \frac{1}{2}-y, -\frac{1}{2}+z$

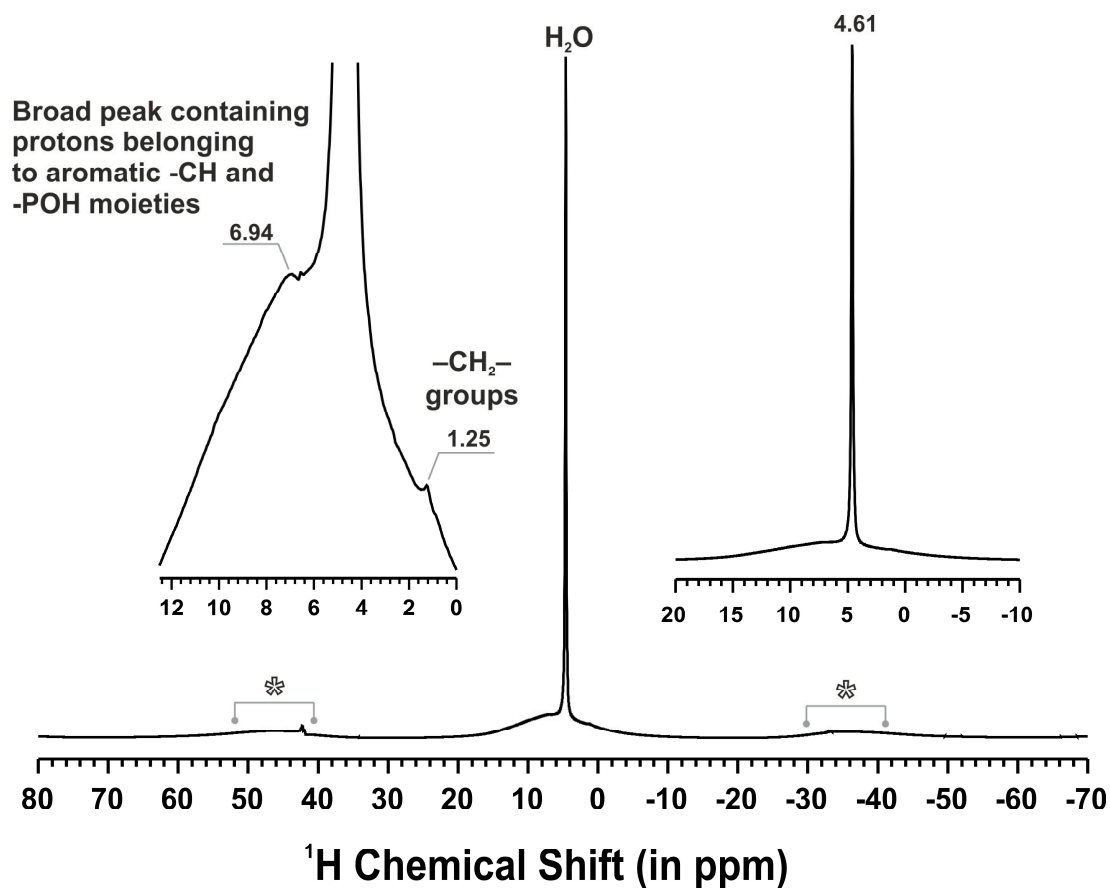


Figure A.2.1 – ^1H MAS spectrum of $[\text{La}_2(\text{H}_2\text{pmd})_3(\text{H}_2\text{O})_{12}]$ (**4**). Spinning sidebands are denoted using an asterisk.

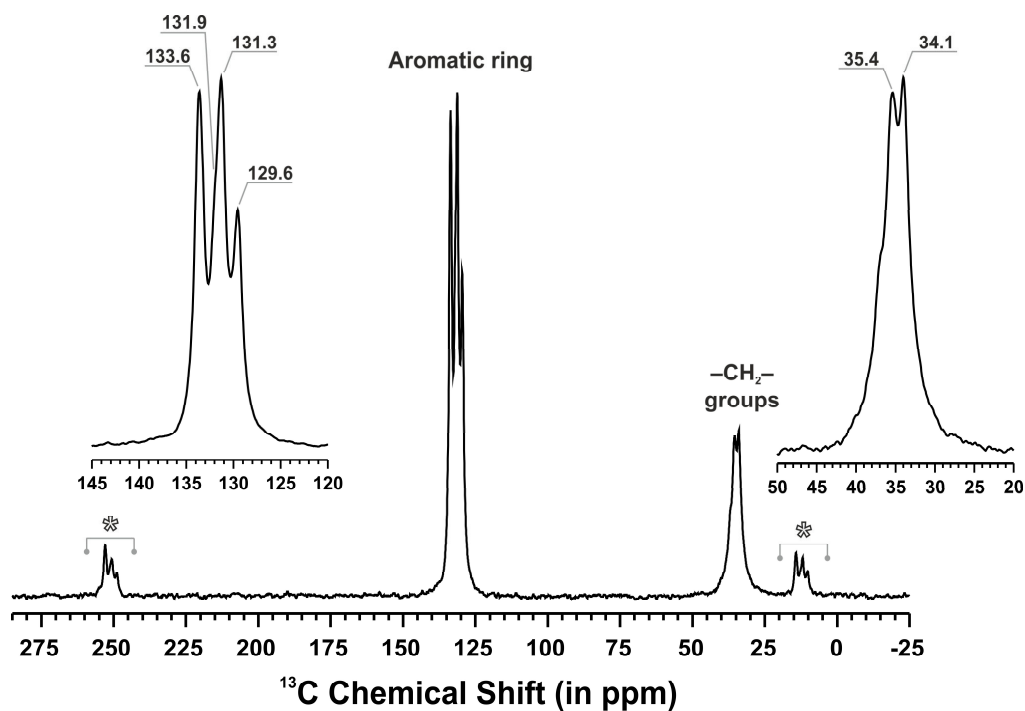


Figure A.2.2 – $^{13}\text{C}\{^1\text{H}\}$ CP MAS spectrum of $[\text{La}_2(\text{H}_2\text{pmd})_3(\text{H}_2\text{O})_{12}]$ (4). Spinning sidebands are denoted using an asterisk.

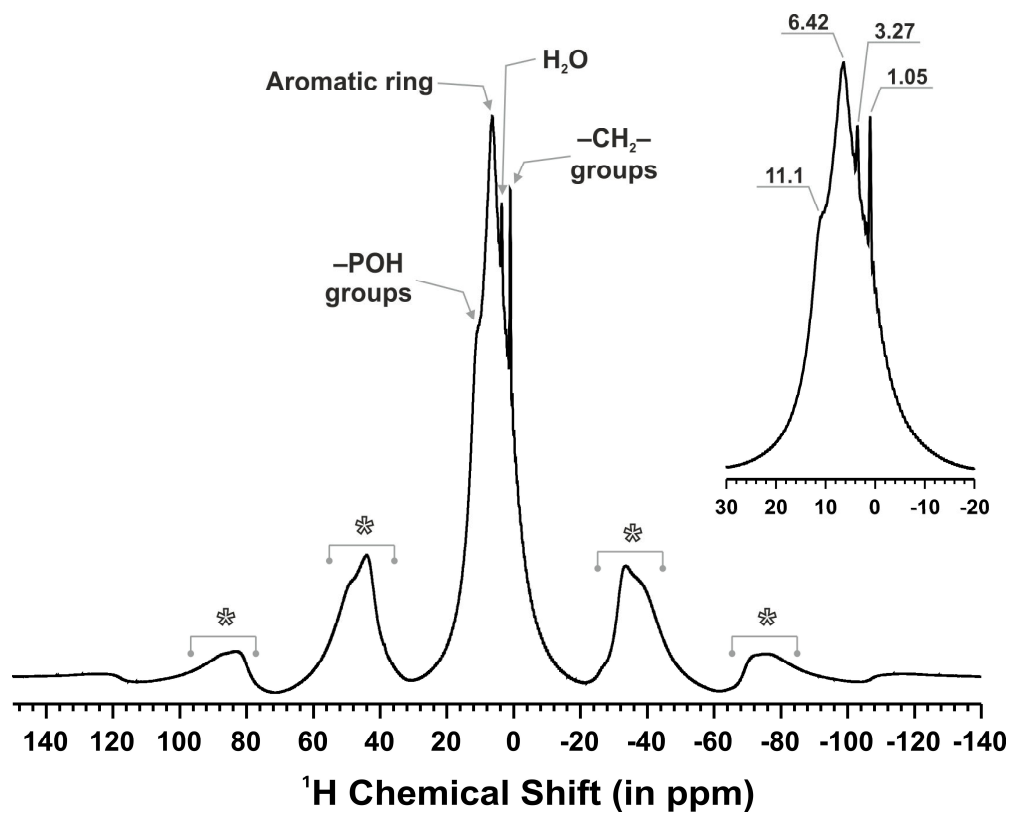


Figure A.2.3 – ^1H MAS spectrum of $[\text{La}_2(\text{H}_2\text{pmd})(\text{pmd})(\text{H}_2\text{O})_2]$ (5). Spinning sidebands are denoted using an asterisk.

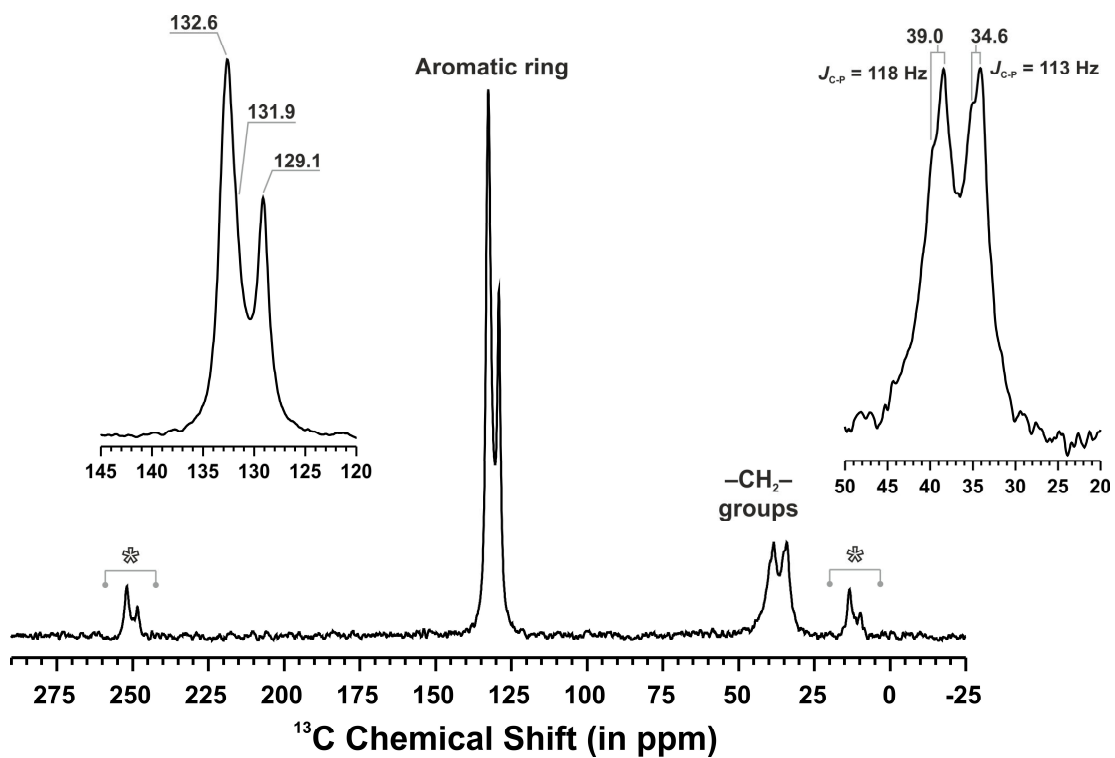


Figure A.2.4 – $^{13}\text{C}\{^1\text{H}\}$ CP MAS spectrum of $[\text{La}_2(\text{H}_2\text{pmd})(\text{pmd})(\text{H}_2\text{O})_2]$ (5). Spinning sidebands are denoted using an asterisk.

Appendix B

B.1. Chapter 4: Microwave-Assisted Synthesis of 1D Lanthanide-Organic Frameworks

B.1.1. Powder X-ray Diffraction

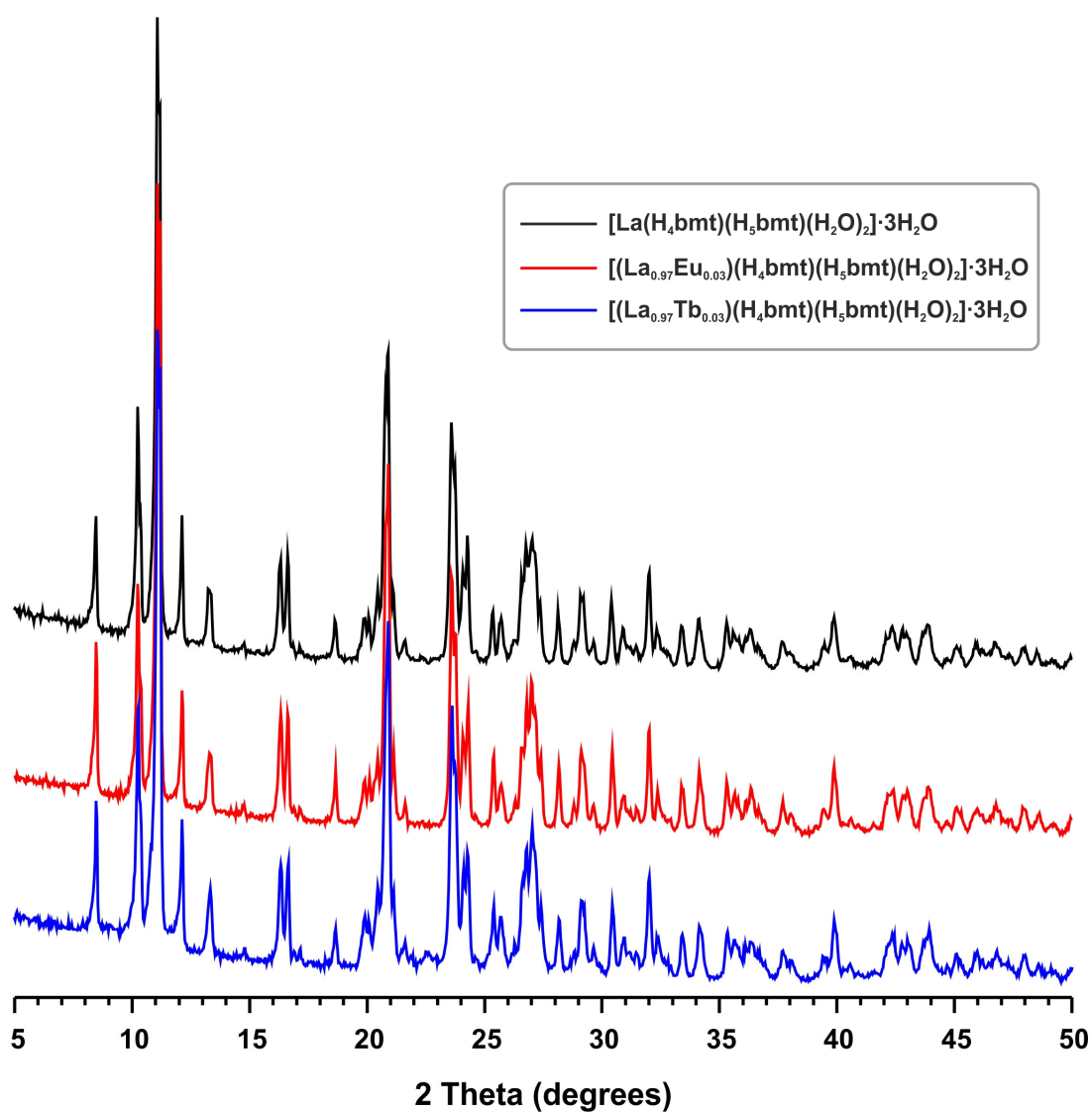


Figure B.1.1 - PXRD patterns of the isotypical $[\text{Ln}(\text{H}_4\text{bmt})(\text{H}_5\text{bmt})(\text{H}_2\text{O})_2] \cdot 3\text{H}_2\text{O}$ materials [where $\text{Ln}^{3+} = \text{La}^{3+}$ (**9**), $(\text{La}_{0.97}\text{Eu}_{0.03})^{3+}$ (**10**) and $(\text{La}_{0.97}\text{Tb}_{0.03})^{3+}$ (**11**)] isolated from microwave-assisted hydrothermal synthesis.

B.1.2. Crystallographic Details

Table B.1.1 - Bond lengths (in Å) and angles (in degrees) in the La³⁺ coordination environment present in compound [La(H₄bmt)(H₅bmt)(H₂O)₂].3H₂O (**9**).^a

La1–O1	2.406(3)	La1–O9 ⁱⁱ	2.488(3)
La1–O1 ⁱ	2.406(3)	La1–O9 ⁱⁱⁱ	2.488(3)
La1–O5 ⁱⁱ	2.437(3)	La1–O1W	2.665(5)
La1–O5 ⁱⁱⁱ	2.437(3)	La1–O2W	2.713(5)
O1–La1–O1 ⁱ	101.70(15)	O5 ⁱⁱ –La1–O9 ⁱⁱ	77.90(10)
O1–La1–O5 ⁱⁱ	82.74(11)	O5 ⁱⁱ –La1–O9 ⁱⁱⁱ	119.72(11)
O1 ⁱ –La1–O5 ⁱⁱ	140.84(11)	O5 ⁱⁱⁱ –La1–O9 ⁱⁱ	119.72(11)
O1–La1–O5 ⁱⁱⁱ	140.84(11)	O5 ⁱⁱⁱ –La1–O9 ⁱⁱⁱ	77.90(10)
O1 ⁱ –La1–O5 ⁱⁱⁱ	82.74(11)	O5 ⁱⁱ –La1–O1W	73.30(12)
O1–La1–O9 ⁱⁱ	80.73(11)	O5 ⁱⁱⁱ –La1–O1W	73.30(12)
O1–La1–O9 ⁱⁱⁱ	141.23(11)	O5 ⁱⁱ –La1–O2W	143.97(8)
O1 ⁱ –La1–O9 ⁱⁱ	141.23(11)	O5 ⁱⁱⁱ –La1–O2W	143.97(8)
O1 ⁱ –La1–O9 ⁱⁱ	141.23(11)	O9 ⁱⁱ –La1–O9 ⁱⁱⁱ	74.68(14)
O1 ⁱ –La1–O9 ⁱⁱⁱ	80.73(11)	O9 ⁱⁱ –La1–O1W	141.95(7)
O1–La1–O1W	71.52(10)	O9 ⁱⁱⁱ –La1–O1W	141.95(7)
O1–La1–O2W	69.96(10)	O9 ⁱⁱ –La1–O2W	74.93(11)
O1 ⁱ –La1–O1W	71.52(10)	O9 ⁱⁱⁱ –La1–O2W	74.93(11)
O1 ⁱ –La1–O2W	69.96(10)	O1W–La1–O2W	116.99(15)
O5 ⁱⁱ –La1–O5 ⁱⁱⁱ	71.11(15)		

^a Symmetry transformations used to generate equivalent atoms: :

(i) $x, 1.5-y, z$; (ii) $-x, 1-y, -z$; (iii) $-x, \frac{1}{2}+y, -z$.

B.1.3. Thermogravimetry

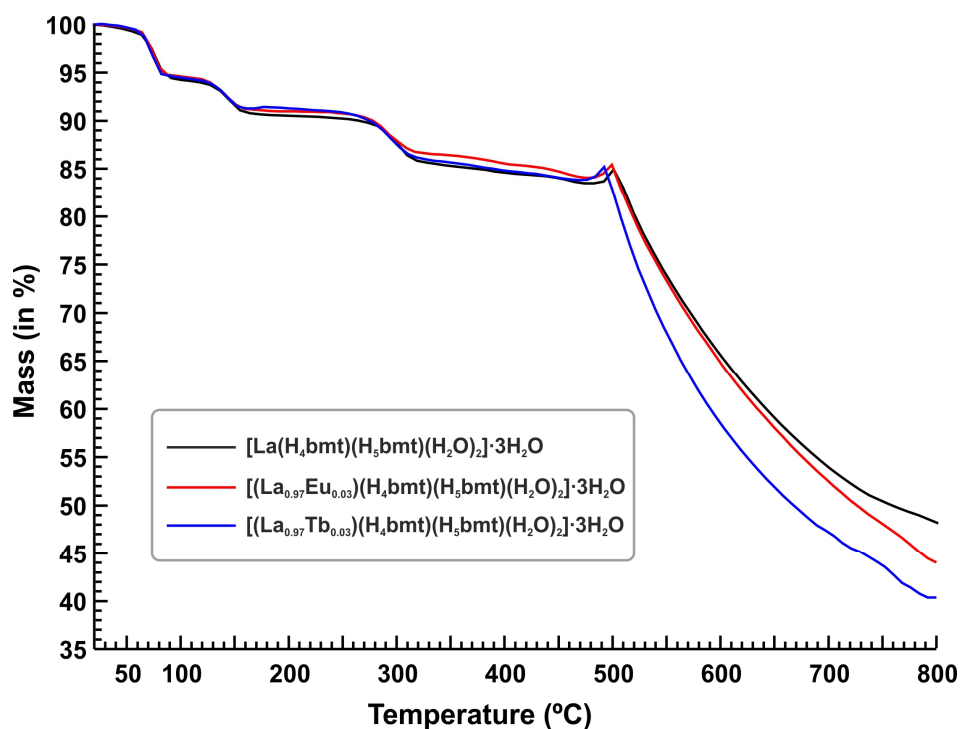


Figure B.1.2 - Thermograms for the $[\text{Ln}(\text{H}_4\text{bmt})(\text{H}_5\text{bmt})(\text{H}_2\text{O})_2] \cdot 3\text{H}_2\text{O}$ materials [where $\text{Ln}^{3+} = \text{La}^{3+}$ (**9**), $(\text{La}_{0.97}\text{Eu}_{0.03})^{3+}$ (**10**) and $(\text{La}_{0.97}\text{Tb}_{0.03})^{3+}$ (**11**)].

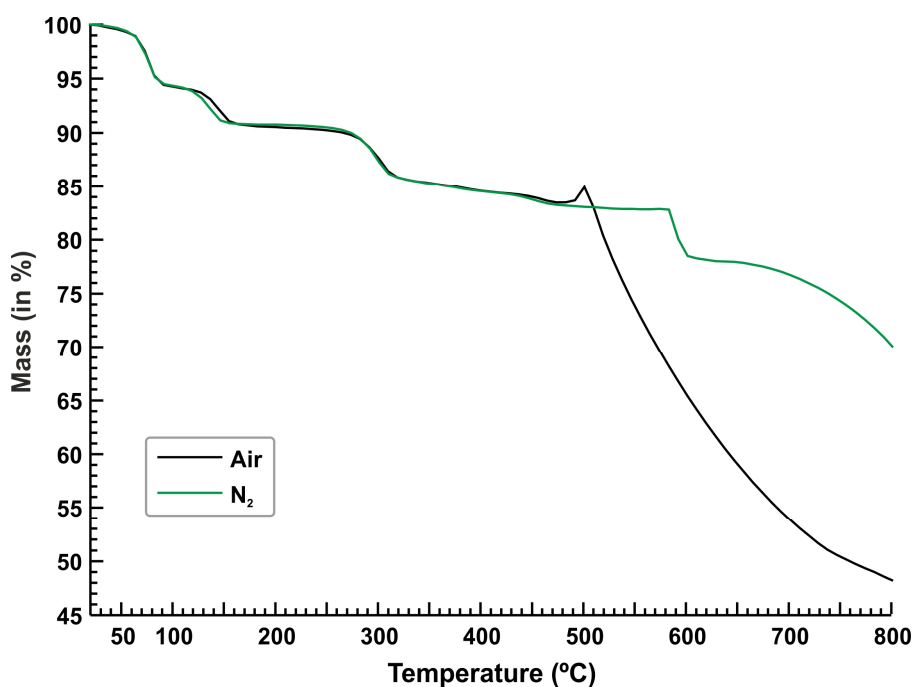


Figure B.1.3 - Thermograms of $[\text{La}(\text{H}_4\text{bmt})(\text{H}_5\text{bmt})(\text{H}_2\text{O})_2] \cdot 3\text{H}_2\text{O}$ (**9**) collected in air (black) and N_2 (green).

B.1.4. Solid-State NMR

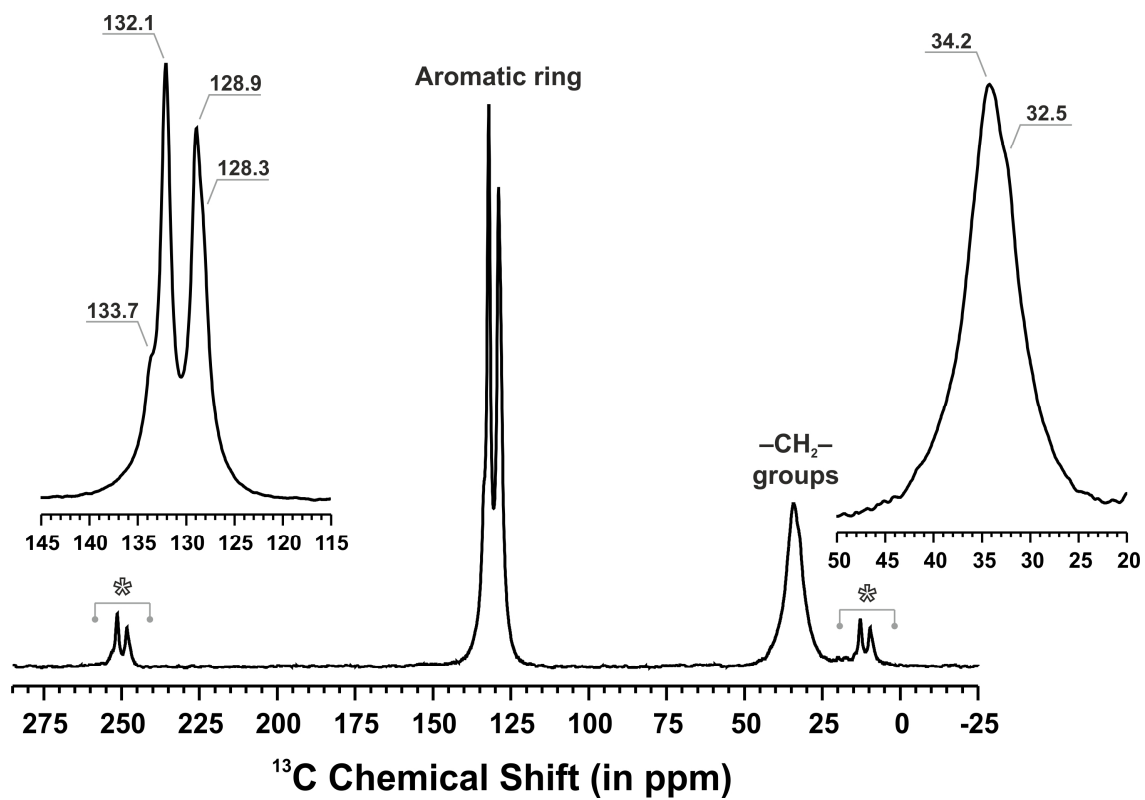


Figure B.1.4 - $^{13}\text{C}\{^1\text{H}\}$ CP MAS spectrum of $[\text{La}(\text{H}_4\text{bmt})(\text{H}_5\text{bmt})(\text{H}_2\text{O})_2]\cdot 3\text{H}_2\text{O}$ (**9**). Spinning sidebands are denoted using an asterisk.

B.2. Chapter 4: Hydrothermal Synthesis of Layered 2D Lanthanide-Organic Frameworks

B.2.1. Thermogravimetry

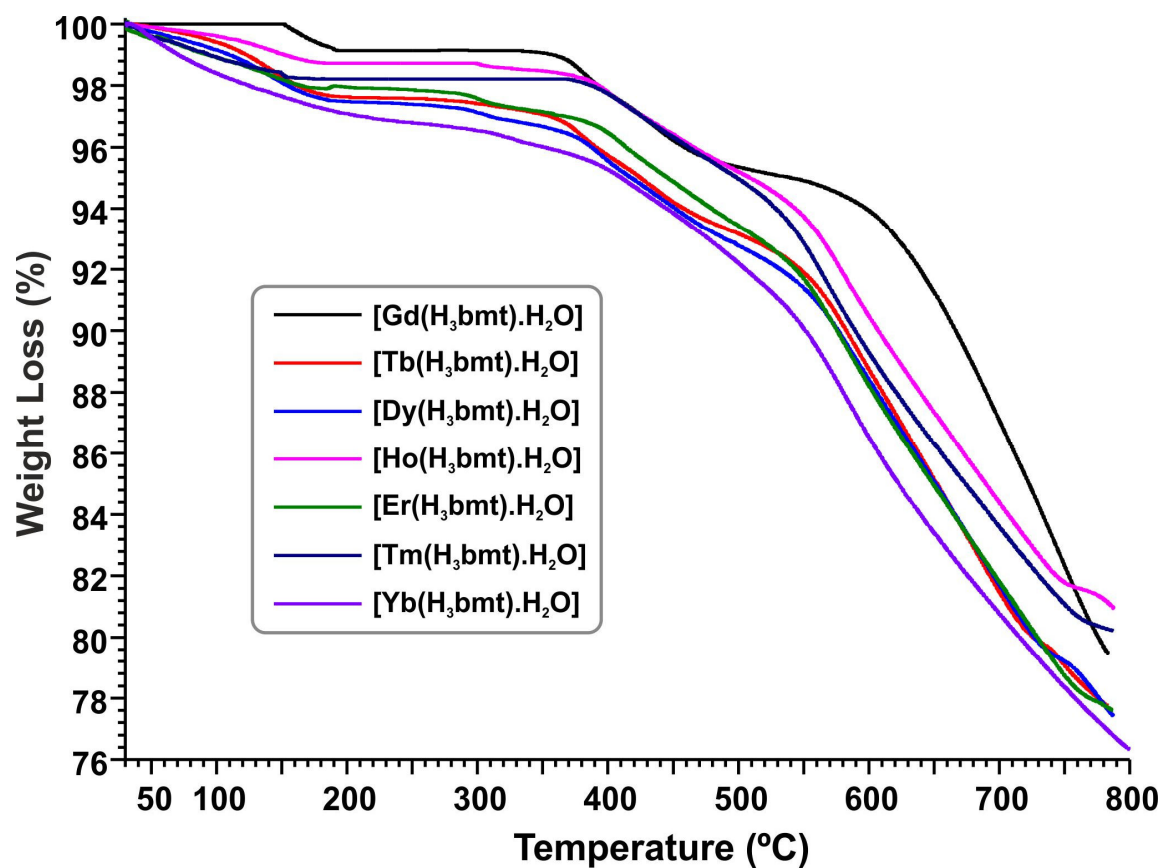


Figure B.2.1 – Thermograms of the $[\text{Ln}_2(\text{H}_3\text{bmt})_2]\cdot\text{H}_2\text{O}$ materials [where $\text{Ln}^{3+} = \text{Gd}^{3+}$ (13), Tb^{3+} (14), Dy^{3+} (15), Ho^{3+} (16), Er^{3+} (17), Tm^{3+} (18) and Yb^{3+} (19)].

B.2.3. FT-IR Spectroscopic Studies

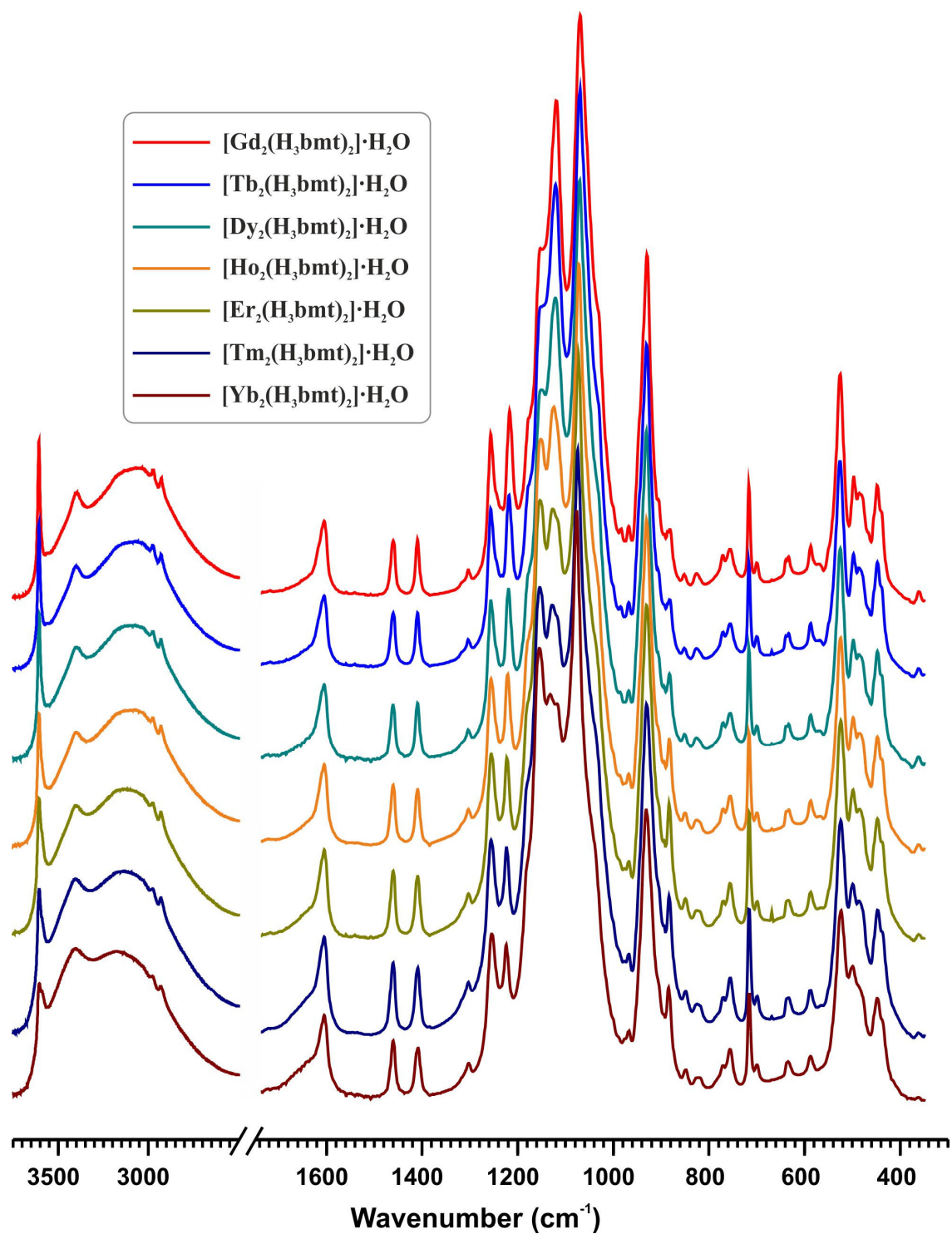


Figure B.2.2 – FT-IR spectra of the $[\text{Ln}_2(\text{H}_3\text{bmt})_2] \cdot \text{H}_2\text{O}$ materials [where $\text{Ln}^{3+} = \text{Gd}^{3+}$ (13), Tb^{3+} (14), Dy^{3+} (15), Ho^{3+} (16), Er^{3+} (17), Tm^{3+} (18) and Yb^{3+} (19)].

B.3. Chapter 4: Conventional Hydrothermal Synthesis of 3D Lanthanide-Organic Frameworks

B.3.1. Crystallographic Details

Table B.3.1 - Bond lengths (in Å) for the La³⁺ coordination environments present in [La₂(H₃bmt)₂(H₂O)₂] \cdot H₂O (**20**) and [La(H₃bmt)] (**20-dehyd**).^a

	La ³⁺ (20)	La ³⁺ (20-dehyd)
La1–O1	2.4660(19)	2.3933(14)
La1–O3 ⁱⁱ	2.417(2)	2.3720(14)
La1–O4 ^{iv}	2.5628(17)	2.4863(13)
La1–O4 ^v	2.6908(17)	2.6459(12)
La1–O5 ⁱⁱⁱ	2.4990(18)	2.4555(13)
La1–O5 ^v	2.6029(16)	2.6012(12)
La1–O8 ⁱ	2.3365(18)	2.3293(14)
La1–O1W	2.559(6)	—
La1–O2W	2.617(6)	—

^a Symmetry transformations used to generate equivalent atoms: (i) $-\frac{1}{2}+x, -\frac{1}{2}+y, z$; (ii) $\frac{1}{2}-x, -\frac{1}{2}+y, \frac{1}{2}-z$; (iii) $\frac{1}{2}-x, 2.5-y, -z$; (iv) $\frac{1}{2}-x, 1.5-y, -z$; (v) $x, 2-y, \frac{1}{2}+z$.

Table B.3.2 - Bond angles (in degrees) for the La³⁺ coordination environments present in [La₂(H₃bmt)₂(H₂O)₂·H₂O (**20**) and [La(H₃bmt)] (**20-dehyd**).^a

	20	20-dehyd		20
O1–La1–O4 ^{iv}	76.16(6)	86.57(5)	O1–La1–O1W	151.44(13)
O1–La1–O4 ^v	84.29(6)	84.64(5)	O1–La1–O2W	145.38(14)
O1–La1–O5 ⁱⁱⁱ	82.18(6)	84.59(5)	O3 ⁱⁱ –La1–O1W	63.09(14)
O1–La1–O5 ^v	75.44(6)	77.62(5)	O3 ⁱⁱ –La1–O2W	62.82(15)
O3 ⁱⁱ –La1–O1	144.45(7)	156.00(5)	O4 ^{iv} –La1–O2W	137.62(14)
O3 ⁱⁱ –La1–O4 ^{iv}	75.90(6)	81.81(5)	O5 ⁱⁱⁱ –La1–O1W	69.26(13)
O3 ⁱⁱ –La1–O4 ^v	94.57(7)	85.68(5)	O5 ⁱⁱⁱ –La1–O2W	68.09(15)
O3 ⁱⁱ –La1–O5 ⁱⁱⁱ	130.84(6)	112.73(5)	O5 ^v –La1–O2W	105.32(16)
O3 ⁱⁱ –La1–O5 ^v	74.86(7)	78.77(5)	O8 ⁱ –La1–O1W	77.46(13)
O4 ^{iv} –La1–O4 ^v	125.71(4)	126.91(3)	O8 ⁱ –La1–O2W	93.70(16)
O4 ^{iv} –La1–O5 ^v	70.64(5)	71.16(4)	O1W–La1–O4 ^{iv}	130.36(13)
O5 ⁱⁱⁱ –La1–O4 ^{iv}	150.85(6)	159.24(4)	O1W–La1–O4 ^v	85.94(12)
O5 ⁱⁱⁱ –La1–O4 ^v	70.16(5)	70.87(4)	O1W–La1–O5 ^v	119.67(13)
O5 ^v –La1–O4 ^v	55.44(5)	55.80(4)	O1W–La1–O2W	16.83(15)
O5 ⁱⁱⁱ –La1–O5 ^v	122.36(4)	124.73(3)	O2W–La1–O4 ^v	69.53(14)
O8 ⁱ –La1–O1	97.23(7)	106.74(5)		
O8 ⁱ –La1–O3 ⁱⁱ	101.99(8)	93.65(6)		
O8 ⁱ –La1–O4 ^{iv}	85.42(6)	87.29(5)		
O8 ⁱ –La1–O4 ^v	147.77(6)	145.09(5)		
O8 ⁱ –La1–O5 ⁱⁱⁱ	78.13(6)	77.37(5)		
O8 ⁱ –La1–O5 ^v	155.97(6)	157.89(4)		

^a Symmetry transformations used to generate equivalent atoms: (i) $-\frac{1}{2}+x, -\frac{1}{2}+y, z$; (ii) $\frac{1}{2}-x, -\frac{1}{2}+y, \frac{1}{2}-z$; (iii) $\frac{1}{2}-x, 2.5-y, -z$; (iv) $\frac{1}{2}-x, 1.5-y, -z$; (v) $x, 2-y, \frac{1}{2}+z$.

Table B.3.3 - Geometrical details (distances in Å and angles in degrees) of the hydrogen bonds present in $[\text{La}_2(\text{H}_3\text{bmt})_2(\text{H}_2\text{O})_2]\cdot\text{H}_2\text{O}$ (**20**) and $[\text{La}(\text{H}_3\text{bmt})]$ (**20-dehyd**).^a

D–H···A	$d(\text{D}\cdots\text{A})$	$\angle(\text{DHA})$
20		
O1W–H2X···O2 ^{vi}	2.866(6)	158
O2W–H1X···O2 ^{vi}	2.800(7)	147
O2–H2···O3W	2.559(5)	155
O2–H2···O3W ^{vii}	3.136(6)	128
O6–H6···O9 ^{viii}	2.571(3)	158
O7–H7···O9 ^{viii}	2.594(3)	169
20-dehyd		
O2–H2···O6 ^{ix}	2.815(2)	177
O6–H6···O9 ^{viii}	2.4906(18)	155
O7–H7···O9 ^{viii}	2.5903(19)	168

^a Symmetry transformations used to generate equivalent atoms:
(vi) $\frac{1}{2}-x, \frac{1}{2}+y, \frac{1}{2}-z$; (vii) $1-x, y, \frac{1}{2}-z$; (viii) $1-x, 2-y, -z$; (ix) $x, 2-y, \frac{1}{2}+z$.

B.3.2. Thermogravimetry

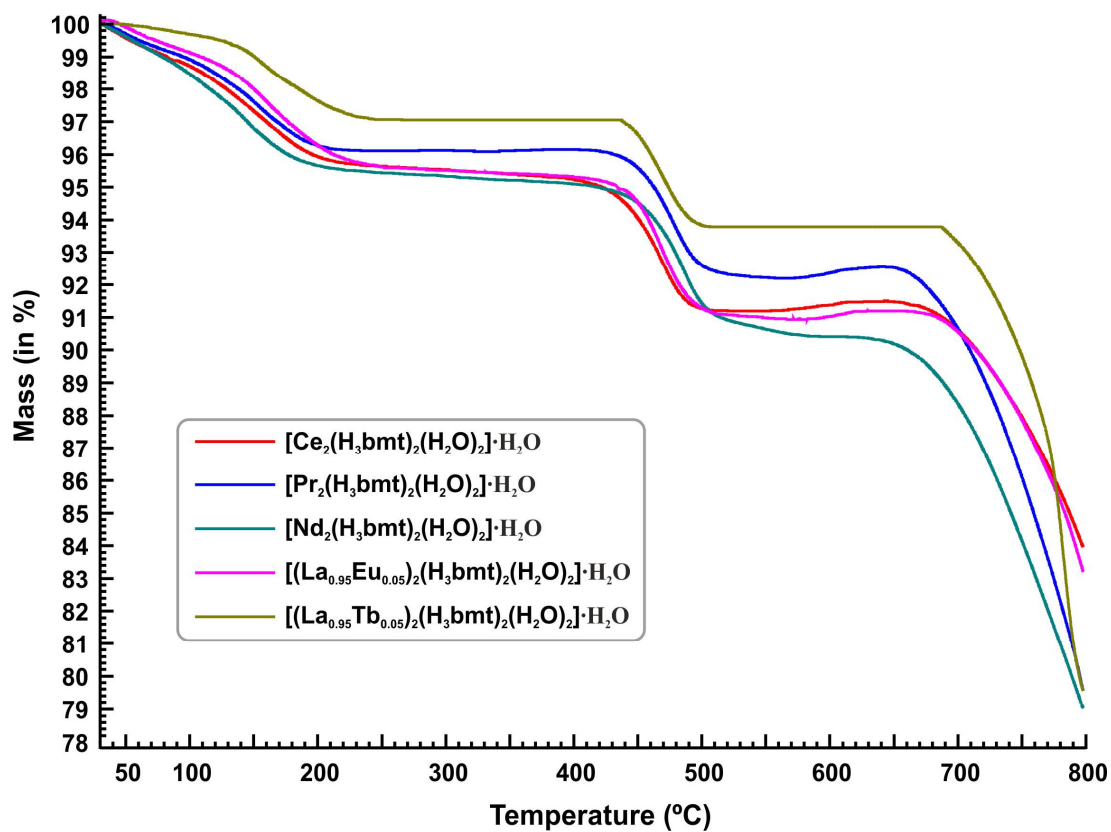


Figure B.3.1 - Thermograms of the $[\text{Ln}_2(\text{H}_3\text{bmt})_2(\text{H}_2\text{O})_2] \cdot \text{H}_2\text{O}$ materials [where $\text{Ln}^{3+} = \text{Ce}^{3+}$ (21), Pr^{3+} (22), Nd^{3+} (23), $(\text{La}_{0.95}\text{Eu}_{0.05})^{3+}$ (24) and $(\text{La}_{0.95}\text{Tb}_{0.05})^{3+}$ (25)].

B.3.3. Solid-State NMR

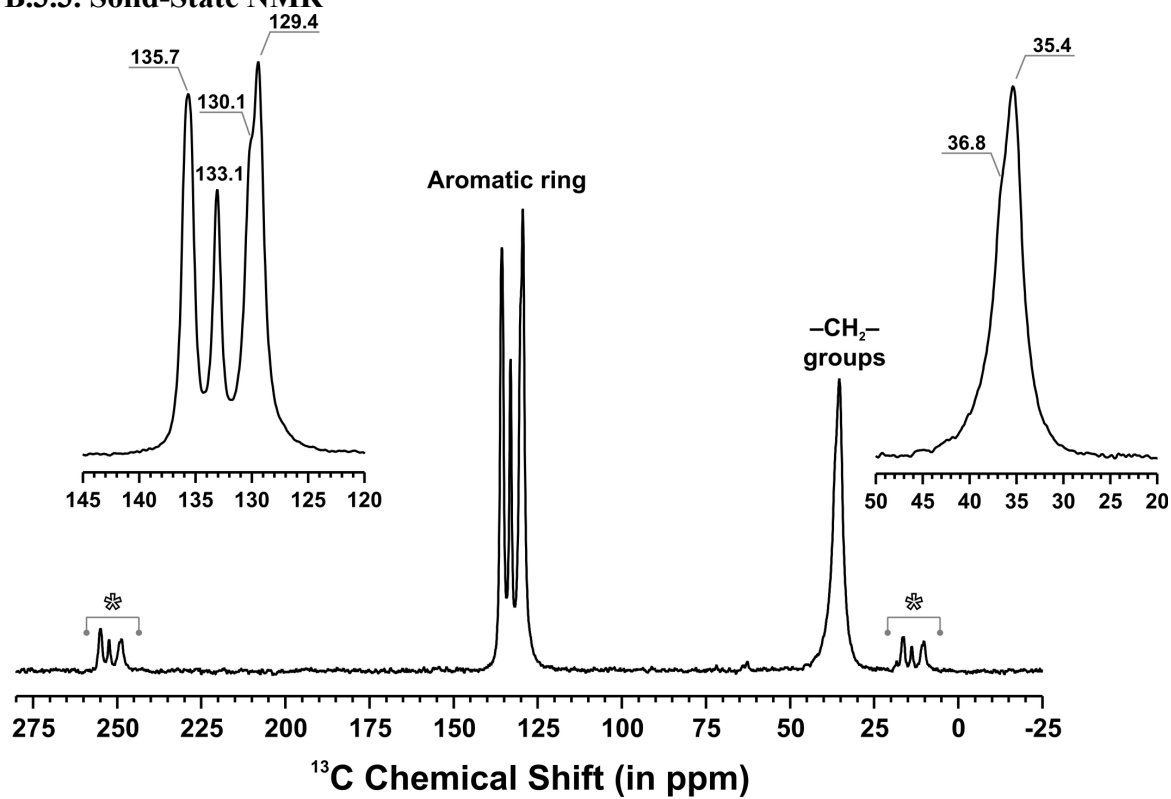


Figure B.3.2 - $^{13}\text{C}\{^1\text{H}\}$ CP MAS spectrum of $[\text{La}_2(\text{H}_3\text{bmt})_2(\text{H}_2\text{O})_2]\cdot\text{H}_2\text{O}$ (**20**). Spinning sidebands are depicted by an asterisk.

B.3.4. FT-IR Spectroscopic Studies

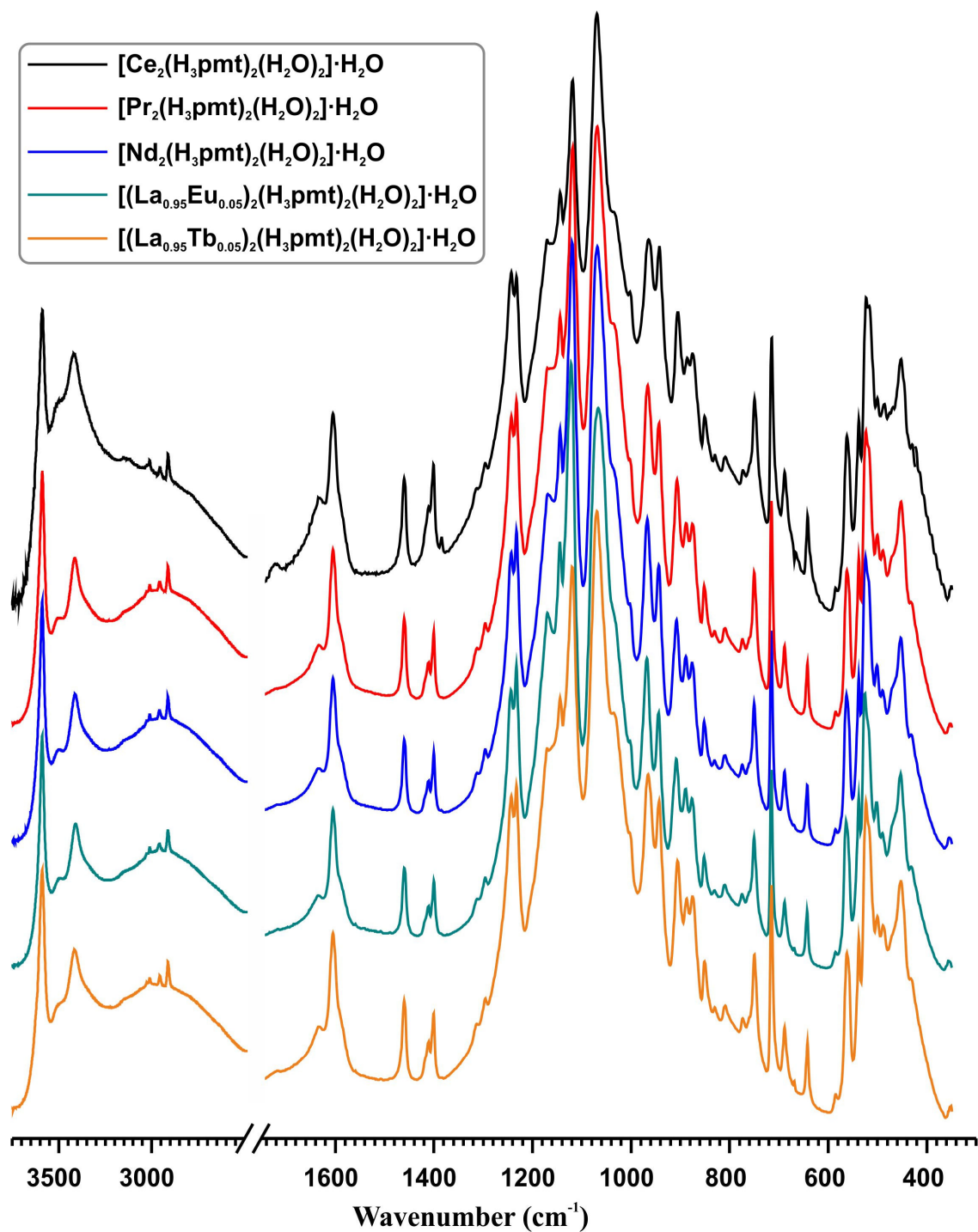


Figure B.3.3 – FT-IR spectra of the $[\text{Ln}_2(\text{H}_3\text{bmt})_2(\text{H}_2\text{O})_2]\cdot\text{H}_2\text{O}$ materials [where $\text{Ln}^{3+} = \text{Ce}^{3+}$ (21), Pr^{3+} (22), Nd^{3+} (23), $(\text{La}_{0.95}\text{Eu}_{0.05})^{3+}$ (24) and $(\text{La}_{0.95}\text{Tb}_{0.05})^{3+}$ (25)].

B.3.5. Photoluminescence

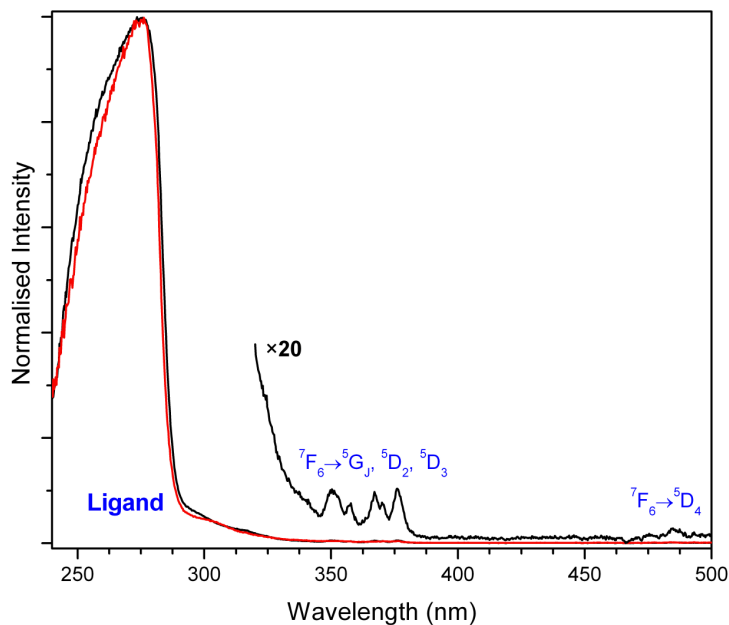


Figure B.3.4 - Excitation spectra of $[(\text{La}_{0.95}\text{Tb}_{0.05})_2(\text{H}_3\text{bmt})_2(\text{H}_2\text{O})_2]\cdot\text{H}_2\text{O}$ (**25**) (black line) and $[(\text{La}_{0.95}\text{Tb}_{0.05})(\text{H}_3\text{bmt})]$ (**25-dehyd**) (red line) at 298 K while monitoring the Tb^{3+} emission at 542 nm.

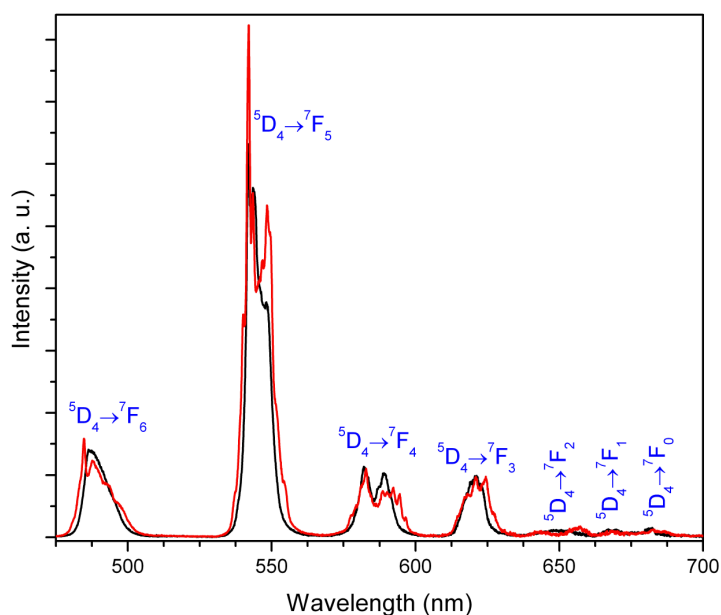


Figure B.3.5 - Ambient temperature (298 K) emission spectra of $[(\text{La}_{0.95}\text{Tb}_{0.05})_2(\text{H}_3\text{bmt})_2(\text{H}_2\text{O})_2]\cdot\text{H}_2\text{O}$ (**25**) and $[(\text{La}_{0.95}\text{Tb}_{0.05})(\text{H}_3\text{bmt})]$ (**25-dehyd**) with excitation at 280 nm: black line, **25** at ambient pressure; red line, **25** after dehydration (**25-dehyd**) at 450 K under a vacuum of 5×10^{-6} mbar.

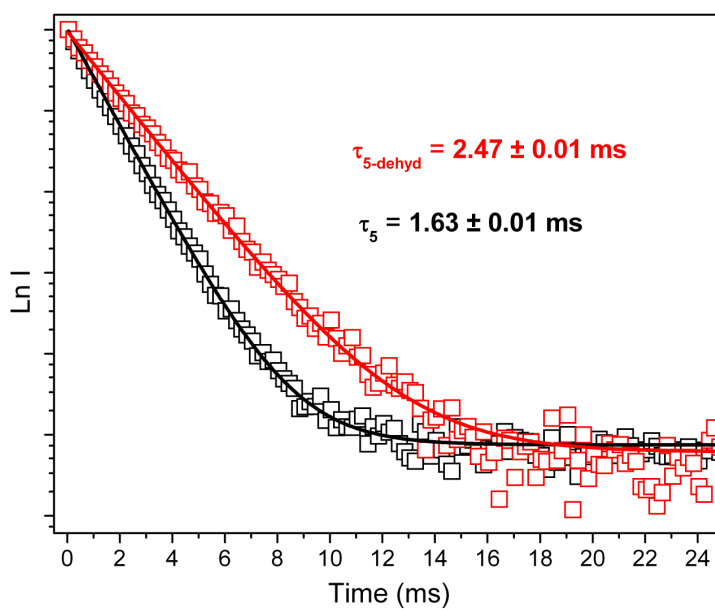


Figure B.3.6 - $^5\text{D}_4$ decay curves of $[(\text{La}_{0.95}\text{Tb}_{0.05})_2(\text{H}_3\text{bmt})_2(\text{H}_2\text{O})_2]\cdot\text{H}_2\text{O}$ (**25**) (black) and $[(\text{La}_{0.95}\text{Tb}_{0.05})(\text{H}_3\text{bmt})]$ (**25-dehyd**) (red) acquired at 298 K while monitoring the emission at 542 nm. Data points were fitted using single exponential decay functions. The excitation was performed at 280 nm.

Appendix C

C.1. Chapter 5: Layered Lanthanide-Organic Frameworks Based on ((2,4,6-Trifluorobenzene-1,3,5-triyl)tris-(methylene))triphosphonic acid

C.1.1. Crystallographic Details

Table C.1.1 - Bond lengths (in Å) and angles (in degrees) for the two crystallographically independent La³⁺ coordination environments present in [La(H₃tftp)(H₂O)] (**26**).^a

La1–O14	2.361(6)	La2–O9 ⁱⁱⁱ	2.374(6)
La1–O8	2.370(6)	La2–O13	2.371(6)
La1–O16 ⁱ	2.443(6)	La2–O1 ^{iv}	2.444(6)
La1–O6	2.458(6)	La2–O12	2.465(6)
La1–O10 ⁱⁱ	2.499(6)	La2–O4	2.505(6)
La1–O18 ⁱⁱ	2.595(7)	La2–O3	2.575(7)
La1–O1W	2.593(6)	La2–O2W	2.591(6)
O14–La1–O8	122.8(2)	O13–La2–O9 ⁱⁱⁱ	122.4(2)
O14–La1–O16 ⁱ	139.4(2)	O13–La2–O1 ^{iv}	86.3(2)
O8–La1–O16 ⁱ	85.7(2)	O9 ⁱⁱⁱ –La2–O1 ^{iv}	139.3(2)
O14–La1–O6	75.7(2)	O13–La2–O12	74.7(2)
O8–La1–O6	74.7(2)	O9 ⁱⁱⁱ –La2–O12	76.1(2)
O16 ⁱ –La1–O6	86.7(2)	O1 ^{iv} –La2–O12	86.3(2)
O14–La1–O10 ⁱⁱ	75.3(2)	O13–La2–O4	73.3(2)
O8–La1–O10 ⁱⁱ	74.1(2)	O9 ⁱⁱⁱ –La2–O4	75.3(2)
O16 ⁱ –La1–O10 ⁱⁱ	144.7(2)	O1 ^{iv} –La2–O4	144.8(2)
O6–La1–O10 ⁱⁱ	114.4(2)	O12–La2–O4	114.3(2)
O14–La1–O1W	128.4(2)	O13–La2–O3	161.5(2)
O8–La1–O1W	88.8(2)	O9 ⁱⁱⁱ –La2–O3	75.8(2)
O16 ⁱ –La1–O1W	74.4(2)	O1 ^{iv} –La2–O3	79.8(2)
O6–La1–O1W	155.9(2)	O12–La2–O3	116.1(2)
O10 ⁱⁱ –La1–O1W	76.4(2)	O4–La2–O3	112.1(2)
O14–La1–O18 ⁱⁱ	75.5(2)	O13–La2–O2W	88.4(2)
O8–La1–O18 ⁱⁱ	161.4(2)	O9 ⁱⁱⁱ –La2–O2W	128.3(2)
O16 ⁱ –La1–O18 ⁱⁱ	80.6(2)	O1 ^{iv} –La2–O2W	74.9(2)
O6–La1–O18 ⁱⁱ	116.8(2)	O12–La2–O2W	155.5(2)
O10 ⁱⁱ –La1–O18 ⁱⁱ	110.7(2)	O4–La2–O2W	76.1(2)

O1W–La1–O18ⁱⁱ

75.4(2)

O3–La2–O2W

76.3(2)

^a Symmetry transformations used to generate equivalent atoms:(i) $-x, 2-y, 2-z$; (ii) $-1+x, y, z$; (iii) $1+x, y, z$; (iv) $-x, 2-y, 1-z$.**Table C.1.2** - Hydrogen bonding geometric details (distances in Å and angles in degrees) for the interactions present in [La(H₃tftp)(H₂O)] (**26**).^a

D–H···A	<i>d</i>(D···A)	<(DHA)
O1W–H1X···O16 ⁱⁱ	2.931(9)	155
O1W–H1X···O15 ⁱⁱ	3.114(9)	113
O1W–H1Y···O12 ⁱⁱ	3.054(10)	129
O1W–H1Y···O13 ⁱⁱ	3.132(9)	146
O2W–H2X···O1	2.960(9)	146
O2W–H2X···O7	3.109(8)	120
O2W–H2Y···O6	3.049(9)	132
O2W–H2Y···O8	3.154(9)	143
O2–H2···O10 ^v	2.682(9)	154
O5–H5···O18 ^{vi}	2.578(9)	152
O7–H7···O11 ^{iv}	2.687(9)	164
O11–H11···O3 ^v	2.568(9)	153
O15–H15···O5 ⁱ	2.692(9)	161
O17–H17···O4 ^{vi}	2.666(8)	159

^a Symmetry transformations used to generate equivalent atoms:(i) $-x, 2-y, 2-z$; (ii) $-1+x, y, z$; (iv) $-x, 2-y, 1-z$;(v) $1-x, 2-y, 1-z$; (vi) $1-x, 2-y, 2-z$.

C.1.2 - Chapter 5: Thermogravimetry

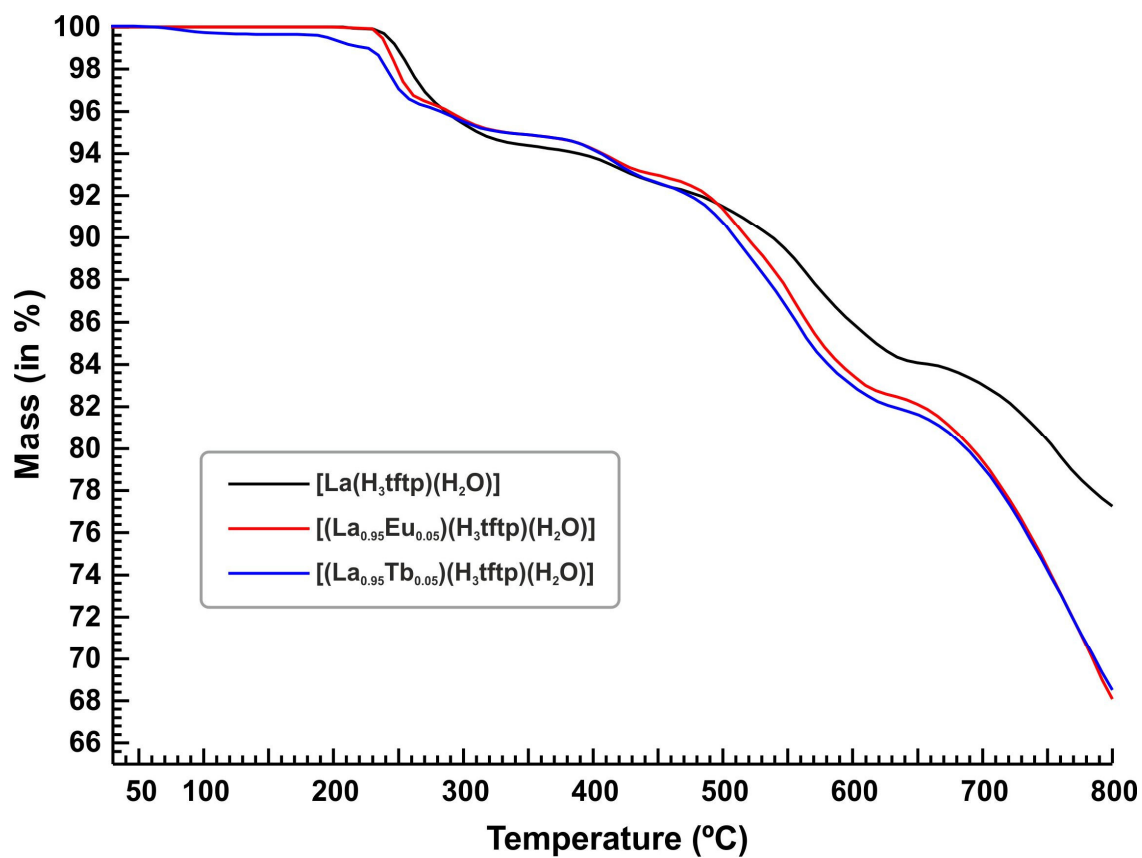


Figure C.1.1 - Thermogravimetric curves of the isotypical materials 26, 27 and 28.

C.1.3 - Chapter 5: Solid-State NMR

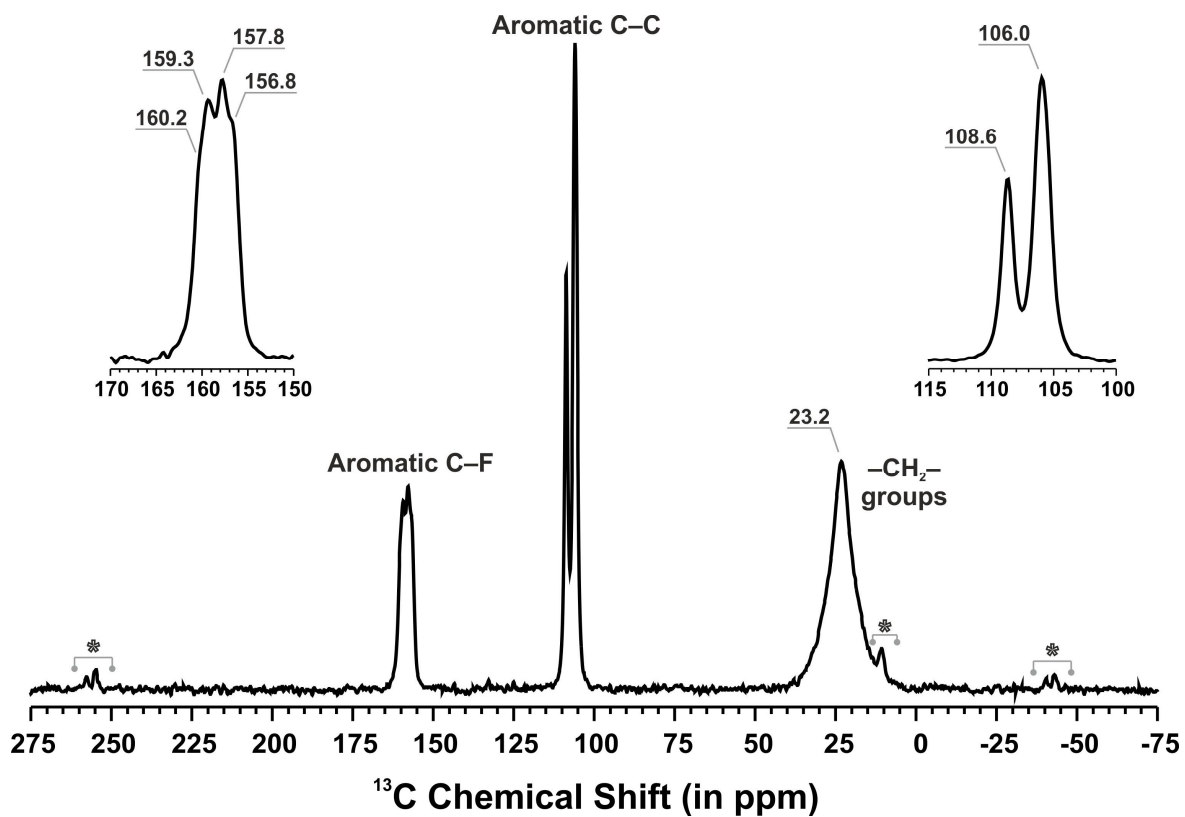


Figure C.1.2 - $^{13}\text{C}\{^1\text{H}\}$ CP MAS spectrum of compound 26. Spinning sidebands are denoted using an asterisk.

Appendix D

D.1. Chapter 6: Porous Yttrium-Triphosphonate MOF: Synthesis and Properties

D.1.1. Adsorption Properties

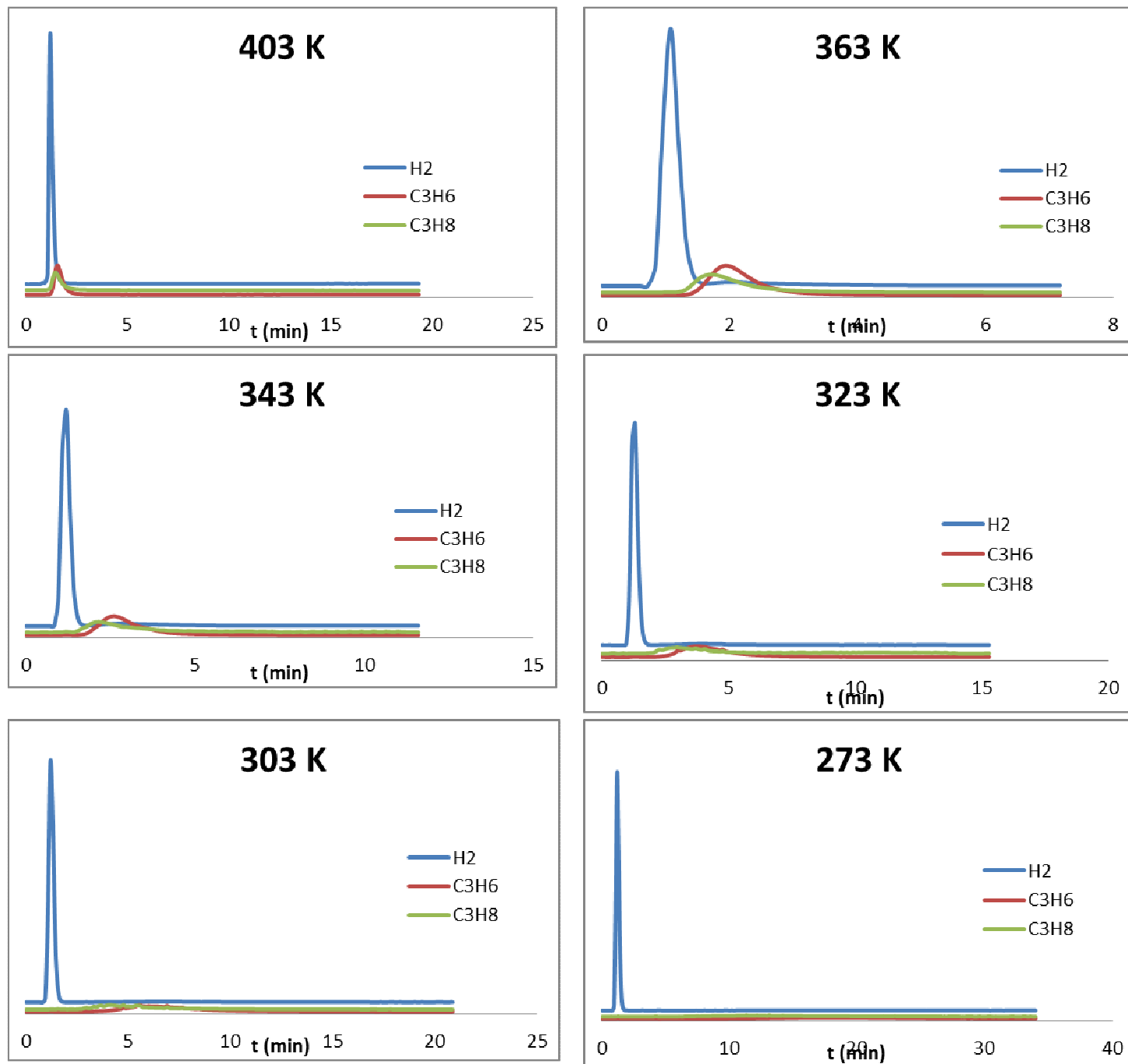


Figure D.1.1. Pulse gas chromatograms for an equimolar mixture of C₃H₈/C₃H₆/H₂ collected at different temperatures using material **29**.

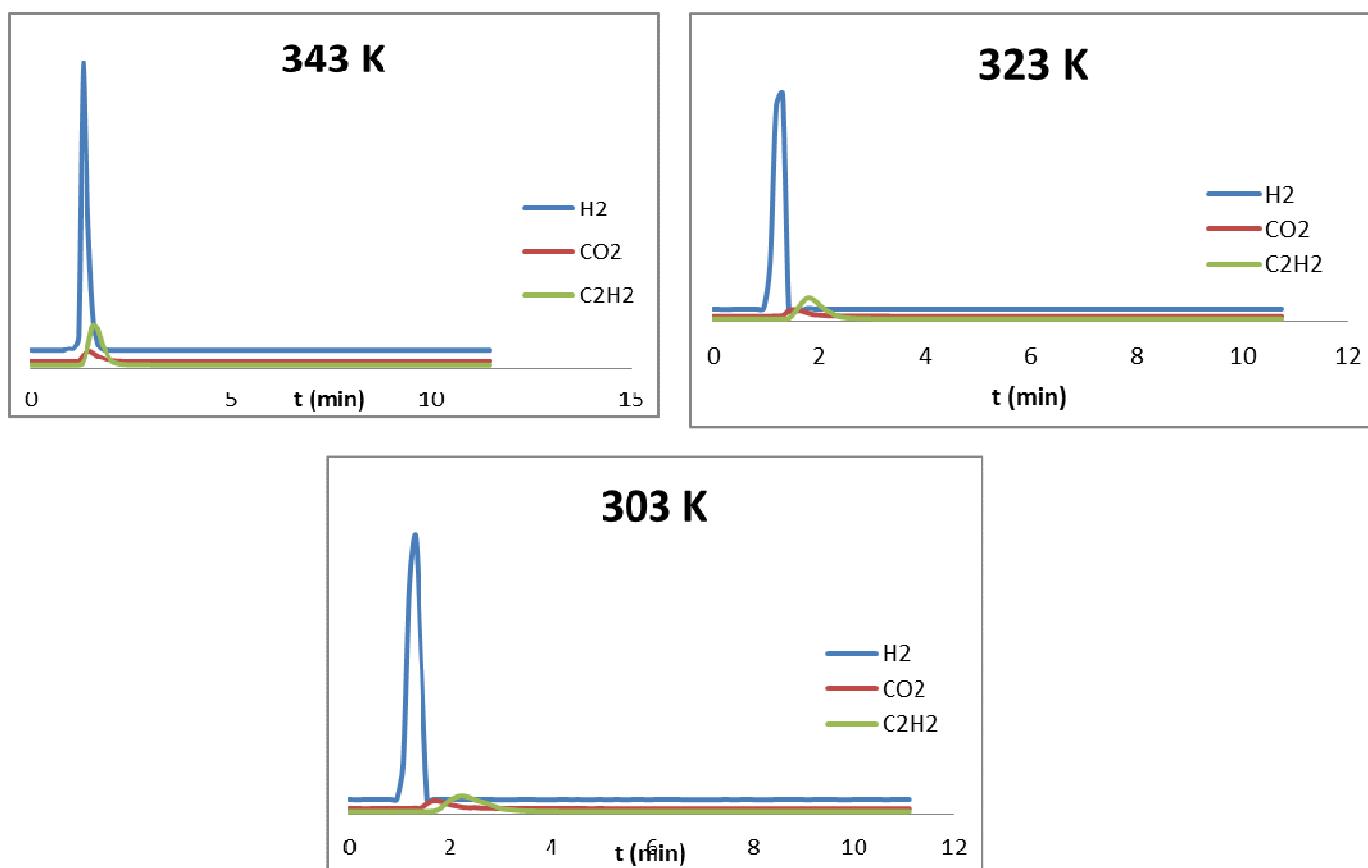


Figure D.1.2. Pulse gas chromatograms for an equimolar mixture of CO₂/C₂H₂/H₂ collected at different temperatures using material **29**.

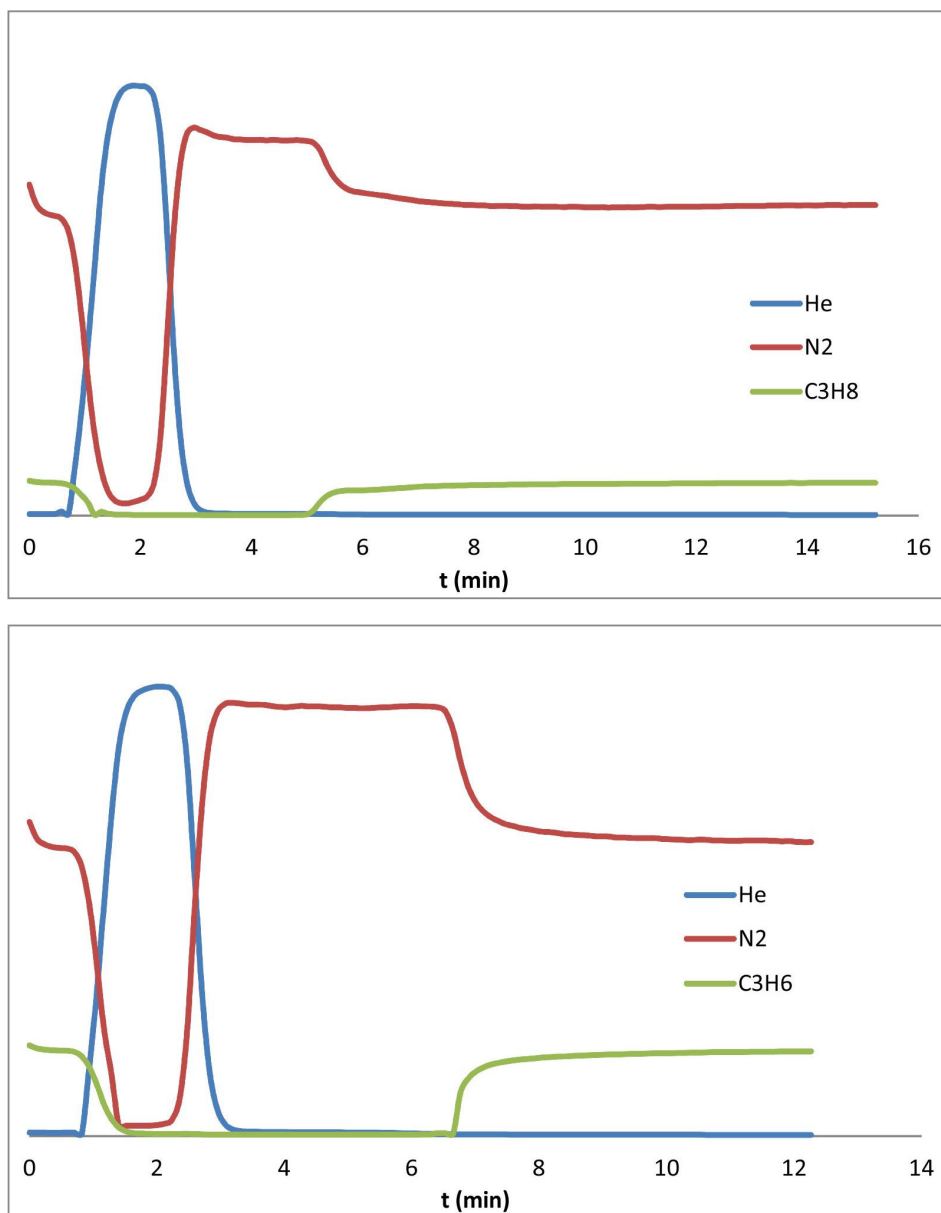


Figure D.1.3. C₃H₆/N₂ (bottom) and C₃H₈/N₂ (top) breakthrough curves measured at 296 K for the porous material **29**.